A Doctoral Thesis submitted in partial fulfilment of the requirements for the award of the degree of Doctor of Philosophy in Chemical Engineering

Investigation of turbulence modulation in solid-liquid suspensions using FPIV and micromixing experiments

by

Heema Unadkat

Product Engineering Group

Department of Chemical Engineering

Loughborough University

December 2009

Dedicated to the most inspirational ladies in my life

My Mum Aruna

Nir

(late) Bena Massi

Jai Ambé

"By perseverance the snail reached the ark"

- Charles H. Spurgeon (1834–1892)

...and so I persevered, one squish at a time

Abstract

The focus of this thesis is the study of turbulent solid-liquid stirred suspensions, which are involved in many common unit operations in the chemical, pharmaceutical and food industries. The studies of two-phase flows present a big challenge to researchers due to the complexity of experiments; hence there is a lack of quantitative solid and liquid hydrodynamic measurements. Therefore, an investigation of turbulence modulation by dispersed particles on the surrounding fluid in stirred vessels has been carried out, via two-phase fluorescent Particle Image Velocimetry (FPIV) and micromixing experiments. The main property of interest has been the local dissipation rate, as well as root-mean-square (rms) velocities and turbulent kinetic energy (TKE) of the fluid.

Initially a single-phase PIV study was conducted to investigate the flow field generated by a sawtooth (EkatoMizer) impeller. The purpose of this study was to gain insight into various PIV techniques before moving on to more complex two-phase flows. Subsequently stereo-, high-speed and angle-resolved measurements were obtained. The EkatoMizer formed a good case study as information regarding its hydrodynamics is not readily available in literature, hence knowledge has been extended in this area.

An analysis of the mean flow field elucidated the general structure of fluid drawn into the impeller region axially and discharged radially; the latter characterised the impeller stream. The radial rms velocity was considered to represent best the system turbulence, even though the tangential rms velocity was greater close to the blade; however the radial component was more prevalent in the discharge stream. Due to differences in rms velocities, TKE estimates obtained from two and three velocity components deviated, being greater in the latter case. Integral (1-D and 2-D) length scales were overestimated by the quantity $W/2$ in the impeller region. Ratios of longitudinal-to-lateral length scales also indicated flow anisotropy (as they deviated from 2:1). The anisotropy tensor showed that the flow was anisotropic close to the blade, and returned to isotropy further away from the impeller. Instantaneous vector plots revealed vortices in the discharge stream, but these were not associated with flow periodicity. Alternatively, the vortex structures were interpreted as low frequency phenomena between 0-200 Hz; macro-instabilities were found to have a high probability of occurrence in the discharge stream.

Dissipation is the turbulent property of most interest as it directly influences micromixing processes, and its calculation is also the most difficult to achieve. Its direct determination from definition requires highly resolved data. Alternative methods have been proposed in the literature, namely dimensional analysis, large eddy simulation (LES) analogy and deduction from the TKE balance. All methods were employed using 2-D and 3-D approximations from stereo-PIV data. The LES analogy was deemed to provide the best estimate, since it accounts for three-dimensionality of the flow and models turbulence at the smallest scales using a sub-grid scale model. This method was carried forward to the analysis of two-phase PIV experiments. Turbulence intermittency of dissipation was assessed against the multifractal

model of Meneveau and Sreenivasan (1991) and on that basis, the global standard deviation filter was considered most suitable for vector validation. The distribution of energy dissipation was calculated; it was estimated that 96% was dissipated in the impeller region. The ratio of maximum-to-mean energy dissipation compared well to other impellers, creating uncertainty about its reported high-shear attributes.

After sufficient analyses of the single-phase EkatoMizer flow had been completed, investigation of two-phase flows began. Fluorescent Particle Image Velocimetry (FPIV) and digital image analysis techniques were combined, to quantify the hydrodynamics of solid-liquid suspensions stirred by a 45° pitched blade turbine impeller. Soda-lime glass spheres of sizes 250-300, 700-750 and 1000 μm were employed for the dispersed phase, up to volumetric concentrations of 0.3, 0.5 and 0.5 vol% in water, respectively. The continuous phase mean velocity did not change significantly in the impeller jet or bulk flow, with the addition of up to 0.5 vol% dispersed phase. The 250-300 and 1000 μm particles were found to suppress the carrier phase turbulence, in terms of rms velocities, turbulent kinetic energy and dissipation rate above particle concentrations of 0.2 vol%. The level of turbulence suppression remained constant up to 0.5 vol%. Greatest impact was on the dissipation rate, which decreased at most 25% in the discharge stream. Continuous phase integral length scales remained unchanged in the presence of solids. The locally averaged particle concentration field showed high concentrations above and below the impeller and at the corner of the vessel base. Particle turbulence levels measured at 0.5 vol% dispersed phase were lower than the corresponding fluid, and showed relatively higher anisotropy. The terminal velocity under estimated the slip velocity of the 1000 and 700-750 μm particles in the impeller discharge, by a factor of five and nine respectively.

Finally, two-phase micromixing experiments were carried out using both Bourne and Villermaux reaction schemes, to determine how the presence of particles affects the by-product distribution. In this way, the consequence on the dissipation rate was inferred indirectly. As these experiments did not depend on transparency of the mixture, experiments could be carried out with up to 1.75 vol% particles in the Bourne scheme and 3 vol% in the Villermaux scheme (operated at 500 and 800 rpm respectively). The common findings were that both small and large size classes (i.e. 70-100, 250-300 and 1000 μm particles) increased the by-product yields and subsequently suppressed the dissipation rate. These results substantiated the earlier two-phase PIV observations. In the case of smaller particles (70-100 and 250-300 μm), the maximum turbulence suppression occurred at ~1 vol%. Above this concentration, the level of suppression decreased and in some cases the regime switched to augmentation, indicating that particle concentration as well as size is important. In both FPIV and micromixing experiments, the finding of larger particles suppressing turbulence contradicts one of the most influential theories of Gore and Crowe (1989), which suggests that particles with diameter-to-integral length scale ratio greater than 0.1 create augmentation. Finally an experimental flow model (to accompany the engulfment model of micromixing) was proposed for a PBT stirred flow and evaluated against the single-phase micromixing results.

Keywords: Multiphase flows; micromixing; turbulence; particle image velocimetry; phase separation; stirred tanks; parallel reactions

Preface

The work presented in this thesis was carried out in the Department of Chemical Engineering, Loughborough University, between October 2006 and September 2009, under the supervision of Professor Chris D. Rielly and Dr Zoltan K. Nagy. I hereby declare that the work presented is, to the best of my knowledge and belief, original, except where acknowledged. The material of this thesis has not been submitted, either in whole or in part, for a degree at this or at any other University. This research was funded by the Engineering and Physical Sciences Research Council, UK.

Heema Unadkat
Department of Chemical Engineering
Loughborough University
December 2009

Acknowledgements

As well as granting a renewed outlook in my personal life, my faith has provided a continuous source of optimism throughout some difficult times outside of my PhD, so first and foremost I thank Sri Krsna (God) for seeing me through my endeavour till its completion.

Before applying for a PhD position, I visited the department to meet Prof Chris Rielly and discuss the potential of my research. I knew from our initial meeting that working with him would be a positive challenge. My first impressions (to be later confirmed) were that Prof Rielly's standards were sky-high and that I would be working relentlessly to meet his expectations; I admired that a lot! Immediately I applied to pursue my PhD under his guidance, and I believe that at that point I had just made the best decision of my life...the rest they say is history. The last three years have gone by incredibly quickly because working with my supervisors has been an absolute pleasure. I thank Prof Rielly for bestowing his wealth of knowledge and teaching me the fundamentals of fluid mixing, whilst bearing patience for me to ask questions and share my thoughts. Many times after engaging in discussions I left his office feeling inspired, perplexed, enlightened all at once, and my research is all the better for it. On numerous occasions I found myself laughing with my supervisor; thanks to his sense of humour and dynamic personality I developed a natural rapport with him. During my PhD Prof Chris Rielly became Head of Department and despite his demanding schedule, he made time to uphold the tradition of weekly meetings with all of his PhD students which I greatly appreciate. I have taken example of his professionalism many times, for instance imitating his conduct when teaching students (who agree that he is ace), and these are the traits I hope to carry with me into the future. I feel privileged to have received the opportunity of working alongside a person with such great reputation and credibility, and who I have utmost respect for. Prof Rielly, there is no doubt in my mind that I will be seeking your professional advice and approval well beyond the course of my PhD and I would be honoured if you agreed to be my mentor in the years to follow.

I want to express my appreciation for my second supervisor Dr Zoltan Nagy for his help in getting me acquainted with Matlab programming; something I was not looking forward to at the start but made so easy due to his expertise. I thank him for always finding the time to help me develop or trouble-shoot some of my failing algorithms and always making me feel comfortable in asking sometimes trivial questions. Without his contribution the computational part of my PhD would have not have been enjoyable. Dr Nagy's advice also benefited my experimental work; some of his suggestions solved practical problems that I had spent weeks trying to fix. I thank him for offering an alternative perspective where I lacked ideas; his recommendations have advanced my work on numerous occasions. Both supervisors complemented different aspects of my research perfectly, and in my opinion it has been a winning combination. I thank both for their attention to detail and hours spent in meticulous corrections of my thesis. I am grateful for the times they gladly worked through problems with me even after hours; that kind of supervision is priceless. Most of all having the independence to explore some of my own ideas and the process of learning from my mistakes has been liberating.

I would like to thank my dearest friends (constituents of the 4 o'clock club) for sharing laughter and procrastination inducing chats over copious amounts of coffee. Mu I will always remember your refreshing honesty, Erum your culinary delights and sisterly words of wisdom, Savita's comical episodes from which we coined the phrase 'Savita-moment', Bahareh with whom I faced some hectic tutorials and Paul's awesome vegetarian BBQ's. You've all made me feel so cheerful. Other friends I would like to acknowledge are Siti, Pawel, Nicoletta, Naeem and Kuhan. My longstanding chums Natasha, Claire, Neeta, Faizal, Altaf, Neel, Guv, Tosin and Lara have made sure that I received a regular dose of love, 'Hush' or that much needed holiday.

The staff at Loughborough University forms the backbone of research activities. The lab technicians, especially Dave and Sean, have helped me greatly. My appreciation is extended to Tony, Chris, Jim, Terry, Kim, Monika, Graham, Mark and Steve, who have at some point fixed something that I have broken; thank you all and sorry! The ladies in the administrative office have been a pleasure to interact and exchange spa ideas with, thanks to Yasmin, Anna, Liz, Becky, Ann, and Janey. Prof Starov, computing tutorials have sometimes been the highlight of my week! Previous colleagues I am grateful for are Liansong, Jolius and Chris Webb; their help kick-started my PhD. My PIV experiments were carried out in the Optical Engineering lab where Prof Hargrave, Ed and Tim trained me on the equipment, whilst Pete and Dave ensured my safety. There I met my ally and subsequent gym partner Matt. Finally big thanks to Prof John Bourne, who personally advised me through the micromixing experiments.

I am grateful to have received the financial backing of the EPSRC which has funded my PhD. Additionally many thanks to members of the IChemE FMPSG subject group who have created opportunities for me to attend the Mixing XXI (2007) conference in Utah, USA in collaboration with the NAMF committee, as well the 13th European Conference on Mixing (2009), London.

My family has been the greatest driving force behind my PhD and I absolutely could not have finished without their boundless support. I am indebted to my Mum Aruna's great love and devotion, and the sacrifices she has made in raising me and my brother. I have always valued her opinion and she is the first person I turn to for advice in turbulent situations; apt for a fluid dynamicist! Over time my mum has become my best friend. She has often bore the brunt of my bad moods usually arising from failed experiments, but nothing a hot dinner hasn't been able to fix. Her own strength, will power and determination have inspired me. Mum you have always watched out for me and there's no way I can repay you, my thesis dedication is the smallest gesture I can offer. The banter that I've shared with my Dad Suman over the years has made my life more jovial and inheriting his insomniac gene has benefited my late nights working. Arvind Mama and Nir you have always made me feel like you are my number one fans and that has been incredibly special. You have always encouraged me to go as far as I possibly can in academia and shown relentless faith in me whatever the circumstance. I am lucky to share this unique bond with you, which adds value to my life immeasurably. I must thank Vinod Mama and (late) Bena Massi for showering on me their well wishes and I know their blessings have brought me this far. My younger brother Mithun, thank you for the constant reminders that 'you haven't finished yet' along with 'don't be silly, when will that PhD kick in?' which have only propelled me to towards the finishing line. Subhash Mama for your 'get a job' remarks as if I wasn't working full time already! Well here's news for you both; I'm done.

Table of Contents

List of Figures

List of Tables

Chapter 1 Introduction

1.1 Background

The study of turbulent flows in multiphase systems has presented a significant challenge to fluid dynamicists, being recognised as one of the most interesting fields of research. Investigating the dynamics of a continuous phase turbulent flow is coupled with the complexity of the response of the dispersed phase. The dispersed phase may modulate the structure of the turbulent environment in terms of fluctuating velocities, turbulent kinetic energy (TKE) and dissipation rate, and simultaneously the continuous phase will have a compounding impact by transferring momentum back to the dispersed phase, referred to as 'two way coupling' (Bachalo, 1994). The main objective of this study is to investigate how solid dispersed particles alter the continuous phase turbulence (i.e. the TKE and dissipation rate) in a stirred vessel.

Previous studies of multiphase flows in geometries other than stirred vessels provide valuable information about the effects of dispersed particles on the continuous phase turbulence. Most of these studies have been conducted in pipe and jet configurations. For instance, Tsuji *et al.* (1984) investigated air-solid flows in a vertical pipe, and reported that small particles attenuate the turbulence intensity, whereas larger particles enhance it. Gore and Crowe (1991) reported up to 50% turbulence damping by small particles, and up to 360% increase by larger particles, and suggested that this transition occurs when the particle diameter to characteristic fluid length scale ratio is equal to 0.1. This has been the most commonly referenced hypothesis to date. Other theories have also been postulated to relate these effects to the particle Reynolds number and wake shedding (Hetsroni, 1989), which will be discussed in detail later.

Some studies of multiphase flows in stirred vessel configurations report both turbulence suppression and augmentation in the presence of dispersed particles (e.g. Nouri and Whitelaw, 1992; Guiraud *et al.*, 1997; Virdung and Rasmuson, 2008). In many cases the observations may be explained by the hypothesis of Gore and Crowe (1991). However, defining the transitional criterion in stirred tanks is challenging, since a problem is encountered in selecting the direction of the most appropriate fluid integral length scale, which is not always measurable. Additionally, integral length scales are not constant throughout the tank volume (Baldi, 2004; Khan, 2005).

The focus of this thesis is the study of turbulent solid-liquid stirred suspensions, which are a common unit operation in the chemical, pharmaceutical and food industries (Guiraud *et al.*, 1997), involving steps such as solid-catalysed reactions, dissolution and crystal growth. In solid-catalysed fluid-phase reactions, velocity and diffusion characteristics are paramount. In particle coating processes, mixing is used to enhance nucleation, crystal growth and precipitation of solid particles; and in the final stages of a polymerization process, mixing is necessary to obtain

good product quality. The optimization of a mixing vessel involves the design of the impeller and tank geometry to provide sufficient solid dispersion throughout the tank, and thorough mixing with minimum power input. All of these factors require understanding of the fluid mechanics within the vessel.

Although solid-liquid mixing is widespread in industry, there is a lack in availability of quantitative measurements of solid and liquid hydrodynamics, especially at elevated concentrations. This is mainly due to the limitations of previously available measurement techniques. However, recent advances in laser diagnostics and digital imagery have improved the prospects of studying two-phase flows, and some experiments have even attempted to characterise turbulence modulation in stirred vessel configurations.

Nouri and Whitelaw (1992) applied laser Doppler anemometry (LDA) to quantify the mean flow and root-mean-square (rms) velocities of the dispersed phase up to 2.5 vol%. Guiraud *et al.* (1997) employed phase Doppler velocimetry to measure velocities of both phases in stirred suspensions up to 0.5 vol%. In both studies, more than one velocity components were obtained, but not simultaneously. The LDA technique was further adapted by Pettersson and Rasmuson (1997), who applied phase Doppler anemometry to obtain simultaneous 3-D velocity vectors of the fluid and suspended particles in a mechanically agitated crystallizer. Micheletti and Yianneskis (2004) also applied LDA for measurements of the continuous phase flow, with solids fraction up to 2 vol%. These examples portray the development of LDA techniques from single-phase to simultaneous multi-phase, and from 1-D to simultaneous 3-D recordings.

In the aforementioned studies, turbulence modulation was investigated in terms of the particles' effect on the fluid rms velocities or turbulent kinetic energy, but not the rate at which the turbulent kinetic energy was dissipated. The latter property is more important in chemical processes, since it governs the degree of micromixing, and subsequently the product selectivity, where parallel competing reactions are involved (Bourne and Yu, 1994). Furthermore, if the key reaction is catalysed by a solid, then inclusion of the dispersed phase may alter the fluid turbulence, and hence the product yield. The dissipation rate is also linked to the crystal size distribution (CSD) in crystallization processes through the breakage and coalescence of kernels, and the mean and minimum drop size in liquid-liquid systems (Zhou and Kresta, 1998). Hence, knowledge of the hydrodynamics of stirred solid-liquid suspensions may enable optimization of the system geometry as well as operating conditions, which may improve, for instance, the product yield in a solid-catalysed reaction, or give better control of a CSD.

The lack of experimental data has also held back the validation of predictive two-phase models. Predictive models of the physical world must be justified by observations of the system under study, but in the case of multiphase flows, data regarding velocity fluctuations and Reynolds stresses have not been recorded with a great deal of specificity or accuracy until recently. The models should include interphase turbulence transfer terms for turbulence modulation. In the absence of such information, most models employ simple extensions of the standard single-phase $k-\varepsilon$ model (e.g. Montante and Magelli, 2007). For instance, the homogeneous $k-\varepsilon$ model assumes that both solid and liquid phases share the same turbulent kinetic energy and dissipation rate, when in reality this may not be the case. Subsequently, experimental results of this nature are highly valuable, as they may provide verifications (or contradictions) to the much contested field of CFD prediction of two-phase flow phenomena.

Particle Image Velocimetry (PIV) techniques are traditionally used to visualise single-phase flows, to determine spatial information regarding their fluid velocities and turbulence levels (Sheng *et al.*, 2000; Sharp and Adrian, 2001; Khan *et al.*, 2006). The opacity of most multiphase systems and increased interphase noise limits the application of PIV to the study of solid-liquid suspensions at low concentrations. However, with optical filtering and/or digital post-processing, some of these challenges may be overcome.

Only a handful of studies have implemented PIV techniques to investigate solid-liquid stirred suspensions thus far. One of the early studies was carried out by Hasan *et al.* (1999) for the solid-phase velocity field in a stirred flow. Eloranta *et al.* (2001) extended the technique by obtaining simultaneous measurements of the dispersed and continuous phases. The latest study has been carried out by Virdung and Rasmuson (2008), who also obtained simultaneous measurements of solid-liquid stirred suspensions solely via digital image processing techniques.

1.2 Aims of current study

The current study aims to advance the knowledge of fluid hydrodynamics and turbulence modulation in solid-liquid stirred suspensions, by presenting a novel PIV experimental technique, which combines fluorescent PIV (FPIV) and digital image analysis, for the simultaneous velocity measurements of both phases. To work towards this goal, single-phase experiments employing variations of stereo-PIV, high-speed PIV and angle-resolved PIV will be conducted first.

The influence of particle size and concentration on fluid turbulence properties such as rms velocities, turbulent kinetic energy, and more importantly dissipation rate, will be investigated. Note that turbulence modulation with respect to dissipation has never been examined before, so the results presented herein aim to provide a deeper understanding of turbulence modulation. PIV experiments will be carried out in water using particles sizes of 250-300, 700-750 and 1000 μm, up to 0.5 vol% without refractive index matching.

Micromixing experiments will also be carried out with the objective of validating the PIV experiments. The Bourne (Bourne and Yu, 1994) and Villermaux (Fournier *et al.*, 1996) reaction schemes will be implemented in particle suspensions and the effect on the by-product yield will be quantified. Solid-liquid micromixing studies in literature have not been reported turbulent modulation at such low concentrations; hence the results shown in this thesis are the first of this nature. Since these experiments do not rely on the transparency of the system, higher particle volumetric concentrations up to 3 vol% will be employed.

1.3 Thesis contribution

The main contributions to knowledge made by the present thesis have been (i) the quantification of fluid turbulence properties such as rms velocities, TKE and crucially the dissipation rate in solid-liquid stirred suspensions and subsequently (ii) evaluating modulation of these properties with changes in dispersed particle size and concentration. These effects have been studied via a combination of fluorescent PIV and digital image analysis, and in doing so a novel measurement technique has been suggested to overcome some of the challenges of complex multiphase experiments. Results have demonstrated turbulence modulation of the

continuous phase by both small (250-300) and large (1000 μm) particles above volumetric concentrations of 0.2 vol%. The greatest impact was on the dissipation rate, which was found to be suppressed by a maximum of 25% in the discharge stream. Besides spatial concentration fields, dispersed phase velocities and turbulence quantities were also determined simultaneously, and results showed their levels to be lower than those of the corresponding continuous phase.

Micromixing experiments carried out using both Bourne and Villermaux reaction schemes (Bourne and Yu, 1994; Fournier *et al.*, 1996) validated the earlier PIV observations, as they also indicated turbulence suppression by both particle sizes. Results of the larger (1000 μm) particles conflict with the theory of Gore and Crowe (1989), which suggests turbulence augmentation by particles whose diameter to integral length scale ratio is greater than 0.1; in this case the equivalent ratio was found to be 0.278. Single-phase PIV results of the velocity and dissipation rate were also utilized to create an experimental flow model (EFM) for the engulfment model (E-model) of micromixing. The model was verified against micromixing experimental data from the single-phase Bourne reaction scheme (whose kinetics are well established) and found to be successful in predicting by-product yields at high impeller speeds (>600 rpm).

1.4 Thesis structure

Chapter 2 describes the development of flow measurement techniques from single- to multi-point, as well as 1-D to 3-D, and the benefits of employing Particle Image Velocimetry (PIV) in the current study become apparent. The challenges of two-phase PIV are discussed, and the techniques used by previous researchers to achieve phase discrimination are reviewed. The choice of phase discrimination for the current study is then highlighted. The main findings of previous studies investigating turbulence modulation of the continuous phase by the dispersed phase in simple geometries such as pipe and jet flows are summarised. Hypotheses put forth by these researchers, which shape interpretation of data to the current day are introduced. A specific literature review of analogous studies in stirred vessel configurations is provided, which sets the agenda to progress knowledge in the current work.

Chapter 3 describes a single-phase PIV study of a sawtooth (EkatoMizer) impeller, for which there is sparse information in literature. The relevance of this work was to gain experience of PIV measurement techniques, data processing, and interpretation of turbulence quantities before progressing to more complex multi-phase systems. Stereo-, high-speed and angle-resolved PIV experiments were implemented and described in this section. Issues such as image acquisition and analysis, followed by data processing in Matlab are discussed. Subsequently mean flow properties, 1-D and 2-D integral length scales, rms velocities, TKE, flow anisotropy, angle-resolved measurements and macro-instabilities of the single-phase flow are presented.

Chapter 4 considers in detail calculation of the dissipation rate, which was the turbulence property of most interest in subsequent two-phase work. Results of the dissipation rate obtained directly from its definition, dimensional analyses, LES analogy (Sheng *et al.*, 2000) and the turbulent kinetic energy balance are presented. Calculations were performed using both two and three velocity components from stereo-PIV measurements and compared. Subsequently an

assessment of using linear scaling factors and isotropic assumptions to estimate unknown quantities is provided. The best calculation method is highlighted for application in proceeding studies. Issues relating to turbulence intermittency and vector validation are considered simultaneously. A method of selecting the most appropriate vector validation filter by judging resultant dissipation rate profiles against the multifractal model of Meneveau and Sreenivasan (1991) is presented. The spatial distribution of energy in different regions of the vessel is calculated, and ratio of maximum-to-mean energy dissipation of the EkatoMizer is evaluated against values reported for other impellers in literature.

Chapter 5 presents the algorithm which had been selected after reviewing literature in Chapter 2, to carry out digital phase discrimination of multiphase Mie scattering images to extract information of the dispersed phase. Steps of the original algorithm by Khalitov and Longmire (2002) are summarised, and modifications of the code to adapt to the current study are incorporated; i.e. to detect fragmented rather than full circular image patterns. The phase discrimination algorithm implemented in the in-house code developed in Matlab, is described step-by-step. The bias and random errors induced by the phase separation algorithm are quantified by performing tests on artificial two-phase images.

Chapter 6 describes two-phase PIV experiments of solid-liquid stirred suspensions. The section gives details of the experimental setup, two-camera measurement technique followed by results of the study. Characteristics of the single-phase flow without addition of particles are provided first and evaluated against literature to validate their consistency. This provides the reference case against which turbulence modulation effects by particles are compared. Subsequently, turbulence modulation by the dispersed phase is discussed first with respect to particle size, and then with respect to particle concentration. Continuous phase 1-D and 2-D integral length scales were also obtained. Dispersed phase information such as locally averaged concentration fields, mean flow patterns, slip velocities, rms velocities and TKE were also calculated and presented in this section.

Chapter 7 investigates turbulence modulation by dispersed particles via an alternative measurement technique; two-phase micromixing experiments. Unlike PIV, which uses flow visualisation to capture fluid hydrodynamics, this class of experiments employ chemical reactions as probes to infer the level of micromixing. The aim of this experimental work was to validate observations made from previous two-phase PIV experiments described in Chapter 6. In this chapter both Villermaux and Bourne reaction schemes are presented sequentially. The reaction kinetics and experimental techniques are described for each scheme, followed by micromixing results in a two-phase stirred flow. The final section of this chapter shows the development of an experimental flow model for a PBT to predict by-product yields in the Bourne reaction scheme.

Chapter 8 forms the final contribution to this thesis. It summarises the main conclusions drawn from this research, and puts forward recommendations for future studies based on the authors own experience.

Chapter 2
Literature review

2.1 Review of flow measurement techniques

Flow measurement techniques may be classified as either single-point or whole flow field. As the name suggests, the former type provides velocity information at a single-point in the domain, whereas the latter provides spatially distributed information. The following discussion briefly describes various types of measurement devices currently available in both categories, and also illustrates their development from single-point to whole flow field analysis.

2.1.1 Single-point techniques

Pitot-static tube

The Pitot-static tube is a device consisting of two concentric tubes; a Pitot and a static tube which simultaneously measure the total (stagnation) and static pressure in a fluid stream. The resulting differential pressure measurement between the stagnation and static pressure is converted into the fluid velocity in accordance with incompressible or compressible fluid theory (Wolf *et al.*, 1966; Hayward, 1979). The advantage of this technique is that it is simple to construct, quite inexpensive and almost no calibration is required. On the other hand, its accuracy and spatial resolution may not be high enough for some applications and the tube must be aligned with the flow velocity to obtain good results. The major drawback however is not encountered in its ability to record velocity, but more with its intrusive nature. The Pitot-static tube disturbs the flow field with its insertion, and in some cases can lead to a pressure drop in the flow (albeit small). In order to minimise the disturbance to the flow field, the diameter of the device should be kept to a minimum.

Hot wire anemometry (HWA)

Hot wire anemometry has been previously applied to measure instantaneous fluid velocities in stirred tanks (Cooper and Wolf, 1968; Gunkel and Weber, 1975; Bertrand and Couderc, 1985). In this technique, an electrically heated sensor or probe is inserted into the system of interest, and the rate of convective heat transfer to the surrounding fluid is measured. If all factors of the flow are assumed to be constant (e.g. temperature) apart from the velocity, then the heat loss may be interpreted as a measure of that variable. HWA was highly popular in the measurement of unsteady flows due to its high frequency response characteristics and was used for many years in the study of laminar, transitional and turbulent boundary layer flows. Like the Pitot-static tube, its major drawback is its intrusive nature.

Laser Doppler anemometry (LDA)

Advancements in laser technology broadened the possibility of obtaining more detailed and accurate measurements of the flow field non-intrusively. The first significant invention was laser

Doppler anemometry (LDA) in 1964 by Yeh and Cummins (1964). Unlike Pitot-tubes, the technique can be applied to flows of unknown direction and provides precise measurements in unsteady and turbulent media, where the velocity is fluctuating with time. Measurements of the continuous phase are achieved by tracing the fluid with small (tracer) particles that are capable of following the mean flow and turbulence-induced accelerations.

The technique involves splitting a single laser beam into two, monochromatic, parallel beams, in the flow being measured. The beams are crossed at a common point by the use of a lens, which becomes the 'measurement volume'. Typical dimensions are 100 μm diameter and 1 mm length (Papadopoulos and Arik, 2004), which defines the spatial resolution. Areas of constructive and destructive interference patterns form in the intersection volume, also known as the fringe pattern, with planar layers of high and low intensity light.

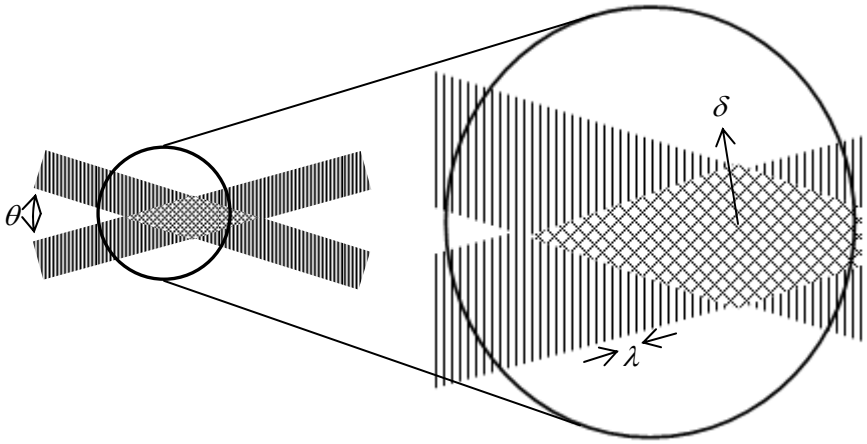

Figure 2.1: Measurement volume formed by the beam intersection

The fringes are separated by a distance known as the fringe spacing (δ) which can be expressed in terms of the laser properties as follows.

$$\delta = \frac{\lambda}{2\sin\left(\theta/2\right)} \tag{2.1}$$

where λ is the wavelength of the laser light, and θ is the angle between the two beams. As particles in the flow move through the fringe pattern, scattering light with a fluctuating intensity is collected by a photo-sensor. The frequency of this fluctuation is equivalent to the Doppler shift (f_D) between the incident and scattered light. It is proportional to the particle velocity component (u) which lies in the plane of the two laser beams and is perpendicular to their bisector. Subsequently, this velocity component may be deduced from the following relationship:

$$u = f_D \delta \tag{2.2}$$

LDA is considered to be an absolute flow measurement method. Knowing the laser wavelength and the intersection angle between the laser beams, the fringe spacing and subsequently

velocity can be easily calculated; it does not require calibration. LDA is able to provide measurements with a high temporal resolution (sampling rates up to 3 kHz). However as with all other single-point techniques, measurements must be obtained at various points in the flow to obtain a full field profile, which would be time-averaged.

Limitations of single-point measurement techniques

Single-point techniques must be adjusted in order to determine turbulence quantities which require simultaneous measurement of the velocity components at a given location, such as the Reynolds stress terms ($\overline{u'v'}$), where u'_i is the fluctuating velocity in the i^{th} direction. In HWA, this is made possible by combining several wires on the same probe, aligned in different directions to measure all three components. In LDA, the inclusion of additional beam pairs within the same measurement volume and associated photomultipliers also enables two or three components to be measured simultaneously. However, a limitation is imposed when simultaneous velocity measurements are required at two separate locations. Spatial gradients can only be inferred via multi-point LDA techniques (Ducci and Yianneskis, 2005). In order to determine spatial gradients from time-series measurements at a single-point, Taylor's frozen turbulence hypothesis is usually applied. This assumes that within a small time interval, the turbulent structure is frozen in space, and advection of a turbulent structure past a fixed point is entirely due to the mean flow (Hinze, 1975). The spatial gradients may be obtained from the temporal derivatives as follows:

$$\overline{\left(\frac{\partial u'_i}{\partial x_i}\right)^2} = \frac{1}{\overline{u_i}^2}\overline{\left(\frac{\partial u'_i}{\partial t}\right)^2} \tag{2.3}$$

For example, this approach may also be used to convert integral time scales to integral length scales (Lee and Yianneskis, 1998). However, in cases where the turbulence intensity is large, such as close to the impeller region of a stirred vessel, Taylor's hypothesis is unlikely to apply (Sheng *et al.*, 2000; Khan, 2005). Turbulence intensity is defined in Equation (2.4), as given by Pettersson and Rasmuson (1997) encompassing all components. If all three velocities are not known, turbulence intensity is calculated in the same way but from only the available components. Subsequently the definition of turbulence intensity is slightly variable in different sources of literature.

$$\mathrm{TU} = \frac{\sqrt{\overline{u'^2} + \overline{v'^2} + \overline{w'^2}}}{\sqrt{\overline{u^2} + \overline{v^2} + \overline{w^2}}} \tag{2.4}$$

2.1.2 Whole flow field techniques

Whole flow field techniques are able to provide detailed spatially distributed information of the velocity and flow pattern over a wide region of the flow at an instant in time (Bachalo, 1994). Examples include particle tracking velocimetry (PTV) and particle image velocimetry (PIV).

Particle tracking velocimetry (PTV)

The experimental configuration of PTV is analogous to that used in PIV, which is described in the following section. PTV is fundamentally an image analysis technique (of tracer particles in

the fluid of interest), and is applicable to low density flows. The method is relatively straight forward: individual particles (in low solids volumetric fraction flows) are identified on the images and their centroids are located. Subsequently, images of the same particle on subsequent exposures are also identified and located. The distance between the centroids is used for the velocity calculation. Algorithms which implement this tracking routine have been developed by Hassan and Canaan (1991), Chen and Fan (1992) and Hassan and Philip (1997). However as the particle density increases, the particle tracking method becomes inaccurate, as it becomes increasingly difficult to identify unambiguously corresponding particle images pairs between the first and second exposures and distinguish them from neighbouring particles. In the case of higher particle density flows, the application of statistical techniques is required, which leads to the development of particle image velocimetry (PIV).

Particle image velocimetry (PIV)

It was not until developments in digital imaging techniques, computational power and high speed cameras that the benefits of laser visualisation were transformed from a qualitative to quantitative basis. Following LDA, the use of laser light sheets to obtain flow visualisation and quantitative data was investigated and led to the development of particle image velocimetry (PIV). PIV provides a solution in which a full field, non invasive analysis of a fluid system may be carried out, whilst the flow field remains completely uninterrupted (Raffel *et al.*, 2007). The non-intrusive nature of PIV compared to previous techniques such as Pitot-static tubes and HWA makes it the most favourable measurement technique to date. Compared to LDA, which is also non-intrusive, the capability of obtaining instantaneous spatial recordings provides a significant advantage. This enables direct determination of velocity gradients, which are used for the calculation of many turbulence properties. However for a short period, LDA techniques sustained the advantage of providing a higher temporal resolution, with sampling rates up to 3 kHz, compared to only 15 Hz for a pulsed laser in a standard PIV set-up. Advancements in digital imaging have made it possible to acquire a sampling rate of up to 2 kHz with high-speed PIV; hence it is becoming more practical in obtaining time-resolved data. For these reasons, PIV will be the chosen measurement technique in the current study.

2.1.3 Single-phase PIV

The entire PIV process, from the experimental set-up to the image analysis is presented schematically in Figure 2.2. A high energy double-pulsed laser is directed through a cylindrical lens, which shapes the resulting beam into a thin sheet of high intensity laser light. The planar light sheet is positioned through the flow under study, parallel to the two dimensional streamlines. The flow itself is traced with small light scattering particles, which are illuminated with the incident planar sheet of laser light. The Mie scattering from the tracer particles is recorded using a CCD (Charged Couple Device) camera at two instances in time. The fundamental premise of PIV is to measure the displacement and hence velocity of these particles. The main components of a single-phase PIV setup comprise (i) tracer particles within the continuous phase (ii) illumination source (iii) image capture device (iv) synchroniser (v) hardware for data acquisition and software for image analysis. The respective components are described as follows.

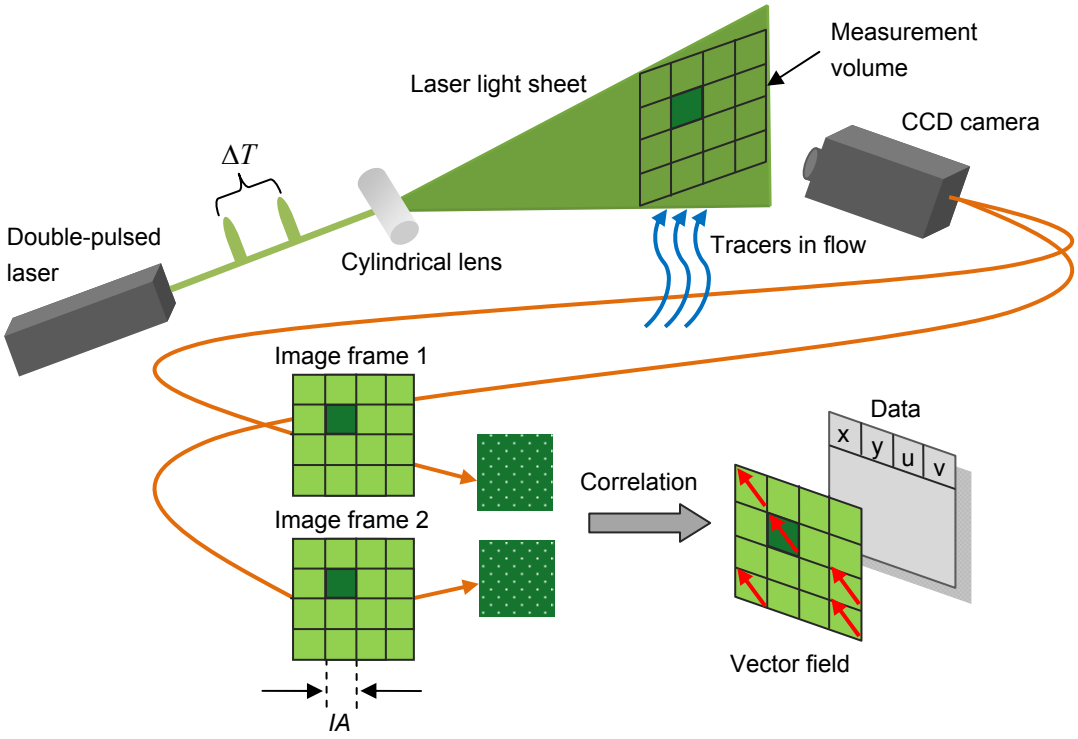

Figure 2.2: Entire PIV process

Tracer particles

Tracer particles are introduced into the system to track the mean flow and turbulence-induced velocity fluctuations. This requires them to be neutrally buoyant and small. Generally speaking, in all Mie-scattering velocimetry techniques, the particles must be big enough to scatter light for signal detection (good signal to noise ratio) but be small enough to follow the flow (laminar or turbulent) faithfully, in-synchronisation with the localised fluid motion. If particles are able to adequately follow the flow, their displacement may be used to infer the flow velocity (Papadopoulos and Guillard, 2003). In water applications the tracers are normally polystyrene, polypropylene, alumina or glass spheres of diameters between 5 and 100 μm (Dantec Dynamics, 2007). General criteria for PIV studies are that they should be non-toxic, non-corrosive, non-volatile and chemically inert.

Time scales of the flow provide a good representation of the particle-fluid interactions. It is desirable to use tracer particles which are able to reach velocity equilibrium with the fluid in a short space of time. The particle response time τ_p represents the time required for a particle to achieve 63% of its terminal velocity starting from rest. Subsequently, particles with a small response time are considered to be effective in following the flow (Micheletti and Yianneskis, 2004). Under the assumption of Stokes regime with particles Reynolds number $\mathrm{Re}_p < 1$, the particle response time is defined as follows:

$$\tau_p = \frac{d_p^2 \rho_p}{18\mu} \tag{2.5}$$

where d_p and ρ_p are the particle diameter and density respectively and μ the fluid viscosity. The Stokes number (St), defined as the ratio of the particle response time to the flow time-scale also provides a quantitative indication of particle-fluid interactions (flow time-scales are discussed in Appendix V). If $St << 1$, the particle response time is much smaller than the characteristic time scale of the flow. Consequently, the particle has sufficient time to respond to changes in the fluid velocity, and tends to follow the motion. Conversely if $St >> 1$, the particle is little affected by the flow field. Thus it is desirable to use particles with $St << 1$. If the Stokes number is defined with respect to the Kolmogorov time scale (and $St << 1$) then particles would be able to follow even the smallest motions of the turbulence spectrum.

Charged Couple Device (CCD) cameras

The CCD technology enables digital recording of the images and their subsequent analysis. The CCD imaging device converts light signals into electrical charge, which is transferred to a personal computing hardware for permanent data storage. Subsequent interpretation and manipulation of the image data may be accomplished using software associated with the image acquisition system. Images may be obtained in two modes. In the first, images are captured on a single frame (*double-exposed single-frame*), which enables a small time delay between subsequent exposures, necessary for recording the dynamics of fast flows. However, this can lead to directional ambiguities when the first image cannot be distinguished from the second. CCD cameras also enable the capture of successive exposures on subsequent frames in sequence (*single-exposed single-frame*), which eliminate these directional ambiguities (Raffel *et al.*, 2007).

Laser

The most commonly used laser is the frequency doubled Nd:YAG which is able to deliver a bright illumination source. It has an extremely short pulse duration (5 to 10 ns) of green light (532 nm) with a high energy per pulse (up to 400 mJ) (Stanislas and Monnier, 1997). In traditional PIV, an exposure of the laser is created to illuminate the particles in a flow, and the image is recorded by a CCD camera. After a short period of time (relative to the flow velocity) a second exposure is created by the laser, and another image of the particles is recorded at their new locations. The separation time between the exposures is selected so that particles travel several pixels such that their displacement can be measured, but the majority of them must remain common to both images. Particles which are not present in two image frames lead to lost cross-correlation, and subsequently loss of velocity information.

The laser beam is expanded into a light sheet by passing it through a series of spherical and cylindrical lenses; at least two are required to adjust the sheet thickness and width. The thickness must be small enough to provide good spatial resolution in the out-of-plane direction and to keep the particle images in focus on the recording optics. Laser sheets which are too thick illuminate all particles within the sheet volume, which could appear unfocussed. However, the thickness should also be large enough to prevent particles with out-of-plane velocity leaving the light sheet between two subsequent exposures. Keane and Adrian (1990a) suggested that the maximum out-of-plane motion of the particles should be limited to 25% of the light sheet thickness.

Synchroniser

Synchronization is an important element of PIV. It allows the laser pulses/exposures and camera acquisition to come together at the correct timing (within nanoseconds) and in sequence for the measurement of relatively high velocity flows (with respect to the image plane). A computer controlled synchroniser activates the laser illumination and image capture components of the camera in a simultaneous and automated fashion. In addition, the system needs to control the camera shutters to reduce background light exposure. Specifically, the synchroniser provides the appropriate trigger output to the lasers and harmonizes this with the frame rate of the CCD camera, such that appropriate images can be captured in sequence. The device enables recording of the first pulse at the end of the first image frame and subsequently the next pulse on the second image frame (Jarvis, 2003). The separation time between the pulses can be manipulated by the synchronizer, which is crucial for the recording of high velocity flows. If the separation time between the exposures is too great, then particles may travel out of the image frame, leading to lost correlation and loss of velocity data. After the images are captured by the camera, the synchroniser prompts the computer to capture the pair of frames, where the data are stored for further analysis.

Image analysis

Since the images are captured in a digitized format, digital analysis may ensue. There are two methods to analyse these images; *auto-correlation* for double-exposed single-frames and *cross-correlation* for single-exposed single-frames. The basis of the correlation procedures is that the image frames are subdivided into regions called interrogation areas (*IA*). Corresponding *IAs* (on either the same or subsequent frames) are correlated pixel by pixel via Fourier transforms. The correlation generates a signal peak, representing the common particle displacement.

The size of the interrogation areas can range between 8×8 and 64×64 pixels. The *IA* must be large enough such that particles undergoing cross-correlation remain within the *IA* of both frames being correlated. However, the cross-correlation technique is most efficient on near-field flows; hence the *IA* must be limited to allow competent tracking. Additionally, the *IA* size determines the spatial resolution (and small resolutions are required to determine turbulence properties). Thus, expanding the *IA* creates a trade-off. As a rule of thumb, Keane and Adrian (1990a) suggested that the interrogation area size should be selected such that the particle displacement is less than 25% of its length.

The average velocity is determined by the displacement divided by the time interval between the two exposures. By attaining average velocities in each *IA*, velocity vector maps may be produced (Lourenco and Krothapalli, 1986). Since velocity distributions are achieved, it is possible to calculate quantities involving velocity gradients, such as the energy dissipation rate of the fluid.

2.2 Two phase PIV with dispersed particles

The application of PIV may be extended to multiphase systems. The premise is essentially the same, in that a high intensity laser light sheet is used to illuminate the flow in the region of interest, and particle images are captured using a CCD camera. The main difference in the flow

facility is the inclusion of the dispersed phase, be it solid, liquid or gas. In solid-liquid flows, careful consideration must be given to the choice of the dispersed phase particle size and material, since these factors affect the fluid transparency and quality of image capture. Dispersed particles are relatively large in size, typically 100 to 1000 μm, and typical materials are glass spheres. In liquid-liquid systems, the liquid phase droplets are self-representative as they scatter the incident light. Their fluid composition and concentration are usually the controlled variables.

The incorporation of dispersed particles within the flow creates a heterogeneous medium, making optical measurements difficult to obtain as there is no clear optical path to the measurement zone. One way in which the problem may be resolved is by using optical fibres, through which the light is conducted to and from the measurement zone. However this method is intrusive. An alternative technique is refractive index (RI) matching of the dispersed phase particles and continuous phase fluid, which renders the entire system transparent. This makes it possible to access the area of interest by reducing the optical distortion and blockage by dispersed phase particles.

Northrup *et al.* (1991) applied RI matching in PIV to obtain clear images of flow fields in porous media. In their study, parameters such as temperature, purity and composition of the RI-matching fluid were optimized to obtain undistorted images of the flowing particles. For instance, the temperature of the medium was adjusted until the most uniform profile of the distorted laser beam was obtained. This indicated good RI matching between the solid and liquid phases, at the desired wavelength. Since the refractive index varies with temperature, control of this quantity is especially important. In another study, Zachos *et al.* (1996) attempted to study fluid mechanical problems in a coal floatation process, by simulating the solid phase with glass spheres whose RI was matched by an organic liquid in the two-phase system. The study determined the limiting value of the solid concentration at which extinction of the light sheet through the cell would be low enough to obtain PIV measurements for the total field of view. They reported that the mass concentration of the solid phase could be increased by a factor of 30 with RI matching, to obtain clear PIV measurements. Similarly, Nouri and Whitelaw (1992) concluded that the maximum concentration at which the solid-phase LDA velocity measurements could be made increased from 0.02 to 2.5% with RI matching.

The dispersed phase concentration must be considered for two reasons. Firstly, it is an important factor where impurities or air bubbles in the particles are present, which would hinder total RI matching between the two phases, and limit the transparency of the mixture. Unsatisfactory surface finishing of the particles have the same effect (Virdung and Rasmuson, 2003). Thus, increasing the solid content would lead to increased scattering from impure materials within the dispersed phase, making it difficult to obtain clear PIV images.

A similar problem to the above was experienced by Northrup *et al.* (1991). Laser light scattering from impurities within the RI-matched medium was of similar intensity to the tracer scattering, producing unclear images. Subsequently, the PIV technique was adapted by using fluorescent, rather than scattering tracer particles. This method is referred to as fluorescent PIV (FPIV). The final results confirmed that a combination of RI-matching and FPIV techniques can be used to quantitatively describe velocity fields within complex media.

As a second effect, an increase in dispersed phase concentration could lead to particle collisions; the extent of which needs to be known to complete the particle momentum balance equation. The threshold below which particle collisions may be neglected is still ambiguous. Batchelor and Green (1972) indicated that two-particle interactions are negligible below solid concentrations of 0.3 vol%. Other recent studies have indicated that particle collisions are important in the redistribution of particle momentum even at low mass loading (Fukagata *et al.*, 2001). Collisions between the dispersed phase particles and tracer particles of the continuous phase must also be considered. For example, Fajardo *et al.* (2006) evaluated the extent of physical processes (e.g. adsorption and diffusion) that would cause the tracer particles and dispersed phase to interact.

Numerous forces exerted on the particles by the fluid affect their dynamic behaviour, such as gravity and drag (which are most important for solid-liquid systems) and Saffman and Magnus forces. These must be accounted for in a realistic force balance on a spherical particle in a turbulent liquid flow. As mentioned before, the majority of solid-liquid studies use spherical glass particles for the solid phase. By employing neutrally buoyant particles, the effect of gravity may at least be eliminated. In their study, Micheletti and Yianneskis (2004) employed neutrally buoyant particles to eliminate density difference effects, and simplify understanding of solid-liquid flow behaviour.

2.3 Review of multiphase PIV separation techniques

PIV image analysis involves calculation of the particle displacement by means of cross-correlation or auto-correlation within an interrogation window. A study by Kiger and Pan (2000) highlighted that the presence of dispersed particles affect displacement calculations of the tracers in the continuous phase. Without any pre-treatment, the PIV calculations yielded erroneous vectors in the vicinity of the dispersed particles, due to significant differences in the motion of both phases.

In recent literature, several examples of the application of PIV techniques for simultaneous measurements of multiphase flows may be found. In all cases, some means of phase discrimination is required to eliminate the interference effects, so that the displacement of the tracers and dispersed phase particles may be obtained independently. The various phase discrimination techniques can be classified according to the stage at which the phase separation is made in the analysis. The first technique described in this section is (i) fluorescence tagging, where phase separation is done at the PIV image capture stage. In this technique, separate images of both phases are acquired independently, with the use of two cameras and optical filtering. Alternatively, a single image can be captured of both phases simultaneously, and post processing techniques such as (ii) masking and (iii) algorithms based on differences in size and/or intensity of the two phases can be employed to separate them before the application of PIV or PTV algorithms. On the other hand, a multiphase PIV image can be cross-correlated without any image processing and (iv) peak separation techniques may be employed to distinguish between the continuous and dispersed phase correlation peaks before generating vector maps. Lastly, a multiphase PIV image can be cross-correlated to yield a multiphase velocity vector map, and (v) vector separation can be employed instead. The principles of all of these techniques are discussed through the following examples.

2.3.1 Fluorescence tagging

Fluorescence tagging involves the use of fluorescent tracer particles/dyes, rather than Mie scattering particles for either one or both phases, such that phase discrimination may be achieved. This is a two-camera technique, whereby separate images of both phases may be acquired independently on each camera, which are equipped with optical filters. The method exploits the wavelength shift of the laser induced fluorescence (LIF) with respect to the Mie scattering to distinguish between the two phases.

In their study, Grunefeld *et al.* (2000) used this novel technique to obtain the velocity fields of gas and liquid simultaneously, in a laminar unsteady two-phase aerosol. Nitrogen oxide was selected as the fluorescent tracer due its stability in combustion, whereas water droplets of the spray provided Mie scattering. The authors noted that an advantage of the LIF technique compared to the Mie scattering is that it can be easily performed very close to the walls, where large amounts of stray light may occur. Results showed that large gas-phase single-shot velocity errors occurred in regions where the LIF signal was below a certain limit and dominated by noise.

In another study, Boedec and Simoens (2001) obtained discrimination of a two phase gas-liquid spray flow. The liquid droplets were tagged with fluorescent dye, whereas the gaseous phase was traced with micrometer-sized tracer particles. Subsequently, fluorescence images of the droplets were recorded by one camera, and Mie scattering images of both phases were obtained by a second camera. Digital image treatment was used to distinguish between the phases. Firstly, the two images produced by fluorescence and Mie scattering were binarized, by applying a threshold on the gray level value for each image. Then, images of the fluorescent liquid droplets were subtracted from the Mie scattering image. After applying a criterion based on the 'apparent diameter' (AD) and centroid, a final representation of the droplets was developed. The study concluded that the AD parameter was reliable enough to achieve phase discrimination. However, this method may be unsuitable for cases without a significant size difference between tracers and dispersed particles, or for particles with a broad size distribution; a point for consideration in the present case.

Driscoll *et al.* (2003) employed a combined PIV-LIF method to determine the simultaneous velocity fields of a two-phase dense fuel spray. The gas phase was traced with ethylene glycol drops doped with fluorescence dye, and the gasoline spray droplets provided Mie scattering. They modified the standard PIV technique by employing different laser wavelengths to illuminate each phase, which were pulsed independently. This enabled the spatial resolution to be optimized based on the velocities of each phase. Specifically, the delays were chosen by limiting the displacement of each phase to approximately 25% of the interrogation area length. This technique is highly useful for multi-phase systems with a large dynamic range, and allows the study of specific regions with increased accuracy. On the other hand, some studies in stirred tanks have reported negligible velocity differences between the dispersed and continuous phase (Pettersson and Rasmuson, 1997) so the added complexity of synchronizing two independently pulsed lasers may not be necessary.

In another adaptation of the LIF technique, Kosiwczuk *et al.* (2005) obtained the velocity field of liquid droplets and gas phase simultaneously from fluorescence images of both phases. The gas phase was traced with small liquid droplets, tagged by a fluorescent dye, whereas droplets

of the liquid phase were tagged by another fluorescent dye. The study highlighted that tracer particles of the gas phase must be small enough to follow the flow. However, the fluorescence intensity is dependent on the droplet diameter and the signal is weaker compared to the corresponding Mie scattering. To overcome this, dye with the highest fluorescence efficiency was used for the gas phase tracers.

In a recent development, Guido *et al.* (2005) performed an experiment whereby simultaneous measurements of solid and liquid velocities in a channel flow were obtained by tagging both phases with fluorescent dye, which also produced distinct spectra. In this case, the dispersed phase comprised solid plastic particles of size 63-105 µm sprayed with Rhodamine dye, and the liquid phase tracers were fluorescent microspheres. This system closely describes the materials suitable for the present study. Analogous to the experiment of Kosiwczuk *et al.* (2005), Guido *et al.* (2005) employed two cameras with optical filters, that enabled transmission of light above a certain cut-off such that fluorescence from both phases could be separated, and images of each acquired independently.

2.3.2 Masking

In standard two-phase PIV employing a single CCD camera, an exposure of the flow contains images of both phases recorded on a single frame. Masking is a form of image processing, with the objective of extracting separate images of each phase from the two-phase image frame. Subsequently, cross-correlation or auto-correlation can be performed on the resulting images, yielding two independent velocity fields. Phase separation techniques by 'masking' are based on particle image size and intensity, where a mask is created over the image to separate the signals between two phases. The examples below discuss different methods of obtaining the masks.

Rottenkolber *et al.* (2002) investigated the hollow-cone spray of a high pressure swirl injector for a direct-injection spark-ignition (DISI) engine using PIV. Fluorescent tracer particles were used to follow the gas phase, and the liquid droplets of the spray provided Mie scattering. Images of both phases were recorded on a single frame. The ratio between the mean grey level of the spray droplet and tracer particle images could be adjusted via optical filters. A comparison between the cumulative histograms of the grey level distributions of the single-phase and two-phase flow showed that the curve of the latter type produced a distinctive step. The characteristic step location and its corresponding grey level could be identified, which provided a threshold to create an appropriate mask. Pixels exceeding the threshold value were prescribed a constant grey level and formed an image of one phase, referred to as the 'mask'. The remaining pixels of the original image were also prescribed a constant grey value, which resulted in an image of the second phase.

Image recording must be optimised to achieve an unambiguous threshold grey level for phase discrimination. One way of achieving this is by rendering the smallest tracer particle brighter than the largest spray droplet by using an optical filter, which *significantly* reduces the Mie scattering intensity. This was done in the study of Rottenkolber *et al.* (2002). A disadvantage of this approach was that the camera was not sensitive enough to record dilute regions of the spray containing the smallest droplets. An alternative could have been to use an optical filter that only *slightly* attenuates the scattering intensity. In this case the dynamic range of the

camera must be sufficient to record tracer particles that are dark enough to resemble a clear threshold, but also light enough to distinguish them from the background noise. Both approaches impose different requirements on the camera, and the final choice depends on the sensitivity range.

The main disadvantage of the histogram-based masking technique is that a minimum concentration of each phase within the same exposure is required, for a reliable determination of the step location, and subsequent identification of the threshold level. As a result, consideration must be given to areas of phase segregation, where a concentration imbalance is expected to occur, as in stirred flows.

Virdung and Rasmuson (2003) achieved phase discrimination through masking in a PIV study of a solid-liquid stirred flow. The first stage involved processing the image pairs separately using an in-house code. The routine determined whether pixels constituted a small or large particle, corresponding to a tracer or dispersed particle respectively. If a pixel was found to correspond to a large particle, a white circle was drawn at the centre of that particle on a completely black image frame, referred to as the 'mask image'. A single mask image contained representations of large particles from both images within an image pair, so that particles moving into or away from the plane were accounted for. The second stage involved subtraction of the 'mask image' from the original image pair, thus eliminating the large particles. This effectively produced images of continuous phase tracers. However, the dispersed phase particle images were extracted by means of a median filter (discussed in §2.3.3).

The masking technique required thresholds and parameters to be specified by the user, such as (i) minimum intensity of a pixel for the program to begin searching for a large particle (ii) minimum average intensity of a cluster of pixels to be recognized as constituents of a large particle and (iii) minimum diameter of large particles. The main disadvantage of this technique is that the variation in intensities of the large particles would lead to some of them being dismissed as small particles of the continuous phase, and not be incorporated into the mask. As a result, the input parameters would need to be specified on a case-by-case basis, meaning that the algorithm is not fully automated.

2.3.3 Algorithms based on differences in particle size and/or intensity

This class of methods is also a form of image processing, and relies on the geometrical properties of the particles to distinguish between the phases. Analogous to the masking technique, the objective of the phase separation algorithm is to generate two separate images of each phase from a single two-phase image frame.

Chen and Fan (1992) wrote a phase discrimination algorithm to discriminate between dispersed solid particles, bubbles, and continuous phase tracer particles, from PIV images taken of a gas-liquid-solid fluidized bed flow facility. The algorithm implemented various tasks in series, starting with image filtering to remove background and electronic noise (by applying both low and high pass filters to the grey levels). Next, the grey scale images were binarized into a pure black and white form by applying a grey level threshold, whereby pixels exceeding the threshold were set as saturated, and those below it were set to zero. The third stage was identification of all particles in the image. To do this, a scanning routine was executed to find a pixel with a saturated grey level value, and trace the boundary of the particle which it formed part of, in a

clockwise direction. The boundary search was completed when the initial pixel was encountered again. Next, integration along the $x-y$ axes was performed to calculate the image area (in pixels) as well as centroid and mean radius.

After all particle images had been identified, the actual phase discrimination between the phases was dependent on particle mean radius. The pre-calibrated PIV image scale factor was used to convert the image size into 'real' particle size. With knowledge of the size distribution of the bubbles, solid particles and tracer particles, the PIV images could then be classified as belonging to one of the three phases. A limitation of this algorithm is that it would not be able to account for the occurrence of dispersed particles appearing relatively small in the image plane (due to them being detected from behind the light sheet) or tracer particles appearing slightly larger (due to them being out of focus). Although there may not be overlap in the physical size distribution of the tracer and dispersed particles, it is common for them to appear distorted in the image plane, causing some ambiguity and errors if discrimination is based on size alone. Including information of their real grey level values would help to solve this problem to some extent.

Kiger and Pan (2000) developed a technique for phase separation of solid-liquid two-phase turbulent flows, which was based on differences in the geometrical properties of the dispersed and tracer particles. The technique involved application of a two-dimensional median filter, which is a non-linear signal processing tool that has been found effective in reducing background noise and periodic interference patterns (Huang, 1981). In this case, the small tracer particles are treated as random noise over a uniform background. The filter operation is performed by convolving a two dimensional stencil over the pixels of a two-phase image. The median filter sorts the grey level values of a particular region in ascending order, and selects the median value to replace the pixel at the central location of that region. If the filter size is large enough, the median value will correspond to the image background, since tracers usually occupy only a few pixels only. In this way, the presence of small tracer particles is removed from the image. After filtering, only dispersed particles are left. Following this, an extraction technique (analogous to masking) was used to obtain a single-phase image of the tracers.

Kiger and Pan (2000) evaluated the separation process as a function of the dispersed particle size (d_p) and filter width (f), at a constant tracer particle size (d_t). The optimal value for tracer evaluation was given by a filter width $f/d_t \geq 2$ for all dispersed particle sizes. On the other hand, the optimal filter for dispersed phase evaluation was found to be $f/d_t = 1.3$, for $d_p/d_t > 3$. Two separate conditions suggest that a single application of the filter cannot satisfy both simultaneously. Instead, for best phase separation, the filter would need to be applied twice, doubling the image processing time.

The filter described above was successful in the identification of dispersed particles, although tracer images were only obtained by subtraction of the dispersed particles from the original image. The filter did not treat the images for noise effects that each phase introduced to the other. This is most prominent in the locality of the dispersed phase elements, making simultaneous measurements less reliable. A more refined algorithm is required for appropriate mapping of the tracers in the variable background. Khalitov and Longmire (2002) developed a

more sophisticated phase discrimination technique that was able to extract reliable tracers and dispersed solids, whilst eliminating background noise and unidentified spots.

The algorithm consisted of two main steps. Firstly, both solids and tracers were identified as 'objects' by conditioning them under second order intensity gradients (defined later in Chapter 5). This condition was based on the conjecture that the image intensity in 'objects' reaches a local maximum. If a pixel satisfied the condition, then it was marked as an object. A threshold intensity was also specified for processing saturated objects. The remaining pixels were assumed to belong to the background and set to a low constant intensity. This eliminated the problem of a variable background. Next, objects were characterized as solids, tracers or other objects, based on their size and brightness; hence the method was named 'two-parameter discrimination.' This was achieved by producing *size-brightness-number* contour plots and identifying distinct peaks for both phases. Subsequently, separation limits were mapped around the peaks to identify regions of the solids and tracers.

Tests showed that a valid data yield of the tracers above 98% could be obtained, but only up to particle volumetric loads of 0.014%. This is extremely small compared to the volumetric fractions that will be employed in the current study (~0.5 vol% dispersed phase), questioning the applicability of the technique to the present case. However, it is important to note that the validity of the data yield was quantified with regards to the continuous phase only. If some other means were employed to obtain information of the continuous phase, and the algorithm was applied to extract only the dispersed phase, then the quoted limit for obtaining a good data yield would become irrelevant, and the method could be extended to higher volume fractions.

2.3.4 Peak separation

Cross-correlation of two-phase PIV images captured on a single frame (without image processing) yields two velocity peaks in each interrogation cell, given that both co-exist. As the name suggests, peak separation involves the identification of the displacement peaks of both phases, and separating them on this basis. The technique relies on the differences between the motions of the two phases at a given location, in order to discriminate between them.

Delnoij *et al.* (1999) developed this method to study dispersed gas-liquid two phase flows. The bubbles provided natural scattering, whereas the liquid phase was tracked with Mie scattering tracer particles. The correlation peaks of both phases did not overlap significantly due to the inherent velocity differences between them. With some *a priori* knowledge of the flow, an interrogation window containing only tracer particles was specified, and used to separate velocity maps for each phase.

The authors found that the signal-to-noise ratio (SNR) of the correlation peak associated with the bubbles was poor due to the limited number of bubbles in the interrogation window. Subsequently, they proposed an ensemble correlation technique, where the ensemble mean of the correlation function for several sequentially recorded PIV images was calculated. This improved detectability of the bubble displacement peak. This consideration is directly relevant to this study of solid-liquid flows, where dispersed phase concentrations are expected to be relatively low compared to the tracers, and may fall below the recommended 10-15 images per interrogation area (Keane and Adrian 1990a). Through ensemble averaging, small time-scale variations exhibited by the dispersed phase particles may be lost. Secondly, as the size of the

correlation set increases, the 'instantaneous' nature of the velocity field decreases, as the images are produced over a period of time.

Rottenkolber *et al.* (2002) also investigated the peak separation technique for a high pressure swirl injector for a DISI engine. Fluorescent tracers were used to mark the gas phase, and liquid droplets provided Mie scattering. Note that although fluorescent tagging was used, images of both phases were recorded on a single image frame. Optical filters partially attenuated Mie scattering of the spray droplets, so that they appeared as brighter spots (relative to the tracers) on the PIV images. This facilitated the identification of interrogation areas containing double-peaks after cross-correlation. Subsequently, the double peaks within the two-phase zones were identified by evaluating their height and width. In general, the shape of a correlation peak is affected by parameters such as properties of the flow pattern and of the particle image. For instance large particles and velocity gradients within a correlation spot cause broadening of the peak (Keane and Adrian, 1990b), whereas image contrast and particle density affect the peak height and noise level respectively (Collicott, 1992).

Rottenkolber *et al.* (2002) identified that the peak separation technique was unsuccessful if the difference in velocity between the gas tracers and droplets was insufficient. Subsequently, this created regions of drop-outs in the vector plots. The method required a similar density and intensity level of both phases in addition to the large difference in velocities, and these conditions may not be fulfilled in all areas of a stirred vessel.

2.3.5 Vector separation

It is possible to cross-correlate multiphase PIV images, and without further intervention, generate multiphase vector maps. These would contain vectors of both phases on a single image frame simultaneously. Then, the vectors may be separated for each phase. Only one such study by Seol *et al.* (2007) has been known to employ this method to process multiphase vector maps of a bubble plume.

In the multiphase vector map, dispersed phase vectors were removed by applying a velocity threshold, followed by a median filter. The filter was used to sort surrounding vectors in ascending order and find the median velocity value. If the vector under consideration was outside a specified range (i.e. a few standard deviations away from the median) then it was removed. The number of neighbouring vectors and specified tolerance from the median were selected by superimposing the resultant vector fields with the raw images, and visually checking that vectors in areas of the bubbles were removed. The results of the vector separation were verified by comparing the extracted dispersed phase vectors to those acquired after digital phase separation of the images (via thresholding), and found to be in agreement.

The main advantage of the method was that it was simple, inexpensive, and employed standard tools which are available in most PIV software packages. Although more detailed phase separation methods were accessible (e.g. those aforementioned), their algorithm was found to be adequate for obtaining mean flow properties. This may be due to the large bubble size (1.5-2 mm) which in turn created sufficiently brighter images and distinct velocity vectors.

2.3.6 Limitations of the phase separation techniques

In order to evaluate interactions between the two phases, continuous phase velocities must be measured very close to the dispersed particles. In the vicinity of the dispersed particles, the noise affecting the tracers becomes stronger and simultaneous measurements become less reliable in these regions. The only technique which is able to overcome the noise problem is fluorescent tagging of the tracers, as independent, unbiased images of the respective phases can be produced. However the application of fluorescent tagging is often limited due to the high potential cost associated with the large quantities of mono-disperse fluorescent particles required. Also, in comparison to Mie scattering, fluorescence emissions have a lower intensity, and images of the smallest particles may not be recorded by the CCD camera. High sensitivity cameras are required to cover the complete range of particles sizes (Boedec and Simoens, 2001). Similarly, in order to produce LIF images of comparable intensity, a greater 'effective' thickness of the laser light sheet would be required (Kosiwczuk *et al*., 2005). The use of two-cameras also necessitates impeccable synchronisation of the camera positions and image capture.

The masking technique of Rottenkolber *et al.* (2002) involved setting threshold values for the grey level intensity to obtain digital masks. The main disadvantage of this technique is that a minimum concentration of each phase within the same image is required for a reliable determination of the threshold. However, many studies in stirred flows have observed the phenomenon of preferential concentration, where the solid phase accumulates forming local inhomogeneities (Eaton and Fessler, 1994; Derksen, 2003; Micheletti and Yianneskis, 2004). Additionally, this technique has no regard for discrimination based on particle size. Variation in intensities of the large particles could lead to some of them being dismissed as small particles. Virdung and Rasmuson (2003) developed the masking technique for dispersed phase particles by specifying more thresholds and parameters for the phase discrimination, which incorporated both size and intensity effects. However, the input parameters would need to be specified for each case, due to the variation in intensity from image to image.

The median filter proposed by Kiger and Pan (2000) did not treat the images for background noise, which was carried through to the filtered images. According to Pahuja and Longmire (1995) simple subtraction of dispersed particle elements from a field of varying background intensity can leave signatures that later cause defect of the correlation fields. In the vicinity of the dispersed particles, the noise affecting the tracers is prominent, making simultaneous velocity measurements unreliable. Thus, although the filter is effective in extracting the dispersed images, a more sophisticated algorithm would be required for proper mapping of the tracers. The two-parameter phase discrimination technique proposed by Khalitov and Longmire (2002) seems to be the best digital image processing technique. Not only did it extract reliable images of the tracers and solid particles, but it also treated the images for high-frequency noise by the application of a blur filter. This method appears to be robust as it accounts for most of the drawbacks of the median filter. The main disadvantage is that to obtain good data yields (98%) of the continuous phase tracers, the technique is limited to extremely low volumetric solids load (0.014%).

The peak separation technique exploits the velocity differences between the two phases at a given location. The application of this technique in two-phase complex turbulent flows may not

always be successful. Pettersson and Rasmuson's (1997) study of stirred flows showed that the absolute difference in magnitude between the 3-D mean velocity of the fluid and dispersed particles was very small. Similarly, Guiraud *et al.* (1997) found that the mean radial velocities of the continuous and dispersed phases were identical for most part of the vessel. To discriminate between the correlation peaks, Delnoij *et al.* (1999) used *a priori* knowledge of the gas-liquid flow field in a bubble column. In stirred multiphase flows however, the lack of experimental data prevents prediction of the flow field. After applying a cross-correlation algorithm on PIV images, Rottenkolber (2002) identified interrogation spots with double peaks, and separated these based on their height and width. However there are no universal criteria for the height and width selection. Rottenkolber *et al.* (2002) emphasized that the strategy is not valid for all kinds of flows. The shapes of the peaks may be influenced by many parameters, and more comprehensive studies investigating their effects have yet to be performed.

Although the vector separation method was simple and inexpensive, Seol *et al*. (2007) identified many limitations. Firstly, the dispersed particles must be bigger than the tracers such that in a given interrogation region, the correlation peak of the dispersed phase is dominant and able to produce a vector; this condition may be fulfilled in the current experiments. At the same time, the dispersed phase images must be smaller than the interrogation area to obtain accurate vectors. However, analogous to the peak separation method, one of the requirements is a velocity difference between the two phases, such that the median filter can pick out the dispersed phase vectors as outliers. This means that in areas where the dispersed and continuous phase velocities are similar, phase discrimination will not be achieved. Given the findings of previous studies in multiphase flows of small or no differences in the velocity fields in certain areas of the vessel (Pettersson and Rasmuson, 1997), both peak separation and vector separation methods are likely to fail for this reason.

2.3.7 Choice of phase-discrimination technique for current study

From the discussion in the previous section, fluorescent tagging of both phases seems to be the most attractive option, as the post-processing stages for phase separation would be eliminated. The superiority of this technique is the removal of noise problems between the two phases, which has been an area of major difficulty experienced with all other single-camera phase separation algorithms. Also, image capture of two phases on separate cameras eliminates the requirement of a large dynamic range, which would be necessary to record both small and large particles on a single camera without saturation effects. This problem would become pronounced for the single camera techniques when using high dispersed phase concentrations and large particle sizes. The two camera technique is more flexible and robust to these changes.

Although the fluorescent tagging method seems to be the most favourable choice theoretically, the high cost of the fluorescent particles is an overriding factor. The economical constraints would need to be considered due to the extensive experimental nature of this work. Therefore it is proposed to implement a combination of both fluorescence tagging and digital image treatment. This system will involve the use of two cameras, but only the continuous phase tracers will be tagged with fluorescent dye. The dispersed particles will be simple Mie scattering spherical elements. Consequently, one camera equipped with an optical filter will capture images of the fluorescent tracers, whilst the other camera will simultaneously capture Mie scattering images of both phases on a single frame. Subsequently, the phase discrimination

algorithm of Khalitov and Longmire (2002) (considered to be the best choice) will be used to process the Mie scattering images, and extract the dispersed phase information based on the criteria of size and intensity. A schematic of the process is illustrated in Figure 2.3.

It is preferred to tag the continuous phase tracers (as opposed to the dispersed particles) with fluorescent dye for two main reasons. Firstly, the tracers used for the continuous phase are relatively small compared to the dispersed particles and a smaller quantity (in terms of both mass and volume) is required, thus reducing the costs. Secondly the phase discrimination algorithm is expected to be superior for the treatment of the dispersed particles, since they are least affected by inter-phase noise compared to the tracers (owing to their larger size and brightness), hence may be extracted with greater accuracy and minimal loss of data. The phase separation algorithm will be developed in-house using Matlab, and tested for various experimental conditions.

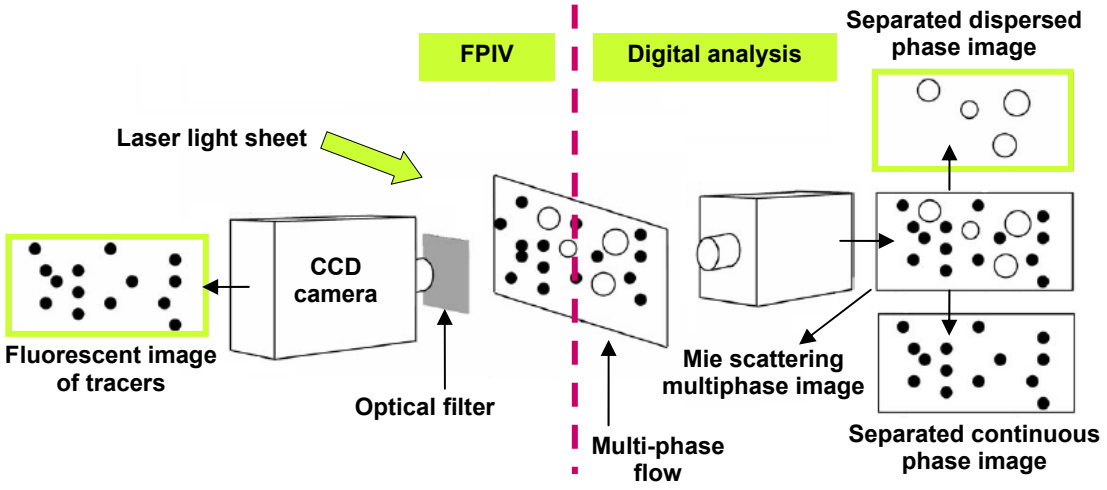

Figure 2.3: Two-camera PIV set-up for phase discrimination

2.4 Review of solid-liquid studies in pipe and jet flows

Studies of multiphase flows in geometries other than stirred vessels, such as pipe and jet flows, have been widely investigated during the last three decades, as the measurement techniques have developed. These studies provide an insight into the interactions between the two phases, and provide hypotheses for turbulence modulation. The theories put forward from such investigations have helped to explain more recent experimental findings of multiphase flow phenomena in stirred vessels. The conclusions drawn from some of the most influential studies are described in this section.

In a review of pneumatic transport through a horizontal pipe, Owen (1969) postulated that the particle Stokes number (St) (defined as the ratio of the particle aerodynamic response time to the characteristic time of an energy containing eddy) was the parameter controlling particle-turbulence interaction. Particles with $St << 1$ have a rapid response to the fluid eddy motion and extract energy from the turbulence, which would be dissipated. For $St \approx 1$ particles respond partially to the velocity fluctuations, and would still be able to dampen turbulence. However

when $St >> 1$ particles are almost insensitive to the turbulent fluctuations. Instead they behave as fixed centres of resistance in the fluid, and distort the turbulence analogous to a gauze screen.

Tsuji *et al.* (1988) performed 1-D LDA measurements of velocities in a mixture containing coarse particles in a downward facing vertical jet. They studied the effect of particles within the size range of 170 and 1400 μm on the time-averaged air mean velocity and turbulence intensity, defined in their case as the root-mean-square of the fluctuating axial velocity component, made dimensionless with the centreline velocity at the nozzle. Results indicated that the decay of the mean (time-averaged) centreline velocity downstream decreased in the presence of particles. This effect was more profound in the presence of small particles compared to larger ones at an equivalent mass loading. The 170 and 243 μm particles were found to decrease the turbulence intensity near the nozzle, and increase it downstream, relative to the single-phase air flow. Conversely, the larger 1400 μm particles had very little effect. The maximum value of turbulence intensity reduced at a high loading ratio. No explanation was given for these effects.

Gore and Crowe (1989) consolidated the experimental data of various researchers in order to produce a physical model that described turbulence modulation of the carrier phase in the presence of dispersed particles. The geometries studied were pipe and jet flows, along the centreline. The researchers correlated the percentage change in turbulence intensity to d_p / L; the ratio of particle diameter to characteristic length of the most energetic eddy; the integral length scale. They identified a critical ratio $d_p / L \sim 0.1,$ below which particles suppressed turbulence (up to ~50%), and above which particles increased turbulence (up to ~380%). The authors suggested that the most energetic eddies impart their energy to the smallest particles that flow with them, resulting in an increase in kinetic energy of the particles, and reduced turbulence intensity of the carrier phase. Conversely, the larger particles generate turbulence in their wake, which is transformed from the mean flow moving the particles to the turbulent kinetic energy of the fluid, and hence there is an increase in the turbulence intensity. The data from the various sources fell into the suggested limits remarkably well, given the extensive range of experimental conditions. However the highest volumetric concentration observed was 0.2 vol%, and particle-particle interactions were (understandably) neglected. Particle-wall and fluid-wall interactions were also excluded. The authors suggested that the inclusion of these phenomena would generate more complex results.

Later, Gore and Crowe (1991) extended the study to examine the effects of particles on turbulence intensity at radial locations other than the centreline, in pipe and jet flows. The results of pipe flows showed that the critical ratio d_p / L increased with radial position from the centreline. Secondly, the percentage change in turbulence augmentation decreased towards the pipe wall. The amount of scatter with regards to data falling outside the proposed segments also increased towards the wall. Gore and Crowe (1991) suggested that this was due to the anisotropic nature of turbulence in that region, which leads to different integral length scales in the different directions, thus reducing the possibility of using a single length scale to correlate the data. On the other hand, the radial position had little or no effect on the critical ratio for the jet flows, which was consistently found to be ~0.1 at all positions. The magnitude of the percentage change in turbulent intensity also remained unaffected.

Levy and Lockwood (1981) used 1-D PDA to obtain velocity measurements of the gas phase and sand particles of various sizes between 215 and 1060 μm in a downward turbulent air jet (information of how they compared to the Kolmogorov length scale was not stated). The authors initially suggested that very small particles would respond well to the turbulent fluctuations, and have no influence on the surrounding flow. Very large particles would increase the carrier phase mean velocity gradients and kinetic energy, whereas particles of intermediate sizes would partially respond to the turbulence fluctuations, and suppress turbulence. Results indicated that the largest particles increased the gas mean and axial rms velocity as expected. However, the smallest particles (with high mass loading) reduced the gas axial rms velocity, and particles of intermediate sizes had a mixed effect. The turbulent kinetic energy of the largest particles was found to be the greatest, and the authors suggested that they reabsorb some of the turbulence energy that they induce during free fall.

Hetsroni (1989) suggested that particles with low Reynolds numbers cause a decrease in turbulence, whereas those with high Reynolds number augment turbulence due to wake shedding. The author recalled the findings of Achenbach (1974), which showed that vortex shedding occurs in the range of $400 < \mathrm{Re}_p < 1000$, and related this phenomenon to the works of other researchers to support his hypothesis. The study of Tsuji and Morikawa (1982) of particles in a horizontal pipe flow showed that turbulence intensity of the air increased in the presence of particles of $d_p = 3.4$ mm. The estimated particle Reynolds number (~470) was within the range where vortex shedding occurs. In a following study of vertical pipe flow, Tsuji *et al.* (1984) found that small particles of $d_p = 200$ μm ($\mathrm{Re}_p \approx \mathrm{O}(0.10)$) always suppressed turbulence, whereas larger particles of $d_p = 3$ mm ($\mathrm{Re}_p \approx \mathrm{O}(1000)$) always increased the turbulence intensity of the carrier phase. However, intermediate size particles of $d_p = 500$ μm ($\mathrm{Re}_p \approx \mathrm{O}(100)$) had a mixed effect; i.e. they increased turbulence in the central part of the pipe, but decreased it in regions closer to the wall. The previous study of Gore and Crowe (1991) which correlated turbulence modification to particle size also could not account for this mixed result.

Elghobashi and Truesdell (1993) modelled interactions of solid spherical particles dispersed in decaying homogeneous isotropic turbulence, using direct numerical simulations. The exact Navier-Stokes and continuity equations for the fluid were discretized in an Eulerian framework. The instantaneous velocity of each particle was obtained from the time integration of the Lagrangian particle equation of motion. In all simulations the particle size was kept below the Kolmogorov length scale ($d_p / \eta < 1$). Results indicated that the particles being smaller than the Kolmogorov length scale impart their energy to the turbulent motion at high wave numbers, thereby increasing the fluid turbulence energy at small scales, with a corresponding increase in dissipation rate. This leads to a subsequent increase in the rate of energy transfer from the large scale motion, and thus an overall decrease in the turbulence kinetic energy compared to the particle-free case. Although the dissipation rate was lower in the particle-laden case at smaller waver numbers; its integral over all wave numbers was greater, giving an overall augmented dissipation rate. The particles had a very low Reynolds number ($\mathrm{Re}_p < 1$), which

opposes the postulate of Hetsroni (1989), for which the underlying mechanisms for turbulence augmentation is attributed to presence of particle wakes.

Hishida *et al.* (1995) investigated interactions between particles and turbulence in a fully developed water channel flow using PIV. Particle sizes were comparable to or slightly greater than the Kolmogorov scale. The following effects were observed in the streamwise direction. Particle mean velocities exceeded the water velocities (which remained unchanged in the two-phase flow) generating substantial slip, and their velocity fluctuations increased with increasing Stokes number. Particles were found to augment the carrier phase turbulence intensity with increased mass loading. The Reynolds stress increased in the presence of particles (to balance the drag force in the fluid-momentum equation and maintain a constant mean fluid velocity), thereby increasing the rate of production of turbulent kinetic energy. Due to the particles' inability to respond well to the turbulent fluctuations, the turbulence intensity in the streamwise direction increased (note that $3.4 < St < 5.3$). The flow power spectra showed that particles augment turbulence at high wave numbers, consistent with the findings of Elghobashi and Truesdell (1993). The authors attributed this effect to the presence of particle clusters (concentration fluctuations) and large particle slip velocities. However in contrast to Elghobashi and Truesdell (1993), the energy also increased in the low wave number region (with increased particle mass loading). Note however that Hishida *et al.* (1995) employed particles that were greater than the Kolmogorov scale.

Atsuhide *et al.* (2007) studied the interactions in a liquid-liquid swirling flow in a horizontal pipe. Droplets generated were moderately large with a mean diameter of $d_p = 4.4$ mm. Experiments were conducted with 0.16 and 0.33 vol% dispersed phase. Results indicated that the presence of the droplets had no effect on the liquid mean velocity. However, an increase in the droplet volume fraction caused an increase in the turbulence intensity of the carrier phase in the streamwise direction. By defining a turbulence ratio that combined turbulent fluctuations in both directions (of continuous phase to only liquid phase fluctuating squared-velocities), the authors showed that the turbulence intensity of the liquid increased in the vicinity of the droplets, but was independent of the dispersed phase volume fraction when considering all droplets. They illustrated that the turbulence ratio was strongly related to the droplet Reynolds number instead, which were in the range $0 < \mathrm{Re}_d < 600$. By summoning upon the DNS results and experimental findings of other researchers (Sakamoto and Haniu, 1990; Mittal, 2000; Sugioka and Komori, 2005), Atsuhide *et al.* (2007) proposed that turbulence enhancement results from vortex shedding from high Re_d droplets, and low-level velocity fluctuations induced by low Re_d droplets. They also found that the effect of volume fraction on the turbulence ratio became evident when considering high Re_d droplets only.

In a recent study, Virdung and Rasmuson (2007a) investigated solid and liquid phase velocities in a confined turbulent jet using PIV. The particles were 1500 μm diameter glass spheres, up to 1.9 vol%. Results were given mainly for the axial velocity, since it dominates the jet flow structure. The study showed that the axial continuous phase centreline velocity remained similar to the single phase jet for up to 1.2 vol% dispersed phase, although its rate of decay was reduced in the presence of 1.9 vol% solids. The rate of decrease of the centreline velocity of the dispersed phase decreased with increasing volume fraction. Due to gravitational effects, the solids lead the continuous phase in all regions of the jet. For both phases, the jet width

increased with particle concentration. The authors suggested that this was because of the increased turbulence created by particles in their wakes (Gore and Crowe, 1989) (Re_p was not stated). Continuous phase axial rms velocities were greatest close to the jet inlet, and increased with dispersed phase content. The authors took the view of Taneda (1956) that a re-circulating zone forms near the rear stagnation point of the spheres, and the laminar wake begins to oscillate sinusoidally to augment turbulence of the continuous phase. However, the continuous phase axial rms velocity remained unchanged at the centreline, but increased with solids fraction at other locations. Dispersed phase rms velocities were generally larger than the continuous phase, independent of axial position, believed to be because of particle collisions. Unlike the case for the continuous phase, the axial rms velocities at the centreline close to the inlet decreased with an increase in volume fraction.

2.5 Review of solid-liquid studies in stirred suspensions

The flow in stirred reactors is usually turbulent, re-circulating and three-dimensional, and the complexity increases for multiphase mixing operations. Although solid-liquid mixing is a common process, there is a lack in availability of quantitative measurements of solid and liquid velocities in stirred tanks, especially at elevated concentrations. Knowledge of the mean and rms velocity fluctuations is crucial for quantifying the influence of dispersed solids on the continuous phase. The data are valuable for calculating turbulence parameters such as the turbulent intensity, Reynolds stress terms, and turbulent kinetic energy (TKE) dissipation rate. All of these factors affect the mixing process and hence knowledge of these hydrodynamic parameters is essential to predict the end result. Many turbulence models have been developed to describe the mixing process, but validation has been held back due to the deficiency in reliable and detailed experimental data. With the advancement of digital imagery and computational power (discussed in §2.1), researchers have attempted to fill this void and provide experimental data starting with low solid fraction suspensions. Examples of such studies are discussed below.

Nouri and Whitelaw (1992) measured particle velocities of a solid-liquid two phase flow in a vessel stirred by a Rushton disc turbine (RDT) using LDA. Two separate working fluids were used for the continuous phase; water and a miscible mixture of tetraline and turpentine which improved light-beam penetration in denser flows, and allowed the particle concentration to be increased from 0.02 to 2.5 vol% with RI matching. Diakon and lead-glass particles of various sizes were used as the dispersed phase in water; only Diakon was used in the mixture. As the liquid and solid velocities could not be measured simultaneously, the apparent velocity (defined as the particle mean velocity minus the corresponding single-phase fluid velocity) was used instead.

Particles lagged the fluid in up flow due to gravity and led the fluid in down flow regions. The lag was more pronounced near the plane of the impeller disc, where the difference between particles and single-phase fluid velocities reached a maximum of $0.075V_{tip}$ (for Diakon particles in the mixture). Particle radial rms velocities were generally lower than the single-phase fluid in the impeller stream, by a maximum of 25% for 232 μm lead-glass particles in water (at 0.02 vol%), and by 15% for the Diakon particles in the mixture (at 2.5 vol%). In the bulk flow, axial turbulence levels of the particles and single-phase fluid were comparable. Variations were

observed in the wall jet, where the particle turbulence levels were lower up to 10%. Note that since only particle velocities were measured, it was not possible to observe their effect on the continuous phase turbulence, or calculate slip velocities.

The study described above measured solely dispersed phase velocities using LDA. Guiraud *et al.* (1997) applied the phase Doppler technique to a solid-liquid suspension stirred by an axial impeller, for simultaneous velocity and particle size measurements for tracer and 253 μm dispersed particles, in water at 0.5 vol%. The liquid axial flow was slightly slowed down in the propeller discharge due to inertia of the glass particles, and close to the vessel wall (where the flow was moving upwards) due to gravity. In agreement with Nouri and Whitelaw (1992) the particles led or lagged parts of the downward and upward flows respectively. In most cases, the mean radial velocities of the continuous and dispersed phase were found to be identical to the single-phase, whilst tangential velocities were relatively small. The axial slip was found to be the most significant because buoyancy force pulled the particles downwards.

The axial rms velocities of the fluid were found to be unaffected by the presence of particles, and were smaller than for the dispersed phase in all areas of the vessel. This does not follow the findings of Nouri and Whitelaw (1992), who noted comparable axial turbulence levels of both phases in the bulk. Guiraud *et al.* (1997) suggested that the contradiction may be based on experimental variations; resulting from a difference in measurement volume size. The rms radial and tangential velocity components of the fluid were not modified by the particles either, and the profiles of both phases were very similar.

The LDA method was further adapted for simultaneous, 3-D velocity measurements by Pettersson and Rasmuson (1997), who applied 3-D phase Doppler anemometry to crystallizers agitated by a pitched blade turbine (PBT). The system comprised six beams, which enabled simultaneous recordings of all three velocity components. Glass particles of 321 μm diameter were suspended in water at 0.06 vol%. Analogous to the previous case, the particle size was recorded synchronously to enable phase discrimination between the tracers and dispersed phase. Results showed that the absolute difference in magnitude between the 3-D mean velocity of the fluid and dispersed particles was very small (of the order of a few cm s^{-1}, compared to fluid velocities reaching ~1 m s^{-1} in the discharge stream. The maximum difference between the two was around 20%). Also, the difference in flow angles between the two phases was no more than a few degrees.

The studies above portray the development of LDA techniques from single- to two-phase systems, and from 1-D to simultaneous 3-D measurements. One of the earlier studies implementing PIV for (only) solid velocity measurements in a two phase solid-liquid stirred flow was carried out by Hasan *et al*. (1999). The continuous phase comprised a mixture of glycerin and water, RI matched to 600 μm glass beads at 1 vol%. The size and concentration of particles was significantly higher than that used in typical PIV applications. The velocity field was determined via cross-correlation of the image pairs. Note that since tracer particles were not employed to track the flow, phase separation was not required. Spatial variations in suspended phase concentration were also examined using an image analysis algorithm developed in-house. Results emphasized segregated regions of particle circulatory flow structures above and below the impeller.

Eloranta *et al.* (2001) extended the PIV technique in RDT stirred flows by obtaining simultaneous measurements of the dispersed and continuous phases. Both optical and digital image processing techniques were implemented for phase separation. The optical technique involved the acquisition of Mie scattering images of dispersed particles on one camera, and LIF images of fluorescent tracers on the other. In the digital technique, both cameras operated in stereo-PIV mode, and tracers and dispersed particles were recorded simultaneously on the same frame. Subsequently this technique yielded simultaneous measurements of three velocity components for each phase. Phase separation was carried out by applying a 2-D median filter (Kiger and Pan, 2000) to obtain dispersed phase images, followed by masking of the dispersed phase to obtain the continuous phase velocity field. A sucrose-water solution was RI-matched to fluorinated ethylene propylene resin (FEP) particles between 1500 to 3000 μm, which is fairly large-scale. Mie scattering glass spheres of 10 μm diameter were used to trace the flow in the digital recordings, which were replaced with fluorescent particles in LIF recordings. Velocity fields of both phases were obtained via cross-correlation.

Axial profiles of the average rms velocity showed lower values for the 2-D Mie-LIF recordings, as in this case the average was determined from two components, compared to all three from pure digital processing. Alternatively, it was suggested that in the digital technique, inadequate masking in some particle neighbourhoods, resulting from strong scattering of the FEP particles may have increased the number of spurious vectors close to the mask edges, which could have biased rms velocity calculations towards higher values. In comparison, rms velocities of the single-phase were less than those obtained from the two-phase digital processing case, indicating that the dispersed phase increases fluid turbulence. The focus of the paper was to evaluate the difference in the measurement techniques hence information of flow scales were not given. Subsequently the d_p / L ratio is not known, but the observed turbulence modulation does conform to Tsuji *et al.*'s (1984) general theory that large particles augment turbulence. However note that the turbulence appeared to be dampened when compared to the continuous phase data obtained from the Mie-LIF recordings. This point is extremely important, as it illustrates contradictory effects observed in the same system, due to a difference in experimental technique, as well as everaging over two or three components.

Micheletti and Yianneskis (2004) investigated velocity characteristics of solid-liquid suspensions in a RDT stirred vessel using LDA. A mixture of tetraline, 1-methylnapthalene and 1-chloronapthalene was RI-matched to 186 μm neutrally buoyant polystyrene particles, up to 2 vol%. The radial mean velocity of the fluid decreased by up to 50% at the impeller tip, where the rms velocity also reduced by 70%. These differences became less pronounced further away from the impeller. Radial profiles of the tangential mean and rms velocity showed that differences between the single- and two-phase fluid were within experimental error. It was suggested that the dispersed phase causes a redirection of the flow in the angular direction near the impeller tip, coupled with the deceleration of the flow in the radial direction. A look at the data rate variation along the vessel radius revealed that it reached a minimum close to the impeller tip, possibly due to a locally high concentration of particles in this region. It was suggested that this may have been responsible for decelerating the continuous phase in the radial direction, and subsequently redirecting the flow. This level of turbulence modulation seems to be the greatest reported so far, but perhaps it is the shift in flow pattern which causes these changes, and not the particles. The shift in flow pattern would mean that corresponding

locations between the single and continuous phase would change, hence comparisons could not be made at the same absolute point between experiments.

Virdung and Rasmuson (2007b) measured only continuous phase axial velocities in a solid-liquid flow stirred by a 45° PBT, using LDV. Dispersed phase glass spheres were made invisible in an RI matched solution of benzyl alcohol and ethanol. Experiments were carried out using particles of 1, 1.5 and 2 mm, up to maximum volumetric concentrations of 6, 9 and 9 vol% respectively. For all particle sizes, an increase in concentration was found to shift the impeller jet radially further away from the impeller and vessel bottom. The axial mean velocities were also found to decrease with an increase in particle concentration. An increase in particle size (at a fixed concentration) also changed the deflection point (i.e. where it hits the vessel base) of the impeller stream.

Generally, both increases in solid particle size and concentration led to an increase in the continuous phase axial rms velocity, which was greater than the single-phase in all locations. The authors estimated the particle diameter to integral length scale ratio for the 1, 1.5 and 2 mm particles to be 0.2, 0.3 and 0.4 respectively. Subsequently, the authors attributed turbulence augmentation to the findings of Gore and Crowe (1989), who suggested that particles with a critical ratio above 0.1 increase the carrier phase turbulence (mechanisms for turbulence modulation discussed in §2.4). The authors identified two regions of maximum axial rms velocity (corresponding to the impeller region and large PBT vortex), whose positions also shifted with increasing solids concentration.

In the most recent two-phase study of this nature, Virdung and Rasmuson (2008) implemented digital PIV to obtain simultaneous velocities of the dispersed and continuous phases in a PBT stirred tank. As before, a mixture of benzyl alcohol and ethanol was RI-matched to 1000 μm glass spheres up to 1.5 vol%. Total matching was not possible due to inhomogeneities in the glass. It is worth recalling that Northrup *et al.* (1991) used fluorescent rather than scattering particles to overcome this problem. Phases were distinguished during post-processing by masking the dispersed phase to obtain the continuous phase, and the use of a median filter to extract the dispersed phase. Note that the author's deemed their previous LDV experiments to be more accurate since they contained fewer sources of errors (arising from phase separation).

The axial velocity decreased by 46% in the impeller jet at a solid concentration of 1.5 vol%, much larger than their LDV study. Such great suppression of the axial velocity was not observed by Guiraud *et al.* (1997) either, although their study employed a lower volumetric concentration of 0.5 vol%. The radial velocity decreased by ~10% compared to the single-phase flow. The overall mean velocities of the solids also decreased with increasing solid content.

The 2-D rms velocities (with contributions from both axial and radial components) of the continuous phase were much higher than those of the single-phase. This observation does not agree with Guiraud *et al.* (1997), who found all rms velocities were unaffected by the presence of particles. The results completely contradict the findings of Micheletti and Yianneskis (2004), who observed turbulence suppression. Since they used small particles (186 μm) relative to Virdung and Rasmuson's (2008) larger size (~1000 μm), the differences may be explained by the hypothesis of Tsuji *et al.* (1984), that small particles attenuate turbulence intensity, whereas larger particles enhance it.

On the other hand, Virdung and Rasmuson (2008) found that rms velocities of the particles were greater than those of the continuous phase, in agreement with Guiraud *et al.* (1997), but at the same time opposing Nouri and Whitelaw (1992), who reported lower particle turbulence levels in the impeller stream compared to the single-phase.

As mentioned previously, Tsuji *et al.* (1984) suggested that small particles suppress turbulence, whereas large particles enhance it, which is now a commonly reported result. Studies in the past have attempted to characterise the transition between the two domains by defining the particle diameter to fluid length scale ratio as a parameter. Gore and Crowe (1991) indicated that this transition occurs when the particle diameter to characteristic fluid length-scale ratio is 0.1. A problem encountered is the selection of the most appropriate fluid length scale corresponding to the size of the most energetic eddy, as this is not straightforward for stirred vessels. More so, time and length scale measurements of turbulent flows using LDA may be inaccurate, since the eddy size could be changing as it passes through the measurement volume; meaning that Taylor's frozen turbulence hypothesis cannot be applied. PIV techniques would be more useful for the determination of such length scales as they provide spatial information of the flow field at an instant in time. One of the objectives of the current study is to take advantage of the superiority of the PIV technique to investigate these effects.

2.6 Conclusions of literature survey

The literature review has illustrated the development of flow measurement techniques from achieving single-point to multi-point capability via laser visualisation. It has been clarified that PIV is the only technique which allows the simultaneous measurement of vectors in a 2-D planar cross section of the flow; hence its application to the current work has been justified. Various methods of phase discrimination techniques have been reviewed for multi-phase PIV applications. Whilst phase separation based on fluorescent tagging of particles in sync with a two-camera system was considered to be the best option due to its efficient elimination of interphase noise, it was also found to be the most costly. From the remaining techniques employing single-camera image capture and subsequent phase separation, computational algorithms for digital image processing seemed to be well developed, and a variety of algorithms were described in literature. Subsequently the combination of fluorescence tagging and digital separation was considered to be the best solution to achieve phase discrimination.

A review of multi-phase studies in pipe and jet flows has shown various attempts at detecting turbulence modulation by the dispersed phase using predominantly LDA techniques, and subsequently correlating these effects to either the particle size or particle Reynolds number. Most studies have suggested that 'small' particles suppress turbulence, whereas 'large' particles augment it. Hetsroni (1989) attributed the latter effect to vortex shedding, which occurs in the range $400 < \mathrm{Re}_p < 1000$ (Achenbach, 1974). The most widely reported finding is that of Gore and Crowe (1989), which suggests that particles with a critical diameter to fluid integral length scale ratio (d_p / L) below 0.1 suppress turbulence, whilst those exceeding the value augment it. This study looked at data obtained at the pipe and jet flow centreline. However it should be noted that when the authors extended their study to examine the effects at radial locations away from the centre line, the critical ratio was not as clearly discernible in pipe flows. This may have been due to the anisotropic nature of turbulence close to the wall, generating

different integral length scales in the different directions, and thus reducing the possibility of applying a single length scale to correlate the data.

Reports of studies in solid-liquid stirred suspensions are the most contradictory, with some reporting turbulence suppression (Micheletti and Yianneskis, 2004), some reporting augmentation (Eloranta *et al.*, 2001; Virdung and Rasmuson, 2008), whilst others report no change by dispersed particles at all (Guiraud *et al.*, 1997). This is unsurprising as the flow in stirred reactors is usually turbulent, re-circulating and three-dimensional, in which fluid-particle interactions would be difficult to quantify, unlike pipe and jet and flows whose streamlines are mainly unidirectional. In the majority of two-phase studies described, the particle volumetric concentrations have been relatively low (of the order 0.1 vol%). Virdung and Rasmuson (2008) achieved 1.5 vol% in their PIV study via RI matching, which is experimentally the most advanced study till date. Moreover, turbulence modulation has only been described in terms of the effects on rms velocities or TKE thus far, but not the TKE dissipation rate.

The current study aims to progress the work described in literature by implementing (transparency-dependent) PIV experiments of solid suspensions in a stirred flow with up to 0.5 vol%, and (transparency-independent) micromixing experiments with up to 3 vol% (micromixing experiments are described in depth in Chapter 7). In this work, turbulence modulation on the fluid dissipation rate will be quantified.

Chapter 3
Single-phase PIV study

3.1 Introduction

Flows in stirred tanks are often complex, multi-dimensional and greatly affect the mixing properties of the fluid. Mechanically agitated tanks are used for a variety of industrial process such as blending of miscible or immiscible solvents, dispersion of gases or solids in liquids, chemical reactions and polymer production to fermentation processes (Kresta and Wood, 1993b). The complexity of stirred flows in chemical reactors has encouraged a number of studies to investigate the mean flow patterns and turbulence properties of the flow fields generated by various types of impellers.

The choice of an impeller is largely dependent on the mixing requirements; the quality of which is defined by the relative distribution of the mean and turbulent kinetic energy (TKE), and more importantly the TKE dissipation rate. The demand for improved impeller designs is driven by the need to enhance the quality and capacity of existing processes, or to satisfy new technologies. One such example is nano-particle technology; a developing field of research that is among the forefront of current investigations, which involves the synthesis and control of particles on a scale smaller than one micrometer. The sawtooth impeller is claimed to be a high shear mixing device, which is used to de-agglomerate nano-particle dispersions. Compared to Rushton disk turbines (RDTs) and pitched blade turbines (PBTs) which have received a lot of attention over the last three decades (Van't Riet and Smith, 1975; Wu and Patterson, 1989; Lee and Yianneskis, 1998; Yianneskis and Whitelaw, 1993; Khan *et al.,* 2004; Gabriele *et al.*, 2009), the hydrodynamics of sawtooth impellers are relatively unknown, and have not been widely investigated. Recently, only a couple of studies have been carried out to study the dispersion of nano-particle agglomerates by the sawtooth impeller (Xie *et al.*, 2007; Xie *et al.*, 2008). This made it a good choice for exploration and contribution to knowledge in the current work. Subsequently, a study has been carried out to investigate the flow field and turbulence properties generated by an EkatoMizer, which is a proprietary type of sawtooth impeller.

Before advanced two-phase experiments could be carried out, it was necessary to gain experience of the PIV apparatus and become familiar with the image processing techniques. Consequently, stereoscopic particle image velocimetry (stereo-PIV) has been employed to obtain three-dimensional flows close to the impeller region of the EkatoMizer. High-speed, two-dimensional PIV experiments were also carried out to obtain better time-resolved velocity fields, as well as angle-resolved measurements. In this chapter, mean flow properties of the impeller will be presented, including integral length scales, root-mean-square (rms) velocities and turbulent kinetic energy (TKE). An analysis of flow anisotropy and macro-instabilities has also been carried out.

Chapter 4 is an extension of the single-phase study and focuses largely on the TKE dissipation rate, as it is responsible for the break-up of nano-particle clusters (Xie *et al.*, 2008), and is the property of most interest in proceeding two-phase studies. Since its calculation is contested, different methods will be compared. The chapter also addresses the issue of spurious vectors in raw PIV measurements, which lead to the calculation of spurious gradients and have a compounding impact on the dissipation rate estimate in gradient based methods. A technique has been developed to distinguish between spurious results and genuine turbulence intermittency, by comparing generalized dimensions of the time-history dissipation rate profiles to the multifractal model of Meneveau and Sreenivasan (1991). High-speed PIV data was crucial for this analysis. The ratio of the maximum and mean dissipation rate for the EkatoMizer has been calculated, and compared to other impellers on this basis.

3.2 Experimental setup and analysis procedures

Stereoscopic PIV is an extension of 2-D PIV for measuring the out-of-plane velocity component in a laser light sheet plane. The main difference is the use of two cameras (rather than one) to obtain two simultaneous viewpoints of the same object plane in order to obtain a three-dimensional perspective. This section describes the experimental setup and various elements of a stereo-PIV system, as well as providing an insight into the practical aspects and data processing.

3.2.1 Vessel arrangement

The vessel was a torispherical-based cylindrical tank, with an inner diameter of $T = 305$ mm, equipped with four equidistant baffles of width $B = 0.1T$. It was constructed of 6 mm thick Perspex which provided an optically transparent path to the measurement volume. Deionised water was filled to a height $H = T$, which was traced with 10 µm hollow glass spheres of 0.014 g l^{-1} density. The EkatoMizer had a diameter of $D = 95$ mm (or $T / D = 3.21$), which operated at a clearance of $C = T / 3$. It had 72 teeth spaced very closely together (see Figure 3.1), making angle-resolved measurements difficult to obtain. The main vessel dimensions are shown in Figure 3.2.

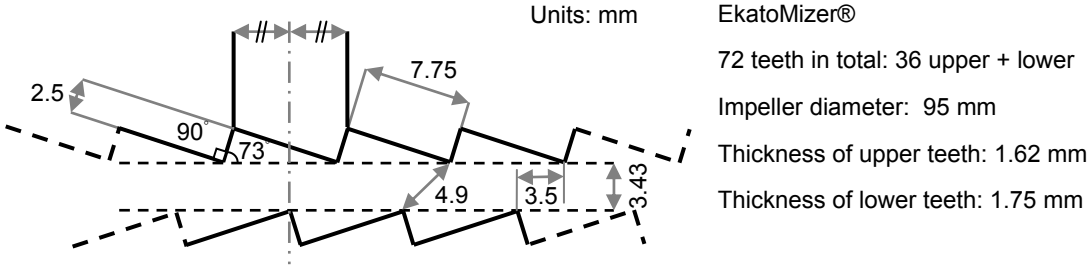

Figure 3.1: Details of impeller teeth dimensions

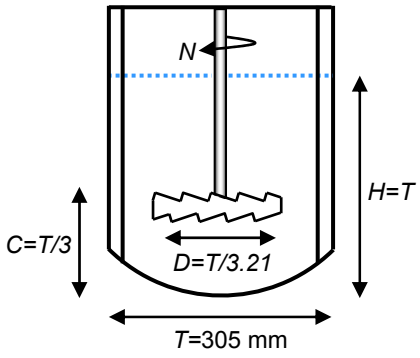

Figure 3.2: Vessel geometry

The vessel was placed inside a larger pentagonal Perspex tank also filled with water, which eliminated refraction of the laser at the curved surface. Instead, the change in RI from air to Perspex occurred over a flat surface. The box comprised five sides, two of which formed an angle at 120°. This arrangement is ideal for 3-D PIV, as the two cameras can be placed perpendicular to these respective faces. In this arrangement, the lens axes of both cameras intersect at 60° on the object plane, forming an off-set half angle of 30°. This arrangement is known as the Scheimpflug configuration, which can provide an accurate measurement of the in- and out-of-plane velocity measurements, for non-uniform magnification. This arrangement is shown in Figure 3.4.

Light reflections off the impeller surface (which would cause errors in the PIV analysis and damage the CCD camera chip) were minimised by painting the impeller matt black. Despite this, strong reflections still occurred. The laser power could have been reduced, but at the expense of reducing the number of tracer particles recorded. According to Keane and Adrian (1990a), approximately 10-15 particles per interrogation area (*IA*) are required for good PIV analysis. Thus, instead of compromising the laser power, black tape was stuck to the outer tank surfaces, creating a mask. The main drawback of masking was that details of the impeller blades were lost.

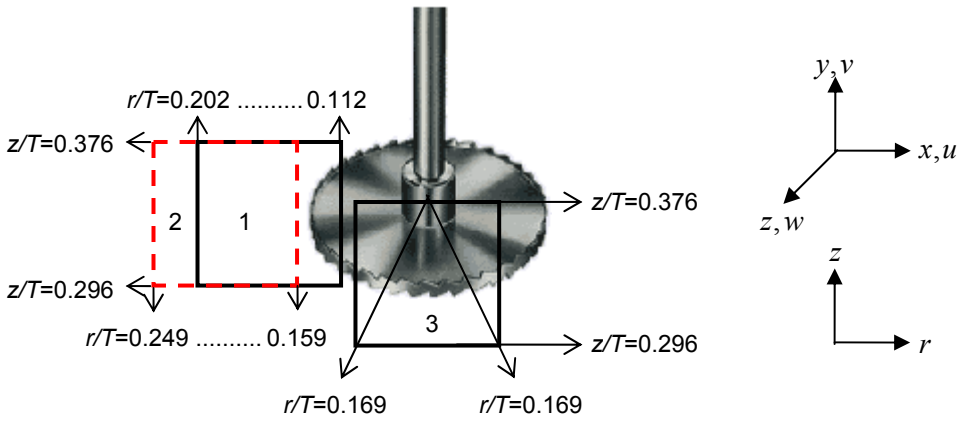

Figure 3.3: Measurement positions

The entire vessel was placed on a sliding table, which enabled the laser and camera positions to be held constant, whilst moving the plate to new locations without altering the arrangement of the tank components. Measurements were obtained at three locations; close to the impeller, further away from it and directly in front of the blade (marked Positions 1, 2 and 3 respectively in Figure 3.3). At each position, the impeller speed was varied between 1500 and 2600 rpm, corresponding to Re between 2.3×10^5 and 3.9×10^5, satisfying operation within the turbulent flow regime ($\mathrm{Re} > 4\times10^3$). Measurements were ensemble-averaged, i.e. taken around 360° of the impeller, since it was not possible to accurately determine the positions of the individual blades.

3.2.2 Stereo-PIV components

The stereo-PIV setup is illustrated in Figure 3.4, and its components are described as follows.

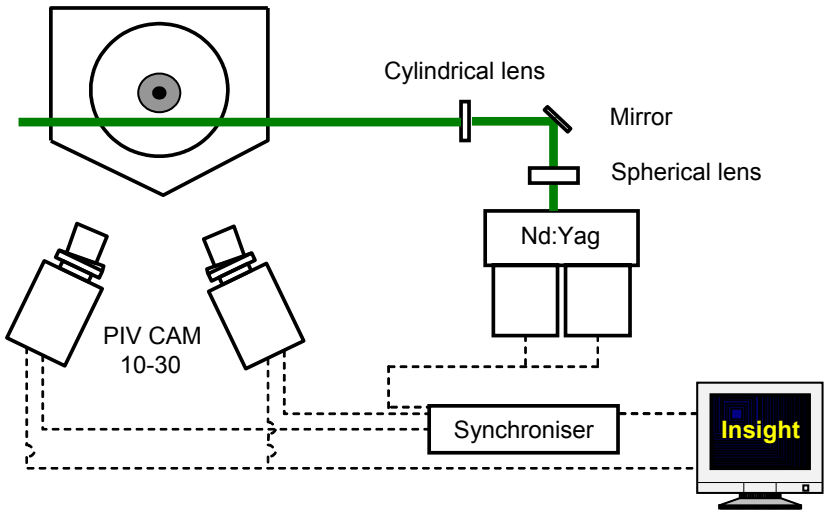

Figure 3.4: Stereo-PIV setup

CCD cameras

The two CCD cameras were from TSI Insight, with a resolution of 1000×1016 pixels and 256 grey scale levels (TSI PIVCAM 10-30 model 630046). Each was fitted with a Nikon Micro-Nikkor 28/F2.8 lens, with an f-number ($f^{\#}$) range between 2.8 and 32, which was manipulated to obtain clear images. Note that the lower the $f^{\#}$, the higher the lens aperture, corresponding to a reduced depth of field, and hence there is a trade off.

The cameras were placed perpendicular to the angled faces of the pentagonal glass box in the Scheimpflug configuration, which provides an accurate measurement of the in- and out-of-plane velocities, for non-uniform magnification. Subsequently their lens axes intersected at 60° on the object plane, forming an off-set half angle of 30°.

As the two cameras viewed the target plane from different angles, the right one received light from forward Mie scattering, whereas the left one received side scattering. Subsequently, particle images from the right camera appeared to be brighter. To compensate for this difference, the $f^{\#}$ of the left camera was dropped, but this resulted in a contrast difference

between the particle images and background. However, the calibration procedure was able to account for this. The $f^{\#}$ of the right and left cameras were set to 22 and 8, respectively.

Laser

A double-pulsed New-Wave Nd:YAG laser of 532 nm wavelength was employed. The light beam was passed through a cylindrical lens, which generated a sheet of ~1 mm thickness. The laser had a maximum repetition rate of 15 Hz (for double pulses) with a pulse width of 5 to 7 ns, and a maximum pulse energy of 50 mJ. At the given repetition rate and in conjunction with the CCD cameras operating at 30 frames per second, a maximum of 15 (single-frame) image pairs could be acquired per second. A total of 500 image pairs were acquired per data set. Preliminary tests showed that a sample size of 100 and 300 instantaneous PIV measurements satisfactorily provided mean flow and rms velocity statistics everywhere in the field of view, respectively. The time-averaged dissipation rate converged to a steady value in the discharge stream after 200 measurements, but only just converged at the blade edge after 450 measurements. Subsequently, 500 measurements were deemed to be sufficient for the statistical convergence of all properties.

Synchroniser

A TSI Insight computer-controlled LASERPULSE synchronizer (Model 610034) was used to provide a sequence of triggers for the activation of the laser pulse and camera. The synchroniser provided a trigger output to the laser, which coordinated the pulse sequence, and ensured that the individual pulses were generated in the appropriate camera frames. Under the frame straddling exposure mode, the synchroniser allowed the camera to capture a pair of images on separate frames, less than 300 μs after the trigger. Both images within the pair had different camera exposure times; 255 μs and 33 ms respectively. The longer exposure time of the second image enabled the camera to transmit the first image to the frame grabber in the PC. The first laser pulse was activated near the end of the first exposure, whereas the second pulse was fired at the beginning of the next exposure. The time between the exposures (ΔT) was selected case by case according to the flow velocity (or impeller speed).

3.2.3 Stereo-PIV Calibration

The most crucial stage for any 3-D PIV system is the calibration, as this determines the accuracy of the out-of-plane velocity component. It accounts for the local magnifications in the three directions, and corrects the centre of the field of view for each camera when not precisely aligned. Even when they are perfectly aligned, the image perspective causes distortions in opposite directions of the left and right images. Calibration software is able to account for this by generating a mapping function which provides a direct relationship between a particle location in the object plane and its corresponding position on the image plane, for both cameras. The calibration was carried out using a PIVCalib program in conjunction with TSI Insight software.

A target grid containing calibration markers (black dots) against a white background, arranged in a Cartesian lattice, was placed in the object plane to coincide exactly with the light sheet. Its main feature was a distinctive mark at the centre called the 'Fiducial point'. Calibration was achieved by acquiring images of the grid on both cameras, as it was traversed through the laser

light sheet in five small increments (of 0.25 mm) in the out-of-plane direction. The centre of the light sheet was defined as $z = 0$. In the first image, the Fiducial mark location [x, y, z] was specified by the user, for instance [0,0,-0.5] or [0,0,+0.5] depending on the start position. Because of the distinctive mark, the program was able to recognize the centre of the grid on each image, identify the remaining markers relative to this central point, and store their pixel locations. Figure 3.5 shows the result of an image analysis. The Fiducial mark is highlighted with a diamond, and the calibration marks are highlighted with boxes.

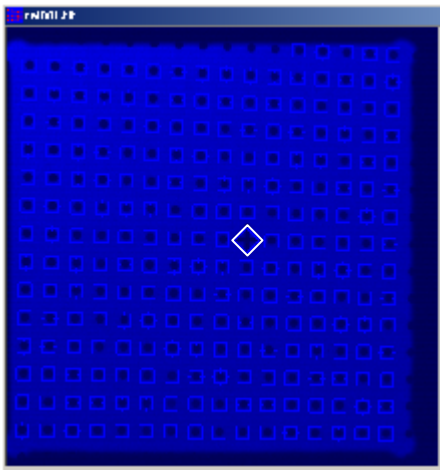

Figure 3.5: Results of a calibration image analysis

By combining the Fiducial mark and calibration point data from all calibration images, the PIVCalib program generated a set of six polynomial equations for each camera, which mapped the object plane (x, y, z) to the image plane (X, Y, Z). This information was stored in a calibration file, displayed schematically in Figure 3.6.

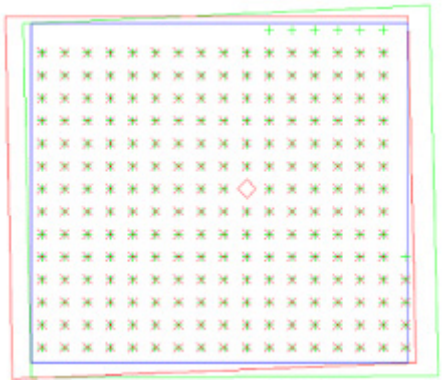

Figure 3.6: Example of a calibration file display

It comprises all calibration images (as in Figure 3.5) superimposed. As expected, the left and right images show distortion, resulting in trapezoidal fields of view for both cameras. The calibration corrects the images for this effect, and aligns them at the centre of the field of view with respect to the Fiducial point. The remaining calibration points also overlap, indicating a

successful calibration. Note that the calibration was performed at each measurement location in the vessel (see Figure 3.3).

3.2.4 Image acquisition and analysis

Following calibration, raw PIV images were captured and stored in files with a (*.TIF) extension. The experimental parameters were laser power and time between exposures for two subsequent frames (ΔT). Sample images captured by the left and right camera simultaneously are presented below.

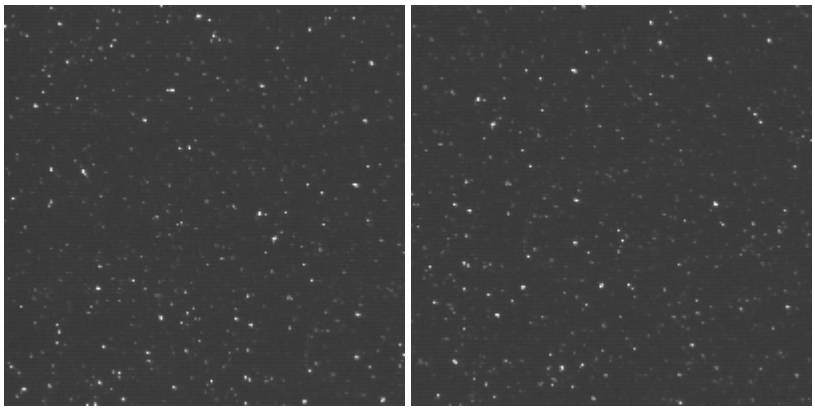

Figure 3.7: Raw PIV images from left and right camera respectively

Raw images were cross-correlated with a Gaussian peak search algorithm for preliminary 2-D PIV velocity fields. The *IA* size was 32×32 pixels with 50% overlap, generating 61×62 vectors. The PIV resolution was 1 mm (corresponding to the length of one *IA*), hence the field of view was 31×31.5 mm. Vector fields obtained from the raw images in Figure 3.7 are shown in Figure 3.8.

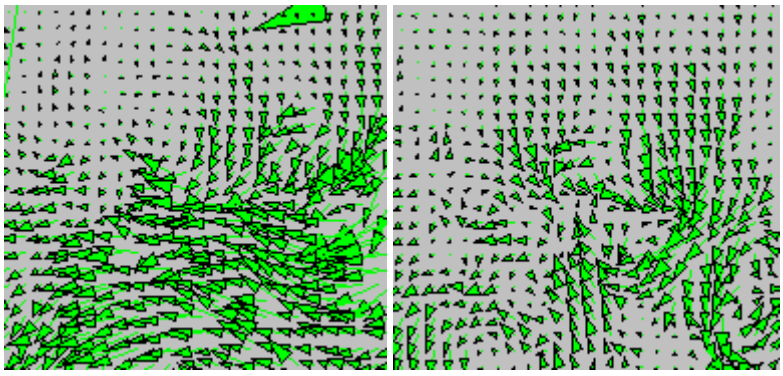

Figure 3.8: 2-D vector plots from left and right images in Figure 3.7 respectively

The quality of 2-D vector fields (in terms of spurious results) was assessed and used to re-adjust the cross-correlation parameters (i.e. peak to noise ratio, peak to average intensity ratio and signal cut off levels). If this was inadequate, images were re-captured with modified laser power and ΔT settings until satisfactory results were obtained. A smaller ΔT was required at greater impeller speeds and close to the impeller region, to limit the number of particles moving

out of the *IA*s between double exposures. Spurious vectors around the image edges were inevitable due to high pixel sensitivity in that region, so the aim was to minimize them in the centre, or close to the impeller blades.

Processing of the 3-D vectors was done automatically in Insight by simply initiating the appropriate command. The function used the calibration file created previously, and generated an output with a (*.V3-D) extension. This is basically an ASCII text file, with columns indicating positions (x, y, z) and velocity vectors (u, v, w), a small portion of which is shown below.

```
TITLE="E:\800rpm 1st Position Stereo\Vector\800rpm 1st Position Stereo
-23.0318, 17.6403, 0, -0.122058, -0.021009, 0.13616, 1, 0.0723488
-22.3652, 17.6403, 0, 9.99e+009, 9.99e+009, 9.99e+009, -1, 0
-21.6985, 17.6403, 0, 9.99e+009, 9.99e+009, 9.99e+009, -1, 0
-21.0319, 17.6403, 0, 9.99e+009, 9.99e+009, 9.99e+009, -1, 0
-20.3652, 17.6403, 0, 9.99e+009, 9.99e+009, 9.99e+009, -1, 0
-19.6986, 17.6403, 0, 9.99e+009, 9.99e+009, 9.99e+009, -1, 0
-19.0319, 17.6403, 0, 9.99e+009, 9.99e+009, 9.99e+009, -1, 0
-18.3652, 17.6403, 0, 9.99e+009, 9.99e+009, 9.99e+009, -1, 0
-17.6986, 17.6403, 0, 9.99e+009, 9.99e+009, 9.99e+009, -1, 0
```

Figure 3.9: Portion of a data file displaying 3-D PIV information

3.2.5 Data processing with Matlab

The data from the (*.V3-D) files were post-processed using self-developed codes in Matlab, whose basic data element is an array which does not require dimensioning. This allows the solution of problems concerning matrix formulations in a fraction of the time required to write a program in a scalar non-interactive language such as C or Fortran. Since it is desirable to study the velocity information in a matrix array, Matlab seemed to be a convenient processing tool.

The vector files generated by TSI insight included a column of 'choice codes' corresponding to each velocity vector, which defined their status. A description of the codes is provided in Table 3.1.

Table 3.1: Description of vector choice codes from TSI Insight

Choice code	*Description*
1	Highest correlation peak used for vector
2	2nd highest correlation peak used for vector
3	3rd highest correlation peak used for vector
4	Interpolated vector
5	Smoothed Measured Vecor. Was code 1, 2 or 3 before smoothing
0	Temporary blank. Vector did not pass validation criteria
-1	SNR* fail. Vector removed as correlation did not pass SNR validation criteria
-2	Removed point. The point has been disabled by a process polygonal grid
-3	3-D vector outside 2-D vector field overlap range

*Signal to noise

No interpolation or vector smoothing was done, hence choice codes 4 and 5 did not exist. Regions in which the impeller was in the field of view were blanked out by creating a digital polygonal grid prior to cross-correlation, which resulted in vectors with a choice code of -2. Those which could be accepted with confidence were labelled with a choice code of 1. The data were then processed using the following steps.

Firstly, two outer rows of vectors were removed from the velocity fields as they contained many spurious results. Next, vectors not corresponding to a choice code of 1 were eliminated. A range filter was also applied to remove obvious spurious vectors whose velocities exceeded $1.5 \times V_{tip}$ (where $V_{tip} = \pi ND$ is the tip velocity). The resultant holes were filled via linear interpolation of the surrounding vectors. Interpolation was considered to be acceptable since the holes were small and distributed within the velocity field, surrounded by many satisfactory vectors of choice code 1. A sample velocity field before and after interpolation is shown below.

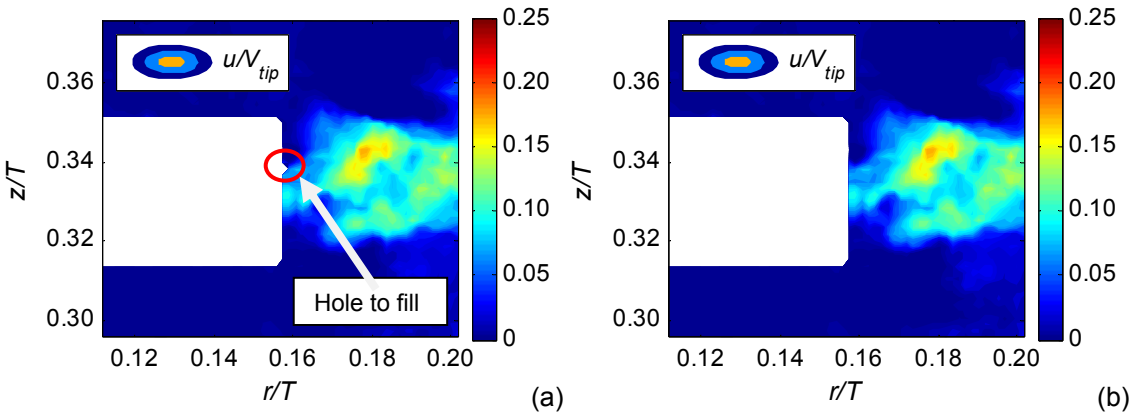

Figure 3.10: Radial velocity field (a) before and (b) after interpolation, from an instantaneous PIV measurement

3.2.6 High-speed PIV

High-speed PIV experiments were also carried out. The components were the same as those used for the stereo-PIV experiments, hence only differences in techniques will be described. The images were acquired using a single camera (analogous to standard 2-D PIV), and two in-plane velocity components were obtained (in the axial and radial directions). The outer pentagonal tank was rotated 90° clockwise such that the camera was aligned perpendicular to a flat surface. The laser used was a New-Wave Nd:YLF Pegasus with a wavelength of 527 nm. For camera calibration, the aforementioned target grid was placed in the centre of the light sheet, and a single image was captured, after which the pixel-to-mm conversion was deduced manually. The image acquisition rate was 5 kHz, and a total of 1000 image pairs were captured in each experiment. For the cross-correlation, *IA* sizes of 16×16 and 32×32 were employed for the first and second images (in each pair) respectively, to improve the correlation around the edges of the *IA* in the first image. No *IA* overlap was introduced. The PIV resolution varied between 0.6-0.7 mm in the various trials (corresponding to the size of an *IA* in the first image). The field of view was approximately 43×43 mm^2.

3.3 Mean flow field

This section describes the mean flow field generated by the EkatoMizer, and its variation with impeller speed and position. For presentation purposes, the data have been plotted on the $r-z$ (radial-axial) plane according to polar coordinates. Also note that this point forward, in the figures, the radial mean and rms velocity is denoted $<u>$ and u_{rms} respectively, and similarly for the axial and tangential velocity components. Throughout this thesis, all velocities have been made dimensionless by the impeller tip speed ($V_{tip}=\pi ND$), the turbulent kinetic energy (k) by V_{tip}^2, and the dissipation rate (ε) by N^3D^2.

3.3.1 Mean flow field

The mean radial velocity $\bar{u}$ (or $<u>$ in figures) normalised by the tip speed ($V_{tip}=\pi ND$), obtained at Position 1 and impeller speed 1500 rpm (corresponding to $\mathrm{Re}=2.3\times10^5$), is presented in Figure 3.11. As may be observed, the radial velocity above and below the impeller is close to being stationary, even at this high rotational speed. However at the impeller level, a strong radial flow moving horizontally away from the blade is evident. The maximum radial velocity ($\sim 0.12V_{tip}$) is found at the blade edge. This radial flow characterises the discharge stream for the EkatoMizer, as it was found to be more significant than the axial and tangential components further away from the impeller (Position 2).

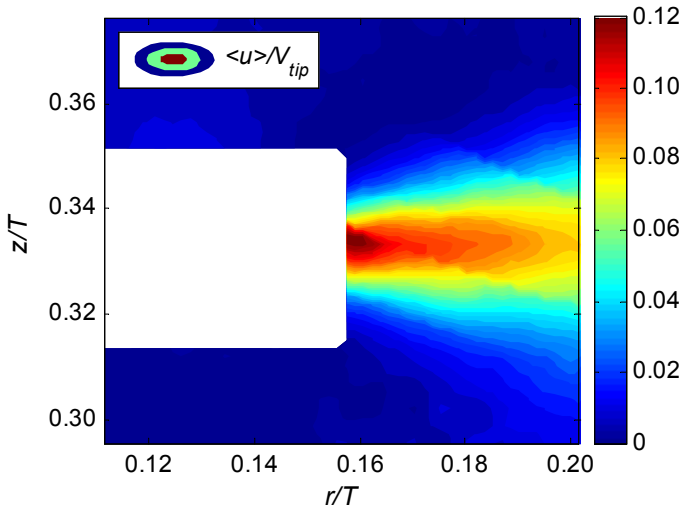

Figure 3.11: Mean radial velocity field obtained at Position 1, 1500 rpm

The mean axial velocity field is shown in Figure 3.12, where the velocity range is comparatively lower than the radial flow. The axial velocity is close to zero in the discharge stream; conversely it reaches a maximum of $\sim 0.03V_{tip}$ above and below the impeller. Note that a positive axial direction is defined as moving upwards, hence negative and positive velocities above and below the impeller suggest the flow moving downward and upwards respectively. Compared to the maximum radial velocity ($0.12V_{tip}$) the maximum axial velocity is relatively small; hence the axial

flow is not considered to be characteristic of the EkatoMizer. The fluid is drawn into the impeller region axially, and discharged radially.

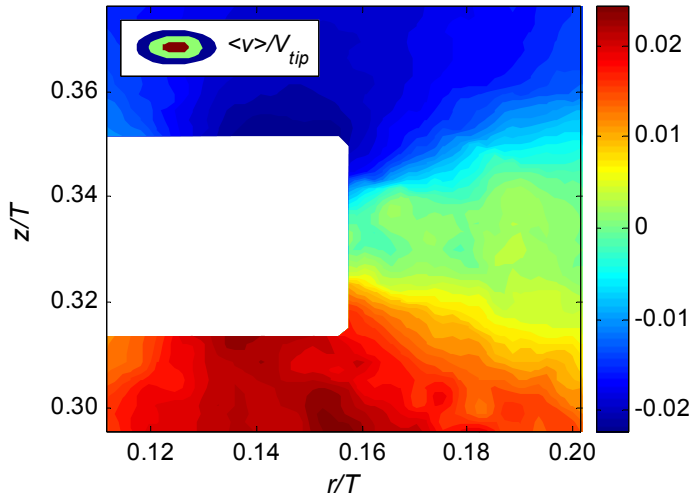

Figure 3.12: Mean axial velocity field obtained at Position 1, 1500 rpm

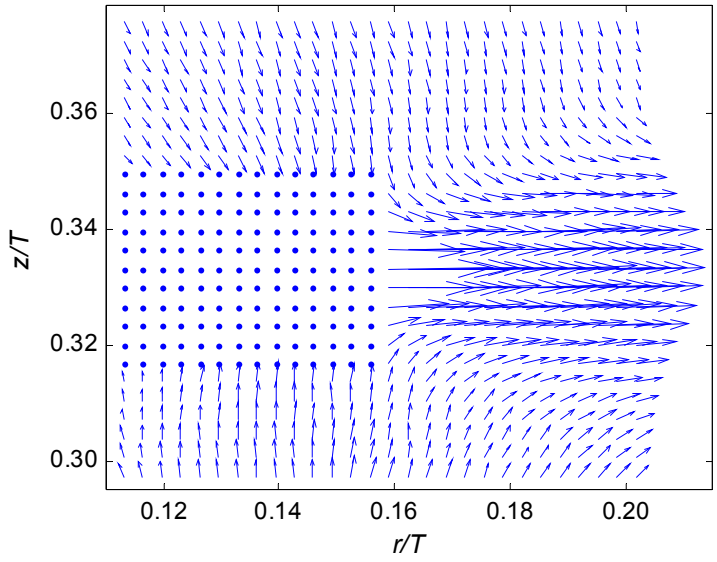

Figure 3.13: Vector plot of mean axial and radial velocity at Position 1, 1500 rpm

Both axial and radial mean components are presented collectively in the vector plot of Figure 3.13. This illustration enables clarification of the discharge stream, and also the relative magnitudes of the velocities with the size of their respective arrows. In the present case the axial and radial velocities appear to be spatially segregated, suggesting no mixed flow; rather a pure radial flow in the discharge stream. However, a vector plot of the axial-radial velocities from an instantaneous PIV measurement suggests otherwise, as shown in Figure 3.14. The picture here is very different to the mean field. Although a strong radial velocity can be observed in the discharge stream, it is combined with axial flow. Secondly, a vortex is identified above the discharge stream. Similar flow structures were identified in many of the instantaneous velocity fields. These turbulent structures are smoothed out during the averaging process, so although

the mean field enables analysis of the dominant flow patterns (such as the suction and discharge streams), they provide no information of unsteady flow structures.

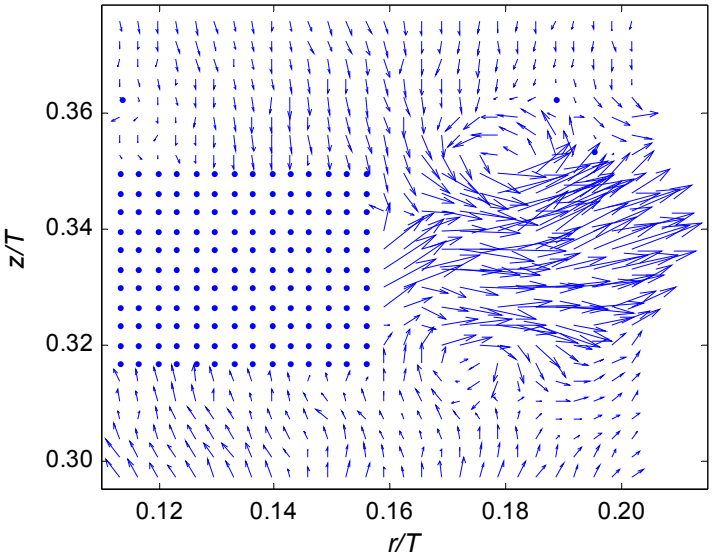

Figure 3.14: Vector plot of instantaneous axial and radial velocity at Position 1, 1500 rpm

Finally, the mean tangential velocity field obtained at the same location is presented in Figure 3.15. It is immediately evident that the range of velocities exceeds that of the radial component. The maximum tangential velocity was found to be $\sim 0.14 V_{tip}$. The negative sign convention represents the flow moving away from the viewer. Although the maximum tangential velocity exceeds the maximum radial velocity, it is not as evenly distributed across the field of view. The maximum tangential velocity is found at the blade edge, similar to the radial velocity, but the large magnitude is confined very much in the impeller region. Thus the strong tangential flow is directly attributable to the impeller motion itself, and is the flow being pushed behind the impeller blade.

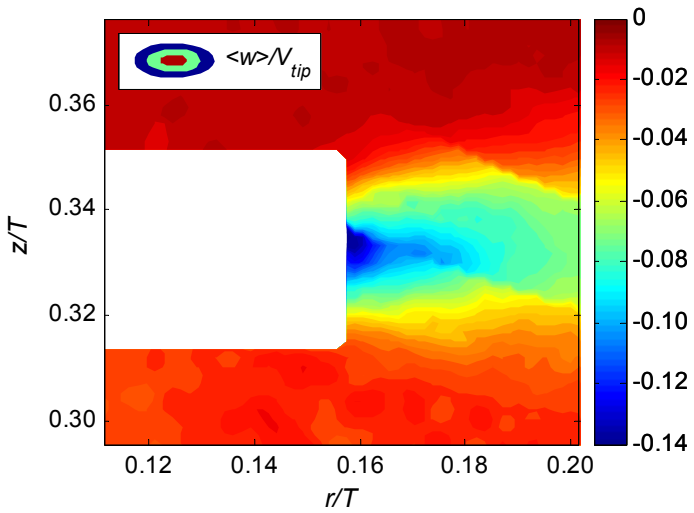

Figure 3.15: Mean tangential velocity field obtained at Position 1, 1500 rpm

3.3.2 Variation of flow with impeller speed and position

Figure 3.16 depicts the mean radial velocities obtained in the impeller region, at impeller speeds 1500, 2000 and 2600 rpm respectively. As may be observed, they scale similarly with the tip speed (although they are not exactly the same). An invariable flow distribution was achieved for all three velocity components across the range of impeller speeds.

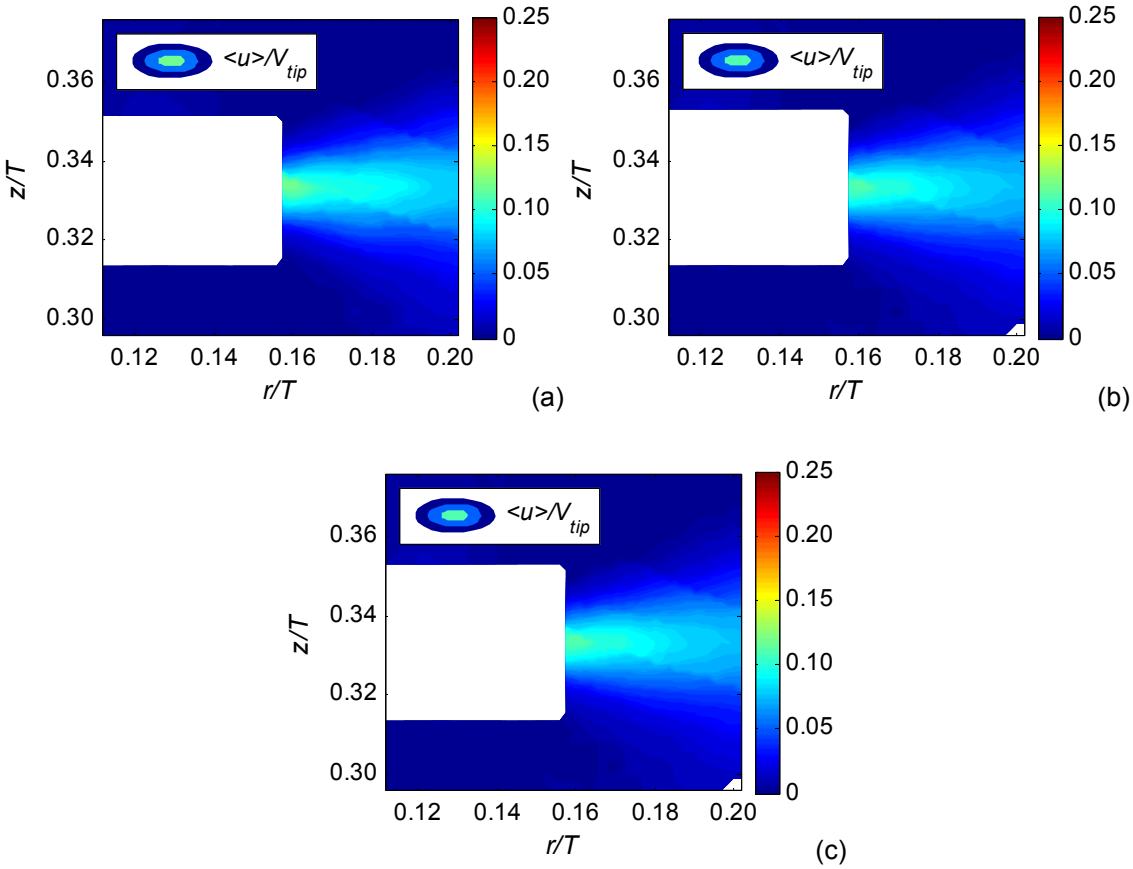

Figure 3.16: Mean radial velocities at Position 1 (a) 1500 (b) 2000 and (c) 2600 rpm

The mean flow field distribution can also be compared between the impeller region and discharge stream (Positions 1 and 2 respectively). Figure 3.17 to Figure 3.19 show the flow fields obtained in both locations, at 1500 rpm. Measurements in the discharge stream were obtained such that the blade edge was positioned at the left hand side of the viewing field. Thus Figure 3.17(a) and (b) may be superimposed at the blade edge. It may be observed that mean velocities scale equivalently with the tip speed at both locations, and the magnitudes and distributions of all three velocity components are consistent. The small structural changes may be due to the the images being processed in a discretized manner. For an exact comparision, the locations of the *IA*s mapped onto the image plane must be identical. With the view further away from the impeller, it is clearer that the relatively strong tangential flow decays more rapidly than the radial flow. It can be seen in Figure 3.17(b) and Figure 3.19(b) respectively that the mean radial flow is approximately $0.08V_{tip}$ horizontally away from the impeller, whereas the tangential velocity is approximately $0.05V_{tip}$ at the same location. This supports the assumption of a characteristic radial discharge stream at the impeller level. The axial flow remains

stationary further into the discharge stream, also confirming that the flow is drawn into the impeller axially, and discharged radially.

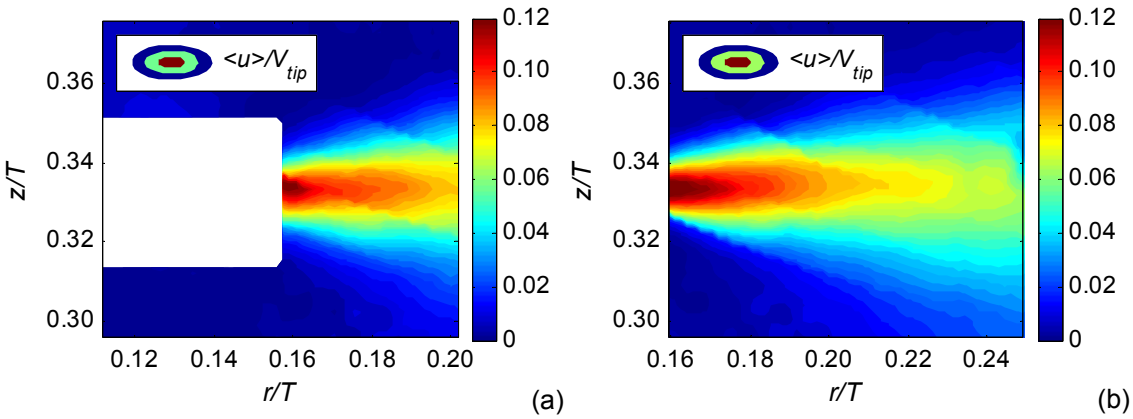

Figure 3.17: Mean radial flow in (a) impeller region and (b) discharge stream at 1500 rpm

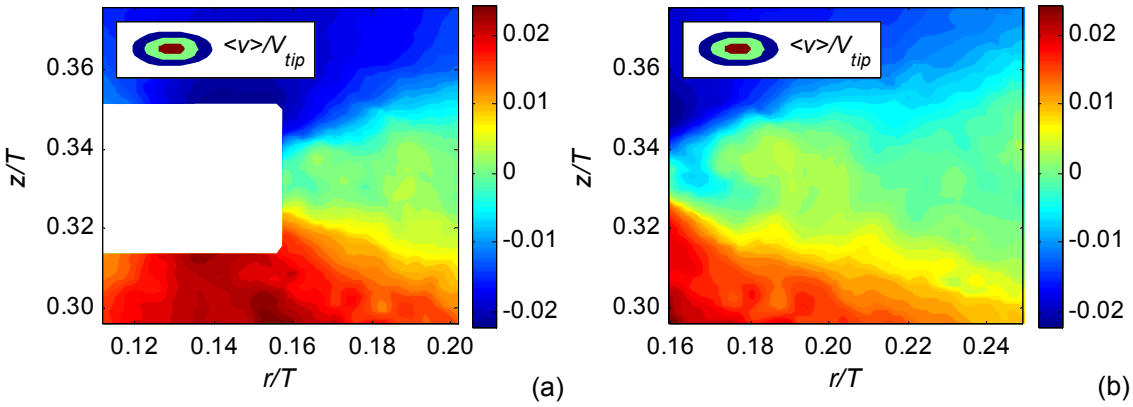

Figure 3.18: Mean axial flow in (a) impeller region and (b) discharge stream at 1500 rpm

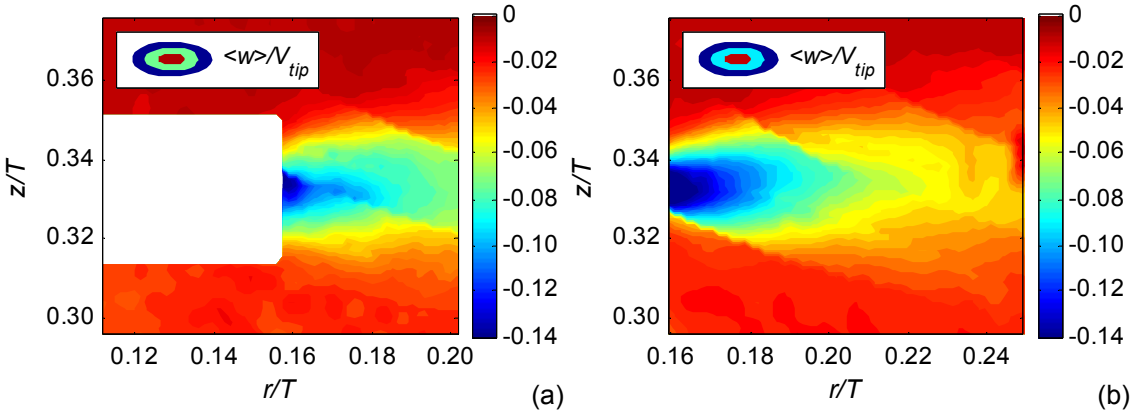

Figure 3.19: Mean tangential flow in (a) impeller region and (b) discharge stream at 1500 rpm

3.4 Integral length scales

In turbulent flows, the turbulent motions range in size from the width of the flow field to much smaller scales. As the Reynolds number of the flow increases, the size of the smaller scales decreases and subsequently the difference in magnitude between the largest and smallest scales also increases. These characteristic turbulent motions (localized within a specific region) are referred to as eddies. Eddies of size l have a characteristic velocity $u(l)$ and timescale $\tau(l)$ (Pope, 2000).

Since energy is dissipated at the smallest scales, calculation of the dissipation rate directly from its definition requires resolution of the velocity field at the Kolmogorov scale, which is the smallest scale of the flow. As previously mentioned, this has proved to be the biggest challenge with the PIV technique. Alternatively, approximations of the dissipation rate based on dimensional analysis have been proposed and widely employed for estimations in stirred tanks. The dimensional relations have a varied form in different sources of literature, but are all dependent on a characteristic velocity and length scale. Most approximations are based on the assumption of a spatially uniform length scale, proportional to the impeller diameter (Laufhutte and Mersmann, 1985; Calabrese and Stoots, 1989; Kresta and Wood, 1991). On the contrary, many studies (Baldi, 2004; Khan, 2005) have shown that this assumption does not hold across the entire vessel volume; rather it over predicts the length scale in the impeller region, and under predicts it in the bulk. In other cases, a uniform integral length scale has been calculated directly, and used instead (Wu and Patterson, 1989, Pettersson and Rasmuson, 1997). As a result, knowledge of the integral length scale is necessary to validate the underlying assumptions, as well as to assess the accuracy of the proportionality constant. The remainder of this section describes calculation of the integral length scale from the autocorrelation function from PIV data.

3.4.1 The 1-D autocorrelation function

Computation of the autocorrelation function is the traditional way to estimate length scales in the flow (Hinze, 1975). The 1-D, two-point autocorrelation function may be expressed as:

$$R_{u_i}\left(x_j,\xi_{x_j}\right)=\frac{\overline{u'_i(x_j)u'_i(x_j+\xi_{x_j})}}{\overline{u'_i(x_j)^2}} \tag{2.6}$$

where u'_i is the fluctuating velocity component in the Cartesian direction i, x_j is a point in the Cartesian direction j, and ξ_{x_j} the distance in the given direction. The denominator normalises the correlation function, such that the correlation coefficient at zero lag is unity. Autocorrelation of the velocity field provides information regarding the correlation distance between two velocity points in the flow field. It follows that as the distance ξ_{x_j} increases, the degree of correlation decreases, and becomes zero where there is no correlation past a finite distance ξ^*. This situation is presented schematically in Figure 3.20.

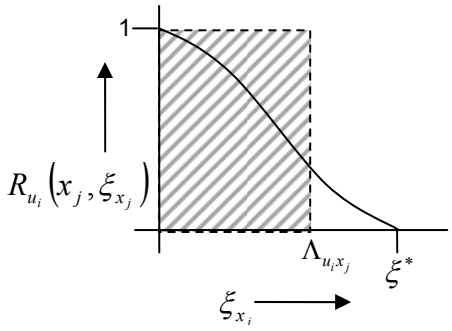

Figure 3.20: 1-D autocorrelation function

The integral length scale may be obtained by integrating the autocorrelation function from zero to infinity as follows:

$$\Lambda_{u_i x_j}\left(x_j\right) = \int_0^\infty R_{u_i}\left(x_j, \xi_{x_j}\right) d\xi_{x_j} \tag{2.7}$$

Two types of integral length scales can be defined; longitudinal or lateral, depending on the velocity component being correlated and the direction of its correlation. In Equation (2.7), if $i = j$, the longitudinal length scale is obtained. Alternatively if $i \neq j$, the lateral length scale is obtained. For instance, the longitudinal length scale of the radial velocity component (u) may be given by:

$$\Lambda_{ux}\left(x\right) = \int_0^\infty R_u\left(x, \xi_x\right) d\xi_x \tag{2.8}$$

For truly isotropic turbulent flows, the ratio of the longitudinal to lateral length scale is 2:1 (Pope, 2000). The autocorrelation function given by Equation (2.6) considers correlation in a single direction, and is appropriate to apply to single-point measurement techniques. More specifically for LDA, the Eulerian integral time scale is obtained by integrating the autocorrelation function of the time-series data (with respect to time), and subsequently converting it to the 1-D length scale via the mean velocity, as was done by Pettersson and Rasmuson (1997). However, this is only possible if Taylor's frozen turbulence hypothesis is invoked, which assumes that for a small time interval, the turbulent structure is frozen in space, and convected along with the mean flow velocity. This approximation is acceptable for flows which have a convective velocity that is large compared to the turbulent fluctuations, but in cases where the turbulence intensity is large (Equation (2.4)), such as close to the impeller region of a stirred vessel, the analogy is unlikely to pertain (Khan, 2005). By applying Taylor's hypothesis, it is only possible to obtain 1-D longitudinal length scales. Wu and Patterson (1989) and Wu *et al*. (1989) suggested corrections to account for three-dimensionality in the length scale, by using a vector sum of the longitudinal length scales determined for all three coordinate directions. With PIV measurements, there is no need to invoke Taylor's frozen turbulence hypothesis, since the information is spatially distributed.

The 2-D velocity vector fields measured by PIV may be taken advantage of in the analysis of turbulent length scales. Calculation of the 2-D autocorrelation function enables determination of

both longitudinal and lateral length scales. The advantage is further extended to the possibility of measuring a 2-D integral length scale, which is not possible with single-point measurement techniques. The following section describes calculation of 2-D integral length scales from the autocorrelation of PIV data.

3.4.2 The 2-D autocorrelation function

2-D and 3-D PIV enable measurement of two (u,v) and three (u,v,w) velocity components in the $x-y$ plane, respectively. As a result, a 2-D autocorrelation function may be computed for an instantaneous turbulent velocity field. The 2-D spatial autocorrelation function for a given fluctuating velocity component u'_i may be expressed as:

$$R_{u_i}\left(x,y,\xi_x,\xi_y\right)=\frac{\overline{u'_i(x,y)u'_i(x+\xi_x,y+\xi_y)}}{\overline{u'_i(x,y)^2}} \tag{2.9}$$

The 2-D autocorrelation function provides the correlation coefficient between two velocity fields, separated by distances ξ_x and ξ_y in the x and y directions respectively, relative to the point of origin (x,y). Since autocorrelation is effectively cross correlation between two identical velocity fields, the autocorrelation coefficients provide information regarding the degree of association between two points in the same field. Inherently, this leads to determination of the integral length scale. 1-D length scales for the velocity components may be obtained as an integral of the autocorrelation function in either the x or y direction.

$$\Lambda_{u_i x_j}\left(x,y\right)=\int_0^\infty R_{u_i}\left(x,y,\xi_x,\xi_y\right)d\xi_{x_j} \qquad \begin{cases} j=x\ \ \xi_y=0 \\ j=y\ \ \xi_x=0 \end{cases} \tag{2.10}$$

If the autocorrelation function of a given velocity component is integrated with respect to its corresponding Cartesian direction (when $i=j$ in Equation (2.10)), the longitudinal 1-D length scale is obtained. When it is integrated with respect to an alternate Cartesian direction (i.e. when $i\neq j$), the lateral 1-D length scale is obtained. For instance, the longitudinal 1-D length scale of the radial velocity component (u) may be expressed as:

$$\Lambda_{ux}\left(x,y\right)=\int_0^\infty R_u\left(x,y,\xi_x,0\right)d\xi_x \tag{2.11}$$

In the above expression, ξ_y is zero as the autocorrelation coefficients being integrated correspond to points of zero lag in the y direction. The autocorrelation function returns a matrix of coefficients since the input velocity field is also a matrix of values. It follows that the autocorrelation function at zero lag in a particular direction (e.g. $\xi_y=0$) is a vector. In a similar fashion, 1-D longitudinal and lateral length scales may be obtained for the axial velocity component. Note that only lateral length scales may be calculated for the tangential velocity (in either the x or y directions); determination of its longitudinal 1-D length scale requires out-of-plane measurements.

2-D and 3-D PIV data also enable determination of a 2-D integral length scale, by integrating the autocorrelation function with respect to both coordinates. This is the integrated volume of the autocorrelation function as follows:

$$\Lambda_{u_i}(x,y) = \left(\int_0^{\infty} \int_0^{\infty} R_{u_i}(x,y,\xi_x,\xi_y) d\xi_x d\xi_y \right)^{1/2} \tag{2.12}$$

The autocorrelation function was calculated from PIV measurements of the instantaneous velocity fields, using an inbuilt Matlab function *xcorr2*. The function performed a two dimensional convolution of the velocity vector matrix with itself, which was based on a 2-D Fast Fourier Transform (FFT) algorithm.

Before the FFT could be applied, the data were treated for 'end effects.' The FFT algorithm assumes that the input data is periodic, whereas in reality the velocity field being convoluted could go on infinitely without repetition, or comprise stretches of non-periodic data. As a result, the convolution theorem could falsely pollute one side of the output data matrix with some 'wrapped-around' data from the opposite side of the input matrix. As a result, a buffer zone was created of zero-padded values at two sides of the input matrix. The general rule is to pad the data with a number of zeros equal to the maximum positive or negative durations of the input data, whichever is larger (Press *et al.*, 1992). This corresponds to the length of the matrix in each direction. The zero padding also ensured that the autocorrelation function always decayed to zero.

Although the limits of integration in Equations (2.10), (2.11) and (2.12) are zero to infinity, in practice the upper limit of integration was set to be the first zero crossing of the autocorrelation function. The negative contribution of the integral beyond this point would reduce the value of the overall integral, and subsequently the integral length scale.

Autocorrelation of the velocity field returns individual autocorrelation coefficients; hence the integration could be performed in two ways. In the first approach, a curve could be fitted to the coefficients and integrated analytically between the limits. This method has been implemented by Pettersson and Rasmuson (1997). A disadvantage of this technique is that curve fitting may cause some smoothing of the data, and peculiarities of the autocorrelation function intrinsic to turbulence flows may be lost. On the other hand smoothing of the autocorrelation function may be a desirable outcome for noisy data, or where decaying periodic fluctuations are evident, as in the case of Pettersson and Rasmuson (1997). In the current study, time averaged measurements around 360° of the impeller were obtained, so periodic fluctuations would automatically be eliminated. Another limitation is that the type of curve fit would have to be specified for the autocorrelation function for each instantaneous velocity field to ensure a good fit. This would require manual intervention and be very time consuming for a data set comprising 500 instantaneous velocity fields. In their study, Pettersson and Rasmuson (1997) had to specify two types of curve fits for the data in case one provided unsatisfactory results.

Alternatively, numerical integration of the raw data could be carried out. This would preserve details of the autocorrelation function (to some degree) and a single algorithm could be applied to the entire data set without further adjustments. In order to carry out both single and double

integration, a simple numerical quadrature technique based on Simpson's rule was applied. The code was self-written in Matlab, details of which are given in Appendix I.

3.4.3 Integral length scale results

The 1-D and 2-D integral length scales were investigated as a function of position in the flow and impeller speed. The velocity fields were not processed using any standard deviation filters as it was preferred to retain fluctuations of the turbulent flow. Only a range filter was applied *a priori* to eliminate vectors exceeding $1.5V_{tip}$. The length scales were calculated for each turbulent velocity field, and subsequently averaged over the PIV data set. In literature the integral length scale is often assumed to be proportional to the impeller diameter or blade width; for instance $\Lambda = D$ (Laufhutte and Mersmann, 1985), $\Lambda = D/2$ (Stoots and Calabrese, 1989) or $\Lambda = W/2$ (equivalent to $D/10$ for a Ruston turbine, Kresta and Wood, (1991)). In the present case the EkatoMizer has teeth rather than blades; hence the width W is defined as that of the impeller. The averaged values normalized by the blade width ($W = 8$ mm) are presented in Table 3.2.

Table 3.2: Integral length scales obtained at various locations and impeller speeds

Position	*rpm*	$*\Lambda_{ux}/W$	Λ_{uy}/W	Λ_u/W	Λ_{vx}/W	$*\Lambda_{vy}/W$	Λ_v/W	Λ_{vx}/W	Λ_{wy}/W	Λ_w/W
1	800	0.41	0.24	0.33	0.33	0.51	0.44	0.28	0.20	0.28
	1500	0.39	0.23	0.33	0.28	0.49	0.38	0.25	0.19	0.25
	2000	0.39	0.23	0.33	0.29	0.51	0.39	0.25	0.19	0.26
	2600	0.38	0.21	0.33	0.31	0.50	0.43	0.23	0.16	0.25
2	800	0.55	0.25	0.40	0.31	0.55	0.45	0.38	0.23	0.33
	1500	0.55	0.25	0.41	0.30	0.55	0.44	0.35	0.21	0.30
	2000	0.54	0.24	0.40	0.30	0.50	0.43	0.35	0.21	0.30
	2600	0.56	0.26	0.41	0.34	0.55	0.48	0.39	0.23	0.33

*1-D Longitudinal length scale

The results indicate that all length scales obtained from the radial velocity component increase with distance away from the impeller. For instance, at 1500 rpm Λ_{ux}, Λ_{uy} and Λ_u increase from $0.39W$ to $0.55W$, $0.23W$ to $0.25W$ and $0.33W$ to $0.40W$ respectively. Comparable increases are evident at all other impeller speeds. Thus it may be concluded that the commonly used factor $W/2$ for approximating the integral length scale provides an over estimate in the impeller region (Position 1). Further into the discharge stream (Position 2), the length scales are comparably larger, with Λ_{ux} slightly exceeding $W/2$. This further emphasizes that a single value cannot realistically represent length scales across an entire flow field.

This trend has also been described in literature, for which 1-D longitudinal length scales were obtained from the radial velocity component. Results from previous findings are summarised in Table 3.3. In one of the earlier works, Cutter (1966) acquired streak photography measurements of the mean and fluctuating velocity components of water in a stirred tank, from which Λ_{ux} was calculated in the impeller stream. Values of approximately $0.2W$ and $0.4W$ were found at radial locations $r/T = 0.17$ and 0.35 respectively. Wu and Patterson (1989)

studied the flow generated by an RDT using LDA, and reported minimum and maximum values of $0.1W$ and $0.4W$ respectively, for Λ_{ux} in the impeller stream. In an analogous fashion, Mahouast *et al*. (1989) reported minimum and maximum values of around $0.48W$ and $1.32W$ for Λ_{ux} close to the impeller and free surface. Later, Lee and Yianneskis (1998) obtained the distribution of Λ_{ux} along the impeller stream, and recorded a minimum value of $0.1W$ at $r/T = 0.17$, and a maximum of $0.3W$ at $r/T = 0.35$. In a more recent study, Khan (2005) investigated the flow generated by a PBT using PIV, which enabled the determination of both 1-D and 2-D integral length scales. From the radial velocity component, Khan (2005) found Λ_{ux} to be approximately $0.3W$ close to the impeller region, $0.5W$ in the bulk and $1.1W$ at the surface. Also, Λ_u increased from $0.4W$ to $1.4W$ between the impeller region and free surface.

Table 3.3: Integral length scales reported in literature

Author	*Length scale*	*Value*	*Region*	*Experiment*
Cutter (1966)	$*\Lambda_{ux}/W$	0.2 (*r/T*=0.17) 0.4 (*r/T*=0.35)	Impeller stream Impeller stream	Photographic
Wu and Patterson (1989)	$*\Lambda_{ux}/W$	0.1 min 0.4 max	Impeller stream Impeller stream	RDT, LDA
Mahouast et al. (1989)	$*\Lambda_{ux}/W$	0.48 min 1.32 max	Impeller Surface	RDT, 2-D LDA
Lee and Yianneskis (1998)	$*\Lambda_{ux}/W$	0.1 (*r/T*=0.17) min 0.3 (*r/T*=0.35) max	Impeller stream Impeller stream	RDT, LDA
Khan (2005)	$*\Lambda_{ux}/W$ Λ_u/W	0.3 1.1 0.4 1.4	Impeller Surface Impeller Surface	PBT, PIV

*1-D Longitudinal length scale

Notwithstanding the different impellers used and different measurement techniques, the results of Cutter (1966), Wu and Patterson (1989) and Lee and Yianneskis (1998) agree reasonably well, as do those of Mahouast *et al*. (1989) and Khan (2005). Results of the current study (specifically Λ_{ux} and Λ_u in the impeller region) are most similar to those reported by Khan (2005).

The analysis above focused primarily on the length scales obtained from the radial velocity component, since this is most commonly cited in literature. In this study, length scales resulting from the axial velocity component conform to the same trend at all impeller speeds except for Λ_{vx} at 800 rpm and Λ_{vy} at 2000 rpm, for which the length scales decreased from $0.33W$ to $0.31W$ and $0.51W$ to $0.50W$ (between Positions 1 and 2 respectively). Since the decreases are relatively small, they could be due to experimental error. Khan (2005) reported the same trend for the axial velocity length scales at 300 rpm. Here, the length scales of the tangential velocity (Λ_{wx}, Λ_{wy} and Λ_w) increase away from the impeller consistently at all impeller revolutions.

The effect of the impeller speed on the length scales may be isolated by analysing results at both locations independently. Figure 3.21(a) and (b) show the length scales obtained at Position 1 and 2 respectively. The bars represent 95% confidence intervals about the mean values.

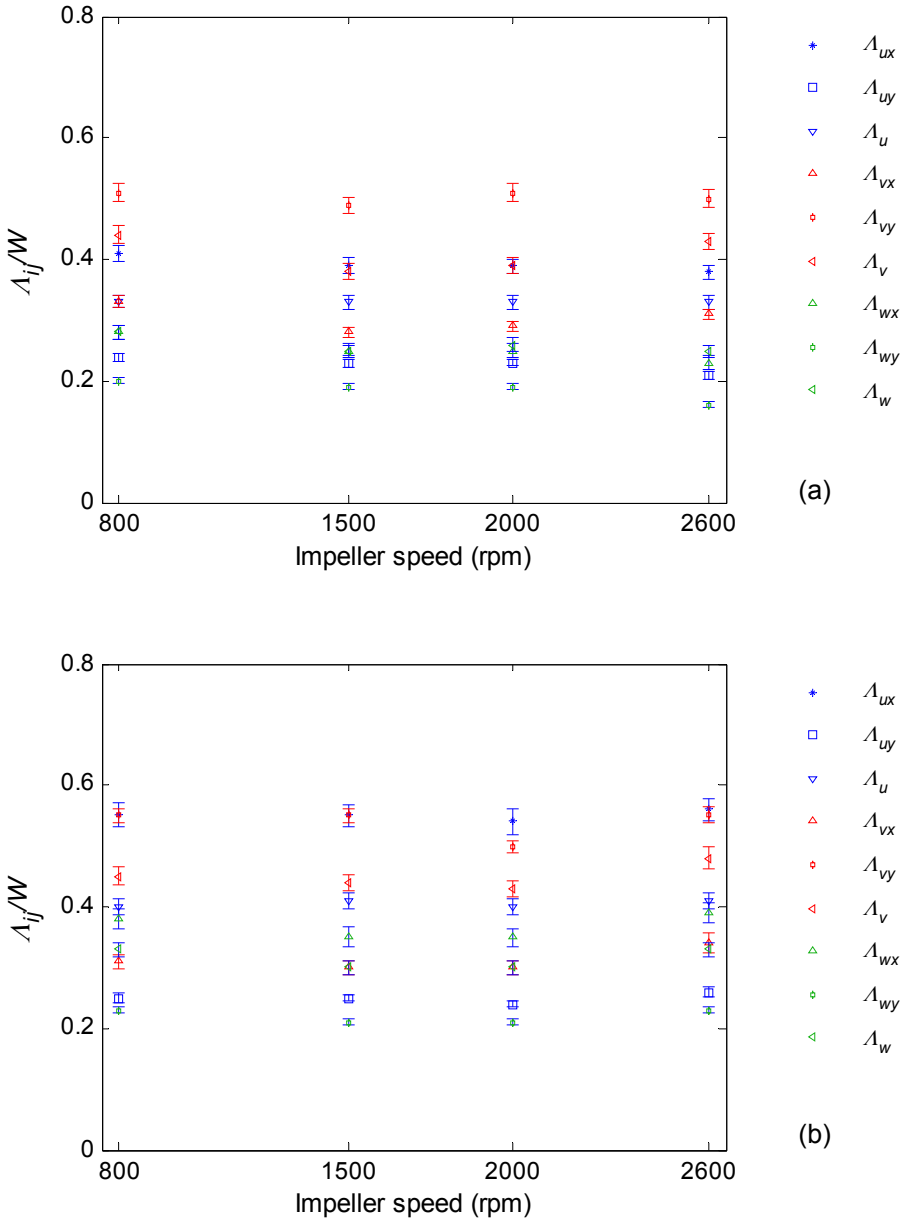

Figure 3.21: Integral length scales at Positions (a) 1 and (b) 2 for various impeller speeds

The impeller speed has a negligible effect on the length scales obtained from the radial velocity component, as they remain approximately constant. An order is maintained across the impeller speeds at both positions being $\Lambda_{ux} > \Lambda_{u} > \Lambda_{uy}$; the 1-D longitudinal length scale is consistently greater than the 1-D lateral length scale, and the 2-D integral length scale is within the limits of the two. For isotropic flow, the ratio of the longitudinal to lateral length scale for any given velocity component is 2:1 (Pope, 2000). At Position 1, the average ratio is 1.73, and at Position 2 it is 2.20. At neither position is the flow perfectly isotropic. The spread between the radial

length scales slightly increased further into the discharge stream. For instance at Position 1 the length scales ranged between $0.21W - 0.41W$, whereas at Position 2 the range increased to $0.24W - 0.56W$.

Trends of the length scales in the axial and tangential directions exhibit some degree of fluctuation with respect to impeller speed. There is no theoretical reason for these fluctuations, although an analysis of the 95% confidence intervals around the mean values indicates that they are approximately constant with variations in impeller speed in most cases.

Despite the slight irregularities, an order is retained at the two positions across all impeller speeds; being $\Lambda_{vy} > \Lambda_{v} > \Lambda_{vx}$. Analogous to the radial case, the 1-D longitudinal length scale is greater than the lateral length scale. The average ratios of the length scales at Position 1 and 2 are 1.67 and 1.72. Considering the confidence intervals, the difference in ratios is not significant. However determination of the anisotropy tensor in §3.6 illustrates that the flow is highly anisotropic near the impeller region, and returns to isotropy further away from it.

For length scales of the tangential velocity component, no clear order is preserved at either location as for the previous two cases. In the discharge stream (Position 2), it appears that $\Lambda_{wx} > \Lambda_{w} > \Lambda_{wy}$, although in the impeller region (Position 1), Λ_{wx} and Λ_{w} overlap between 800 and 1500 rpm. In this case both Λ_{wx} and Λ_{wy} are 1-D lateral length scales. To evaluate isotropy of the flow in terms of length scale ratios, the longitudinal length scale Λ_{wz} is required, which cannot be obtained from planar stereo-PIV measurements.

The main conclusions may be summarised as follows:

- 1-D longitudinal length scales are greater than the lateral length scales obtained from both axial and radial velocity components. In both cases, an evaluation of the ratios suggests anisotropic flow.
- Generally, the range and magnitude of length scales obtained from the axial velocity are greater than those obtained from the radial velocity, which are in turn greater than those obtained from the tangential velocity component, at both locations in the vessel.
- The value $W/2$ over estimates the length scales in the impeller region.
- A single value such as $W/2$ cannot be used to represent length scales across the entire flow field of a flow generated by a rotating impeller.

3.5 rms velocities and TKE

To obtain the root-mean-square (rms) velocities, first ensemble averages were obtained from the set of 500 vector fields. These were subtracted from the instantaneous velocities for the fluctuating components, which were squared, averaged and square-rooted, point-by-point over the field of view. The rms velocity for the i^{th} component is defined as follows, where u'_i is the fluctuating velocity in the i^{th} coordinate direction.

$$\tilde{u}_i = \sqrt{\overline{u'^2_i}} = \sqrt{\overline{(u_i - \overline{u_i})^2}} \tag{2.13}$$

Normalized axial and radial rms velocities in the impeller region (Position 1) at 1500 rpm are shown in Figure 3.22(a) and (b) respectively. As may be observed, the axial and radial rms velocity distributions are similar, although they differ slightly in magnitude. Their maximum values are $0.05V_{tip}$ and $0.06V_{tip}$ respectively; a difference of 20%. Stereo-PIV enables deduction of the tangential rms velocity as well, displayed in Figure 3.22(c).

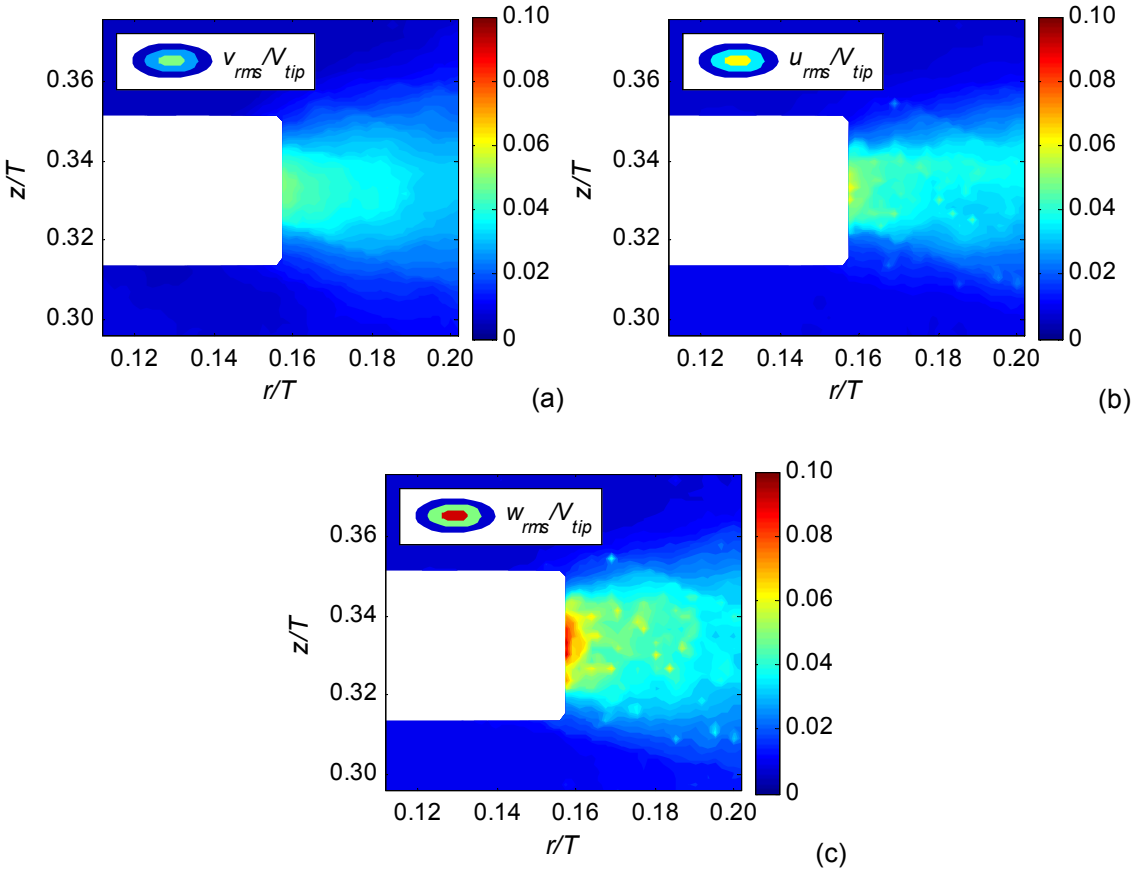

Figure 3.22: (a) Axial and (b) radial and (c) tangential rms velocities, Position 1, 1500 rpm

The tangential rms velocity is larger than the axial or radial components, with a maximum of $0.1V_{tip}$. For truly isotropic flows $\tilde{u}^2 \approx \tilde{v}^2 \approx \tilde{w}^2$. Under this assumption, the tangential rms velocity may be approximated as $\tilde{w}^2 = \left(\tilde{u}^2 + \tilde{v}^2\right)/2$. If the assumption was valid for the flow in question, the maximum tangential rms velocity would be $\sim 0.055V_{tip}$. The true value clearly indicates anisotropy of the flow, and suggests that the isotropic assumption underestimates the turbulence level. Subsequently, although standard 2-D PIV may provide a reliable estimate of the measurable components, it is inadequate in predicting the turbulence in the unknown direction using an isotropic assumption.

The full definition of the turbulent kinetic energy (TKE) k encompassing all three fluctuating velocity components is given following:

$$k = \frac{1}{2}\left(\overline{u'^2} + \overline{v'^2} + \overline{w'^2}\right) \tag{2.14}$$

Since standard 2-D PIV provides only two of three velocities (namely the axial and radial components), the turbulent kinetic energy may be estimated using the pseudo-isotropic assumption, given below:

$$k = \frac{3}{4}(\overline{u'^2} + \overline{v'^2}) \tag{2.15}$$

In stereo-PIV, the pseudo-isotropic assumption is not required, and the correct definition of the TKE should be used instead. The TKE estimates from two and three rms velocity components are shown in Figure 3.23(a) and (b) respectively.

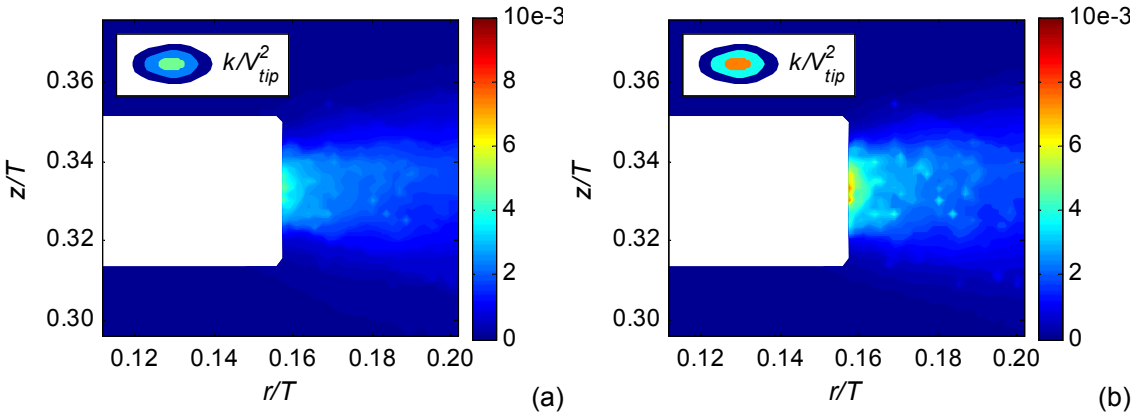

Figure 3.23: TKE (a) pseudo-isotropic assumption (b) full definition, Position 1, 1500 rpm

From Figure 3.23(a), the maximum TKE was found to be $0.005V_{tip}^2$ at the blade edge, consistent with the axial and radial rms velocity regions of maxima. In Figure 3.23(b), it is evident that the TKE is much higher, with a maximum value of $0.008V_{tip}^2$ (60% greater than the pseudo-isotropic result). As expected, this is because the isotropic assumption underestimates the tangential rms velocity (by approximately 45% in the present case). However, the difference between the TKE obtained from two and three components is not significant across the entire field of view. Horizontally away from the blade the TKE reduces to approximately $0.002V_{tip}^2$ in both cases. This is logical, given that the tangential rms velocity is only significantly greater than the axial and radial counterparts close to the blade edge. Subsequently, the TKE estimate would only be affected appreciably within this region. A previous study of Khan (2005) showed that the TKE was predicted very well using the pseudo-isotropic assumption for a PBT stirred flow, but evidently this is not a general result.

3.6 Anisotropy of the flow

In the previous sections, isotropy of the flow has been generally assessed by analysing ratios of the longitudinal to lateral integral length scales, and observation of the rms velocities. The ratios were found to deviate from the isotropic value of 2, whilst the rms velocities varied in magnitude

and distribution. Both results suggested that the turbulent flow field is anisotropic. Alternatively, anisotropy of the flow may be examined through the anisotropy tensor a_{ij} which is characterized using the Reynolds stresses (Pope, 2000):

$$a_{ij} = \overline{u_i u_j} - \frac{2}{3} k \delta_{ij} \tag{2.16}$$

In Equation (2.16) above, δ_{ij} is the Kronecker delta, which is 1 if $i = j$ and 0 if $i \neq j$. The normalized anisotropy tensor is defined as:

$$b_{ij} = \frac{a_{ij}}{2k} = \frac{\overline{u_i u_j}}{\overline{u_k u_k}} - \frac{1}{3}\delta_{ij} \tag{2.17}$$

The normalized anisotropy tensor has zero trace ($b_{jj} = 0$), meaning that the first invariant is zero by definition. The second and third invariants are given below respectively.

$$b_{ii}^2 = 6\eta^2 = b_{ij} b_{ji} \tag{2.18}$$

$$b_{ii}^3 = 6\xi^3 = b_{ij} b_{jk} b_{ki} \tag{2.19}$$

From the above equations, anisotropy may then be characterized by the two variables denoted ξ and η. For all points in the flow field, ξ and η may be determined from the Reynolds stresses and plotted as points on the $\xi - \eta$ plane. There exist particular states of the Reynolds stress tensor that correspond to particular points and curves in this plane, which in turn describe the state of turbulence.

When axisymmetric turbulence is present, the kinetic energy in two orthogonal directions is equal. Subsequently, the anisotropy tensor may be written as:

$$b_{ij} = \begin{pmatrix} -\alpha & 0 & 0 \\ 0 & \alpha/2 & 0 \\ 0 & 0 & \alpha/2 \end{pmatrix} \tag{2.20}$$

The parameter α describes the energy content in the three coordinate directions. The energy contained in the first direction is $\left(\frac{1}{3} - \frac{1}{2}\alpha\right)k$ (Derksen *et al*., 1999). In this case, the invariants maybe written as $b_{ii}^2 = \frac{3}{2}\alpha^2$ and $b_{ii}^3 = -\frac{3}{4}\alpha^3$. It follows that when $\alpha < 0$, $b_{ii}^3 = 6\left(\frac{b_{ii}^2}{6}\right)^{3/2}$. For this case, the energy contained in the direction of symmetry is greater than $k/3$. Conversely, when $\alpha > 0$, $b_{ii}^3 = -6\left(\frac{b_{ii}^2}{6}\right)^{3/2}$ and the energy in the direction of symmetry is less than $k/3$. The equivalent expressions for these conditions in terms of the variables ξ and η are $\eta = \xi$ and

$\eta = -\xi$ respectively, for the anisotropic flow with an axisymmetric state of turbulence. These curves create a boundary for the anisotropic conditions, and represent the Lumley triangle (Lumley, 1978). The bottom corner of the triangle where $\eta = \xi = 0$ corresponds to an isotropic state of turbulence. This suggests that for three-dimensional isotropic flows, all invariants of the Reynolds anisotropy tensor are essentially zero. The values of ξ and η for the flow field measured at Position 1, 1500 rpm, are shown in Figure 3.24. The coloured points correspond to different sections of the flow field. In order of increasing distance from the impeller, the colours are blue, red, yellow, dark green and bright green.

All points within the Lumley triangle correspond to physically realizable Reynolds stresses, whereas outliers correspond to non-realizable Reynolds stress. As may be observed, all of these points are found near the right hand side of the Lumley triangle, across most of the boundary. The first conclusion that may be derived is that some points within the flow field are highly anisotropic. Secondly the state of turbulence may be categorized as axisymmetric, with positive ξ. This further suggests that the direction of symmetry has the highest energy content. An analysis of the b_{ij} components indicated that the tangential plane was the direction of symmetry for the flow generated by the EkatoMizer. No points within the flow field satisfy the condition of isotropy; hence the bottom corner of the Lumley triangle is empty.

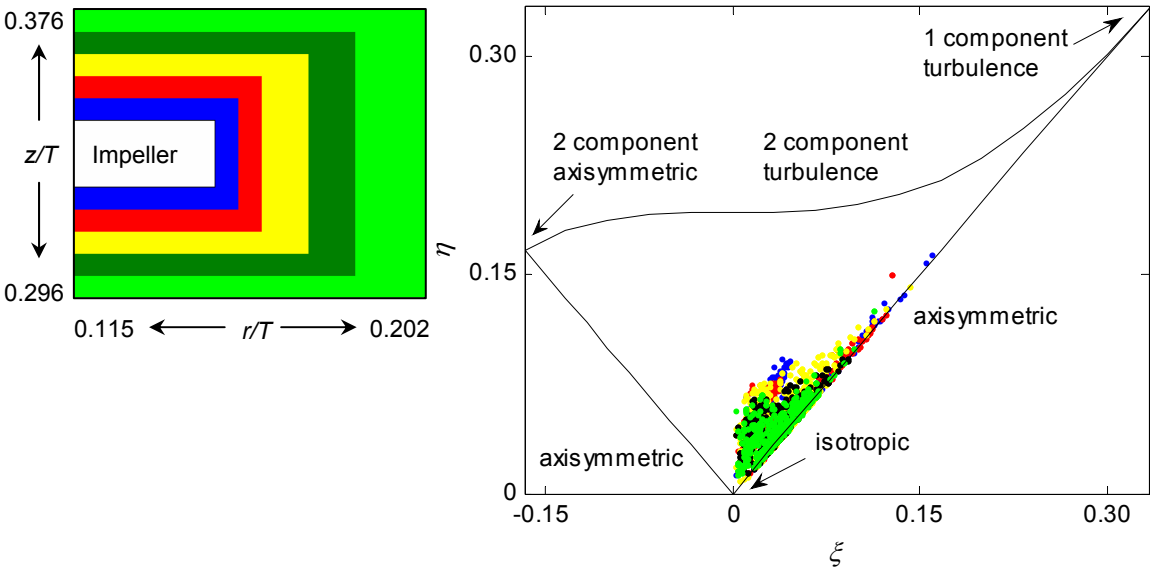

Figure 3.24: Invariant parameters ξ and η from 3-D PIV time averaged measurements, Position 1, 1500 rpm. Solid lines indicate the Lumley triangle.

As expected the blue points, corresponding to the immediate vicinity of the impeller, display the highest state of anisotropy, and fall closest to the region $\eta = \xi = 1/3$. Conversely, the bright green points located furthest away from the impeller show the highest degree of isotropy, and are located close to $\eta = \xi = 0$ (although they are not exactly isotropic). The remaining red, yellow and dark green points fall between these two limits, and in that order show return-to-isotropy behaviour. A flow field further away from the impeller may be more indicative of this

effect, where isotropy of the flow may be more evident, since the entire field of view obtained at Position 1 is very close to the impeller. Subsequently a similar analysis was carried out for all points in the flow field obtained at Position 2 (further into the discharge stream), results are shown in Figure 3.25. Note that in this case the impeller was not in the field of view, the left hand side of the image was immediately adjacent to the blade. As may be observed, now all coloured points are closer to isotropy, and occupy a larger area in the bottom corner of the Lumley triangle. Some points even satisfy conditions of isotropy. It is expected that a coherent analysis for a larger flow field in the bulk flow would result in more overlap between the coloured points, and greater concentration close to $\eta = \xi = 0$.

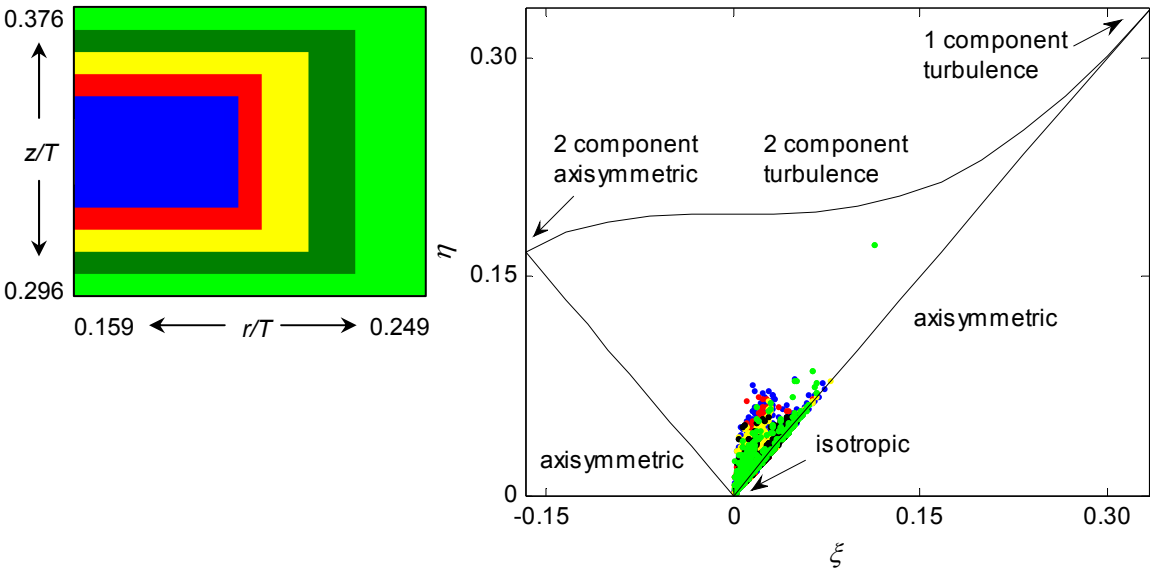

Figure 3.25: Invariant parameters ξ and η from 3-D PIV time averaged measurements, Position 2, 1500 rpm. Solid lines indicate the Lumley triangle.

3.7 Angle-resolved velocity fields

An analysis of the instantaneous velocity fields confirmed the presence of vortex structures in the flow, as illustrated in Figure 3.14. Since the stereo-PIV measurements were ensemble-averaged, it was not possible to correlate the vortices to blade position; instead they appeared to be smoothed out after averaging over the entire data set (Figure 3.13). In order to elucidate these flow structures, angle-resolved measurements were obtained at 5 kHz from high-speed PIV experiments, at impeller speeds 1500 and 2600 rpm. The EkatoMizer had 36 teeth around the circumference of both upper and lower surfaces of the disc (Figure 3.1), distributed uniformly 10 degrees apart. Thus it was decided to allocate the PIV data within ten equal intervals between two reference teeth; i.e. at one degree intervals behind the leading tooth. In this context, the angle behind the reference tooth is denoted θ, as shown in Figure 3.26.

In the angle-resolved measurements, an encoder was employed to trigger image acquisition. The signal was sent to the LASERPULSE synchroniser, which co-ordinated the timing of the laser and camera to obtain 1000 PIV image pairs at a frequency of 5 kHz after the primary pulse. With knowledge of the blade angle at starting position and impeller speed, the sequence

of images could be manually categorized into one-degree intervals with respect to the reference tooth. In theory, this method of 'binning' would work efficiently at a constant impeller speed. However the slight instability of the motor created a variation of ±5 rpm from the nominal impeller speed. Consequently, assuming a constant speed may cause the angle-resolved data to be out of phase within the various bins, and vortex structures (if present) would be smoothed out just as in the case of the ensemble-averaged measurements. For this reason, it was important to determine the precise rotational speed.

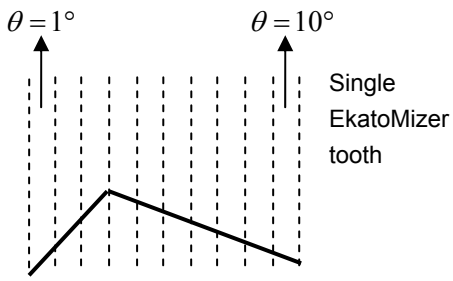

Figure 3.26: Angle-resolved positions with respect to leading tooth

In order to identify the real frequency of the impeller blade passage, a periodogram estimate of the (power spectral density) PSD was obtained from velocity time-series data at a point near the edge of the upper set of teeth, from the high-speed PIV measurements. The PSD obtained at $r/T = 0.16$ and $z/T = 0.35$, at 1500 rpm, is shown in Figure 3.27.

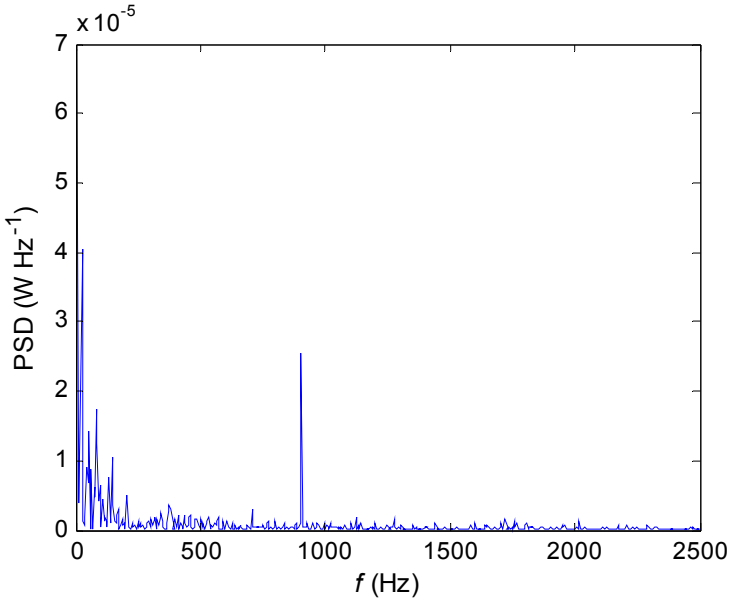

Figure 3.27: PSD of the radial velocity time series at $r/T = 0.16$ and $z/T = 0.35$, 1500 rpm, from high-speed PIV at 5 kHz

A nominal impeller rotational speed of 1500 rpm corresponds to 25 rps. Since the impeller has 36 teeth on each surface, the tooth passage frequency is 900 Hz. From Figure 3.27, a peak in the PSD may be observed at 903.32 Hz, which is very close to the nominal frequency. When

inverted, this frequency corresponds to an impeller rotational speed of 1505.5 rpm, which is within the variability range of the motor. The frequencies on either side of the dominant peak in the PSD correspond to impeller speeds of 1497.4 and 1513.7 rpm. Subsequently, the data was angle-resolved assuming different impeller speeds within this range.

To obtain a measure of the degree of correlation within the ten intervals of each angle-resolved case, the variance of the time-series radial velocity was calculated for each one-degree 'bin' and subsequently summed, at the point $r/T = 0.16$ and $z/T = 0.35$. This is the same location where the PSD was first obtained and the dominant peak corresponding to the tooth passage identified. Consequently at this point, periodicity of the flow due to impeller rotation would be certain. It follows that the angle-resolved data set with minimum total variance at that point should yield vortex structures in the entire field of view after averaging the data, if periodicity of the flow is present.

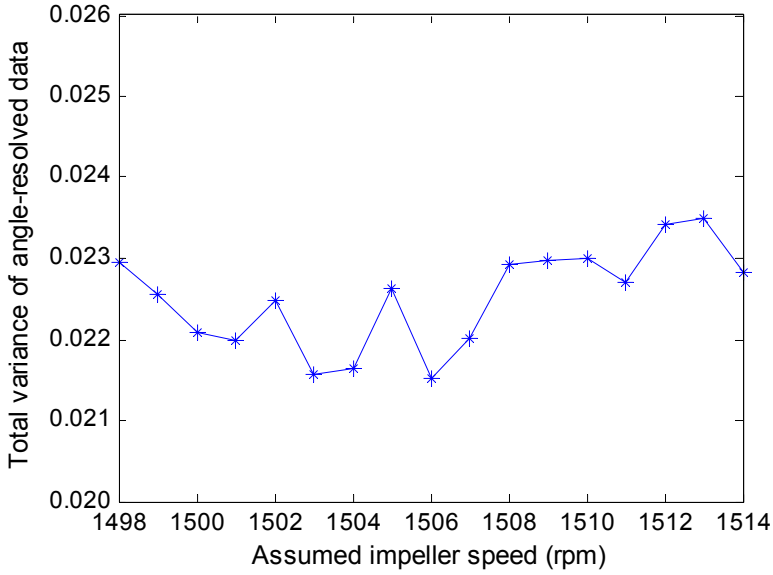

Figure 3.28: Total velocity variance versus impeller speed of angle-resolved data sets at $r/T = 0.16$ and $z/T = 0.35$

Results of total velocity variance against impeller speed are shown in Figure 3.28. It may be observed that the angle-resolved data sets obtained when assuming impeller speeds of 1503 and 1506 rpm have the smallest total variance of the radial velocity at point $r/T = 0.16$ and $z/T = 0.35$. The resulting angle-resolved velocity vector plots corresponding to an impeller speed of 1503 rpm, at $\theta =$ 1°, 2°, 4° and 6° are given in Figure 3.29(a) to (d).

It may be observed that the vector plots do not exhibit the vortices which were evident in the instantaneous velocity fields. The angle-resolved velocity fields obtained from assuming an impeller speed of 1506 rpm provided similar results. This suggests that the vortices have a frequency different to the tooth passage, and that the flow pattern is not truly periodic with respect to the impeller revolution. On the other hand, the impeller speed may not have been sufficiently constant to deduce angle-resolved measurements in this way. The encoder used in these experiments provided only the initial trigger for image capture. Instead employing an

optical encoder which generates a trigger at every impeller revolution would have given precise angle-resolved measurements, and may have enabled the detection of vortices in phase with the tooth passage.

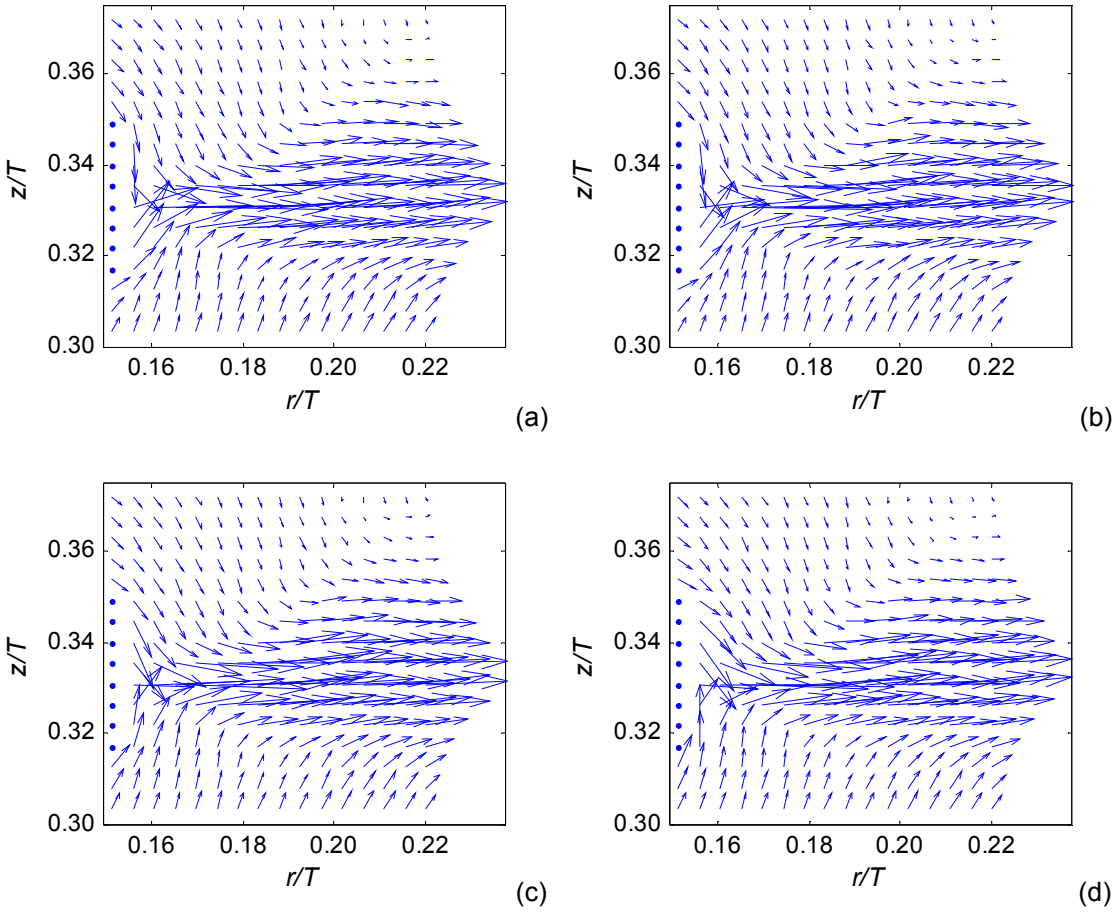

Figure 3.29: Angle-resolved velocity fields at (a) 1° (b) 2° (c) 4° and (d) 6° behind the leading tooth, assuming impeller speed 1503 rpm (nominal 1500 rpm)

3.8 Macro-instabilities

It is possible that the vortices found in the instantaneous PIV results correspond to the low-frequency phenomena observed in the PSD estimate in Figure 3.27; hence macro-instability of the flow was investigated next. Macro-instabilities (MI) are large-scale, low-frequency flow instabilities whose time and length scales are greater than those associated with the impeller blade rotation and small scale turbulence eddies. Earlier findings suggest that MI are responsible for slowly changing the flow pattern in stirred vessels about its mean. The effects are manifested in quantities such as the local heat flux (Haam *et al.*, 1992) or mass fluxes in multiphase systems (Bittorf and Kresta, 2003). Consequently, an understanding of the degree, nature and mechanisms of MI formation are of great importance in the mixing field.

Previously, many researchers have attempted to quantify MI by means of observational measurement techniques such as high speed video tape recording (VTR) (Winardi and Nagase, 1991), Tuft flow visualisation (Chapple and Kresta, 1994), and LDA (Montes *et al.*, 1997). However, since mechanically stirred flows are time-varying, complex, and somewhat stochastic,

it is difficult to determine useful information from visual measurements alone. More recently, signal processing methods such as spectral analysis and wavelet transform have been developed to exploit the random velocity signal (Myers *et al.*, 1997; Montes *et al.*, 1997; Nikiforaki *et al.*, 2003).

In literature, studies implementing spectral analysis of LDA time-series data to investigate MI are commonly cited, such as those mentioned above. However, in recent literature, spectral analysis of PIV time-series measurements have also been reported (Myers *et al.*, 1997, Khan, 2005). PIV measurements are not usually suitable to obtain temporal information of a stirred flow, due to its low sampling rate (~15 Hz) with respect to the time scale of turbulent fluctuations. In this respect, PIV is considered inferior to LDA techniques, whose sampling rate can be of the order of a few kHz. However, since MI phenomena are rather slow, measurements of the higher order frequency are not necessary, and the temporal resolution offered by PIV is deemed sufficient. What is more important is the sampling time, and this aspect will be discussed later.

Macro-instabilities may cover a large portion of the stirred vessel. Subsequently, spatial, as well as temporal information is required to study the full extent of its breadth and intensity. The conventional LDA technique provides only single-point measurements. Due to this, PIV techniques provide a significant advantage, notwithstanding the lower temporal resolution. A study by Fan *et al.* (2004) describes a spatio-temporal analysis of MI in a stirred vessel via PIV, for a flow generated by an RDT. The study aimed to elucidate the distribution of MI across the vessel, as well as obtaining a measure of its respective intensity. A similar approach of studying MI will be adopted in the current study, to take full advantage of the information carried in PIV data.

3.8.1 Characterisation of dominant MI frequency

The PSD was obtained for the velocity time series at discrete points in the flow field (at 1500 rpm) to observe the qualitative nature of the PSD at different locations in the vessel, and identify trends with respect to position.

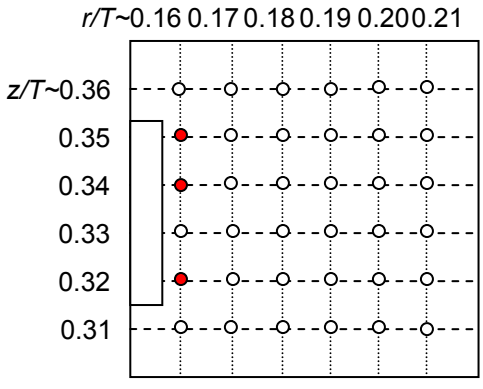

Figure 3.30: Locations of obtaining PSD from time-series radial velocity data

In Figure 3.30, the filled red circles indicate locations where a dominant peak corresponding to the blade passage frequency (~900 Hz) was identified in the PSD estimate. At all other

locations, peaks at much lower frequencies could be observed. These suggest the presence of macro-instabilities (MI) in the flow field. However, an analysis of the PSD at various points showed that the spectra at the low frequency varied with measurement location. Dominant peaks in the low frequency region were not identifiable at all points; instead two or three significant peaks occurred simultaneously. In locations where a single dominant peak could be identified, the frequency was not always the same.

Similar types of difficulties in determining the dominant MI peak have been noted in the works of Montes *et al*. (1997), Hasal *et al*. (2000) and Nikiforaki *et al*. (2003). Khan (2005) suggested that this was due to the random formation and breakage of multiple vortices, which caused a number of harmonic peaks in the spectra. In their studies, Nikiforaki *et al*. (2003) and Khan (2005) were able to visualise precessional vortices which form behind the baffles and travel to the surface. No such structures could be identified in the impeller region of the current study (where the PSD estimates were obtained). However, it must be noted that the frequency (f) of the MI in the current study was found to be within the range of 0-200 Hz (or $f' = 0 - 8$, where $f' = f / N$), which is much greater than that observed for the PBT induced flow by Khan (2005) ($f' \sim 0.011$). It is also greater than that typically reported for RDTs; ~0.016 by Nikiforaki *et al*. (2003), ~0.016 by Khan (2005) and 0-0.4 by Fan *et al*. (2004). The relatively higher MI frequency of the EkatoMizer flow would make visual quantification more difficult.

To demonstrate the variability of MI peaks, the PSD estimate obtained at two separate locations is shown in Figure 3.31(a) and (b). Identification of the dominant peak is more difficult due to the presence of noise; i.e. less significant peaks co-existing with the prominent peak.

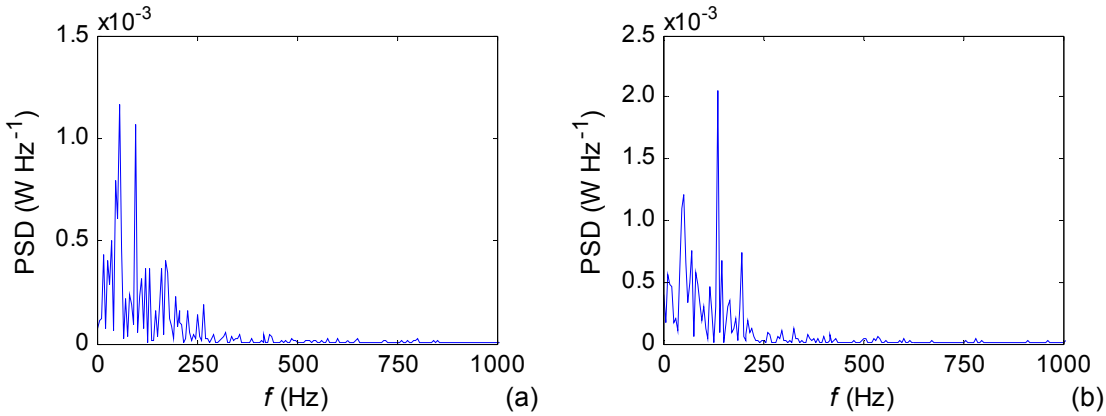

Figure 3.31: PSD of the radial velocity time series at (a) $r/T = 0.17$**,** $z/T = 0.34$ **and (b)** $r/T = 0.18$**,** $z/T = 0.34$ **, 1500 rpm, 5 kHz**

In an earlier investigation, Nikiforaki *et al*. (2003) studied the influence of measurement time on MI frequency detection, for a PBT induced flow. The velocity time-series was recorded using LDA for various sampling times between 50 and 800 s, to establish that enough data had been collected for statistically independent results. The period of one MI cycle was approximately 10 s, so the measurement times varied between 5 and 80 MI cycles. Results indicated that by increasing the sampling time, lower frequencies became more pronounced. The most dominant MI peak became more identifiable in the PSD distribution, and the noise peaks became less

distinct. Based on this observation, Khan (2005) later suggested that a measurement time greater than 10 MI cycles should be used to decrease noise effects. On another note, the PSD itself was obtained from a periodogram estimate, employing a subroutine in Matlab for FFT analysis. For the accurate detection of lower frequencies with FFT methods, higher data rates are required, compared to those for higher frequencies (Randall, 1977).

A single dominant peak corresponding to the MI frequency can be observed in Figure 3.31(b). Noise corresponding to the blade passage frequency is not evident, indicating that it is not strongly influencing the flow at this point. Subsequently, the velocity time series at this point was assessed to obtain an estimate of the MI period, as shown in Figure 3.32.

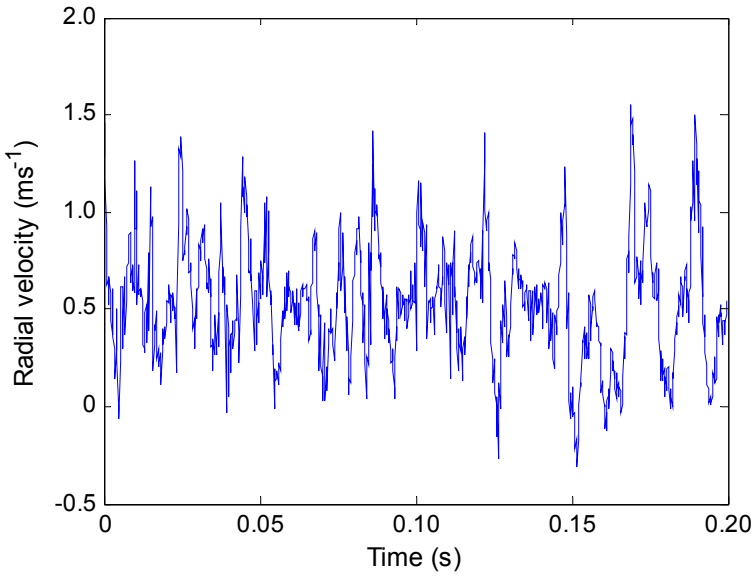

Figure 3.32: Instantaneous radial velocity time-series at $r/T = 0.18$, $z/T = 0.34$, 1500 rpm, 5 kHz

The cyclic variation of the mean flow is not obvious. Consequently, the low frequency data were analysed by applying a moving-window averaging technique. A moving-average filter smoothes data by replacing each data point with the average of the neighbouring points defined within a certain span or window size. This process is equivalent to low-pass filtering. Various window-sizes of 25, 50, 75 and 100 points were employed to remove turbulent fluctuations corresponding to frequencies of 200, 100, 66.7 and 50 Hz respectively, leaving data at the lower frequencies. The filtered velocities are shown in Figure 3.33.

The filtered data illustrate the short-period high-frequency fluctuations being smoothed out as the window size is increased. There is no standard practice to identify the velocity signal corresponding to the main macro-instability cyclic variation, and as such, no one dominant peak corresponding to MI frequency was detected previously. Instead, it is appropriate to determine the number of cycles corresponding to all of the averaged velocity signals within the observed MI frequency range. The velocity signal obtained after applying the 25-point filter has a cycle time of approximately 0.015 s. Thus, the original data series would comprise 13 MI cycles, for

the MI occurring at a maximum frequency of 200 Hz. This count agrees with the recommendation of Khan (2005).

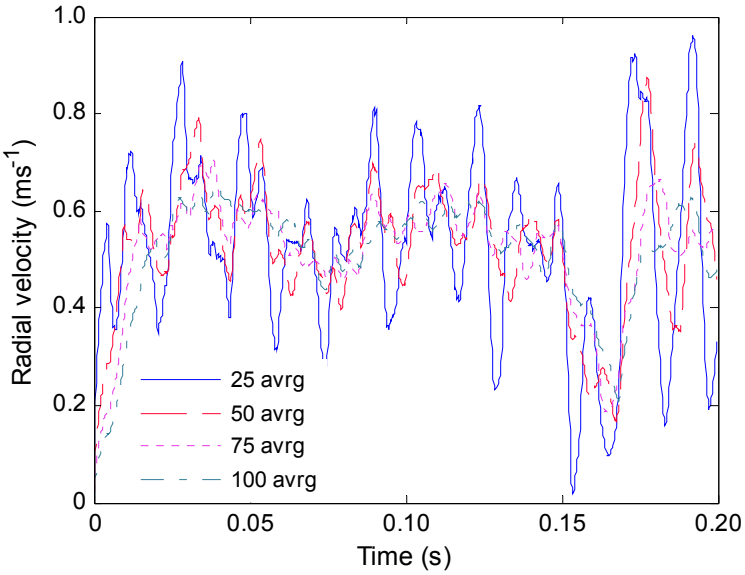

Figure 3.33: Averaged (low-pass filtered) velocity signal $r/T = 0.18$, $z/T = 0.34$, 1500 rpm, 5 kHz

Note that the MI depicted here are quite high frequency compared to studies with PBT and RDTs, for which typical periods would be O(10)s (Yianneskis *et al.*, 1997; Khan, 2005). This is due to a combination of a much higher f' and impeller speed N. On the other hand, the underlying trend of the velocity signal obtained after applying the 100-point filter has a longer cycle time of approximately 0.08 s. The sampling time would then comprise only ~2.5 MI cycles occurring at the lower frequency of 50 Hz. It is apparent that a longer sample time is required to better estimate the MI peaks at frequencies lower that 200 Hz. However, the next section deals with the probability of MI occurrence, where the MI frequency *range* is the more important factor. At this stage, it can be assumed that the MI frequency range of 0-200 Hz is an arbitrary but acceptable estimate, since the amplitude of the higher frequency peaks in the PSD is significantly smaller at all locations in the measurement region.

3.8.2 Probability distribution of MI

In a manner analogous to Fan *et al*. (2004), it was decided to obtain a spatial representation of the MI intensity across the field of view, using a spectral distribution function $P(f)$ to extract information from the time series of the vorticity, given in Equation (2.21). The z component of vorticity was calculated for every point in the velocity field, and for each instantaneous PIV measurement in series. The spatial gradients of the axial and radial instantaneous velocities were calculated using central difference approximations to the derivatives.

$$\omega_z = \frac{\partial v}{\partial x} - \frac{\partial u}{\partial y} \tag{2.21}$$

Subsequently, it was possible to obtain a time series of the vorticity at every point in the flow field (with $t = 0$ s at the instant of the first PIV measurement, and $t = 0.2$ s at the last PIV measurement). A total of 1000 PIV measurements were obtained, meaning that each vorticity time-series consisted of 1000 data points. The signals were processed by calculating the PSD $h(f)$ from a periodogram estimate. The normalized PSD $F(f)$ was obtained by dividing the non-normalized PSD by the variance of the vorticity time series. Finally, the spectral distribution function $P(f)$ was calculated to quantify the MI. According to Fan *et al*. (2004) $P(f)$ may be regarded as the proportion of the total power contributed by the components with frequencies within the range 0 and f. In this case f is 200 Hz.

$$F(f) = \frac{h(f)}{\sigma^2} \tag{2.22}$$

$$P(f) = \int_0^f F(\theta) D\theta \tag{2.23}$$

The authors also suggested that from a mathematical perspective, $P(f)$ is equivalent to a probability distribution function. For instance, $P(f) = 0.5$ means that the MI dominates 50% of the total measurement period, at that measurement location. The MI is as likely to occur as the other fluctuations, also with a probability of occurrence equal to 0.5. $P(f)$ could even be interpreted as the MI intensity. It follows that MI in the vorticity fluctuations would have a high probability of occurrence at the lower frequencies. Similar to the results shown in Figure 3.31, the PSD spectra of the vorticity exhibited variation in the low frequency region, with respect to position in the field of view. An explicit value of the dominant MI frequency could not always be determined. However, this was not crucial in the analysis. The MI frequency existed within the range of 0-200 Hz in the normalized PSD spectra; hence these provided the limits for integration in Equation (2.23). Thus, all fluctuations within this range are characterised as MI.

The 2-D distribution of the probability of MI occurrence in the measurement region is depicted in Figure 3.34. It may be observed that MI intensity is significantly higher in the discharge stream compared to the surrounding flow, with a magnitude of approximately 0.8. In other words, MI contributes to around 80% of the total power within that region. With reference to visual observations of the instantaneous velocity fields (Figure 3.14), vortices were found to appear randomly within the discharge stream. Frequently, two vortices formed simultaneously; one was located in the upper half of the discharge stream whilst the second remained in the lower half. The vortices had a maximum displacement of around 7×10^{-4} m between image frames (equivalent to one vector node in the radial direction), resulting in a velocity of 0.35 m s^{-1}. Within that region, the radial velocity was approximately $0.06V_{tip}$ (see Figure 3.11) or in absolute terms 0.45 m s^{-1}. Thus, vortices were advected with approximately 80% of the mean radial velocity. The result in Figure 3.34 suggests that these vortical structures may be the low frequency MI detected in the PSD distribution, since the region of high intensity matches their location.

The above description of MI may be in contrast with the type of MI phenomena commonly reported in literature for RDT and PBT impellers. Yianneskis *et al*. (1987) identified a 'whirlpool' type of vortex moving around the shaft axis of an RDT, with a period of around 10 s, and

$f' = 0.02$. Haam *et al*. (1992) reported a vortex precessing on the free surface of a flow generated by an RDT, with $f' = 0.036$. Guillard *et al*. (2000) used LIF techniques for flow visualisation, and observed large amplitude concentration oscillations, induced by the interactions of the flow emanating from the RDT impeller and baffles. The authors also identified large coherent structures near the surface and around the baffles, similar to those reported by Yianneskis *et al*. (1987). Nikiforaki *et al*. (2003) reported a whirlpool-type vortex circulating the shaft of an RDT impeller, with a period of 16 s and $f' = 0.017$. Similar types of MIs were reported for the PBT, although their cyclic variation was not as easily discernable.

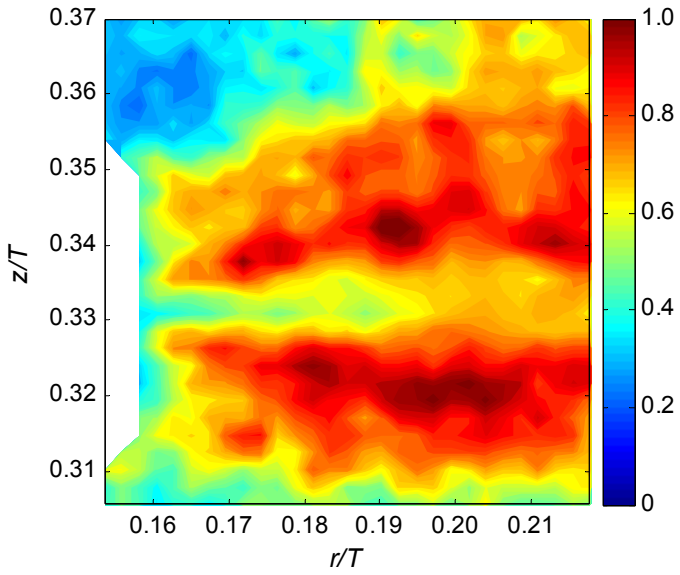

Figure 3.34: Two-dimensional distribution of probability of MI occurrence between 0 and 200 Hz, from high-speed PIV measurements at 1500 rpm, 5 kHz

A common factor amongst the aforementioned studies is that MIs persist close to the liquid surface, circulate around the shaft or form behind the baffles, whereas in the present case, the MIs have a relatively larger probability of occurrence in the discharge stream. Secondly, the MI frequencies (both absolute and normalized by N) recorded previously for the RDT and PBT impellers are approximately two orders of magnitude smaller than that found in the present case (reaching $f' = 8$ in the current study, compared to only ~0.02 for the other impellers). During the visual observations, it was found that vortices persisted for approximately 2 ms before disappearing, and instantly reforming at other positions within the discharge stream. This type of behaviour does not conform to the traditional view of MI. The only firm conclusion that can be drawn thus far is that low frequency phenomena (between 0-200 Hz, lower than the tooth passage frequency of 900 Hz) have been detected for the EkatoMizer. The results of the current study create the possibility of characterising another form of low frequency phenomena, which appropriately describes the flow behaviour of the sawtooth impeller.

The following chapter continues study of the EkatoMizer turbulence properties, specifically the dissipation rate. Various methods will be investigated for its calculation, and the best one will be selected to carry forward into the study of two-phase flows. Turbulence intermittency of the

dissipation rate will also be investigated. Intense fluctuations of the dissipation rate will be evaluated against the multifractal model of Meneveau and Sreenivasan (1991) which describes the dissipative nature of turbulence. On this basis a suitable vector validation filter will also be identified. Finally the spatial distribution of energy dissipation will be considered, and ratio of maximum-to-mean dissipation evaluated. This work will facilitate understanding of turbulence before more complex two-phase flows are investigated in proceeding chapters.

Chapter 4
Dissipation rate study

4.1 Introduction

Determination of the TKE dissipation rate (ε) is paramount for the optimization of fluid mixing processes. The distribution of ε across a stirred vessel determines breakage of droplets, particles and bubbles in liquid-liquid, solid-liquid and gas-liquid flows respectively. The selectivity of competing chemical reactions may be highly dependent on the level of micromixing, which is governed by the local dissipation rate near the feed point. The region of interest is the impeller stream, where vigorous mixing is expected to occur due to the presence of trailing vortices. TKE dissipation occurs at the smallest scales of motion, the Kolmogorov scale, which must be resolved experimentally for the true evaluation of ε. PIV has enabled acquisition of spatially distributed, instantaneous data of turbulent flow fields, but the spatial resolution of this technique is still a limiting factor. For this reason, the determination of ε imposes a significant challenge.

In the literature, various methods for calculating ε have been proposed: (a) dimensional analysis, (b) direct determination from its definition, (c) large eddy simulation (LES) analogies and (d) determination from the TKE balance. In this section, all of these methods will be employed to estimate the dissipation rate of the single-phase EkatoMizer flow (discussed in Chapter 3), and the method deemed best will be applied to subsequent multi-phase studies of a PBT flow. It is assumed that the conclusions derived from the EkatoMizer study are applicable to a PBT stirred flow.

It is expected that acquisition of the third velocity component in stereo-PIV improves the estimate of ε compared to that obtained from standard 2-D PIV, in which the out-of-plane velocity component is unknown. For 2-D PIV calculations, methods often employ isotropic assumptions or scaling factors to estimate unknown quantities. For each method, the dissipation rate will be calculated assuming knowledge of only two velocity components, imitating standard 2-D PIV. Relevant assumptions will be applied to estimate the unknown terms where necessary. The dissipation rate will also be calculated using all three velocity components from the same stereo-PIV data set, enabling assumptions to be eliminated in some cases. However, since stereo-PIV measurements are obtained in a single plane, velocity gradients in the out-of-plane direction are not available, so not all assumptions can be entirely eliminated. The two test conditions will be referred to as the 2-D and stereo-PIV cases respectively. By comparing these, the validity of the isotropic assumptions will be assessed.

4.2 Average dissipation rate

The most generalised way to calculate the volume-averaged dissipation rate is via the total energy input per unit mass.

$$\bar{\varepsilon} = \frac{P}{\rho_l V} \tag{4.1}$$

where, P is the power consumption, ρ_l and V the liquid density and volume, respectively. It is convenient to define a dimensionless group called the power number (P_o), which normalizes the power consumption for various impellers and provides a basis for comparison.

$$P_o = \frac{P}{\rho_l N^3 D^5} \tag{4.2}$$

The variables N and D are the impeller speed and diameter, respectively. If the power number is known, then the power consumption may be estimated, and the average dissipation rate calculated. For the EkatoMizer impeller (Figure 3.1), the shaft diameter was too small to enable an accurate measurement of the torque using strain gauges. Subsequently the power number was measured by recording the temperature change in 5 litres of water at 1500 rpm. The system was assumed to be perfectly insulated, resulting in negligible heat loss. The temperature was measured using a thermocouple, which confirmed a fully mixed system, as the temperature was the same near the impeller and in the bulk flow. The power number was found to be 0.11, consistent with the estimate provided by the BHR Group (Clements *et al.*, 2006). The assumption of an adiabatic system was also justified, as the temperature increase maintained a linear dependency on time. Thus, at 1500 rpm, the mean dissipation rate was found to be 0.6 W kg^{-1} or $0.0042N^3D^2$.

The average dissipation rate is frequently used in the scale up of stirred vessels. However, it is well known that the dissipation rate distribution is non uniform throughout the vessel, and the maximum and minimum can deviate significantly from the mean value. The average dissipation rate provides no insight into the micro-mixing processes, which require knowledge of the local values instead. This calls for more sophisticated techniques to approximate the dissipation rates in the vicinity of the impeller and discharge stream, which are the regions of most interest and certainly the most important in mixing processes.

4.3 Dimensional analysis with the rms velocity

The dimensional argument is perhaps the most widespread energy dissipation estimation tool. It employs an equation relating the dissipation rate to length scales. The TKE content of the flow is described by u'^2, and the rate of energy transfer determined by u'/Λ. By assuming flow isotropy, various authors (e.g. Kresta, 1998) have used the following dimensional relation:

$$\varepsilon = A\frac{u'^3}{\Lambda} \tag{4.3}$$

where A is a constant, u' and Λ the characteristic turbulent velocity and length scale respectively. Various expressions for A, u' and Λ have been employed in earlier investigations. For example, Laufhutte and Mersmann (1985) employed $A = 6.6$. In most cases however, A is assumed to be unity for isotropic turbulence (Cutter, 1966). The characteristic velocity is usually the rms velocity in the main flow direction. The length scale can be taken as proportional to the impeller diameter or blade width; for instance $\Lambda = D$ (Laufhutte and Mersmann, 1985), $\Lambda = D/2$ (Calabrese and Stoots, 1989) or $\Lambda = W/2$ (Kresta and Wood, 1991). In this study, A will take the value of unity, and the length scale is assumed to be constant at $W/2 = 4$ mm. Impellers such as the commonly studied RDTs generate an obvious radial characteristic flow. However for the EkatoMizer, no single rms component could represent the turbulence of the general flow, hence all three rms velocities were used to represent it sequentially.

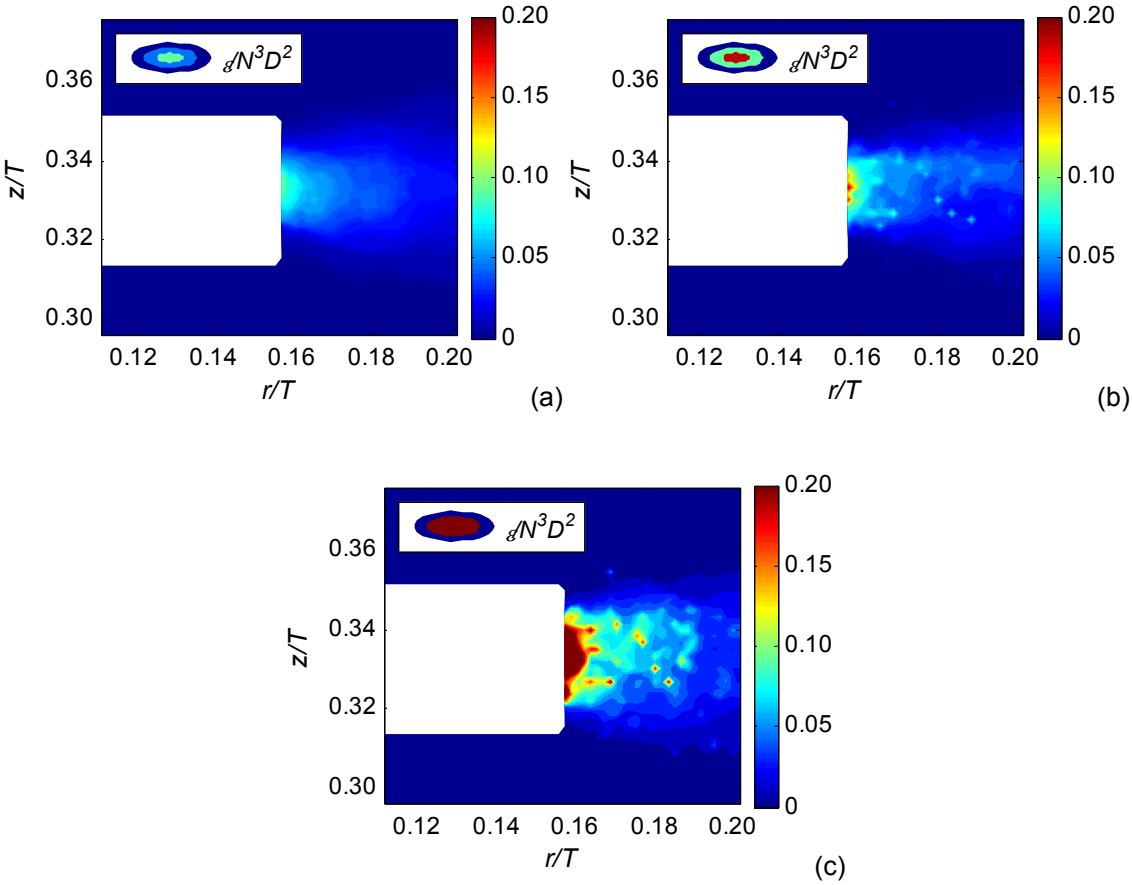

Figure 4.1: Dissipation rate from dimensional analysis using (a) axial (b) radial and (c) tangential rms velocities, Position 1, 1500 rpm

Axial and radial rms velocities were illustrated in Figure 3.22(a) and (b) respectively, which maintained a difference of 20% in their maximum values. It is inherent that this difference is manifest in the dissipation rate calculations; see Figure 4.1(a) and (b). The maximum dissipation rate ($\varepsilon_{\max}$) from the axial rms velocity is $\sim 0.09 N^3 D^2$, that obtained from the radial component is $\sim 0.18 N^3 D^2$. The difference in velocities is magnified due to the cubic power in

Equation (4.3). Nevertheless, their distributions are similar; in both cases $\varepsilon_{\max}$ is found near the blade edge, which decays horizontally away from the impeller.

The dissipation rate resulting from the tangential rms velocity (given by stereo-PIV) is shown in Figure 4.1(c). The maximum value is $\sim 0.7N^3D^2$, almost four times greater than that obtained from the radial component. The maximum is also found at the blade edge, however it diminishes considerably closer to the blade compared to the distributions illustrated in Figure 4.1(a) and (b). This is reasonable when recalling that the mean radial velocity contour plot exhibited a strong radial discharge stream in line with the impeller ($\sim 0.12V_{tip}$). Although an equally strong tangential velocity was observed ($\sim 0.14V_{tip}$), it was restricted to the blade edge.

It is apparent that dimensional analysis should only apply to flows which are approximately homogenous and isotropic. In reality turbulent flows are complex and rarely satisfy these conditions, so it becomes debatable which rms component is characteristic of the flow field. In the present case, the radial rms velocity may appear to be the most representative after considering the mean flow pattern; although it does not characterize the *highest* turbulence level in the same way as the tangential component. Additionally, it was shown that the length scale cannot be represented by a single value, since it varies throughout the vessel for highly turbulent flows (see §3.4.3).

4.4 Dimensional analysis with TKE

In order to account for flow anisotropy, all three velocity components should be used to estimate the dissipation rate. Subsequently, the characteristic velocity in Equation (4.3) may be replaced by the turbulent kinetic energy k. Additionally, Wu and Patterson (1989) used the 'resultant' macro-scale L_f, which is a combination of the 1-D integral length scales in all three directions. The authors integrated the local values of $k^{2/3}/L_f$ in the impeller stream, and after comparing the integral with the energy dissipation rate (obtained from the kinetic energy flows), found $A = 0.85$. Subsequently, they proposed the following relationship to estimate the dissipation rate.

$$\varepsilon = A\frac{k^{3/2}}{L_f} \tag{4.4}$$

In line with this finding, A will now take the value of 0.85. Lee and Yianneskis (1998) employed this relationship, but replaced the denominator with the 1-D longitudinal integral length scale. A similar method will be implemented here. However, the denominator will incorporate the 2-D integral length scale Λ_u from the radial velocity field (found to be 2.6 mm in the field of view, details given in §3.4.3) as follows:

$$\varepsilon = A\frac{k^{3/2}}{\left(3\Lambda_u^2\right)^{1/2}} \tag{4.5}$$

In the 2-D PIV case, k is obtained under the pseudo-isotropic assumption, Equation (2.15). For stereo-PIV, the correct interpretation of k may be used instead, Equation (2.14). Results from both estimates are compared below.

4.4.1 2-D PIV estimate

The dissipation rate obtained from the pseudo-isotropic assumption of k is displayed in Figure 4.2, which exhibits a maximum of $\sim 0.18 N^3 D^2$. The range and spatial distribution is comparable with the dimensional analysis estimate using the radial rms velocity in Figure 4.1(b). This is because the TKE is calculated from the sum of the squared rms velocities, and is expected to resemble their distribution. Since the radial rms velocity is dominant over the axial component, its dissipation rate distribution is similar to that shown here.

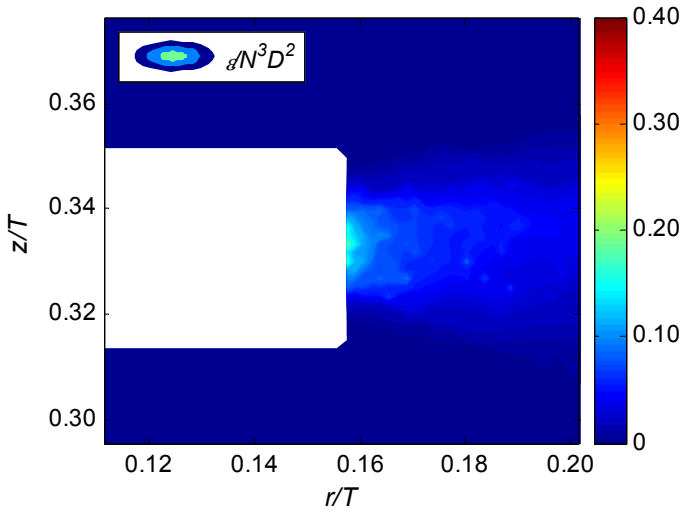

Figure 4.2: Dissipation rate from dimensional analysis using TKE from pseudo-isotropic assumption, assuming 2-D PIV ensemble-averaged measurements, Position 1, 1500 rpm

4.4.2 Stereo-PIV estimate

Figure 4.3 illustrates the dissipation rate from dimensional analysis, employing the full definition of k, made possible via stereo-PIV. It was shown in §3.5 that the local isotropy assumption employed for 2-D PIV methods underestimates the tangential rms velocity component, and consequently the true TKE. Thus as expected, the full k evaluation provides a greater dissipation rate profile, reaching a maximum of $\sim 0.4 N^3 D^2$ at the blade edge. The spatial distribution no longer resembles that obtained from radial rms velocity in Figure 4.1(b), due to the inclusion of the real tangential component.

The constant A in Equation (4.4) was assumed to be 0.85 instead of unity for isotropic flows. However, the 2-D integral length scale (2.6 mm) was found to be smaller than that estimated from the factor $W/2$ (4 mm), which more than offsets the smaller constant, yielding an overall greater dissipation rate. This result supports previous findings which suggest that $W/2$ overestimates the length scale in the impeller region, and subsequently underestimates the dissipation rate (Baldi and Yianneskis, 2003; Khan 2005).

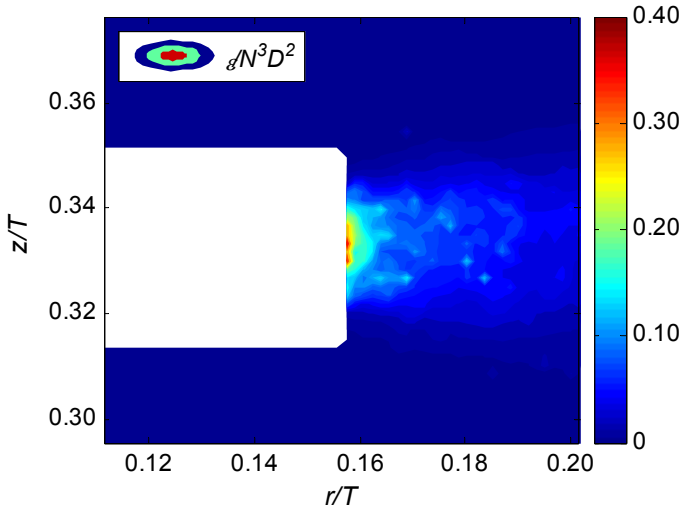

Figure 4.3: Dissipation rate from dimensional analysis using TKE from the full definition, with stereo-PIV ensemble-averaged measurements, Position 1, 1500 rpm

4.5 Direct evaluation

The local dissipation rate may be calculated directly from its definition as given in Equation (4.6) (Hinze, 1972). Expansion into Cartesian coordinates yields Equation (4.7).

$$\varepsilon = \nu \overline{\left(\frac{\partial u'_i}{\partial x_j} + \frac{\partial u'_j}{\partial x_i} \right) \frac{\partial u'_i}{\partial x_j}} \tag{4.6}$$

where, ν is the kinematic viscosity and u'_i the instantaneous fluctuating velocity component in the i^{th} direction. Expanding the equation into Cartesian coordinates yields:

$$\varepsilon = \nu \left\{ \begin{array}{l} 2\left(\overline{\left(\frac{\partial u'}{\partial x} \right)^2} + \overline{\left(\frac{\partial v'}{\partial y} \right)^2} + \overline{\left(\frac{\partial w'}{\partial z} \right)^2} \right) + \overline{\left(\frac{\partial u'}{\partial y} \right)^2} \\ + \overline{\left(\frac{\partial u'}{\partial z} \right)^2} + \overline{\left(\frac{\partial v'}{\partial x} \right)^2} + \overline{\left(\frac{\partial v'}{\partial z} \right)^2} + \overline{\left(\frac{\partial w'}{\partial x} \right)^2} + \overline{\left(\frac{\partial w'}{\partial y} \right)^2} \\ + 2\left(\overline{\left(\frac{\partial u'}{\partial y} \right)\left(\frac{\partial v'}{\partial x} \right)} + \overline{\left(\frac{\partial u'}{\partial z} \right)\left(\frac{\partial w'}{\partial x} \right)} + \overline{\left(\frac{\partial v'}{\partial z} \right)\left(\frac{\partial w'}{\partial y} \right)} \right) \end{array} \right\} \tag{4.7}$$

PIV measurements may be used to obtain gradients of the Reynolds stresses, provided that they have been taken over volumes sufficiently small and comparable to the Kolmogorov scales. The use of either 2-D or stereo-PIV determines the number of terms which may be calculated directly, and those which must be approximated.

4.5.1 2-D PIV estimate

In 2-D PIV, only the axial and radial velocity components can be measured in the $x-y$ plane. Subsequently, only five of twelve terms may be calculated in Equation (4.7); specifically 1, 2, 4, 6, and 10. The remaining unknown terms may be estimated using the statistical isotropy assumptions of Sharp and Adrian (2001) as follows:

$$\overline{\left(\frac{\partial w'}{\partial z}\right)^2} = \frac{1}{2}\left\{\overline{\left(\frac{\partial u'}{\partial x}\right)^2} + \overline{\left(\frac{\partial v'}{\partial y}\right)^2}\right\} \tag{4.8}$$

$$\overline{\left(\frac{\partial u'}{\partial z}\right)^2} = \overline{\left(\frac{\partial w'}{\partial x}\right)^2} = \overline{\left(\frac{\partial v'}{\partial z}\right)^2} = \overline{\left(\frac{\partial w'}{\partial y}\right)^2} = \frac{1}{2}\left\{\overline{\left(\frac{\partial u'}{\partial y}\right)^2} + \overline{\left(\frac{\partial v'}{\partial x}\right)^2}\right\} \tag{4.9}$$

$$\overline{\left(\frac{\partial u'}{\partial z}\right)\left(\frac{\partial w'}{\partial x}\right)} = \overline{\left(\frac{\partial v'}{\partial z}\right)\left(\frac{\partial w'}{\partial y}\right)} = -\frac{1}{4}\left\{\overline{\left(\frac{\partial u'}{\partial x}\right)^2} + \overline{\left(\frac{\partial v'}{\partial y}\right)^2}\right\} \tag{4.10}$$

Consequently, the expression for the dissipation rate (assuming statistical isotropy) becomes:

$$\varepsilon = \nu\left\{2\overline{\left(\frac{\partial u'}{\partial x}\right)^2} + 2\overline{\left(\frac{\partial v'}{\partial y}\right)^2} + 3\overline{\left(\frac{\partial u'}{\partial y}\right)^2} + 3\overline{\left(\frac{\partial v'}{\partial x}\right)^2} + 2\overline{\left(\frac{\partial u'}{\partial y}\right)\left(\frac{\partial v'}{\partial x}\right)}\right\} \tag{4.11}$$

It is important to note that the assumptions of Sharp and Adrian (2001) were derived from a study of a Rushton turbine. The impeller used here is an EkatoMizer, which is not supported with much experimental data from previous literature.

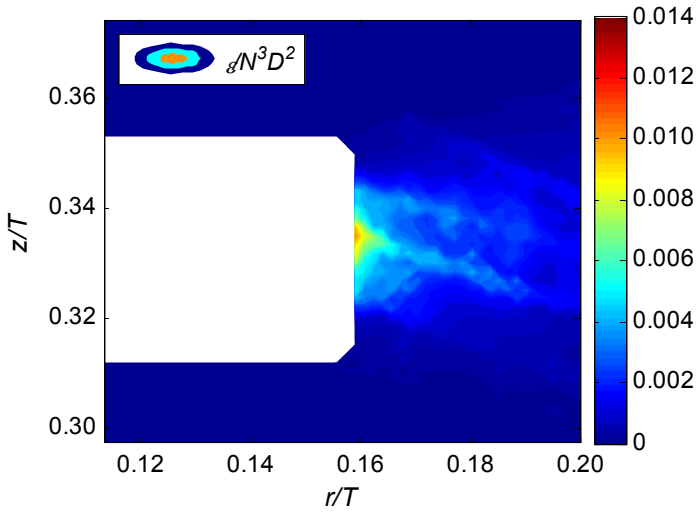

Figure 4.4: Dissipation rate from direct evaluation assuming 2-D PIV ensemble-averaged measurements, Position 1, 1500 rpm

Figure 4.4 illustrates the dissipation rate calculated from the 2-D approximation, where the maximum is $\sim 0.01N^3D^2$ at the blade edge. Similar to the results from dimensional analysis, the dissipation rate decays horizontally away from the impeller, corresponding to the discharge stream in the radial direction. However, the estimate of $\varepsilon_{\max}$ from direct evaluation is an order of magnitude smaller than that obtained from dimensional analyses.

For an accurate estimate of ε from its definition, velocity gradients must be measured over length scales comparable to the Kolmogorov scale, where TKE dissipation occurs and viscous forces dominate. According to Saarenrinne *et al*. (2001), a spatial resolution of 9η is required to estimate approximately 65% of the true dissipation rate; an improved resolution of 2η would provide 90%. Later, Baldi (2004) showed an exponential decrease of the dissipation rate estimate with decreasing resolution.

The Kolmogorov length scale cannot be inferred *a priori*, since the dissipation rate is required in its calculation. However, the mean Kolmogorov length scale in the bulk flow may be estimated from the mean dissipation rate, and for the EkatoMizer was found to be 36 µm at 1500 rpm. It follows that the PIV filtering scale (1 mm) provides a resolution of 28η in the bulk. In view of the findings of Saarenrinne *et al*. (2001) and Baldi (2004), the current resolution is insufficient to determine the dissipation rate directly from its definition. This provides an explanation for the poor result and huge underestimate of the local ε values.

It is important to note that the Kolmogorov scales decrease in regions of high turbulence, where even poorer resolutions are to be expected at the same PIV filtering scale. The Kolmogorov length scale calculated from $\varepsilon_{\max}$ (of the direct estimate) was found to be 29 µm, translating to a PIV resolution of 35η. The result suggests that not only is the ε estimate poor in the bulk region, but even more inaccurate at the blade edge, corresponding to the highest turbulence levels and subsequently greatest dissipation rates.

According to Baldi (2004), an increase in spatial resolution would benefit the calculation of the dissipation rate in both areas, but not equally. This is because the spatial resolution affects the dissipation rate estimate in regions of high turbulence the most. In line with this observation, an increase in resolution would have the greatest impact on the dissipation rate estimate in the impeller discharge stream.

4.5.2 Stereo-PIV estimate

With stereo-PIV, gradients of the tangential velocity component w in the axial and radial directions may be calculated. The new known terms (8 and 9 of Equation (4.7) respectively) are $\overline{\left(\frac{\partial w'}{\partial x}\right)^2}$ and $\overline{\left(\frac{\partial w'}{\partial y}\right)^2}$. However, since these measurements are also taken in a single $x-y$ plane, gradients in the out-of-plane z direction remain unknown. The isotropic assumptions of Sharp and Adrian (2001) must be retained to estimate these (via Equations (4.8) and (4.9)). The cross product terms are a combination of unknown out-of-plane and known in-plane gradients which cannot be separated. Subsequently they must also be estimated from Equation (4.10). Substituting the new terms into Equation (4.7) provides:

$$\varepsilon = \nu \left\{ \begin{array}{l} 2\overline{\left(\frac{\partial u'}{\partial x}\right)^2} + 2\overline{\left(\frac{\partial v'}{\partial y}\right)^2} + 2\overline{\left(\frac{\partial u'}{\partial y}\right)^2} + 2\overline{\left(\frac{\partial v'}{\partial x}\right)^2} \\ + \overline{\left(\frac{\partial w'}{\partial x}\right)^2} + \overline{\left(\frac{\partial w'}{\partial y}\right)^2} + 2\overline{\left(\frac{\partial u'}{\partial y}\right)\left(\frac{\partial v'}{\partial x}\right)} \end{array} \right\} \tag{4.12}$$

The direct estimate of the dissipation rate from stereo-PIV is shown in Figure 4.5. The spatial distribution is similar to that obtained assuming 2-D PIV, with the highest values in the discharge stream. However, stereo-PIV provides a higher estimate of ε, reaching a maximum of $0.014 N^3 D^2$ at the blade edge. This implies that the isotropic assumptions underestimate the tangential velocity gradients of the flow under consideration.

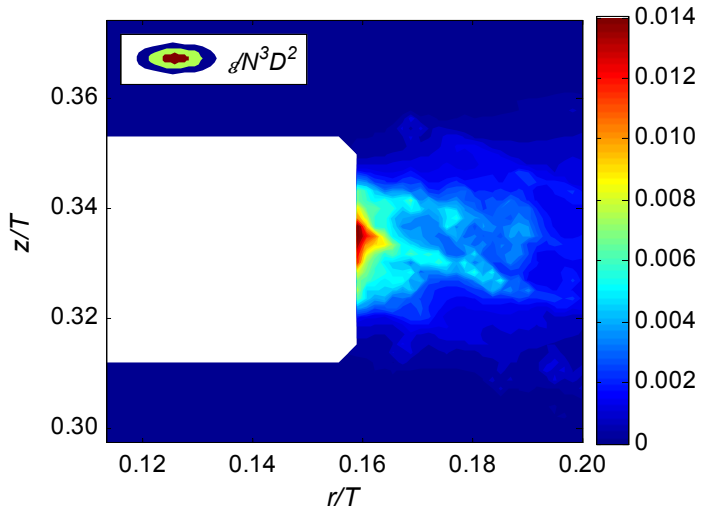

Figure 4.5: Dissipation rate from direct evaluation with stereo-PIV ensemble-averaged measurements, Position 1, 1500 rpm

The isotropic relations of Sharp and Adrian (2001) may be expressed as ratios with respect to the gradient of the radial velocity component in the radial direction, or coefficients K_{ijhk}. When the flow is locally isotropic, the coefficients summarized below are equal to one (Hinze, 1975):

$$K_{jjjj} = \overline{\left(\frac{\partial u'_i}{\partial x_j}\right)^2} \Bigg/ \overline{\left(\frac{\partial u'}{\partial x}\right)^2} = 1 \qquad \text{for } i = j \tag{4.13}$$

$$K_{ijij} = \frac{1}{2}\overline{\left(\frac{\partial u'_i}{\partial x_j}\right)^2} \Bigg/ \overline{\left(\frac{\partial u'}{\partial x}\right)^2} = 1 \qquad \text{for } i \neq j \tag{4.14}$$

$$K_{ijji} = -2\overline{\left(\frac{\partial u'_i}{\partial x_j}\right)\left(\frac{\partial u'_j}{\partial x_i}\right)} \Bigg/ \overline{\left(\frac{\partial u'}{\partial x}\right)^2} = 1 \qquad \text{for } i \neq j \tag{4.15}$$

Axial and radial profiles of these ratios are presented in Figure 4.6(a) and (b), taken immediately adjacent to the blade and above the impeller respectively. From these profiles, it may be concluded that the flow is anisotropic everywhere as the ratios deviate from unity, hence the application of Equations (4.8) to (4.10) is not valid. The maximum deviation from isotropy was a ratio of 2.7 for the estimate of the term $\left(\frac{\partial w'}{\partial y}\right)^2$, and of the same order of magnitude for the term $\left(\frac{\partial w'}{\partial z}\right)^2$. On the other hand the ratios are close to unity for the terms $\left(\frac{\partial v'}{\partial y}\right)^2$, $\left(\frac{\partial u'}{\partial y}\right)^2$ and $\left(\frac{\partial v'}{\partial x}\right)^2$. Profiles of the ratios obtained at other locations in the vessel showed a similar result. This suggests that the flow is anisotropic in the tangential direction. An assessment of the Lumley triangle in §3.6 had already indicated that turbulence was axisymmetric, and that the tangential plane was the direction of symmetry for the EkatoMizer.

Ducci and Yianneskis (2005) also investigated the departure of turbulence from local isotropy from ensemble-averaged data, and reported anisotropy of the flow generated by an RDT in all areas. However, the deviation from isotropy was not to the extent found in the present case; they reported a maximum deviation value of 0.25.

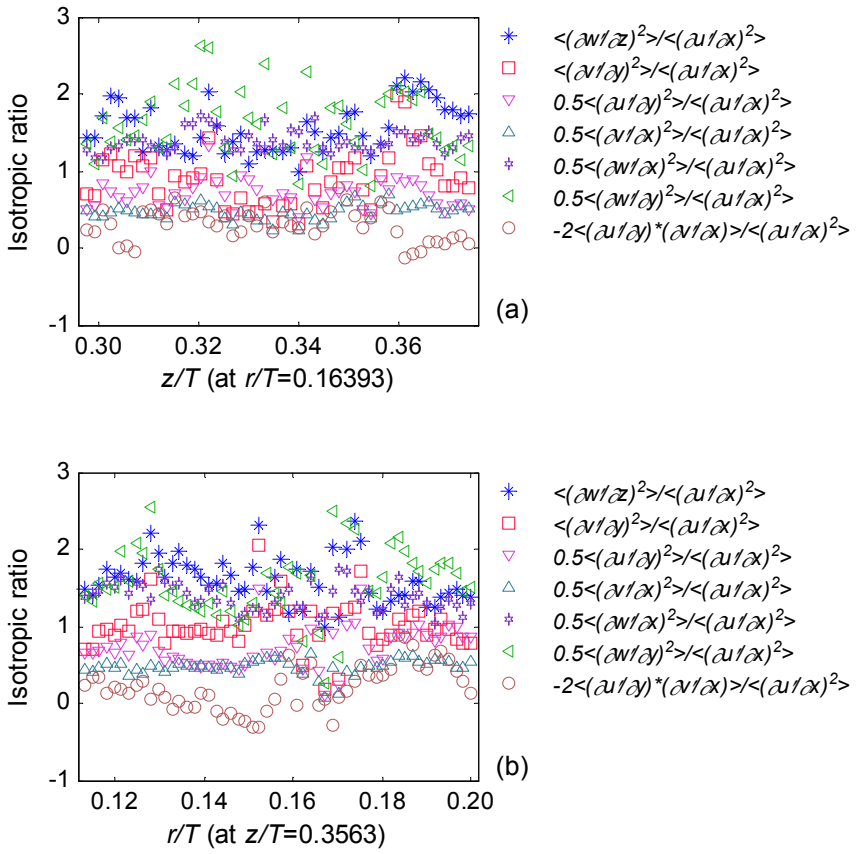

Figure 4.6: (a) Axial ($r/T = 0.16$) and (b) radial ($z/T = 0.36$) profiles of isotropic ratios from stereo-PIV ensemble-averaged measurements, Position 1, 1500 rpm

Since stereo-PIV provides a higher estimate of ε compared to the 2-D PIV case, at first glance it may lead to the conclusion that its resolution is superior. Further analysis proves that this is not the case. From $\varepsilon_{\max}$ of the stereo-PIV estimate, the Kolmogorov length scale was found to be 26 μm. At the same filtering scale (1 mm), this provides a resolution of 38η, worse than the 2-D PIV equivalent of 35η. Note that this is because the estimate of ε is higher in the stereo-PIV case leading to a smaller estimate of η, but the real η is the same in both cases. Baldi and Yianneskis (2004) obtained 2-D and stereo-PIV measurements, and also found that the latter resulted in a poor resolution. Thus although the stereo-PIV resolution is limited in comparison to the assumed 2-D case, measure of the tangential velocity component (at poorer resolution) is still able to provide a greater estimate.

4.6 LES analogy of Sheng *et al.* (2000)

Sheng *et al*. (2000) proposed a large eddy PIV method for dissipation rate estimation based on an analogy with large eddy simulation (LES). In the cascade theory, the largest eddies in high Reynolds number turbulent flows absorb energy from the mean flow, and transport it to smaller eddies. These large eddies have a tendency to be highly anisotropic, vortical in nature and strongly flow-dependent. Conversely, the smallest eddies involved in TKE dissipation tend to be flow-independent. Direct numerical simulation (DNS) requires resolution of all length scales, from the smallest Kolmogorov scales to the largest integral scales, which would be difficult for high Reynolds number flows as they have a broad spectrum of eddy sizes. For this reason, DNS can only be performed at low Reynolds numbers and for simple flow geometries, which reduce the flow complexity and spectrum width of eddy sizes. LES attempts to overcome this by resolving only large scale flow structures. The Navier-Stokes (NS) equations are solved directly for the large scales, whereas the small scales are modelled via sub-grid-scale (SGS) models. A low pass filter is applied to the NS equation to separate the resolved scales from the sub-grid scales.

The spatial resolution of PIV usually exceeds the smallest eddy sizes that govern the dissipation rate. Thus, by adopting the LES analogy, it is possible to measure the resolved velocity field (analogous to solving the NS equations), and model the unresolved scales. The interrogation cell size is naturally the spatial filter.

In between the integral and Kolmogorov scales, there exists an inertial sub-range which transfers energy between the two. The LES analogy assumes a dynamic-equilibrium between the sub-integral scales, such that the flux of TKE through the inertial sub-range is equal to the dissipation rate. To estimate this, only length scales within the inertial sub-range are required and it is not necessary to resolve the velocity field down to the Kolmogorov scale. Sheng *et al*. (2000) derived the resolved-scale kinetic energy balance, comprising the eddy dissipation term. They suggested that the turbulence dissipation rate ε can be approximated by computing the Reynolds averaged SGS dissipation rate $\overline{\varepsilon_{SGS}}$ at the PIV resolution:

$$\varepsilon \approx \overline{\varepsilon_{SGS}} = -2\overline{\tau_{ij} s_{ij}} \tag{4.16}$$

In practice, the Reynolds average on the right hand side of Equation (4.16) is an ensemble average over a PIV data set. This means that the average is taken after the multiplication of instantaneous $\tau_{ij} \times s_{ij}$, rather than $\overline{\tau_{ij}} \times \overline{s_{ij}}$. Since the result of the product is non-linear, the result from both averages is different, hence important to note. The variable s_{ij} is the resolved scale strain rate tensor calculated from gradients of the instantaneous velocity fields:

$$s_{ij} = \frac{1}{2}\left(\frac{\partial u_j}{\partial x_i} + \frac{\partial u_i}{\partial x_j} \right) \tag{4.17}$$

The SGS stress tensor τ_{ij} must be modelled by a SGS turbulence model. When the PIV resolution is comparable to the Kolmogorov scale, the SGS stress is replaced with the viscous shear stress, and the resolved velocity field directly provides the dissipation rate. Various SGS models have been suggested to estimate the stress tensor such as the Smagorinsky model (Smagorinsky, 1963), similarity model (Lui *et al*., 1994) and gradient model (Clark *et al*., 1979). Sheng *et al.* (2000) tested the Smagorinsky and similarity models and found that both yielded consistent results of the dissipation rate. Subsequently in this study only the Smagorinsky model will be used:

$$\tau_{ij} = -C_s^2 \Delta^2 \left| s_{ij} \right| s_{ij} \tag{4.18}$$

where C_s is the Smagorinsky constant, equal to 0.17, Δ the filter width (or interrogation cell size) and $\left| s_{ij} \right|$ the characteristic filtered strain rate, defined as $\sqrt{2 s_{ij} s_{ij}}$.

4.6.1 2-D PIV estimate

In the LES method, u, v, w are now the resolved scale instantaneous velocities rather than the fluctuating components, used in dimensional analyses or the direct calculation. The strain rate tensor consists of a total of nine components. Expanded into Cartesian coordinates, these are:

$$\begin{aligned}
s_{11} &= \left(\frac{\partial u}{\partial x} \right) \qquad s_{12} = s_{21} = \frac{1}{2}\left\{ \left(\frac{\partial u}{\partial y} \right) + \left(\frac{\partial v}{\partial x} \right) \right\} \\
s_{22} &= \left(\frac{\partial v}{\partial y} \right) \qquad s_{13} = s_{31} = \frac{1}{2}\left\{ \left(\frac{\partial u}{\partial z} \right) + \left(\frac{\partial w}{\partial x} \right) \right\} \\
s_{33} &= \left(\frac{\partial w}{\partial z} \right) \qquad s_{23} = s_{32} = \frac{1}{2}\left\{ \left(\frac{\partial v}{\partial z} \right) + \left(\frac{\partial w}{\partial y} \right) \right\}
\end{aligned} \tag{4.19}$$

2-D PIV enables measurement of only five components. The non-diagonal component s_{12} (equal to s_{21} due to symmetry) and diagonal components s_{11} and s_{22} may be calculated. The third diagonal component s_{33} may be derived from continuity. The five known strain rate tensor components for each instantaneous velocity field were multiplied with the corresponding stress tensor components (represented by the SGS turbulence model). The product terms were time-

averaged over the data set, which provided five averaged dissipation rate tensor components ε_{ij}. For instance, the components ε_{11} and ε_{12} may be written as:

$$\varepsilon_{11} = C_s^2 \Delta^2 2\overline{\left(\frac{\partial u}{\partial x}\right)^2} \quad \varepsilon_{12} = C_s^2 \Delta^2 \overline{\left(\frac{\partial u}{\partial y} + \frac{\partial v}{\partial x}\right)^2} \tag{4.20}$$

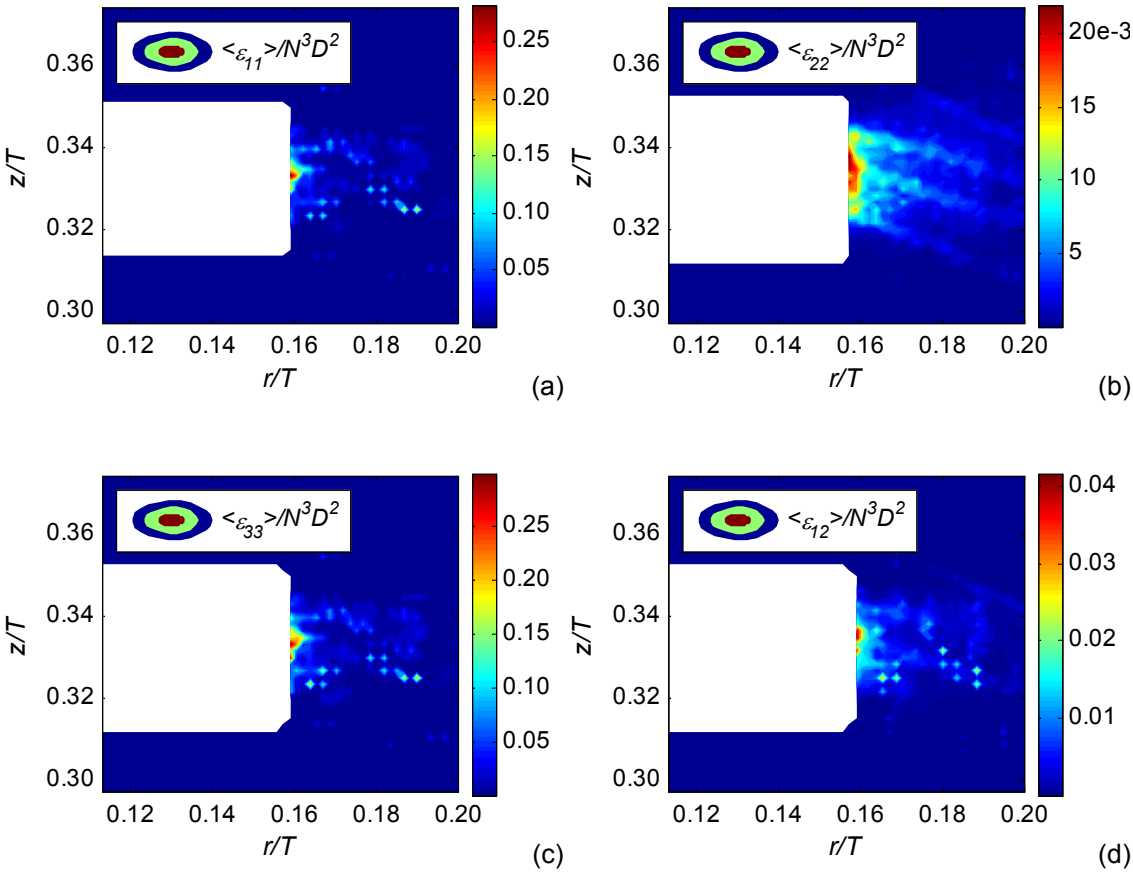

Figure 4.7: Components of the dissipation rate tensor (a) ε_{11} (b) ε_{22} (c) ε_{33} (d) $\varepsilon_{12} = \varepsilon_{21}$ assuming 2-D PIV ensemble-averaged measurements, Position 1, 1500 rpm

Sheng *et al*. (2000) examined the five known components of the dissipation rate tensor, and found that all had similar distributions and magnitudes. Subsequently, they assumed that the total dissipation rate could be approximated by multiplying the sum of the known components by a factor of 9/5. However, analysis of the dissipation rate tensors in the present case shows that linear scaling is inappropriate. As may be observed in Figure 4.7(a) to (d), there exists an order of magnitude difference between the normalized dissipation rate tensors ($\varepsilon_{11,\max} \approx 0.25$ and $\varepsilon_{22,\max} \approx 0.02$), although their spatial distribution appears to be similar. Kilander and Rasmuson (2005) also noted such differences between the tensor components in their study, but applied the 9/5 factor to estimate the dissipation rate nevertheless. The same will be done here in the absence of any better approximation.

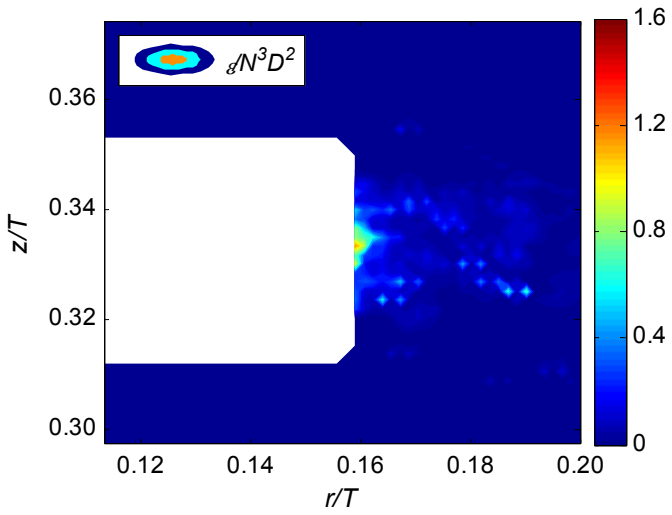

Figure 4.8: Dissipation rate from the LES analogy of Sheng *et al.* (2000) assuming 2-D PIV ensemble-averaged measurements, Position 1, 1500 rpm

The result obtained after scaling is shown in Figure 4.8 where $\varepsilon_{\max} \approx 1.1 N^3 D^2$; an order of magnitude greater than both dimensional analysis methods. Conversely, Sheng *et al*. (2000) found that the LES analogy corresponded reasonably well with their dimensional analysis case ($\varepsilon_{\max} \approx 0.006 N^3 D^2$ for both). It is worth noting that their PIV resolution was 5 mm, resulting in an equally large filter width. However, they claimed that the large-eddy PIV approach is inherently more accurate for inhomogeneous and anisotropic flows, such as the present case. The spatial distribution between these two methods is also very different. The LES approach creates large gradients in the vicinity of the impeller, which rapidly decrease in the main flow direction, whereas dimensional analysis produces a more even distribution of ε along the discharge stream. The comparison between the LES result and dimensional analysis is in agreement with the findings of Kilander and Rasmuson (2005), who obtained a five-times greater mean dissipation rate from the LES analogy, and also noted a difference in distribution between the two methods.

An interesting result is the "spottiness" of the distribution in Figure 4.8, corresponding to regions of intense dissipation. These estimates may have been influenced by a small number of very high velocity gradients in the averaging process. The gradients exist locally, and do not seem to be representative of the surrounding flow. It is not known if these extreme results are caused by genuinely high velocity gradients arising from turbulence intermittency, or if they are artefact. This issue will be revisited in §4.8.

4.6.2 Stereo-PIV estimate

Direct substitution of the strain rate tensor and modelled SGS stress tensor definitions into Equation (4.16) provides:

$$\varepsilon = C_s^2 \Delta^2 \overline{\left(2 s_{ij} s_{ij}\right)^{3/2}} \tag{4.21}$$

Expanding Equation (4.21) into Cartesian coordinates gives the total dissipation rate.

$$\varepsilon = C_s^2 \Delta^2 \overline{\left\{ \begin{array}{l} 2\left(\left(\frac{\partial u}{\partial x}\right)^2 + \left(\frac{\partial v}{\partial y}\right)^2 + \left(\frac{\partial w}{\partial z}\right)^2\right) \\ +\left(\frac{\partial u}{\partial y}\right)^2 + \left(\frac{\partial u}{\partial z}\right)^2 + \left(\frac{\partial v}{\partial x}\right)^2 + \left(\frac{\partial v}{\partial z}\right)^2 + \left(\frac{\partial w}{\partial x}\right)^2 + \left(\frac{\partial w}{\partial y}\right)^2 \\ +2\left(\left(\frac{\partial u}{\partial y}\right)\left(\frac{\partial v}{\partial x}\right) + \left(\frac{\partial u}{\partial z}\right)\left(\frac{\partial w}{\partial x}\right) + \left(\frac{\partial v}{\partial z}\right)\left(\frac{\partial w}{\partial y}\right)\right) \end{array} \right\}^{3/2}} \tag{4.22}$$

As mentioned previously, stereo-PIV does not provide information of derivatives in the out-of-plane direction. If the magnitudes and distributions of known terms are approximately equal, then a scaling factor may be used to approximate the unknown derivatives. Note that one cross product term (i.e. 10 of Equation (4.22)) may be determined directly since it comprises in-plane gradients. However all cross product terms will be neglected (following the justification of Khan (2005) described later), and a scaling factor of 12/10 will be employed to estimate the remaining mean-squared gradients. The final relationship maybe written as:

$$\varepsilon = C_s^2 \Delta^2 \overline{\left\{ \frac{12}{10}\left(\begin{array}{l} 2\left(\frac{\partial u}{\partial x}\right)^2 + 2\left(\frac{\partial v}{\partial y}\right)^2 + 2\left(\frac{\partial w}{\partial z}\right)^2 \\ +\left(\frac{\partial u}{\partial y}\right)^2 + \left(\frac{\partial v}{\partial x}\right)^2 + \left(\frac{\partial w}{\partial x}\right)^2 + \left(\frac{\partial w}{\partial y}\right)^2 \end{array} \right) \right\}^{3/2}} \tag{4.23}$$

To assess the similarity between the mean-squared velocity gradients, profiles were obtained along six sections of the flow field, as illustrated in Figure 4.9. The impeller had been blanked out during vector processing hence profiles crossing this region resulted in no data points.

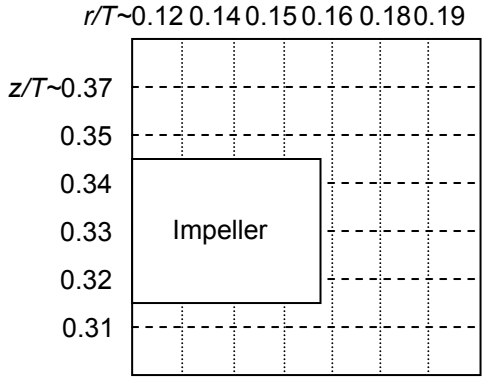

Figure 4.9: Schematic representation of axial and radial profile locations

Axial profiles of instantaneous velocity gradients

Figure 4.10(a) to (c) show that all mean-squared gradients increase between $0.31 > z/T > 0.37$ (coinciding with the axial position of the impeller blade) and reach a maximum at $z/T = 0.34$. The tangential velocity gradients show the greatest increases, followed by the radial and axial components respectively. This may be understood when considering the strong tangential flow behind the impeller blades, and the discharge stream in the radial direction. The EkatoMizer did not generate a strong axial flow.

The maximum values of the gradients also depend on distance from the impeller blade. For example, the tangential velocity gradient $\overline{\left(\frac{\partial w}{\partial x}\right)^2}$ reaches maxima of 15×10^4 s^{-2}, 20×10^4 s^{-2} and 45×10^4 s^{-2} in the bulk, discharge and near the blade edge respectively. Note that this gradient is the greatest close to the impeller tip, which is to be expected since a plot of the rms velocities (Figure 3.22) showed that the tangential component was the most turbulent near the blade.

Figure 4.10(d) to (f) show that not all mean-squared gradients are close to zero above and below the impeller, and the spread between them also increases. The profile obtained at $r/T = 0.12$ (next to the impeller shaft) in Figure 4.10(f) displays the largest spread. A common realization amongst all axial profiles is that the cross-product gradient $\overline{\left(\frac{\partial u}{\partial y}\right)\left(\frac{\partial v}{\partial x}\right)}$ retains an approximately zero value, which is why they were neglected in Equation (4.23).

Radial profiles of instantaneous velocity gradients

Directly above and below the impeller (Figure 4.11(b) and (f) respectively), all velocity gradients are negligibly small up to $r/T = 0.16$, the blade edge location. Further away from the blade the gradients gradually increase, with the exception of $\overline{\left(\frac{\partial w}{\partial y}\right)^2}$ which exhibits a sharp rise, as the tangential velocity diminishes very quickly above and below the impeller (Figure 3.15). Analogous to the axial profiles, the gradients reach their maximum values to different extents, in descending order of tangential, radial and axial components. The reverse trend is noticed in the discharge stream shown in Figure 4.11(c), (d) and (e); all gradients retain their maximum close to the blade edge and gradually decrease with distance away from it. The variation in distribution and magnitude is also the most prominent in this region compared to above and below the impeller.

Of the three impeller stream profiles, that obtained nearest to the blade centreline (Figure 4.11(d)) exhibits the largest gradients. For instance, $\overline{\left(\frac{\partial w}{\partial x}\right)^2}$ is 5.5×10^5 s^{-2} at the blade tip, compared to 3.3×10^5 s^{-2} and 7.5×10^4 s^{-2} in Figure 4.11(c) and (e) respectively. The cross product gradient $\overline{\left(\frac{\partial u}{\partial y}\right)\left(\frac{\partial v}{\partial x}\right)}$ maintains a relatively negligible value consistently.

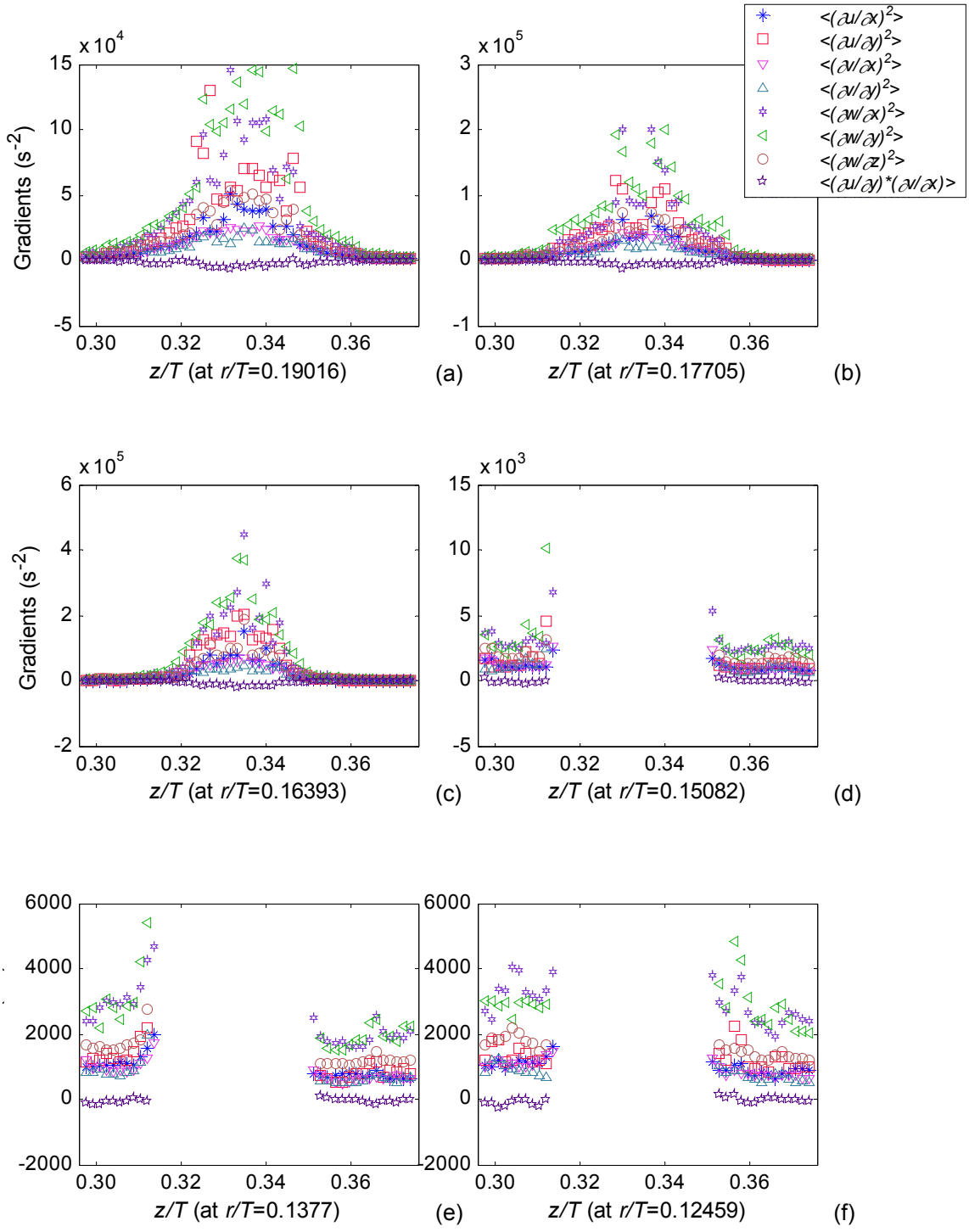

Figure 4.10: Axial profiles of instantaneous velocity gradients from stereo-PIV ensemble averaged-measurements, Position 1, 1500 rpm (a) $r/T = 0.19$ **(b)** $r/T = 0.18$ **(c)** $r/T = 0.16$ **(d)** $r/T = 0.15$ **(e)** $r/T = 0.14$ **and (f)** $r/T = 0.12$

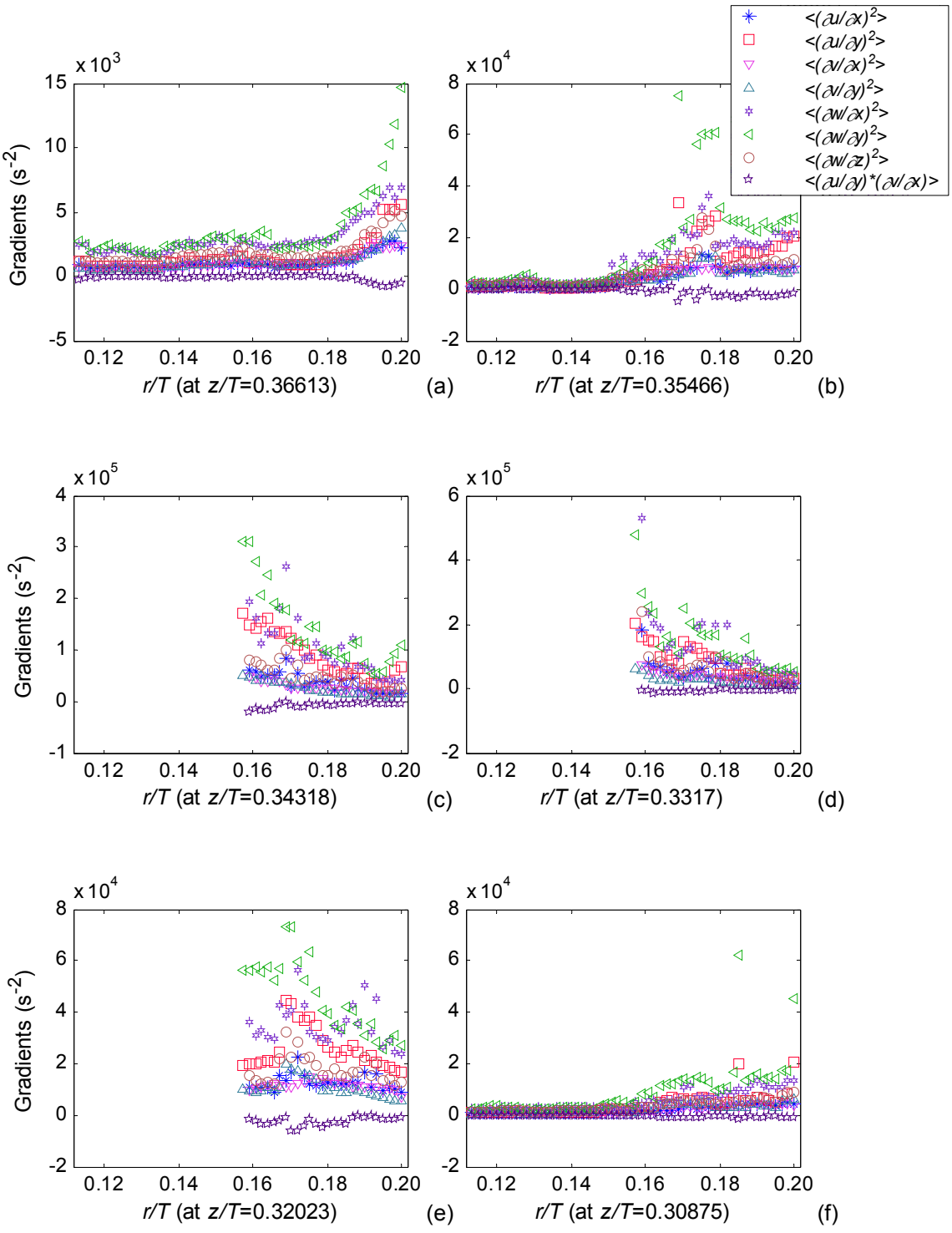

Figure 4.11: Radial profiles of instantaneous velocity gradients from stereo-PIV ensemble averaged-measurements, Position 1, 1500 rpm (a) $z/T = 0.37$ **(b)** $z/T = 0.35$ **(c)** $z/T = 0.34$ **(d)** $z/T = 0.33$ **(e)** $z/T = 0.32$ **and (f)** $z/T = 0.31$

Treatment of unknown terms

From the observations made above, it is justified to neglect the known cross-product term in Equation (4.22). However, the treatment of the unknown cross-products is ambiguous. Khan (2005) hypothesized that these terms take both positive and negative values (unlike mean-squared gradients which are always positive), since in all cases their values were small compared to the other squared gradients; hence cancel each other out in the time averaging process. Subsequently in all cases their values were small compared to other squared gradients.

This hypothesis could be evaluated against one other cross-product term. PIV measurements obtained in front of the impeller in the $y-z$ plane enabled calculation of gradients in the axial and tangential directions. The term $\frac{\partial u}{\partial x}$ was obtained from continuity, and the known cross-product gradient was $\overline{\left(\frac{\partial w}{\partial y}\right)\left(\frac{\partial v}{\partial z}\right)}$. Axial and radial profiles obtained at $r/T=0.16$ and $z/T=0.35$, are displayed in Figure 4.12(a) and (b) respectively.

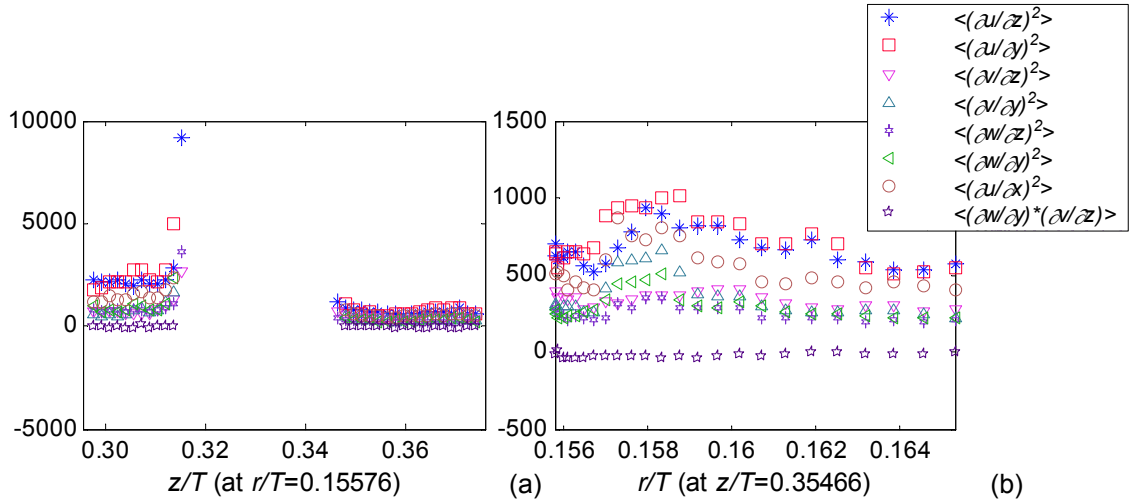

Figure 4.12: (a) Axial ($r/T=0.16$) and (b) radial ($z/T=0.35$) profiles of instantaneous velocity gradients from stereo-PIV ensemble-averaged measurements, Position 3, 1500 rpm

As may be observed, the cross-product gradients maintain negligible values along both profiles. The third cross-product term $\overline{\left(\frac{\partial u}{\partial z}\right)\left(\frac{\partial w}{\partial x}\right)}$ remains unknown, but is assumed to follow trends similar to those depicted already. By accepting Khan's (2005) hypothesis for all cross-product terms, their contribution to the dissipation rate may be eliminated.

The profiles of Figure 4.10 to Figure 4.12 indicate that simple scaling is not an appropriate measure to approximate unknown gradients in the out-of-plane direction, as their magnitudes are not equivalent. The spread in data is considerable in the vicinity of the impeller and

discharge stream. However since the stereo-PIV estimate of the dissipation rate comprises more known terms (10 of 12 after excluding the cross-product terms) compared to the 2-D PIV estimate (with 5 of 9 known terms), it is believed to provide a more accurate estimate, notwithstanding the linear scaling. Note that the scaling factor 12/10 does not actually imply that 83% of the real measure has been obtained, since the unknown gradients could contribute significantly more to the total dissipation rate. The result from this method is presented in Figure 4.13.

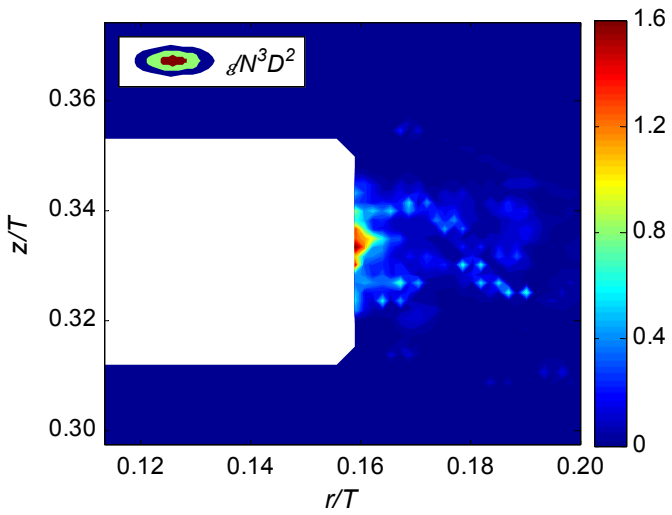

Figure 4.13: Dissipation rate from the LES analogy of Sheng *et al.* (2000) using stereo-PIV ensemble-averaged measurements, Position 1, 1500 rpm

The spatial distribution of ε is almost identical to that portrayed in Figure 4.8 from the 2-D PIV case. However $\varepsilon_{\max}$ obtained from stereo-PIV is $\sim 1.76N^3D^2$; 60% greater than the 2-D equivalent. This suggests that the 2-D scaling factor underestimates the unknown gradients. Intense dissipation is confined to the blade edge, which is unsurprising since axial profiles of the tangential velocity gradients portrayed their maximum values close to the blade. Simple scaling in 2-D PIV would not account for these unusually high gradients. It is anticipated that stereo-PIV combined with the LES analogy of Sheng *et al*. (2000) provides the closest estimate of the true dissipation rate compared to all methods discussed thus far. However as some scaling was still employed, the actual dissipation rate may be different to that illustrated in Figure 4.13.

4.7 TKE balance

Due to the dissipative nature of TKE, a continuous supply of turbulent energy is required to maintain the turbulence, otherwise it would decay. A statistical steady state is only possible when there is equilibrium between the energy supplied to the turbulent motion, diffusion and dissipation of TKE. The balance in Equation (4.24) assumes the steady flow of an incompressible Newtonian fluid.

In a stirred tank, there usually co-exist three types of motion; mean flow (or global recirculation pattern), turbulent fluctuations (that dissipate TKE) and periodic fluctuations (induced by the

impeller blade rotation). Escudie and Line (2003) carried out a triple decomposition of the velocity, and solved separately the energy balance equations for each motion. In the EkatoMizer case, the PIV measurements were ensemble-averaged. Since they do not account for flow periodicity, it is more appropriate to apply the standard Reynolds decomposition to the velocity field, which comprises the mean and turbulent motions only. The turbulence kinetic energy balance may then be expressed as:

$$\underbrace{\frac{\partial}{\partial t}\left(\frac{1}{2}\overline{u'_i u'_i}\right)}_{\text{Accumulation}} + \underbrace{\overline{u_j}\frac{\partial}{\partial x_j}\left(\frac{1}{2}\overline{u'_i u'_i}\right)}_{\text{Transport}} = \underbrace{-\frac{\partial}{\partial x_j}\left(\overline{\frac{1}{2}u'_j u'_i u'_i}\right)}_{\text{Turbulent\_diffusion}} \underbrace{-\frac{\partial}{\partial x_j}\left(\overline{u'_j \frac{p}{\rho}}\right)}_{\text{Pressure\_diffusion}}$$
$$\underbrace{-\overline{u'_i u'_j}\frac{\partial \overline{u_i}}{\partial x_j}}_{\text{Transfer}} \underbrace{+\nu\frac{\partial}{\partial x_j}\left(\overline{u'_i\left(\frac{\partial u'_i}{\partial x_j}+\frac{\partial u'_j}{\partial x_i}\right)}\right)}_{\text{Viscous\_diffusion}} \underbrace{-\nu\overline{\frac{\partial u'_j}{\partial x_i}\left(\frac{\partial u'_i}{\partial x_j}+\frac{\partial u'_j}{\partial x_i}\right)}}_{\text{Viscous\_dissipation}} \quad (4.24)$$

Equation (4.24) states that the rate of change in turbulence kinetic energy per unit mass is equal to the convective diffusion by turbulence of the total turbulence energy, pressure and viscous diffusion, plus the transfer of energy from the mean to turbulent motion through turbulence shear stresses, plus the work done by the viscous shear stress of turbulent motion per unit mass and time, plus the dissipation by the turbulent motion per unit mass. In this method, the dissipation rate may be obtained from the balance of TKE, in which all other terms are derived experimentally. Thus, the requirement to resolve the flow down to the Kolmogorov scales is eliminated.

The following discussion of the TKE balance is based on stereo-PIV measurements only. 2-D PIV does not provide enough data for a basis of comparison. As will be observed, stereo-PIV itself leaves many quantities unspecified due to the requirement for out-of-plane gradients. 2-D PIV would only extend the problem in cases where the w velocity component is required in isolation, for example in the triple velocity correlations and for the Reynolds stress tensor.

In the TKE balance given in Equation (4.24), at steady state there is no accumulation, and hence the first term is zero. The transport term expressed in Cartesian coordinates comprises the convection of TKE in and out of the control volume as below:

$$\text{Transport} = \bar{u}\frac{\partial}{\partial x}\left(\frac{1}{2}\left(\overline{u'^2}+\overline{v'^2}+\overline{w'^2}\right)\right)+\bar{v}\frac{\partial}{\partial y}\left(\frac{1}{2}\left(\overline{u'^2}+\overline{v'^2}+\overline{w'^2}\right)\right)+\bar{w}\frac{\partial}{\partial z}\left(\frac{1}{2}\left(\overline{u'^2}+\overline{v'^2}+\overline{w'^2}\right)\right) \quad (4.25)$$

The turbulent diffusion term comprises a triple velocity correlation:

$$\text{Turbulent\_diffusion} = \begin{array}{l} -\frac{\partial}{\partial x}\left(\frac{1}{2}\left(\overline{u'u'^2}+\overline{u'v'^2}+\overline{u'w'^2}\right)\right) \\ -\frac{\partial}{\partial y}\left(\frac{1}{2}\left(\overline{v'u'^2}+\overline{v'v'^2}+\overline{v'w'^2}\right)\right) \\ -\frac{\partial}{\partial z}\left(\frac{1}{2}\left(\overline{w'u'^2}+\overline{w'v'^2}+\overline{w'w'^2}\right)\right) \end{array} \quad (4.26)$$

In both of the previous two expressions, the third term involving the tangential gradient is unknown. The pressure diffusion term comprises a pressure-velocity correlation, which cannot be measured directly from PIV data. Escudie and Line (2003) referred to the DNS results of Eggels *et al*. (1994) who concluded that its contribution is negligible in the TKE balance. The same assumption will be applied here.

The kinetic energy transfer term involves a product of the Reynolds stress tensor and gradients of the mean flow:

$$\text{Transfer} = \begin{Bmatrix} -\overline{u'^2}\frac{\partial \bar{u}}{\partial x} & -\overline{u'v'}\frac{\partial \bar{u}}{\partial y} & -\overline{u'w'}\frac{\partial \bar{u}}{\partial z} \\ -\overline{v'u'}\frac{\partial \bar{v}}{\partial x} & -\overline{v'^2}\frac{\partial \bar{v}}{\partial y} & -\overline{v'w'}\frac{\partial \bar{v}}{\partial z} \\ -\overline{u'w'}\frac{\partial w}{\partial x} & -\overline{v'w'}\frac{\partial w}{\partial y} & -\overline{w'^2}\frac{\partial w}{\partial z} \end{Bmatrix} \tag{4.27}$$

All nine Reynolds stresses may be calculated with stereo-PIV data, but since out-of-plane gradients are unknown, only six of nine transfer terms may actually be determined. Lastly, the viscous diffusion term is expressed as:

$$\begin{aligned} \text{Viscous\_diffusion} = & +\nu\frac{\partial}{\partial x}\left(2\overline{u'\left(\frac{\partial u'}{\partial x}\right)}+\overline{v'\left(\frac{\partial u'}{\partial y}+\frac{\partial v'}{\partial x}\right)}+\overline{w'\left(\frac{\partial u'}{\partial z}+\frac{\partial w'}{\partial x}\right)}\right) \\ & +\nu\frac{\partial}{\partial y}\left(\overline{u'\left(\frac{\partial u'}{\partial y}+\frac{\partial v'}{\partial x}\right)}+2\overline{v'\left(\frac{\partial v'}{\partial y}\right)}+\overline{w'\left(\frac{\partial v'}{\partial z}+\frac{\partial w'}{\partial y}\right)}\right) \\ & +\nu\frac{\partial}{\partial z}\left(\overline{u'\left(\frac{\partial u'}{\partial z}+\frac{\partial w'}{\partial x}\right)}+\overline{v'\left(\frac{\partial v'}{\partial z}+\frac{\partial w'}{\partial y}\right)}+2\overline{w'\left(\frac{\partial w'}{\partial z}\right)}\right) \end{aligned} \tag{4.28}$$

This expression comprises the most unknown quantities. When the gradients are expanded into a total of nine terms, only four are known comprising second-order derivatives of in-plane gradients. These derivatives are calculated using a second order central differencing scheme.

In all aspects of the TKE balance, scaling of the known terms (by a factor of known to unknown terms) was applied to approximate the unknown quantities, and evaluate the budget of TKE. Note that terms which had a factor of say two already, were counted as two terms. The result is illustrated in Figure 4.14. The dissipation rate has some very distinct features compared to other methods. Firstly it creates an intense spot of dissipation near the impeller, reaching a maximum of $\sim 3.8N^3D^2$; much greater than that obtained from the 3-D LES analogy ($\sim 1.76N^3D^2$). Secondly, high magnitude regions are not spread evenly in the flow field and instead are scattered discretely. Within the discharge stream, the dissipation rate is $\sim 1N^3D^2$, but for the majority of the flow field, there appears to be very little dissipation.

The biggest failure of this method is evident from the negative values (shaded blue in Figure 4.14). Escudie and Line's (2003) dissipation rate estimate from the TKE balance did not generate this discrepancy. However they obtained PIV measurements in multiple planes, which

enabled full quantification of the TKE balance. In this case, the extensive scaling used is not really applicable to anisotropic flows. Ducci and Yianneskis (2005) completed the budget of TKE (using the dissipation rate from direct evaluation), and found that the total balance was negative. The authors attributed this deficit to the missing pressure diffusion term, which was also unknown in the present case. Thus, the anomalous results may be a direct consequence of an incomplete balance and/or inappropriate scaling of unknowns. In this case, if the negative dissipation rate is due to the missing pressure diffusion term only, then it suggests that the pressure diffusion term must be negative.

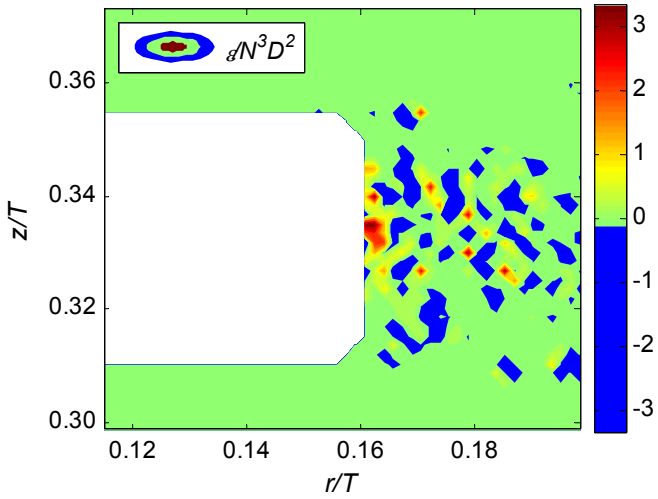

Figure 4.14: Dissipation rate from the TKE balance using stereo-PIV ensemble-averaged measurements, Position 1, 1500 rpm

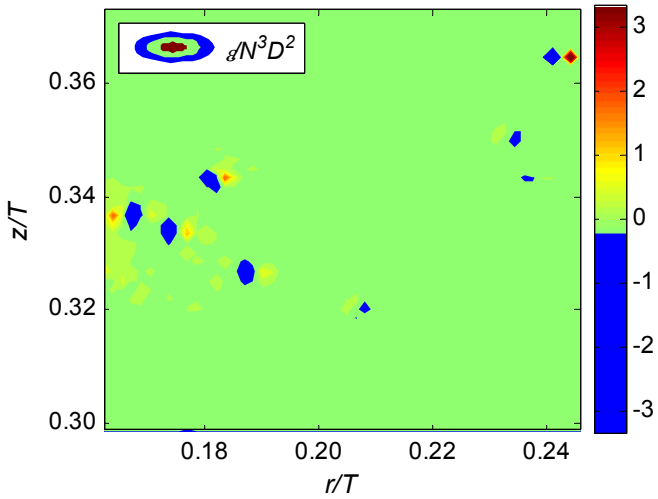

Figure 4.15: Dissipation rate from the TKE balance using stereo-PIV ensemble-averaged measurements, Position 2, 1500 rpm

Ecudie's (2001) study of an RDT showed that pressure diffusion varied significantly along the radial direction. The dissipation rate estimate further into the discharge stream (Position 2) from

the TKE balance is shown in Figure 4.15, where there are fewer negative evaluations. Thus it is possible that the pressure diffusion term decreases with radial distance away from the impeller, and its contribution to the balance is less significant. Overall, it is clear that even stereo-PIV is insufficient to estimate the dissipation rate from the TKE balance.

4.8 Turbulence intermittency and vector filtering

Figure 4.16 shows the time-history of the instantaneous dissipation rate from the LES analogy of Sheng *et al.* (2000), at a point in the discharge stream over 500 PIV measurements. It is apparent that some fluctuations reach between $50-250N^3D^2$. Although these high values are infrequent, they bias the mean ($1.76N^3D^2$), which would be significantly lower without their contribution. Outlying vectors generating high velocity gradients could be eliminated using filters if assumed to be erroneous, or retained if considered to be genuine fluctuations arising from turbulence intermittency. Both issues will be considered simultaneously in this section.

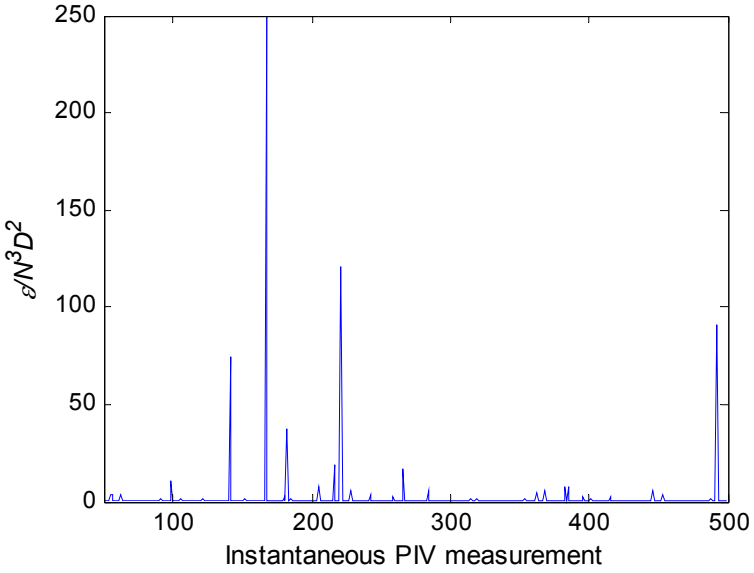

Figure 4.16: Time-history of instantaneous normalized dissipation rate at a point in the discharge stream, over 500 PIV measurements, 1500 rpm

There are various types of vector validation filters; i.e. range, standard deviation, local mean and local median filters. Of these, standard deviation filters are the most comprehensive and popular. They evaluate vectors against the velocity mean, and eliminate them if they exceed a specified tolerance, i.e. a few standard deviations from the mean. These statistics could be obtained globally (over the entire velocity field), locally (around neighbouring vectors of a specific point), or temporally (over sequential PIV measurements at a fixed node). Figure 4.17 shows points in the velocity field which are used to calculate statistics for each type of filter.

Preliminary tests were carried out to eliminate erroneous vectors in the velocity field by applying these standard deviation filters. The tolerance was set to three standard deviations for all of them, which is the default level used by TSI Insight vector processing software. All three types altered the dissipation rate in a different way. For instance, the global and temporal filters

significantly affected the magnitude and distribution, whereas the local filter eliminated a few outlying points only (results in Appendix II). Consequently, an assessment method is required for selecting the most appropriate filter, and also to check that genuine fluctuations inherent to turbulent flows are not removed. It is possible to represent turbulence intermittency via the multifractal model of Meneveau and Sreenivasan (1991). Dissipation rate profiles resulting from filtering may be compared to this model, and the most suitable filter selected on this basis.

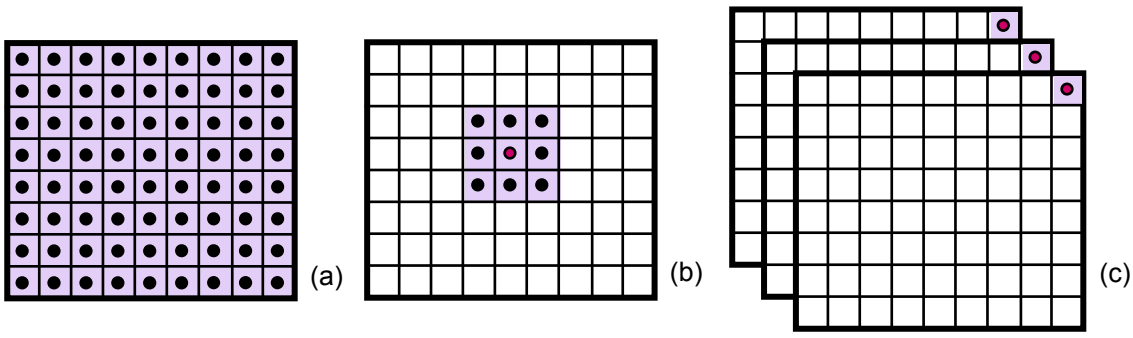

Figure 4.17: Points in the PIV velocity fields used to calculate statistics in the (a) global (b) local and (c) temporal standard deviation filters

4.8.1 Multiplicative process and cascade theory

It is well known that small scales of turbulence are intermittent. Since the observation of Batchelor and Townsend (1949) of strongly intermittent bulges in velocity derivative signals, many models have been proposed to account for small-scale intermittency. The dissipation rate has received the most attention over the last 30 years. Most turbulence models are based on the theory of transfer of kinetic energy from large to small scales in a self-similar cascade, with an associated multiplicative process.

In the multiplicative process, large eddies break down into smaller eddies sequentially. Each eddy is given a characteristic linear dimension $r(n)$, where n is the generation step. At each stage, the characteristic scale may be estimated as the product of n numbers called 'length multipliers l_j', which are ratios of consecutive length scales. Hence the characteristic linear dimension is given by:

$$r(n) = r(0)\prod_{j=i}^{n} r(j)/r(j-1) = r(0)\prod_{j=1}^{n} l_j \tag{4.29}$$

Secondly, when an eddy (or piece) decays, the smaller ones are assumed to receive a fraction of the total dissipation rate E_t, equal to E_r. Similar to the characteristic scales, the total dissipation on a piece of size $r(n)$ may be given in terms of the product of n numbers, referred to as the 'measure multipliers M_j', which are ratios of consecutive measures.

$$E_{r(n)} = E_{r(0)}\prod_{j=i}^{n} E_{r(j)} / E_{r(j-1)} = E_{r(0)}\prod_{j=1}^{n} M_j \tag{4.30}$$

Thus a multiplicative process may be considered as the disintegration of a large piece into smaller ones, with each smaller piece receiving a fraction of the measure of the larger unit, which is the product of the multipliers l_j and M_j from previous stages. The multipliers are considered to be random variables, with a certain probability distribution. When the distributions are independent of the level or generation step j, self-similarity appears, and power-law behaviour occurs in the moments and distribution function of E_r.

4.8.2 Multifractal model of Meneveau and Sreenivasan (1991)

Meneveau and Sreenivasan (1991) provided a detailed account of the development of cascade models for turbulence intermittency and highlighted their shortcomings. Previous models were oversimplified by assuming that the measure multipliers at a given stage were equal, implying non-intermittency (Kolmogorov's 1941 theory) or that they were non-zero and equal for a fraction of the new eddies (β model).

Meneveau and Sreenivasan (1991) proposed a self-similar binomial model, which assumes that the multiplicative process occurs in one dimension. An initial eddy of size L breaks down into two equal segments of size $L/2$, yielding a length multiplier $l_j = 1/2$. The distribution of energy over eddies is assumed to be unequal, by assigning the measure multipliers a bimodal distribution. The authors found that spatial fluctuations of the dissipation rate could be well quantified by the multipliers $M_1 = p_1 = 0.7$ and $M_2 = p_2 = 0.3$. These correspond to the simplest possible fluctuations that reproduce most of the experimental observations. Whether a multiplier takes the value 0.7 or 0.3 is random. However, at each cascade step, a conservation of the measure is imposed such that the sum of M_j is always unity.

The measure of a multiplicative process may be characterised in terms of moments q. By introducing an exponent D_q, the sum of the dissipation rate E_r^q over disjoint segments of size r may be given as proportional to:

$$\sum E_r^q \sim E_L^q (r/L)^{D_q(q-1)} \tag{4.31}$$

where E_L is the total dissipation contained in pieces of fluid size L. The exponents D_q are called 'generalized dimensions'. High positive values of q accentuate regions of intense dissipation; whereas negative values of q emphasize regions of low dissipation. For the binomial case in particular, the analytical model of D_q is given as:

$$D_q = \log_2\left[p_1^q + p_2^q\right]/(1-q) \tag{4.32}$$

Anselmet *et al*. (2001) assessed the fractal nature of energy distribution at scales r with respect to all of the above mentioned cascade models. They reported that the best predictions were given by the multifractal model at the highest orders, whereas Kolmogorov's 1941 theory and the β model departed from the multiplicative process at quite low orders. In light of this,

the multifractal model of Meneveau and Sreenivasan (1991) was selected to represent turbulence intermittency in the present case.

4.8.3 D_q exponents of dissipation from stereo-PIV

It is possible to obtain the multifractal exponents D_q at the last cascade step of a multiplicative process, by analysing the dissipation rate at varying degrees of resolution. In the binomial case the process occurs on pieces of size 2^{-n} starting at the origin. However in most experiments dissipation is obtained at an unknown level in the multiplicative process, in which case knowledge of the last cascade step, or size and position of pieces at different levels is lacking. Nevertheless, Meneveau and Sreenivasan (1991) showed that it is still possible to use box sizes different from the natural partition 2^{-n}, and the results remain unaffected.

In practice, the dissipation rate ε obtained from experimental data at the resolved scale is integrated over disjoint segments of length r, yielding dissipation E_r. The segmented dissipation is normalized by the total dissipation in the data set E_t:

$$E_r = \int \varepsilon dr\,, \qquad E_t = \int \varepsilon dx \tag{4.33}$$

The scaling range r should be greater than the Kolmogorov length scale η and contained within the inertial range where self-similarity appears. Here the distribution functions of the multipliers l_j and M_j becomes independent of the cascade step (or characteristic size r). In the current PIV experiments, the flow was not resolved down to the Kolmogorov scale; hence the aim was to ensure that it was resolved within the inertial range at least.

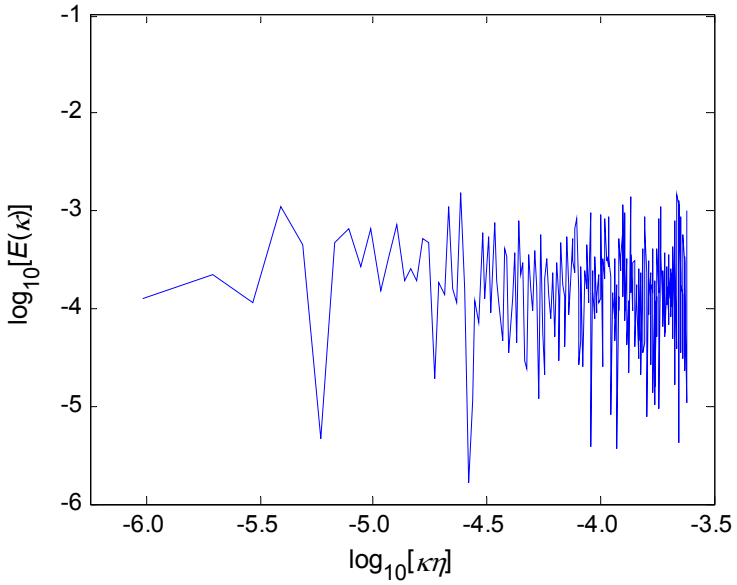

Figure 4.18: Power spectrum of the radial velocity at point $r/T = 0.161$, $z/T = 0.335$ in the discharge stream, from stereo PIV measurements at 15 Hz and 1500 rpm

To convert the time separation between PIV image pairs (ΔT) into longitudinal separation (Δr), Taylor's hypothesis was applied such that $\Delta r = \bar{u}\Delta T$, where $\bar{u}$ is the time-averaged mean radial velocity at that point in the flow field. The power spectrum of the radial velocity time-series obtained at the point $r/T = 0.161$, $z/T = 0.335$ in the discharge stream is presented in Figure 4.18.

A periodogram estimate of the power spectral density (PSD) was obtained. Note that the wave number $\kappa = f/\bar{u}$ where f is the sampling frequency 15 Hz. As may be observed, the cut-off range of the PSD is within the energy containing range, meaning that an appropriate scaling range r cannot be defined for the current dissipation field. In order for this analysis to be carried out, better time resolved information is required. The next section describes the calculation of the generalized dimensions of the dissipation rate from high-speed PIV data.

4.8.4 D_q exponents of dissipation from high-speed PIV

2-D high-speed PIV experiments were carried out at 5 kHz; details are given in §3.2.6. The PSD from the radial velocity at the point $r/T = 0.167$, $z/T = 0.333$ in the discharge stream is shown in Figure 4.19. In this case, the time separation between double-image frames (2×10^{-4} s) was found to produce a power spectrum with an identifiable inertial range. The solid line indicates the -5/3 slope. The dashed vertical lines enclose the scaling range $-2.25 < \log_{10}[\kappa\eta] < -1.5$, corresponding to $32 < r/\eta < 178$. Subsequently D_q exponents of the instantaneous dissipation rate at that point (from the 2-D LES analogy of Sheng *et al*. (2000)) could be calculated.

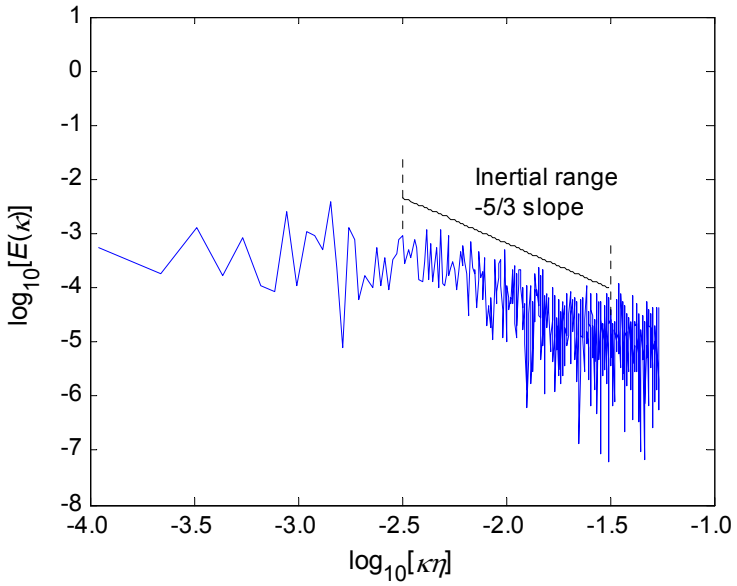

Figure 4.19: Power spectrum of the radial velocity at point $r/T = 0.167$, $z/T = 0.333$ in the discharge stream, from high-PIV measurements at 5 kHz and 1500 rpm

Instantaneous velocity fields from high-speed PIV were processed using the global, local and temporal standard deviation filters, and the dissipation rate re-calculated. Details of the filtering

operations are given in Appendix II. The profiles before and after filtering are shown in Figure 4.20(a) to (d). In Figure 4.20(a), extreme fluctuations up to $200N^3D^2$ may be observed, whereas the mean is only $0.37N^3D^2$.

The dissipation rate profiles from the filtered and unfiltered velocity fields were integrated over arbitrary disjoint segments of length r within the scaling range. The sums $\sum(E_r/E_t)^q$ for q values between 0 and +5 were computed. Relevant quantities in determining the D_q exponents are the logarithm of the moments divided by $(q-1)$. Then, log-log plots of $\left[\sum(E_r/E_t)^q\right]^{1/(q-1)}$ as a function of r/η were constructed for various q values, where the slope of the linear regions provided the D_q exponents.

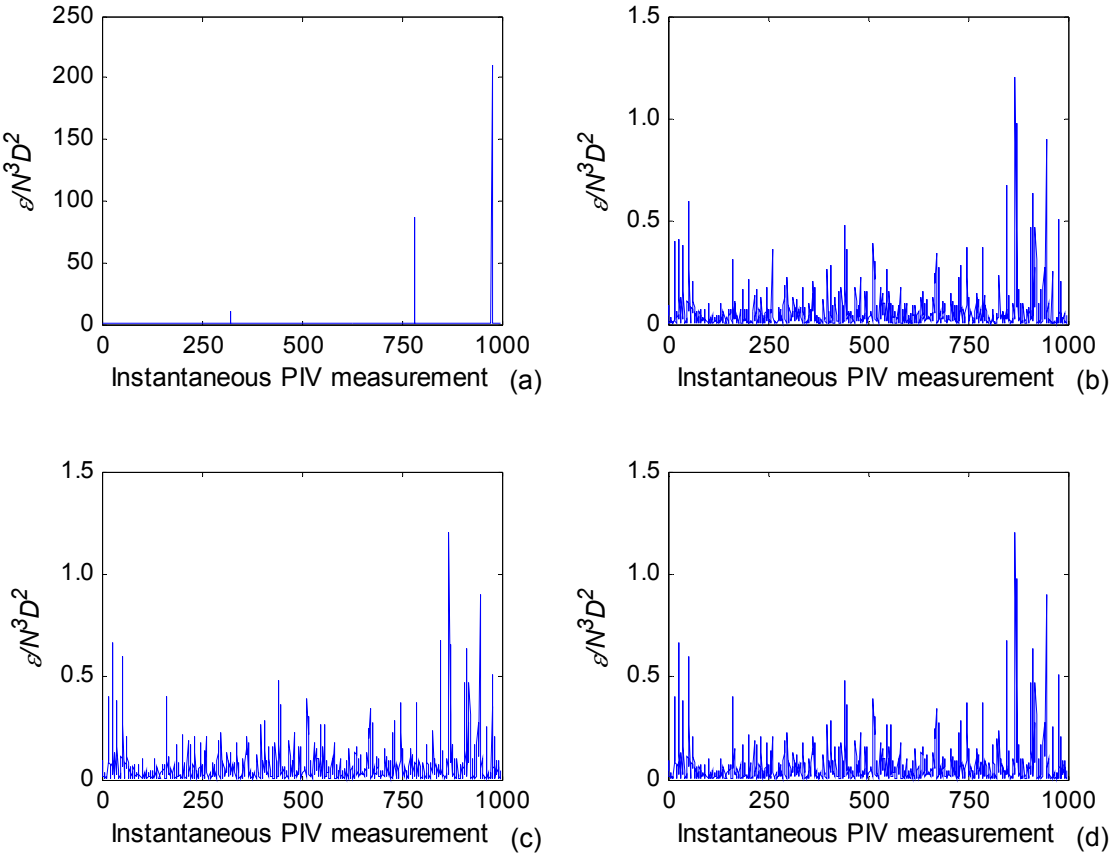

Figure 4.20: Time-history of instantaneous normalized dissipation rate at $r/T=0.167$, $z/T=0.333$, over 1000 high-speed PIV measurements, at 5 kHz and 1500 rpm (a) before and after applying the (b) global (c) local (d) temporal standard deviation filters

Meneveau and Sreenivasan (1991) suggested that averaging over tens of samples improves the statistical convergence of D_q. Additionally, data lengths of a few tens of integral length scales improve the scaling; long sets of data make it increasingly difficult to identify the power-law behaviour between $\left[\sum(E_r/E_t)^q\right]^{1/(q-1)}$ and r/η. These recommendations also enable

computation of D_q for $q<0$. Consequently it would be ideal to compute sums $\sum(E_r/E_t)^q$ over a data length $\sim 100\Lambda_u$, and average results over ~10 such samples. However, after converting the cumulative time steps between PIV image pairs to spatial separation (via $r=(1000-1)\bar{u}\Delta T$), the data length was found to be only $\sim 130\Lambda_u$. Since only one full sample could be obtained, the spectrum of generalised dimensions was calculated for $0<q<+5$ only. Meneveau and Sreenivasan (1991) stated that high positive q values emphasize regions of intense dissipation, whereas negative values accentuate low dissipation. In the present case, as the aim is to quantify the nature of intense dissipation, the negative q range is unimportant.

The log-log plots of $\left[\sum(E_r/E_t)^q\right]^{1/(q-1)}$ versus r/η are shown in Figure 4.21(a) to (d) for $-5<q<+5$. The plots for $q<0$ are shown to exemplify that power-law behaviour cannot be identified unambiguously within this range for any dissipation rate profile. Subsequently these moments were excluded from further analysis.

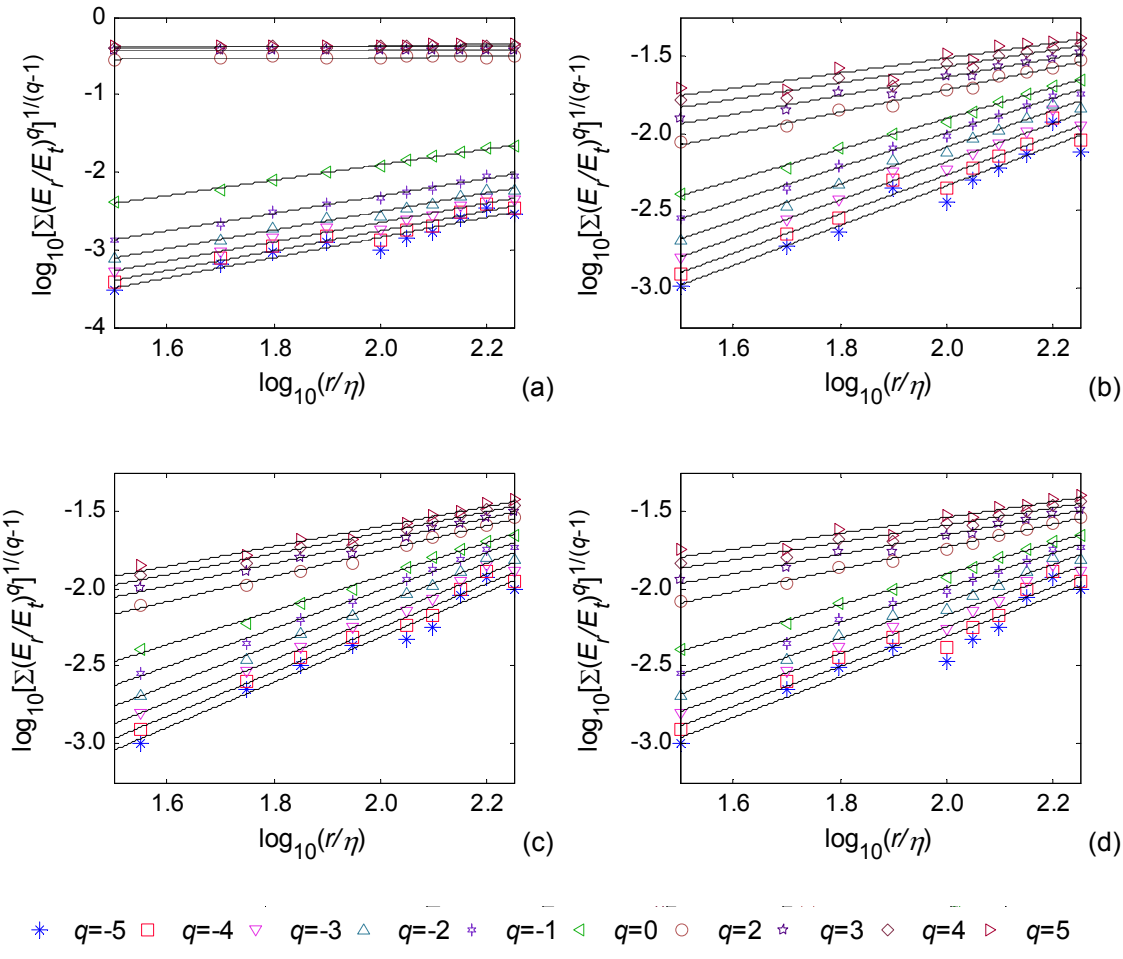

Figure 4.21: Log-log plots of $\left[\sum(E_r/E_t)^q\right]^{1/(q-1)}$ versus r/η for several q values, from the dissipation rate profiles obtained (a) before and after applying the (b) global (c) local (d) temporal standard deviation filters

In Figure 4.21(a) scaling of the higher-order moments does not vary noticeably between $2 < q < +5$, indicating that generalized dimensions would be similar. Thus it may be anticipated *a priori* that the unfiltered velocity field does not represent real turbulence intermittency. Results of the filtered profiles show that scaling behaviour of the higher-order moments has improved, and it may be ascertained which conforms best to the multifractal model.

The moment exponents D_q obtained from the slopes of the lines between $0 < q < +5$ for all four profiles are plotted in Figure 4.22, against the analytical model of Meneveau and Sreenivasan (1991). It may be observed that the generalized dimensions from the unfiltered profile depart significantly from the multifractal model, indicating that the intense fluctuations observed in Figure 4.20(a) were not genuine intermittency. Instead they arise from velocity gradients of spurious vectors. The removal of this noisy data necessitates the application of a type of standard deviation filter.

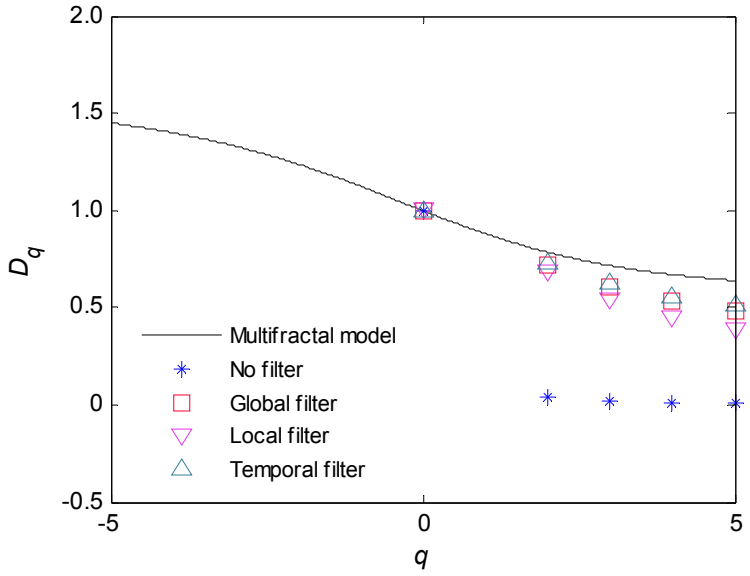

Figure 4.22: Moment exponents D_q from the analysis of dissipation rate profiles before and after the application of various standard deviation filters. The solid line represents the multifractal model of Meneveau and Sreenivasan (1991).

The generalized dimensions of the filtered profiles are much closer to the analytical model. The result is surprising since the D_q exponents were obtained from a single sample and no averaging was performed to improve the statistics. The improvement suggests that all three filters appear adequate in removing the spurious vectors, and the dissipation rate profiles shown in Figure 4.20(b) to (d) are more plausible illustrations of intermittency. The D_q exponents from the globally filtered profile agree most with the multifractal model, indicating that this is the best type for the present case. The result may be surprising since the global field of view contains a wide range of velocities.

The dissipation rate in the entire field of view after applying the global standard deviation filter is portrayed in Figure 4.23. The maximum dissipation rate is now $\sim 0.08 N^3 D^2$, an order of magnitude lower than that shown in Figure 4.8.

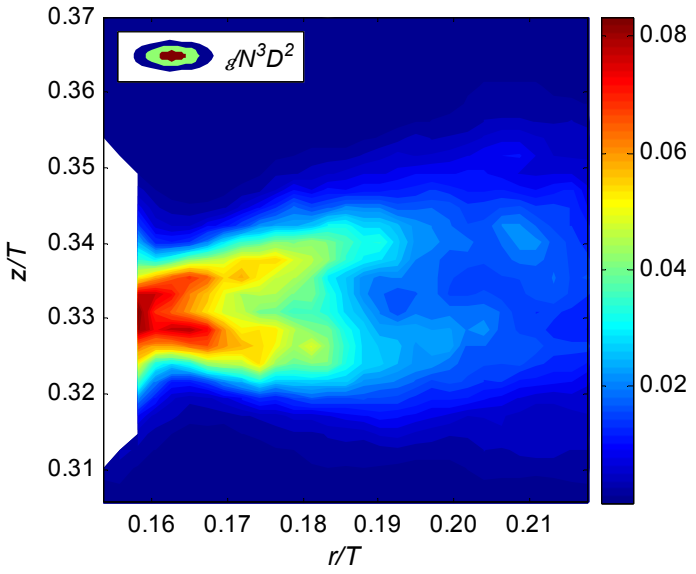

Figure 4.23: Dissipation rate from the 2-D LES analogy of Sheng *et al.* (2000), using high-speed PIV ensemble-averaged measurements, after applying a global standard deviation filter to the velocity field

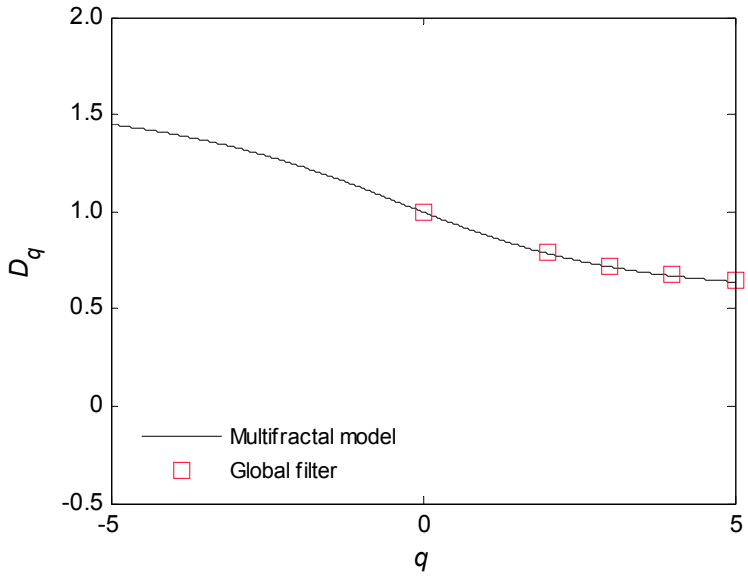

Figure 4.24: Moment exponents D_q from the analysis of the dissipation rate profile at the point of maxima ($r/T = 0.158$, $z/T = 0.331$) in Figure 4.23. The solid line represents the multifractal model of Meneveau and Sreenivasan (1991).

To further validate the efficiency of the global filter, the instantaneous dissipation rate profile obtained at the point of maxima was also validated against the multifractal model, as shown in Figure 4.24. The D_q exponents from this analysis coincide exactly with the model of Meneveau and Sreenivasan (1991), providing confidence in the filter choice as well as the maximum dissipation rate estimate.

The recommendation herein is that the best filter should be selected on a case-by-case basis, since this is largely dependent on the degree of turbulence and inhomogeneity of the flow field, as well as experimental parameters such as tracer number density and time-delay between image frames, which in turn influence the cross correlation procedures. After selecting the best filter, the multifractal model may also be used to optimise filter parameters, such as tolerance level of the global filter or neighbourhood size of the local filter. One such example is shown in Figure 4.25, where the generalised dimensions arising from different tolerance levels of the global standard deviation filter are plotted; these are 2, 3 and 4 standard deviations. Note that that in all cases described previously, the tolerance was set to 3 standard deviations. It may be observed that the various tolerance levels produce different fits against the multifractal model. The tolerance of 4 standard deviations departs most from the model, whereas 2 standard deviations provide the closest fit.

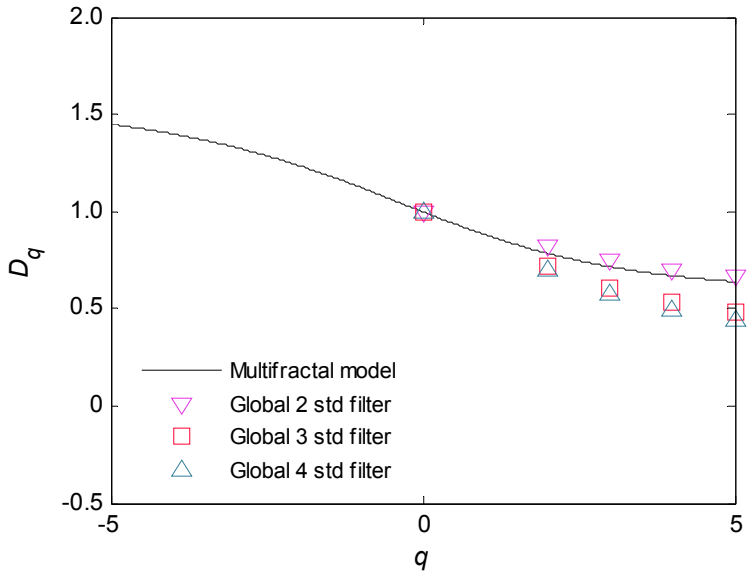

Figure 4.25: Moment exponents D_q from the analysis of dissipation rate profiles before after the application of the global standard deviation filter with various tolerance levels. The solid line represents the multifractal model of Meneveau and Sreenivasan (1991).

The overall dissipation rate distribution arising from 2 and 4 standard deviation tolerances is shown in Figure 4.26(a) and (b), for which $\varepsilon_{\max}$ is $0.07N^3D^2$ and $0.09N^3D^2$ respectively. As expected, more intense fluctuations of turbulence are retained by the 4 standard deviation filter; hence it portrays higher dissipation in the discharge stream. It may appear that the 2 standard deviation filter is the best choice, but the generalised dimensions obtained from its profile at $\varepsilon_{\max}$ did not generate a fit as good as the one illustrated in Figure 4.24. For this reason, a

tolerance of 3 standard deviations is considered to be the optimum level in the present case. In light of this finding, PIV measurements displayed from this point forward will be processed using the global standard deviation filter with a tolerance of 3 standard deviations.

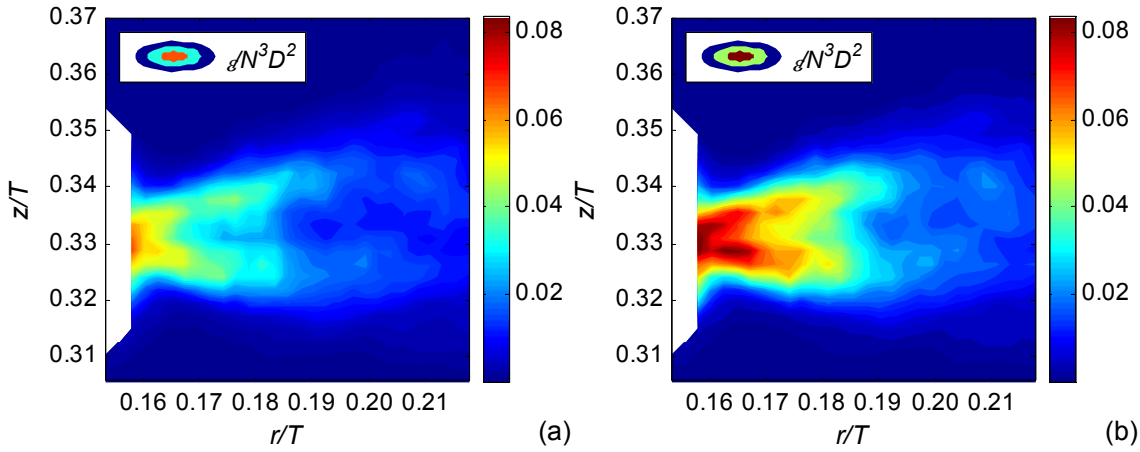

Figure 4.26: Dissipation rate from the 2-D LES analogy of Sheng *et al.* (2000), after applying a global standard deviation filter with a tolerance of (a) 2 and (b) 4 standard deviations

4.9 Distribution of energy dissipation

Knowledge regarding the distribution of ε (specifically $\varepsilon_{\max}$) in stirred vessels is important for understanding droplet break up in liquid-liquid dispersions, particle de-agglomeration in solid-liquid dispersions, as well as mixing of two co-existing phases. Additionally, understanding how the magnitude and variation of ε is affected by operating variables (e.g. impeller speed) is important for efficient process design (Ng and Yianneskis, 2000). There are two ways in which energy dissipation in various zones may be estimated. The first method is by performing a total kinetic energy balance around a control volume in the vessel, and obtaining the amount of energy consumed within the zone, which is assumed to be totally dissipated. Alternatively, volume-weighted average dissipation values may be obtained from calculations of ε from experimental data within specific regions. The vessel is considered to comprise three main regions, for which Ng and Yianneskis (2000) have provided approximate boundaries:

- Impeller swept region: $0 < r < R$ and $(C - W/2) < z < (C + W/2)$
- Impeller stream: $R < r < 2R$ and $(C - W/2) < z < (C + W/2)$
- Bulk flow region: remainder of the vessel

where r and z are the radial and axial cylindrical coordinates (measured from the centre of the vessel base), R the impeller radius, C the clearance between the impeller centreline and vessel base, and W the blade width. In this study, both methods were employed to determine the average dissipation rate in the impeller stream of the flow field generated by the EkatoMizer. Stereo-PIV measurements obtained at 1500 rpm in the impeller region (i.e. Position 2) were used for this calculation. Note that the field of view did not extend to $2R$; only $1.6R$. Boundaries of the control volume are illustrated in Figure 4.27. The global standard deviation

filter was applied to the velocity fields for vector validation, prior to calculating turbulence properties.

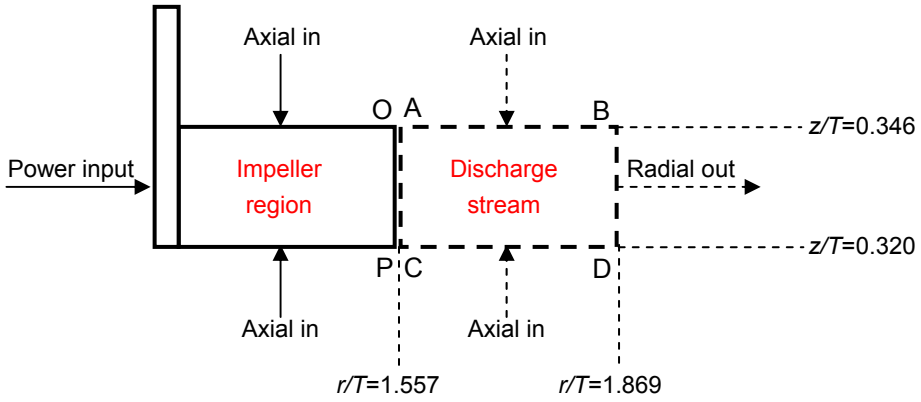

Figure 4.27: Control volume ABCD of Position 2 for energy dissipation measurement

4.9.1 Total kinetic energy balance

Khan *et al*. (2006) performed a total kinetic energy balance for the flow generated by a PBT to obtain the average dissipation rate in the impeller region; a similar analysis will be conducted here. A total kinetic energy balance was performed over the control volume depicted in Figure 4.27. The standard Reynolds decomposition was applied to describe the velocities, where the instantaneous velocity is divided into the ensemble-averaged mean and fluctuating components.

$$u_i = \overline{u_i} + u_i' \tag{4.34}$$

The total kinetic energy (K) obtained from the instantaneous velocities may be expressed as:

$$K = \frac{1}{2}\left(u^2 + v^2 + w^2\right) \tag{4.35}$$

Expanding the equation above in terms of Reynolds decomposition provides:

$$K = \frac{1}{2}\left(\left(\overline{u} + u'\right)^2 + \left(\overline{v} + v'\right)^2 + \left(\overline{w} + w'\right)^2\right) \tag{4.36}$$

Then, the kinetic energy flow in the radial direction (via surfaces AC and BD) and axial direction (via surfaces AB and CD) may be given by Equations (4.37) and (4.38) respectively:

$$KE_r = 2\rho\pi R \int_{C-W/2}^{C+W/2} K u dz \tag{4.37}$$

$$KE_z = 2\rho\pi \int_{R}^{2R} K v r dr \tag{4.38}$$

After substituting the full definition of the kinetic energy and averaging over all instantaneous results, the mean kinetic energy flows are given by:

$$KE_r = \rho\pi R \int_{C-W/2}^{C+W/2} \left(\begin{array}{l} \bar{u}^3 + 3\bar{u}\overline{u'^2} + \overline{u'^3} + \bar{u}\bar{v}^2 + \overline{v'^2}\bar{u} + 2\overline{vu'v'} \\ +\overline{v'^2 u'} + \bar{u}\bar{w}^2 + \overline{w'^2}\bar{u} + 2\overline{wu'w'} + \overline{w'^2 u'} \end{array} \right) dz \tag{4.39}$$

$$KE_z = \rho\pi \int_{R}^{2R} \left(\begin{array}{l} \bar{v}^3 + 3\bar{v}\overline{v'^2} + \overline{v'^3} + \bar{v}\bar{u}^2 + \overline{u'^2}\bar{v} + 2\overline{uu'v'} \\ +\overline{u'^2 v'} + \bar{v}\bar{w}^2 + \overline{w'^2}\bar{v} + 2\overline{wv'w'} + \overline{w'^2 v'} \end{array} \right) rdr \tag{4.40}$$

LDA and 2-D PIV measurements do not enable calculation of the second- and higher-order velocity cross-correlation terms, which are usually neglected from Equations (4.39) and (4.40) (Wu and Patterson, 1989; Zhou and Kresta, 1996). In the present case, knowledge of all three velocity components enables a complete estimate of the kinetic energy flows via Equations (4.39) and (4.40). However it should be noted that Khan *et al*. (2006) found that neglecting the cross-correlation terms does not significantly affect the kinetic energy flow estimations.

The mean kinetic energy flow entering the control volume in the axial direction via surfaces AB and CD was found to be 0.061 W and 0.052 W respectively. The mean kinetic energy flow in and out of the control volume in the radial direction via surfaces AC and BD was found to be 0.576 W and 0.233 W respectively. Thus, the amount of kinetic energy consumed in the control volume was 0.456 W. Note that diffusion terms in the total TKE balance were neglected, only convective transfer was considered. The consistency of these estimates was checked by comparing the radial flow of kinetic energy out of the impeller region (via surface OP in Figure 4.27) from a separate set of stereo-PIV measurements (Position 1, 1500 rpm), to that entering the control volume via surface AC. If PIV estimates are reliable, then flows through adjacent surfaces should be comparable. The kinetic energy flow through surface OP was found to be 0.547 W, giving a total error of 5% between the estimates. The results are in good agreement considering that they were obtained from two independent trials, which could sustain inevitable experimental discrepancies (such as differences in stereo-PIV calibration). Subsequently the power consumed within the control volume could be compared to the total power input to the impeller at 1500 rpm, found to be 13.30 W via Equation (4.2). From this it may be deduced that approximately 3.4% of the total power input is dissipated in the impeller stream.

Calculation of the energy dissipated in the impeller region requires integration of the axial flow over the surface $0 < r < R$, above and below the impeller. However PIV measurements did not include the entire impeller in the field of view. Since the axial kinetic energy flows in the impeller stream were relatively small compared to the radial direction, they were simply neglected in the impeller region as a crude approximation. Given a power input of 13.30 W, and radial kinetic energy flow out of the impeller region via surface OP of 0.547 W, it may be assumed that approximately 12.75 W is consumed within the impeller region. This is equivalent to around 96% of the total energy.

Previous ε distributions from experimental and modelling results of RDT and PBT studies were collected by Togatorop (1995) and Ng and Yianneskis (2000); Table 4.1 is an updated version of their compilation. It should be noted that the control volume limits in the listed studies are not

identical and there are differences in impeller geometry also. The method of calculating ε also varies. This could explain the wide variation in the estimates of ε distribution across the regions, even for common impeller types. Despite the differences, it is evident that a significant amount of energy is dissipated in the impeller region of the sawtooth, and the least amount dissipated in the impeller stream. The average dissipation rate in the impeller region may be obtained as follows:

$$\overline{\varepsilon_{CV}} = \frac{P_{CV}}{\rho V_{CV}} \tag{4.41}$$

where V_{CV} is the volume occupied by the impeller region, found to be 7.76×10^{-5} m^3. Consequently the average dissipation rate in this control volume is 164 W kg^{-1}, which is about 273 times greater than the average dissipation rate in the entire vessel (0.6 W kg^{-1}, volume 2.228×10^{-2} m^3). Similarly, the average dissipation rate in the impeller stream was found to be 1.87 W kg^{-1} (for a volume of 2.436×10^{-4} m^3); only ~3 times greater than the average dissipation rate in the vessel.

Table 4.1: Distributions of ε reported in literature for various impeller types

Author	*Impeller*	*Dissipation rate distribution (%)*		
		Impeller region	*Impeller stream*	*Remaining volume*
Cutter (1966)	RDT	20	50	30
Fort et al. (1972)	RDT	60	-	-
Gunkel and Weber (1975)	RDT	-	38	-
Laufhutte and Mersmann (1985)	RDT	30	30	40
Wu et al. (1989)	RDT	30	30	40
Ranade and Joshi (1990)	RDT	30	34	36
Kresta and Wood (1991)	RDT	54	35	11
Togatorop (1995)	RDT	36	30	34
Zhou and Kresta (1996)	RDT	15.3	28.2	-
Ng and Yianneskis (2000)	RDT	12	31	57
Zhou and Kresta (1996)	PBT	52		
Khan et al. (2006)	PBT	44	-	-
Current study (2009)	Sawtooth	96	3.4	<1

4.9.2 Average of calculated ε

The average dissipation rate in the impeller stream may also be obtained from the volume averaged estimate of the calculated ε in §4.6.2, after applying a global filter to the velocity fields. The average dissipation rate is obtained in a control volume defined by the same limits mentioned previously:

$$\overline{\varepsilon_{CV}} = \frac{1}{V_{CV}} \int_0^{2\pi} \int_{C-W/2}^{C+W/2} \int_R^{2R} \varepsilon r dr dz d\theta \tag{4.42}$$

Note that ε in Equation (4.42) is actually an ensemble-average from 500 instantaneous PIV measurements. Since angle-resolved measurements were not taken, the flow is assumed to be homogeneous around 360° of the impeller, such that Equation (4.42) reduces Equation (4.43).

$$\overline{\varepsilon_{CV}} = \frac{2\pi}{V_{CV}} \int_{C-W/2}^{C+W/2} \int_{R}^{2R} \varepsilon r dr dz \tag{4.43}$$

In this way, the average dissipation rate in the control volume was found to be 0.64 W kg^{-1}. This is almost the same as the average dissipation in the entire vessel (0.6 W kg^{-1}) and about three times smaller than the magnitude obtained from the kinetic energy balances.

It should be noted that linear scaling was employed to estimate the unknown gradients to calculate the dissipation rate via the LES analogy of Sheng *et al*. (2000). In the same discussion it was highlighted that simple scaling of gradients leads to an underestimate of ε. Consequently, the volume-average in the impeller stream from Equation (4.43) is also expected to be an underestimate. Secondly, the kinetic energy balance around the control volume considered only convective flows. Diffusion and pressure terms have not been included, which would reduce the amount of kinetic energy dissipated in the control volume. Therefore, the average given by Equation (4.41) may actually be lower than that calculated. Notwithstanding these discrepancies, the average dissipation rates calculated via both methods are comparable to within the same order of magnitude, which is an encouraging result. The main point from both results is that the vast majority of energy dissipation occurs in the impeller swept volume, unlike many other impellers reported in Table 4.1.

4.10 Ratios of maximum and mean energy dissipation

The mean dissipation rate is often used in the scale up of stirred vessels; however it provides no information about the distribution or maximum value throughout the tank. The maximum dissipation rate may deviate significantly from the mean, which may determine, for instance, the minimum drop size in dispersed gas or liquid flows (Zhou and Kresta, 1998). After processing the stereo-PIV velocity fields using a global standard deviation filter, and applying the LES analogy of Sheng *et al.* (2000) to the 3-D data, $\varepsilon_{\max}$ was found to be $\sim 0.17 N^3 D^2$ at 1500 rpm. The mean dissipation rate was $0.004 N^3 D^2$, giving $\varepsilon_{\max} / \overline{\varepsilon} \approx 40$. The sawtooth impeller is a high shear mixing device, so a large maximum-to-mean ratio is expected. It is of interest to compare this ratio with other impeller types, to evaluate the relative order of magnitude. The mean and maximum dissipation rates cited in literature are summarised in Table 4.1, and $\varepsilon_{\max} / \overline{\varepsilon}$ calculated from this data. There is a significant variation in $\varepsilon_{\max} / \overline{\varepsilon}$ even between common impeller types. Three main factors contribute to these variations; differences in tank geometry, flow measurement technique and dissipation rate calculation method.

Zhou and Kresta (1996) employed 1-D LDA to measure flow velocities generated by a PBT with $D/T = 0.333$. They used dimensional analysis to obtain the dissipation rate and found $\varepsilon_{\max} / \overline{\varepsilon} \approx 38$. Khan (2005) used PIV and employed the 2-D LES analogy resulting in $\varepsilon_{\max} / \overline{\varepsilon} \approx 118$. Since the impeller geometry was identical in both studies, the difference must be

due to the calculation method. Note in the present case, ε_{max} from dimensional analysis was an order of magnitude smaller than the LES method. However Sheng *et al*. (2000) found $\varepsilon_{max}/\overline{\varepsilon} \approx 8$ from their LES analogy for a PBT, which is surprisingly smaller than the dimensional result of Zhou and Kresta (1996). In fact Sheng *et al*. (2000) found that both LES and dimensional analysis yielded similar results. Their PIV resolution was 5 mm, compared to only 1.08 mm in Khan's (2005) study. In the LES method, turbulence statistics at scales smaller than the PIV resolution are filtered and modelled, so the low result is not unexpected when taking this into account.

Table 4.2: Maximum and mean dissipation rates of various impellers reported in literature

Author	*Impeller*	*D/T*	P_o	$\overline{\varepsilon}/N^3D^2$	*Calc method for* ε	ε_{max}/N^3D^2	$\varepsilon_{max}/\overline{\varepsilon}$
Current study (2009)	Sawtooth	0.311	0.11	0.004	3-D LES analogy of Sheng *et al*. (2000)	0.17***	40
Baldi and Yianneskis (2003)	Hydrofoil	0.333	0.22	0.01	Directly from definition	0.02-0.8*	2 - 80
Kilander and Rasmuson (2005)		0.330	0.3	0.016	Modified 2-D LES analogy	14.57	921
Zhou and Kresta (1996)	PBT-4 45°	0.333	1.35	-	Dimensional analysis	2.44**	38
Sheng et al. (2000)		0.349	1.4	0.071	2-D LES analogy of Sheng *et al*. (2000)	0.58	8
Khan (2005)		0.333	1.52	0.078	2-D LES analogy of Sheng *et al*. (2000)	9.2	118
Zhou and Kresta (1996)	RDT-6	0.333	5.4	-	Dimensional analysis	12.14**	48
Sharp and Adrian (2001)		0.333	4.5	0.209	Directly from definition	3.35	16
Escudie and Line (2003)		0.333	5.5	0.313	TKE balance	14	45
Baldi and Yianneskis (2004)		0.333	4 4.1 4.7	0.189 0.193 0.222	Directly from definition	10 11 6.4	53 57 29

*From PIV measurements at varying spatial resolution

**Average ε_{max} for 5 impeller speeds

***at 1500 rpm

All RDT studies listed in Table 4.2 were carried out using $D/T = 0.333$. The lowest result was obtained from the direct evaluation of Sharp and Adrian (2001) of $\varepsilon_{max}/\overline{\varepsilon} \approx 16$, at a PIV resolution of 0.5 mm. Baldi and Yianneskis (2004) also employed direct calculation of ε for various Re flows under a PIV resolution of 0.1 mm. The authors noted that the Kolmogorov length scale decreases in the most turbulent regions as Re increases; hence the accuracy of ε decreases at a fixed PIV resolution for direct evaluation. The most reliable measure was

assumed to be at $\mathrm{Re} = 20 \times 10^3$, where $\varepsilon_{max} / \bar{\varepsilon} \approx 57$. As a final consideration, note the various P_o values used to estimate the mean dissipation rate. The power number (hence $\bar{\varepsilon}$) of RDTs is dependent on Re up to $\mathrm{Re} \sim 70 \times 10^3$ stated by Chapple *et al*. (2002) and up to $\mathrm{Re} \sim 60 \times 10^3$ as found by Khan (2005). Since the listed experiments were carried out in varying Re flows below $\mathrm{Re} = 60 \times 10^3$, $\varepsilon_{max} / \bar{\varepsilon}$ is expected to deviate even for identical ε_{max} estimates due to the differences in $\bar{\varepsilon}$. For instance, the ε_{max} estimates from dimensional analysis of Zhou and Kresta (1996) and TKE balance of Escudie and Line (2003) are greater than the direct calculations. However since both employ higher P_o values for the same impeller, the final $\varepsilon_{max} / \bar{\varepsilon}$ ratios are smaller; 48 and 45 respectively.

It has been found that $\varepsilon_{max} / \bar{\varepsilon} \approx 40$ for the EkatoMizer is within the range of ratios reported for PBT and RDT impellers. Subsequently it is debatable whether the EkatoMizer really sustains a high shear advantage. However note that before calculating the dissipation rate, a global standard deviation filter was applied to the velocity field for validation, which eliminated some large magnitude vectors. This affected ε_{max} significantly. Without applying the filter, $\varepsilon_{max} \approx 1.76 N^3 D^2$ at 1500 rpm, giving $\varepsilon_{max} / \bar{\varepsilon} \approx 416$. It is believed that the global standard deviation filter provides a more realistic representation of turbulence intermittency, in line with the multifractal model of Meneveau and Sreenivasan (1991) (refer to §4.8.2). Subsequently the ratio obtained after filtering is accepted as the best estimate in the present case. It follows that PIV experiments of the aforementioned authors may be subjected to the same argument, in that their data could possibly benefit from filtering. Since vector validation techniques have such a profound impact on the dissipation rate results, a comprehensive comparison of $\varepsilon_{max} / \bar{\varepsilon}$ is not really possible.

A hydrofoil impeller was studied by Baldi and Yianneskis (2003), with PIV resolution between 1.25 and 0.111 mm. Direct estimates of the dissipation rate gave $0.02 < \varepsilon_{max} / N^3 D^2 < 0.8$ with corresponding $2 < \varepsilon_{max} / \bar{\varepsilon} < 80$, emphasizing the importance of resolution. Kilander and Rasmuson (2005) also investigated a hydrofoil via PIV and a modified large eddy method to obtain the dissipation rate. Their results indicated $\varepsilon_{max} / \bar{\varepsilon} \approx 921$; the greatest reported yet for any mixer. This is especially surprising for a hydrofoil which is thought of as a low-shear device. Aside from the issue of vector validation, the enormity of this result may be attributed to the fact that the authors took the space between vectors after 75% overlap to be the filter width, which is incorrect; it should be equal to the *IA* length.

On a final note it must be considered that the ratio $\varepsilon_{max} / \bar{\varepsilon}$ has been evaluated from PIV results in the EkatoMizer impeller stream. Given the discussion in §4.9.1, it is suggested that ε_{max} actually occurs in the impeller swept volume. PIV experiments were not possible in this region as the impeller completely obstructed the field of view, so this cannot be experimentally validated in the present case. The total KE balance revealed that $\varepsilon_{max} / \bar{\varepsilon}$ could be as high as 273 in the swept volume. If this is true then the EkatoMizer could be considered as a high shear

impeller. However dissipation rate estimates would also be required in the swept volume of the other impellers to enable an equivalent assessment.

4.11 Angle-resolved measurements

Angle-resolved PIV experiments were carried out, as described in §3.7. The data were binned in ten equal intervals between two reference teeth of the impeller, in bin widths 1° each. The dissipation rate in some angle-resolved planes is illustrated in Figure 4.28. All spatial distributions appear to be similar beyond $r/T > 0.18$. Slight variation is evident with respect to angular position only at radial distances closer to the blade. Intense dissipation up to $0.1N^3D^2$ was found to occur 1°, 3°, 6° and 8° behind the leading blade. To obtain these results, sequential PIV measurements were manually angle-resolved assuming an impeller speed of 1503 rpm, which gave minimum variance of the radial velocity in the bins. However data were also resolved assuming 1506 rpm (another speed which gave low variance). In the latter case, maximum dissipation was found 1°, 3° and 7° behind the leading blade. Overall in both cases, the angle-resolved dissipation rate was very similar to the ensemble-average (Figure 4.23). The flow does not seem to exhibit periodicity with respect to the blade passage, but the distributions also show that it is not entirely homogeneous around 360° of the impeller.

4.12 2-D planes in front of impeller

High-speed PIV measurements were obtained directly in front of the impeller (as close as possible to Position 3 outlined in Figure 3.3, but not exactly as this is a different experiment). The light sheet scraped the blade edge in the first measurement, subsequent 2-D planes were taken at 7 mm intervals in front. The velocity fields were validated with a global standard deviation filter, and the dissipation rate calculated from the 2-D LES analogy of Sheng *et al.* (2000). Results from these 2-D slices are shown in Figure 4.29. In Cartesian coordinates y and z represent the axial and tangential directions respectively. The image centre corresponds to the blade centreline where $z/T = 0$. The disc plane is at $y/T = 0.33$.

In Figure 4.29(a) the clearly discernible region where $\varepsilon > 0.05N^3D^2$ corresponds to the impeller disc, where the dissipation rate reaches a maximum of $\sim 0.3N^3D^2$. However these instances are very rare, and can only be seen as small spots of high intensity. Generally the dissipation rate is around $0.1-0.2N^3D^2$ in the impeller region, consistent with the magnitude observed at the blade edge in Figure 4.23. It is evident that the maximum intensity is distributed along two horizontal layers; these correspond to the blade teeth around the upper and lower perimeter of the disc. This observation also supports the double-jet like distribution emerging from the blade edge in Figure 4.23. With a view 7 mm in front of the impeller in Figure 4.29(b), the high intensity spots disappear. However it can be seen that the dissipation rate corresponding to the location of the upper teeth remains greater than that observed at the bottom teeth. Note that the teeth geometries on the upper and lower surface are different, which could be the reason for this uneven distribution. The upper and lower teeth have a thickness of 1.62 and 1.75 mm respectively, suggesting that the smaller teeth have a relatively high shear impact on the surrounding flow. At views a further 14 and 21 mm in front of the impeller, Figure 4.29(c) and (d) respectively, the dissipation rate decreases further, and the high intensity layers merge. This

behaviour is also evident in Figure 4.23, at $r/T \sim 0.2$, equivalent to 13.5 mm in front of the blade edge. This confirms consistency between PIV results obtained from completely different observational planes.

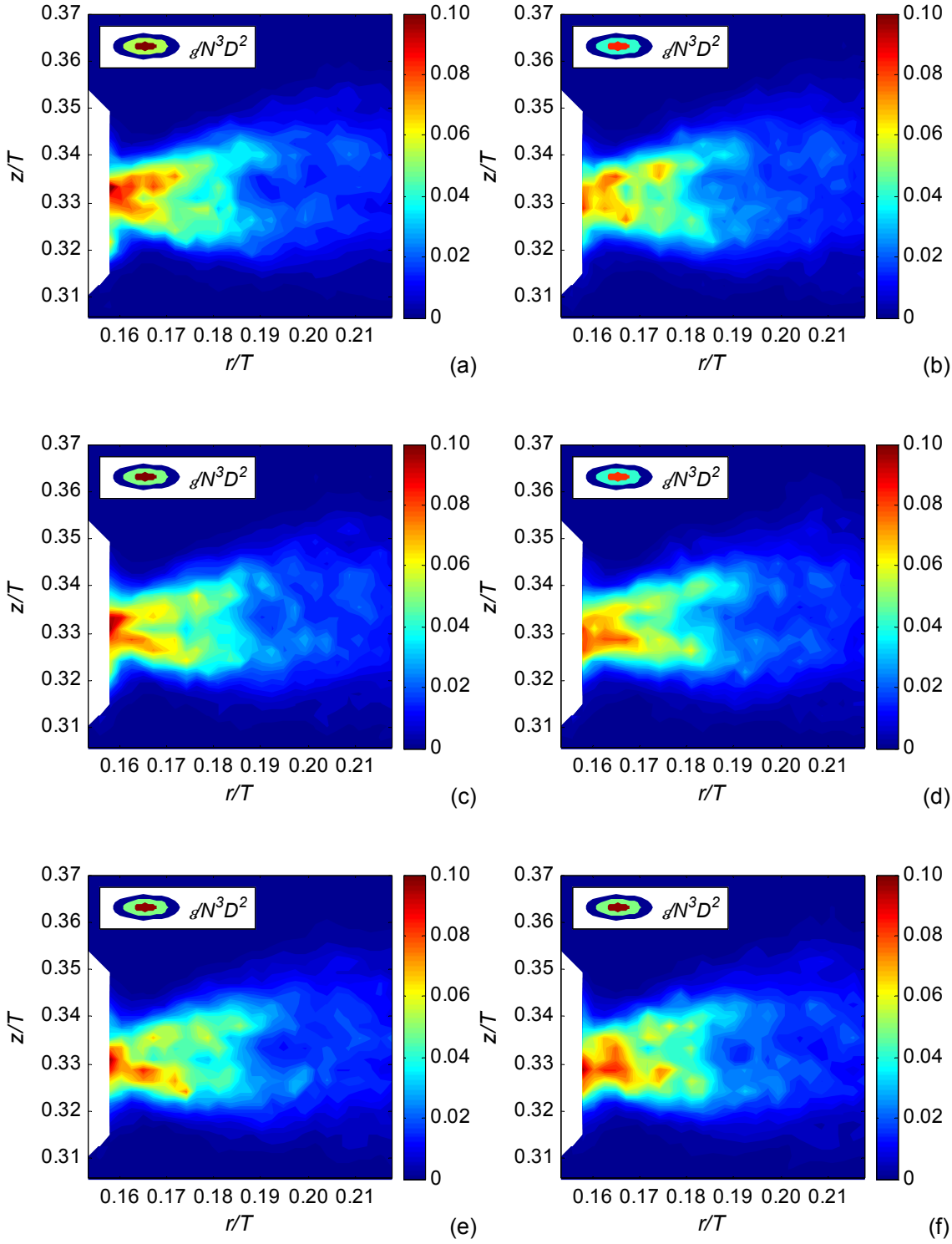

Figure 4.28: Angle-resolved dissipation rate (a) 1º (b) 2º (c) 3º (d) 4º (e) 5º and (f) 6º behind the leading tooth, assuming impeller speed 1503 rpm (nominal 1500 rpm)

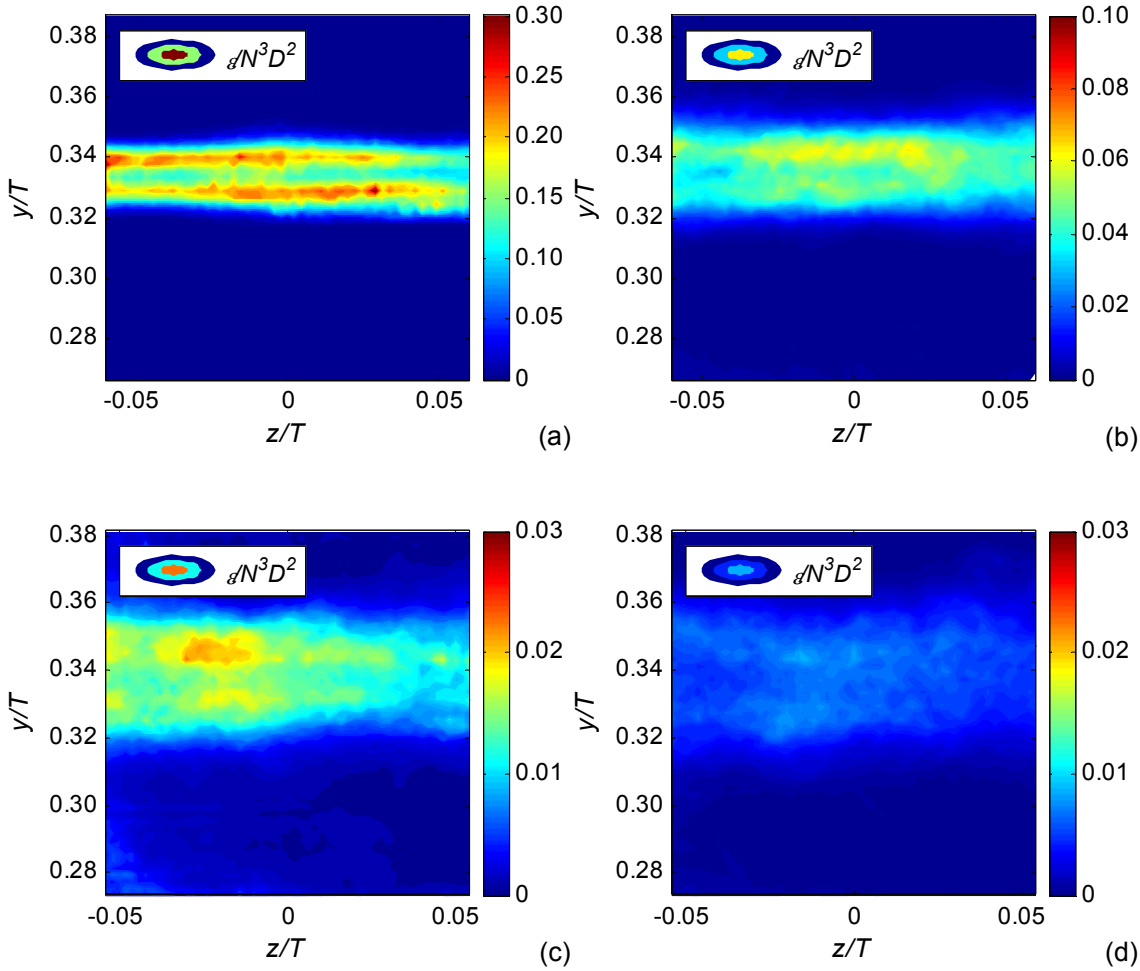

Figure 4.29: Dissipation rate from 2-D LES analogy of Sheng *et al.* (2000) in $y-z$ planes (a) 0 mm (b) 7 mm (c) 14 mm and (d) 21 mm in front of the impeller

4.13 Conclusions of dissipation rate study

Various methods for dissipation rate calculation have been explored; namely dimensional analysis, direct evaluation, LES analogy of Sheng *et al*. (2000) and deduction from the TKE balance. Where relevant, comparisons between (assumed) 2-D and 3-D estimates were made.

Dimensional analysis employing a characteristic rms velocity and length scale $W/2$ generated different dissipation rates, rendering the method unsuitable for anisotropic flows. The tangential component provided the highest estimate but only in a region confined to the blade tip and did not extend into the radial discharge stream, considered to be the main flow direction. Dimensional analysis employing the TKE and integral length scale from autocorrelation accounted for three-dimensionality of the flow. The isotropic assumption was applied to estimate the TKE in the assumed 2-D case, but the full evaluation from stereo-PIV provided a higher dissipation rate. The integral length scale was also found to be smaller than $W/2$, which may have provided an overestimate previously. Direct calculation of the dissipation rate from both 2-D and stereo-PIV provided the lowest results, due to the poor PIV resolution. The

dissipation rate obtained from the TKE balance yielded negative results, indicating that even stereo-PIV does not provide enough information for its evaluation using this method.

The LES analogy of Sheng *et al*. (2000) is believed to provide the most comprehensive measure of the dissipation rate. The calculation accounts for three-dimensionality of the flow by incorporating all three velocity components, but more importantly, it accounts for the turbulence at the smaller scales via a SGS model. Subsequently, this method will be employed to determine the local ε in proceeding two-phase PIV studies. Dissipation rate estimates from stereo-PIV were greater than those obtained from the assumed 2-D case, indicating that the simple scaling underestimates the unknown velocity gradients. However the 2-D scaling factor will have to be retained as two-phase experiments will not be possible in stereo-PIV mode.

An analysis of intense fluctuations of the dissipation rate against the multifractal model of Meneveau and Sreenivasan (1991) suggested that they were a result of spurious PIV vectors rather than genuine intermittency. The filtered dissipation rate created more plausible profiles of intermittency against the multifractal model. On this basis, the global standard deviation filter was selected to be the best type. A similar analysis of selecting the best vector validation filter can only be carried out in subsequent two-phase experiments if high-speed PIV is implemented (since highly resolved data are required for the calculation of fractal dimensions).

Finally, a comparison of the $\varepsilon_{max} / \overline{\varepsilon}$ ratio of the EkatoMizer with other common impellers such as PBTs and RDTs suggest that it does not really bear a high shear advantage. However the estimate of ε_{max} was obtained in the impeller stream where PIV experiments were possible. The real ε_{max} may be in the impeller region, making $\varepsilon_{max} / \overline{\varepsilon}$ significantly higher.

Chapter 5
Phase discrimination algorithm

Khalitov and Longmire's (2002) algorithm was selected for digital phase separation of two-phase PIV images in §2.3.7. The main steps are (i) object detection of particles followed by (ii) their separation into solids and tracers according to parametric combinations of size and brightness. The image processing toolbox in Matlab was used to develop an in-house code based on these principles.

5.1 Object detection

Khalitov and Longmire (2002) employed second-order intensity gradients to identify the internal pixels of objects, based on the consideration that the intensity I reaches maxima in two-dimensional images of tracers and solids. To identify maxima, the intensity distribution must be smooth and approximately Gaussian, such that second-order spatial derivatives satisfy the condition:

$$\frac{\partial^2(\ln I)}{\partial x_i^2} < 0 \tag{5.1}$$

Successful application of this approach also necessitates the capture of circular images of the objects. However in the current experiments, tracers occupied only a few pixels of approximately constant intensity. Dispersed particle clusters, broken particles or those at the edge of the light sheet did not appear to be circular in the image plane. As illustrated in Figure 5.1, the dispersed particles appeared as two adjacent 'half moon' shapes rather than full circles, due to the refraction of light at the edges.

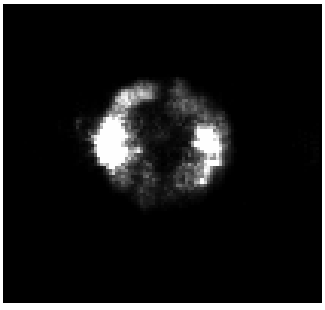

Figure 5.1: PIV image of a dispersed particle in water

In these cases, neither tracers nor dispersed particles would be picked up using second-order derivatives. Consequently, an alternative approach was sought for object detection, described below.

Step 1: Create a uniform background

Figure 5.2 shows an original two-phase PIV image with dispersed phase particles and tracers for the continuous phase. Although it is not obvious, the background intensity is variable. The first stage is to make it uniform, which facilitates object detection.

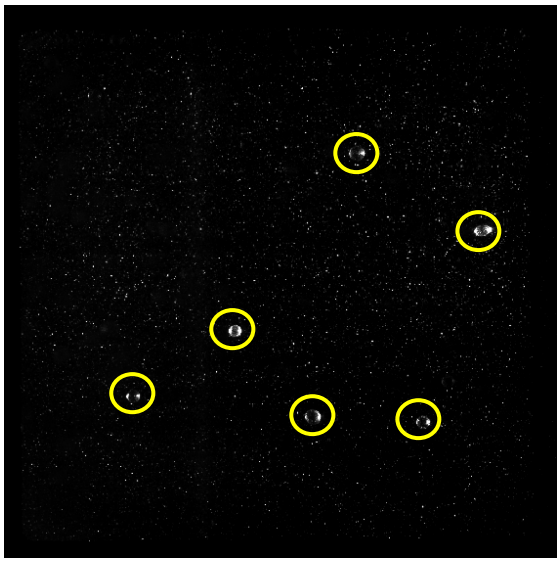

Figure 5.2: Original two-phase PIV image of dispersed particles in water (highlighted with yellow circles) and tracers

To extract the background, a disk-shaped structuring element was created using the *strel* function, and passed over the image. Matlab uses a 'morphological opening operation' that removes objects which do not completely saturate the structuring element. The element size is an input parameter, and must be larger than the objects for them to be filtered out. The objective is to remove both tracers and dispersed particles so that only the background is remaining. In Figure 5.2, the average object size (over all particles) is 2.8 pixels. As a rough measure, the 250-300, 700-750 and 1000 μm particles were found to have a maximum total diameter of around 30, 60 and 80 pixels respectively, which were made up of smaller objects. Thus a disc radius of 15 pixels was sufficient to eliminate all objects in the given example. The 'estimated' background image with its intensity distribution (displaying non-uniformity on the left-hand side) is shown in Figure 5.3(a) and (b). Although it looks uniform, in reality it is not. The non-uniformity becomes apparent in the Figure 5.3(b).

In the surface display of Figure 5.3(b), [0,0] represents the upper left corner of Figure 5.3(a). The brighter regions of the background can be clearly identified. To make it more uniform, the background image is subtracted from the original image; the result is shown in Figure 5.4.

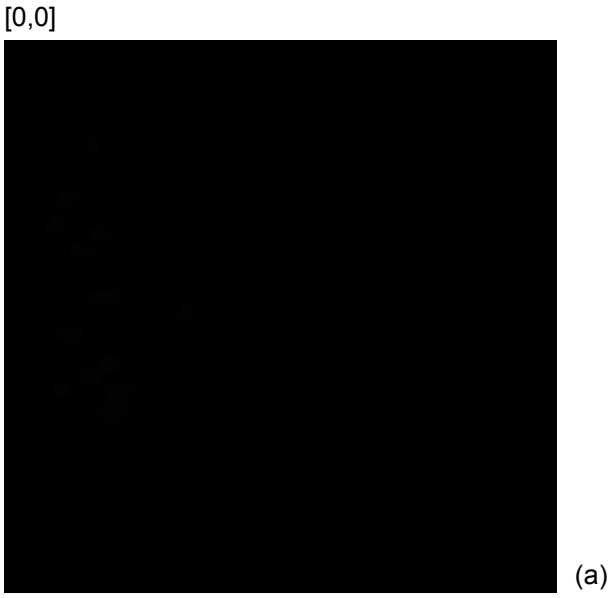

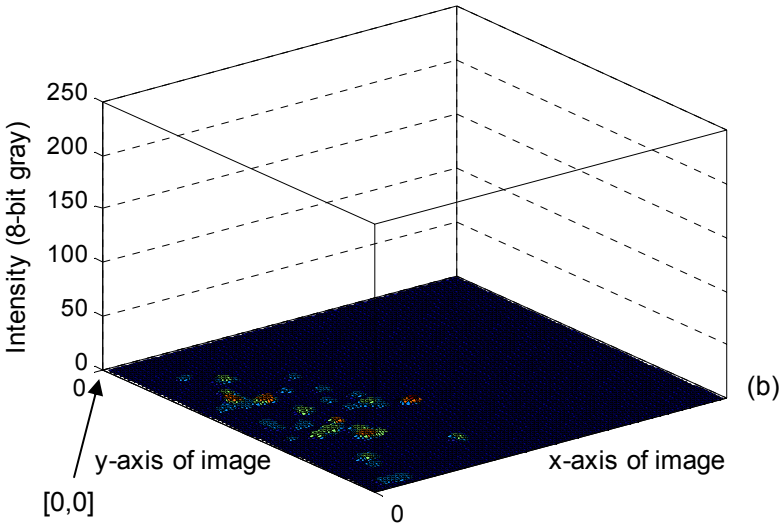

Figure 5.3: (a) Estimated background (b) Background intensity distribution

Figure 5.4: Background-subtracted PIV image

Step 2: Increase image contrast

Figure 5.5 displays the intensity range of the background-subtracted image in Figure 5.4, which is very narrow, with the majority of pixels at the lower intensity (black). The histogram does not cover the potential gray level range of 0-255 and is missing the high values that would result in good contrast. To maximize object detection, the contrast in Figure 5.4 is increased by saturating 1% of the data at both low and high intensities, and by stretching the intensity values to fill the dynamic range. The function *imadjust* was used for this purpose.

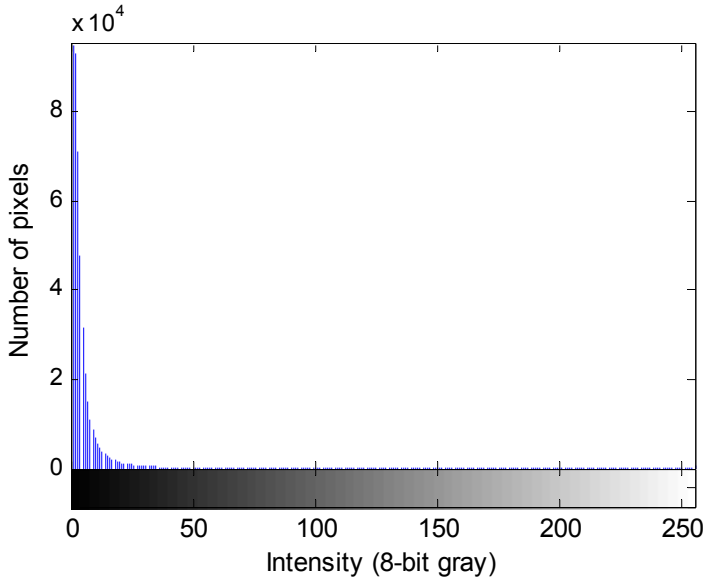

Figure 5.5: Intensity range of background-subtracted image

The contrast-adjusted image and corresponding intensity range is shown in Figure 5.6(a) and (b) respectively.

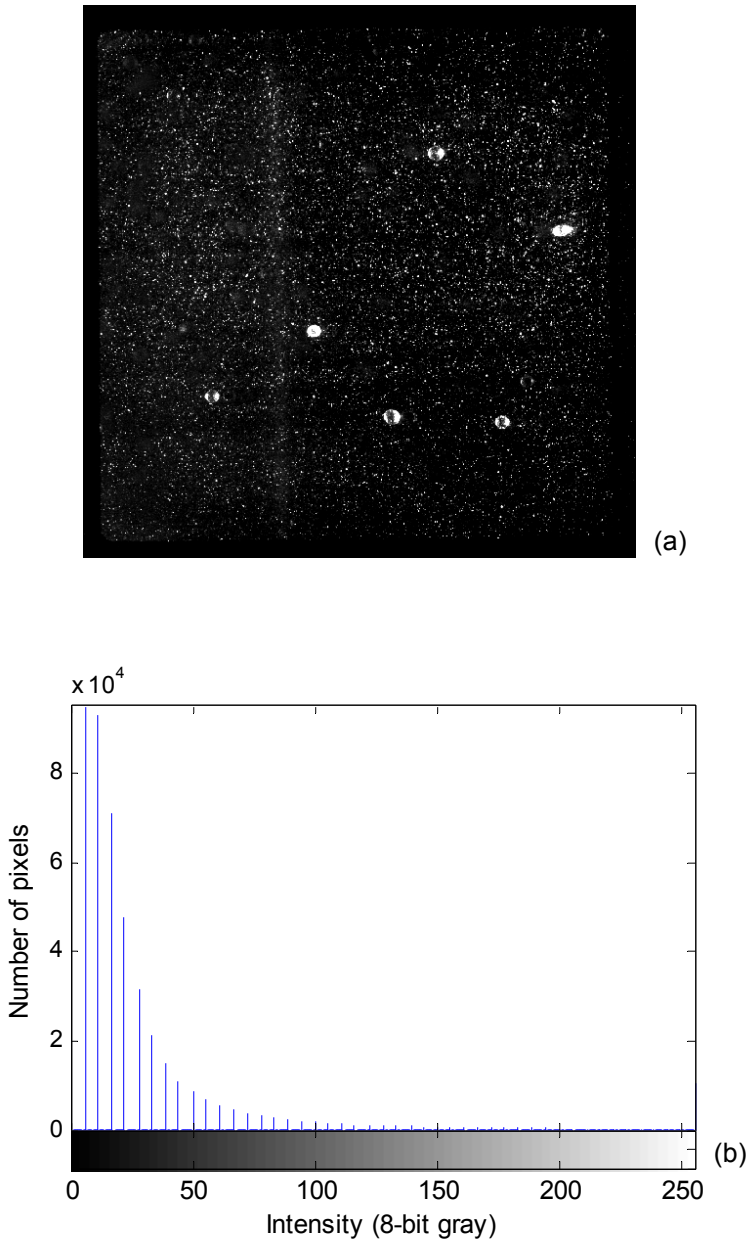

Figure 5.6: (a) Contrast-adjusted image and its (b) Intensity range

Step 3: Binarize image for object detection

After the contrast had been adjusted, the image was binarized by 'thresholding'. The Matlab function *graythresh* automatically computes an appropriate threshold to convert the gray-scale image to a binary black-white form, as illustrated in Figure 5.7.

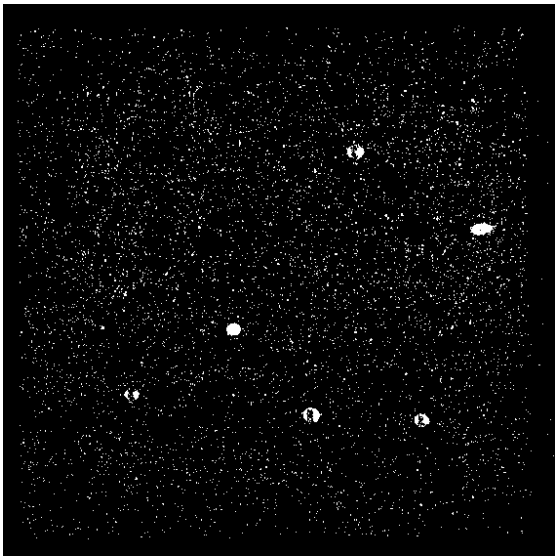

Figure 5.7: Binarized image

The binarized image enables application of the *bwlabel* function to determine the number of objects and tag/label them. Subsequently, the *regionprops* command may be used to obtain object properties such as 'object area' or size (in pixels). The 'pixel connectivity' option was set such that diagonal and adjacent pixels were counted as part of the same object.

Figure 5.8: Image with objects on a low intensity background

A search algorithm was used to locate pixels corresponding to objects in the original image. Their gray scale intensities were extracted and placed on a constant low intensity background at the same locations. Subsequently, the average gray scale intensity or brightness of each object was calculated (from the original image pixels). This completes the object detection

stage. A sample image of objects with their original gray levels, placed on a pure black background, is shown in Figure 5.8.

5.2 Phase discrimination

The objects in Figure 5.8 may be separated into tracers, dispersed particles, and unidentified objects, following the routine of Khalitov and Longmire (2002). In the object detection stage, all particles were assigned the following parameters: S (object area in pixels) defining size and B (object average intensity) defining brightness.

Next, a size-brightness contour map is constructed. The map indicates the total signal carried by objects with a given combination of size and brightness (Khalitov and Longmire, 2002). For the total signal density, the authors found the most effective measure to be:

$$\iint_{\text{all\_objects}} IdS = S \times B \times N \tag{5.2}$$

where N is the number of particles with a particular size and brightness. The logarithm of the total signal density is shown in Figure 5.9. Note that only objects from the sample PIV image (Figure 5.8) were used for this plot, but in reality an entire PIV data set comprises a few hundred images.

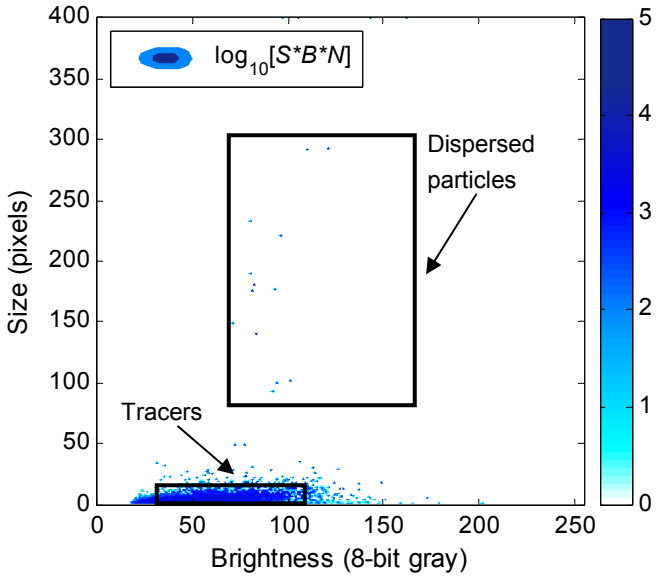

Figure 5.9: Size-Brightness map constructed from the objects in Figure 5.8

The size-brightness map is expected to yield two distinct peaks for tracers and dispersed particles. As a single image (with many tracers but few dispersed particles) was used in this example, only one distinct peak (corresponding to tracers) may be observed. However, a few discrete points lying far away from the peak can also be identified, corresponding to dispersed particles. The signal peak of the dispersed phase (if present) would be located in the top-right region of the map, representing larger, brighter objects. There may also be a region of overlap

between the two peaks, with low signal density. These signals could arise from tracer particle clusters, or broken dispersed particles as show in Figure 5.10, classified as 'unidentified objects'. It is desirable to distinguish between the dispersed and tracer particles, whilst discarding other objects.

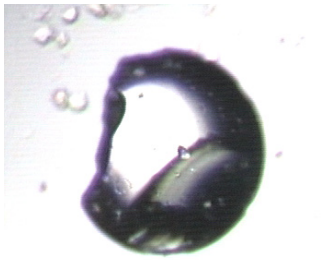

Figure 5.10: Broken dispersed particle

Phase separation limits may be obtained by defining two non-overlapping rectangles in the map, confining the signal peaks. Although there is no 'peak' for the dispersed phase, the data observed in Figure 5.9 are sufficient to classify the dispersed particles. Note that there is a large amount of scatter for the dispersed particle data, because many of them appear as 'half moon' shapes in the images rather than complete circles. These half moon shapes may also be made of collections of bright object pixels, which could be counted as independent objects if separated by one or more black pixel; this was found to be a common occurrence. Nevertheless, even dispersed particle fragments are significantly larger than the tracers to be clearly distinguished.

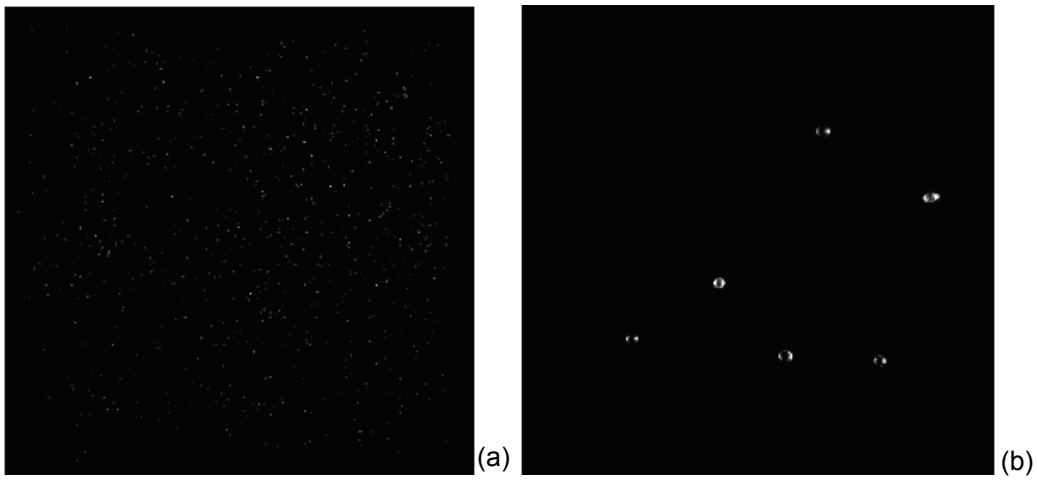

Figure 5.11: Separated (a) tracers and (b) dispersed phase images

Every object in the solids rectangle was picked out from the original image and written to a 'solids-only' image file with a low uniform intensity background (and likewise for the tracers). The refined/separated images of the continuous and dispersed phase are shown in Figure 5.11(a) and (b) respectively. As may be observed, all of the dispersed particles have been successfully detected, even though some comprised multiple fragments in the original image.

This suggests that the two-parameter algorithm of Khalitov and Longmire (2002) with the modified object detection routine may be successfully implemented for phase discrimination in the current study.

Particle centroid location and tracking

'Solids-only' images may be processed for velocity vector maps of the dispersed phase. Particle tracking is preferred (compared to correlation techniques) due to the low number per image frame. The routine calculates the displacement of individual particles across numerous frames in sequence, thereby creating trajectories. The information required for tracking is the centroid location of all particles. Khalitov and Longmire (2002) suggested using the weighted centroid vector $x_{c,i}$:

$$x_{c,i} = \frac{\iint\limits_{\text{object}} x_i I dS}{\iint\limits_{\text{object}} dS} = \frac{\sum\limits_{\text{object}} x_i \times I \times \text{pixels}}{\sum\limits_{\text{object}} \text{pixels}} \tag{5.3}$$

In the present case, since dispersed particles appear as disconnected objects, Equation (5.3) does not hold, since it requires a completely connected image with an approximate Gaussian intensity profile. Subsequently, an alternative method was employed to calculate the centroid coordinates by obtaining Hough transforms of the particle boundaries. The code was self-written in Matlab (details in Appendix III).

5.3 Error estimates with artificial images

Bias and random errors induced by the phase separation algorithm should be assessed before application on real images. Khalitov and Longmire (2002) evaluated the reliability and accuracy of their algorithm with respect to errors on the continuous phase; the dispersed phase was not the main focus. In this study, continuous phase images will be captured exclusively via FPIV. The phase discrimination algorithm will be applied to multiphase Mie scattering images to extract dispersed particle pixels only; hence errors for this phase must be investigated.

Khalitov and Longmire (2002) performed solids-only experiments with various particle sizes, and increased their concentration artificially by overlapping images. This method fails to include reflections between dispersed particles at high concentrations. Secondly, the authors quantified the error on the streamwise (continuous phase) velocity. Stirred flows are highly complex and multi-dimensional; hence it is necessary to express the error with respect to all three directions (if possible). Subsequently, the errors will be re-evaluated using real PIV images of increasing particle concentration, and incorporate both x and y directions. Tests were carried out with particles as large as 1025 μm up 0.5 vol% (compared to 63 μm and 0.0022 vol% reported previously).

5.3.1 Experimental setup

The set-up comprised a baffled cylindrical glass vessel with a flat base and inner diameter $T = 101$ mm. A steel 4-bladed PBT impeller with $D = T/3$ was operated at a clearance of

$C = T/4$. The Perspex baffles had a width $w_b = 0.1T$, located at 90° intervals around the tank wall. Deionised water was filled to a height $H = T$ and open to the atmosphere. The cylindrical tank was placed inside a larger square tank filled with the same fluid, to minimise refraction of the light sheet at the curved surface. The impeller was painted matt black to minimise reflections off the shiny surface.

2-D high-speed experiments were carried out. A CCD camera from TSI Insight with a resolution of 1024×1024 pixels was positioned perpendicular to the front face of the outer tank. The system was equipped with a New-Wave Nd:YLF Pegasus laser with wavelength 527 nm. For calibration, a target grid of known spacing was placed in the centre of the light sheet and a single image was captured, after which the pixel-to-mm conversion was deduced manually. The image acquisition rate was 1500 Hz (for double pulses), with a pulse width of 5 to 7 ns and pulse delay of 310 μs. The time between two exposures in an image pair was 50 μs.

In single-phase experiments, water was traced with 10 μm diameter hollow glass spheres. In solids-only experiments, three different particle diameters were employed: 200-300, 500-750 and 1000-1250 μm of density 2500 kg m^{-3}. Experiments commenced at 0.01 vol% and increased until distortion of the light sheet was too severe to obtain satisfactory images. For the three sizes, upper limits were 0.3, 0.5 and 0.5 vol% respectively. Particles were fully suspended in the flow by operating at 1100 rpm, where $\mathrm{Re} > 2.05 \times 10^4$ (just-suspended speed and flow Re calculations are provided in Appendix V).

5.3.2 Artificial images

Suppose that tracer and solid images have intensities $I_t(x,y)$ and $I_s(x,y)$ respectively. Then artificial two-phase images may be created by overlapping, analogous to the method proposed by Khalitov and Longmire (2002) as follows:

$$I_{\text{overlap}}(x,y) = \max[I_t(x,y), I_s(x,y)] \tag{5.4}$$

The equation above suggests that at each pixel location, the maximum pixel intensity out of the two images is selected to construct the two-phase image. Since dispersed particles are (usually) brighter than tracers, they would overwrite the tracer locations. Similarly, tracer images would overwrite pure background in the solids-only images.

Comparing size-brightness maps of real and artificial two-phase images

A comparison between a real and artificial image with identical dispersed particle size (500-750 μm) and concentration (0.1 vol%) can be made in Figure 5.12(a) and (b). Artificial images do not include inter-phase noise (between tracers and solids). This is unimportant at low concentrations in the real two-phase images. If present, the reflections would cause a local increase in background intensity, and subsequently a less uniform background. However, the algorithm is robust and able to deal with background non-uniformities. It is more important that the artificial images generate signal peaks similar to those of real two-phase images. The size-brightness maps constructed from 10 image pairs of real and artificial images (with conditions matching Figure 5.12) are shown in Figure 5.13(a) and (b).

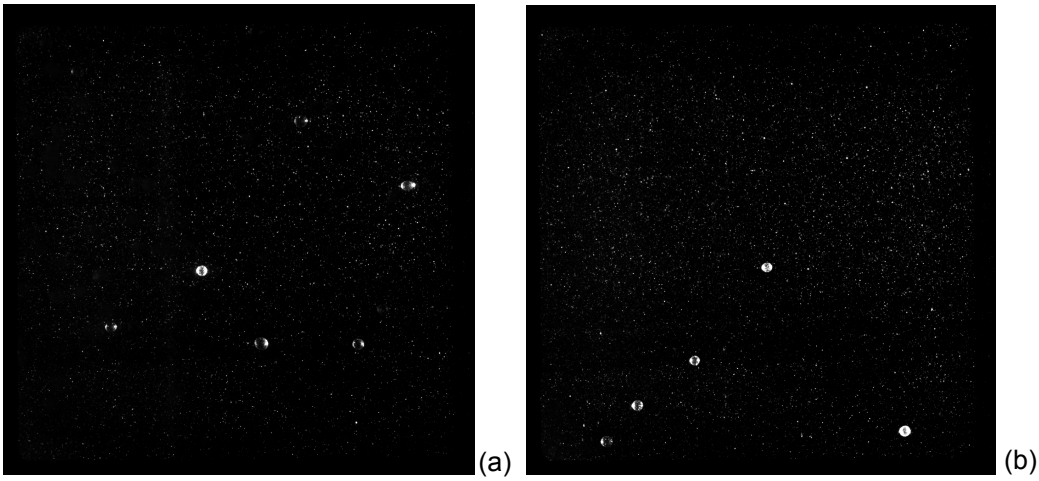

Figure 5.12: (a) real and (b) artificial raw two-phase images

It may be observed from Figure 5.13(a) that the size-brightness map of real images contains a stronger signal in the area of overlap between the rectangular boxes, compared to that obtained from artificial images (Figure 5.13(b)). This is due to scattering between the two phases, described above. However, object pixels within this region would be classed as 'unidentified' and eliminated. Inevitably, some information about real objects could be discarded this way. However, the main regions of consideration are the rectangles forming separation limits. The tracer signal peak and dispersed particle scatter in both cases appear to be very similar. In light of this observation, the use of artificial images is acceptable for testing purposes.

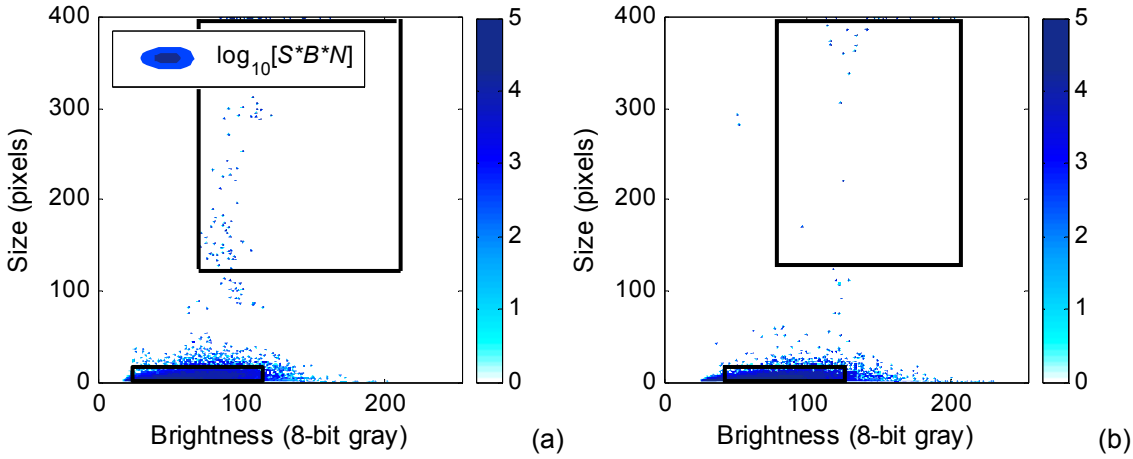

Figure 5.13: Size-brightness maps of (a) real and (b) artificial two-phase images, constructed from 10 PIV image pairs, particle size 500-750 µm and loading 0.1 vol %

Comparing signal peaks of single- and artificial two-phase images

Size-brightness maps were also constructed from tracer- and solids-only images, shown in Figure 5.14(a) and (b) respectively (for 500-750 µm dispersed particles at 0.1 vol%). Differences in signal intensity may be observed between the solids-only (Figure 5.14(b)) and artificial two-phase map (Figure 5.13(b)). Khalitov and Longmire (2002) suggested that in both real and artificial two-phase images, tracers that appear in contact with dispersed particles

would be recognised as a single object during detection. In the present case, it was found that tracers in direct contact with a dispersed particle could add up to ~100 pixels to the individual dispersed particle size. Note that a tracer particle occupies between 1-15 pixels (shown by the limits in Figure 5.14(a)), and as many as 10 of them could appear to be in direct contact with the dispersed particles in the images. Since the tracer light scattering intensity is relatively small (between 20-120 8-bit gray), their effect would be to reduce the 'average intensity' of the solid. For this reason, the signal from the dispersed particles in Figure 5.14(b) appears to be shifted to the centre in the size-brightness map of artificial images Figure 5.13(b). The important point is that both real and artificial two-phase images show this effect. The consequence of the attached tracers is that they would also be written to the 'solids-only' file, and included in the calculation of solid particle centroid locations. However, the Hough transform is robust to these additions, as only the dominant signal (arising from the real particle boundary) would be picked out from the Hough space. In cases where tracers may skew the centroid location, solid velocities could be slightly altered.

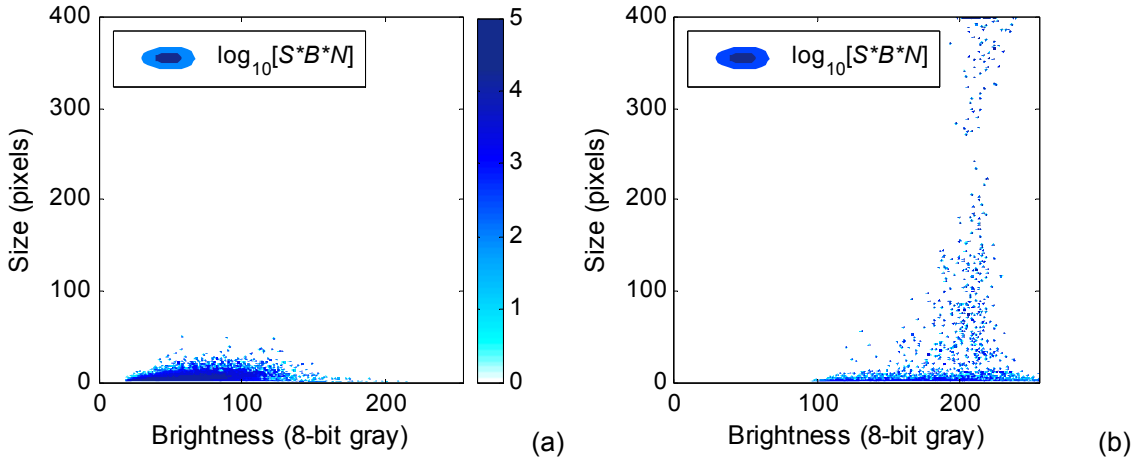

Figure 5.14: Size-brightness maps of (a) tracers- and (b) solids-only, constructed from 10 raw PIV image pairs, particle size 500-700 µm and loading 0.1 vol %

The signal in the solids-only size-brightness map spreads across the region of small, dimmer objects, possibly resulting from miscellaneous remnants originally attached to the solids, as highlighted in Figure 5.15. The patterns could also be a result of Mie scattering from inhomogeneities within the dispersed particles (such as air bubbles). This residual signal coincides with the tracer peak, hence would be included in the tracer separation limits. If they appear to be attached to the tracers, they would be counted as part of the tracer object. Although the magnitude of this signal is relatively small compared to the tracer-only peak, the random objects are likely to induce some error in the cross-correlation procedure of resultant tracer images. In this way, both phases influence the velocity of each other; the following section attempts to evaluate the extent of these errors. Note that information from separated tracers will not be used anyway, since continuous phase velocities will be obtained from cross-correlation of FPIV images. The remaining discussion focuses on the error of dispersed phase velocities only.

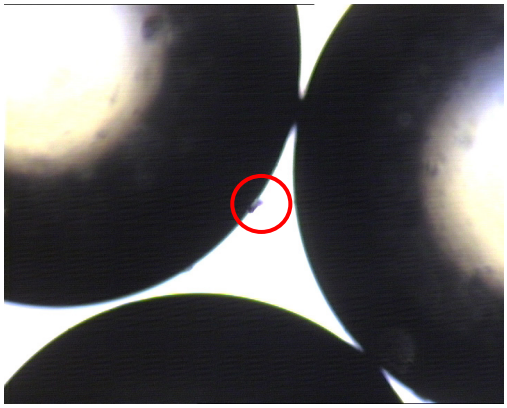

Figure 5.15: Dispersed particles under a microscope, 10× magnification, showing remnants attached to the solid surface

5.3.3 Error estimates

To estimate the error induced by the phase separation algorithm on the dispersed phase, velocity profiles from solids-only images may be directly compared to those obtained from artificial two-phase images *after* phase separation. Initially, solids-only images were post-processed with the separation algorithm to eliminate broken particles and remnants. Size-brightness maps were constructed for each combination of particle size and concentration. The rectangles obtained from these maps were also used as separation limits for corresponding artificial two-phase images. In this way, only information within the rectangles was compared.

The treated images were post-processed using the particle tracking algorithm of Pastor (2007) (Appendix IV) to obtain velocity fields. Subsequently, solids-only and phase-separated solid velocities could be compared. Radial velocities before and after phase separation will be denoted u_s and $u_{s,sep}$ respectively, as depicted in Figure 5.16.

One way of evaluating the error is by calculating the absolute difference between the two velocity fields in the axial and radial directions (Kiger and Pan, 2000). Then, the average absolute error may be calculated stepwise as:

$$u_{err} = \frac{1}{V_t}\sum_{i=1}^{V_t}\left|u_{s,i} - u_{s,sep,i}\right| \tag{5.5}$$

$$v_{err} = \frac{1}{V_t}\sum_{i=1}^{V_t}\left|v_{s,i} - v_{s,sep,i}\right| \tag{5.6}$$

$$s_{err,k} = \sqrt{u_{err,k}^2 + v_{err,k}^2} \tag{5.7}$$

$$\overline{s_{err}} = \frac{1}{N_t}\sum_{k=1}^{N_t} s_{err,k} \tag{5.8}$$

In Equations (5.5) to (5.8), V_t is the total number of vectors in a given velocity field, and N_t the total number of velocity fields in the data set. In this way, the error between vectors is calculated at each vector location and an average error is obtained for an instantaneous velocity field. Then, the total error for all image pairs in a data set is computed and subsequently averaged. The final velocity error will be expressed in pixel displacement (using the time delay between two exposures, and pixel-to-mm conversion).

A range filter was applied to the velocity fields to remove vectors whose magnitude exceeded $1.5V_{tip}$ for both u and v components, prior to calculating the errors. This filter ensured that only obviously spurious vectors were eliminated, which would distort the velocity field and skew the error if not removed.

Note that cross-correlation produces vectors spaced uniformly over the images. However, particle tracking generates velocities at random locations on a point-by-point basis. Subsequently, errors for particle vectors whose $x-y$ co-ordinates match within one pixel are computed using Equations (5.5)-(5.7). On the other hand, some dispersed vectors that appear as u_s might not appear as $u_{s,sep}$, and vice versa. These will be quantified separately as drop-out (x_{out}) and drop-in (x_{in}) vectors respectively, and expressed as a percentage of the number of vectors originally detected in the solids-only velocity field. The entire process of constructing artificial images to evaluating the error is described schematically in Figure 5.16.

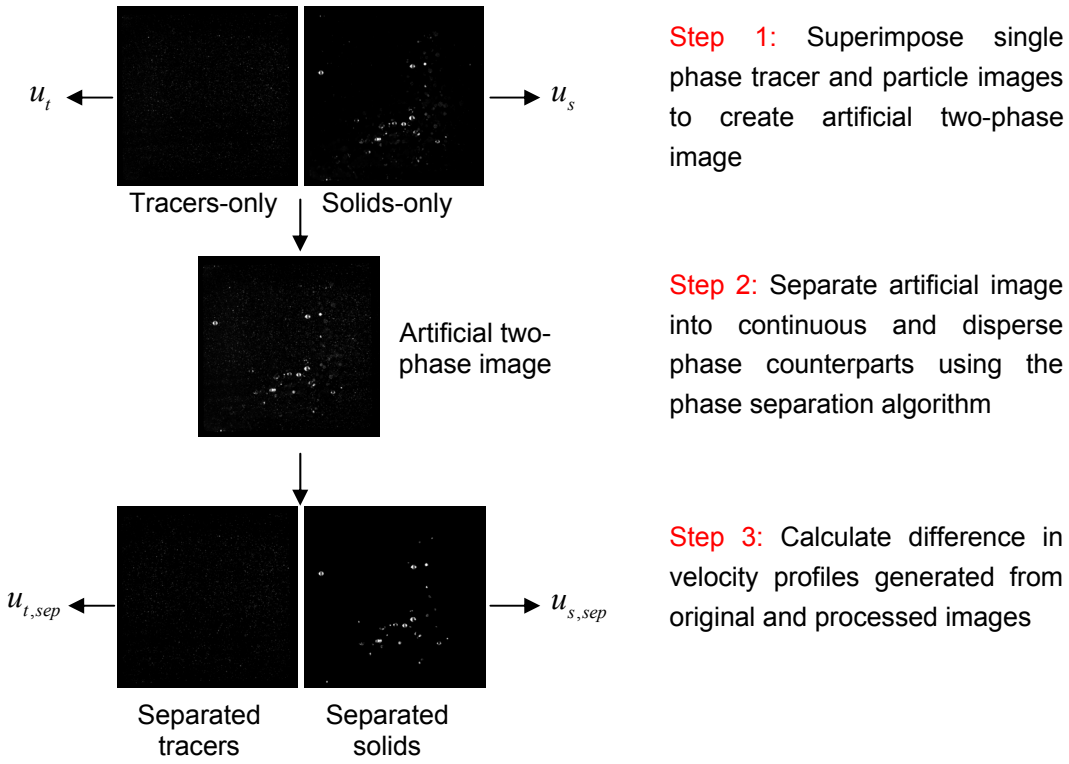

Figure 5.16: Error evaluation process

According to Westerweel *et al.* (1997), typical uncertainties in locating PIV cross-correlation peaks in a 32×32 pixel spot with Gaussian fit is approximately 0.1 pixels in good quality experiments. This order of magnitude may be taken as a standard to evaluate the error of the phase discrimination algorithm.

Figure 5.17(a) illustrates the error induced by the phase separation algorithm in the dispersed phase velocities, with respect to volumetric concentration. Each trend line corresponds to a different particle size. There is no observable correlation between the displacement error and particle concentration, except between 0.01 and 0.1 vol%, where the errors for all three size classes increases up to 0.2 pixels. However, this trend is not consistent along the range of concentrations studied. It is evident that the displacement error of the 300 µm particles is always greater than the two larger size classes (750 and 1250 µm) at all particle concentrations. This trend is clearly demonstrated in Figure 5.17(b), where the error is plotted against particle size (different lines correspond to different concentrations).

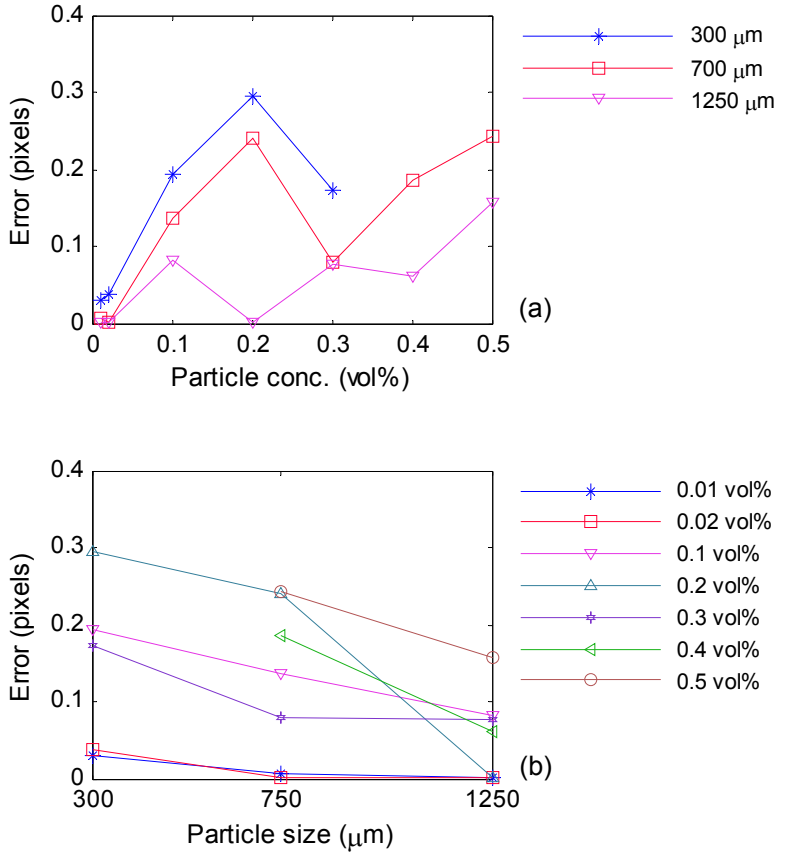

Figure 5.17: Average displacement error of the dispersed phase velocity fields (a) as a function of volumetric concentration and (b) particle size

At all concentrations, the error for the 300 µm particles is larger than that for the 750 µm particles. In most cases, the error for the 750 µm particles is also greater than for the 1250 µm particles. A possible source of these errors (also suggested by Khalitov and Longmire (2002)) is that tracers become attached to dispersed particles, and are counted as a single object during object detection. This can cause a small discrepancy in the centroid location. In the current study, the smallest particles may be the most sensitive to these tracer particle additions at the

boundaries, since the Hough transform uses only the boundary pixels for the centroid location. The attached tracer particles would constitute a larger fraction of the boundary of a small particle, than that of a larger particle, and hence have a greater impact on the centroid location. For the larger particles, the additions become unimportant, and the Hough transform of the processed images would yield peaks at approximately the same locations as the original images. Khalitov and Longmire (2002) noticed that brighter tracer particles caused a larger displacement error compared to dimmer ones, because their calculation of the centroid location included the gray scale intensity as well (Equation (5.3)). This problem is eliminated in the current study, as the boundary pixels are binarized prior to boundary detection, and their gray scale intensity is irrelevant in the Hough transform calculation (details in Appendix III).

Figure 5.18(a) and (b) show the percentage of 'drop-out' vectors in the dispersed phase images with respect to particle concentration and size respectively. Drop-out vectors are those which appear in the velocity field of the raw unprocessed images, but not in the velocity field of the phase separated images. From Figure 5.18(a) it can be seen that the percentage of drop-outs are not related to particle concentration. However, the percentage of drop-out in the 300 μm particles case is consistently greater than larger particles, which is also more evident in Figure 5.18(b). There is no clear distinction between the drop-out percentages of the 750 and 1250 μm particles as their trends overlap, often crossing to show an increase at some concentrations and a decrease at others.

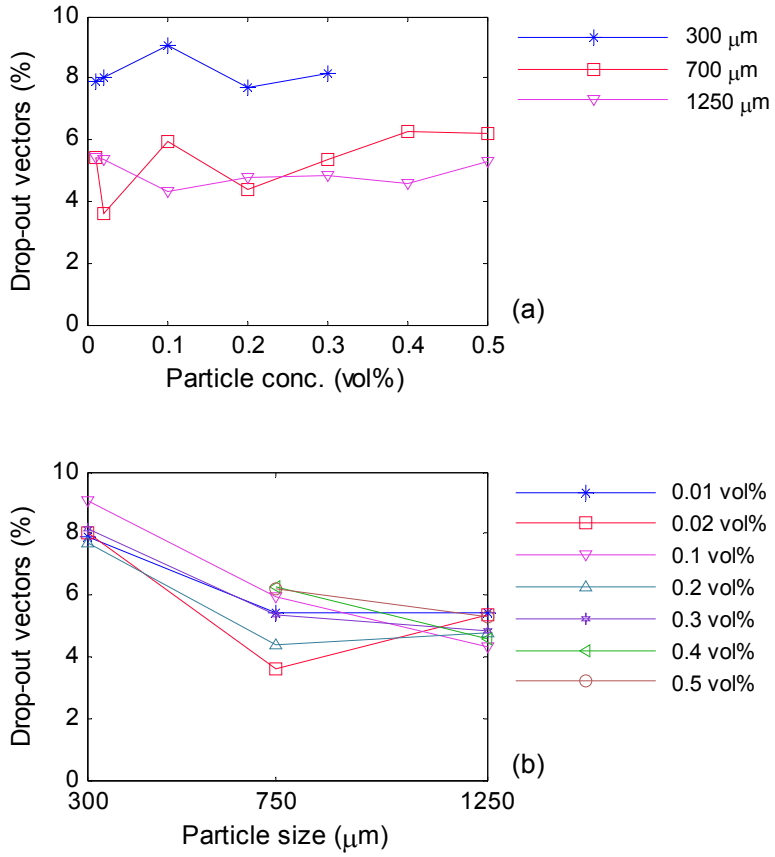

Figure 5.18: Average percentage of drop-out vectors in the dispersed phase velocity fields as a function of volumetric concentration and particle size

It was mentioned previously that dispersed particle images appear as two adjacent 'half moon' shapes, which may also be made up of smaller fragments. The smaller the particle size, the smaller these constituent fragments. The smallest fragments could be of the same size as a cluster of tracer particles. For this reason, the size-brightness contour map of the objects detected in images of the 300 μm particles yielded a greater signal in the area of overlap between the two rectangular boxes which formed the separation limits. Consequently, there was more information removed from images of the smallest particles after phase separation, which was discarded as random objects or noise. A lot of this information could have corresponded to reliable dispersed particle fragments. However, the small loss of reliable data is acceptable, since much of the signal in the region of overlap arises from clusters of tracers, which would cause relatively more spurious vectors. Note that the phase separation limits from the size-brightness maps were adjusted to minimize the loss of overlapping information for each experimental condition.

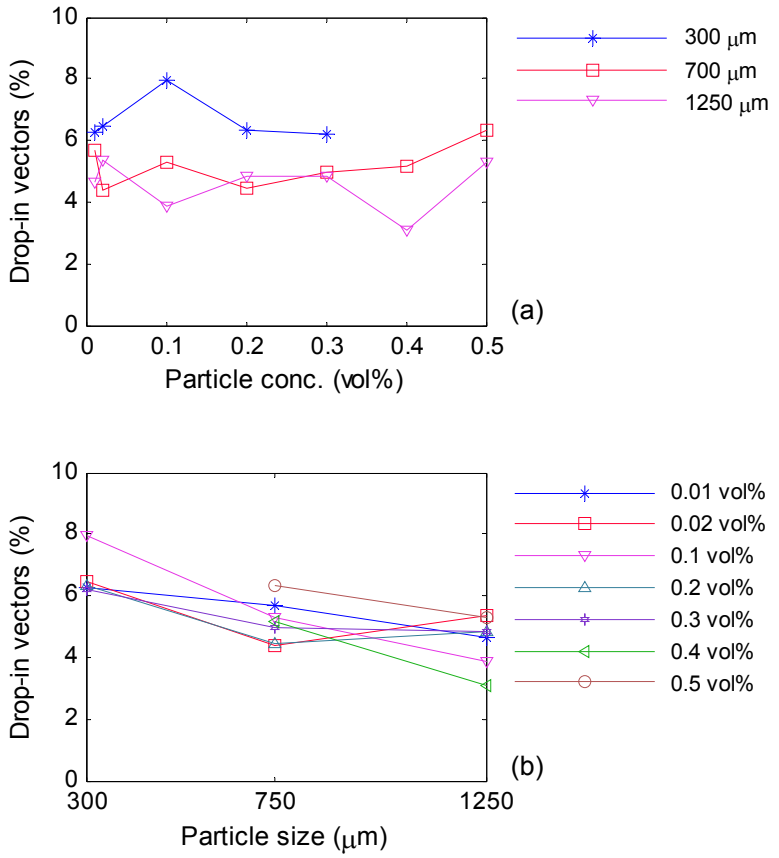

Figure 5.19: Average percentage of drop-in vectors in the dispersed phase velocity fields as a function of volumetric concentration and particle size

In the case of the larger particles, it is believed that the drop-out vectors are mainly dispersed particles whose centroids have shifted by more than one pixel in the processed images (probably due to tracers attached at the boundaries). A visual analysis of the particle trajectories supports this assumption. Subsequently this information is not really 'lost'; it is just not matched with the original solid images within pixel accuracy. As a result, these vectors were not included in the analysis of displacement errors of matching particles before and after phase separation.

Instead these would appear as ‘drop-in’ vectors in the processed images, shown in Figure 5.19(a) and (b) with respect to particle concentration and size.

For the two larger particle sizes, the percentage of drop-in and drop-out vectors are approximately equal in magnitude and show similar trends to the drop-out percentage at all concentrations, supporting this conjecture. In the rare instances where there is a small surplus of drop-in vectors over drop-out vectors, as in the case of 750 μm particles at 0.2 vol%, these are due to large clusters of tracers which are mistakenly classified as dispersed particles and appear in the phase separated particle images. There are generally more drop-out than drop-in vectors for the 300 μm particles, further suggesting that this deficit is in fact lost information from the images.

Note that drop-out vectors are not necessarily a bad result, as the phase separation limits serve to remove noise (as well as some reliable data). In some cases, particle trajectories of the phase separated images appeared to be a lot more consistent, or smoother, than those generated from the raw single-phase images, because spurious objects were removed.

To conclude, Khalitov and Longmire’s (2002) phase separation algorithm operates best on the two larger particle sizes; 500-750 and 1000-1250 μm. Their difference in size from the tracer particles facilitates phase separation by minimizing the region of overlap in the size-brightness maps. Secondly, the detrimental effect of artificial tracer additions to their image boundaries is less significant. The error on the 200-300 μm particles is greatest, reaching a maximum of 0.3 pixels. However since this error is of the same order as the recommended benchmark for good quality PIV of 0.1 pixels (Westerweel *et al.*, 1997), the algorithm may still be applied to achieve phase discrimination of the smallest particles without significant bias in the dispersed phase velocity. To improve phase discrimination and shorten the width of the size-brightness separation limits, the aforementioned particles will be physically filtered to achieve narrower size distributions of 250-300, 700-750 and 1000 μm. Consequently, these are the dispersed particle sizes which will be referred to in the following chapters concerning two-phase PIV and micromixing experiments.

Chapter 6
Two-phase PIV Study

Two-phase PIV experiments to measure velocity fields in solid-liquid stirred suspensions have been carried out. This chapter describes the observed turbulence modulation by solids on the continuous phase, especially in terms of the dissipation rate, the property of most interest.

6.1 Experimental setup

6.1.1 Experimental apparatus

Experiments were carried out in a flat-base stirred tank of diameter $T = 101$ mm, with four baffles (width $T/10$) placed equidistantly around the vessel circumference. A small tank (relative to the EkatoMizer study with $T = 305$ mm) was selected to reduce the path length of the light sheet, to the measurement region. This is because the dispersed particles obstruct the laser light sheet, and subsequently hinder its penetration depth into the flow. Distilled water was filled to a height $H = T$ and open to the atmosphere. The cylindrical tank was placed inside a larger square tank filled with the same working fluid, to minimise refraction of the laser at the curved surface. The vessel was made of cylindrical glass; all other components were made of acrylic. The experimental setup and measurement plane are illustrated in Figure 6.1. The final tank dimensions incorporating baffles are given in Table 6.1.

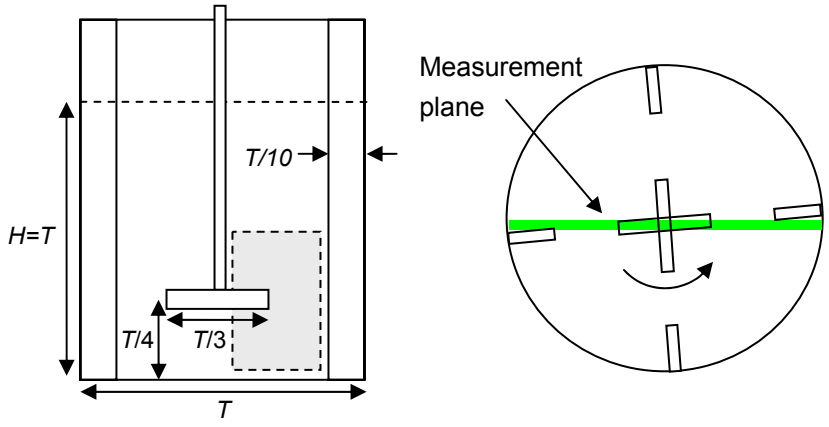

Figure 6.1: Impeller and tank geometry, and measurement plane as viewed from above

Different impeller designs are able to achieve different degrees of solid suspension for a similar power input, due to variations in mean flow pattern. High efficiency axial impellers (e.g. Lightnin A310, Chemineer HE3) are the most capable of achieving solid suspension at lower impeller

speeds, followed by PBTs. RDTs are a relatively poor choice (Magelli *et al.*, 1991). For a given impeller type, the degree of suspension is dependent on the impeller geometry and clearance and hence depends on the D/T and C/T ratios at constant power input. Atiemo-Obeng *et al.* (2004) showed that a large diameter PBT with $D/T = 0.75$ is poor at suspending solids due to the resulting flow pattern, whereas $D/T < 0.4$ is better. If impellers are mounted too near the base, fluid velocities in the upper half of the vessel may not be strong enough to balance the downwards force of settling solids, since fluid velocities decrease away from the impeller. On the other hand, impellers at high clearance may not create enough turbulence near the base to lift the settled solids. In general small PBTs located near the vessel base are generally good for solid suspension (Atiemo-Obeng *et al.*, 2004). Following this recommendation, a down-pumping acrylic 45° PBT of $D = T/3$ was selected to operate at $C = T/4$. The impeller dimensions are provided in Table 6.2.

Table 6.1: Tank dimensions

Parameter	*Notation*	*Size (m)*
Tank Diameter	T	0.101
Water fill height	H	T
N° of baffles	n_b	4
Baffle width	w_b	T/10
Baffle thickness	t_b	T/67

Table 6.2: Impeller geometry

Parameter	*Notation*	*Size*
Impeller swept diameter	D	T/3
N° of blades	n_{bl}	4
Blade angle	α	45°
Blade length	L	0.351D
Blade width	W	0.219D
Blade thickness	b_t	0.045D
Shaft diameter	S_d	0.30D
Impeller clearance	C	T/4

Dispersed particles were soda-lime glass spheres of density 2500 kg m^{-3} and RI 1.51 at the sodium D-line ($\lambda = 589.3$ nm) at 20 °C (Duke Scientific Corporation). Three sizes were employed; 250-300, 700-750 and 1000 µm. Experiments were initiated with particles suspended in the fluid at a concentration of 0.01 vol%, and increased incrementally until the laser light sheet extinction was too severe to enable satisfactory PIV measurements. The upper limits were 0.3, 0.5 and 0.5 vol% respectively. In all experiments the impeller speed was set at 1600 rpm, which is well above the just-suspended speed characterised by the Zwietering (1958) criterion of ~1087 rpm for 0.5 vol% of 1000 µm particles suspended in water (calculation in Appendix V). This ensured complete off-bottom suspension. Fluorescent particles of 30 µm diameter were used to trace the water. The particles were manufactured in-house from polystyrene (PS) cross-linked with divinyl benzene (DVB) and doped with pyrromethene 597-8C9 dye (Exciton). The dye has an absorption peak at 527.8 nm (close to the laser excitation

wavelength of 532 nm), and a fluorescence peak at 590 nm in diesel fuel. The dyes are not very solvochromatic, hence wavelength changes would be small (5-10 nm at most) in the PS/DVB material. Details of the particle manufacturing methods are given in Appendix V.

6.1.2 Measurement technique

The measurement technique involved a combination of fluorescence tagging and digital image treatment, depicted previously in Figure 2.3. The system employed a two-camera PIV setup. One was fitted with two long-pass Schott OG550 filters (UQG Ltd) with a cut-off at 550 nm, meaning that it blocked Mie scattering at the lower wavelength (532 nm) and transmitted fluorescence at higher wavelengths. In this way, the camera captured images of fluorescent tracers without interphase noise, which were processed to obtain velocity fields without any further treatment. PIV analysis was conducted using cross-correlation techniques with interrogation area (*IA*) sizes of 32×32 pixels, with 50% overlap. At the given resolution (33 pixels per mm), the length of the interrogation areas was 0.97 mm. The largest particle diameter (1 mm) was comparable to the *IA* spatial resolution. However, the majority of particles appeared as two 'half moon' shapes rather than filled circles in the images (see Figure 5.1). They did not always occupy the entire *IA* and enabled enough fluorescence from the tracers to be transmitted for cross-correlation. In cases where particles overlapped or where particles saturated the *IA*, no additional measures were taken to avoid the problem of insufficient tracers. Instead, the cross-correlation signal peak-to-noise ratio was set relatively higher than the single-phase case, so that vectors from these low tracer regions would be eliminated. Obvious spurious vectors exceeding a magnitude of $1.5 \times V_{tip}$ were also filtered, and the holes later filled in via linear interpolation of the surrounding vectors.

The second camera was equipped with a short-pass dielectric cut-off filter (Melles Griot) which also had a cut-off at 550 nm. In contrast to the first camera, this filter was used to partially block fluorescence and transmit mainly Mie scattering from the dispersed and tracer particles. Subsequently, fluorescent tracers appeared less bright in the images, which in turn facilitated digital phase separation. This camera simultaneously captured Mie scattering images of both phases on a single frame, which were digitally post-processed to extract bright pixels corresponding to the dispersed phase, using the algorithm of Khalitov and Longmire (2002) (discussed in Chapter 5). Particle velocities were obtained via cross-correlation, in a similar fashion to the continuous phase, using 32×32 pixel *IA*s with 50% overlap.

The cameras were two 8-bit TSI PIVCAM 10-30 Model 630046 cross-correlation cameras, with a resolution of 1000×1016 pixels. Both were fitted with a Nikon Micro Nikkor 105 mm lens ($f^{\#}$ 2.8-32). The system was equipped with a double-pulsed New-Wave Nd:YAG Solo III laser of 532 nm wavelength and 50 mJ pulse energy. The laser was passed through a series of cylindrical and spherical lenses (focal lengths -15 and 500 mm respectively), which shaped the resulting beam into a light sheet of ~1 mm thickness. The two cameras were synchronised using a TSI LASERPULSE synchroniser Model 610034. For camera calibration, a target grid of known grid spacing was placed in the centre of the light sheet and both cameras were adjusted to obtain the same field of view (with an accuracy of ±2 pixels at the edges). The calibration yielded a resolution 33 pixels per mm in the field of view. The image acquisition rate was 15 Hz (for double pulses), with a pulse width of 6 ns and pulse delay of 263 μs. The time separation

between two exposures in an image pair was 50 μs in each experiment. Ensemble-averaged measurements (averaged around 360º of the impeller) were obtained in the impeller region, where the highest turbulence level was expected. The field of view was 28×28 mm^2 and included the blade. The baffle at the edge of the field of view was positioned just behind the light sheet, such that its reflections did not appear in the images. A recent study revealed that the mean flow and turbulence properties can be characterised by a sample comprising a minimum of 575 vector fields (Virdung and Rasmuson, 2008). Consequently, 600 double image pairs were obtained in each evaluation, and considered to be sufficient to obtain turbulence statistics.

6.2 Single-phase flow

This section describes the flow field and turbulence properties generated by a PBT for a single-phase flow at 1600 rpm. For the PBT impeller geometry (see Table 6.2) $\mathrm{Re} = 3.08 \times 10^4$, meaning that the flow is fully turbulent. When operating under this regime, flow velocities should scale with the impeller tip speed. Statistical properties were calculated by averaging over 600 instantaneous PIV measurements obtained around 360° of the impeller. In this and following sections, data have been plotted on the $r - z$ (radial-axial) plane according to polar coordinates and in the figures, $< u >$ and u_{rms} denote the radial mean and rms velocity respectively (similarly for the axial component).

6.2.1 Mean flow field

Figure 6.2 displays the ensemble-averaged mean velocity field generated by the PBT for a single-phase flow at 1600 rpm.

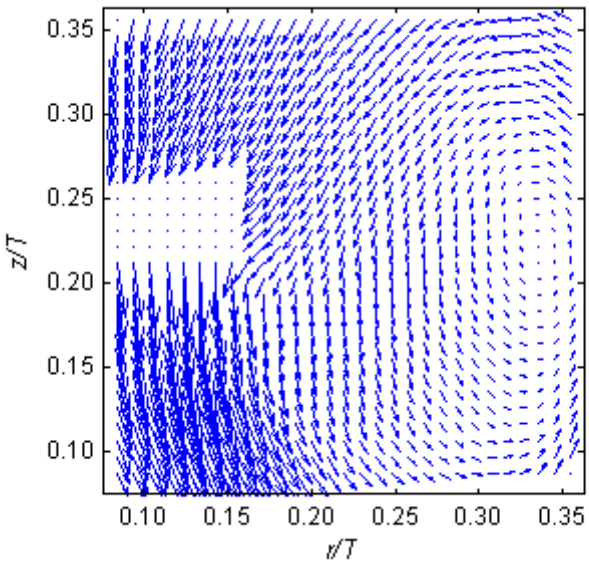

Figure 6.2: Ensemble-averaged mean velocity vectors of the single-phase flow

The main feature is the primary circulation loop characteristic of a PBT. It may be observed that the impeller generates a strong axial flow in the downwards axial direction. The stream flows

along the bottom of the vessel radially towards the wall, and then flows up the vessel wall before returning to the top of the impeller. Since the flow is fully turbulent, the same general flow pattern was observed for every experiment regardless of the impeller speed. If the flow was not fully turbulent, the impeller stream flow direction would become more axial as Re increases through the transitional regime (Schafer *et al.*, 1998) making comparisons between experiments difficult. The field of view is not large enough to observe the entire circulation loop, but the top has been reported to reach a height $z/T = 0.55 - 0.65$ (Shafer, *et al.*, 1998).

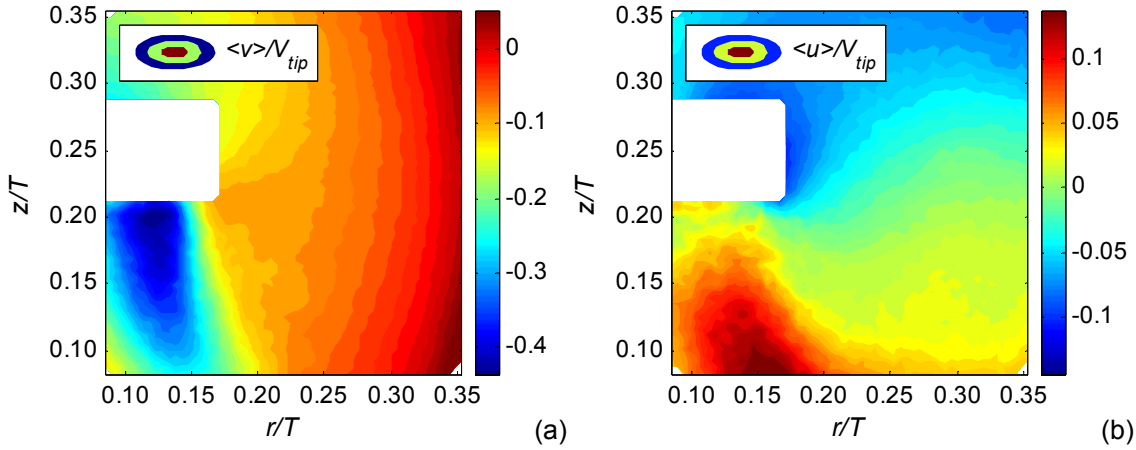

Figure 6.3: Ensemble-averaged (a) axial and (b) radial mean velocity of single-phase

Figure 6.3(a) shows a contour plot of the mean axial velocity. The strongest flow is directly beneath the impeller, reaching a maximum of $0.45V_{tip}$ at $z/T = 0.197$ and $r/T = 0.119$. This is in very close agreement with the value reported by Kresta and Wood (1993a). Schafer *et al.* (1998) also found the peak axial mean velocity to be $\sim 0.45V_{tip}$ beneath the impeller, where $r/T = 0.125$. Axial velocities in the upward flow close to the wall are $\sim 0.1V_{tip}$. However the field of view extends only to $r/T = 0.356$ and not as far as the vessel wall where $r/T = 0.5$. In the wall jet, velocities can be as high as $0.2V_{tip}$ (Shafer *et al.*, 1998). Apart from in the impeller discharge, the axial velocity close to the centre of the vessel base ($z/T = 0.09$, $r/T = 0.09$) is relatively small at around $0.1V_{tip}$, and would decrease as $r/T \to 0$. Schafer *et al.* (1998) suggested that there may be difficulties in lifting solids off the vessel base in this area in solid-liquid systems.

In previous studies, the axial discharge for a single-phase PBT flow has been reported to reach the vessel base and change direction towards the wall at around $r/T = 0.25$ (Fort, 1986; Virdung and Rasmuson, 2008). Schafer *et al.* (1998) observed this behaviour at $\mathrm{Re} > 1100$. In the present case however, the jet is found to deflect towards the wall directly underneath the impeller blade. The contour plot of the radial mean velocity in Figure 6.3(b) illustrates this more clearly. It may be observed that the strongest radial flow (coinciding with the change in direction of the impeller jet) occurs at $r/T = 0.15$. The difference may be due to the smaller clearance from the vessel base in this study ($T/4$) compared to the standard geometry used in the

aforementioned studies ($T/3$). It seems as if the jet reaches the vessel base while it is still predominantly axial, meaning that it is deflected radially at a position further away from the wall.

6.2.2 rms velocities and TKE

The ensemble-averaged axial and radial rms velocities of the single-phase flow are shown in Figure 6.4(a) and (b) respectively.

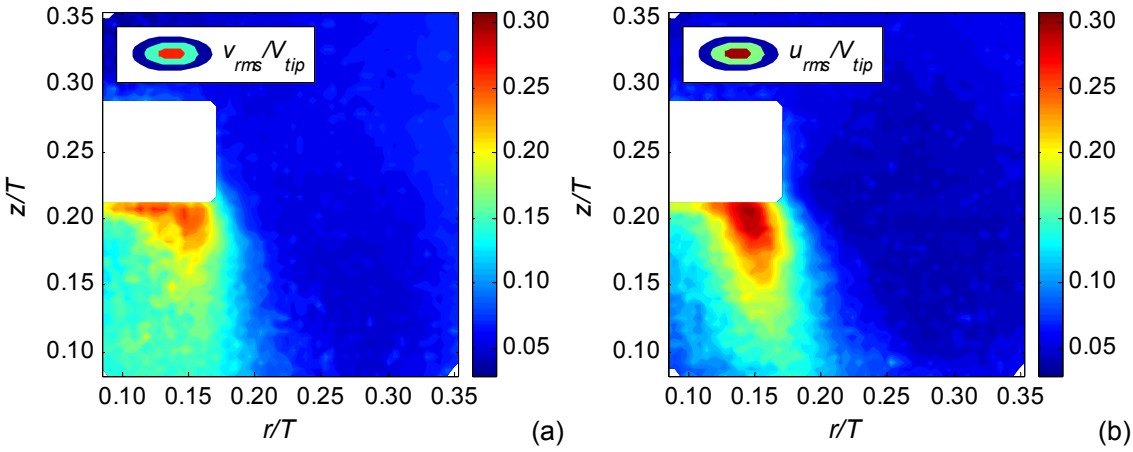

Figure 6.4: (a) Axial and (b) radial rms velocities of the single-phase flow

It may be observed that rms velocities are strongest below the impeller blade reaching $0.3V_{tip}$, and are an order of magnitude smaller $\sim 0.03V_{tip}$ in the bulk. Differences in distributions of the axial and radial rms velocities are evident. Regions of high axial rms velocity are found under the lower blade edge between $0.175 < z/T < 0.216$ and up to $r/T = 0.167$, whereas regions of high radial rms velocity are narrower (confined within a width $\sim 0.026T$), extending axially downwards from the lower blade edge to $z/T = 0.16$. Secondly, the maximum values of the axial and radial rms velocities are unequal; $0.27V_{tip}$ and $0.30V_{tip}$ respectively. The radial rms velocity is greater, which is unusual since the primary flow direction (in this case axial) is normally considered to represent the system turbulence when estimating the dissipation rate via dimensional analysis methods. This also involves the assumption of isotropic turbulence, since the turbulence in one direction is assumed to represent the turbulence in the orthogonal directions too.

In order to determine whether the flow can be classified as isotropic or anisotropic, direct comparisons have been made between the axial and radial rms velocities. The absolute differences between the two velocity components normalized by the tip speed i.e. $|u_{rms} - v_{rms}|/V_{tip}$, are plotted in Figure 6.5.

In the bulk differences are only a small fraction of the tip velocity (i.e. $\sim 0.02V_{tip}$). Larger differences are found under the blade edge and close to the centre of the vessel base ($r/T = 0.1$); however even in these areas, the maximum difference is only $0.08V_{tip}$. Khan

(2005) also found a maximum difference of $0.08V_{tip}$ in the discharge stream of a PBT impeller, where measurements were angle-resolved exactly between two blades. In absolute terms, the rms velocities in this experiment differ at most by 27%. In their study, Kresta and Wood (1993b) found absolute differences between the three rms velocity components of a PBT flow to be between 25-50%. The authors stated that rms velocities in highly anisotropic flows are expected to differ by up to 200%. Against this criterion, the single-phase flow of the current study may be considered as approximately isotropic. On the other hand, Schafer *et al.* (1998) found values of $\left|u_{rms} - v_{rms}\right| / V_{tip}$ to be as high as 0.15, and suggested anisotropy of the flow. Subsequently, the demarcation between the two definitions is a matter of the author's own judgement.

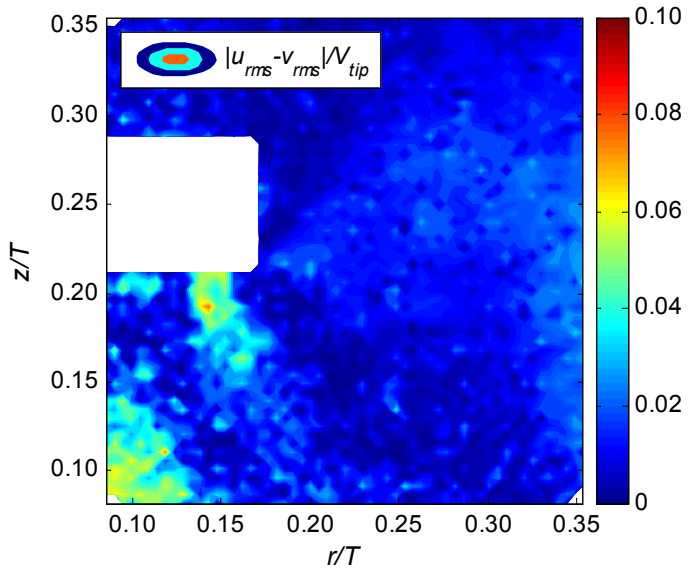

Figure 6.5: Difference in the axial and radial rms velocities of the single-phase flow

The turbulent kinetic energy (TKE) was calculated using a pseudo-isotropic assumption, given in Equation (2.15). Ideally, the TKE would be calculated using all three fluctuating components, but since 2-D PIV does not provide the tangential velocity, Equation (2.15) was used out of necessity. However, since the comparison between the axial and radial rms velocities in Figure 6.5 indicate isotropy of the flow, scaling for the tangential velocity component may be acceptable in this case. Khan (2005) also showed that the TKE was predicted very well using the pseudo-isotropic assumption for a PBT stirred flow.

A contour plot of the normalized TKE is displayed in Figure 6.6. As may be observed, regions of high TKE are located under the lower blade edge where $0.125 < r/T < 0.167$ and $0.175 < z/T < 0.216$. This is naturally a combination of regions of high axial and radial rms levels, whose square roots are constituents of the 2-D TKE. The spatial distribution agrees reasonably well with the turbulence distribution provided by Virdung and Rasmuson (2008) (defined as $\sqrt{\overline{u'^2} + \overline{v'^2}}$), even though their experiments were angle-resolved between two baffles. Angle-resolved measurements of Khan (2005) also yielded high values of the TKE in the impeller discharge stream at all blade angles.

The maximum value of k/V_{tip}^2 was found to be 0.12 where $z/T = 0.207$ and $r/T = 0.148$. In the bulk, normalized TKE levels are close to zero. Schafer *et al.* (1998) reported maximum k/V_{tip}^2 of 0.085 from their ensemble-averaged measurements, which is lower than the present case. However, their ensemble-averages were taken over 90° of revolution, opposed to 360° in this case which could include blade-to-blade variations. More importantly, their impeller clearance was $T/3$ compared to $T/4$ here. Kresta and Wood (1993b) operated a PBT at a clearance of $T/4$, and their 360° ensemble-averaged maximum k/V_{tip}^2 was around 0.1 at the impeller discharge. Note that their impeller diameter was $T/2$. Studies which have employed angle-resolved measurements (e.g. Schafer *et al.*, 1998; Khan, 2005) have reported even lower maximum k/V_{tip}^2 levels (0.058 and 0.06 respectively). This is almost certainly because ensemble-averaged measurements can overestimate turbulence levels due to the contribution of the mean flow periodicity. Overall, turbulence levels and TKE distributions presented here agree well with similar studies cited in literature.

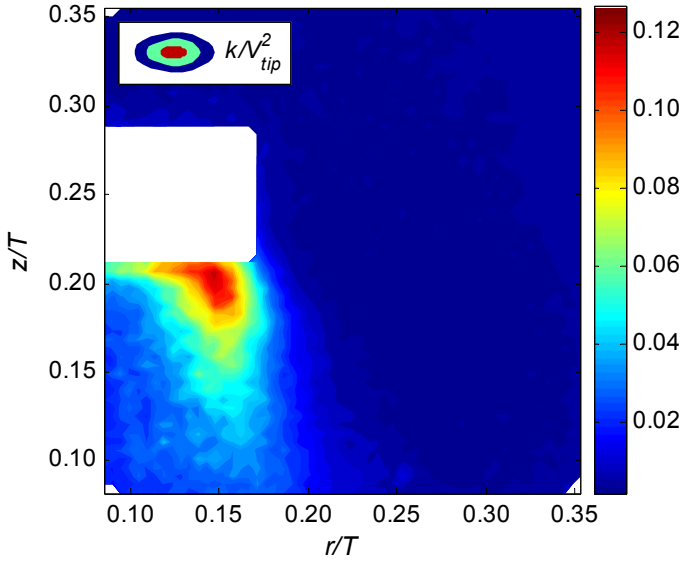

Figure 6.6: 2-D TKE estimate of the single-phase flow

6.2.3 Dissipation rate

The dissipation rate was estimated using the 2-D LES analogy of Sheng *et al.* (2000), Equation (4.16). Note that vector validation filters were not applied to the velocity field before its computation. This is because the best filter must be selected on a case by case basis, since it is dependent on the experimental conditions (e.g. field of view, ensemble-averaged vs. angle-resolved data), and the fluid hydrodynamics (e.g. level of turbulence and inhomogeneity). The global filter was was identified as the most suitable in the EkatoMizer study (§4.8.4) but cannot be assumed to be the best choice for the PBT flow. In the EkatoMizer study, the field of view was relatively small compared to the size of the vessel (43×43 mm^2 and $T = 305$ mm). In the present case, the relatively larger field of view (28×28 mm^2 and $T = 101$ mm) would certainly affect the degree of filtering, as it would contain a wider range of velocites. An assessment of

the filter efficiency against the multifractal model of Meneveau and Sreenivasan (1991) (discussed in §4.8.2) necessitates high-speed PIV data. Since the two-phase PBT experiments employed a 15 Hz system, such an analysis could not be performed. Consequently the data were not manipulated further, as the effects of filtering could not be ascertained.

The final result is displayed in Figure 6.7(a). Regions of intense dissipation are confined very close to the lower blade edge, where $0.181 < z/T < 0.216$ and $0.120 < r/T < 1.150$. The normalized dissipation rate $\varepsilon/(N^3D^2)$ reaches a maximum value of ~54 below the impeller at $z/T = 0.212$ and $r/T = 0.138$, and decays to approximately 10-20 in the rest of the discharge stream. In all other regions of the bulk $\varepsilon/(N^3D^2) < 1$.

The maximum dissipation rate generated by 45° 4-PBT impellers are an order of magnitude lower in literature than the present case. Zhou and Kresta (1996) employed 1-D LDA to measure a PBT flow, and dimensional analysis to obtain the dissipation rate. In their study, $\varepsilon_{max}/(N^3D^2)$ was ~2.44 (an average over five impeller speeds). The PIV study of Sheng *et al.* (2000) which first implemented the LES analogy indicates $\varepsilon_{max}/(N^3D^2)$ of only 0.58. Khan (2005) used PIV and employed the LES analogy, for which $\varepsilon_{max}/(N^3D^2)$ was ~9.2. Already between these estimates, there is an order of magnitude difference. There are three main factors that contribute to these variations; differences in tank geometry, flow measurement technique and dissipation rate estimation method. Although the current estimate seems relatively high, an independent experiment produced a similar distribution within the same order of magnitude, shown in Figure 6.7(b). The repeatability confirms reliability of the data, hence single-phase results illustrated in this section will be taken as a basis of comparison for the following multiphase measurements.

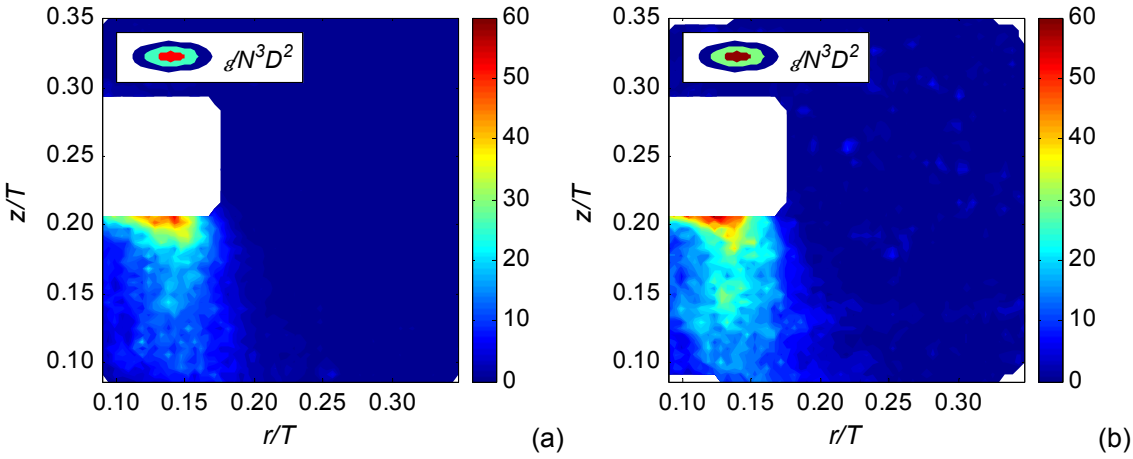

Figure 6.7: Dissipation rate from the 2-D LES analogy of Sheng *et al.* (2000) from two independent single-phase experiments carried out under the same operating conditions

6.2.4 Comparison between single-phase experiments

Three independent PIV experiments were carried out for each solid particle size class investigated. In each experiment, the particle size was kept constant and its concentration

varied. Between each set of experiments, the vessel and impeller had to be removed to drain the contents and be cleaned, and replaced back into the original configuration for the proceeding run. It is important that the location of the baffle relative to the light sheet and impeller clearance were constant in each experiment to enable cross-comparison between the results. To verify this, PIV measurements of the single-phase flow were obtained whenever the experimental setup was reconfigured, which could be directly compared with each other.

The radial profile of the mean axial velocity at $z/T = 0.106$ and axial profile of the mean radial velocity at $r/T = 0.258$ are shown in Figure 6.8(a) and (b) respectively. Note that Exp1, Exp2 and Exp3 correspond to single-phase velocities obtained under the same operating conditions, after reconfiguration. It may be observed that the trends overlap along both dimensions of the vessel, suggesting that the setup was maintained relatively constant throughout the trials. Subsequently, it is possible to cross-compare results between each set of experiments.

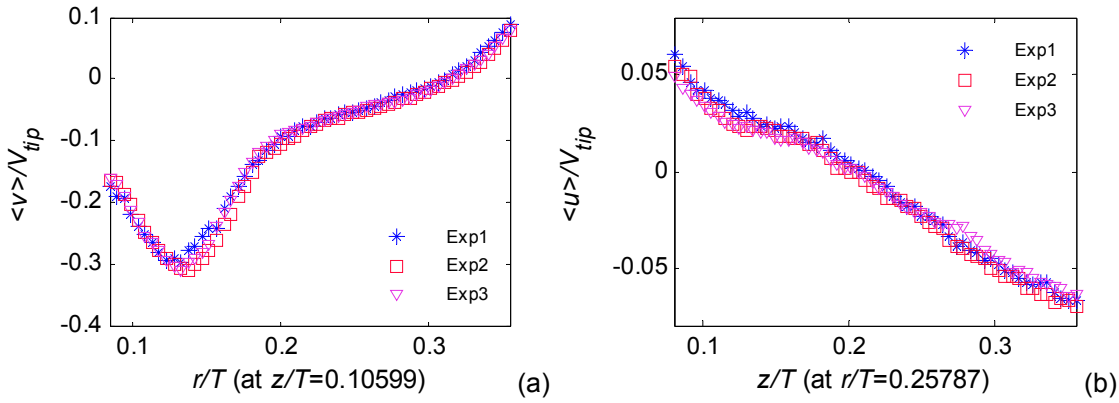

Figure 6.8: (a) Radial profile of the mean axial velocity at $z/T = 0.106$ and (b) axial profile of the mean radial velocity at $r/T = 0.258$ of three independent experiments

6.3 Turbulence modulation: Effect of particle size

This section evaluates turbulence modulation of the continuous phase relative to the single-phase flow, with respect to particle size 250-300, 700-750 and 1000 μm, at 0.3 vol%. The single-phase mean flow field and turbulence properties used for comparison were averages of the three single-phase data sets, which were obtained at the start of each experiment. So for instance, the mean axial velocity profile in the radial direction at $z/T = 0.106$, would be an average of the three single-phase trend lines depicted in Figure 6.8(a). The variation between the three sample means is shown by dashed lines representing plus and minus one standard deviation from the overall mean in proceeding figures.

6.3.1 Mean flow field

Figure 6.9(a) and (b) illustrate radial profiles of the mean axial velocity of the single and continuous phase with 250-300, 700-750 and 1000 μm particles at 0.3 vol%. The profiles were taken in regions above and below the impeller respectively.

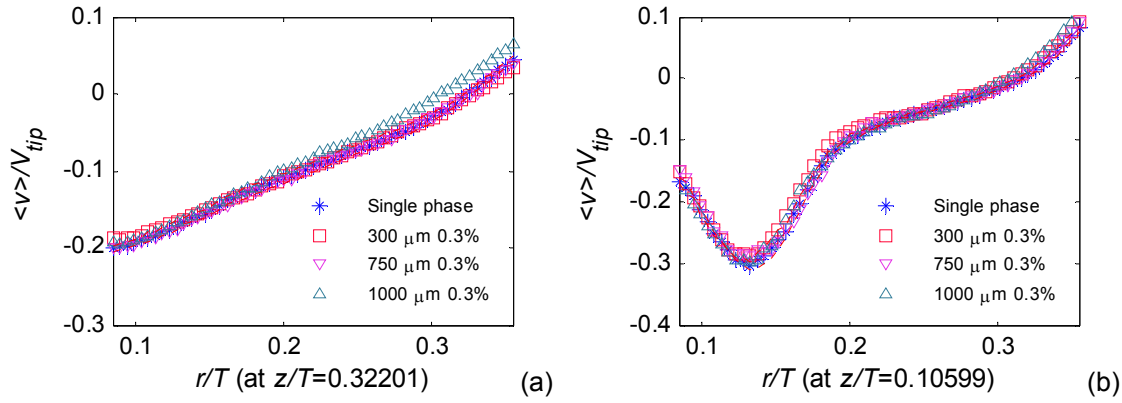

Figure 6.9: Radial profiles of the mean axial velocity of the single and continuous phase flows with varying particle size obtained at (a) $z/T = 0.322$ **and (b)** $z/T = 0.106$

In both graphs the trends overlap, apart from the continuous phase mean axial velocity with 1000 µm particles, at $r/T > 0.20$ and $z/T = 0.322$, Figure 6.9(a). This difference in axial velocity decreases vertically down the vessel, and the trends in Figure 6.9(b) taken below the impeller coincide within one standard deviation of the single-phase data. It is unclear what is causing the slightly greater (upward) continuous phase velocity with 1000 µm particles, but since the difference is not appreciable and also not observed along the entire vessel wall, the effect is considered to be unimportant.

Similarly, axial and radial profiles of the mean radial velocity are depicted in Figure 6.10(a) and (b). Velocity profiles of the single and continuous phase show the same trends, but do not coincide as well as the mean axial velocities. However it should be noted that the standard deviation of the single-phase radial mean velocity is also slightly greater than the axial component. With this in mind, it can be concluded that mean velocities of the continuous phase are not altered significantly in the impeller suction or jet, with the incorporation of various particle sizes at 0.3 vol%.

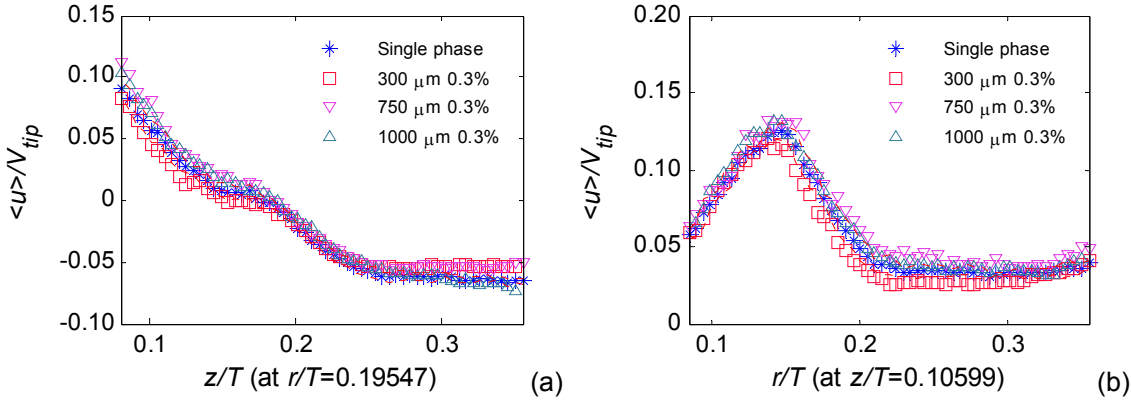

Figure 6.10: (a) Axial ($r/T = 0.195$**) and (b) radial (**$z/T = 0.106$**) profiles of mean radial velocity of the single and continuous phase flows with varying particle size**

The result is in contrast to the study of Guiraud *et al.* (1997), who investigated the effect of 253 µm particles suspended in water at 0.5 vol%. They reported that the axial velocity decreased slightly in the impeller jet due to inertia of the glass particles, and also in the upward wall jet due to gravity. However, the continuous phase mean radial velocities were found to be identical with the single-phase flow for most parts of the vessel. Virdung and Rasmuson (2008) reported a maximum decrease in the axial and radial velocity of 46 and 10% respectively in the impeller jet, when 1000 µm particles were present in the flow at 1.5 vol%. They also found that the impeller jet diverted towards the tank wall further away from the vessel base when particles were present, but attributed this effect to particles resting on the bottom, thus reducing the clearance. In the present case however, particles were agitated well above the just-suspended speed defined by Zwietering (1958), ensuring off-bottom suspension, so this effect was not observed.

6.3.2 rms velocities and TKE

This section describes turbulence modulation of the continuous phase, relative to the single-phase fluid, caused by the presence of dispersed particles (250-300, 700-750 and 1000 µm) at 0.3 vol%. Figure 6.11(a) and (b) show radial profiles of the axial and radial rms velocities below the impeller respectively (at $z/T = 0.106$). It may be noticed that the standard deviation of the three single-phase rms velocities (shown by dashed lines) is greater than that of the mean velocities in Figure 6.9, where it can be barely distinguished from the data. This is expected since rms velocities are calculated from fluctuating components, which would be unstable relative to the mean flow.

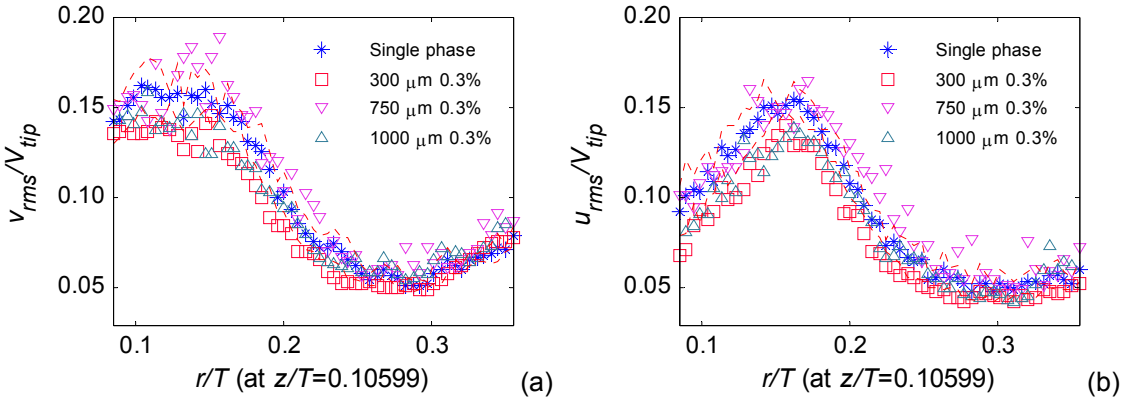

Figure 6.11: Radial profiles of the (a) axial and (b) radial rms velocities of the single and continuous phase flows with varying particle size obtained at $z/T = 0.106$

From both graphs it may be observed that the smallest and largest particles (i.e. 250-300 and 1000 µm) decrease both rms velocities below the impeller. The 250-300 µm particles suppressed the maximum axial and radial rms velocities by 8.7 and 4.3% respectively. Similarly, the 1000 µm particles suppressed the maximum axial and radial rms velocities by 2.8 and 4.8% respectively. Even at this low particle concentration (0.3 vol%), the trend lines of the continuous phase lie outside the standard deviation of the single-phase rms velocities. For this reason, there is confidence that the observed turbulence suppression is a genuine effect, and not an artefact of the unsteady nature of the fluctuating velocities. Conversely, rms velocities of

the intermediate size class (750 μm) fall within the standard deviation boundaries, so turbulence modulation cannot be clearly distinguished. These trends were consistent in the discharge stream. Above the impeller, only 300 μm particles caused turbulence suppression. Modulation was not significant in any experiment radially away from the impeller (in the bulk region and close to the vessel wall), and all trend lines fell within the single-phase standard deviation boundaries.

Gore and Crowe (1989) postulated that particles with a 'diameter to fluid integral length scale ratio' $d_p / L < 0.1$ cause turbulence suppression, whereas those with $d_p / L > 0.1$ cause augmentation. In their study, L was defined as the integral length scale of the single-phase, although the authors used this mainly out of necessity, since data of length scales after the addition of particles were not available. Following this comment, 2-D-integral length scales of the continuous phase were used to evaluate this ratio in the present case. The computation involved determination of the 2-D autocorrelation function of the instantaneous axial fluctuating velocity fields, and integration with respect to both coordinates (Equation (2.12)). The average length scale of all instantaneous results in the data set provided the 2-D length scale Λ_v. This is for the field of view shown in Figure 6.2. Continuous phase integral length scales are discussed in detail in §6.5. For experiments with 250-300 and 1000 μm particles, Λ_v of the continuous phase was found to be 0.0038 and 0.0035 m respectively (or $0.514W$ and $0.475W$). Corresponding ratios of d_p / Λ_v were 0.079 and 0.285 respectively. According to Gore and Crowe's (1989) criterion the smallest particles suppress turbulence as expected. However the result of the largest particles is unusual since they fall into the regime of turbulence augmentation.

Hetsroni (1989) suggested that particles with a low Reynolds number decrease turbulence, whereas those with a high Reynolds number augment turbulence due to wake shedding. The author stated that vortex shedding does not occur when $\mathrm{Re}_p < 110$; instead it occurs in the range $400 < \mathrm{Re}_p < 1000$ (Achenbach, 1974). Re_p was estimated from the particle terminal velocity, since the slip velocity is unknown at this stage, and found to be 4.92 and 105 for the 300 and 1000 μm particles respectively (calculations in Appendix V). Since Re_p is almost the same as or less than O(100), turbulence damping by these particles is correctly predicted.

Previous reports in literature have provided mixed results. Guiraud *et al.* (1997) studied 253 μm particles in water at 0.5 vol%, and found that they did not disturb the axial, radial or tangential rms velocities of the continuous phase. Micheletti and Yianneskis (2004) suspended 186 μm particles in water at 0.5 vol% and also showed turbulence suppression; the radial rms velocity in the impeller disc plane decreased by 50%. This difference is considerable compared to the amount of suppression observed in the present and other cases. The authors reported a particle diameter to fluid integral length scale ratio of 0.15. Although it may be argued that the ratio is close to (or of the same order as) the transitional value of 0.1, the study of Gore and Crowe (1989) depicts $d_p / L = 0.1$ to be a clear demarcation point. Conversely, the results of Virdung and Rasmuson (2008) showed that 1000 μm particles at 0.5 vol% increased turbulence and their calculated ratio d_p / L was greater than 0.1, where an increase in turbulence is to be

expected. In the aforementioned studies only the effects of particles on rms velocities were reported. Mechanistic models for turbulence modulation were not provided.

Radial profiles of the 2-D TKE of the single and continuous phase, taken above and below the impeller are shown in Figure 6.12(a) and (b) respectively. As in the case of the rms velocities, the 250-300 and 1000 µm particles decrease the TKE below the impeller. As mentioned earlier, these effects are considered to be genuine as the trend lines are outside the standard deviation of the single-phase TKE results.

The reduction of TKE is only appreciable between $0.085 < r/T < 0.20$. For $r/T > 0.2$, the difference is small and within experimental error. Nouri and Whitelaw (1991) also found that turbulence damping (in terms of rms velocities) became insignificant radially away from the RDT blade.

Figure 6.12(a) demonstrates an earlier point that above the impeller, only 250-300 particles dampen turbulence. This may be due to the fact that the smallest particles are suspended more easily, and would be dispersed above the impeller level more effectively. Subsequently, there would be a higher probability of finding a larger concentration of the smallest particles above the impeller, in order for them to cause a noticeable change. It should also be noted that although the impeller speed was above the just-suspended speed (Appendix V), particles were not suspended homogeneously throughout the vessel. There were evidently higher concentrations above and below the impeller; this is discussed in §6.7.1. The 700-750 µm particles do not modify turbulence outside of the bounds of the single-phase standard deviation, analogous to the rms velocities.

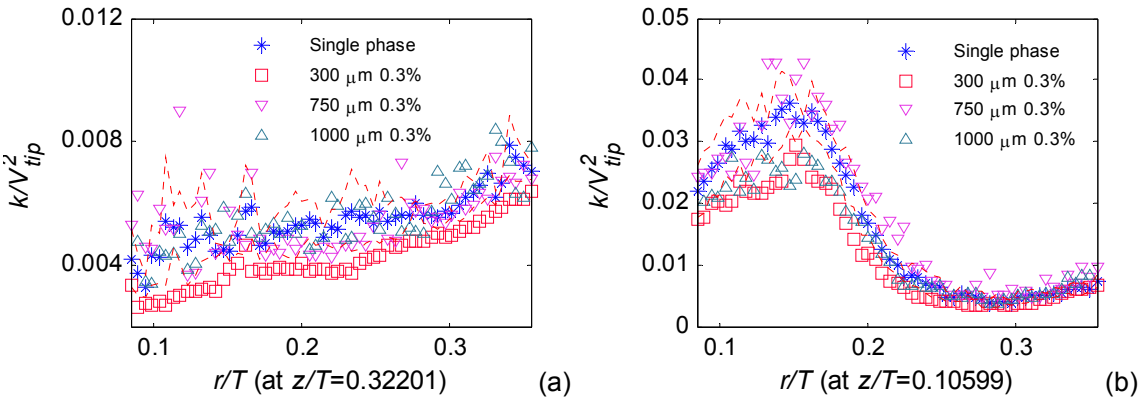

Figure 6.12: Radial profiles of the 2-D TKE of the single and continuous phase flows with varying particle size obtained at (a) $z/T = 0.322$ **and (b)** $z/T = 0.106$

The 250-300 and 1000 µm particles decrease the maximum single-phase TKE by 18.4 and 9.3% respectively. Contour plots of the single and continuous phase TKE with 300 µm particles at 0.3 vol% are shown in Figure 6.13(a) and (b), respectively. It is evident that the greatest turbulence reduction occurs directly below the impeller in the jet stream, whereas the bulk is less affected. The spatial distribution of the TKE with 1000 µm particles was similar; only the maximum reduction was to a lesser extent.

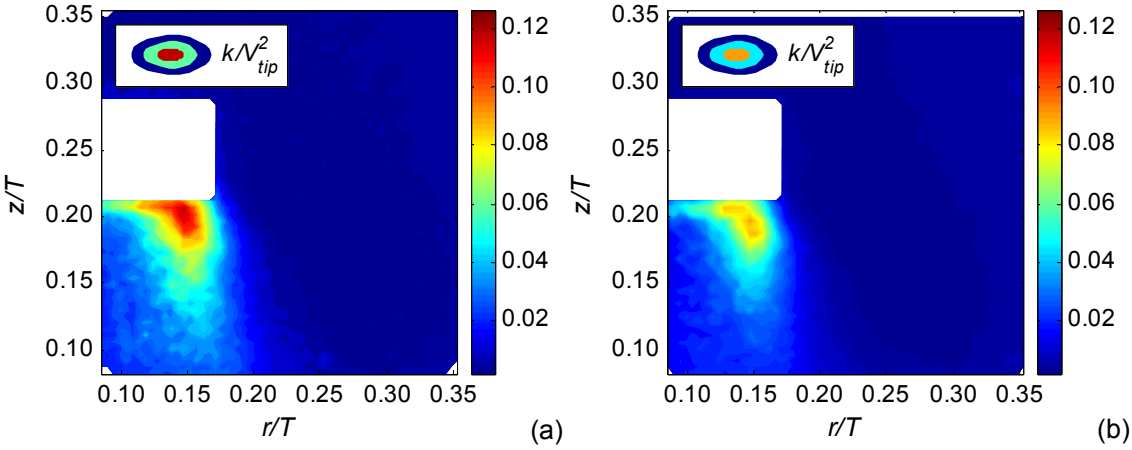

Figure 6.13: Contour plots of the 2-D TKE of the (a) single and (b) continuous phase flows with 300 µm particles at 0.3 vol%

6.3.3 Dissipation rate

The author is not aware of any other study which has experimentally investigated the effect of particles on the dissipation rate of a stirred continuous phase flow, relative to the single-phase fluid. Axial and radial profiles of the dissipation rate are presented in Figure 6.14(a) and (b) respectively. Note that in Figure 6.14(a) the area of no results (between $0.216 < z/T < 0.293$) corresponds to the region occupied by the impeller.

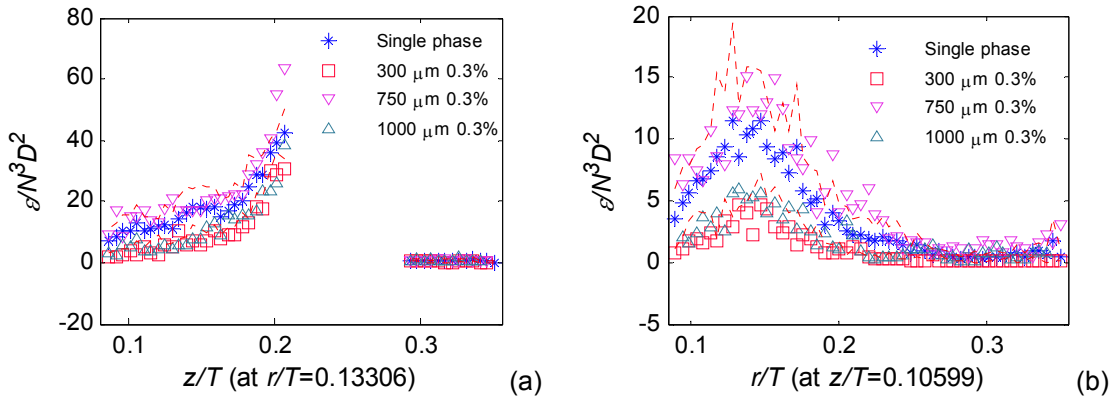

Figure 6.14: (a) Axial ($r/T = 0.133$) and (b) radial ($z/T = 0.106$) profiles of the dissipation rate from the 2-D LES analogy of Sheng *et al.* (2000) for the single and continuous phase flows with varying particle size

Consistent with results presented thus far, the smallest and largest (250-300 and 1000 µm) particles decrease the dissipation rate, whereas the intermediate size class does not cause changes outside the single-phase standard deviation boundaries. The standard deviation of the single-phase dissipation rate is much greater than that of the mean and rms velocities. This is because its calculation involves a gradient based method (Sheng *et al.*, 2000) which is more susceptible to velocity fluctuations, and amplifies their deviation from neighbouring vectors in the flow field. In general, dissipation is known to have an intermittent nature (Meneveau and

Sreenivasan, 1991), so a larger standard deviation is to be expected compared to properties of the mean flow. The 250-300 and 1000 µm particles suppress the maximum dissipation rate by 24.6 and 12.2% respectively. It may be noted that similar to the TKE, the smallest particles decrease the fluid turbulence more than the largest particles, by a factor of ~2.

Spatial distributions of the dissipation rate for the single and continuous phase flow with 250-300 µm particles (0.3 vol%) are shown in Figure 6.15(a) and (b). It may be observed that the decrease in dissipation is not as pronounced as the decrease in TKE in the entire discharge stream below the impeller. The largest turbulence suppression occurs directly underneath the blade. This suggests that the presence of the particles decrease the velocity gradients in the immediate vicinity of the impeller blades, as well as causing a general decrease in the fluctuating velocities throughout the impeller discharge jet.

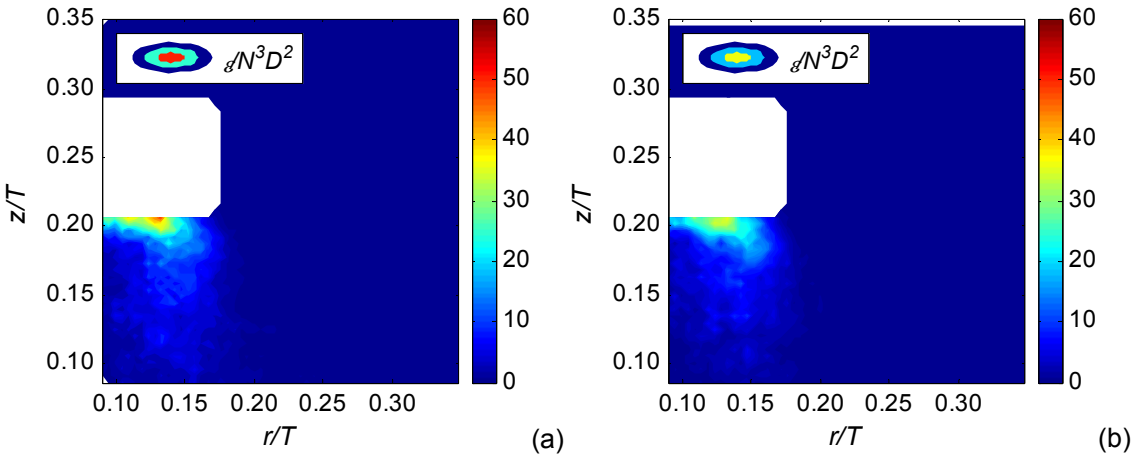

Figure 6.15: Contours of the dissipation rate from the 2-D LES analogy of Sheng *et al.* (2000) for the (a) single and (b) continuous phase flows with 300 µm particles at 0.3 vol%.

6.4 Turbulence modulation: Effect of particle concentration

This section describes the effect of particles on the continuous phase fluid turbulence, with respect to the particle concentration. Three size classes 250-300, 700-750 and 1000 µm were studied up to volumetric concentrations of 0.3, 0.5 and 0.5 vol% respectively. The discussion will be based primarily on experiments carried out with 1000 µm particles, and observations of the other two size classes will be summarised.

6.4.1 Mean flow field

Figure 6.16(a) and (b) depict radial and axial profiles of the mean axial and radial velocities of the continuous phase respectively, with the incorporation of 1000 µm particles at various volumetric concentrations. It was previously shown that particle size had no significant effect on the mean velocities (at 0.3 vol%). In Figure 6.16(a) the trend lines coincide almost exactly, meaning that particle concentration is also unimportant, at least up to the maximum solids volume fractions studied here. The mean radial velocity trend lines of the continuous phase in Figure 6.16(b) show slight variations from the single-phase, but all deviations are within experimental error and no significant effects are evident. Mean velocity profiles of the

continuous phase with 250-300 and 700-750 µm particles also showed no relation to particle concentration, at these low volume fractions.

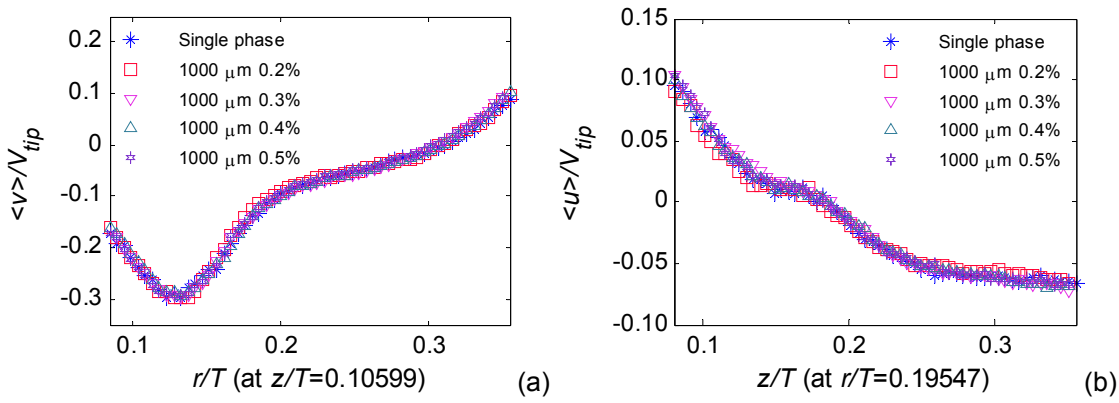

Figure 6.16: (a) Radial profile ($z/T = 0.106$) of the mean axial velocity and (b) axial profile ($r/T = 0.195$) of the mean radial velocity of the continuous phase with 1000 µm particles, increasing concentration up to 0.5 vol%

6.4.2 rms velocities and TKE

Axial and radial profiles of the radial and axial rms velocities of the continuous phase are shown in Figure 6.17(a) and (b) respectively, in the presence of 1000 µm particles, up to 0.5 vol%. Although the fluctuation of these turbulence properties is large (relative to the mean flow), it may still be observed that the rms velocities decrease above particle concentrations of 0.2 vol% in both directions. The degree of turbulence suppression remained relatively constant between 0.3-0.5 vol%. This is portrayed more clearly in the TKE contour plots, Figure 6.18(a) to (d).

Figure 6.18(a) and (b) show the TKE of the single and continuous phase with 0.2 vol% of 1000 µm particles respectively; the magnitudes and distributions of both are comparable. However with the incorporation of 0.3 vol%, turbulence suppression in the impeller jet is immediately evident, in Figure 6.18(c). When the concentration is increased to 0.5 vol% in Figure 6.18(d), there is no noticeable further change. The results suggest that at the low concentrations studied, particle-particle interactions are unimportant, and do not contribute to the observed phenomenon of turbulence suppression. Instead it is a direct consequence of the interactions between individual particles and the flow. In particulate suspensions with higher volumetric concentrations, where particle-particle interactions are expected to be significant, the degree to which turbulence is modulated would also depend on the particle volume fraction.

Micheletti and Yianneskis (2004) who also observed turbulence suppression found that concentrations of 0.5 and 1 vol% of 186 µm particles decreased the radial rms velocity of the fluid in the impeller disc plane by 50 and 70% respectively. On the other hand, Virdung and Rasmuson (2008) found that increasing the concentration of 1000 µm particles from 0.5 to 1.5 vol% increased the amount of turbulence augmentation of the continuous phase, as well as making their spatial distributions more homogeneous. Although these studies show opposing effects, it is suggestive that particle-particle interactions become relevant in the mechanisms which modulate turbulence, above volumetric concentrations of 0.5 vol%. However Micheletti

and Yianneskis (2004) also noted that turbulence levels did not decrease further when the concentration was increased to 2 vol%, indicating that inter-particle interactions no longer governed turbulence suppression.

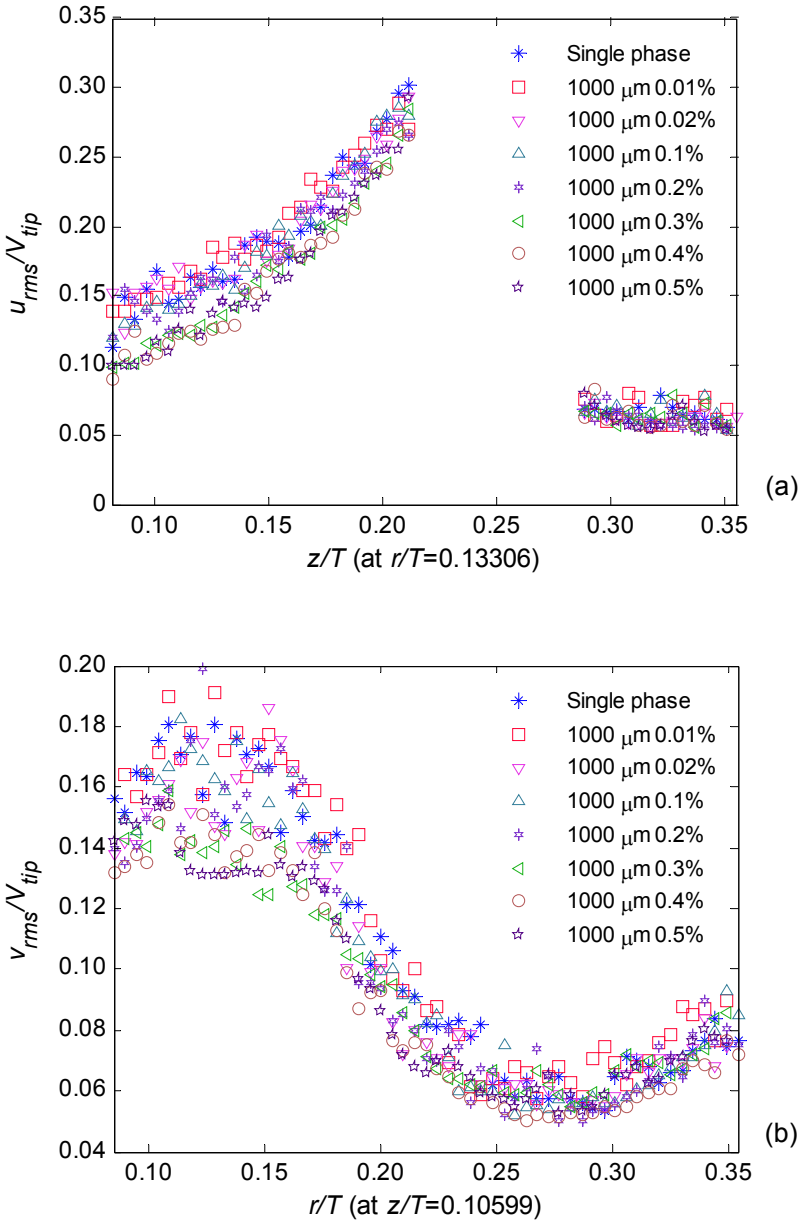

Figure 6.17: (a) Axial profile ($r/T = 0.133$) of the radial rms velocity and (b) radial profile ($z/T = 0.106$) of the axial rms velocity of the continuous phase with 1000 µm particles, increasing concentration up to 0.5 vol%

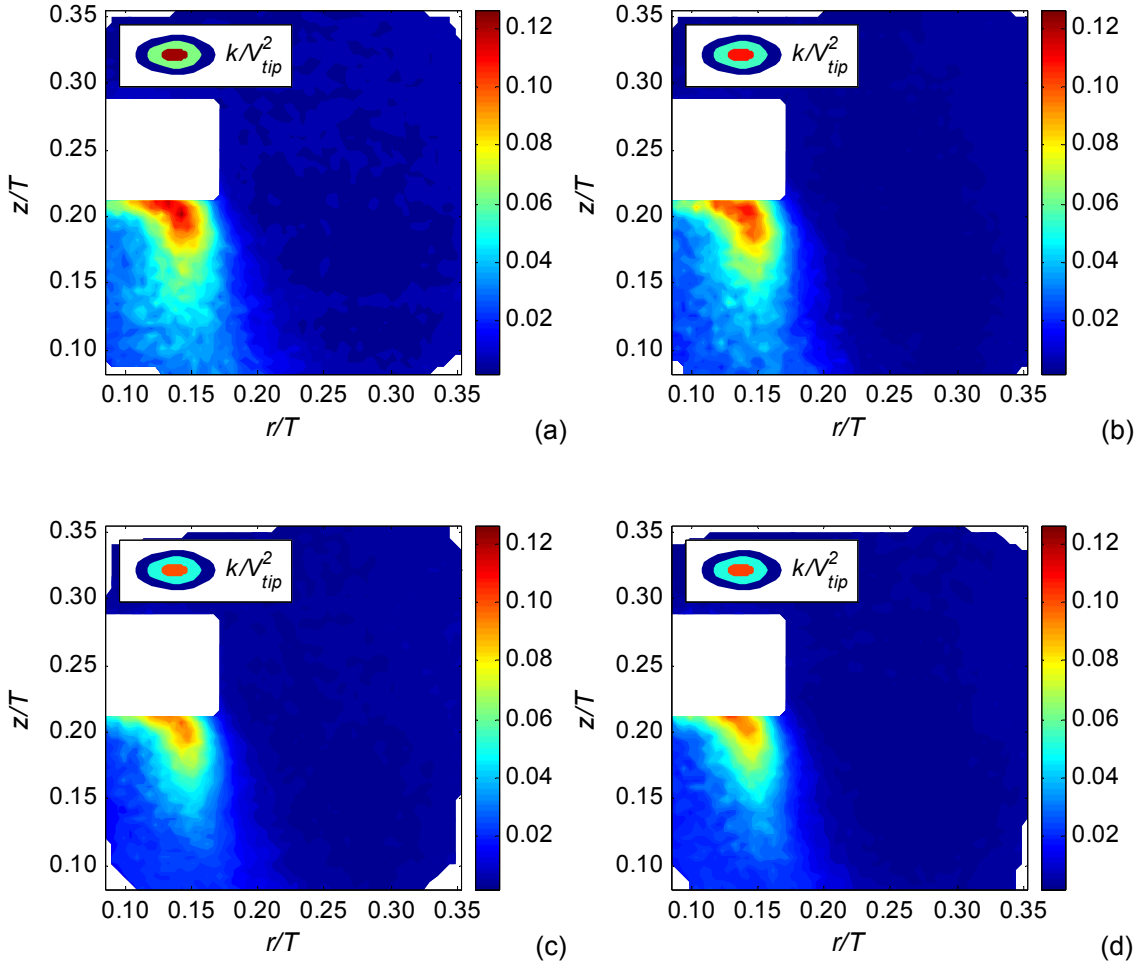

Figure 6.18: Contour plots of the 2-D TKE of the (a) single and continuous phase flows with 1000 µm particles at concentrations of (b) 0.2 (c) 0.3 and (d) 0.5 vol%

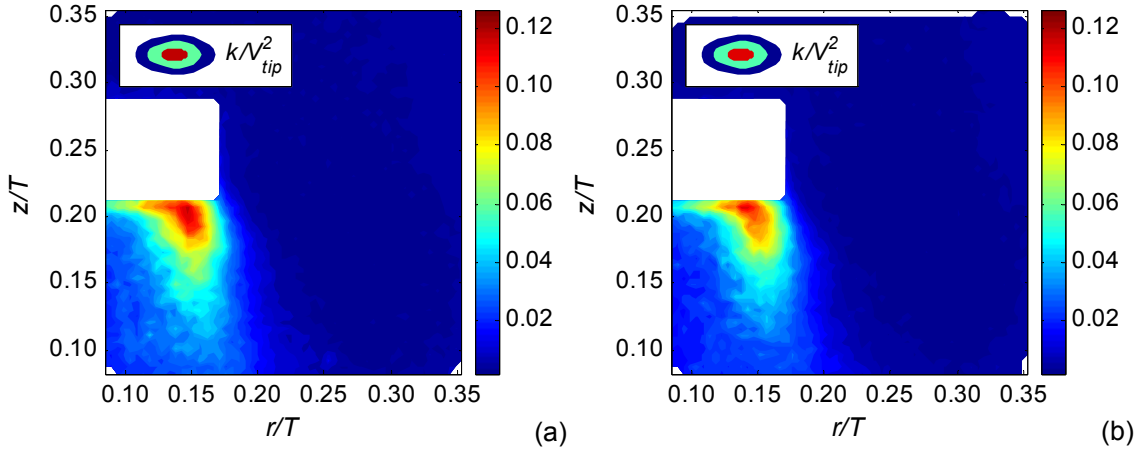

Figure 6.19: Contour plots of the 2-D TKE of the (a) single-phase and (b) continuous phase flows with 750 µm particles at a concentration of 0.5 vol%

Results for the 300 μm particles also showed turbulence suppression at 0.3 vol%. This was the highest concentration studied for the smallest particle class, as at an equivalent concentration to a larger size, there were more particles in the flow which obstructed the laser light sheet. Subsequently, the effect of increasing concentration of smaller particles cannot be deduced at this stage (but will be later investigated via two-phase micromixing experiments in Chapter 7). When observing analogous trends of experiments carried out with 750 μm, there was also evidence of turbulence suppression at concentrations >0.2 vol%. However, compared to the continuous phase TKE with 1000 and 300 μm at the same concentration, the degree of turbulence suppression is much less significant. This point is illustrated in Figure 6.19(a) and (b), which show the TKE of the single and continuous phase with 750 μm particles at 0.5 vol%. Here the turbulence has not been suppressed down to the level shown in Figure 6.18(d), which has 1000 μm particles. This supports the previous observation that the effect of 750 μm particles (at 0.3 vol%) is negligible compared to the other two size classes.

6.4.3 Dissipation rate

Following the trends of the rms velocities and TKE, the dissipation rate also decreases in the presence of 1000 μm particles at concentrations >0.2 vol%. Turbulence suppression is clearly distinguishable from the single and continuous phase experiments with lower particle concentrations, shown by the axial and radial profiles in Figure 6.20(a) and (b) respectively. In the analysis of the effect of particle size on turbulence properties (§6.3), it was also noticed that suppression of the dissipation rate was greater than that of the TKE and rms velocities close to the lower blade edge.

Once again, the extent of turbulence damping remains approximately constant with increasing dispersed phase concentration up to 0.5 vol%. Contour plots of the dissipation rate in Figure 6.21(a) to (d) show hardly any turbulence damping when 0.2 vol% are present in the flow, but suppression is obvious when adding 0.3 vol%, which remains constant up to 0.5 vol%. The maximum dissipation rate is decreased by 21% in the presence of 1000 μm particles at 0.5 vol%.

Observations of the dissipation rate for the 250-300 and 700-750 μm particles are the same as for the TKE, in that the smallest particles show turbulence suppression at 0.3 vol%. The intermediate size class also causes slight turbulence suppression above 0.2 vol%, but not to the extent of the smallest and largest size classes. The continuous phase dissipation rate in the presence of 0.3 vol% of 250-300 μm, and 0.5 vol% of 700-750 μm particles is displayed in Figure 6.22(a) and (b) respectively, where it can be seen that smaller particles dampen turbulence relatively more at a lower concentration.

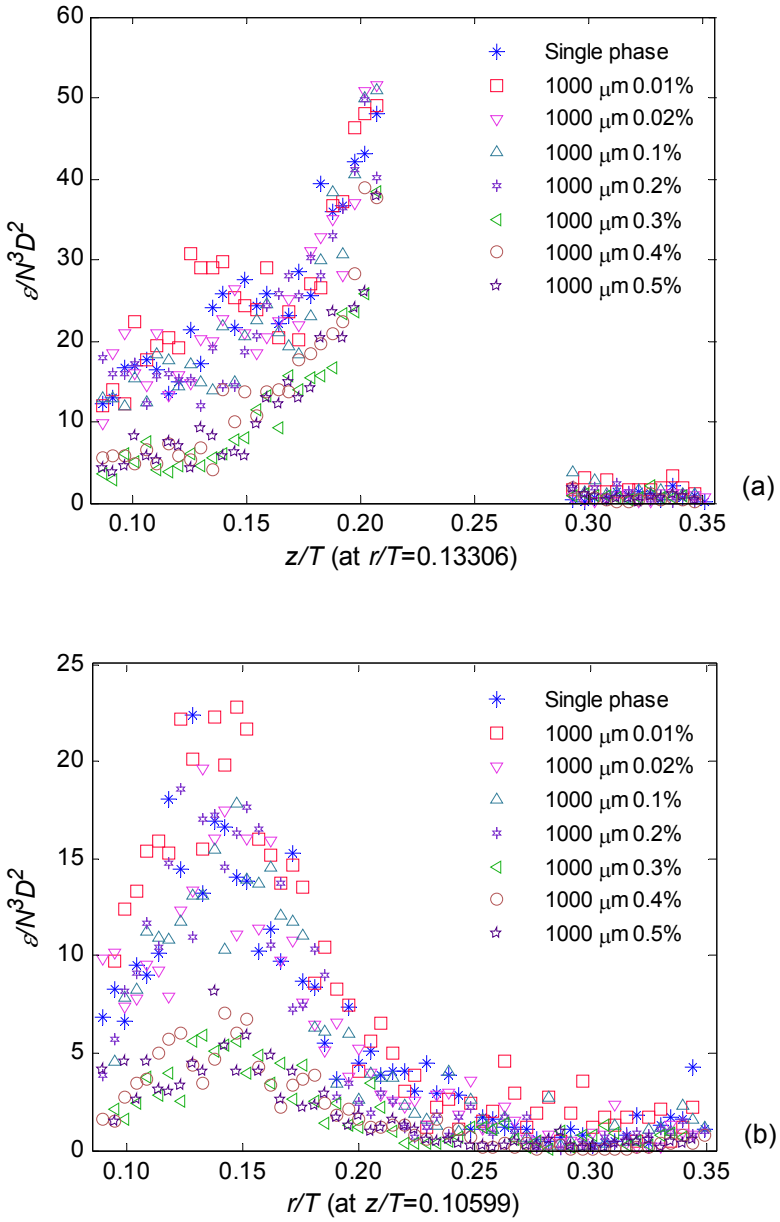

Figure 6.20: (a) Axial ($r/T = 0.133$) and (b) radial ($z/T = 0.106$) profiles of the dissipation rate from the 2-D LES analogy of Sheng *et al.* (2000), for the continuous phase flow with 1000 µm particles, increasing concentration up to 0.5 vol%

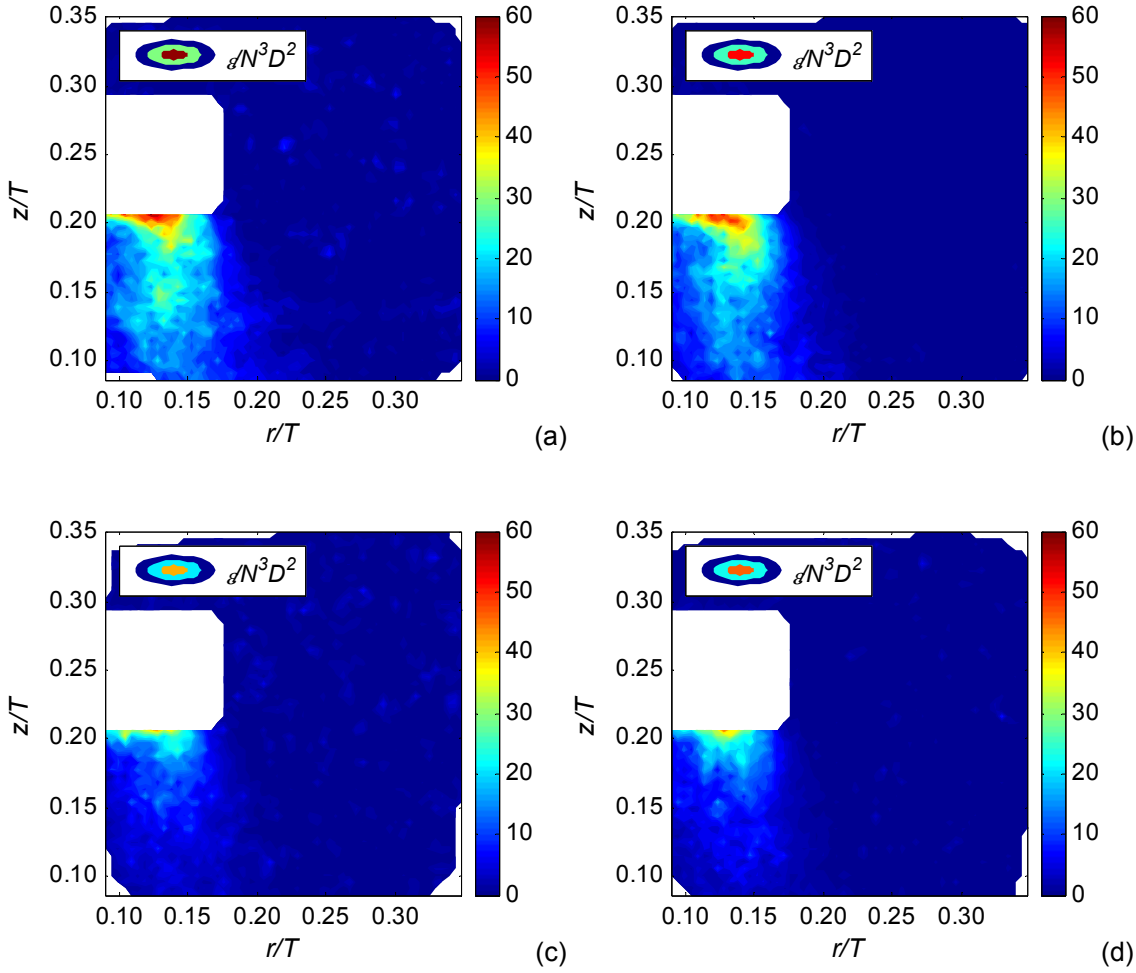

Figure 6.21: Contour plots of the dissipation rate from the 2-D LES analogy of Sheng *et al.* (2000), of the (a) single and continuous phase flows with 1000 µm particles at concentrations of (b) 0.2 vol% (c) 0.3 vol% and (d) 0.5 vol%

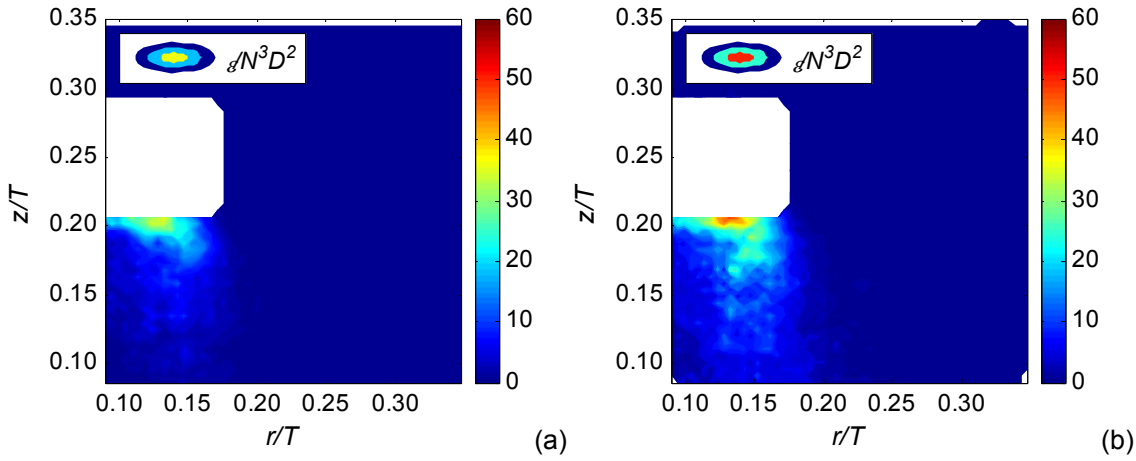

Figure 6.22: Contour maps of the dissipation rate from the 2-D LES analogy of Sheng *et al.* (2000), of the continuous phase flow with (a) 0.3 vol% of 250-300 µm particles and (b) 0.5 vol% of 700-750 µm particles

6.5 Continuous phase integral length scales

In this study, the continuous phase integral length scale was used to evaluate the d_p / L ratio of Gore and Crowe (1989). Changes in these length scales change after the addition of particles will be assessed, which may in turn affect the value of the transitional parameter, which defines the change in regime from turbulence suppression to augmentation. Both 1-D longitudinal ($\Lambda_{u_i x_i}$) and transverse ($\Lambda_{u_i x_j}$) integral length scales of the u and v fluctuating velocity components, as well as their 2-D length scales (Λ_{u_i}) were calculated (details given in §3.4).

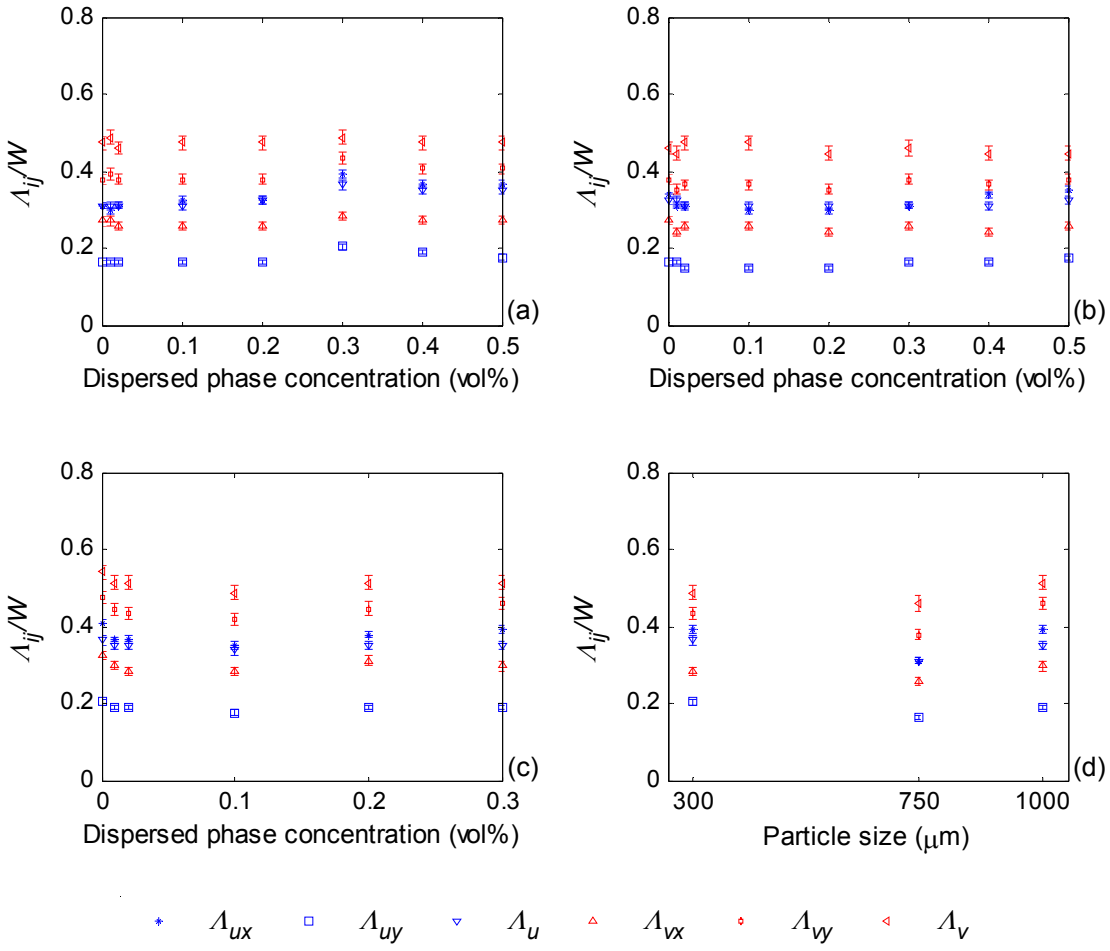

Figure 6.23: Integral length scales of the continuous phase with respect to particle concentration for (a) 1000 μm (b) 700-750 μm (c) 250-300 μm particles and with respect to (d) particle size at 0.3 vol%

Figure 6.23(a) to (c) illustrates the length scales with respect to particle concentration for 1000, 700-750 and 250-300 μm particles respectively. General trends in each case are that the 2-D length scales are greater than the 1-D longitudinal length scales (although for the radial component they overlap at some points in all three size classes), which are in turn greater than the 1-D transverse length scales. So for instance in the case of the axial velocity component

$\Lambda_v > \Lambda_{vy} > \Lambda_{vx}$. Secondly, 2-D length scales in the primary (axial) flow direction are always greater than the 2-D length scales in the radial direction, i.e. $\Lambda_v > \Lambda_u$. Similarly, $\Lambda_{vy} > \Lambda_{uy}$ and $\Lambda_{ux} > \Lambda_{vx}$, suggesting that longitudinal length scales are always greater than transverse length scales, even when comparing between different velocity components.

For isotropic turbulence, the ratio of the longitudinal to transverse length scale is 2:1 (Pope, 2000) even when comparing different velocity components (regardless of which is considered to be the primary flow direction). From experiments with 1000 μm particles, the average ratio from the radial velocity component ($\overline{\Lambda_{ux} / \Lambda_{uy}}$) was found to be 1.95, but the equivalent ratio from the axial velocity ($\overline{\Lambda_{vy} / \Lambda_{vx}}$) was 1.47, indicating some anisotropy of turbulence. Similarly, the ratios of $\overline{\Lambda_{vy} / \Lambda_{uy}}$ and $\overline{\Lambda_{ux} / \Lambda_{vx}}$ were found to be 2.29 and 1.26 respectively. The 2-D length scales in the primary (axial) flow direction were always greater than the 2-D length scales in the radial direction, i.e. $\Lambda_v > \Lambda_u$.

In some cases, there are fluctuations in the magnitude of the length scales with respect to particle concentration, but the majority of these are retained within the 95% confidence intervals about the mean values of adjacent results. Even when considering these fluctuations, there is no indication of the length scales consistently increasing or decreasing with respect to particle concentration. Similar observations can be made for trends of the length scales with respect to particle size, in Figure 6.23(d). It may be concluded that the integral length scales of the continuous phase are unaffected by the presence of particles at these low concentrations, and they may be estimated from a comparable single-phase flow.

The average 2-D length scale of the axial velocity components (Λ_v) from all continuous and single-phase measurements was found to be $0.48W$. This supports the conjecture that the characteristic integral length scale may be approximated as half the blade width ($W/2$) in the impeller discharge (Kresta and Wood, 1993b). However it should be noted that this result was derived from the autocorrelation of the entire field of view, which expands from the impeller jet towards the tank wall (up to $r/T = 0.35$). It was found previously that this ratio over estimates the integral length scales within the impeller region, and under estimates them in the bulk (Cutter, 1966; Wu and Patterson, 1989; Mahouast *et al*., 1989; Khan, 2005). In light of these observations, it is expected that if autocorrelation was performed on sections of the field of view both close to and further away from the impeller, the measured length scales would have been different. Dividing the velocity field into smaller sections would reduce the number of instantaneous vectors available for the autocorrelation, providing less reliable results; hence this notion was not explored further. For all other measured 2-D and 1-D integral length scales, the factor $W/2$ provides an overestimate in the field of view.

6.6 Power dissipated in field of view

The total power dissipated in the field of view (FOV) of the single- and two-phase experiments was calculated according to Equation (7.68). Here the dissipation rate was integrated over the FOV, which was assumed to be homogeneous around 360° of the impeller (since the

measurements were ensemble-averaged). Results of the dissipation rate from two different calculation methods were employed for the integration: (a) the 2-D LES analogy of Sheng *et al.* (2000) and (b) dimensional analysis using the TKE and 2-D integral length scale. Results from both calculation methods are shown in Figure 6.24(a) and (b) respectively. The different trend lines correspond to independent experiments carried out with different particle sizes, where the apparatus was dismantled and reconfigured. Each trend line is plotted with respect to particle concentration on the abscissa.

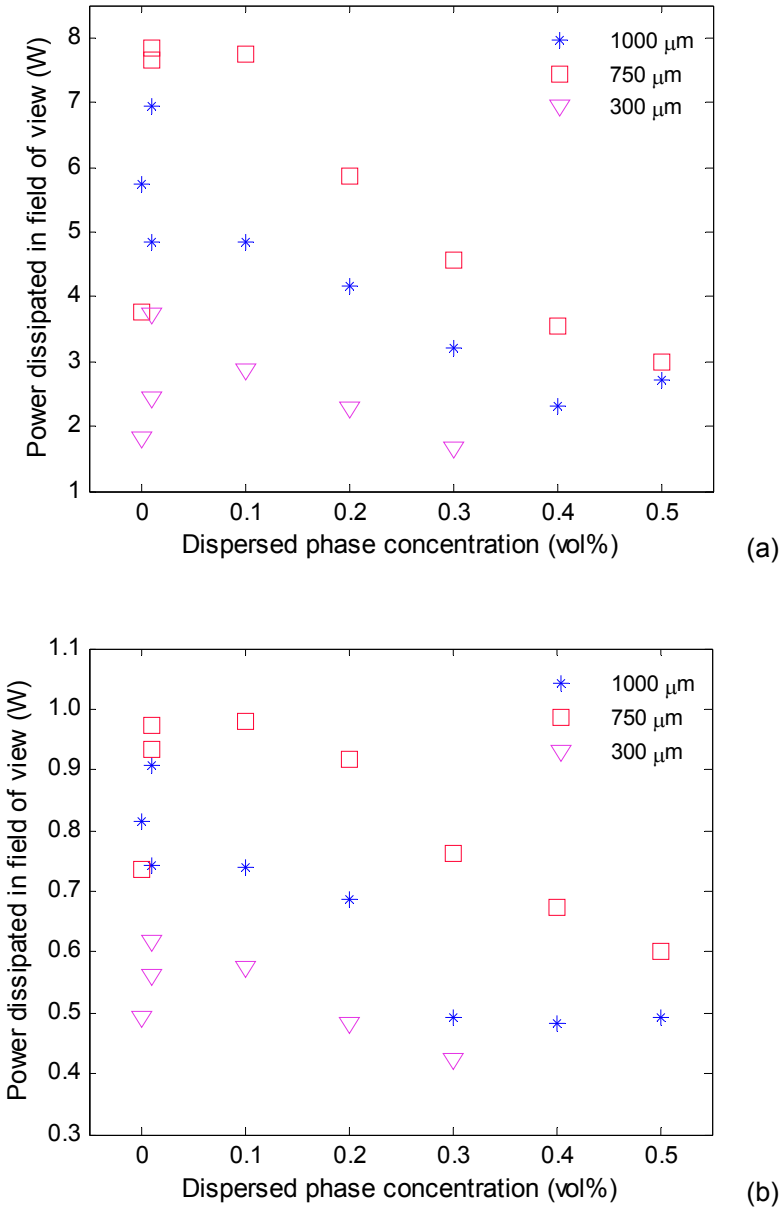

Figure 6.24: Power from the integrated dissipation rate in the field of view calculated from (a) the 2-D LES analogy of Sheng *et al.* (2000) and (b) dimensional analysis with the TKE and 2-D integral length scale

It may be assumed that if the three sets of experiments were comparable, the total power dissipated in the FOV in the single-phase cases would be almost equivalent. However in Figure

6.24(a), the power estimates vary by a factor of ~4. It was shown in §6.2.4 that the three independent single-phase experiments were comparable on a point-by-point basis, as the trend lines of the axial and radial velocities almost superimposed in Figure 6.8. It must be noted that in this calculation the discrepancy between the estimates are owed to accumulated differences in velocity gradients, as the dissipation rate is integrated over the FOV. In Figure 6.24(b), the single-phase power estimates deviate by a factor of ~2. In this case the fluctuating velocity components were used to calculate the TKE, the sum of which was is raised to the power of 3/2 in Equation (4.5), further amplifying the accumulated differences between experiments.

Notwithstanding the differences in the power estimates between independent single-phase experiments, all three trend lines depict similar trends with respect to particle concentration, in both Figure 6.24(a) and (b). Note that in a given two-phase PIV experiment, the apparatus was not disturbed; only the particle concentration was increased before new measurements were taken, hence the experimental errors between the independent experiments described above are not pertinent along the trend lines. The total power dissipated in the FOV decreases as the particle concentration is increased. This agrees with the observations made in §6.3 and 6.4 that both small and large particles suppress the dissipation rate. When the data are compared in this way, the same trend is apparent for experiments with 750 µm particles, whose effects were not found to be as significant when analysing data along discrete sections of the vessel.

A peculiar result which was not evident before, is the sharp increase in power dissipation at very low particle concentrations (i.e. 0.01 and 0.02 vol%) relative to the single-phase case. There is no theoretical justification for this result. An evaluation of the data revealed a greater dissipation rate (at most 9% at a given point) in the vessel bulk, at all particle concentrations, compared to the single-phase fluid. Note that the dissipation rate is very small in the bulk $\sim 0.01N^3D^2$ (compared to $54N^3D^2$ at $\varepsilon_{\max}$ in the discharge stream) so the percentage differences are expected to be high in this region. The differences in the bulk between single- and two-phase experiments were of the same order of magnitude as the experimental fluctuations, and could not be isolated from evaluation of profiles visually, for example in Figure 6.20(b) where $r/T > 0.25$. However in Equation (7.68), the dissipation rate in the bulk is integrated over a larger volume, and has a higher contribution to the total integral compared to the discharge stream. In experiments with very low particle concentrations where the dissipation rate in the discharge stream is relatively unaffected, the total power increases compared to the single-phase. As the particle concentration is increased, the turbulence in the discharge stream is dampened. Note that the maximum dissipation rate in the discharge stream was suppressed by 21% with 1000 µm particles in the flow at 0.5 vol%. Consequently the total dissipated power also decreases with respect to particle concentration. However due to the opposing effects in the discharge stream and bulk, and larger contribution of the bulk, the total power dissipated at even the highest particle concentration (0.5 vol%) is not significantly lower than the single-phase experiment. For this reason, power draw measurements (from the torque on the shaft using strain gauges) are not expected to reflect the turbulence suppression in the discharge stream.

6.7 Dispersed phase flow

Dispersed phase velocities (of phase-separated solids-only images) were obtained via cross-correlation, using *IA* sizes of 16×16, 32×32 and 32×32 pixels with 50% overlap, for 250-300, 700-750 and 1000 μm particles respectively. Only particle images from experiments carried out at the highest volumetric concentrations for each size class were processed, to ensure enough particle signals in the images for cross-correlation. These were 0.3, 0.5 and 0.5 vol% for the 250-300, 700-750 and 1000 μm particles respectively. When calculating mean fields, areas unoccupied by particles, and hence not containing vectors, were excluded from the average. Consequently, regions where particles never passed the field of view over the entire data set resulted in holes in the mean fields.

6.7.1 Locally-averaged concentration fields

One of the most important aspects of solid-liquid mixing is the distribution of solid particles throughout the volume, since it may affect the reactor performance and thus efficient reactor design. The solids distribution is a result of a balance between two competing effects; particle lift due to their interaction with the liquid flow and turbulence, and the particles' tendency to settle (Nocentini *et al.*, 2002). The solids distribution affects a variety of industrial processes such as suspension polymerization, reactive crystallization and particle coating processes. Take for example catalytic slurry reactors, in which the solid particles carrying catalytic material are suspended throughout the turbulent flow induced by the impeller. It is important to obtain a good distribution of particles in the medium so that enough particle surface area is exposed, to enable heat and mass transfer between solids and liquid. Knowledge of the particle distribution in a stirred vessel may also be useful to interpret turbulence modulation of the continuous phase.

Locally averaged particle concentration fields were obtained for experiments carried out with the highest volumetric fractions of the dispersed phase for each size class; i.e. 1000 μm at 0.5 vol%, 700-750 μm at 0.5 vol% and 250-300 μm at 0.3 vol%. The following procedure was adopted. Phase-separated solids-only images were binarized and divided into small non-overlapping rectangular regions (analogous to *IA*s in cross-correlation) of size 30×30 pixels. The number of bright pixels per region was obtained across the entire image, and for all instantaneous images. Subsequently an average was obtained in each 30×30 pixel region across all (600×2) images in the data set, and the result normalized by the total number of pixels in that area (900 pixels). In this way, the fraction of bright pixels per region in the 2-D image was interpreted as the 3-D local volume fraction within that region. Spatial distributions of the local concentration fields are provided in Figure 6.25(a) to (c), where 100% on the colour scale would indicate that particles fully occupied a particular region in all image frames.

Note that the absolute value of the local concentration obtained from image analysis in the vicinity of the impeller region does not provide a reliable measure. Reflections from the blade were found to be strong when the impeller was captured in the field of view. Consequently, this area was blanked out during vector processing. However, reflections off the blade also distorted images of dispersed particles surrounding the blade, and their projected image was larger than what the PIV calibration factor would suggest. Therefore, the concentration maps should only be interpreted to assess the relative distribution of particles in the field of view, but not as an

absolute measure. Notwithstanding this effect, the volume-averaged concentration of 1000 µm particles in the field of view in Figure 6.25(a) was found to be 0.48 vol%, very close to the experimental value of 0.5 vol%.

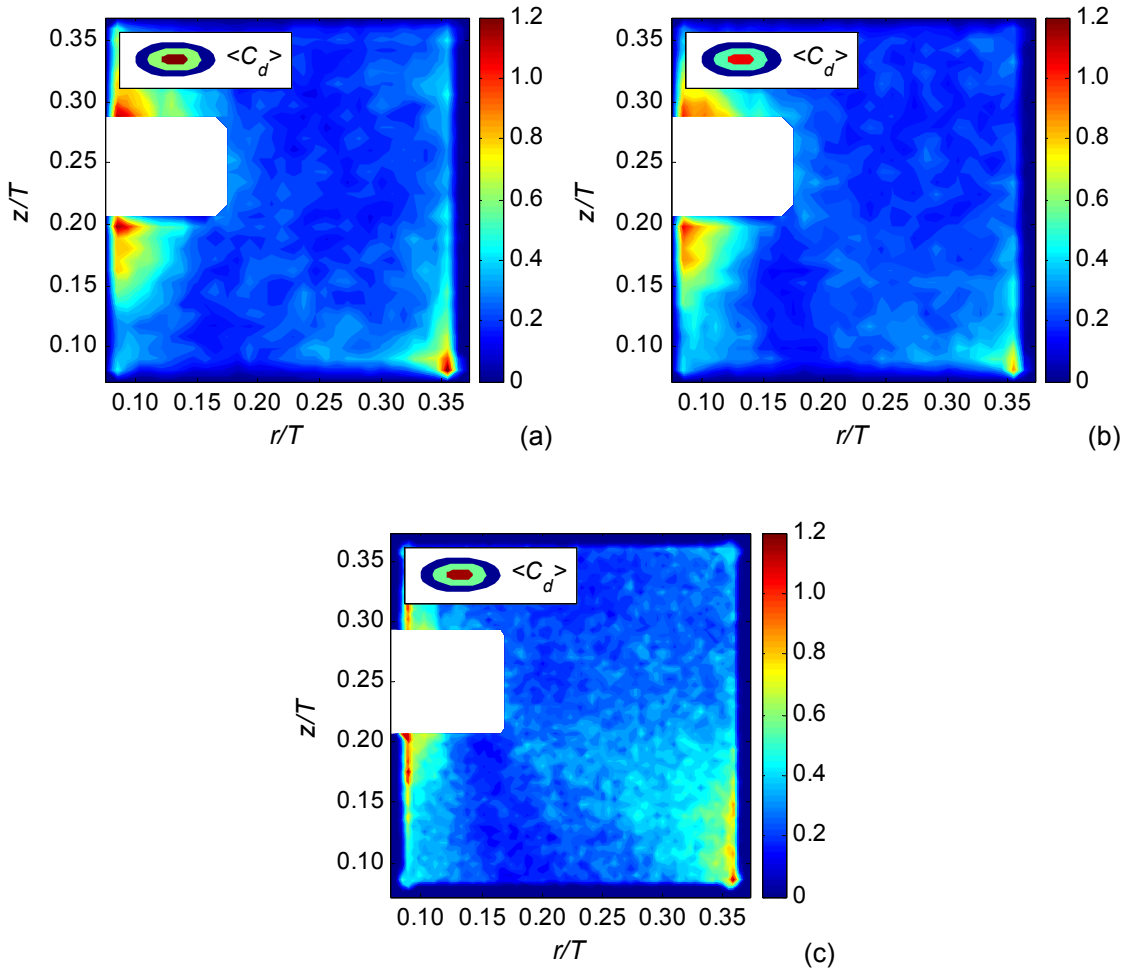

Figure 6.25: Locally averaged volumetric concentration maps of the dispersed phase with (a) 1000 µm 0.5 vol% (b) 700-750 µm 0.5 vol% and (c) 250-300 µm 0.3 vol% in water

It may be observed that 1000 µm particles are not distributed homogeneously in the fluid. Instead, there are locally high concentration regions above and below the impeller, as well as a stagnation point at the bottom right corner of the vessel. The apparent stagnation region in the bottom corner could be a result of a combination of two factors. Firstly there was found to be a local accumulation of particles underneath the baffles, and in the narrow space between the baffles and the wall. Secondly, the laser light reflections off the baffles caused a strip of bright pixels along the right vertical edge of the image, which would artificially enhance the grey scale level in that area. Note that that the outer two rows of vectors were removed before analysing the velocity fields, so these artefacts were eliminated from the flow field analysis.

A similar particle distribution may be observed for the 700-750 µm particles at an equivalent volumetric fraction in Figure 6.25(b). However, the maximum values of the locally averaged volumetric concentrations in the three accumulation zones are not as significant as for the 1000 µm particles, suggesting that the 700-750 µm particles are distributed slightly more evenly

throughout the circulation loop. The simulation results of Derksen (2003) also showed that larger particles generated more pronounced concentration profiles at the impeller level.

The spatial distribution of the smallest particles (250-300 μm) in Figure 6.25(c) suggests that they are distributed much more evenly throughout the tank, since their locally high concentration zones occupy smaller regions above and below the impeller. The fluid surrounding the stagnation region at the bottom-right corner of the tank also appears to contain more solids, relative to the 1000 and 700-750 μm particles. The concentration gradually decreases from being locally high at the corner to relatively low in the surrounding fluid (which covers the bottom-right quarter of the image), in contrast to the 1000 μm particles which exhibit a steeper concentration decrease. However, even the smallest particles are not completely homogeneously distributed, with the three high concentration zones still evident. This suggests that the observed turbulence suppression of the continuous phase is a genuine effect, and a direct consequence of the presence of particles in the discharge stream, particularly beneath the impeller.

The Eulerian-Lagrangian simulation results of Derksen (2003) for a turbulently agitated solid-liquid suspension by an RDT showed high solids concentrations in front and underneath the impeller, as well as accumulation around the tank wall due to centrifugal forces. However unlike PBTs, RDTs generate an up-flow below the impeller, which may carry highly concentrated slurries with it. Experimental studies employing an optical technique to measure average solid concentration profiles of RDTs, conducted by Magelli *et al.* (1990) and Nocentini *et al.* (2002), also reported locally high solids concentrations in the vicinity of the impeller, and midway between turbines for multi-impeller configurations. Interestingly, the concentration profiles of particles generated by multiple PBT impellers (Montante *et al.*, 2001) showed trends similar to the RDT studies, despite differences in flow patterns between the two impellers.

6.7.2 Mean flow field

The ensemble-averaged mean velocity vector fields of the dispersed particles are shown in Figure 6.26(a) to (c), for the 1000 μm 0.5 vol%, 700-750 μm 0.5 vol% and 250-300 μm 0.3 vol% particles in water respectively. It is evident that the dispersed phase velocity fields are noisier than equivalent single or continuous phase velocity fields (e.g. Figure 6.2), since the average values have been obtained from fewer vectors; O(10) instead of O(100). Also, at the same concentration (0.5 vol%), the total number of 1000 μm particles in the fluid is less than the number of 700-750 μm particles; for this reason the vector field depicted in Figure 6.26(a) is not as smooth as that in Figure 6.26(b). On the other hand, a lower concentration (0.3 vol%) was studied for the 250-300 μm particles, which created the most erratic flow field with significantly more holes in the data, as shown in Figure 6.26(c). However, even at the low concentrations studied, cross-correlation of the dispersed phase images was able to provide some qualitative information of the flow field, and enabled further calculation of slip velocities, particle rms velocities and TKE.

All three vector maps depict the general flow field, namely the downward pumping flow circulation loop generated by the PBT. Particle velocities are strongest underneath the impeller blade and in the discharge stream, and change direction from being predominantly axial to radial at $r/T = 0.15$, analogous to the point of change in direction of the single and continuous

phase jets (Figure 6.2). Relatively smaller upward axial velocities are attained in the wall jet, which eventually becomes radial and returns to the top of the impeller, completing the circulation loop. Note that since continuous phase velocities remain largely unchanged from the single-phase at these low particle concentrations, the latter may be used as a basis of comparison in this section.

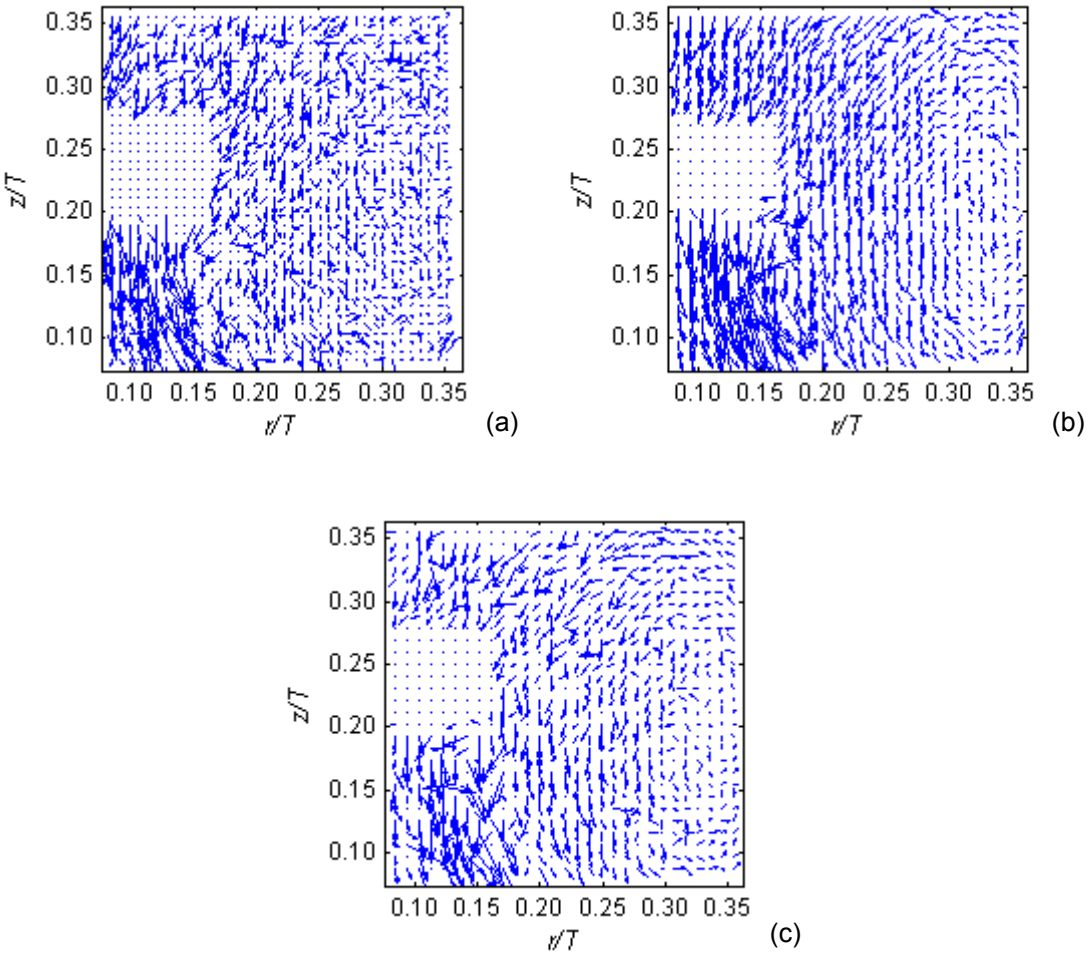

Figure 6.26: Ensemble-averaged mean velocity vectors of the dispersed phase flow field for (a) 1000 µm 0.5 vol% (b) 700-750 µm 0.5 vol% and (c) 250-300 µm 0.3 vol%

Since the 700-750 µm particles produced the most reliable and complete flow field, their axial and radial mean velocity contours are portrayed in Figure 6.27(a) and (b) respectively. For the same reasons described above, the dispersed phase contours are not as smooth as the single and continuous phase (e.g. Figure 6.3), and a few holes are present in the data. The maximum axial velocity of the 700-750 µm particles was found to be $-0.64V_{tip}$ where $r/T = 0.143$ and $z/T = 0.197$, which is very close to the blade edge. The exact magnitude and location of the maximum velocity is not a reliable measure to quantify the dispersed phase on its own, since the average is obtained over only a few vectors. Instead it is more useful to look at general aspects of the flow.

In Figure 6.27(a) the high axial velocity region occurs underneath the blade at $r/T \sim 0.15$, extending down to the vessel base. On the other hand, the greatest axial velocity of the single and continuous phase jet is located slightly more towards the centre of the vessel at $r/T = 0.119$, which also extends from the impeller to the base. The particle axial velocities appear to be weaker in the down flow region above the impeller, compared to the fluid, Figure 6.3(a). Pettersson and Rasmuson (1997) suggested that whilst the mean flow direction of both phases is the same (within a few degrees), the absolute difference in the 3-D mean velocity can be as much as 20% relative to the fluid, at a given position. In Figure 6.27(b), the strongest radial flow region coincides with the point at which the impeller jet deflects towards the tank wall ($r/T = 0.15$, $z/T = 0$), similar to the fluid (Figure 6.3(b)). The absolute differences in the dispersed and continuous phase velocities are discussed in the next section.

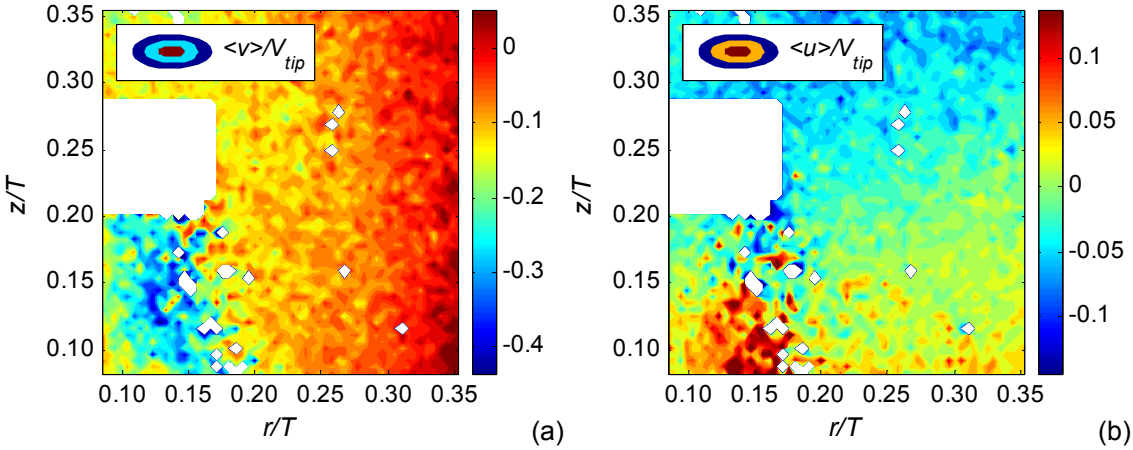

Figure 6.27: Ensemble-averaged (a) axial and (b) radial mean velocity contour plots of the dispersed phase flow, 700-750 µm 0.5 vol%

6.7.3 Slip velocities

The slip velocity around a dispersed particle is defined as the difference between the instantaneous velocity of that individual particle, and its surrounding continuous phase fluid. Ideally, this would require information of dispersed particles on a point-by-point basis, which can only be obtained via particle tracking. In the present case, dispersed phase velocities were obtained from cross-correlation, which generates 'local velocity vectors' in regular grid spacing. Secondly, the interpretation of the velocity of the surrounding fluid may be debated, since it is also obtained from cross-correlation, giving vectors at discrete and regular nodes. Two different methods may be adopted, depending on the particle size. If (a) a particle is larger than the *IA*, the fluid velocity may be taken as the mean of the surrounding instantaneous vectors in the corresponding continuous phase image. On the other hand if (b) a particle is smaller than the *IA*, the fluid velocity may be taken as the vector at that exact location in the continuous phase image. If a particle fully occupies an *IA*, either method (a) or (b) could be implemented.

In the current study, all particle sizes were equal to or less than the *IA*s used for their cross correlation, hence it was decided to adopt method (b). Consequently, the instantaneous slip velocity is only an estimate at a given vector node. Average slip velocities were calculated as below:

$$\left\langle u_{i,slip} \right\rangle = \left| \overline{u_i - u_{i,p}} \right| \tag{6.1}$$

where u_i is the instantaneous continuous phase velocity in the i^{th} direction, and $u_{i,p}$ the equivalent dispersed phase velocity at that vector position. Taking differences in this way provided no information of whether particles led or lagged behind the fluid, hence only the absolute mean slip velocities were analysed to compare relative magnitudes. Particle lead and lag is considered later.

Mean axial and radial slip velocities were calculated for the 1000 μm 0.5 vol%, 700-750 μm 0.5 vol% and 250-300 μm 0.3 vol% particles, shown in Figure 6.28 to Figure 6.30 respectively. Similar to the mean dispersed phase velocities, averages were a result of only a few vectors, since slip velocities could only be calculated at positions where particles were present. Once again, the holes in the contour plots are a result of the consistent absence of particle vectors at those points in all image frames in the data set. Slip velocities have been normalized by the particle terminal velocity, which may be used to estimate the axial slip when the dispersed phase velocity is not known. In this way, the particle terminal velocity was used to estimate the particle Reynolds number (Appendix V) previously. The conjecture can now be assessed.

In Figure 6.28(a) it is apparent that slip velocities are not constant throughout the tank; they are largest in the impeller discharge stream and underestimated by the terminal velocity by a factor of five. At radial distances further away from the impeller into the bulk, slip velocities range from zero to the same value as the terminal velocity. In the wall jet, axial slip velocities are up to two times the terminal velocity. Similar observations can be made for the radial slip velocity distribution in Figure 6.28(b), which are also relatively higher in the discharge stream than the bulk. The radial slip reaches the same order of magnitude as the axial slip, but only in isolated regions throughout the discharge stream.

Nouri and Whitelaw (1992) calculated apparent relative velocities (defined as particle mean minus equivalent single-phase velocities) of 0.02 vol% particle suspensions stirred by an RDT. They found that radial apparent velocities were underestimated by the particle terminal velocity at the impeller disc plane, by a factor of ~2.5 and ~1.7 for 725 μm Diakon and 232 μm lead-glass particles respectively, whereas 272 μm Diakon particles had negligible slip. Axial apparent velocities were relatively smaller (than the radial). The authors stated the continuous phase velocities would remain unaffected by the presence of particles at these low concentrations, so single-phase velocities may be accepted as a basis of comparison. Therefore apparent relative velocities may be interpreted as slip velocities. The results are similar to the present case, that slip velocities are under-predicted mostly in the main flow direction (axial for the PBT and radial for the RDT). Conversely, Guiraud *et al*. (1997) observed slip velocities which were the same order of magnitude as the terminal velocity for 253 μm 0.5 vol% particles in water stirred by an axial propeller. Once again, the axial slip was most significant, because buoyancy pulled the particles downwards.

Figure 6.29(a) and (b) and Figure 6.30(a) and (b) show the axial and radial slip velocities of the 700-750 μm (0.5 vol%) and 250-300 μm (0.3 vol%) particles respectively. The trend of higher slip velocities in the discharge stream still holds for the 700-750 μm particles, but the quality of data for the smallest particles is poor, and insufficient to draw any firm conclusions. Figure

6.29(a) shows that the axial slip velocity of the 700-750 μm particles reaches a factor of nine times their terminal velocity, and up to thirteen times for the smallest size class in Figure 6.30(a). Since the maximum slip velocities of the smallest particles are distributed in a random and spotty manner around the impeller region, they could be artefact results of a few spurious particle vectors, which are not smoothed out in the averaging process, since the average itself is taken over only a few vectors. In Figure 6.29(b) and Figure 6.30(b), the maximum radial slip velocities are consistently five times greater than the corresponding terminal velocities in the discharge stream.

From the discussions above it may be concluded that the particle terminal velocity does not provide a reliable estimate of the axial slip velocities in stirred flows, since these are highly variable in different regions of the tank. The terminal velocity generally underestimates the axial slip velocity, mainly in the impeller jet stream where slip velocities are the greatest. Additionally, it seems that the smaller the particle size, the greater the slip relative to the terminal velocity in the jet stream.

The particle Reynolds numbers quoted in §6.3.2 had been estimated from the terminal velocity, and evaluated against the theory of Hetsroni (1989). The theory suggests that particles augment turbulence due to wake shedding when $400 < \mathrm{Re}_p < 1000$. Since the slip velocity of the 1000 μm particles is underestimated by the terminal velocity by a factor of five in the discharge stream, it follows that Re_p was also underestimated in this region. The true slip velocity suggests that Re_p (original estimate ~105) could be as high as ~525. This value falls within the limit of wake shedding; hence the larger particles would be expected to augment turbulence according to Hetsroni (1989). However the PIV results show turbulence suppression, and consequently contradict the theory. Similarly, the 300 μm particles could have Re_p up to 63.96. This result still correctly falls within the regime of turbulence suppression. An important point to note is that Hetsroni (1989) did not actually correlate turbulence modulation to Re_p since information of slip velocities in the literature was absent. Instead, changes in turbulence intensity were generally discussed with respect to the particle size. Changes in turbulence intensity were only related to Re_p from the study of Tsuji and Morikawa (1982), where particles with $\mathrm{Re}_p \sim 470$ augmented the carrier phase turbulence in a horizontal pipe. In order to substantiate Hetsroni's (1989) theory, turbulence modulation must be directly correlated to Re_p, for which knowledge of slip velocities is required, but is relatively scarce. In the present case, the theory does not support the experimental results for large particles, but holds for the smaller size.

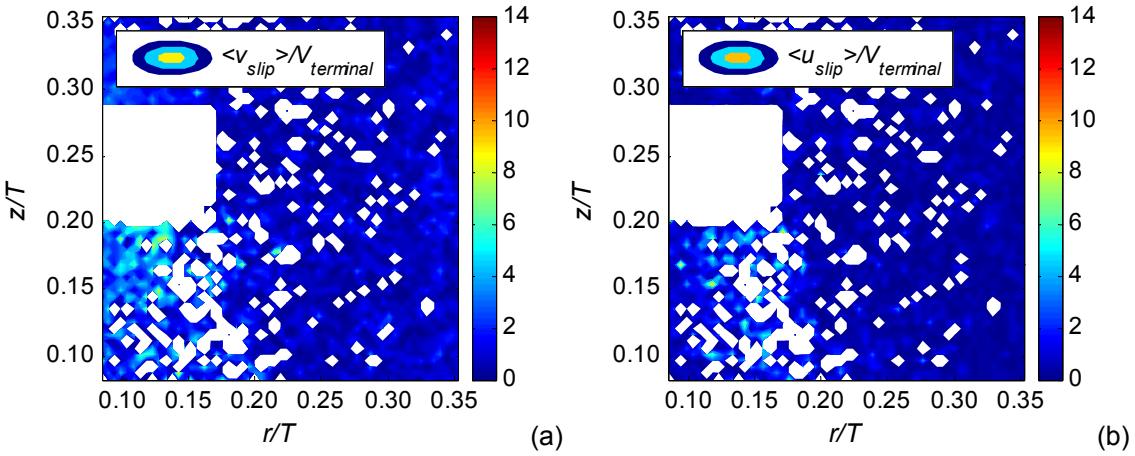

Figure 6.28: Mean (a) axial and (b) radial slip velocities around 1000 µm particles 0.5 vol%, normalized by the terminal velocity

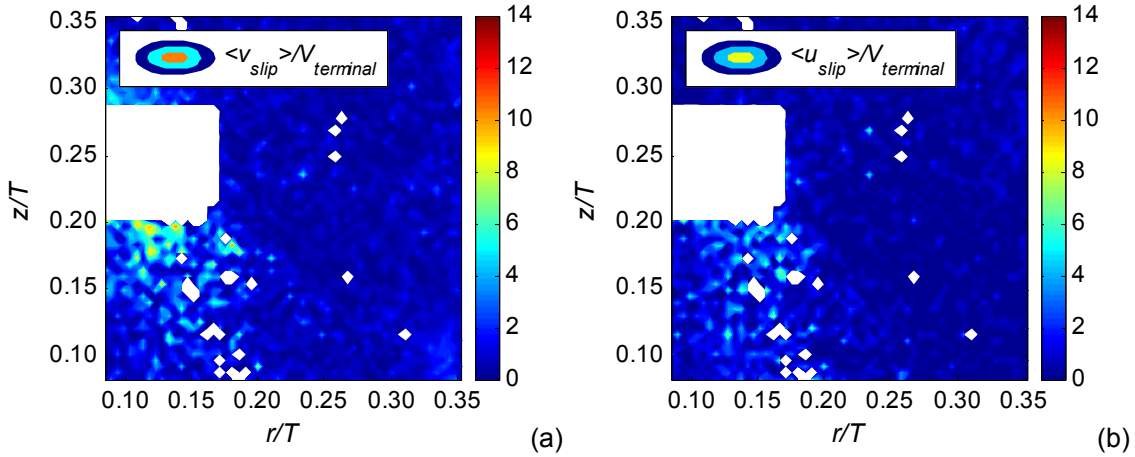

Figure 6.29: Mean (a) axial and (b) radial slip velocities around 700-750 µm particles 0.5 vol%, normalized by the terminal velocity

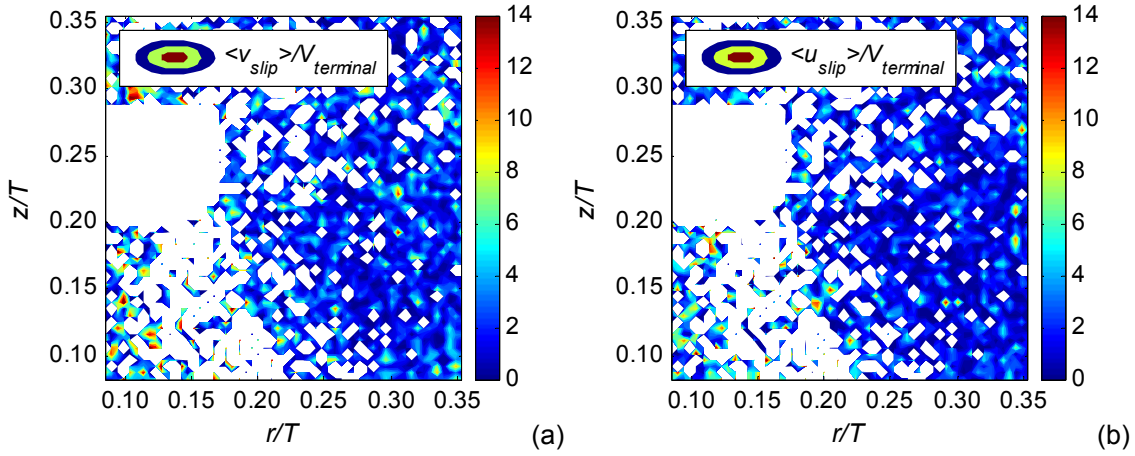

Figure 6.30: Mean (a) axial and (b) radial slip velocities around 250-300 µm particles 0.3 vol%, normalized by the terminal velocity

Mittal (2000) carried out DNS to study the response of a sphere wake to freestream fluctuations. In these simulations, the frequency and amplitude of the freestream fluctuations of the flow past a sphere, and particle Reynolds number was varied. The results indicated that natural vortex shedding only occurred when the freestream fluctuation level was low (and when $\mathrm{Re}_p > 300$). At higher turbulence intensities of the carrier phase, vortex shedding was completely disrupted. This observation complicates the argument of Gore and Crowe (1989) and Hestroni (1989) which attribute turbulence augmentation to vortex shedding, as this phenomenon is related to the fluid turbulence intensity as well as particle Reynolds number. It is possible that the vortex shedding reported in pipe and jet flows ($\mathrm{Re}_p > 400$) may not occur in stirred flows, which are more complex and almost certainly have a higher turbulence intensity. In this context, it follows that turbulence augmentation can not be expected from the 1000 µm particles, even for $\mathrm{Re}_p > 400$.

In order to discern regions where particles led or lagged behind the fluid, differences were taken between absolute values of the instantaneous vectors and subsequently averaged, according to Equation (6.2).

$$\left\langle u_{i,slip} \right\rangle = \overline{|u_i| - |u_{i,p}|} \tag{6.2}$$

Thus, regardless of the general flow direction, mean slip velocities were always positive when particles lagged behind the fluid and negative when they led the fluid. However in order for this to be true, it was assumed that both particles and fluid travelled in the same direction at any given point.

The newly defined mean axial slip velocities around the 700-750 µm particles at 0.5 vol% are shown in Figure 6.31(a). It may be observed that particles lag behind the fluid in the majority of the discharge stream and also directly above the impeller. In the bulk particles lead the fluid, whereas near-zero slip is obtained close to the vessel wall. Particle inertia, particle-particle collisions and gravity would be the main contributing factors towards these effects. As they are deflected by the impeller into the discharge stream, particles do not travel as fast as the fluid initially due to their inertia, even though gravity is acting in the same direction. Also it was shown previously in Figure 6.25(b) that there exists a locally high concentration of particles underneath the impeller. Consequently, particle-particle collisions may be important in this region, causing a reduction in the particle velocities, and hence a lag behind the fluid whilst in down flow. In the space between the impeller and the wall, the fluid axial velocity is downwards until $r/T = 0.255$ (Figure 6.3(a)). In this region, particle-particle collisions become irrelevant and gravity acts in the same direction as the flow; subsequently the particles lead in the downward flow. In the near wall region where $r/T > 0.255$, the upward fluid flow balances gravity acting on the particles, and they become fluidised. Finally, particles lag behind the fluid as they return to the top of the impeller with the downward fluid flow. Figure 6.25(b) also indicates a locally high concentration of particles in that region; hence particle-particle collisions may again be responsible for reducing the fluid velocities.

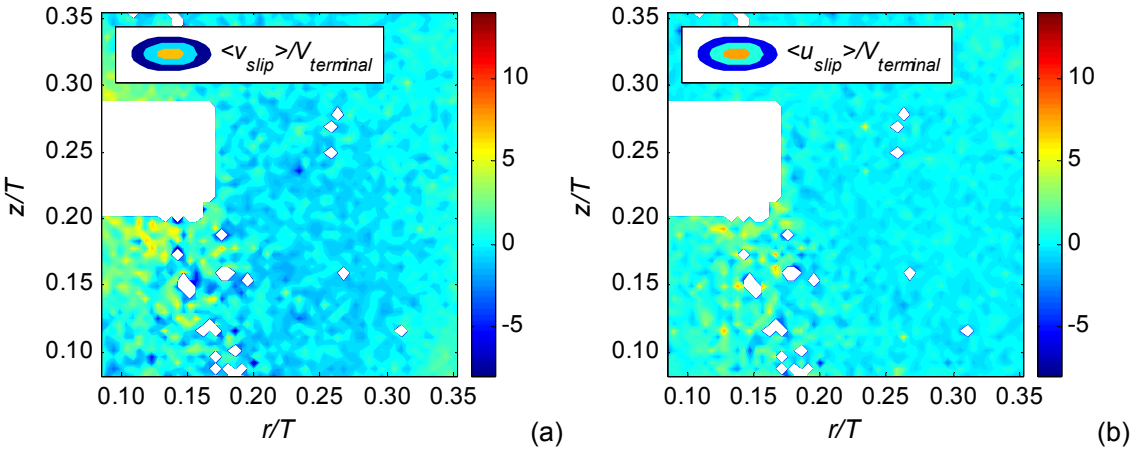

Figure 6.31: Mean (a) axial and (b) radial slip velocities showing regions of lag (+ve) and lead (-ve) for the 750-700 µm particles 0.5 vol%, normalized by the terminal velocity

Nouri and Whitelaw (1992), Guiraud *et al*. (1997) and Virdung and Rasmuson (2008) all found that particles led the fluid in down flow regions. However in the studies of Guiraud *et al*. (1997) and Virdung and Rasmuson (2008), this also included the down flow region underneath the impeller (since they also employed axial propellers), as opposed to the particle lag observed in the present case. Nouri and Whitelaw (1992) suggested that the lead in down flow was due to gravity acting on the particles, Guiraud *et al*. (1997) concurred with this suggestion. However analogous to the current study, Ljungqvist and Rasmuson (2004) also observed particle lag in the down pumping flow of a PBT, which was also the region of greatest slip. The authors also attributed particle lag to their inertia, as they are accelerated more slowly than the fluid from the impeller motion. However as the flow is redirected from axial to radial (near the bottom), the particle inertia causes them to lead instead, as they are still travelling faster axially downwards relative to the fluid, which gains a stronger radial velocity. In general, the authors concluded that both particle lead and lag may be found in the downflow region.

Figure 6.31(b) shows near-zero mean radial slip velocities in the vessel bulk, wall jet and directly above the impeller region, whereas particle radial velocities are less than the fluid in the discharge stream. The radial lag is not as significant as that in the axial direction, which is understandable since the fluid mean radial velocity is less than the mean axial velocity (see Figure 6.3(a) and (b)).

6.7.4 rms velocities and TKE

The rms velocities and TKE of dispersed particles were calculated from the particle velocity fields, in a similar way to the treatment of the single and continuous phase flows. Only contour plots of the 700-750 µm particles (0.5 vol%) will be shown in this section, since their images produced the most complete velocity fields. The corresponding continuous phase rms velocities and TKE will also be displayed.

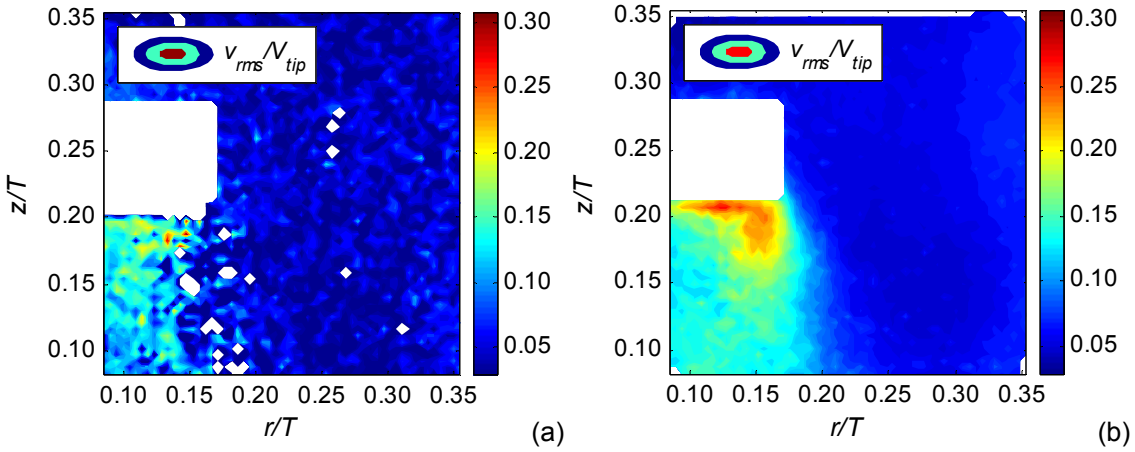

Figure 6.32: Normalized axial rms velocity contours of (a) dispersed particles, 700-750 µm at 0.5 vol% and (b) corresponding continuous phase fluid

Figure 6.32(a) and (b) show the normalized axial rms velocity contours of the particles and continuous phase respectively. It may be observed that the dispersed phase axial rms velocities are the greatest in the discharge stream, reaching $\sim 0.15V_{tip}$. Some infrequent spotty regions reach as high as $0.2-0.3V_{tip}$. Away from the impeller, rms velocities are comparably small, between $0-0.06V_{tip}$. It should be noted that the zero results may be artefact of there being only one particle vector at that point (since the rms velocity is calculated from the difference between the instantaneous and mean velocity, and when only one vector is present, these two values are equal). The continuous phase axial rms velocity distribution is similar to the dispersed phase, but the fluid attains higher turbulence levels directly underneath the blade up to $\sim 0.3V_{tip}$. Note that the continuous phase axial rms velocity is also comparable to the single-phase (Figure 6.4(a)), since the 700-750 µm particles were not found to modify the fluid turbulence.

Nouri and Whitelaw (1992) found that axial and radial rms velocities of 232 µm 0.2 vol% lead-glass particles were up to 25 and 15% lower than the single-phase in the impeller stream and wall jet respectively. Note that they compared particle turbulence levels to the single-phase due to experimental difficulties in measuring the two-phase fluid. Pettersson and Rasmuson (1997) obtained simultaneous 3-D two-phase measurements of 325 µm particles in water at 0.06 vol%, and found that the total rms values of particles were significantly lower than the fluid in the impeller region, supporting the current observations. On the other hand, Guiraud *et al.* (1997) simultaneous two-phase measurements of 253 µm 0.5 vol% particles in water showed that particle axial rms velocities were always greater than fluid, sometimes by a factor of two. No significant differences were observed for the radial or tangential components. The contradictory result was supported by Virdung and Rasmuson (2008), who found that the total rms values of 1000 µm particles between 0.5-1.5 vol% in benzyl alcohol and ethanol were greater than the fluid. Explanations were not provided in either studies for these observed phenomena.

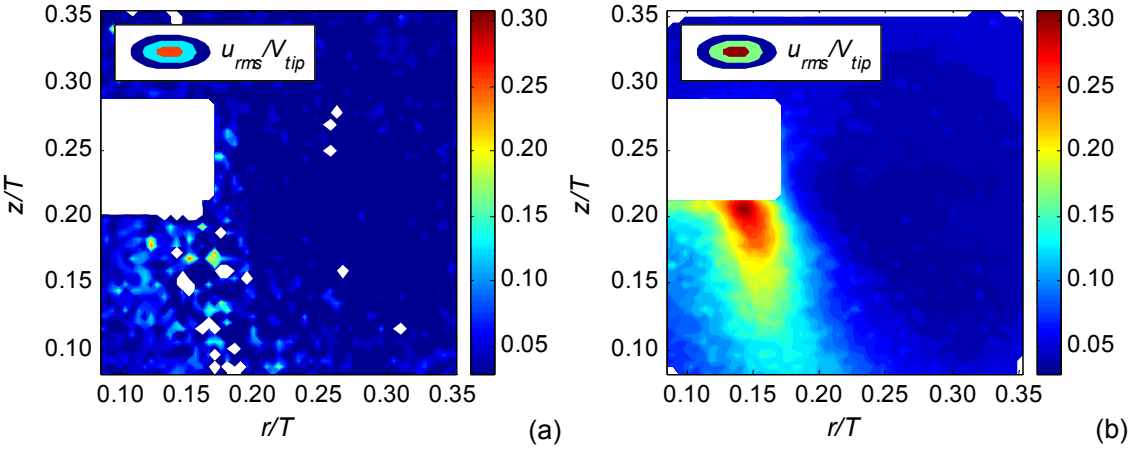

Figure 6.33: Normalized radial rms velocity contours of (a) dispersed particles, 700-750 µm at 0.5 vol% and (b) corresponding continuous phase fluid

In Figure 6.33(a), the radial rms velocities of particles are significantly lower than their axial counterparts, and the high magnitude turbulence level in the discharge stream is no longer prominent. Instead, the radial rms velocities reach up to $0.125V_{tip}$ only at some points in the discharge stream. The bulk rms turbulence levels are also slightly lower, between $0-0.05V_{tip}$. This suggests anisotropy of the dispersed phase turbulence. On the other hand, the continuous phase rms velocities shown in Figure 6.33(b) preserve the high turbulence region underneath the blade and in the jet stream, which also reaches $\sim 0.3V_{tip}$ as found in the fluid axial rms velocities. An assessment of turbulence anisotropy can be made by calculating the difference in the axial and radial rms velocities and normalizing by the tip speed, i.e. $|u_{rms}-v_{rms}|/V_{tip}$.

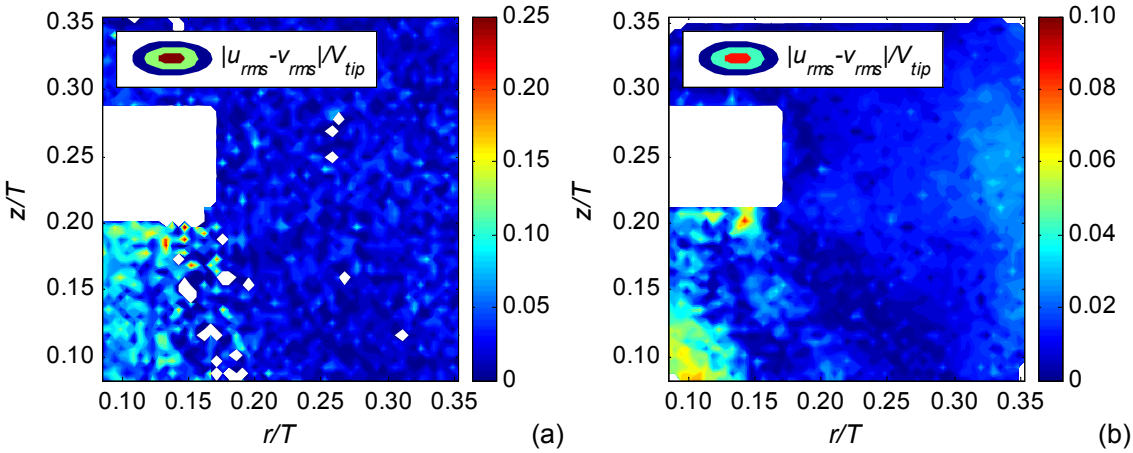

Figure 6.34: Difference in the axial and radial rms velocities normalised by V_{tip} for the (a) 700-750 µm dispersed particles and (b) corresponding continuous phase

Figure 6.34(a) and (b) show anisotropy maps of the dispersed and continuous phases respectively. Note that they are plotted on different scales. Kresta and Wood (1993b) stated that

rms velocities in highly anisotropic flows are expected to vary up to 200%, so anisotropy will be judged against this criterion. It may be observed that turbulence of the dispersed particles is slightly anisotropic; differences in both rms velocity components reach between $0.1-0.15V_{tip}$ in the discharge stream. The particle turbulence in the bulk of the flow is relatively isotropic, where the difference is at most $0.05V_{tip}$. On the other hand, the continuous phase preserves much higher isotropy, as shown in Figure 6.34(b). For the fluid, rms components differ by only $0.02V_{tip}$ in the bulk, and reach a maximum of $0.08V_{tip}$ underneath the blade, and close to the centre of the vessel base. This observation is analogous to the single-phase fluid (Figure 6.5), and again reaffirms the previous finding that 700-750 μm particles do not modify the flow's turbulent structure.

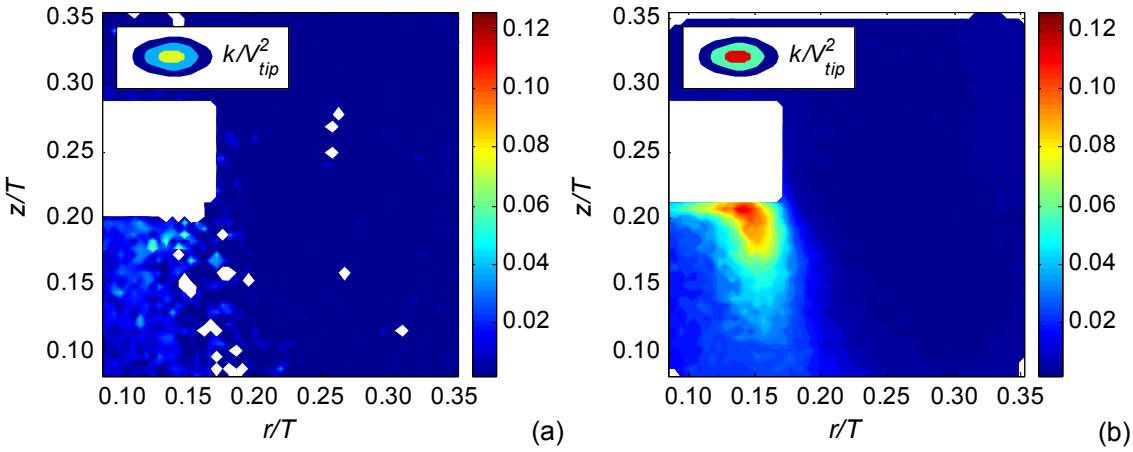

Figure 6.35: Contour maps of the 2-D TKE of (a) dispersed particles, 700-750 μm at 0.5 vol% and (b) corresponding continuous phase fluid

Finally, the 2-D TKE calculated via Equation (2.15) is illustrated in Figure 6.35(a) and (b) for the dispersed and continuous phases respectively. It is evident that the particle TKE levels are much lower than the corresponding fluid. They are slightly higher in the jet stream relative to the bulk flow, but reach only $0.05V_{tip}^2$ compared to $\sim 0.115V_{tip}^2$ in the continuous phase. It is expected that the TKE of the particles would increase with respect to its concentration, due to particle-particle collisions, referred to as the 'granular temperature' (Crowe *et al.*, 1996).

6.8 Conclusions of two-phase PIV study

This study of solid-liquid stirred flows at dilute concentrations of the dispersed phase up to 0.5 vol%, has provided some information about the effect of particles on the fluid turbulence. Analysis of the continuous phase has indicated that both small (250-300 μm) and large (1000 μm) particles suppressed turbulence, in terms of the rms velocities, TKE and dissipation rate, above volumetric concentrations of 0.2 vol%. The level of turbulence suppression remained approximately constant when the particle concentration was gradually increased to 0.5 vol%, suggesting that particle-particle interactions did not contribute to the observed phenomenon. This kind of information is valuable in the development of CFD codes for predictions of two-phase flow phenomena, as it highlights a particle volumetric concentration below which

turbulence modulation effects of the dispersed phase may be neglected, and thus when one-way coupling models are acceptable to implement.

The greatest impact has been on the dissipation rate, which shows turbulence suppression between 20-25% in the discharge stream, in the presence of particles. In light of the finding that the length scales remain unchanged, even simple dimensional analysis calculations of the dissipation rate would be able to show this effect from the TKE. The intermediate size particles (700-750 μm) also showed some suppression of the turbulence properties, but their effect was minor compared to the other two size classes, and may be deemed negligible. The observation that the largest particles decreased turbulence contradicts one of the most the most influential theories in literature (Gore and Crowe, 1981) as well as some previous experimental studies (Virdung and Rasmuson, 2008), but at the same time is supported by some other findings (Micheletti and Yianneskis, 2004). Two-phase micromixing experiments will be carried out to verify the current observations.

Digitally phase-separated images of the particles (at their maximum concentrations) were also processed. Spatial distributions of the locally averaged volumetric concentration field revealed three zones of locally high concentrations; one of which was the discharge stream. This supported the notion that the presence of particles was responsible for modulating the turbulence in that region. Particle velocities were obtained from cross correlation of dispersed phase images. The 700-750 μm particles created the most complete flow field. Their average particle slip velocities varied throughout the impeller region and were found to be greatest in the discharge stream. In this region the particle slip was nine times greater than the terminal velocity; hence this parameter does not provide a reliable estimate of axial slip velocities in stirred flows. The rms velocities and TKE of the particles were found to be lower than the corresponding continuous phase fluid; the former also exhibited slight anisotropy of turbulence.

Chapter 7
Two-phase micromixing study

Mixing is a general term which implies homogenization, i.e. the spatial redistribution of materials to achieve certain objectives. For instance, blending one material with another to achieve uniform properties, mixing to accelerate the rate of heat transfer for an exothermal process, or the dispersion of two immiscible phases. Mixing involves the reduction of inhomogeneities, and may occur over various scales of the flow. Macromixing occurs on the scale of the vessel, and determines large-scale distributions, such as the residence time and mean concentration in the Eulerian frame. Mesomixing describes the turbulent exchange between a fresh feed and its surrounding. The feed plume is large relative to the Kolmogorov microscale, but fine compared to the scale of the vessel, and its spatial evolution may be expressed in terms of turbulent diffusion (Guichardon and Falk, 2000). Finally, micromixing is the process of homogenization at the molecular scale, which has a direct influence on the course of chemical reactions, and subsequently product quality (Baldyga and Bourne, 1999). For instance, in crystallization, the chemical reaction and nucleation stages are directly dependent on micromixing, which determines the crystal size distribution and structure, which may in turn alter the functionality of the product. In polymerization, micromixing may control the incorporation of the initiator, as well as the molecular weight distribution (Fournier *et al.*, 1996). For this reason it is important to obtain experimental data which characterizes micromixing efficiency, and enables validation of sophisticated models developed for micromixing dependent processes, at the scale of the local fluid mechanics. This is not to say that macroscale homogenisation is irrelevant in reactions, as it determines the environment within which meso- and micromixing will occur. However, this study considers only the direct effects of molecular scale mixing on the selectivity of chemical reactions. The main objective is to quantify how micromixing rates are affected by the presence of solids in agitated suspensions. This study is a continuation of the work presented in Chapter 6, where turbulence modulation by dispersed particles was investigated via fluorescent PIV experiments.

A variety of experimental techniques have been employed in the past to characterize micromixing efficiency, ranging from condumetric, optical, and chemical methods. Chemical methods involve chemical reactions, which behave as molecular probes. A good test reaction must satisfy the following criteria (Fournier *et al.*, 1996):

- simple reaction scheme to avoid analysis of many products;
- easy analysis of reaction products;
- known reaction kinetics;
- good sensitivity and reproducibility.

There are three main classes of reactions; single, competing and parallel. The latter have the advantage of providing an indication of the mixing efficiency through the distribution of products. In parallel competing reactions, if the micromixing time scale is shorter than the characteristic reaction time of the limiting reaction, the product distribution always favours the faster reaction, since the yield is kinetically controlled. On the other hand if micromixing is slow and segregation of the chemical species at the molecular scale is intense, the reaction kinetics become unimportant. The rates of reaction depend on the instantaneous concentrations of the reactants, and by-products of the slower reaction begin to form. Since the degree of micromixing is governed by the dissipation rate, chemical reactions may be used as molecular probes to infer how the presence of particles affects the product distribution, and subsequently the dissipation rate.

To date, only a handful of two-phase micromixing experiments have been carried out to ascertain the effects of suspended solids on chemical reactions. Guichardon *et al.* (1995) reported a negliglible effect of solid glass particles (20 to 1300 μm) up to 6 mass%. Barresi (1997) studied the influence of three different types of solid particles in a RDT stirred flow and found that glass particles had a significant impact on the product selectivity. They dampened the fluid turbulence, but only at very high concentrations (above 11 vol%). Secondly at a fixed concentration (11 vol%), small glass particles (100-177 μm) and large PET particles (3 mm) had a relatively small impact compared to the large glass particles (425-500 μm). Explanations of the behaviour based on turbulence modulation mechanisms by the particles were proposed.

In a later study Barresi (2000) investigated turbulence modulation via micromixing experiments in both PBT and RDT stirred flows, and reported condratictory effects. Results showed that small glass particles (150-212 μm at 12 vol%) dampened turbulence in the PBT flow, but enhanced turbulence in the RDT flow under the same conditions. In the PBT experiment a clear fluid layer formed on top of the dense slurry. Subsequently the turbulence suppression was attributed to the change in fluid circulation. It was suggested that the particles increased the mixing time of the liquid, and homogenization in the clear layer was slower than in the slurry volume. Under these conditions the system could not be assumed to be perfectly macromixed, and this caused an increase in the by-product selectively. Barresi (2000) reconsidered the findings of the previous study (Barresi, 1997), and suggested that the increased by-product yield in the RDT flow was also due to a change in the fluid circulation rather than turbulence damping by the particles (as suggested initially), since in that case a clear fluid layer was also observed. Note however that in the more recent study (Baressi, 2000) the RDT experiment employed a lower liquid level and solids were dispersed in the whole volume. Consequently, the observed turbulence augmentation could be a direct effect of the solids (although a mechanism was not proposed).

Brilman *et al.* (1999) studied the effect of a range of glass particle sizes between 70-500 μm at 21 mass%, and reported a complex effect with respect to particle size. The dispersion was considered to behave like a pseudo-fluid with small particles. Energy was assumed to be dissipated mainly via particle-particle interactions, meaning a decrease in the fluid dissipation rate, and a corresponding increase in the by-product yield. However with increasing particle size, the amount of turbulence suppression was found to decrease. The justification was that at a fixed concentration, an increase in particle size (and reduced particle number) would decrease the number of collisions. At larger particle sizes the level of turbulence suppression

then increased. It was suggested that larger particles are less able to follow the fluid motion, and more energy is required to re-suspend them, and more energy is dissipated in particle-particle collisions. Alternatively there could be an increase in the amount of stagnant fluid moving with the particles.

From the above discussion it is evident that a small number of two-phase micromixing experiments have been carried out at relatively high concentrations. In the present case, the maximum concentration studied will be 3 vol%, where turbulence modulation has not been reported in literature. Two different parallel reaction schemes will be implemented with inert dispersed particles in the fluid. The first described is the Villermaux reaction scheme developed by Fournier e*t al.* (1996), followed by the Bourne scheme (Bourne and Yu, 1994) in the proceeding section.

7.1 Villermaux reaction scheme

The Villermaux reaction scheme (Fournier *at al.,* 1996) is given below:

$$H_2BO_3^- + H^+ \underset{}{\overset{k_1}{\rightleftharpoons}} H_3BO_3 \tag{7.1}$$

$$5I^- + IO_3^- + 6H^+ \underset{}{\overset{k_2}{\rightleftharpoons}} 3I_2 + 3H_2O \tag{7.2}$$

$$I_2 + I^- \underset{k_3'}{\overset{k_3}{\rightleftharpoons}} I_3^- \tag{7.3}$$

Prior to mixing, the tank contains iodide (I^-), iodate (IO_3^-) in stoichiometric proportions, and borate ions ($H_2BO_3^-$), to which the limiting reagent sulphuric acid is added. The first reaction is a neutralisation between borate ions and acid, which competes with the (second) Dushman reaction between iodide, iodate and acid, liberating the by-product iodine (I_2). The iodine complexes with iodide to form triiodide (I_3^-) according to Equation (7.3); its concentration may be measured photometrically. A material balance on the iodide ions yields the following expression:

$$c_{I^-} = c_{I_0^-} - \frac{5}{3}\left[c_{I_2} + c_{I_3^-}\right] - c_{I_3^-} \tag{7.4}$$

Above c_{I^-}, c_{I_2} and $c_{I_3^-}$ are the molar concentrations of iodide, iodine and triiodide after reaction, and $c_{I^-,0}$ the initial iodide concentration. Subsequently, knowledge of Equation (7.4) combined with the equilibrium constant for the third reaction (Equation (7.10)), together with the measured triiodide concentration, allows the iodine concentration to be determined from the algebraic equation as follows:

$$-\frac{5}{3}c_{I_2}^2 + \left[c_{I,0} - \frac{8}{3}c_{I_3^-}\right] \times c_{I_2} - \frac{c_{I_3^-}}{K_3} = 0 \tag{7.5}$$

7.1.1 Reaction kinetics

The first reaction is almost instantaneous, with a second order rate constant $k_1 \sim 10^{11}$ $m^3\,mol^{-1}\,s^{-1}$. Its rate is given as follows:

$$r_1 = k_1 \left\{ c_{H_2BO_3^-} c_{H^+} \right\} \tag{7.6}$$

The second reaction is fast but has a time scale of the same order of magnitude as the micromixing process. If mixing is rapid and intense, only the first instantaneous reaction occurs, and iodine is not formed since the second reaction is relatively slower. On the other hand, if mixing is slow and not achieved down to the molecular scale, there remains a local excess of the acid, which may react through the second reaction, forming iodine, and subsequently triiodide.

The rate constant of the second reaction k_2 depends on the ionic strength of the reaction zone I (mol l^{-1}), which changes during the micromixing process. The kinetics of the second reaction have been determined as a function of the medium composition by Guichardon *et al.* (2000), but they are still uncertain (Bourne, 2008):

$$\begin{aligned} \log k_2 &= 9.28 - 3.66\sqrt{I} \\ \log k_2 &= 8.38 - 1.51\sqrt{I} + 0.23I \end{aligned} \quad \text{for} \quad \begin{cases} I < 0.16 \\ I > 0.16 \end{cases} \tag{7.7}$$

for which the rate law may be expressed as:

$$r_2 = k_2 \left\{ c_{I^-}^2 c_{IO_3^-} c_{H^+}^2 \right\} \tag{7.8}$$

The rate of the third reaction is given by:

$$r_3 = k_3 c_{I_2} c_{I^-} - k_3^{'} c_{I_3^-} \tag{7.9}$$

for which k_3 and $k_3^{'}$ are equal to 5.6×10^6 $m^3\,mol^{-1}\,s^{-1}$ and 7.5×10^6 s^{-1}, respectively (Ruasse *et al.*, 1986). The values of the rate constants for the forward and backward reactions are consistent with the equilibrium constant characterising the third reaction at 25 °C (Palmer and Lietzke, 1982):

$$K_3 = \frac{k_3}{k_3^{'}} = \frac{c_{I_3^-}}{c_{I_2} c_{I^-}} \tag{7.10}$$

The dependency of the equilibrium constant K_3 on temperature (units K) has also been given by Palmer *et al.* (1984):

$$\log_{10}(K_3) = \frac{555}{T} + 7.355 - 2.575\log_{10}(T)\text{, units l mol}^{-1} \tag{7.11}$$

7.1.2 Segregation index

From this point forward, the amount of iodine produced will be expressed in terms of the segregation index. The segregation index is defined as the *relative* amount of acid consumed in the second reaction Equation (7.2) to produce iodine, which depends on the efficiency of the micromixing process. When mixing is imperfect, the yield of iodine may be expressed as follows:

$$Y = \frac{2n_{\mathrm{I}_2}}{n_{\mathrm{H}^+,0}} = \frac{2\left(n_{\mathrm{I}_2} + n_{\mathrm{I}_3^-}\right)}{n_{\mathrm{H}^+,0}} \tag{7.12}$$

In Equation (7.12) n_{I_2} and $n_{\mathrm{I}_3^-}$ are the number of moles of iodine and triiodide after reaction, and $n_{\mathrm{H}^+,0}$ the initial number of moles of acid. Under totally segregated conditions, the yield of iodine is governed by the ratio Y_{TS} of the initial number of moles of $\mathrm{H_2BO_3^-}$ to $\mathrm{IO_3^-}$:

$$Y_{TS} = \frac{6n_{\mathrm{IO_3^-},0}}{6n_{\mathrm{IO_3^-},0} + n_{\mathrm{H_2BO_3^-},0}} \tag{7.13}$$

The segregation index, X_S, may be expressed as:

$$X_S = \frac{Y}{Y_{TS}} \tag{7.14}$$

It follows that when mixing is perfect, no iodine is produced meaning that $Y = 0$ and thus $X_S = 0$. Under totally segregated conditions $Y = Y_{TS}$ and $X_S = 1$. For imperfect mixing $0 < X_S < 1$.

7.1.3 Experimental method

The tank geometry in the micromixing study was kept the same as in the PIV experiments in §6.1.1 (important dimensions being $T = 0.101$ m, $D = T/3$ and $C = T/4$). The feed location was selected to be in the discharge stream of the impeller, where the highest degree of turbulence modulation by the particles was detected in the PIV study. Locations directly under the blade were avoided, since this region contains the strongest spatial gradients. Consequently minor changes in the feed location between new experimental runs could lead to substantial changes in the product selectivity, even if all other experimental parameters (such as impeller speed) were held constant. At locations too far away from the impeller, turbulence modulation is not expected to be considerable, so the discharge stream seemed appropriate. The co-ordinates of the feed outlet were $z/T = 0.178$ and $r/T = 0.129$, as shown in Figure 7.1. The pipe was manufactured from stainless steel, and had an inner diameter of 1 mm. The experimental set-up is depicted in Figure 7.2.

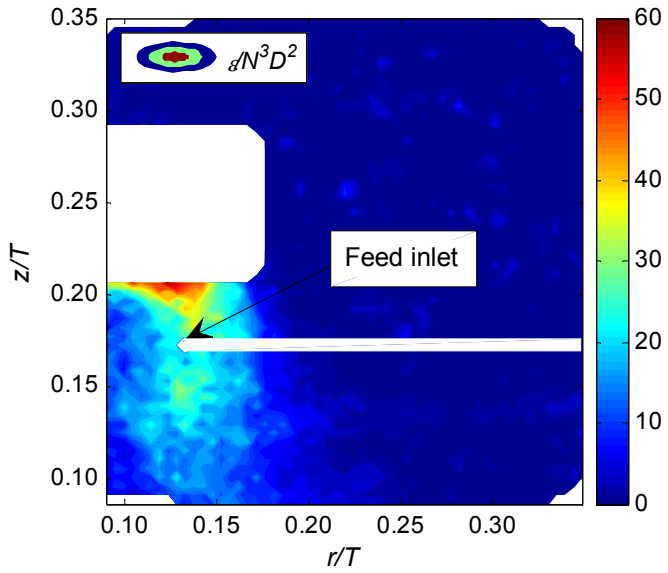

Figure 7.1: Location of the feed pipe superimposed onto the dissipation rate map

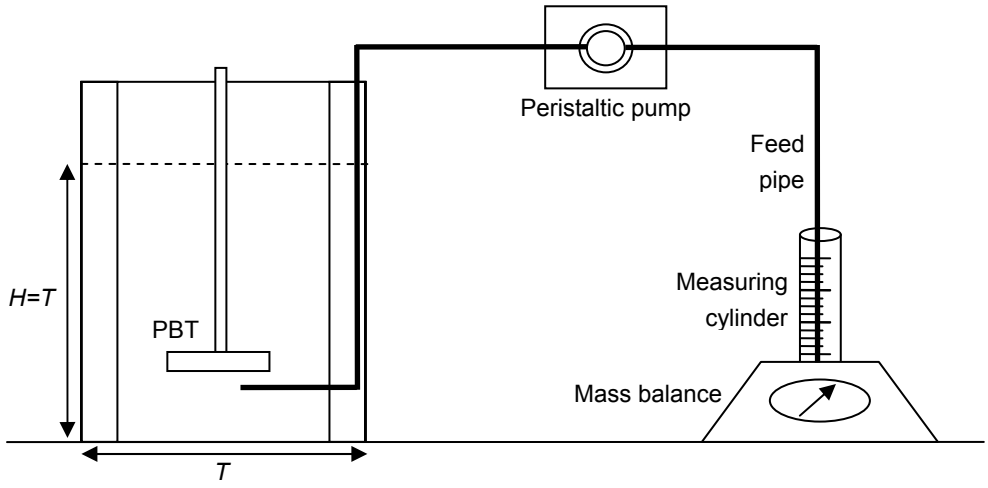

Figure 7.2: Micromixing experimental setup

Table 7.1: Initial reactant concentrations in the 1 l tank

Reactant	*Concentration (mol l^{-1})*
I^-	0.116
IO_3^-	0.023
$H_2BO_3^-$	0.056
H^+	0.020

Before mixing, the tank contained solutions of iodide, iodate and borate ions, which had been prepared individually. All reagents were purchased from Fisher Scientific and were of analytical grade. The combined volume of these solutions was 1 litre (giving a liquid fill height of

$H = 1.24T$); the final concentrations in the 1 litre vessel are summarised in Table 7.1. These concentrations were used previously by Fournier *et al.* (1996).

The iodide and iodate solutions were made by dissolving potassium salts in ultra pure water (at ambient temperature) and stored in separate glass vessels. The iodide solution was prepared just before the start of the reaction to limit its oxidation. A buffer solution containing the borate ions was obtained by mixing boric acid with sodium hydroxide, resulting in three equilibria for borate ions (Fournier *et al.*, 1996). It is assumed that $H_2BO_3^-$ is the predominant borate ion as in Equation (7.15), characterised by the equilibrium constant $K_{b1} = 1.36 \times 10^{-5}$ mol l^{-1}.

$$H_3BO_3 + OH^- \rightleftarrows H_2BO_3^- + H_2O \tag{7.15}$$

The precise concentration of the borate ion may then be determined from the equilibrium relation below:

$$c_{H_2BO_3^-}^2 - \left(c_{H_3BO_3,0} + c_{OH^-,0} + K_{b1}\right)c_{H_2BO_3^-} + \left(c_{H_3BO_3,0}c_{OH^-,0}\right) = 0 \tag{7.16}$$

The initial boric acid and sodium hydroxide concentrations were 0.0909 and 0.0560 mol l^{-1} respectively, giving a borate ion concentration of 0.0560 mol l^{-1}. Finally, a 0.02 mol l^{-1} solution of sulphuric acid was prepared by diluting a commercially available solution of 0.1 mol l^{-1}.

After the reagents were prepared, the buffer solution containing the borate ions were first introduced to the tank, followed by solutions of iodate and iodide respectively. The order of addition was important, to ensure that the iodide and iodate ions co-existed in a basic solution, thereby preventing the premature formation of iodine. The sulphuric acid feed was added to this medium after it had been mixed for around two minutes.

In addition to being a reactant in the neutralisation reaction, the concentration of borate ions determines the solution pH. Owing to the potential-pH diagram of the iodine-water system, the formation of iodine is thermodynamically possible when $\mathrm{pH} < \mathrm{pH}^*$ (Fournier *et al.*, 1996), where pH^* is the critical pH. Subsequently if the pH of the buffer is below pH^*, iodine may form even in the absence of the sulphuric acid feed, due to the reaction between iodide, iodate and H^+ released by the boric acid (shifting the equilibrium of the $H_2BO_3^-/H_3BO_3$ system to the left). Thus, it is necessary that the initial pH (governed by the buffer solution) is greater than pH^* if micromixing efficiency of the sulphuric acid is to be detected. In the present case, pH^* is close to 8, as shown in the potential-pH diagram for the given iodine-water system in Figure 7.3 (refer to the Appendix of Fournier e*t al*., (1996) for calculations). From knowledge of the equilibrium concentrations of $H_2BO_3^-$ and H_3BO_3 (0.0560 and 0.0349 mol l^{-1} respectively) and $pK_{a1} = 9.14$, the initial pH of the solution was calculated according to Equation (7.17), and found to be 9.35.

$$\mathrm{pH} = pK_{a1} + \log\left(\frac{c_{H_2BO_3^-}}{c_{H_3BO_3}}\right) \tag{7.17}$$

Therefore, the condition of $pH>pH^*$ was satisfied. The final solution pH is determined by the quantity of sulphuric acid added. This value should be closer to (but not less than) pH^* to limit the dissociation of formed iodine. In any given experiment, a maximum of 80 ml of 0.02 mol l^{-1} acid could be added to the tank (for reasons explained later). After this addition, the final pH of the solution was found to be 9.31, still above the limit of pH^*, hence satisfying the second criterion.

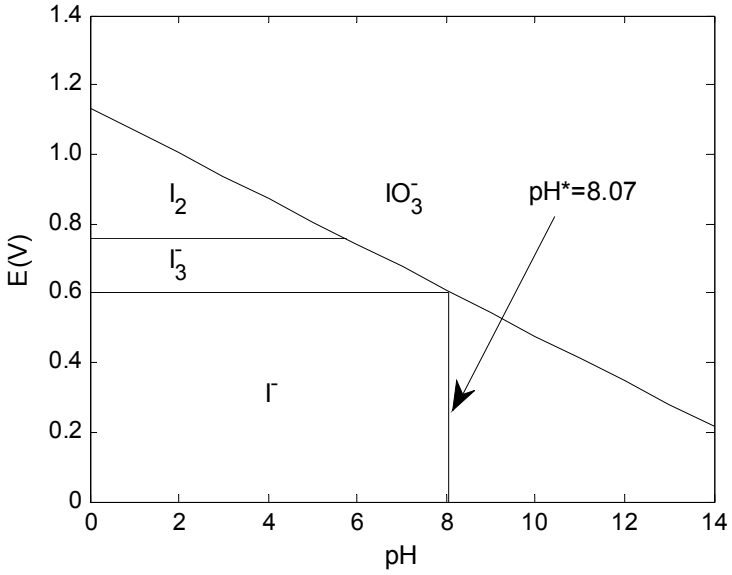

Figure 7.3: Potential-pH diagram of the iodine-water system. The potential iodine concentration is 0.0699 mol l^{-1}.

7.1.4 Semi-batch operation

The experiment was carried out in a semi-batch operation, where 10 ml acid injections were introduced sequentially into the same solution (giving a total of 80 ml after a maximum of 8 injections). The advantages of this technique include reductions in the preparation time of the reagents, as well as experimental costs. A semi-batch operation also eliminates errors which may be incurred when attempting to replicate the setup each time the experiment is reconfigured, instead enabling a straightforward comparison between results obtained from a series of consecutive feeds.

Two minutes after the end of each injection, a sample of the solution was taken (the position in the tank being unimportant since the contents are well mixed) and the triiodide absorption measured using a spectrophotometer at 353 nm. By taking into account the amount of iodine and triiodide formed after the previous injection, a measure of the segregation index could be obtained after each individual addition. The initial reactant concentrations before each injection must be updated for this purpose.

Let i represent the index for the i^{th} acid injection. First consider the tank volume increases due to the additions of acid feed, noting that the sample taken for spectrophotometry was always replaced so this need not be taken into account. Before the i^{th} injection, the tank has a volume:

$$V_i = V_0 + (i-1)V_{inj} \tag{7.18}$$

where V_0 and V_{inj} are the initial tank and injection volumes, respectively. The initial concentrations of iodide, iodate and borate ions before the i^{th} injection may be obtained from material balances as follows:

$$c_{\mathrm{I},0,i} = \frac{\left[V_{i-1}c_{\mathrm{I},0,i\text{-}1}\right] - \frac{5}{3}\left[n_{\mathrm{I}_2,i-1} + n_{\mathrm{I}_3^-,i-1}\right] - n_{\mathrm{I}_3^-,i-1}}{V_i} \tag{7.19}$$

$$c_{\mathrm{IO}_3^-,0,i} = \frac{\left[V_{i-1}c_{\mathrm{IO}_3^-,0,i\text{-}1}\right] - \frac{1}{3}\left[n_{\mathrm{I}_2,i\text{-}1} + n_{\mathrm{I}_3^-,i\text{-}1}\right]}{V_i} \tag{7.20}$$

$$c_{\mathrm{H_2BO_3},0,i} = \frac{\left[V_{i-1}c_{\mathrm{H_2BO_3},0,i\text{-}1}\right] - \left[n_{\mathrm{H}^+,0} - 2\left(n_{\mathrm{I}_2,i\text{-}1} + n_{\mathrm{I}_3^-,i\text{-}1}\right)\right]}{V_i} \tag{7.21}$$

where $n_{\mathrm{I}_3^-,i-1}$ and $n_{\mathrm{I}_2,i-1}$ are the number of moles of triiodide and iodine formed *exclusively* from the $(i-1)^{th}$ injection, not the cumulative total number of moles in the bulk after the $(i-1)^{th}$ injection. After the first injection, these quantities are known and can be carried forward to the material balances of the next injection and so forth, as given in Equations (7.19) to (7.21).

The concentration of triiodide in the bulk after the i^{th} injection, denoted $c_{\mathrm{I}_3^-,i}$, may be inferred from its absorption (discussed in the next section). Following, the equilibrium concentration of iodine in the bulk may be determined from the quadratic equation below:

$$-\frac{5}{3}c_{\mathrm{I}_2,i}^2 + \left[c_{\mathrm{I},0,i} - \frac{8}{3}c_{\mathrm{I}_3^-,i}\right]\cdot c_{\mathrm{I}_2,i} - \frac{c_{\mathrm{I}_3^-,i}}{K_3} = 0 \tag{7.22}$$

Note that Equation (7.22) has a form similar to Equation (7.5), but now the iodide concentration corresponds to that at the start of the i^{th} acid injection. Subsequently, the yield of iodine after the i^{th} injection under imperfect mixing conditions is:

$$Y_i = \frac{2\left[\left(n_{\mathrm{I}_2,i} + n_{\mathrm{I}_3^-,i}\right) - \left(n_{\mathrm{I}_2,i-1} + n_{\mathrm{I}_3^-,i-1}\right)\right]}{n_{\mathrm{H}^+,0,i}} \tag{7.23}$$

Similarly, the yield of iodine under totally segregated conditions is:

$$Y_{TS,i} = \frac{6n_{IO_3^-,0,i}}{6n_{IO_3^-,0,i} + n_{H_2BO_3^-,0,i}} \tag{7.24}$$

where $n_{IO_3^-,0,i}$ and $n_{H_2BO_3^-,0,i}$ are the initial number of moles of iodate and borate ions before the i^{th} injection. As mentioned before, the segregation index is the ratio between these two yields.

In the two-phase micromixing experiments, the first acid injection was introduced into a single-phase liquid medium. After the first injection had been completed and a sample of the solution analysed by a spectrophotometer, inert solid soda-lime glass spheres were added to the fluid, followed by the second acid injection. Thereafter, the concentration of particles was increased between consecutive acid injections.

7.1.5 Calibration and product analysis

It was explained previously that the major by-product yield to be measured in the Villermaux reaction scheme is iodine. However some of the iodine further reacts to form triiodide, and these two species coexist at equilibrium. The by-products may be analysed via spectrophotometry, but of the two it is easier to determine the concentration of triiodide, as it has a globally higher extinction coefficient (Awtry and Connick, 1951). The iodine concentration in equilibrium with the triiodide may then be determined from the relationship given in Equation (7.10).

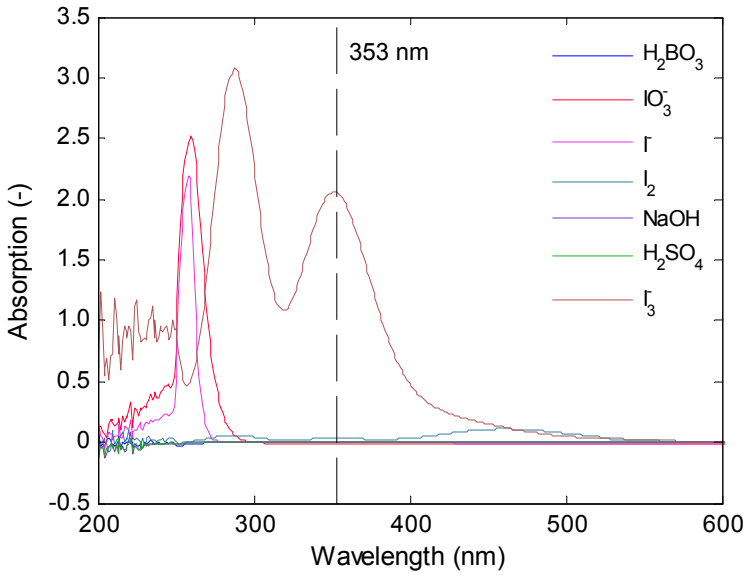

Figure 7.4: Absorption spectra of all species in the Villermaux reaction scheme

The absorption spectra of all species (at various concentrations) in the chemical test reaction are shown in Figure 7.4, in the visible and ultraviolet range. From this is it apparent that the triiodide ion has absorption peaks at 288 and 353 nm. At the higher wavelength there is less interaction from other species, hence the product will be analysed at 353 nm.

According to the Beer-Lambert law, the light absorption of the triiodide ion D_{353} at 353 nm, across a quartz cell of optical path length l, is linearly dependent on its concentration c_{I_3} and molar extinction coefficient ε_{353} (also at 353 nm) as follows:

$$D_{353} = \varepsilon_{353} l c_{I_3} \tag{7.25}$$

The molar extinction coefficient was determined through a calibration procedure, where absorption readings of solutions containing known concentrations of triiodide and iodine were obtained at 353 nm.

To begin, a solution was prepared by dissolving measured quantities of iodine and potassium iodide in water, and the equilibrium relation given in Equation (7.10) was used to infer the equilibrium triiodide concentration. After measuring the absorption of this solution, it was serially diluted, absorption readings were taken and so forth. After each dilution, the equilibrium relation was taken into account to re-determine the iodine concentration. The variation of the equilibrium triiodide concentration with increasing water content throughout the calibration procedure is shown in Figure 7.5. The points circled in red are concentrations at which the absorption was measured.

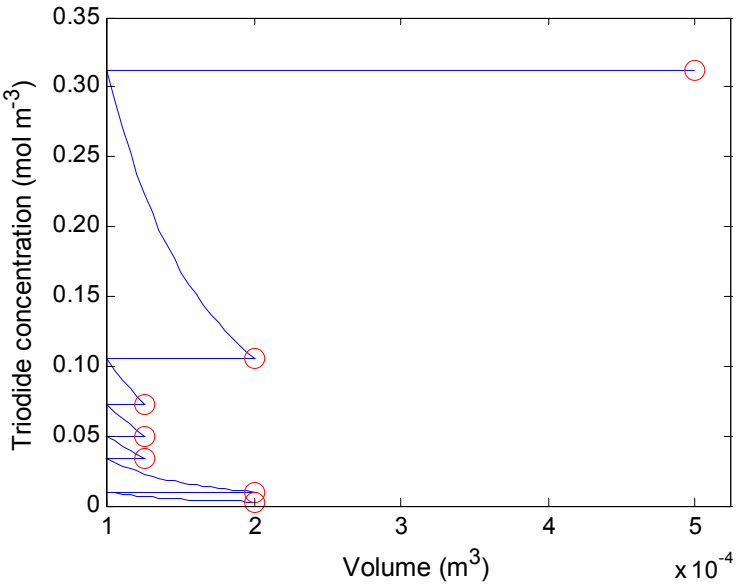

Figure 7.5: Triiodide concentration after serially diluting a known solution of iodine and iodate. Red circles mark points at which absorption measurements were obtained.

Finally the relation between absorption of the triiodide ion versus its concentration is displayed in Figure 7.6. The straight line proves that the Beer-Lambert law is applicable up to a triiodide concentration of ~0.1 mol m^{-3}, at which the absorption is ~3. The limit found here is consistent with that recommended by Guichardon and Falk (2000), and at 353 nm the extinction coefficient of the triiodide ion was found to be 2686 m^2 mol^{-1}. The value compares well with those reported in literature (Guichardon and Falk, 2000).

Preliminary tests of micromixing experiments carried out with reagent concentrations given in Table 7.1 showed that up to 8 acid injections (of 10 ml and 0.02 mol l^{-1} each) could be added to the tank before the maximum absorption limit of the triiodide ion under the Beer-Lambert law was reached.

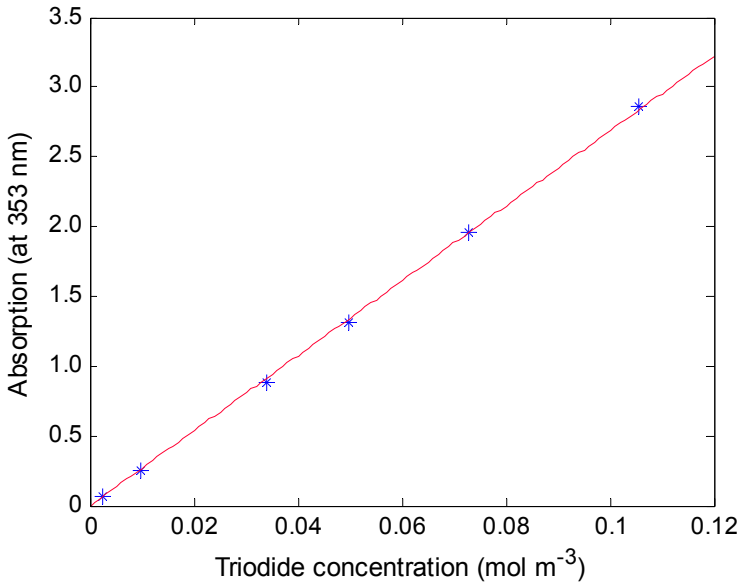

Figure 7.6: Calibration curve of the triiodide ion

Adsorption of the reactants and products on the glass beads was also tested and found to be neglible. Solutions of potassium iodide (0.116 M), potassium iodate (0.023 M), and a mixture of iodine and potassium idiode (forming 1×10^{-4} M triiodide at equilibrium) were prepared and stirred in sealed vessels containing 1000 µm particles at 4 vol%. Absorption of the species was measured over 2 hours (a typical experiment lasts ~1 hour) and found to be constant.

7.1.6 Critical feed time and temperature variation

Before experiments can be carried out, it must be ensured that micromixing is the mechanism controlling the product distribution, and that it is free from macromixing influences. The effects of macromixing can be tested by gradually increasing the feed time (or decreasing the feed rate) of the sulphuric acid solution. It has previously been established (Bourne and Yu, 1994; Baldyga and Bourne, 1999; Guichardon and Falk, 2000) that at high feed rates, the plume of acid is first distributed through the vessel via macromixing mechanisms, which may cause large scale concentration gradients and consequently high by-product yields. Therefore, it is desirable to add the feed slowly enough so that it is well dispersed as soon as it enters the tank, and macromixing effects are eliminated. The segregation index decays as the feed time of the acid is increased, and the time at which it becomes constant is referred to as the critical feed time. At shorter times, the segregation index is under the control of both macro and micromixing influences, whereas at longer feed times it is micromixing dependent only. This test was carried out at two impeller speeds of 800 and 1000 rpm (under ambient temperature conditions); results are shown in Figure 7.7. In both cases a feed time of 300 s (corresponding to a feed rate of 2 ml min^{-1}) was found to be the critical point, and fixed for following experiments.

The yields of iodine (and hence the segregation index) obtained in experiments at 1000 rpm are lower than those obtained at 800 rpm across all feed times, since micromixing is more efficient at higher speeds (ε is greater) and less by-product is generated. At 1000 rpm at the critical feed time, $X_S = 0.13$. The value is similar to that reported in literature for a feed in the discharge stream and RDT operated at the same average power per unit volume; $\bar{\varepsilon} = 0.304$ W kg^{-1} and $X_S \sim 0.15$ (Fournier *et al.*, 1996). Consequently, the single-phase segregation index is considered to be a reliable estimate, at both impeller speeds.

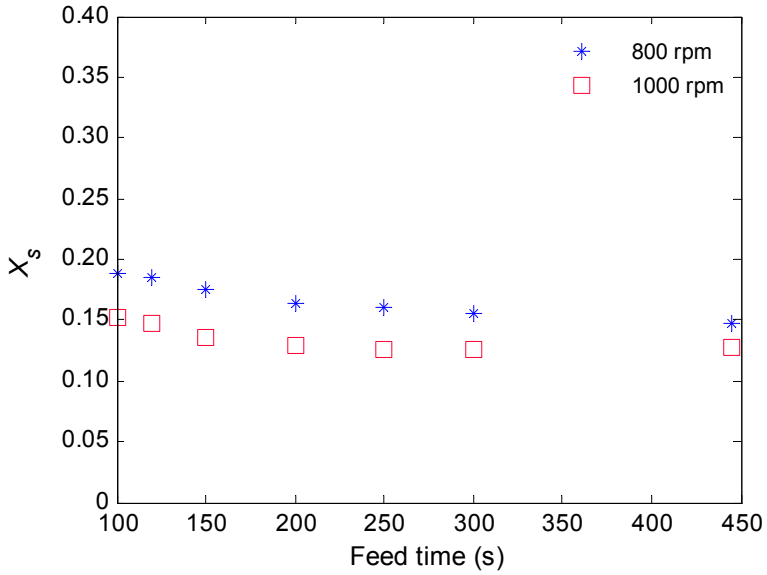

Figure 7.7: Effect of feed time on segregation index at impeller speeds 800 and 1000 rpm

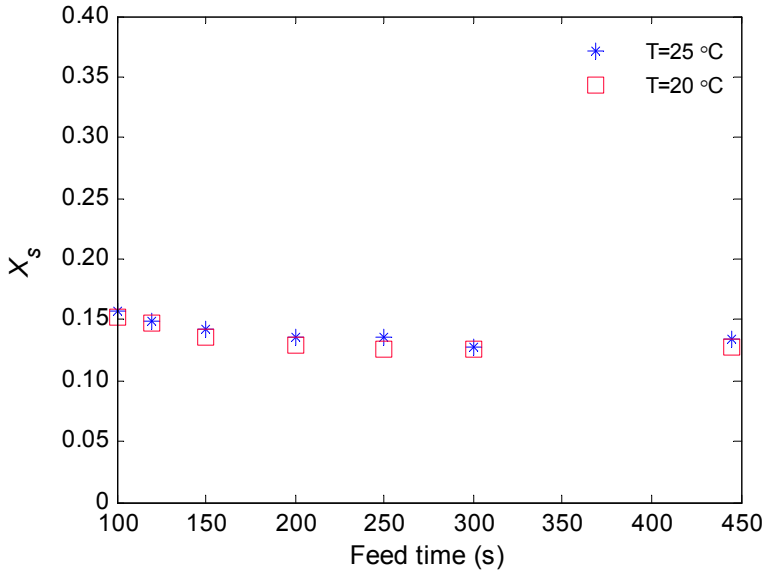

Figure 7.8: Influence of temperature on segregation index. Impeller speed 1000 rpm

The effect of minor changes in temperature on the by-product yield was also assessed, since temperature control was not implemented. Two more experiments showing the decreasing segregation index with increasing feed time were carried out under ambient conditions (20 °C at the time of experiment) and 25 °C, at an impeller speed of 1000 rpm. Since the temperature dependency of the equilibrium constant K_3 for the iodine/triiodide system was known via Equation (7.11), the concentration of iodine could be accurately determined in each case. The results in Figure 7.8 show that temperature has no significant effect on the by-product yield (up to a variation of 5 °C). Guichardon *et al.* (2000) had also showed that there was no change in the rate constant k_2 for the Dushman reaction within the temperature range of 293 and 308 K. For this reason, temperature control was not deemed to be necessary in the micromixing experiments, and they were carried out under ambient conditions.

7.1.7 Sensitivity of product distribution

After determining the critical feed time, the next step was to ensure that the reaction scheme is sensitive to the fluid hydrodynamics, since the objective is to detect changes in the local dissipation rate due to the presence of particles.

Figure 7.9(a) illustrates the segregation index versus impeller speed, and it is evident that the yield shows a general sensitivity to the system turbulence, since the segregation index is decreasing with an increase in impeller speed. However the sensitivity declines at high impeller speeds. The reduced sensitivity becomes more apparent when the relative yield is plotted versus the mean power dissipation rate (at the respective impeller speeds) shown in Figure 7.9(b).

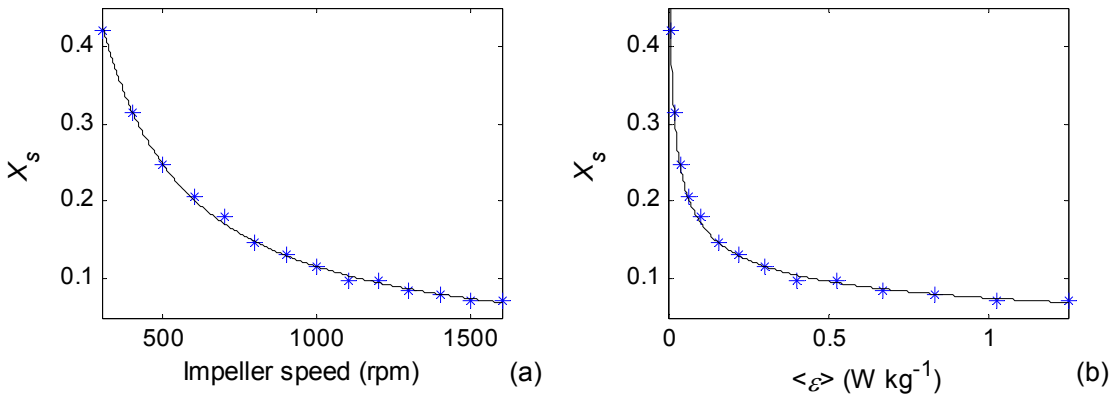

Figure 7.9: Variation of segregation index with respect to (a) impeller speed and (b) mean power dissipation rate

It is preferable to conduct the two-phase micromixing experiments at high speeds to be able to suspend the solid particles effectively. Note that the just suspended speed for 1000 micron particles at 3 vol% (calculated from the Zwietering (1958) criterion) is around 1300 rpm, which provides an average power dissipation rate of 0.67 W kg^{-1}. This falls into the flatter region of the curve where the mixing conditions have relatively little influence on the selectivity of the chemical test reaction.

In principle, for this method to work, there should be a competition between the Dushman chemical reaction and the fluid mixing process. This would result in a variation of the product selectivity with respect to the fluid hydrodynamics, and subsequently impeller speed and dissipation rate. Optimum sensitivity is obtained when the characteristic time of the second reaction is almost equal to the micromixing time (Guichardon and Falk, 2000). Since the variation of the yield is very small at high impeller speeds, it is indicative that mixing conditions are very efficient.

The sensitivity of the chemical test method may be increased to match the mixer efficiency, by adjusting the reactant concentrations. Following the recommendations of Guichardon and Falk (2000), first the acid concentration was increased, followed by the iodine potential, defined as follows:

$$(I_2)_{potential} = 3IO_{3,0}^- = \frac{3}{5} I_0^- \tag{7.26}$$

The iodine potential was increased by a factor of two and four to increase the kinetics of the second reaction. Above this limit too much triiodide was produced and exceeded the absorption threshold for which the Beer-Lambert law was still applicable (i.e. $D_{353} = 3$). The results are illustrated in Figure 7.10, and show that the plateau at the high impeller speeds is still prevalent under all tested conditions. Thus, even after adjusting the reactant concentrations, the sensitivity of the yield was not improved at such high impeller speeds. For this reason an impeller speed of 800 rpm (corresponding to an average dissipation rate of 0.156 W kg^{-1}) was selected for the two-phase experiments, where reasonable sensitivity of the yield was attainable.

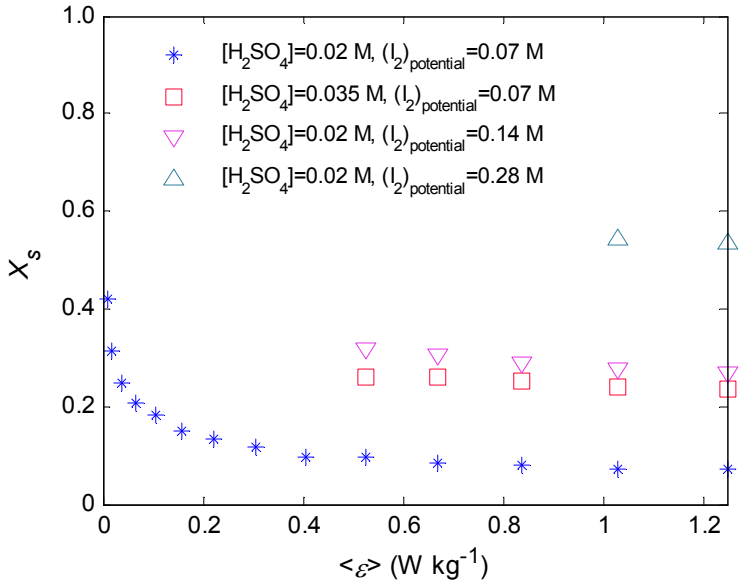

Figure 7.10: Influence of reactant concentration on the segregation index sensitivity

Note that the just suspended speed of 300 μm particles at 0.5 vol% is 817 rpm according to the Zwietering correlation (1958). Nevertheless, two-phase micromixing experiments were carried

out with up to 3 vol% of particles in the flow, with even larger particle sizes, meaning that they were not suspended homogeneously. The main disadvantage is that the mean volume fraction of particles near the feed pipe would not be known. However in §6.7.1 it was also shown that even when particles were suspended at an N well above the just suspended speed, there remained concentration gradients of solids throughout the vessel, with particle accumulation close to the blades and vessel corners. In light of this, the true volume fraction of particles near the feed would not be known even if higher impeller speeds were used. Nevertheless the effect of the presence of particles could still be determined through the micromixing experiments.

7.1.8 Experimental error estimate

The method of feeding sulphuric acid in a semi-batch operation was tested by adding successive injections into the same solution at the critical feed rate of 2 ml min^{-1} and a constant impeller speed of 800 rpm. No variables were altered between injections, so after applying the material balances in §7.1.4, one would expect a constant yield of iodine after each injection. In this way, the experimental error could also be evaluated. Figure 7.11 illustrates the accuracy of the method. The maximum deviation in the segregation index between successive injections was found to be ~5% which may be interpreted as the experimental error, possibly arising from fluctuations in the impeller rotation (± 3 rpm). Note that iodine may also be forming due to the oxidation of potassium iodide instead of a result of imperfect micromixing. Additionally there may be the disproportionation of iodine, which will be discussed in the next section. The experiment takes approximately one hour from the start of the first acid injection.

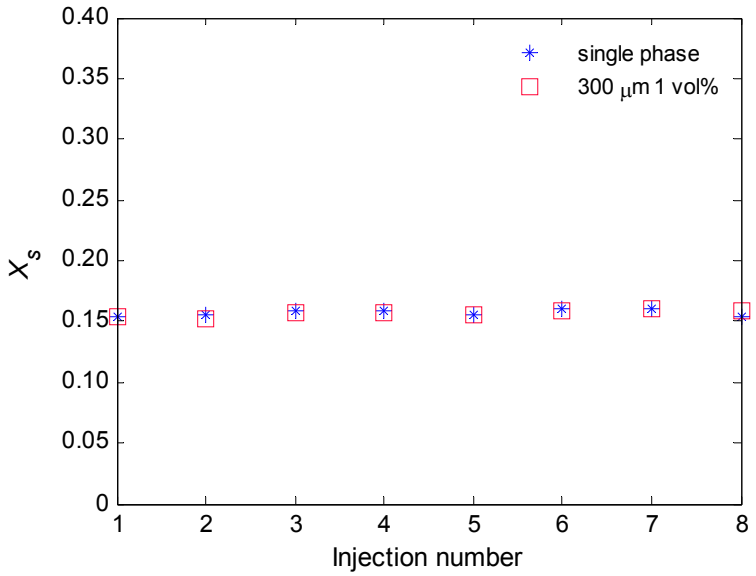

Figure 7.11: Repeated injections of sulphuric acid feed into the same solution both in the absence and presence of 300 μm particles 1 vol%. Impeller speed 800 rpm.

An identical test was carried out with 300 μm particles in the flow throughout all injections at a concentration of 1 vol%. As shown in Figure 7.11, the accuracy of the method remained unchanged, and the deviation did not exceed 5%.

7.1.9 Dissociation of iodine

In the Villermaux reaction scheme, the Dushman reaction (Equation (7.2)) is assumed to be irreversible. An analysis of the Gibbs free energy for the reaction also supports this conjecture. The enthalpies of formation and entropies (under standard-state conditions) of the aqueous reactants and products are given in Table 7.2. The Gibbs free energy under standard-state conditions was then determined using this information via Equation (7.27).

$$\Delta G^o = \Delta H^o - T\Delta S^o \tag{7.27}$$

The Gibbs free energy for Equation (7.2) was found to be -308 kJ. The highly negative value suggests that the forward Dushman reaction is favoured and spontaneous, whereas the reverse reaction (or disproportionation of iodine) is unfeasible.

Table 7.2: Standard enthalpies and entropies of compounds in the Dushman reaction at standard state of 25 °C

Compound (aq)	ΔH_f^o *(kJ mol^{-1})*	*reference*
I^-	-56	Negi and Anand (1985)
IO_3^-	-229.44	Stern and Passchier (1962)
H^+	0	Negi and Anand (1985)
I_2	13.52	Chase (1998)
H_2O	-285.83	Chase (1998)

Compound	ΔS^o *(kJ mol^{-1} K^{-1})*	*reference*
I^-	0.13	Conway (1978)
IO_3^-	0.14	Greensfelder and Latimer (1931)
H^+	-0.02	Rockwood (1987)
I_2	0.15	Chase (1998)
H_2O	0.07	Chase (1998)

It is important to remember that iodine is formed in a basic medium where thermodynamically this should not be possible (since $pH_{bulk} > pH^*$). Only the locally high acid feed concentration creates an environment where $pH < pH^*$, and subsequently enables the formation of iodine under imperfect mixing conditions. Within a matter of seconds, the reaction zone and its contents is mixed with the bulk. As a result, the sample must be analysed rapidly (Fournier *et al.*, 1996). This requirement was fulfilled by obtaining a sample of the solution within a minute after the end of the acid injection. However, an experiment carried out in semi-batch operation takes approximately 1 hour to complete, meaning that iodine formed from the first injection and onwards may be dissociating in the tank over this time duration. The loss of iodine through disproportionation should be accounted for in the mass balances given in §7.1.4, to obtain an accurate estimate of the yield after successive injections.

In order to quantify the disproportionation of iodine in the mixture, its decay was studied over a long time period. 70 ml of 0.02M acid was fed to a 1 litre of solution containing the reagents outlined in Table 7.1, and the resultant concentration of iodine was determined from Equation (7.5). A sample of the product was obtained and its absorption measured continuously over a

period of 24 hours. The quartz cell was sealed with a lid to prevent evaporation. The concentration profile of the sample is shown in Figure 7.12. It may be observed that there is a definite decrease in the concentration of iodine over time, and thus disproportionation is confirmed. To model the decay as a rate law with respect to the iodine concentration, the integrated rate law for a general n^{th} ($n \neq 1$) order reaction was fitted to the data, shown in Equation (7.28).

$$c_{I_2} = \left\{ \left(\frac{c_{I_2,0}^{-n+1}}{-n+1} - k_2' t \right) (-n+1) \right\}^{\frac{1}{-n+1}} \qquad n \neq 1 \tag{7.28}$$

The optimum value of the rate constant k_2' and reaction order n was obtained by minimising the sum of the squared differences between the model prediction and experimental data. By doing so, n was found to be 1.00115, indicating a first order reverse reaction with respect to iodine, and k_2' equal to 8.86×10^{-6} m^3 mol^{-1} s^{-1}. The fitted model is plotted with the experimental data in Figure 7.12.

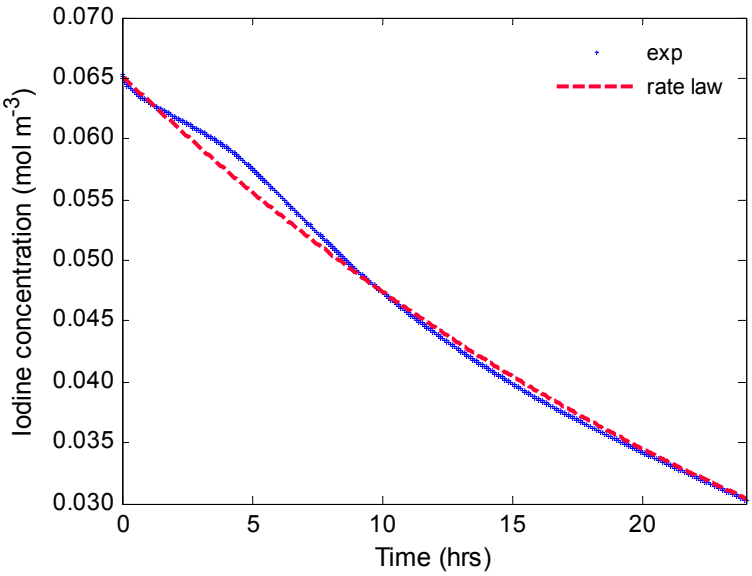

Figure 7.12: Disproportionation of iodine in basic medium

Theoretically, Equation (7.28) is not valid for $n=1$, although the converged solution $n=1.00115$ is very close to this value. If the order of iodine disproportionation is in fact unity (with respect to its concentration), then a plot of $\ln\left(c_{I_2} / c_{I_2,0}\right)$ versus t should be linear, and its slope equal to $-k_2'$. Figure 7.13 clearly confirms this, and the slope yielded $k_2' = 8.94\times10^{-6}$ m^3 mol^{-1} s^{-1}.

Finally, since the time elapsed between the successive samples after each acid injection was known, the disproportionation of iodine over that time period could be calculated using Equation (7.28) and the fitted parameters, and incorporated in the mass balances.

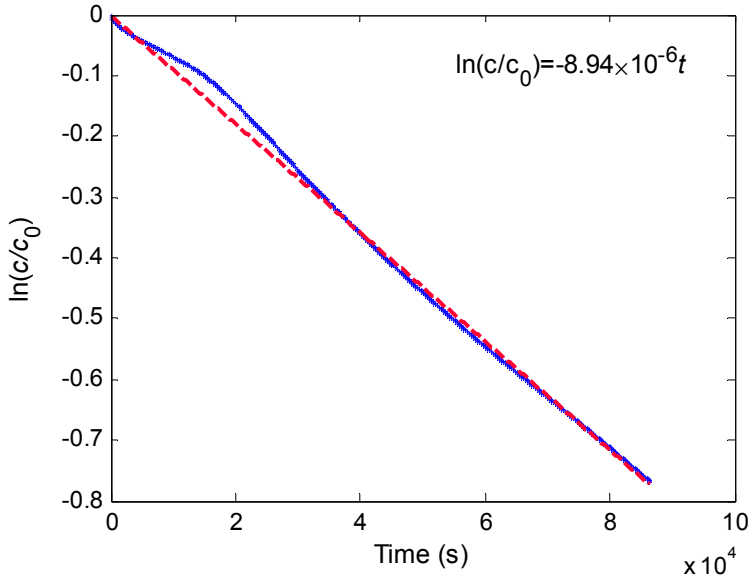

Figure 7.13: Plot of $\ln(c/c_0)$ of iodine concentration versus time

7.1.10 Two-phase micromixing results

Two-phase micromixing experiments were carried out with the same solid particles employed in the PIV experiments; soda-lime glass spheres of upper sizes 300, 750 and 1000 μm. The semi-batch operation was employed in such a way that the first injection of the acid feed entered a pure single liquid phase. After this injection had completed and a sample of the solution extracted for absorption measurement, particles of a given size class were introduced to the medium. Subsequently, the particle concentration was increased between each successive injection. For all three size classes, the maximum percent of particles fed to the tank was 3 vol%; above this level no additional particles could be suspended and a solid slurry accumulated at the vessel base.

Result are expressed as the percentage change in the segregation index (δX_s) compared to the single-phase experiment (i.e. the first injection from that series of semi-batch experiments), shown in Equation (7.29). A positive percentage change in the segregation index would arise from turbulence augmentation; conversely a negative change would arise from turbulence suppression.

$$\delta X_s = \frac{X_s|_L - X_s|_{LS}}{X_s|_L} \tag{7.29}$$

where $X_s|_L$ and $X_s|_{LS}$ is the segregation index from a pure liquid phase reaction, and an analogous reaction in the presence of solids, respectively. Figure 7.14 shows the results of micromixing experiments with 300 μm particles in the tank, up to 3 vol%. Each trend line depicts a repeated experiment. The deviations between repeats could arise from even a small difference in the location of the feed position, each time the experiment is reconfigured. Note that a deviation of 1 mm in the feed position would change the turbulence level of the

environment by up to 45%, and the degree of turbulence modulation at that position may also be variable. Notwithstanding this difference, all of the trend lines appear to follow the same pattern. The particles seem to dampen the turbulence at lower concentrations, but have the reverse effect of increasing turbulence at larger concentrations. This transition seems to occur at approximately 1 vol%. If it is true that the regime changes for a given particle size with respect to concentration, this may explain the many contradictions reported in literature, for which experiments are carried out at discrete volume fractions.

According to the criterion of Gore and Growe (1989), turbulence augmentation is not expected from particles of this size. However, the critical ratio ($d_p / L < 0.1$) put forward by these authors does not take into account particle concentration. There is confidence that the experimental results shown here are not due to experimental error, which has been quantified and found to cause a maximum change in the segregation index of 5%. The percentage change in yield observed in the two-phase experiments with 300 µm particles is double the maximum error, at around 10%.

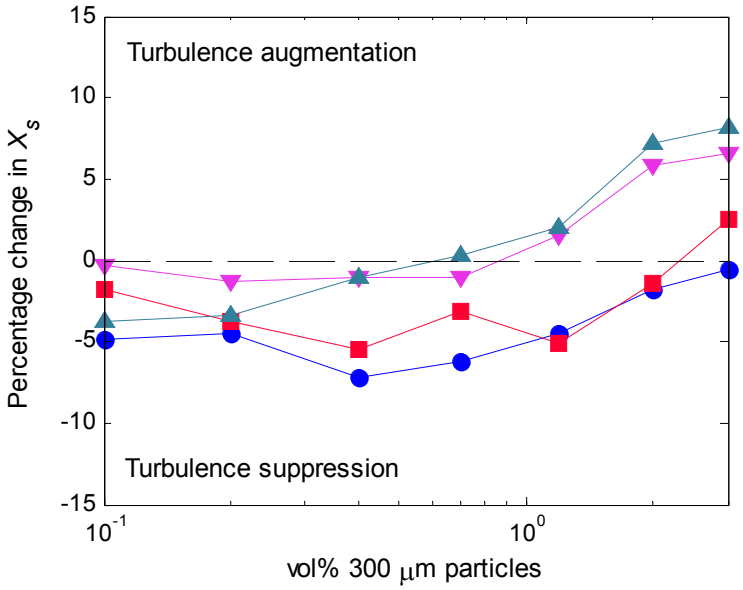

Figure 7.14: Percentage change in segregation index relative to a single-phase experiment, in the presence of 300 µm particles up to 3 vol%. Each trend line depicts a repeated experiment.

In the event that iodine forms in the tank due to oxidation of potassium iodide, the segregation index would increase, or alternatively the percentage change in segregation index would decrease. This effect would be strongest at the highest volumetric concentrations, as the solution would have been exposed to the atmosphere for the longest period of time when 3 vol% had been reached (since the concentration of particles was increased gradually over the time). Despite this, the yield of iodine is showing the opposite effect and decreasing. So even with the possible oxidation of potassium iodide, there must be a genuine increase in the dissipation rate to promote micromixing. Secondly, the smallest particles might be expected to increase the fluid mean viscosity; hence a decrease in the segregation index could be an artefact of this change in fluid properties. The viscous-convective deformation of fluid elements

is considered to be the most important feature of micromixing, and discussed in §7.3. Instead, the results are counteracting this idea, suggesting that there is a real interaction between the particles and turbulence, causing augmentation at high concentrations.

Some preliminary experiments carried out over smaller ranges of particle concentration, starting arbitrarily either above or below 1 vol%, showed the same trend. These shorter discrete sets of data are plotted in Figure 7.15. From these results it may be observed that regardless of the start point of the experiment, particles suppressed turbulence below ~1 vol% and augmented it above ~1 vol%. By allowing the experiment to start at concentrations above the 1 vol% mark, the effect of time dependent factors (such as oxidation of KI or disproportionation of I_2) are safely neglected, and validate the observations of the longer time experiments in Figure 7.14.

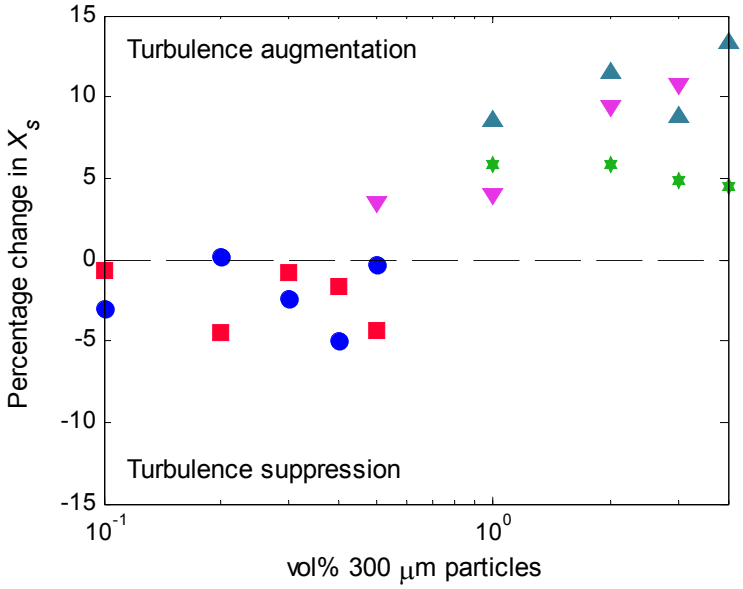

Figure 7.15: Preliminary results of change in segregation index relative to a single-phase experiment, in the presence of 300 μm particles, over discrete ranges of vol%

The change in regime of turbulence suppression to augmentation may be linked to particle concentration, if it is assumed that the two-phase flow changes from being dilute to dense over the concentration range studied (the transition occurring ~1 vol%). In a dilute flow, the motion of particles would be governed by the surface and body forces on that particle exerted by the fluid, but in a dense flow the motion may be controlled by particle-particle collisions. Note that 3 vol% would not normally be considered as dense, but in practice the particles were not suspended homogeneously throughout the tank, and there were much higher concentrations near the impeller region and bottom quarter of the vessel. Subsequently, a dense flow may be more descriptive of the region of interest.

At low particle concentrations, Gore and Crowe's theory may be applied to interpret the turbulence suppression by the 300 μm particles, for which $d_p / L < 0.1$. At higher particle concentrations, a cloud of particles could be causing a laminar displacement of the fluid, and the momentum flux associated with the displaced fluid may behave like a Reynolds stress in the carrier phase (Crowe *et al.*, 1996). Alternatively, the dispersed phase may have a fluctuating

velocity associated with it, due to particle-particle collisions. The fluctuating kinetic energy of these particle-particle collisions is referred to as the 'granular temperature', which may also affect the turbulence of the continuous phase (Crowe *et al.*, 1996).

Figure 7.16 shows similar results of changes in the segregation index with 750 µm particles in the flow. In this case there is no obvious trend with respect to particle concentration, so the observed fluctuations may be due to experimental error, which could give rise to a 5% change in yield. Most of the percentage changes in yield are below 5%, but exceed it when the particle concentration reaches 3 vol%. Despite there being no apparent trend, the yields obtained in the two-phase mixture do suggest turbulence suppression. However, the results are considered to be inconclusive. Ferrante and Elghobashi (2003) performed DNS simulations to study modulation of isotropic turbulence by particles with $0.1 < St < 5$ (defined relative to the Kolmogorov time scale). Results showed that dispersed particles with $St = 0.25$ modified the TKE and its dissipation rate spectra in such a way that these properties remained nearly identical to that of the particle-free case. The authors stated that turbulence modulation by these particles would not be detected by examining only the temporal behaviour of the TKE spectra $E(t)$ experimentally, even though the energy spectra $E(k)$ showed suppression at low wave numbers, and augmentation at high wave numbers. Subsequently these were denoted 'ghost particles'. It is possible that the 750 µm particles in the current experiments behave in an analogous manner. However their energy spectra $E(k)$ would have to be analysed, which would require data resolved down to the Kolmogorov scale to view the entire wave number range. Note that the value $St = 0.25$ is not universal, but depends on the microscale Reynolds number, mass fraction, magnitude of gravitational acceleration, so it is entirely plausible that the 750 µm particles could be 'ghost particles' at a higher St in the present case.

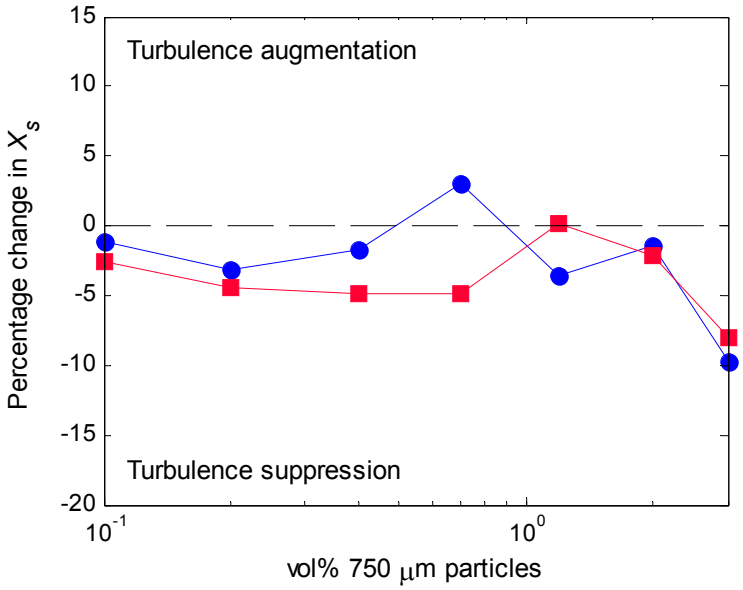

Figure 7.16: Percentage change in segregation index relative to a single-phase experiment, in the presence of 750 µm particles up to 3 vol%. Each trend line depicts a repeated experiment.

Finally, repeated experiments with the 1000 µm particles show great consistency. In Figure 7.17, all trend lines fall into the regime of turbulence suppression, and the percentage change in yield increases continuously with respect to particle concentration. As was mentioned before a general increase in the by-product yield (or negative percentage change in segregation index) may be due to the oxidation of potassium iodide. However once again, the level of change observed in the two-phase experiments (12-13% at 3 vol% particles) exceeds the change which may be attributed to oxidation and/or experimental error (~5%). Ferrante and Elghobashi (2003) showed that particles with $St > 1$ decrease the TKE and dissipation rate. Specifically, particles with $St = 5$ were found to dampen the TKE by 30% at concentrations as low as 0.1 vol%. This finding supports the current results that large particles suppress turbulence. At the same time their results showed that particles with $St = 0.1$ augmented turbulence, which would contradict the vortex shedding theories of Hetsroni (1989) and Owen (1969). The authors provided a mechanism for turbulence modulation for the particles which were smaller than the Kolmogorov scale, and involved their interaction with vortices also at that scale. Consequently the mechanism is not applicable here.

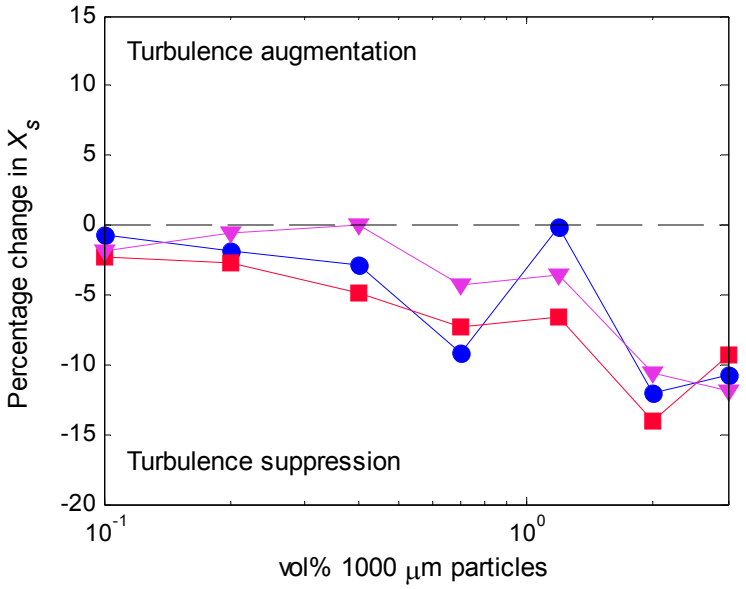

Figure 7.17: Percentage change in segregation index relative to a single-phase experiment, in the presence of 1000 µm particles up to 3 vol%

The previous PIV results had also shown turbulence suppression by the large particles, but there were initial reservations in judgement because this finding contradicts the commonly adopted theory of Gore and Crowe (1989). However, the micromixing experiments presented here also show turbulence damping by large particles, supporting the earlier PIV observations.

7.2 Bourne reaction scheme

Two-phase micromixing experiments were also carried out using the Bourne reaction scheme, to check whether similar turbulence modulation effects could be detected. The scheme consists of two parallel reactions; an acid-base neutralisation and the alkaline hydrolysis of ethyl

chloroacetate, as shown in Equations (7.30) and (7.31) respectively. Ethyl chloroacetate is a toxic substance, which limits its application, and makes the Villermaux scheme more attractive.

$$\mathrm{NaOH} + \mathrm{HCl} \xrightarrow{k_1} \mathrm{NaCl} + \mathrm{H_2O} \tag{7.30}$$

$$\mathrm{NaOH} + \mathrm{CH_2ClCOOC_2H_5} \xrightarrow{k_2} \mathrm{CH_2ClCOONa} + \mathrm{C_2H_5OH} \tag{7.31}$$

Both reactions are assumed to be second-order and irreversible Yu (1993), and their kinetics have been well identified. The acid-base neutralisation is considered to be instantaneous relative to the hydrolysis and also the micromixing time, with a rate constant $k_1 = 1.3 \times 10^8$ m^3 mol^{-1} s^{-1} (Eigen and DeMaeyer, 1955). A detailed discussion of the ester hydrolysis kinetics may be found in the work of Yu (1993). The main point is that the rate of alkaline hydrolysis is significantly faster than the rates of neutral and acid-catalyzed hydrolyses. Subsequently, the rate law for this reaction may be expressed as:

$$r_2 = -k_2 c_{\mathrm{NaOH}} c_{\mathrm{ECA}} \tag{7.32}$$

The second-order rate constant for the acid hydrolysis has been given by Nolan and Amis (1961) as below:

$$k_2 = 2 \times 10^5 \exp\left(-3.891 \times 10^4 / RT\right), \text{ units m}^3 \text{ mol}^{-1} \text{ s}^{-1} \tag{7.33}$$

The current work considers the experimental case where a small volume of concentrated sodium hydroxide solution is added to a relatively large volume of pre-mixed hydrochloric acid and ethyl chloroacetate solution in the tank. After completion of the feed addition, the product distribution X_Q of the sodium salt may be obtained if the residual concentration of ethyl chloroacetate is known.

$$X_Q = \frac{V_0 c_{\mathrm{ECA},0} - (V_0 + V_{\mathrm{NAOH}}) c_{\mathrm{ECA}}}{V_{\mathrm{NAOH}} c_{\mathrm{NaOH},0}} \tag{7.34}$$

In Equation (7.34), ECA denotes ethyl chloroacetate, V_0 the liquid volume in the tank at the start of the reaction and V_{NaOH} the total volume of sodium hydroxide fed to this mixture.

When mixing is rapid and intense, the product distributions are determined only by the kinetics. Since the acid-base neutralisation is deemed to be instantaneous relative to the hydrolysis, ethyl chloroacetate does not react, hence $X_Q = 0$. On the other hand in a fully segregated regime, the kinetics become unimportant and $X_Q = 0.5$. In partially segregated mixtures arising from insufficient micromixing $0 < X_Q < 0.5$.

7.2.1 Chemical analysis

Samples of the reaction mixture were analysed via GCMS. The column used was from Restek, type Rtx-5MS (Crossbond 5% diphenyl – 95% dimethyl polysiloxane). Details of the method are summarised in Table 7.3.

Table 7.3: Details of the GCMS method

Column	
Length	50 m
Internal diameter	0.25 mm
Film thickness	0.25 µm
Chromatograph	
Column initial temp	35 °C (6 mins)
Column ramp temp	10 °C per min
Column final temp	200 °C (1 min)
Injection	
Injector temp	230 °C
Split (purge:column) ratio	50:1
Detector	
MS source setpoint	230 °C
MS Quad setpoint	150 °C
Acquisition mode	Scan

The reactive mixture contains unreacted HCl and $CH_2ClCOOC_2H_5$ as well as the primary and secondary products $NaCl$ and H_2O, and primary and secondary by-products $CH_2ClCOONa$ and C_2H_5OH. The chromatogram of a sample solution containing 2000 ppm of ethyl chloroacetate, ethanol, monosodium salt and butanone is illustrated in Figure 7.18.

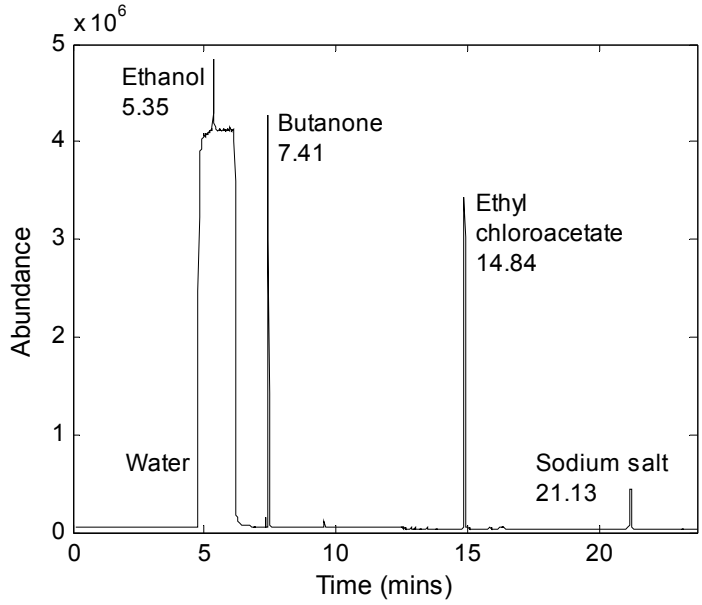

Figure 7.18: Chromatogram of a sample reactive mixture

From this it may be observed that the chromatogram has a relatively flat baseline, and that the ethyl chloroacetate peak is well resolved. Note that the ethanol peak is lost in the broader signal generated by water. This is not problematic as either the residual reactant or primary by-product concentration may be used to evaluate X_Q, and in this case the former may be quantified. Thus the method described in Table 7.3 is satisfactory to analyse the reaction mixture. Butanone, ethyl chloroacetate and sodium salt have retention times 7.41, 14.84 and 21.13 mins respectively. The peak areas may be determined from the output of the digital integrator with the GCMS software.

The following discussion describes the technique of analysing the reactant mixture to obtain the concentration of residual ethyl chloroacetate.

7.2.2 Internal standard technique

An internal standard method was applied to make quantitative determination of a given substance (in this case the ethyl chloroacetate) more efficient. In this technique, a known amount of standard solution is mixed with the sample prior to the GCMS injection. The ratios of the corresponding areas of the standard and analyte may then be used to determine the unknown concentration. The ratios of the areas are proportional to their respective molar concentrations as below:

$$\frac{A_a}{A_s} \propto \frac{c_a}{c_s} \tag{7.35}$$

where the subscript a denotes the analyte and s denotes the internal standard. If the concentrations do not vary significantly, the ratio of the number of moles to area of a given substance is a constant:

$$r_i = \frac{\text{mols}_i}{A_i} \tag{7.36}$$

Given that the volume injected into the GCMS column is the same for each sample, which contains the unknown solution as well as the internal standard, the moles in Equation (7.36) may be replaced with concentration. It follows that Equation (7.36) may be expressed as:

$$\frac{A_a}{A_s} = \frac{r_s}{r_a}\frac{c_a}{c_s} \tag{7.37}$$

The ratio r_a / r_s will be referred to as the response factor RF. If this is known *a priori* with the concentration of the standard solution and peak areas from the GCMS chromatogram, then the unknown concentration of the analyte may be determined as:

$$c_a = \frac{A_a}{A_s} RF c_s \tag{7.38}$$

The response factor may be determined via a calibration procedure, through the analysis of solutions of known concentrations of both the analyte and the internal standard.

The requirement of an internal standard is that it should be stable in the reactive mixture, have a retention time close to the primary by-product ethyl chloroacetate, be soluble in water (as it is an aqueous system) and produce a distinguishable peak. Butanone was found to be suitable for this purpose, as it fulfils these criteria, and is shown in the chromatogram Figure 7.18. An aqueous solution containing 2000 ppm butanone and ethyl chloroacetate was analysed using GCMS, at time intervals of 1 hour for 3 hours. The peak ratios were found to be 1.16, 1.15, 1.16 and 1.16 respectively, confirming its stability. Samples were analysed within this time scale at the end of each experiment. Similar tests for adsorption of ethyl chloroacetate and butanone on the particles were also carried out, with 1000 μm particles at 4 vol% in the mixture. The peak ratios remained stable over 3 hours, verying the absence of adsorption.

7.2.3 Calibration

For the calibration, various aqueous solutions of known concentrations of ethyl chloroacetate and butanone internal standard were prepared. The concentrations were interpreted as molar, however all chemicals were measured on a mass basis to obtain higher accuracy of the measurement, and converted to molar concentrations later. The calibration procedure allows determination of the ethyl chloroacetate concentration range where RF is constant.

The initial ethyl chloroacetate concentration in the micromixing experiments was 90 mol m^{-3} or ~11,000 ppm. Considering that not much reacts (as it is involved in the secondary reaction), the residual ester concentration is of a similar magnitude. This would overload the GCMS column; hence samples were diluted 4 times using water. Assuming no conversion, the maximum residual ethyl chloroacetate concentration injected into the column would be ~22.5 mol m^{-3}, or 2750 ppm. Subsequently, calibration samples were prepared up to this limit, and the butanone concentration was fixed as 20.76 mol m^{-3} or ~1500 ppm in each. The total injected volume into the GCMS was 1 μl. For each calibration sample, average results from a total of 3 consecutive injections were obtained.

Referring back to Equation (7.38), c_a and c_s of the calibration samples are known. Their respective areas A_a and A_s are obtained from digital integration of their peaks, arising from the sample chromatograph after injection. It follows that a plot of c_a versus $\frac{A_a}{A_s}c_s$ generates a straight line, whose gradient is the response factor RF. Calibration results are displayed in this form in Figure 7.19, in which $RF = 0.6998$.

On a final note, peak heights or areas of the internal standard and analyte should be of the same order of magnitude to enable a reasonable comparison of their ratios. During the calibration procedure it was found that peak heights of 2000 ppm (~16.3 mol m^{-3}) ethyl chloroacetate and 1500 ppm (~20.8 mol m^{-3}) butanone were comparable.

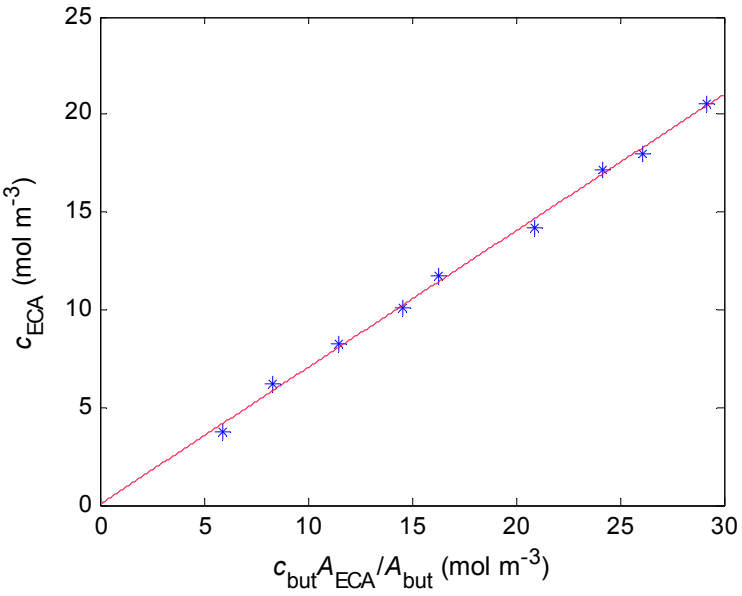

Figure 7.19: GCMS calibration curve of ECA and butanone in water

7.2.4 Experimental method

The experimental set-up was identical to that used in the Villermaux reaction scheme, as shown in Figure 7.2. The feed point was also the same as in Figure 7.1. The by-product yield is affected by the initial concentration of reagents (Bhattacharya and Kresta, 2004). The starting conditions must be selected based on the following two considerations:

1) The product distribution X_Q is the most sensitive to micromixing (i.e. between the perfectly mixed and perfectly segregated regimes) when the reactant quantities are equimolar (Baldyga and Bourne, 1990). Consequently, an equal number of moles of sodium hydroxide, ethyl chloroacetate and hydrochloric acid will be added to the tank.

2) The maximum solubility of ethyl chloroacetate in water is 150 mol m^{-3} at 30.8 °C (Stephenson and Stuart, 1986).

Therefore, an ester concentration of 90 mol m^{-3} corresponding to 60% of the maximum solubility was selected, which is the standard employed in most previous studies (Bourne and Yu, 1994; Baldyga *et al.*, 2001; Battacharya and Kresta, 2004). Naturally the hydrochloric acid concentration should also be 90 mol m^{-3} in the 1 litre vessel. The sodium hydroxide feed volume was 20 ml; hence it was prepared to have a concentration of 4,500 mol m^{-3} to satisfy equimolar conditions. Feed concentrations are summarised in Table 7.4.

Table 7.4: Initial reactant concentrations in the 1 l tank

Reactant	*Concentration (mol l^{-1})*
$CH_2ClCOOC_2H_5$	0.09
HCl	0.09
NaOH	4.50

As the $NaOH$ feed was equimolar, only 1 injection could be added to the tank per experiment. This is a significant disadvantage of the Bourne scheme compared to that developed by Villermaux. For successive injections to be possible as in the Villermaux scheme (§7.1.4), the feed would need to be more dilute, to ensure an excess of the non-limiting reagents already present in the tank, which is not recommended.

The sequence of events was carried out as follows:

- 11.03 g of ethyl chloroacetate was added to 1 litre of reverse-osmosis water and stirred for 30 minutes in the vessel to ensure complete dissolution (Battacharya and Kresta, 2004).
- 90 ml of concentrated 1 M HCl solution was added to the tank and stirred for 2 minutes before a 5 ml sample was extracted for GCMS analysis, from which the initial ester concentration could be deduced.
- If the experiment was to be carried out in the presence of inert glass particles, then they were added to the tank at this stage. If the experiment was conducted in a single liquid medium, no particles were added and the next step was implemented.
- 20 ml of the feed solution (prepared by dissolving $NaOH$ pellets in reverse-osmosis water) was injected into the tank. At the end of feed injection, the solution was allowed to stir for 2 minutes to ensure homogenization of the tank contents. Finally another 5 ml sample was removed to obtain the residual ester concentration.
- The 5 ml samples were diluted 4 times by adding 15 ml of pure water, and doped with the butanone internal standard of known concentration. Specifically, 1500 ppm butanone was added, to generate a peak height comparable to the ester in the GCMS chromatogram, which was expected to have a concentration near 2000 ppm.
- Once the initial and final concentration of ester was inferred from Equation (7.38), X_Q could be calculated via Equation (7.34).

Note that comparisons of X_Q from single- and two-phase systems had to be made between different experiments. As the vessel requires cleaning between each run, slight differences in reconfiguration (e.g. impeller clearance or feed location) could influence the yield. This problem was completely eliminated in the Villermaux scheme, which allowed successive feed injections and subsequently cross-comparison of data from the same experiment.

7.2.5 Critical feed time

The relevance of the critical feed time was discussed in §7.1.6. Experiments to determine this parameter were carried out at 500 rpm. Results of X_Q versus feed time for the Bourne reaction scheme are shown in Figure 7.20.

As expected, the by-product yield decreases with feed time, and stabilises towards its minimum value when $t = 1200$ s, corresponding to a feed rate 1 ml min^{-1} for a 20 ml injection. The experiment with feed rate 1 ml min^{-1} was repeated, and is also shown in the plot with a different

marker (red circle). The difference between X_Q at these identical conditions is 3.3% which provides an indication of the experimental error. Subsequently, all following experiments were carried out at with feed time $t = 1200$ s.

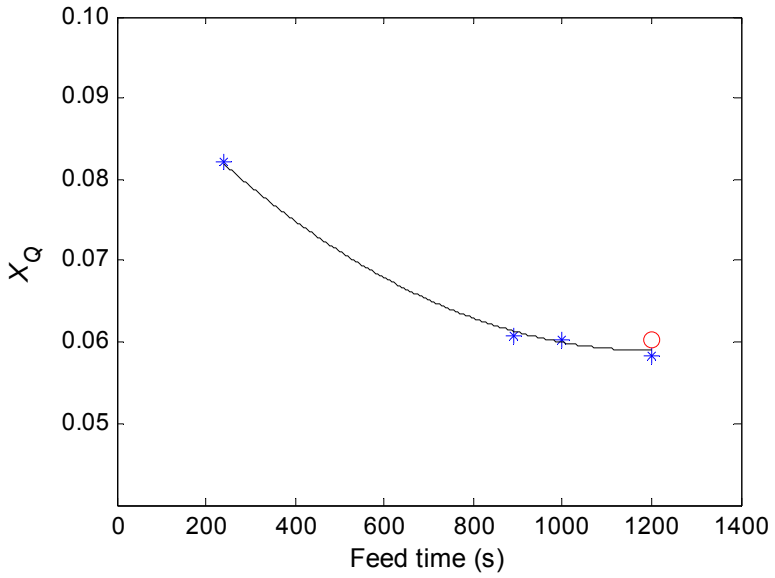

Figure 7.20: Effect of feed time on product distribution at impeller speed 500 rpm. The red circle represents a repeated experiment at feed time 1200 s.

The average of the two product distributions obtained at the critical feed time is $\overline{X_Q} = 0.06$. This value is similar to that reported in literature for a feed in the discharge stream and RDT operated at the same Damköhler number; $Da = 10.2$ and $X_Q \sim 0.07$ (Bourne and Yu, 1994). The Damköhler number is the ratio of characteristic micromixing and chemical reaction times, defined in Equation (7.53). Subsequently, the single-phase product distribution is thought to be a reliable estimate, and used a basis of comparison in proceeding two-phase experiments.

7.2.6 Sensitivity of product distribution

The responsiveness of the reaction scheme to the fluid hydrodynamics is shown in Figure 7.21(a). Yield sensitivity to the system turbulence is demonstrated, since the product distribution decreases with increasing impeller speed. However the sensitivity declines at high impeller speeds, as is shown more clearly in Figure 7.21(b), where the yield is plotted versus the mean power dissipation rate. From this chart yield sensitivity is lowest when $N = 700$ rpm and $\bar{\varepsilon} = 0.104$ W kg^{-1}. Note that $N = 800$ rpm and $\bar{\varepsilon} = 0.156$ W kg^{-1} was found to be optimum in the Villermaux scheme, making it more appropriate to the application of two-phase flows where particles need to be suspended at relatively high speeds. Secondly, the absolute measure of yield in the Bourne scheme is quite low; $X_Q = 0.06$ compared to $Y = 0.18$ or $X_S = 0.25$ in the Villermaux scheme, both at 500 rpm. Under these chemical conditions, the Bourne scheme appears even less suitable at high impeller speeds, as product yields would decline to such small levels that measurement errors could become significant.

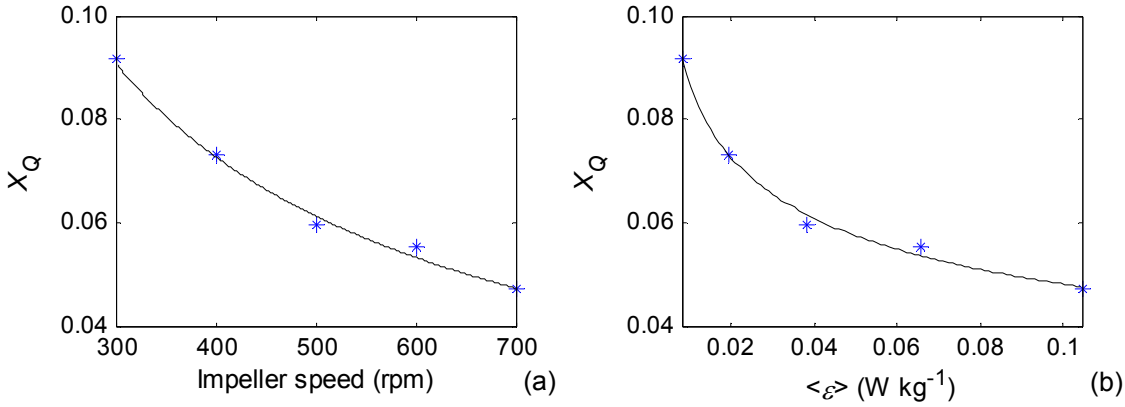

Figure 7.21: Variation of product distribution with respect to (a) impeller speed and (b) mean power dissipation rate

For the reasons outlined above, two-phase experiments were carried out at 500 rpm and $\bar{\varepsilon} = 0.04$ W kg^{-1}, where good yield sensitivity could be attained. The limitation is that lower particle concentrations could be suspended compared to the Villermaux experiments (just suspended speed of 300 μm particles in water at 0.02 vol% is 537 rpm, compared to 817 rpm for 0.5 vol% according to the Zwietering correlation).

In the two-phase experiments employing the Bourne scheme, 70-100 μm particles were suspended up to 1.75 vol% and 250-300 μm up to 1.2 vol%. One set of repeated-injection experiments was also run using the Villermaux scheme with 70-100 μm particles up to 3 vol%, to enable cross-comparison with the new data presented in this chapter.

7.2.7 Two-phase micromixing results

The percentage change in yield from the Bourne reaction scheme after adding particles to the reactive mixture was defined as follows:

$$\delta X_Q = \frac{X_Q\big|_L - X_Q\big|_{LS}}{X_Q\big|_L} \tag{7.39}$$

where $X_Q\big|_L$ is the product distribution from a pure liquid phase reaction, and $X_Q\big|_{LS}$ the distribution from an analogous reaction in the presence of solids. Although X_Q and X_S from the Bourne and Villermaux reactions schemes respectively are different quantities (the former is an absolute yield and latter is relative), Equation (7.39) and (7.29) are directly comparable, as both express *changes* in yield. Results of micromixing experiments carried out with 100 and 300 μm particles in both reaction schemes are presented in Figure 7.22.

Looking at the Bourne scheme alone, both 100 and 300 μm particles have the effect of damping turbulence. The peculiar trend which was observed in the Villermaux scheme for the 300 μm solids is once again repeated here. At concentrations below 1 vol%, particles increasingly suppress the dissipation rate with respect to concentration. Above 1 vol% however the regime alternates; the level of turbulence damping decreases. Previously Figure 7.14 showed that not

only did the level of suppression decrease, but in some experiments the particles caused turbulence augmentation, such that the percentage change in yield became positive. The 100 µm particles have a much greater effect than the 300 µm particles at equivalent concentrations, suggesting that particle size is an important factor. At 0.75 vol%, they caused a change in yield of -26.63 and -8.88% respectively.

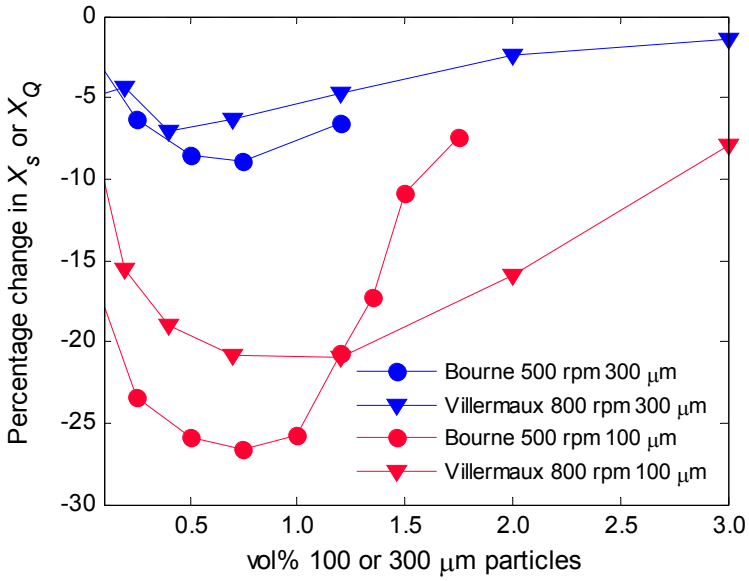

Figure 7.22: Percentage change in yield relative to a single-phase experiment, in the presence of 100 or 300 µm particles, in both Bourne and Villermaux reaction schemes

Results from the Villermaux experiments are plotted in the same graph. Note that four repeated experiments were carried out with the 300 µm particles but only one set is displayed here for clarity. The trends are in very good agreement with the Bourne scheme, as are the percentage changes in yield. In most cases, at equivalent concentrations, the levels of changes agree within 5%, which was evaluated to be experimental error in the Villermaux scheme with repeated feed injections. Differences up to 10% would not be unusual, as this was found to be the maximum error in yield between identical experiments due to reconfiguration of the vessel. Notwithstanding the deviations, the pattern of turbulence damping is evident below ~1 vol%, and reduction in turbulence above 1 vol%. Again 100 µm particles have a greater impact on the dissipation rate.

An alternative interpretation for the difference in percentage changes between the two size classes may be owed to particle number, which is indirectly linked to size. For the smaller size, there are more particles in the fluid than the larger size at the same volume fraction. Following on from the theory of Gore and Crowe (1989), the most energetic eddies would be able to impart their energy to more particles, which would reduce the turbulence intensity of the carrier phase to a greater extent. At higher concentrations where collisions become important, the smaller particles would have a higher collision frequency due to the larger number, thereby increasing the granular temperature of the particles, which is transferred back to the fluid.

7.3 Engulfment model of micromixing

Micromixing consists of the viscous-convective deformation of fluid elements, followed by molecular diffusion. The viscous-convective process accelerates molecular diffusion; the former effect is considered to be the most important feature of micromixing. Baldyga and Bourne (1989) showed that for $Sc < 4000$, the effects of molecular diffusion become negligible compared to the effects of viscous-convective stretching, which results in fluid incorporation into the reaction zone. Baldyga and Bourne (1989) have also suggested that the mechanism which dominates environment incorporation in turbulent mixing is the process of engulfment into the vortex.

By analysing the time spectrum of turbulence, the aforementioned authors showed that the most hydrodynamically active eddies (with the highest vorticity) have a characteristic size of $\sim 12\eta$, and are thought to form an important part in the dissipating structure of turbulence. Vortices of this characteristic length scale are quite stable, as they undergo stretching and dissipation in equilibrium. The stretching process of the stable size leads to elongation of concentration spots within the eddy, which results in the intake of the fluid environment via convection. This process of environment incorporation within the reaction zone (or turbulent eddy) is called 'engulfment'. The supposition that engulfment controls mixing at scales smaller than or comparable to the Kolmogorov scale, has lead to the development of the engulfment or E-model.

The current section employs the E-model to estimate product distributions resulting from the Bourne reaction scheme, for which information of the mean flow field and dissipation rate from single-phase PIV experiments will be utilised. Predicted yields will be compared to single-phase micromixing experimental data; in this way the quality of PIV results may be assessed.

7.2.8 E-model equations for the Bourne reaction scheme

The E-model considers the situation where a small volume of a reactant with high concentration in the feed, is added to a large volume of a more dilute second (or third) reactant within the vessel. The volume of the reaction zone (V) then grows according to the engulfment relation given in Equation (7.40).

$$\frac{dV}{dt} = EV \tag{7.40}$$

where E is the engulfment rate coefficient, which is related to the local dissipation rate and fluid viscosity as follows:

$$E = 0.058\left(\frac{\varepsilon}{\nu}\right)^{0.5} \tag{7.41}$$

A material balance for substance α (for any reactant) within the growing eddy is:

$$\frac{d(Vc_\alpha)}{dt} = EV < c_\alpha > + r_\alpha V \tag{7.42}$$

where $< c_\alpha >$ is the concentration of substance α in the environment of the reaction zone, c_α without parentheses the concentration of substance α within the reaction zone, and r_α the rate of reaction of substance α. The first term on the r.h.s. of Equation (7.42) is the rate of addition of α into the eddy via engulfment, and the second term is the production via reaction. Substitution of Equation (7.40) into (7.42) provides the evolution equation for concentration in the reaction zone:

$$\frac{dc_\alpha}{dt} = E(< c_\alpha > - c_\alpha) + r_\alpha \tag{7.43}$$

Equation (7.43) does not include self engulfment between eddies of the feed reactant, which may be neglected when only small volume fractions of the feed are added to the vessel.

The Bourne reaction scheme and kinetics were provided in §7.2, whereby NaOH reacts with HCl and $\mathrm{CH_2ClCOOC_2H_5}$ (or ECA), to give the primary product NaCl and by products $\mathrm{CH_2ClCOONa}$ and $\mathrm{C_2H_5OH}$ (denoted 'salt' and EtOH here on). On the basis of Equation (7.43), the material balance for each reactant within the reaction zone may be written as:

$$\frac{dc_{\mathrm{NaOH}}}{dt} = E(< c_{\mathrm{NaOH}} > - c_{\mathrm{NaOHA}}) - k_1 c_{\mathrm{NaOH}} c_{\mathrm{HCl}} - k_2 c_{\mathrm{NaOH}} c_{\mathrm{ECA}} \tag{7.44}$$

$$\frac{dc_{\mathrm{HCl}}}{dt} = E(< c_{\mathrm{HCl}} > - c_{\mathrm{HCl}}) - k_1 c_{\mathrm{NaOH}} c_{\mathrm{HCl}} \tag{7.45}$$

$$\frac{dc_{\mathrm{ECA}}}{dt} = E(< c_{\mathrm{NaOH}} > - c_{\mathrm{NaOH}}) - k_2 c_{\mathrm{NaOH}} c_{\mathrm{ECA}} \tag{7.46}$$

Given that E_{av} is the engulfment rate coefficient evaluated at the average power per unit volume in the tank, and $c_{\mathrm{NaOH},0}$ the initial concentration of limiting reagent NaOH, the following dimensionless variables may be defined.

$$T = tE_{av} \tag{7.47}$$

$$C_\alpha = \frac{c_\alpha}{c_{\mathrm{NaOH},0}} \tag{7.48}$$

Equations (7.47) and (7.48) may then be used to obtain dimensionless mass balance equations for all reactants as follows:

$$\frac{dV}{dT} = \phi^{0.5} V \tag{7.49}$$

$$\frac{dC_{\mathrm{NaOH}}}{dT} = \phi^{0.5} \left[< C_{\mathrm{NaOH}} > - C_{\mathrm{NaOH}} \right] - Da_1 C_{\mathrm{NaOH}} C_{\mathrm{HCl}} - Da_2 C_{\mathrm{NaOH}} C_{\mathrm{ECA}} \tag{7.50}$$

$$\frac{dC_{\mathrm{HCl}}}{dT} = \phi^{0.5}\left[< C_{\mathrm{HCl}} > - C_{\mathrm{HCl}}\right] - Da_1 C_{\mathrm{NaOH}} C_{\mathrm{HCl}} \tag{7.51}$$

$$\frac{dC_{\mathrm{ECA}}}{dT} = \phi^{0.5}\left[< C_{\mathrm{ECA}} > - C_{\mathrm{ECA}}\right] - Da_2 C_{\mathrm{NaOH}} C_{\mathrm{ECA}} \tag{7.52}$$

where the parameter Da_i is the Damköhler number for reaction i. The Damköhler number represents the degree of micromixing; it is the ratio of characteristic times for micromixing and chemical reaction. The greater the Damköhler number, the smaller the extent of micromixing relative to the reaction rate. The parameter ϕ is the ratio of local-to-average dissipation rate. These parameters are defined in Equations (7.53) to (7.55) as follows:

$$Da_i = \frac{k_i c_{\mathrm{NaOH},0}}{E_{av}} \text{ where } i = 1 \text{ or } 2 \tag{7.53}$$

$$\phi = \frac{\varepsilon}{\bar{\varepsilon}} \tag{7.54}$$

$$\frac{E}{E_{av}} = \left(\frac{\varepsilon}{\bar{\varepsilon}}\right)^{0.5} = \phi^{0.5} \tag{7.55}$$

For a certain degree of micromixing (or at a constant impeller speed), the concentration of reagent ECA at the end of reaction may be obtained from the solution of Equation (7.52), solved simultaneously with Equations (7.50) and (7.51), given that the engulfment rate coefficient E is known along the trajectory of the reaction zone. The product distribution of ECA (denoted X_Q) may then be determined through Equation (7.34) shown previously.

7.2.9 NaOH added to premixed HCl and ECA

Consider the addition scheme used in the current micromixing experiments, where pure NaOH was added to premixed HCl and ECA in a semi-batch process, depicted in Figure 7.23.

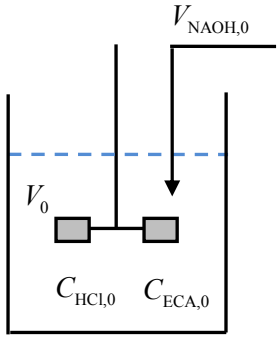

Figure 7.23: NaOH **added to pre-mixed** HCl **and** ECA

The initial dimensionless concentrations of reagents in the reaction zone are:

$$C_{\mathrm{NaOH}}(0) = C_{\mathrm{NaOH},0} = 1$$

$$C_{\mathrm{HCl}}(0) = 0 \tag{7.56}$$

$$C_{\mathrm{ECA}}(0) = 0$$

The initial dimensionless concentrations of reagents in the vessel bulk are:

$$< C_{\mathrm{NaOH}} > (0) = 0$$

$$< C_{\mathrm{HCl}} > (0) = C_{\mathrm{HCl},0} \tag{7.57}$$

$$< C_{\mathrm{ECA}} > (0) = C_{\mathrm{ECA},0}$$

Baldyga and Bourne (1989) proposed the following procedure to calculate the concentration of the reactants in the bulk, as the reaction proceeds. It is assumed that the volume of NaOH solution is added to the reactor in a discretized manner with a total of σ parts, each of initial volume $V(0) = V_{\mathrm{NaOH},0} / \sigma$ and concentration $C_{\mathrm{NaOH}}(0) = C_{\mathrm{NaOH},0} = 1$. After any part has been added to the vessel, engulfment proceeds; the environment remains constant during engulfment. Subsequently, the environment concentration $< C_\alpha >$ of all reagents remains unchanged during the application of Equations (7.49) to (7.52) to any part of the feed. After each packet of reactant has completely reacted (i.e. when all of NaOH has been depleted in the reaction zone), it is mixed with the environment. Note that macroscopic and mesoscale concentration gradients in the bulk are excluded from this analysis. Also since diffusion is relatively rapid, C_α is assumed to be uniform throughout the reaction zone. Thus, after the addition and reaction of one part, the environment concentration must be updated by a mass balance, before the application of Equations (7.49) to (7.52) to the next feed part entering the vessel. In this way, $< C_\alpha >$ is updated at the start of the integration from one part to the next, but remains constant during the integration process. The mass balance is computed as follows:

- Suppose that the j^{th} part of the feed has been added to the vessel. The volume of the vessel before the addition of the j^{th} part ($V_{B,j}$) may be described as:

$$V_{B,j} = V_0 + \frac{V_{\mathrm{NaOH},0}}{\sigma}(j-1) \tag{7.58}$$

- The j^{th} part of the feed completely reacts in (dimensionless) time $T = T_j$. Then, the concentration of NaOH, HCl and ECA in the eddy, $C_{\mathrm{NaOH}}(T_j) = 0$; $C_{\mathrm{HCl}}(T_j)$ and $C_{\mathrm{ECA}}(T_j)$ are obtained from the solutions of Equations (7.51) and (7.52) respectively, when the aforementioned condition is reached. Each eddy grows according to Equation (7.49), and hence the eddy volume at the end of reaction is:

$$V(T_j) = \frac{V_{\mathrm{NaOH},0}}{\sigma}\left[\exp\int_0^{T_j}\phi^{0.5}dT\right] \tag{7.59}$$

- The volume engulfed by the eddy may be written as:

$$V_{\mathrm{eng}}(T_j) = V(T_j) - V_{\mathrm{NaOH},0}/\sigma \tag{7.60}$$

- The volume of the environment after engulfment is then:

$$V_{\mathrm{env}}(T_j) = V_{B_j} - V_{\mathrm{eng}}(T_j) \tag{7.61}$$

Or in full notation as:

$$V_{\mathrm{env}}(T_j) = V_0 + \frac{V_{\mathrm{NaOH},0}}{\sigma}j - \frac{V_{\mathrm{NaOH},0}}{\sigma}\left[\exp\int_0^{T_j}\phi^{0.5}dT\right] \tag{7.62}$$

The concentration of substance α in the vessel after the j^{th} eddy is mixed with its environment, $<C_\alpha>_j$, may be obtained from Equation (7.63). Subsequently, $<C_\alpha>_j$ is the environment that the $(j+1)^{th}$ feed part enters into, engulfs, and reacts with.

$$<C_\alpha>_j = \frac{<C_\alpha>_{j-1} V_{\mathrm{env}}(T_j) + C_\alpha(T_j)V(T_j)}{V_0 + \frac{V_{\mathrm{NaOH},0}}{\sigma}j} \tag{7.63}$$

7.2.10 Experimental flow model (EFM) for a PBT

Turbulence in a stirred tank exhibits significant inhomogeneity, and is found to be greatest in the discharge stream of a flow agitated by a PBT (shown in §6.2.3). The turbulence level, specifically the dissipation rate, affects the mixing intensity at the microscale. Subsequently after the addition of feed into the stirred tank, reaction takes place under different levels of mixing intensity, as the feed travels along the flow circulation loop. The E-model must account for this inhomogeneity by incorporating the change of the engulfment rate coefficient (E) along the trajectory of the reaction zone. Thus, characterization of micromixing requires experimental evaluations of the spatial distributions of the dissipation rate, as well as the trajectory of the reaction zone.

The concept of an experimental flow model (EFM) was originally developed by Bourne and Yu (1994) for the flow generated by a RDT. The EFM comprises information of the mean velocity and local energy dissipation rate, in different flow zones of the vessel. The mean flow in each of these zones is characterized by plug flow circulation along a streamline. The trajectory of the reaction zone can be evaluated from the velocity field in the EFM, with the dissipation rate along the path. Subsequently, Equations (7.49) to (7.52) may be solved with knowledge of ϕ in a Lagrangian framework.

The current experimental study employs a down-pumping PBT (of standard geometry), for which there is no suggested EFM in literature yet. Consequently, a new EFM has been constructed from the single-phase PIV data introduced in §6.2, and proposed as follows.

Mean velocity

The mean single-phase flow field generated by the respective PBT was shown previously in the vector plot of Figure 6.2. Based on the observed flow pattern in the field of view, the flow was divided into nine regions as shown in Figure 7.24. Note that the PIV field of view only covered part of the vessel, between $0.085 < r/T < 0.354$ and $0.082 < r/T < 0.356$. In order to construct flow regions outside the field of view, the mean velocity flow field obtained by Khan (2005) for a down-pumping PBT was assessed. The author had employed a multi-block approach for a complete view in half of the vessel. In the respective study, the impeller operated at a clearance of $C = T/3$ from the vessel base ($C = T/4$ in the present case). Notwithstanding this difference, the flow field in the top half of the vessel is expected to be comparable.

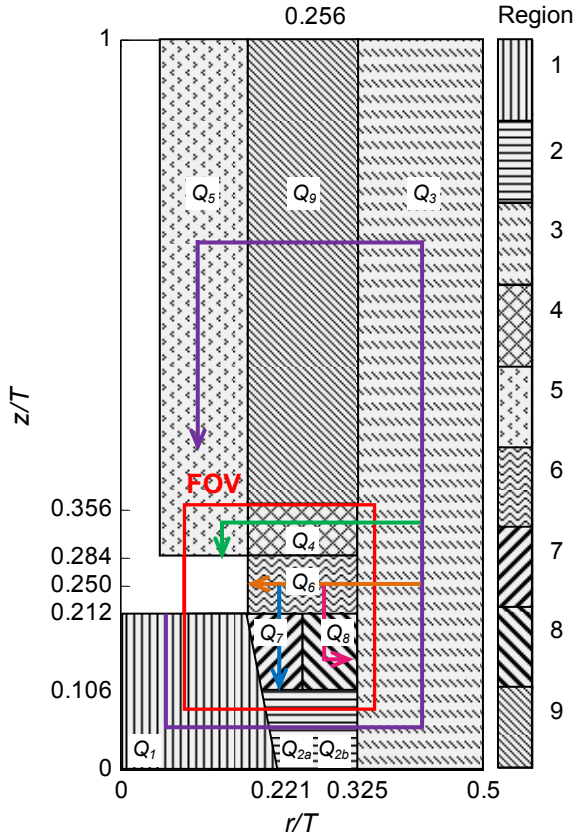

Figure 7.24: Schematic of EFM for the PBT employed in current study (FOV = field of view). The different coloured lines represent five trajectories of the reaction zone.

The flow boundaries in Figure 7.24 were selected such that continuity was satisfied as much as possible between the various regions, from the experimental mean velocity field. The volumetric flows across the boundaries in the radial (Q_{radial}) and axial (Q_{axial}) directions were calculated using Equations (7.64) and (7.65) respectively:

$$Q_{\text{radial}} = 2\pi R \int \left| \bar{u} + \bar{v} \right| dz \tag{7.64}$$

$$Q_{\text{axial}} = 2\pi \int \left| \bar{u} + \bar{v} \right| r dr \tag{7.65}$$

In this way, continuity was checked between all flow regions, and found to be satisfied within 5-15%. Some discrepancy was expected since the tangential velocity component (hence the flow entering or leaving regions in the out-of-plane direction) was unknown.

After the flow boundaries were fixed, the impeller pumping capacity was calculated by integrating the velocity in the horizontal plane directly underneath the blade. The calculation was done analogous to Equation (7.65). However, it may be observed from Figure 7.24 that the field of view (shown by the red line) did not extend as far as the shaft; some flow information was missing. The PIV field of view only covered $0.085 < r/T < 0.354$ and $0.082 < r/T < 0.356$. In order to obtain the unknown velocity data, CFD predictions of the flow field were made (with the assistance of Dr J. Gimbun, Loughborough University).

The stirred vessel was simulated by adopting the multiple reference frame method, implemented in the CFD code Fluent 6.3, which provides a converged steady-state solution of the fluid. The non-linear set of equations (formed via discretization of the Navier-Stokes equations) was solved by a finite control volume technique. The standard $k-\varepsilon$ model was employed for turbulence (Gimbun, 2009). The vessel and tank geometry were modelled for the dimensions specified in §6.1.1, and the working fluid was water. The impeller speed was set at 1600 rpm.

The computational grid comprised two meshes; an inner cylindrical volume enclosing the impeller and an outer volume forming the rest of the vessel separated by an interface. It was assumed that the flow pattern repeats itself over 90° sectors, hence the calculation was restricted to a quarter of the vessel, with cyclic boundaries applied on its exposed surfaces. The computational mesh consisted of 344,248 tetrahedral cells over an azimuthal extension of π/2. The GAMBIT mesh generation tool was employed to create the grid. Care was taken to put additional mesh elements in the regions of high velocity gradients around the blades and in the discharge stream. The effect of grid density has been previously assessed by many researchers (e.g. Scargiali *et al.*, 2007). Generally, a grid consisting of more than 200,000 computational cells can produce a grid independent solution for RANS modelling. In the present case two different meshes were used. The first one comprised 78,486 cells (coarse) and the second one comprised of 344,248 cells (fine). The only difference between the two grids was a local refinement in the impeller discharge region for the finer grid. The results presented below have been obtained by employing the fine mesh.

The current simulation took approximately 12 hours on a quad-core 3.8 GHz processor with 3 GB RAM. In order to make the CFD data comparable with the ensemble-averaged PIV results, the mean velocities at a given grid location were averaged azimuthally over the grid cells. A comparison of the axial velocity underneath the blade edge (where $z/T = 0.212$) resulting from the CFD simulation and 2-D PIV experimental data is shown in Figure 7.25.

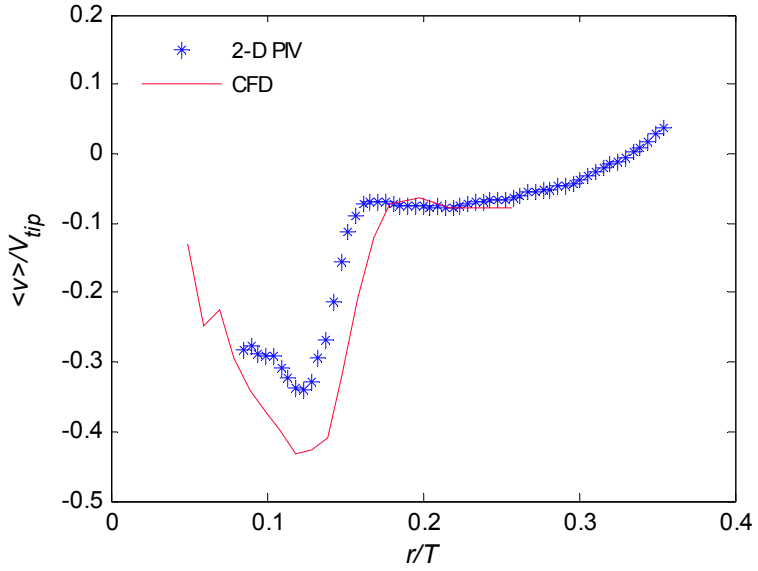

Figure 7.25: Comparison between CFD and PIV data for mean axial velocity of a single-phase fluid, underneath the blade where $z/T = 0.212$

From Figure 7.25 it may be observed that the CFD predictions are in close agreement with the experimental data. The impeller blade edge is located at $r/T = 0.167$. The simulation over predicts the mean axial velocity under the blade at $r/T = 0.124$ by approximately 25%, which is the maximum deviation. However in both directions away from this point, the experimental data is more accurately predicted. Following this observation, the CFD data close to the shaft ($0.05 < r/T < 0.085$) combined with the PIV experimental data under the blade ($0.085 < r/T < 0.167$) (both on the plane $z/T = 0.212$) was integrated radially to achieve a more complete estimate of the pumping capacity. The flow number was obtained from the pumping capacity via Equation (7.66), and found to be 0.552. The value is lower than those reported in literature for PBTs; 0.93 by Ranade and Joshi (1989), 0.88 by Hockey and Nouri (1996) and 0.86 by Khan (2005). Khan (2005) showed that the flow number calculated at a greater distance from the blades is higher than that calculated closer to blades, due to entrainment of fluid into the discharge stream. It should be noted that in this case the flow number was calculated at the blade edge, which could be the cause of the lower estimate.

$$N_Q = Q/ND^3 \tag{7.66}$$

The pumping capacity provided a starting point of the flow volume driven by the impeller in region 1, Q_1. The split fractions of the flow at conjunctions with other regions were obtained from the experimental data in the field of view (FOV). Outside the FOV the mass balance was completed to ensure that continuity was always satisfied. So for instance, consider the axial flow along the vessel wall Q_3, which sequentially splits into Q_8, Q_6, Q_4 and Q_9. The flows Q_8, Q_6 and Q_4 were determined from the integration of the experimental velocity at the respective boundaries using Equation (7.64). Then, for Q_9 which is outside the FOV, $Q_9 = Q_3 - Q_8 - Q_6 - Q_4$. After volumetric flows in all regions were established, velocities were

simply obtained by dividing through by the cross sectional areas at the boundaries. The resultant velocities (normalized by V_{tip}) are given in Table 7.5. Note that region 2 has been further divided into '*a*' and '*b*'.

Table 7.5: Dimensionless mean velocities in each region of EFM

Region	$v^* = \bar{v} / V_{tip}$	$u^* = \bar{u} / V_{tip}$
1	-0.5588*z** - 0.1271	0
2a	0	3.995*r** - 0.2979
2b	0	-2.253*r** + 1.313
3	-1.694*z** + 0.603	0
4	0	-0.3217*r** + 0.04307
5	0.029*z** - 0.152	0
6	0	0.257*r** - 0.1035
7	0.2055*z** - 0.1204	0
8	0	-0.08127*r** + 0.04777
9	0	-0.01616*r** - 0.01125

Local dissipation rate

The dissipation rate obtained from the 2-D LES analogy of Sheng *et al.* (2000) for a single-phase flow generated by the PBT was illustrated in Figure 6.7. In order to determine whether the magnitude of the estimates were reliable, the power dissipated in the field of view was compared to the total power input by the impeller, obtained from the power number as follows:

$$P_{\text{input}} = \rho P_o N^3 D^5 \tag{7.67}$$

The power number of the PBT was taken as 1.52 (Khan, 2005). At the given impeller speed (26.67 s^{-1}) and impeller diameter (0.0337 m), the power input was found to be 1.247 W, giving an average dissipation rate $\bar{\varepsilon} = 1.541$ W kg^{-1}. The power dissipated in the FOV was obtained as:

$$P_{\text{FOV}} = \rho \int_0^{2\pi} \int_{z=0.008}^{z=0.036} \int_{r=0.008}^{r=0.036} \varepsilon r dr dz d\theta = 2\pi\rho \int_{z=0.008}^{z=0.036} \int_{r=0.008}^{r=0.036} \varepsilon r dr dz \tag{7.68}$$

As a simplification, it was assumed that the dissipation rate in the field of view was axisymmetric (consistent around 360° of the impeller). Since the results were ensemble-averaged, the generalization may hold. The integration on the r.h.s of Equation (7.68) was performed using Simpsons rule in 2-D (Appendix I). In this way, the power dissipated in the field of view was found to be 5.73 W, giving a volume-averaged dissipation in the FOV of $\langle \varepsilon \rangle|_{\text{FOV}} \sim 58.93$ W kg^{-1}. Consequently, the power dissipated in the field of view is overestimated by a factor of $P_{\text{FOV}} / P_{\text{input}} = 4.6$. In theory, the power dissipated in the entire vessel should equal the power input by the impeller, so the power dissipated in the field of view alone should be $P_{\text{FOV}} / P_{\text{input}} < 1$. In their study, Gabriele *et al.* (2009) found that the LES method over estimated the power dissipated in half of the vessel by a factor of ~2.

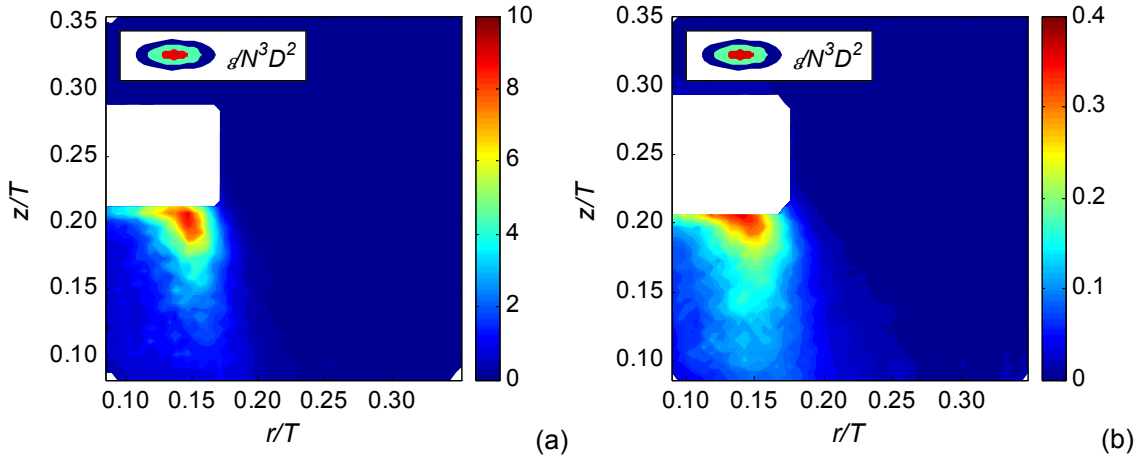

Figure 7.26: Dissipation rate calculated from (a) dimensional analysis and (b) from its definition, for a single-phase flow generated by a PBT

For comparison purposes, the local dissipation rate was also calculated from dimensional analysis (using the TKE and integral length scale from autocorrelation, Equation (4.5)) and from its definition (using isotropic assumptions for unknown gradients, (4.11)). The spatial distributions of ε / N^3D^2 from these methods are shown in Figure 7.26(a) and (b).

It may be observed that the spatial distributions of dissipation from all methods including the LES analogy of Sheng *et al.* (2000) are similar, but their maximum estimates have an order of magnitude difference between each other. The dimensional analysis and direct estimation methods yielded $P_{\text{FOV}} / P_{\text{input}}$ ratios of 0.65 and 0.044 respectively. Gabriele *et al.* (2009) found these ratios to be 4 and 0.2 respectively (note that their dimensional analysis result provided an over estimate).

Since most of the power is expected to be dissipated in the turbulent discharge stream (captured in the FOV), it is apparent that the direct calculation provides an underestimate. This is expected since the direct estimate requires the PIV resolution to be $\mathrm{O}(\eta)$ for an accurate determination. Based on the average dissipation rate from the power input ($\bar{\varepsilon}$), the Kolmogorov length scale was found to be 28.38 μm. Therefore, the PIV resolution (*IA* length 0.97 mm) is $\sim 34\eta$. In order to measure ~90% of the dissipation rate from its direct calculation, the PIV spatial resolution should be $\sim 2\eta$ (Saarenrinne *et al.*, 2001). On the other hand, the dimensional analysis method provides a reasonable ratio of the power dissipated in the field of view. However, it was decided not to use these results when constructing the E-model, because the estimate should ideally come from a gradient-based method.

To preserve information from the gradient-based LES calculation, an alternative approach of scaling-down the dissipation rate was adopted. Firstly, the dissipation rate outside the FOV had to be approximated. Results of Khan (2005) and Gabriele *et al.* (2009) showed that the dissipation rate of a PBT flow sustains a very high magnitude in the discharge stream, and along the lower half of the circulation loop. Subsequently, the dissipation in the high magnitude area (between $0.090 < r / T < 0.210$ and $0.092 < z / T < 0.202$) was extrapolated into regions 1

and 2. The Matlab surface fit function *biharmonicinterp* provided an adequate result. The dissipation rate in all other zones was assumed to be equal to that in the bulk of the FOV.

Although this approximation is crude, most of the reaction is expected to proceed in the vicinity of the feed in the discharge stream, where real inhomogeneities in dissipation have been sufficiently captured. Secondly, peculiarities in the top half of the vessel are not expected, so a constant bulk value of the dissipation rate is acceptable there.

Next, the total power dissipated in half of the vessel was obtained via integration of the extended ε map, using Equation (7.68) with limits $0 < r/T < 0.5$ and $0 < z/T < 1$. Finally, the dissipation in the entire map was scaled-down such that $P_{\text{map}} / P_{\text{input}} = 1$. The resultant local dissipation rate, normalized by $\overline{\varepsilon}$ (equal to ϕ in the E-model equations) is shown in Figure 7.27.

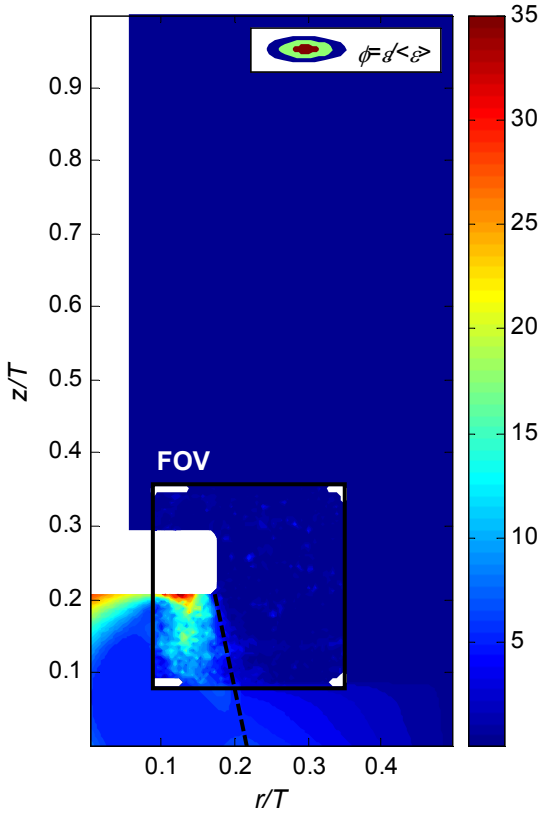

Figure 7.27: Construction of local dissipation rate in half of vessel from 2-D LES analogy of Sheng *et al.* (2000), after scaling such that $P_{\text{map}} / P_{\text{input}} = 1$

Following, the variation of ϕ with respect to either $r^* = r/T$ or $z^* = z/T$ (depending on the flow direction) in each region could be determined. From Figure 7.27, it is evident that ϕ only varies across regions 1 and 2 (with respect to z^* and r^* respectively). In region 1, the local dissipation was radially averaged according to Equation (7.69) on each vertical plane, and a third-order polynomial was fitted to the average data with respect to z^*.

$$\bar{\phi} = \frac{2}{r_2^2 - r_1^2} \int_{r_1}^{r_2} \phi r dr \tag{7.69}$$

$$\bar{\phi} = \frac{1}{z_2 - z_1} \int_{z_1}^{z_2} \phi dz \tag{7.70}$$

The profile of ϕ along region 1 with respect to z^* is shown in Figure 7.28, with its fitted trend line. Similarly in region 2, the dissipation rate was axially averaged according to Equation (7.70) at each radial position, and a relationship determined between the average ϕ and r^*. A summary is provided in Table 7.6.

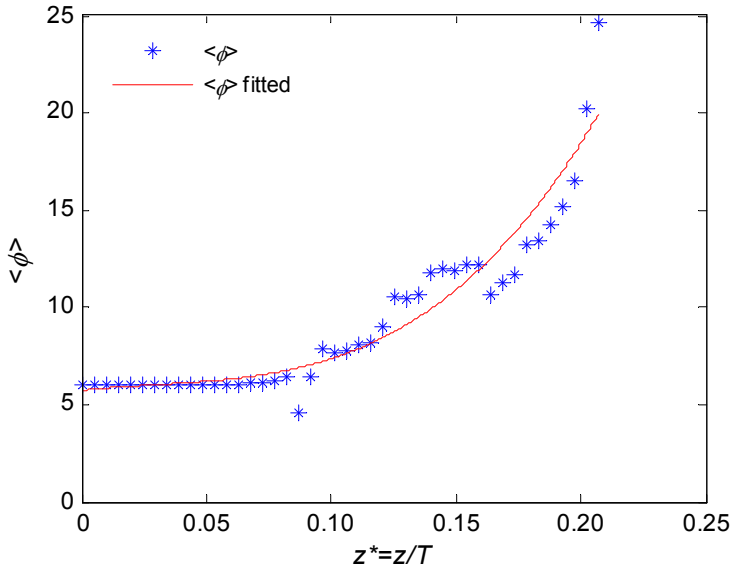

Figure 7.28: Variation of radially averaged ϕ in region 1 with respect to $z^* = z/T$

Table 7.6: Mean relative dissipation rate in each region of the EFM

Region	$\bar{\phi}$
1	$2594z^{*3} - 229.6z^{*2} + 15.83z^* + 6.635$
2	$-15.09r^* + 8.116$
All other	0.6411

The resultant values of ϕ are in a range close to those compiled by Bourne and Yu (1994) for a RDT. Their suggested ϕ in the impeller region was 33.8. In this case, the maximum value at the blade edge (where $z/T = 0.212$) is ~25 (see Figure 7.28). The similar orders of magnitude provide confidence that scaling-down of the dissipation rate to match the power input supplied by the impeller has provided a reasonable estimate of the true value of ε, and will be employed in the E-model to predict the by-product distribution of the Bourne reaction scheme.

7.2.11 Multiple trajectories in the EFM

In the PBT-EFM described above, it is assumed that the reaction zone splits at each boundary, creating five separate trajectories. The partition of the reaction zone at each intersection was determined by assuming an incompressible fluid and conservation of mass throughout the circulation loop.

Subsequently, the mass balance in Equation (7.63) is redefined to account for the variation in eddy concentration C_{α_i}, eddy reaction time T_{j_i} and eddy growth volume $V_i(T_{j_i})$ between each fraction of the reaction zone passing through a different trajectory. The subscript i denotes the trajectory. The eddy volume at the end of reaction in trajectory i is defined as:

$$V_i(T_{j,i}) = x_i \frac{V_{\mathrm{NaOH},0}}{\sigma}\left[\exp\int_0^{T_{j,i}} \phi^{0.5} dT\right] \tag{7.71}$$

where x_i is the split fraction of the eddy. Subsequently, the concentration of substance α in the vessel $< C_\alpha >_j$ after mixing all five parts of the j^{th} eddy with the environment may be updated as:

$$< C_\alpha >_j = \frac{< C_\alpha >_{j-1}\left[V_0 + \frac{V_{\mathrm{NaOH},0}}{\sigma} j - \sum_{i=1}^{i=5} V_i(T_{j,i})\right] + \sum_{i=1}^{i=5} C_{\alpha_i}(T_{j,i}) V_i(T_{j,i})}{V_0 + \frac{V_{\mathrm{NaOH},0}}{\sigma} j} \tag{7.72}$$

For a given impeller speed and hence a certain degree of micromixing (given by Da_2), the final concentration of reagent α in the vessel is the solution of Equation (7.72) after the addition of the last part of the feed (i.e. when $j = \sigma$).

7.2.12 E-model Results

The E-model described above was employed to estimate the product distribution resulting from the Bourne reaction scheme. The modelled conditions were set to match experimental parameters, i.e. the tank geometry specified in §6.1.1 and initial reagent concentrations listed in $7.2.4. The tank to feed volume ratio matched the experimental value of $V_0 / V_{\mathrm{NaOH}} = 50$, and the feed location in the EFM was identical to the micromixing experiments, i.e. at $z/T = 0.178$ and $r/T = 0.129$. Following the recommendation of Baldyga and Bourne (1990), the feed was discretized such that $\sigma = 100$. Simulations were run to emulate micromixing conditions between 300 and 700 rpm; the experimental range shown previously in Figure 7.21(a). Two different situations were modelled:

(a) Homogeneous turbulent energy dissipation throughout the tank (where $\phi = 1$)

(b) Inhomogeneous distribution of turbulent energy dissipation throughout the tank (where ϕ is given by the newly constructed PBT-EFM summarised in Table 7.6)

In the homogeneous dissipation case, only a single trajectory is required to model the environment of the reaction zone, and it is not necessary to define the feed point, since all points in the vessel have the same dissipation. However in case (b), the feed point determines the turbulence intensity which the eddy experiences upon entrance to the vessel, and five separate trajectories were specified to describe the level of mixing intensity that the feed experienced as it fractionated through the various flow zones. The modelled results are plotted with the experimental data in Figure 7.29.

It may be observed that product distributions from the EFM predictions are lower than the homogeneous case at all impeller speeds. In light of the previous discussion this is expected, as the EFM describes more intense micromixing at the feed point. Predictions from the inhomogeneous case are close to the experimental values, indicating success of the constructed EFM, despite the simple extrapolation technique and scaling to achieve the correct magnitude of ϕ.

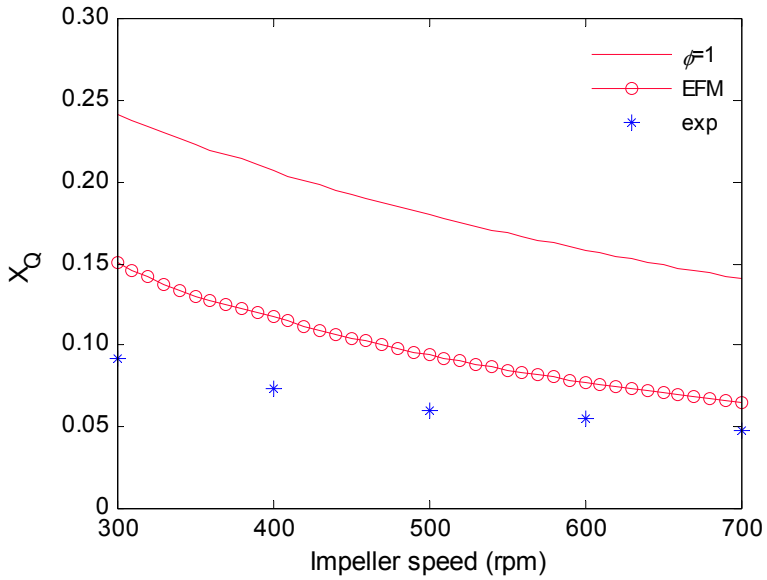

Figure 7.29: Variation of by-product distribution with impeller speed from E-model predictions and experimental results employing the Bourne reaction scheme

The deviation between EFM model predictions and experimental data increases at lower impeller speeds. This is because at relatively low mixing intensity, the eddy does not completely react in the discharge stream captured in the PIV field of view, where dissipation rates were calculated. The reactive eddy traverses Region 1, and at 300 rpm the reaction even proceeds through to Region 2 of the EFM, where it eventually diminishes. In these areas the dissipation rate was extrapolated. Since the product distributions are over predicted in these cases, it is suggested that the extrapolation technique underestimates the real dissipation rate at the end of Region 1 and in all of Region 2. This is more apparent when comparing the extrapolated magnitudes to experimental data of Khan (2005) and Gabriele *et al.* (2009), whose results show that the high intensity dissipation near the impeller trails further into the downwards circulation loop of the PBT.

The fact that the product distribution is predicted reasonably well at higher impeller speeds (~700 rpm) supports the assumption that enough information was captured in the PIV field of view to model these cases. At higher impeller speeds, the model showed that the reaction was completed in the field of view, where real PIV data were used to estimate ϕ. Subsequently, the EFM proposed herein may be applied to estimate product distributions at high impeller speeds (>600 rpm) where the reaction is expected to complete in the immediate vicinity of the feed point, located in the discharge stream. Most studies investigating stirred flows focus on regions close to impeller, but in order to predict by-product distributions more accurately at lower mixing intensities, experimental data of the dissipation rate would be required further away from the blade.

7.4 Conclusions of micromixing experiments

Two-phase micromixing experiments have been carried out using the Bourne and Villermaux reaction schemes. Bourne reactions were carried out with single feed injections and impeller speed 500 rpm, where the maximum concentration suspended was 1.75 and 1.2 vol% for 100 and 300 μm particles respectively. Villermaux experiments were carried out with multiple feed injections and impeller speed 800 rpm, where 100, 300, 750 and 1000 μm particles were suspended up to 3 vol%. In both reaction schemes, the by-product yield was measured in the absence and presence of inert glass particles in the flow. Results were expressed in terms of the percentage changes in yield of the two-phase experiments, relative to a single-phase reference case. The Bourne and Villermaux reaction schemes produced comparable results. In both cases, changes in yield could be detected in the presence of 100 and 300 μm particles. Below ~1 vol%, the particles dampened turbulence, causing a negative percentage change in by-product yield. However above ~1 vol%, the level of suppression decreased, and in the Villermaux experiments turbulence augmentation became evident at ~3 vol% for 300 μm particles. The theory of Gore and Crowe (1989) correctly predicts the initial turbulence damping by these particles according to the d_p / L ratio. Note that Gore and Crowe (1989) developed the criterion based on experimental observations up to a maximum of 0.2 vol% particles in the flow. The parameter does not account for the change in turbulence modulation regime at higher concentrations. The 100 μm particles had a considerably larger effect on the fluid turbulence compared to the 300 μm particles in both reactions schemes, indicating that particle size or alternatively number is important.

In the Villermaux experiments, 750 μm particles did not show consistent changes in yield, and the observed fluctuations were within experimental error 5%. It is possible that they behaved as ‘ghost particles’ described by Ferrante and Elghobashi (2003). The 1000 μm particles repeatedly showed turbulence damping of the continuous phase. Their respective d_p / L ratio being greater than 0.1 opposes the hypothesis of Gore and Crowe (1989). The micromixing experiments validate earlier PIV observations that both small and large particles suppress the dissipation rate at low concentrations at least. The results presented highlight the need for more comprehensive theories of turbulence modulation, which take into account effects of size and concentration to predict the levels of change.

The E-model of micromixing was employed to predict the by-product yields of the single-phase experiments resulting from the Bourne reaction scheme. To make this possible, an

experimental flow model describing the mean flow field and dissipation rate distribution in different regions of the vessel was constructed specifically for the PBT, using experimental data of the PIV study presented in Chapter 6. Data which was not available outside of the field of view was extrapolated, and the integrated power from the dissipation rate was scaled down to match the power input by the impeller. The E-model predictions compared well with experimental data at high impeller speeds, where turbulence levels were high and most of the reaction completed near the feed point in the discharge stream. In this case the dissipation rate was estimated from experimental data along most of the trajectory of the reaction zone. Conversely the deviation between E-model predictions and experimental data increased at low impeller speeds, where the reaction zone travelled out of the discharge stream, and hence the local dissipation rate was estimated mainly from extrapolated data.

Chapter 8 Conclusions and recommendations

8.1 Conclusions

8.1.1 Single-phase PIV study

The primary objective of this thesis was to investigate the effects of dispersed particles on the fluid turbulence in solid-liquid stirred suspensions, via two-phase PIV and micromixing experiments. In order to gain experience of the PIV measurement techniques before studying a more complex two-phase system, a single-phase PIV study was carried out. The flow field generated by a sawtooth impeller (EkatoMizer) was investigated in the impeller region, via single-phase stereo-, high-speed and angle-resolved PIV experiments. The aim was to identify the best calculation method for the dissipation rate from the outcomes of this study, which could be carried forward to the investigation of two-phase flows.

An analysis of the EkatoMizer mean flow field revealed that fluid was drawn into the impeller region axially both above and below the impeller, and discharged radially; the latter characterised the impeller stream. The mean tangential velocity was found to be greatest near the impeller blade, but decayed close to the impeller relative to the radial velocity, and hence was not considered to be the primary flow direction.

Two-dimensional velocity fields enabled calculation of both 1-D and 2-D integral length scales from the spatial autocorrelation function of fluctuating velocity components in all three directions. 1-D longitudinal length scales were found to be greater than lateral length scales obtained from both axial and radial velocity components. In both cases, an evaluation of the ratios (which deviated from 2:1) suggested anisotropic flow. The parameter $W/2$ over estimated the integral length scales in the impeller region.

The tangential rms velocity was found to be greater than the axial and radial components. For this reason, the characteristic turbulence level could not be identified unambiguously. However as in the case of the mean flow, high turbulence in the tangential direction was only significant close to the blade edge. Consequently the radial rms velocity, which was prevalent in the discharge stream, was considered to represent best the system turbulence. Due to differences in rms velocities, the 2-D and 3-D estimates of the TKE were different. Under the pseudo-isotropic assumption the maximum TKE was $0.005V_{tip}^2$ whereas it reached $0.008V_{tip}^2$ from the full estimate.

Anisotropy of the flow was further investigated via the anisotropy tensor. A plot of the invariant parameters on Lumley's triangle showed that the flow was anisotropic in the immediate vicinity of the impeller blade, and moved closer to isotropy as the flow progressed from the discharge stream into the bulk.

Snap shots of instantaneous velocity vector plots elucidated vortices in the discharge stream, which became smoothed out after averaging and were not apparent in the phase-averaged flow. Angle-resolved velocity fields at 1° intervals behind the reference tooth did not reveal periodicity of the flow with respect to these vortex structures. Instead macro-instability (MI) of the flow was investigated to determine whether the vortices corresponded to low frequency phenomena. The power spectral density (PSD) of the radial velocity time-series revealed multiple dominant peaks in the low frequency region at various point in the flow. It was more appropriate to identify the MI range; 0-200 Hz in this case. A spatial representation of the MI intensity across the field of view showed a high probability of MI occurrence in the upper and lower sections of the discharge stream; the same location where vortices were found.

Various calculation methods for the dissipation rate were investigated thoroughly, since this turbulence property was to be inferred in the following two-phase PIV and micromixing experiments. Estimates were obtained directly, from dimensional analyses, LES analogy (Sheng *et al*., 2000) and the TKE balance using both two and three velocity components from stereo-PIV data. In all cases, estimates from three velocity components yielded higher dissipation rate values than from two components due to flow anisotropy, suggesting that linear scaling and isotropic relations were not applicable to the EkatoMizer flow. The LES analogy of Sheng *et al*. (2000) was believed to provide the most comprehensive measure of the dissipation rate. The calculation accounts for three-dimensionality of the flow by incorporating all three velocity components, but more importantly, it accounts for turbulence at the smaller scales via a sub grid scale (SGS) model. Note that linear scaling of the unknown gradients was not deemed to be suitable for the tangential velocity gradients, but was implemented due to the absence of a better alternative. The purpose of identifying the best calculation method was achieved, and the LES method was employed to determine the local ε in proceeding two-phase PIV studies.

The application of the multifractal model of Meneveau and Sreenivasan (1991) to represent turbulence intermittency of dissipation, and select an appropriate vector validation filter for PIV data, is a novel approach. High-speed PIV data were required to calculate fractal dimensions of the dissipation rate. Time-series profiles of dissipation were evaluated against this model after applying global, local and temporal standard deviation filters to the instantaneous velocity fields. Results showed that the unfiltered profile deviated most from the multifractal model, suggesting that intense fluctuations in the instantaneous dissipation rate were a result of measurement or processing errors rather than genuine intermittency. The global standard deviation filter created a profile which aligned more closely to the multifractal model, and hence was considered to be the best type for the flow under investigation. The maximum dissipation rate estimate dropped from $1.76N^3D^2$ to $\sim 0.1N^3D^2$ after global filtering. This study highlights the need for other researchers to consider the treatment of PIV errors, especially where gradient-based calculations of ε are involved, as the type of filter dramatically affects the result. The method of validating filtered profiles may be implemented by other researchers if high time-resolved data is obtained, such that the power spectrum may be resolved down to the inertial range.

Globally filtered velocity profiles and subsequent dissipation rate estimates from the LES analogy were used to investigate the distribution of energy dissipation. A kinetic energy (KE) balance around the impeller discharge stream suggested that 3.4% of the total power input was dissipated in that zone. It was estimated that 96% of the energy was dissipated in the impeller region. From the calculated power consumed in the control volume, the average dissipation rate in the discharge stream was found to be 1.87 W kg^{-1}. An equivalent measure from the already calculated dissipation rate found the average to be 0.64 W kg^{-1} in the same region. The ratio of maximum-to-mean dissipation rate (~40) in the discharge stream was of comparable magnitude to analogous ratios found in literature for RDTs and PBTs, raising doubt about its reported high-shear characteristics. However this ratio was estimated to be at least 273 in the impeller region from the KE balance, suggesting that the vast majority of energy dissipation occurs in the impeller swept volume.

The conclusions summarised above provide new information regarding the EkatoMizer flow field, which has not been investigated in detail before. Sufficient experience was obtained from the single-phase PIV study to progress with a more complex two-phase flow, and the best method for calculating the dissipation rate had been identified (i.e. the LES analogy). Therefore, the interim objectives were achieved.

8.1.2 Two-phase PIV study

Phase separation techniques were reviewed for solid-liquid PIV experiments. It was decided to employ florescent PIV (FPIV) for continuous phase tracers via one camera, combined with digital image processing of two-phase Mie scattering images to extract the dispersed phase from a second camera. The digital phase discrimination algorithm of Khalitov and Longmire (2002) was deemed to be the best choice from those available in literature, as it performed separation using information of both particle size and light scattering intensity simultaneously. The combination of FPIV with this specific algorithm presents a novel experimental technique, as it has not been implemented before. The original algorithm was written for object detection of spherical particles with a Gaussian intensity distribution. In the present case the code was adapted for object detection of fragmented image patterns.

Two-phase PIV experiments of soda-lime glass dispersed particles of sizes 250-300, 700-750 and 1000 μm were carried out up to concentrations of 0.3, 0.5 and 0.5 vol% respectively, and effects on the continuous phase turbulence were examined. The modulation of the dissipation rate has not been quantified before, so the current study advances knowledge in this field.

Both small (250-300 μm) and large (1000 μm) particles suppressed turbulence, in terms of rms velocities, TKE and dissipation rate (relative to the single-phase fluid), above volumetric concentrations of 0.2 vol%. The level of turbulence suppression remained approximately constant when the particle concentration was increased to 0.5 vol%, suggesting that particle-particle interactions did not contribute to the observed phenomenon. The dissipation rate was modulated most, which showed suppression up to 25% in the discharge stream, in the presence of particles. Integral length scales of the continuous phase were unaffected, indicating that simple dimensional analysis calculations of the dissipation rate would be able to reflect this change from the TKE. The intermediate size particles (700-750 μm) also showed some suppression of the turbulence properties, but their effect was insignificant compared to the other

two size classes. The observed turbulence suppression by the 1000 μm particles contradicts the widely adopted theory of Gore and Crowe (1989), which suggests that particles with a diameter to characteristic fluid length scale ratio greater than O(0.1) enhance turbulence; the ratio in this case was 0.278.

Digitally phase-separated images of dispersed particles at their maximum experimental concentrations were processed. Spatial distributions of the locally averaged volumetric concentration field portrayed three zones of locally high concentrations; one of these was the discharge stream. This supports the belief that the presence of particles is responsible for modulating turbulence in that region. Dispersed phase velocities were obtained from cross correlation; the 700-750 μm particles at 0.5 vol% produced the most complete flow field. Their average particle slip velocities varied throughout the field of view and were found to be largest in the discharge stream. In this region the terminal velocity underestimated the particle slip velocity by a factor of nine times. Consequently the particle terminal velocity does not provide a reliable estimate of the axial slip in stirred flows. Particle rms velocities and TKE were found to be lower than the corresponding continuous phase fluid. The dispersed phase also exhibited higher anisotropy of turbulence.

8.1.3 Two-phase micromixing study

In order to validate the two-phase PIV experiments, two-phase micromixing experiments were also carried out using the Bourne and Villermaux reaction schemes, with the aforementioned dispersed particles suspended in the reactive mixture. Two-phase micro-mixing experiments have not reported turbulence modulation at low particle concentrations before, so the conclusions drawn from this study are novel. The by-product yield was measured after reaction with particles present in the fluid and compared to a particle-free reference case. Bourne micromixing experiments were carried out at 500 rpm and Villermaux experiments at 800 rpm; the impeller speeds were selected based on sensitivity of the chemical schemes to the fluid hydrodynamics. Due to the relatively low impeller speed, only 100 and 300 μm particles were fully suspended in the Bourne two-phase experiments.

Both reaction schemes produced similar results. The 100 and 300 μm particles increased the by-product yield which is an indication of turbulence suppression. This trend was observed up to 1 vol% particles in the fluid, where the level of suppression reached a maximum. Above this concentration, the amount of turbulence damping decreased. In the Villermaux reaction scheme, at 3 vol% the same particles decreased the by-product yield, indicating a change in regime to turbulence augmentation. Overall the 100 μm particles showed greater turbulence suppression compared to the 300 μm, suggesting that particle size is an important factor, or particle number at an equivalent volumetric concentration. The d_p / L ratios of both particles were below 0.1, hence the theory of Gore and Crowe (1989) rightly predicts the effects at low concentrations. Note that their theory was developed using experimental data up to a maximum of 0.2 vol% particles, and does not explicitly include effects of concentration as were observed in this study.

In the Villermaux reaction scheme, 750 μm particles did not generate consistent changes in yield, and the observed fluctuations (up to 5%) were within the experimental error. The 1000 μm particles consistently decreased the by-product yield, indicating turbulence damping of the fluid.

Subsequently, the micromixing experiments validated earlier PIV observations that both small and large particles suppress the dissipation rate at low concentrations at least. The results draw attention to the need for more comprehensive theories of turbulence modulation which incorporate effects of size and concentration to model the levels of turbulence change.

8.2 Recommendations for future work

In PIV, spurious velocity vectors may result from lost particle pairs due to in- and out-of-plane motion, or low tracer number density, which in turn leads to poor correlation signal strength. When spurious vectors are produced, the highest correlation peaks are not a result of pairs of particles moving with the flow, but instead arise from the random pairing of particle images producing the greatest signal. Therefore, velocity fields may benefit from the application of vector validation filters to remove erroneous vectors. However, it was explained in §4.8 that velocity statistics for validation (such as the mean, median or standard deviation) may be obtained in different ways, each impacting the flow to a different extent. It is useful to have some criteria to validate the filtering efficiency and subsequently select the best filter, and also ensure that genuine fluctuations are not smoothed out.

The multifractal model of Meneveau and Sreenivasan (1991) proved to be a good representation of turbulence intermittency, as it enabled identification of an appropriate vector validation filter. The fractal dimensions of the dissipation rate obtained from a globally filtered velocity profile matched closely against the model; hence the global standard deviation filter was selected to be the best option in the present case. The author recommends that the choice of the most appropriate filter should be made on a case-by-case basis, since this is largely dependent on the degree of turbulence and inhomogeneity of the flow field, as well as experimental parameters such as tracer number density and time-delay between image frames, which in turn influence the cross correlation procedures. After selecting the best filter, the multifractal model may also be used to optimise the filter parameters (such as tolerance level of the global filter or neighbourhood size of the local filter).

The two-phase PIV experiments carried out in the present study did not employ refractive index (RI) matching. Soda-lime glass spheres of RI 1.51 were suspended in water which has a RI of 1.333 at 21 °C. Distortion of the laser light sheet caused by particle blockage and subsequent extinction of its path length through the vessel limited the dispersed phase concentration to be studied up to a maximum of 0.5 vol%. Future two-phase PIV experiments could exploit RI matching which renders the system transparent, and enables study of higher particle concentrations. An organic system has been recommended herein. A high RI may be attained by mixing Tetraline and Turpentine oil, which has been employed previously by Nouri and Whitelaw (1992) to obtain a RI of 1.49. Preliminary tests in the present case revealed that a RI of 1.51 matching the soda-lime glass spheres could be obtained by mixing 60 vol% Tetraline with 40 vol% Turpentine oil, at 21 °C. The measured mixture density was found to be 927 kg m^{-3} at ambient conditions. The mixture viscosity (measured using a u-tube type viscometer of capillary diameter 0.64 mm and nominal constant 0.01 from Technico Inc.), was found to be 1.720 mPa s at 21 °C. Since both properties are close to those of water (998 kg m^{-3} and 1.002 mPa s) high Reynolds numbers may be attained in the stirred vessel without additional difficulty. However since RI varies with temperature, control of this parameter would be important. Further tests revealed the relationship between temperature and RI of the organic fluid; for a

temperature increase of 1 °C, the RI drops by 0.0005. Melamine resin particles of 23 μm diameter, doped with fluorescent Rhodamine B dye from Sigma Aldrich were found to be stable in the organic fluid and compatible with the optical filters described in §6.1.2.

Secondly, the experimental setup used for the non-RI matching experiments was not suited for subsequent particle tracking of dispersed phase images which give rise to point-wise velocities. This kind of information is required to compute slip velocities. Since only one double-pulsed laser was used to illuminate the flow, the time separation between image pairs was optimized for cross-correlation of the continuous phase tracers. This was not large enough to allow detectable displacement of the solid particles. Their displacement appeared to be very small, and within the error of the object detection algorithm (± one pixel). A compromise could not be found where images of both phases could be captured accurately at any given time separation; the dispersed phase particles required ~1 ms between image frames for noticeable displacement, whereas tracers required a time of O(50) μs. As a recommendation, two independent double-pulsed lasers could be used to illuminate the flow in future experiments, which may be adapted to suit the velocity ranges of both phases. Although PIV measurements of both phases would be obtained from laser pulses triggered at different moments in time, the data sets could be obtained within the same overall time frame, hence the two-phase information may be considered as quasi-simultaneous.

Finally, after conducting a review of particle tracking algorithms employed in literature, the approach based on an ‘artificial neural network’ of Hassan and Philip (1997) was thought to be the best choice, and is recommended for future application. It overcomes the major limitation of most other particle tracking algorithms by comparing all possible tracks resulting from one particle simultaneously, and selects the one with the least error. The underlying assumption of this algorithm is that short particle tracks may be represented as almost linear regressions. Subsequently, groups of particles that are roughly aligned may be picked out by performing the Hough Transform (of a line). Another requirement is four consecutive image frames to form a particle track comprising three velocity vectors. Hassan and Philip (1997) tested the performance of this algorithm and showed that it is able to handle turbulent flows with large velocity gradients, hence suited to track particles in stirred flows.

Appendix I
Simpson's integration rule

I.1 Simpson's rule for 1-D integration

Simpson's rule provides a numerical approximation of a definite integral using quadratic polynomials (i.e. parabolic arcs instead of the straight line segments used in the trapezoidal rule). For one-dimensional integration, Simpson's rule involves fitting a third order polynomial fit to the function at three equally spaced points. Since it uses quadratic polynomials to approximate functions, Simpson's rule yields exact results when approximating integrals of polynomials up to cubic degree. Specifically, consider a function $f(x)$ defined within the limits a and b. The definite integral between the upper and lower limits may then be expressed as:

$$I = \int_a^b f(x)dx \tag{I.1}$$

Let the points $x_0 = a$ and $x_2 = b$, separated by a distance Δ_x. Assume that the function may be tabulated at three equally spaced points such that the mid-point $x_1 = x_0 + \Delta_x/2$. Subsequently, Simpson's rule states that the integral may be approximated as:

$$I \approx \frac{\Delta_x}{6}\left(f(x_0) + 4f(x_1) + f(x_2)\right) \tag{I.2}$$

The function may be further decomposed into a sum of integrals over smaller equal intervals, each comprising three equally spaced points. Equation (I.1) then becomes:

$$I \approx \frac{\Delta_x}{6}\sum_{i=0}^{2M_x} Q_i f(x_i) \tag{I.3}$$

where M_x is the number of intervals, $\Delta_x = (b-a)/M_x$ the length of the intervals, and $x_i = x_0 + i\Delta_x/2$ where $(i = 0,...,2M_x)$ are the equally spaced points within the intervals. The coefficients in Q_i follow the pattern 1,4,2,4,2….2,4,2,4,1 such that $Q_0 = Q_{2M_x} = 1$, $Q_i = 2$ if i is even ($i \neq 0$, $i \neq 2M_x$) and $Q_i = 4$ if i is odd. The full derivation of the formula may be found in Bregains *et al*. (2004). A Matlab script was written to perform the integration using the principles of Simpson's rule and fit quadratic polynomials to every three data points of the autocorrelation function. The coefficients of integration followed the same pattern as specified by Q_i and the points $f(x_i)$ were the autocorrelation coefficients. Simpson's rule is applicable to the entire data set since the autocorrelation coefficients are equally spaced. It is important to note that

although real data points are used within the integration, the technique of fitting quadratic polynomials would lead to smoothing to some extent. However, since the polynomials fit exactly through the data points (unlike simple curve fitting), the degree of smoothing would be minimal.

I.2 Simpson's rule for 2-D integration

Simpson's rule may be extended to double integrals for calculating the 2-D integral length scales. Instead of integrating over intervals in one dimension, the integration is performed over rectangular areas in two dimensions. For a function $f(x,y)$ defined with the limits (a,b) and (c,d) respectively, the definite integral may be expressed as:

$$J = \int_{c}^{d}\int_{a}^{b} f(x,y)dxdy \tag{I.4}$$

After decomposing the above into a sum over equal rectangles and applying a (3×3)-point quadrature formula to each rectangle, the integral may be approximated as:

$$J \approx \frac{\Delta_x \Delta_y}{36} \sum_{i=0}^{2M_x} \sum_{j=0}^{2M_y} Q_{i,j} f(x_i, y_j) \tag{I.5}$$

Table I.1: The Q_{ij} coefficient matrix for the two dimensional Simpson's rule

Q_{ij}	i=0	i=1	i=2	i=3	…	$i=2M_x-3$	$i=2M_x-2$	$i=2M_x-1$	$i=2M_x$
j=0	1	4	2	4	…	4	2	4	1
j=1	4	16	8	16	…	16	8	16	4
j=2	2	8	4	8	…	8	4	8	2
j=3	4	16	8	16	…	16	8	16	4
.	.	.	.	.	…	.	.	.	.
.	.	.	.	.	…	.	.	.	.
.	.	.	.	.	…	.	.	.	.
$j=2M_y-3$	4	16	8	16	…	16	8	16	4
$j=2M_y-2$	2	8	4	8	…	8	4	8	2
$j=2M_y-1$	4	16	8	16	…	16	8	16	4
$j=2M_y$	1	4	2	4	…	4	2	4	1

The full derivation of the approximation may be found in Bregains *et al*. (2004). As in Equation (I.3), M_x and M_y are the number of intervals in the x and y directions respectively. The interval lengths (and hence the sides of the rectangles) are given by $\Delta_x = (b-a)/M_x$ and $\Delta_y = (d-c)/M_y$ respectively. Here, $y_j = y_0 + j\Delta_y/2 \ \ (j = 0,...,2M_y)$ are the equally spaced points in the y direction, and x_i similarly in the x direction. The coefficient matrix Q_{ij} follows the one-dimensional Simpson's pattern along boundaries of the integration domain. For the interior of the domain, $Q_{ij} = Q_{0,j}Q_{i,0}$. A sample coefficient matrix is provided in Table I.1. Extending the Matlab script to perform 2-D integration was straightforward. The coefficient

matrix followed the same pattern as Q_{ij} and the points $f(x_i, y_j)$ were predetermined values of the autocorrelation function in 2-D.

I.3 Adjustments to Matlab script for Simpson's rule

To successfully implement Simpson's quadrature, the Matlab script was adjusted. In theory, the autocorrelation function is integrated to the first zero crossing for calculation of the length scales. However, this requirement must be relaxed when applying Simpson's rule. The rule necessitates an odd number of data points in the integration, such that full intervals (in one dimension) or rectangles (in two dimensions) can be created, since the period of one interval is 3 points, and a rectangle comprises 3×3 points. Figure I.1(a) and (b) show the construction of intervals arising from an odd and even number of data points in the autocorrelation function respectively, in one dimension. Three equal intervals can be formed in Figure I.1(a), whereas the last two points cannot form a complete interval in Figure I.1(b). Subsequently, in these cases the numerical quadrature terminated at the point *before* the first zero crossing.

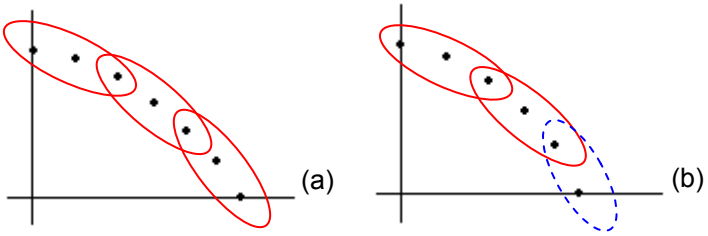

Figure I.1: Simpson's rule with an (a) odd and (b) even number of data points

The situation above presumes a definite zero crossing of the autocorrelation function. It is true that the autocorrelation function always decays to zero because of the zero padding added to the vector field *a priori*. However, the autocorrelation function could fall below zero before decaying towards it, without a definite zero crossing, as depicted in Figure I.2. In this case, it is desirable to integrate the autocorrelation function up to the first negative value. The two loops worked in conjunction to ensure that both conditions were satisfied simultaneously. If the first negative value resulted in an even number of data points, the algorithm would integrate to the previous point instead, circled blue in Figure I.2. In practice the autocorrelation function was rarely integrated to a definite zero crossing, either because it did not exist, or because it did not satisfy the condition of generating an odd number of data points in series.

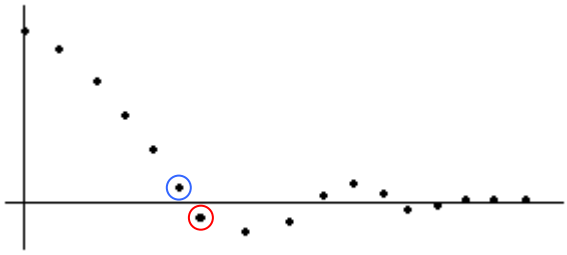

Figure I.2: Example of an oscillating autocorrelation function

Appendix II
Filtered dissipation results

In PIV, spurious velocity vectors may result from lost particle pairs due to in- and out-of-plane motion, or low tracer number density which in turn leads to poor correlation signal strength. When spurious vectors are produced, the highest correlation peaks are not a result of particle pairs moving with the flow, but arise from the random pairing of particle images producing the greatest signal. The time-history of instantaneous velocity gradients obtained at the same point in Figure 4.16, is depicted in Figure II.1.

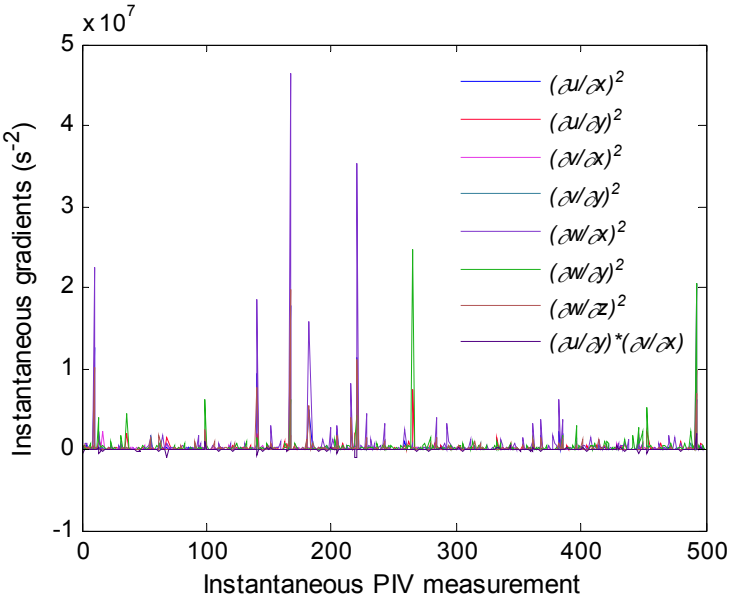

Figure II.1: Time-history of instantaneous velocity gradients at a point in the discharge stream, over 500 PIV measurements, 1500 rpm

High values of the dissipation rate in Figure 4.16 coincide with instances of extremely high velocity gradients, which may have been a result of spurious velocity vectors. An interesting point is that the highest gradients are of the tangential velocity. In order to obtain a more stable and accurate profile of the instantaneous dissipation rate, outlying vectors have to be removed. Three types of standard deviation filters (i.e. global, local, and temporal) were applied to the flow field shown in §3.3.1, and the dissipation rate recalculated. Results are presented below.

II.1 Global standard deviation filter

The global standard deviation filter uses all points in the instantaneous velocity field to calculate the mean and standard deviation for each instantaneous measurement. This example shows the result of filtering when the tolerance was set as three standard deviations from the global

mean; vectors exceeding this value were eliminated. A tolerance of three standard deviations has been commonly reported in literature, and is also the default level in TSI Insight software. Resultant holes were filled in via linear interpolation of the surrounding vectors.

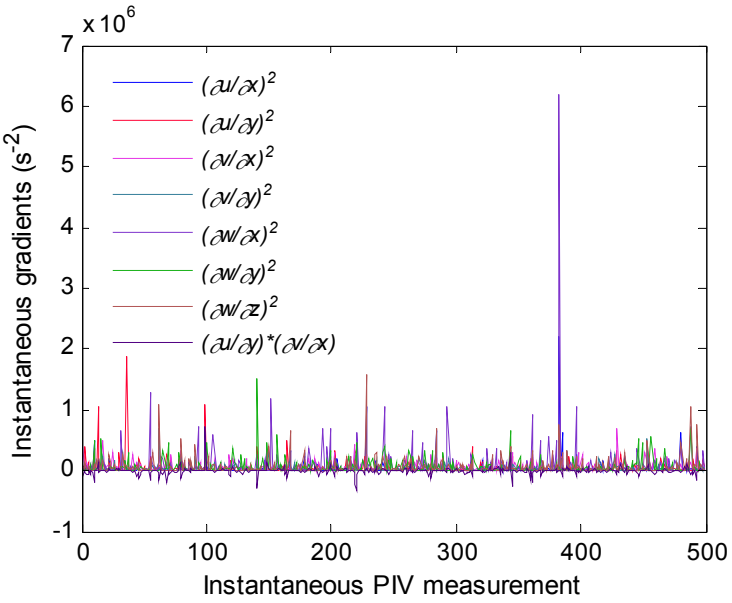

Figure II.2: Time-history of instantaneous velocity gradients at a point in the discharge stream, over 500 PIV measurements, after applying the global standard deviation filter

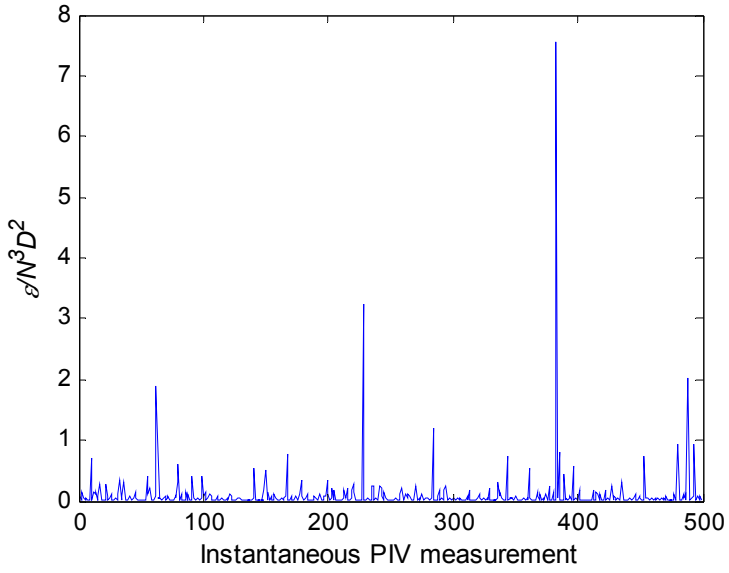

Figure II.3: Time-history of instantaneous dissipation rate at a point in the discharge stream, over 500 PIV measurements, after applying the global standard deviation filter

In Figure II.2, the most extreme instantaneous velocity gradients have been eliminated, and their order of magnitude has reduced from 10^7 to 10^6. A radical change was also found in the instantaneous dissipation rates; in Figure II.3 the scale has decreased from $250N^3D^2$ to

$8N^3D^2$. Although the change is drastic, the instantaneous dissipation rate profile after filtering still has an appreciable degree of fluctuation, since the majority of values are closer to zero. The profile could be smoothed further by decreasing the tolerance level (e.g. two standard deviations) which would filter more vectors. However, this would be at the cost of eliminating genuinely high gradients, characteristic of a turbulent velocity field. The effect of changing the tolerance level on this dissipation rate was illustrated in the §4.8.4. The instantaneous profiles presented above correspond to only one point within the flow field, and are not sufficient to evaluate the effect of the filter alone.

Figure II.4 provides a global view of the average dissipation rate. It is evident that the filter has a greater impact within the discharge stream, since the bulk remains unaffected (compared to Figure 4.13). The maximum dissipation rate after applying the global standard deviation filter is approximately $0.17N^3D^2$ compared to $1.76N^3D^2$ without filtering.

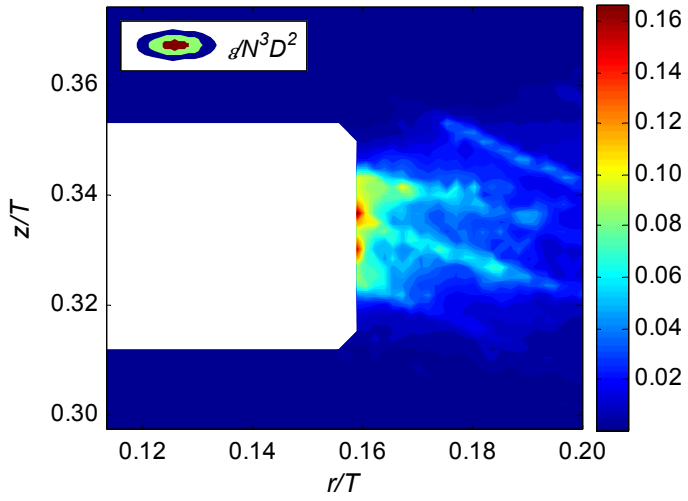

Figure II.4: Dissipation rate from the LES analogy of Sheng *et al.* (2000) using stereo-PIV ensemble-averaged measurements, after applying the global standard deviation filter

A limitation of the global standard deviation filter is that since underlying statistics are obtained from data in the entire measurement plane, the filter does not account for real variations in velocity over the flow field. Assigning a single mean and standard deviation to represent the flow field is equivalent to suggesting that all velocity vectors conform to the same distribution. For a laminar or stagnant flow or within the bulk region the simplification may hold, but is highly unlikely for a turbulent flow in the vicinity of the impeller. There would always be a certain number of vectors which lie outside of the tolerance level, since the statistics are calculated from a field with large variations. Consequently, if the filter was applied recursively, all data would be eliminated eventually.

II.2 Local 3×3 standard deviation filter

The local standard deviation filter calculates the mean and standard deviation of vectors surrounding a single point in the flow field (not including the central point). The tolerance compares the central point to its neighbouring statistics. The neighbourhood size could

comprise 3×3, 5×5, 7×7 etc vectors. In turbulent flows where large velocity gradients are expected, it is preferable to use the smallest neighbourhood size, hence 3×3 was selected. Using a large neighbourhood size may be helpful in cases where large holes are present in the vector field, or if velocity gradients are not expected to be large (e.g. in the bulk). A tolerance of three standard deviations from the mean was selected.

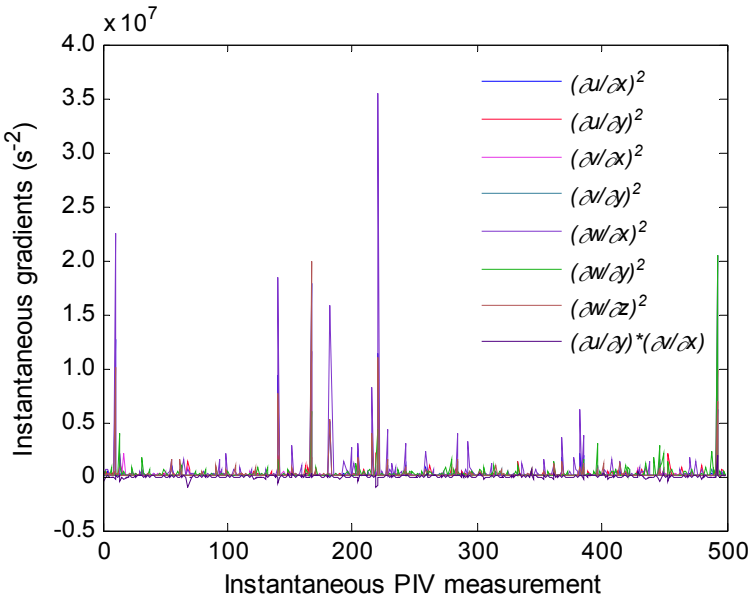

Figure II.5: Time-history of instantaneous velocity gradients at a point in the discharge stream, over 500 PIV measurements, after applying the local 3×3 standard deviation filter

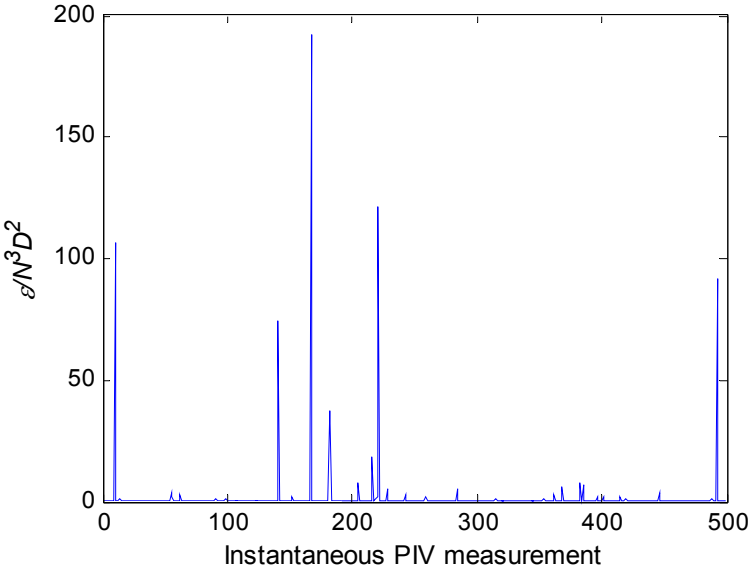

Figure II.6: Time-history of instantaneous dissipation rate at a point in the discharge stream, over 500 PIV measurements, after applying the local 3×3 standard deviation filter

Figure II.5, suggests that the local standard deviation filter has a very small impact on the instantaneous velocity gradients. Their order of magnitude remains the same, implying that

hardly any vectors were eliminated. Naturally, the profile of the instantaneous dissipation rates in Figure II.6 remains very similar to the original shown in Figure 4.16. However, the highest peak has been removed. The maximum dissipation rate in Figure II.7 is now $\sim 1.6 N^3 D^2$. In the discharge stream, small regions of intense dissipation rate have been removed, reducing the 'spottiness' of the distribution.

The result implies that most of the high velocity gradients are genuine, since they fall within the specified tolerance level. Since the mean and standard deviation were calculated from surrounding points, it is evident that large velocities (hence velocity gradients) are not stand-alone spurious results; instead they must exist in small colonies.

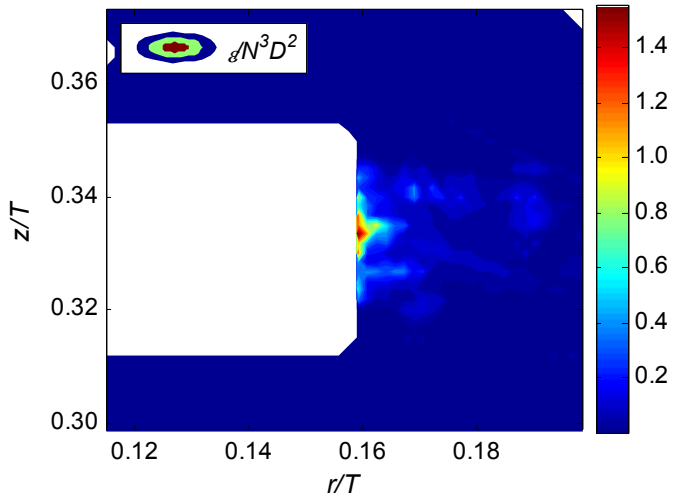

Figure II.7: Dissipation rate from the LES analogy of Sheng *et al.* (2000) using stereo-PIV ensemble-averaged measurements, after applying the local 3×3 standard deviation filter

II.3 Temporal standard deviation filter

The filters described above acquired the mean and standard deviation spatially (either globally or locally). Another approach is to obtain the statistics at every point in the flow field with respect to time, or in this case over sequential PIV measurements at a fixed vector node. At each vector position, the mean velocity was obtained over 500 image pairs. Again, the filter tolerance was set as three standard deviations from the mean.

From Figure II.8, it may be observed that extreme values of the velocity gradients have been removed. Their order of magnitude has reduced from 10^7 to 10^6. Velocity gradients resulting from the temporal filter are greater than those arising from the global filter (apart from one tangential velocity gradient at the ~390th PIV measurement). This is because the standard deviation of measurements at a single point is lower than that obtained over the whole field. In Figure II.9 the maximum has reduced from $250 N^3 D^2$ (without filtering) to $8.2 N^3 D^2$.

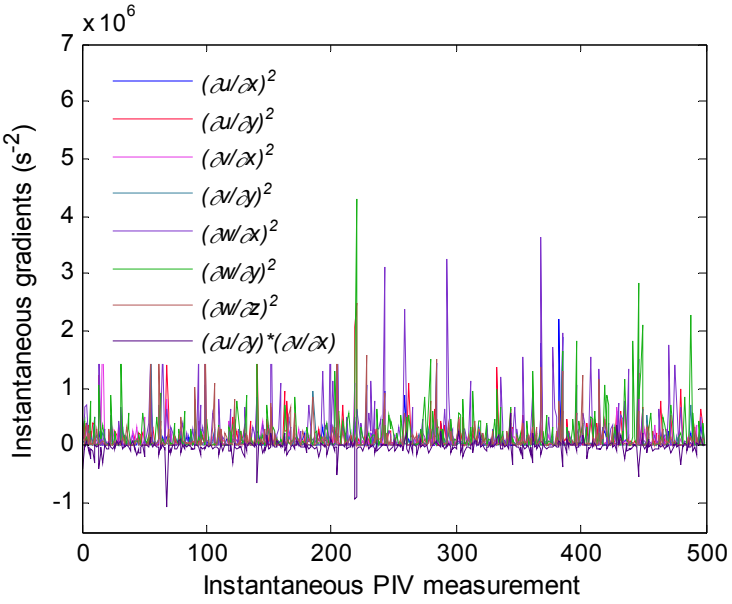

Figure II.8: Time-history of instantaneous velocity gradients at a point in the discharge stream, over 500 PIV measurements, after applying the temporal standard deviation filter

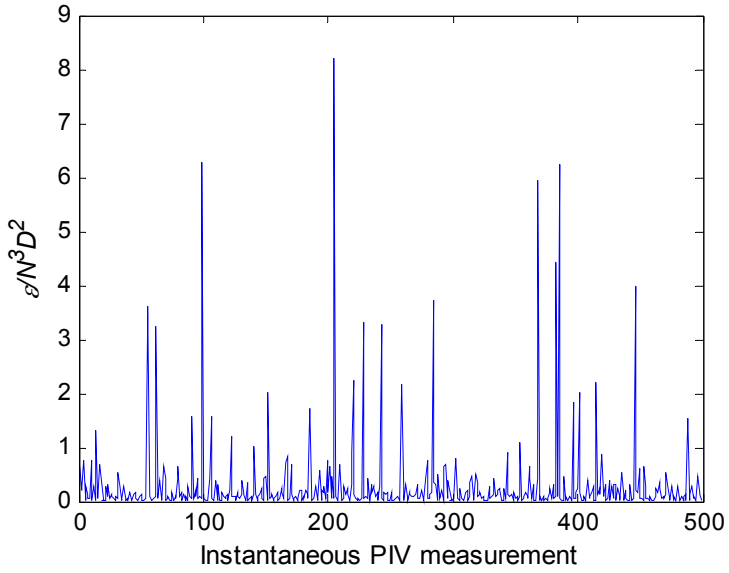

Figure II.9: Time-history of instantaneous dissipation rate at a point in the discharge stream, over 500 PIV measurements, after applying the temporal standard deviation filter

Figure II.10, shows that the average dissipation rate in the discharge stream has been affected. The maximum has decreased from $1.76N^3D^2$ to $0.45N^3D^2$ at the blade edge. Note that the blank regions in the outer areas of the flow field are due to failed interpolations. The code in Matlab was unable to interpolate over excessively large blank regions, which this filter seems to create.

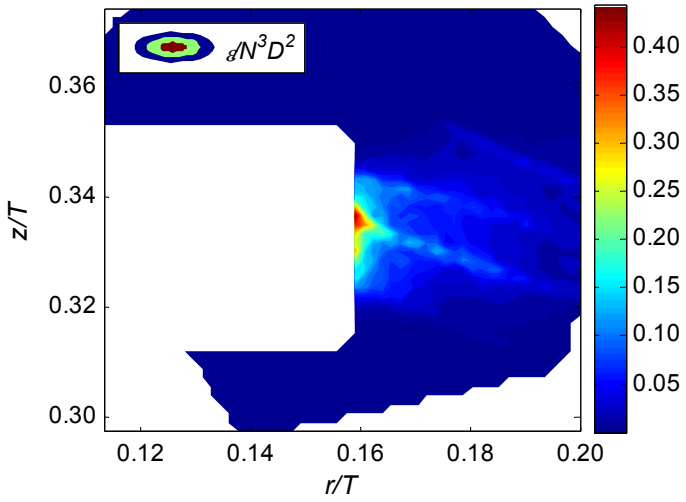

Figure II.10: Dissipation rate from the LES analogy of Sheng *et al.* (2000) using stereo-PIV ensemble-averaged measurements, after applying the temporal standard deviation filter

It is questionable whether the temporal filter provides reliable statistics to represent the flow field. Since PIV measurements were not angle-resolved (they were 360° ensemble-averaged), it may be argued that turbulence properties are smoothed-out during the averaging process, leading to the loss of real velocities when applying the filter. On the other hand, it has been shown that ensemble-averaged measurements can lead to an overestimation of turbulence properties in the impeller stream by up to 400% (Yianneskis and Whitelaw, 1993) since they include relatively high gradients specific to the blade angle. In light of this, it may be beneficial to eliminate the high gradients, even if they are not spurious results, since they are not representative of the 'general' flow field. It should be noted that in order to obtain mean velocities from ensemble-averaged data, 'stationarity' of the flow was assumed, requiring that physical processes do not change with time. If stationarity breaks down, it is necessary to change the analysis method to account for the time-varying characteristics, e.g. by obtaining angle-resolved measurements.

For the current ensemble-averaged measurements, it is preferred not to remove any true vectors from the velocity field, so use of the temporal filter may be unsuitable. It may be a useful tool for removing spurious vectors from angle-resolved measurements, for which the expression 'pseudo turbulence' may be applied. Pseudo turbulence refers to a flow field with a regular pattern that exhibits a distinct constant periodicity in time (and space). Thus, if angle-resolved measurements are obtained, the time-averaged mean may be calculated, since a 'quasi-steady' state may be assumed.

In §4.8.4, fractal dimensions of the filtered and unfiltered dissipation rate profiles were compared to the multifractal model of Meneveau and Sreenivasan (1991). The global standard deviation filter with a tolerance level of three standard deviations from the mean was found to create the most plausible representation of intermittency, as it aligned best with the multifractal model. Consequently, this filter was used to treat the high-speed PIV data in the remainder of Chapter 4.

Appendix III
Hough transform

The idea behind the Hough technique for shape detection, is that each input measurement (the object pixel grey level) forms part of a globally consistent solution (the perimeter of a circle), which gives rise to that image point. A circle can be expressed in Cartesian form according to Equation (III.1), where $[x, y]$ are coordinates of the object pixel, $[a, b]$ the coordinates of the circle centre with radius r, which the object pixel is assumed to form part of. It follows that object pixels which outline the same circle have a unique solution for $[a, b]$ and r.

$$(x-a)^2+(y-b)^2=r^2 \tag{III.1}$$

Thus all object pixels in the image (with known $[x, y]$) serve as constants in the calculation of possible $[a, b]$ for a specified r. Figure III.1 illustrates this calculation schematically.

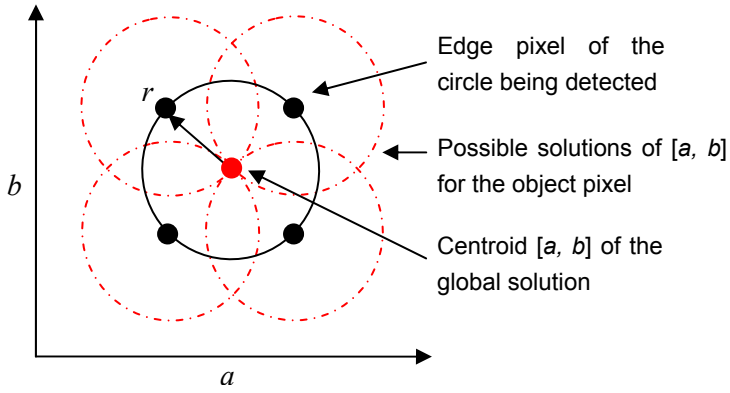

Figure III.1: Hough transform of a circle

Four object pixels lie on the boundary of the circle drawn with the black solid line, which has a radius r. The red dashed lines around each object pixel depict possible solutions of $[a, b]$ in the $a-b$ parameter space, which would arise if the co-ordinates of those pixels were used to solve Equation (III.1) for the given radius r. The solutions overlap at a common point, which is the centroid of the circle in question. In this way, possible solutions of $[a, b]$ were calculated for all object pixels in the dispersed phase images. Object pixels constituting the same circle boundary provided common solutions. Solutions were stored in a 3-D histogram (accumulator array), and the circle centroids manifested as the highest points. A contour plot of the calculated parameters $[a, b]$ (for a specified r) is called the Hough transform, which in discretized form is

equivalent to the histogram. When viewed in the Hough parameter space, points forming part of the same circle boundary generate a peak.

The Matlab code was written to calculate the coordinate a to sub-pixel accuracy, for prescribed r and b values at pixel level. The code could be forced to perform calculations with parameters r and b at sub-pixel accuracy at the expense of increased computational time; only worthwhile if the input data (object pixels coordinate) had sub-pixel accuracy itself.

As the analysis treats each input as part of a boundary, pixels forming the inside of dispersed particles may be considered as noise; their solutions are irrelevant. Therefore, a boundary detecting Matlab operator was used to extract pixels of object edges which were subjected to the Hough technique. The boundary detector was selected over the Matlab edge detector function, as it may be coupled with a fill operation for holes or secondary spots in the image. This reduces detection of unwanted boundaries inside the desired object, which could also be regarded as noise. A limitation of both boundary detection and edge functions is that they detect boundaries at pixel accuracy (not sub-pixel level). An example of boundaries detected by the Matlab operator for an image comprising 1000-1250 μm dispersed particles (0.01 vol%) is given in Figure III.2.

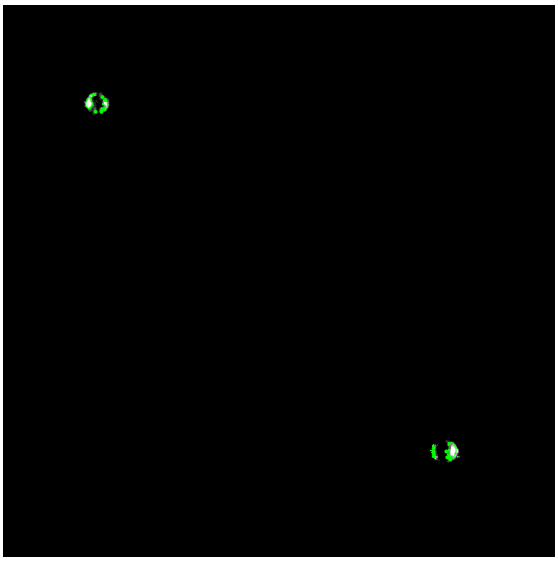

Figure III.2: Boundaries detected on a dispersed particle image

An advantage of the Hough transform is that it is able to identify parameters of a curve which best fit a set of given edge points containing multiple fragments of a single whole feature. Subsequently, outer edges of the ‘half moon’ shapes observed for the dispersed particle images would be recognised as part of the same circle and form peaks in the Hough space for their unique solutions (given that these edges are circular). Of course the Hough transform is sensitive to gaps in the boundary of the dispersed particle image, as a more complete boundary yields a stronger Hough peak. The Hough transform of the frame shown in Figure III.2, for an approximated particle radius of 25 pixels in image space, is shown in Figure III.3.

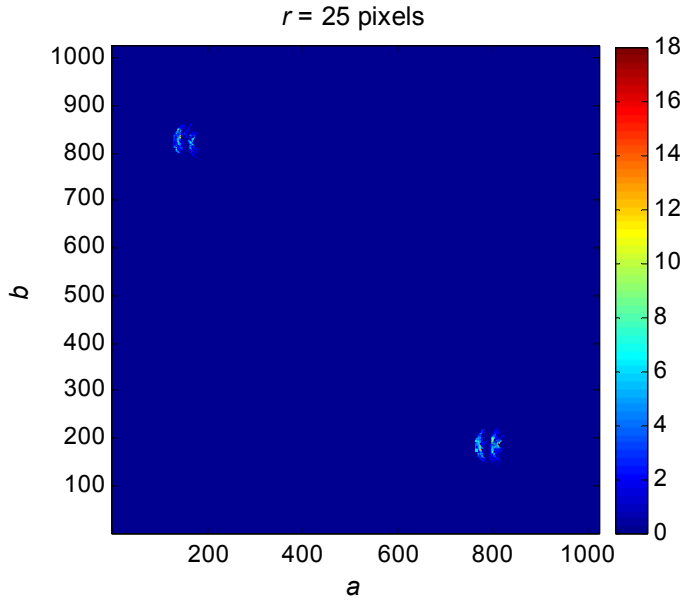

Figure III.3: Hough transform image shown in Figure III.2, for $r = 25$ pixels

Here parameters $[a,b]$ have been calculated for a single r value. In principle, this operation is carried out for a range of r, generating many Hough transform planes, as the exact particle radius (in pixels) is not known *a priori*. The Hough transform plane containing the strongest peak from all results is the one corresponding to the most probable r ($r_{\max}$). Due to the polydispersity of particles and nature of images, there exists a variation of r (around $r_{\max}$) that could provide a true fit around the particles. Subsequently a threshold T_1 was defined to pick out Hough transform planes calculated using r values which satisfy Equation (III.2).

$$r_{\text{peak}} = (1 - T_1) r_{\max} \le r \le (1 + T_1) r_{\max} \tag{III.2}$$

Typical values of T_1 were ~0.05-0.2. A second search operation was carried out to locate the maximum peak on each of these Hough planes, denoted $[a,b]_{\max}$. This peak corresponds to the particle centroid which generates the strongest signal (on the Hough plane where $r = r_{\text{peak}_i}$). Relative to this maximum, locations of other particles $[a,b]_{\text{peak}}$ of the same radius may be identified by applying a global threshold T_2 to the entire 2-D Hough space as follows:

$$[a,b]_{\text{peak}} = [a,b] \ge T_2 \times [a,b]_{\max} \tag{III.3}$$

Typical values of T_2 are ~0.65-0.85. Note that the search is performed on all Hough transform planes corresponding to $r = r_{\text{peak}}$ independently. In this way, particles of various radii at different locations can be picked out. Result of circles created by this routine is shown in Figure III.4. As may be observed, information from a single dispersed particle could yield multiple solutions, whose centroids are within close vicinity of each other. This is because object boundaries are not perfectly circular. Subsequently, a local comparison of Hough peaks is required. The

maximum peak of solutions which coexist within a distance $2 \times r_{\max}$ (or particle diameter) is taken to be the best solution. A drawback of this technique is that for true overlapping particles whose centroids will inevitably be close together, only the one with the dominant Hough peak will be picked out. Refined results after the local comparison of peaks are given in Figure III.5.

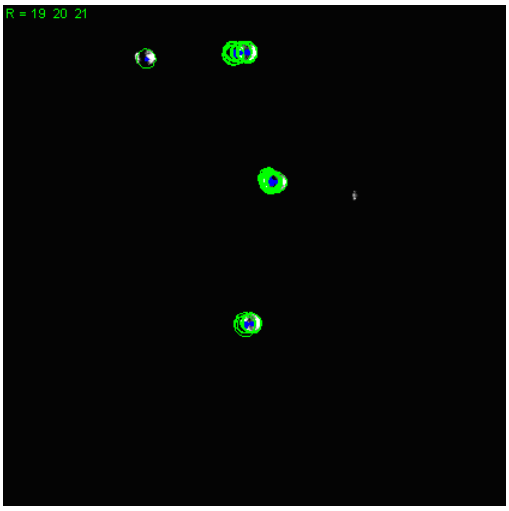

Figure III.4: Circles generated from the Hough transform for a prescribed range of r, after applying global thresholds T_1 and T_2

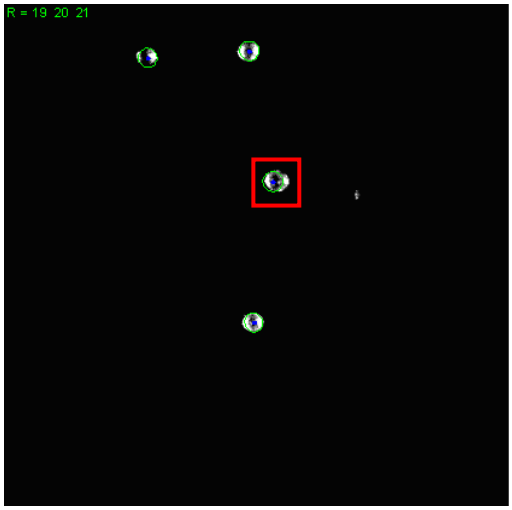

Figure III.5: Circles obtained after a local comparison of Hough transform peaks

A problem encountered is that circles often fit around inner boundaries of the 'half moon' shapes, and may be picked out as the final solution if their peaks are stronger than those which arise from fits around the outer boundaries. This is evident for the particle highlighted in a red box in Figure III.5. In some cases, blurring images before commencing the Hough routine by softening the inner boundaries gives an improved fit of circles around the outer edges. To add blur, the image was convolved with a point spread function using the Matlab function *fspecial*, where the disc filter was found to be the most suitable option. The filter radius defined the

extent of blur. An example of improvements made by the blur filter is portrayed in Figure III.6(a) and (b).

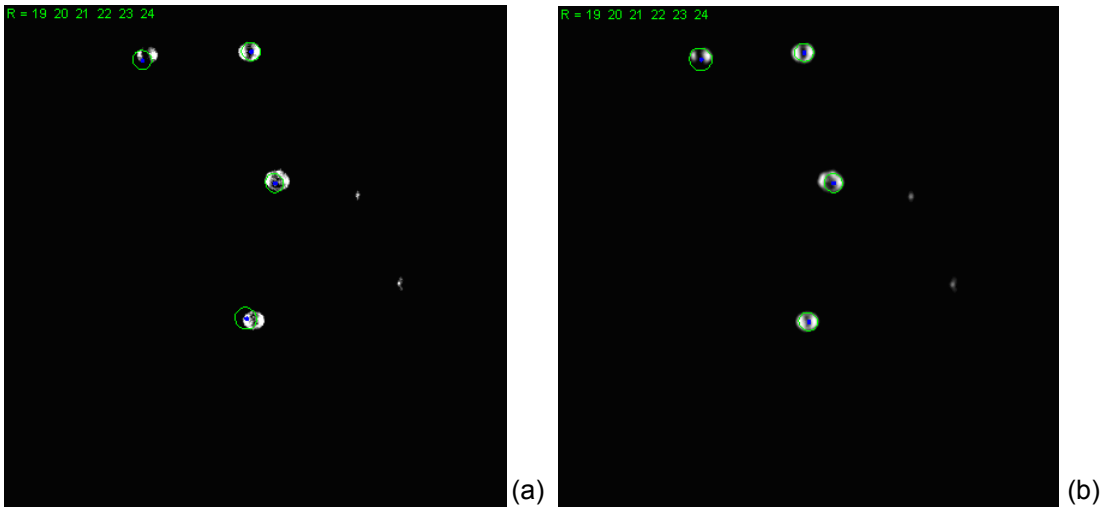

Figure III.6: Circles obtained (a) before (b) and after applying a blur filter to the image. Note the improved fitting around outer object boundaries.

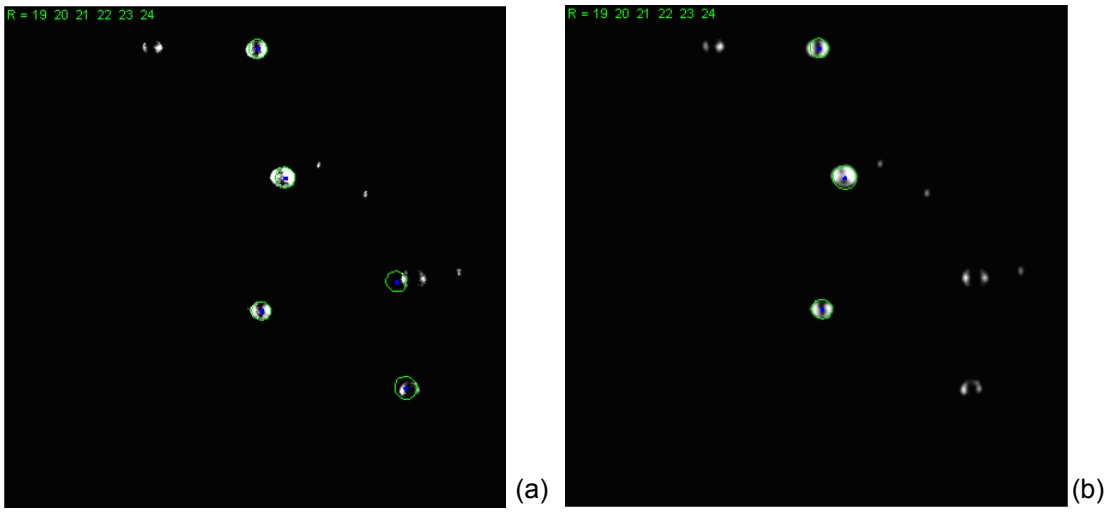

Figure III.7: Centroids and circles obtained (a) without applying a blur (b) and after applying a blur filter to the image. Note the removal of fitting around noise.

The blur filter is also useful for removing noise from large bright non-circular objects (resulting from particles scraping the light sheet), which could be recognised as dispersed particles in the phase separation limits. Other sources of noise are fragments within the 'half moon' shapes, which result in fitting circles around smaller bright circular spots. The blur filter smoothes out such spots, and eliminates fitting circles around them, as shown in Figure III.7(a) and (b). However, the blurring operation is not always advantageous. In some cases it decreases the fit around real particle boundaries, and shifts the true centroid location (albeit only slightly). If faint particles moving in or out of the light sheet plane are blurred, their boundaries are sometimes not detected and their information is lost.

Whether a blur filter should be applied or not depends on whether decreasing the fit around some particles and/or loss of other particles is outweighed by the removal of noise and consequently spurious vectors. At the moment, statistical criteria to evaluate this have not been developed, so the user's visual observations must suffice. It was noticed that blurring was only required for PIV images of the largest particles (1000-1250 μm), whereas it was disadvantageous for the smallest size (200-300 μm). This is because the distance between two opposing edges of a smaller particle is relatively short, and enables the refraction of light (as it enters and exits a particle) to merge together forming a type of fringe pattern. This creates a more complete object, and reduces the likelihood of observing 'half moon' shapes with defined inner boundaries as in the case of bigger particles. Thus, applying the blur filter to images of the smaller particles leads to a deterioration of the outer particle boundaries instead.

The technique could be improved by using mono-disperse and/or opaque particles in PIV experiments, which would reduce the range of r in the Hough calculations, and the threshold T_1 could be reduced with confidence. Subsequently, the particles were physically filtered to obtain narrower size distributions, which were used in following two-phase experiments. The 1000-1250, 500-750 and 200-300 μm size classes were reduced to sets of 1000, 700-750 and 250-300 μm particles. The parameters T_2 and disc filter radius in the blurring operation also have a bearing on the accuracy of results, and require optimisation.

Appendix IV
Particle tracking algorithm

Particle tracking is the process by which individual spots of dispersed particles on consecutive image frames are matched and connected. Velocity vectors are generated on a point-by-point basis, each corresponding to a separate dispersed particle. Tracking can also be carried out over a series of image frames in sequence, yielding Lagrangian particle trajectories.

A readily available tracking algorithm developed by Pastor (2007) was implemented in this study. The input information comprised the $[x, y]$ coordinates of particle centroid locations (in pixels) in the entire sequence of images. This information was obtained *a priori* from the image processing and object detection stages (employing the phase discrimination algorithm of Khalitov and Longmire (2002) described in Chapter 5). The data were arranged in the form shown in Table IV.1.

Table IV.1: Format of particle centroid information passed to the particle tracking routine

Image no.	*x coordinate*	*y coordinate*	
1	356	198	Coordinate positions of all particles in Image 1
:	:	:	
2	742	865	
:	:	:	

The first, second and third columns represent the image frame in which the respective particle appears, and the horizontal and vertical coordinates of the centroid location in pixels, respectively. Each line of the table corresponds to information of a separate particle. The data are arranged in sequence such that information of particles that appear in the first image is recorded first; those that appear in the second image are recorded next, and so on. The individual rows are ordered with respect to the x and y coordinates respectively. Basic principles of the algorithm are explained in a step by step fashion below.

- The algorithm starts at the first line of Table IV.1, which corresponds to the first particle in the first image frame. The algorithm creates a circular 'search area' around the particle centroid in the second frame. If a particle exists within the search area, it is accepted as the matching particle. A trajectory is created by joining a linear path between the pair.

- Next, the algorithm creates a search area in the third image (with respect to the second particle's coordinates) and the process is repeated. The trajectory is constructed until no particle is located in the search area of a subsequent image, or conversely, if more than one particle is found. The latter criterion reduces the possibility of matching particles falsely and also accelerates the process.

- At this point, the algorithm restarts at the second line of the table (corresponding to the second particle in the first image) and a new trajectory is created. All information used to create trajectories is marked and not recalled, so the same particle cannot appear in two separate tracks. This process is shown schematically in Figure IV.1.

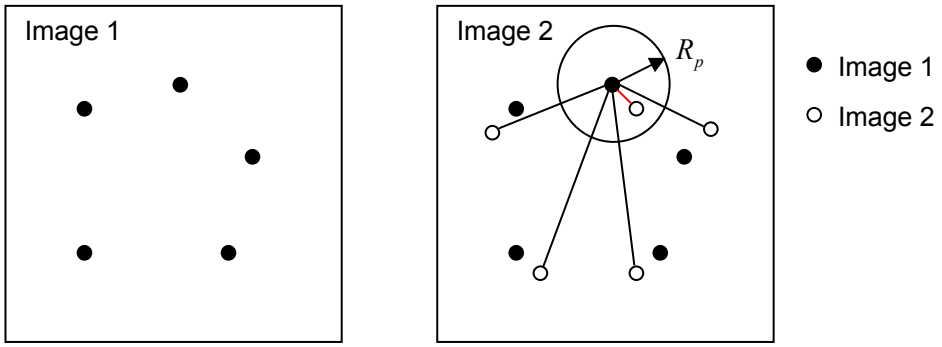

Figure IV.1: Schematic of particle tracking algorithm by Pastor (2007)

The algorithm enables control of three key parameters. The first is the search radius R_p (in pixels or metres depending on units of input data), which would theoretically be the maximum expected displacement of particles. The second parameter is the trajectory length T_l, which enables the user to specify the minimum number of points that should form a trajectory. For instance if a path contains less than T_l points after construction, it is not accepted as a valid trajectory and the information can be used again in the search for new trajectories. In the present case, it is only necessary to join particles between two consecutive image frames to create a velocity vector; hence T_l is set as 2. The third parameter 'jump' or J enables the user to define the number of image frames a particle can 'skip' in sequence before reappearing in another. For instance, suppose that J is set as 3. Then, if in the previous example a particle appears in images 1 and 2, but not in 3 to 5; rather than the trajectory stopping at frame 2 it is continued through to frame 6. The missing points in the trajectory (between frames 3 and 5) are created from linear interpolation (of the particle locations in frames 2 and 6). In the present case, it is not desired to allow the particles to skip any images, hence J is set as zero.

Of the parameters mentioned above, the one which requires most consideration is the search radius, since the algorithm is based on the 'condition of proximity', meaning that a track is only joined between two particles if they appear within a certain distance from each other. If R_p is too small then no particles will be found in the search area and if it is too big, more than one particle may be identified; both leading to termination of the particle track. It is desirable to limit both in- and out-of-plane displacements of dispersed particles between successive image frames. This has further implications on the PIV experimental conditions, such as capturing images at a very high frame rate, and limiting the exposure time between two double-image frames.

IV.1 Tracking algorithm tests

IV.1.1 CFD Model for artificial tracks

The effect of search area size and particle number density on the efficiency of the particle tracking algorithm was evaluated via the test cases presented below. Artificial particle tracks were generated from the predictions of the CFD code Fluent 6.3 (with the assistance of Dr J. Gimbun, Loughborough University). The impeller blade and baffle interactions were simulated via the multiple reference frame model, which provides a converged steady-state solution of the continuous phase fluid. In order to simulate the particle distribution within the stirred vessel, the solid phase was treated with a Lagrangian approach, where particles were released into the steady-state flow field, and information regarding their position and velocity was obtained by integrating the particle equation of motion for a number of time steps (Crowe *et al.*, 1996). Turbulence of the two-phase system was modelled using a realizable $k-\varepsilon$ model. The numerical model for the fluid-particle interactions was based on one-way coupling, where it was assumed that the dispersed phase has negligible impact on the continuous phase. This assumption may be reasonable as all simulations were performed with a relatively low particle volume fraction. The validity of this conjecture was not important, as the aim was to evaluate the efficiency of the particle tracking algorithm given random trajectories, independent of the continuous phase dynamics. It was assumed that the flow pattern repeated over 180° segments; hence calculations were performed in only one half of the vessel.

The geometry modelled was a stirred vessel to create a complex flow as would be observed in real experiments, of dimension $T = 0.26$ m, with four equi-distant baffles of $B = T/10$ around the tank periphery. The simulated tank was filled with 14 litres of water, and agitated using a RDT of $D = T/3$ which operated at a clearance of $C = T/3$ at an impeller speed of 700 rpm. This impeller generates two characteristic circulation loops, providing a bigger challenge for the tracking algorithm.

The resulting information of the particle positions at each time step (i.e. the transient solution) was transformed to a layout similar to Table IV.1, where each time step was interpreted as a transition between successive image frames (i.e. t_0, t_1, t_2 corresponding to images 1, 2, 3 respectively). The simulation generated solutions at regular time intervals of 3.74×10^{-4} s. Subsequently, the particle tracking routine was run with this information as input, and new trajectories were created. Finally, simulated trajectories and the output from the tracking algorithm could then be compared.

IV.1.2 Effect of search area size

In the test for evaluating the impact of search area size, the particle number was maintained relatively low (15 particles in half of the vessel volume). The simulated mono-dispersed particle diameter and density was 10 μm and 1500 kg m^{-3} respectively. The average displacement of all particles in the x and y directions was 27 μm and 19 μm respectively; the same order of magnitude as the particle diameter. The simulation generated particle tracks with 5000 time steps.

The tracking routine was implemented on the output data under four different conditions; the parameter R_p was set as 10^{-5}, 10^{-4}, 10^{-3} and 10^{-2} m respectively (whilst T_L and J were held constant at 2 and 0 respectively). In this way, the effect of increasing R_p could be identified independently. Results are shown in Figure IV.2(a) to (d). The coloured points correspond to simulated particle trajectories (with a different colour for each particle) and the black lines are trajectories from the particle tracking algorithm.

In Figure IV.2(a) it may be observed that the tracking routine is unable to create particle trajectories because the search radius ($R_p = 10^{-5}$ m) is smaller than the mean particle displacements in the $x-y$ plane, and particles cannot be found in the circular search area. When the search radius is increased ($R_p = 10^{-4}$ m), it may be observed that particle tracks are beginning to form near the impeller region in Figure IV.2(b). In this case, the search area is closer to the mean displacements of all trajectories in the $x-y$ plane. However, a global average is not very useful in characterising the motion of a stirred flow in such a large field of view (0.26×0.13 m^2), where the variation in velocities is expected to be large.

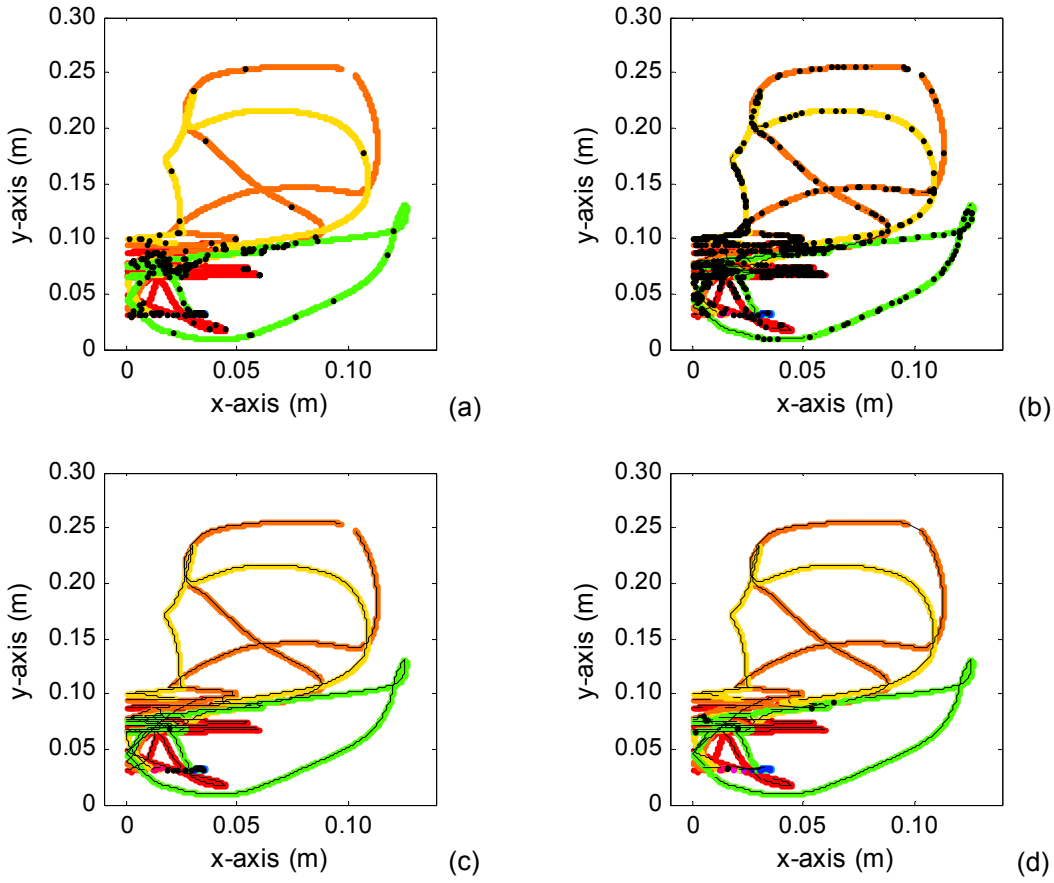

Figure IV.2: Simulated particle trajectories in coloured points (different colour for each particle) and superimposed trajectories from tracking algorithm shown as black lines using (a) $R_p = 10^{-5}$ (b) $R_p = 10^{-4}$ (c) $R_p = 10^{-3}$ (d) $R_p = 10^{-2}$ m

A further increase in the search radius proves to be sufficient for tracking all 15 particle tracks accurately, shown in Figure IV.2(c). In this case, the search radius is ($R_p = 10^{-3}$ m) is two orders of magnitude greater than the mean displacements in the x and y directions O(10^{-5} m). Note that the algorithm is able to cope exceptionally well with the curved path lines, is able to continue along a given trajectory when path lines cross, and is able to track particles along two independent circulation loops. It is also surprising that complete tracks are generated, given that each track comprises as many as 5000 time steps (equivalent to 5000 image frames). Standard PIV experiments and high speed PIV yield approximately 500 and 2000 frames respectively, hence there is confidence that the algorithm will be able to track over long image sequences (given short time separations between them). When the search radius is increased more ($R_p = 10^{-2}$ m), the efficiency of the algorithm deteriorates in the impeller region, where some particle trajectories are lost (Figure IV.2(d)). This is due to the high number density in that region, causing more than one particle to be identified in the search area at an early stage, and leading to premature termination of the trajectories.

Given that $D = 0.087$ m and $N = 700$ rpm, the impeller tip speed was $V_{tip} = 3.18$ m s^{-1}. The maximum particle radial velocity (in the main flow direction for a RDT) was 3.32 m s^{-1}. For the time interval $\Delta T = 3.74 \times 10^{-4}$ s, and average displacement of 27 μm in the x direction, the average particle radial velocity was found to be 0.072 m s^{-1}. At the optimum search area size ($R_p = 10^{-3}$ m), the parameter $R_p / \Delta T$ was calculated as 2.68 m s^{-1}. This value compares well with the tip speed and maximum particle velocity, rather than the particle mean velocity.

From this review, it is apparent that there exists an optimum search radius, which depends on the particle displacement. For real PIV experiments, it will be easier to estimate the search radius. Cross correlation of the continuous phase fluid will be performed first, hence knowledge of the flow field will be obtained prior to tracking. The dispersed particle velocity is not expected to deviate from the fluid motion significantly (Pettersson and Rasmuson, 1997). The search area size will be selected such that $R_p / \Delta T$ (where ΔT is now the time separation between two image frames) is just below the maximum fluid (and hence particle) velocity. In the absence of fluid velocities, the impeller tip speed could also be used as a basis of comparison.

IV.1.3 Effect of particle number density

The number of particles in the image influences the tracking efficiency, as more than one particle in the search area terminates the particle track. The objective of this test was to evaluate the limit (dispersed phase volume fraction) above which tracking was unfeasible using this algorithm. Mono-dispersed particles of 1000 μm diameter were simulated for approximately 200 time steps. The particle density was set as 500 kg m^{-3}, making them buoyant, so that they dispersed throughout the vessel quickly.

In PIV experiments, a 1 mm thick laser light sheet is directed through the measurement region, and light scattering particles in the field of view are captured by the CCD camera. Assuming that the light sheet traverses through half of the vessel, it would comprise a volume of 3.4×10^{-5} m^3. Thus, given a total vessel volume of 14 l, particle diameter of 1000 μm and homogeneous dispersion, there would be 13 and 65 particles in the light sheet at volumetric concentrations of

0.02 and 0.1 vol% respectively. The number of particles (N_p) was artificially varied between 12 and 75, and particle tracking was performed on the simulated data. The search radius was kept constant in all trials ($R_p = 10^{-2}$ m was best for this case). Results of the simulated trajectories (projected on the $x-y$ plane) and those from the tracking routine are shown in Figure IV.3(a) to (d). Results of Figure IV.3(a) to (d) indicate that the algorithm is able to track particle trajectories reasonably well up to dispersed phase volumetric concentrations of 0.1 vol%. The tracking routine works relatively poorly in the impeller region for the reasons explained above and in other cases where particle displacements are too large. This is independent of the number of particles in the flow field.

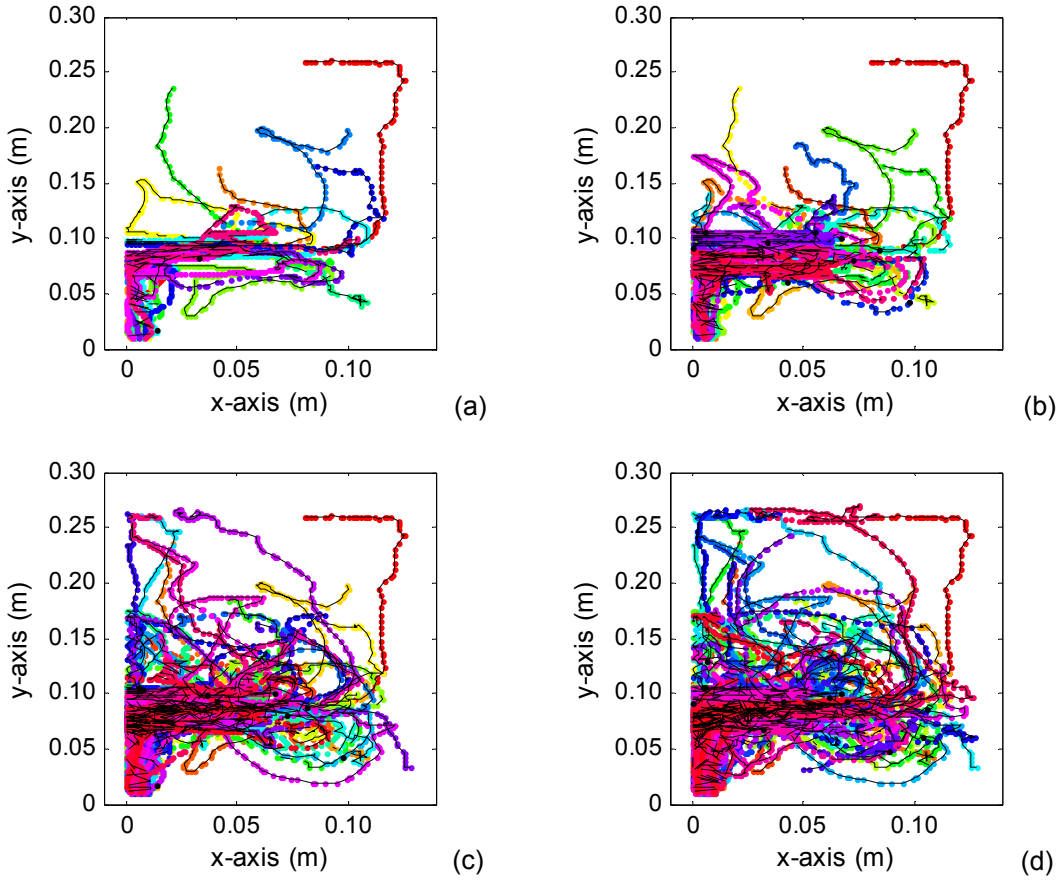

Figure IV.3: Simulated particle trajectories in coloured points (different colour for each particle) and superimposed trajectories from tracking algorithm shown as black lines using (a) $N_p = 12$ **(b)** $N_p = 25$ **(c)** $N_p = 50$ **(d)** $N_p = 75$ **particles.**

Overall, the algorithm of Pastor (2007) is considered to be appropriate for tracking particles in flows which have a relatively small dispersed phase concentration, and where the particle displacement can be estimated and is around the same order of magnitude as the particle diameter. However at high dispersed phase concentrations where there is a possibility of detecting more than one particle within a given search area, the performance of the algorithm deteriorates. This tracking code was employed only in the investigation of the phase discrimination algorithm (Chapter 5), where two-phase PIV experiments were carried out up to only 0.5 vol% dispersed phase.

Appendix V
Solid and tracer properties

V.1 Dispersed phase particles

In two-phase PIV experiments, soda-lime glass spheres were employed for the dispersed phase, of density 2500 kg m^{-3} and RI 1.51 at the sodium D-line ($\lambda = 589.3$ nm) at 20 °C (Duke Scientific Corporation). Three size classes were employed: 250-300, 700-750 and 1000 μm.

V.1.1 Just suspended speed

In complete suspension, particles are in constant motion and none remain on the vessel base for more than 1-2 s (Atiemo-Obeng *et al.*, 2004). This state is optimal, as it requires minimum agitation for full suspension, referred to as the 'just suspension' speed N_{js}. At this speed, it is assumed that there exists equilibrium between particles lifted from the vessel base and settling back down. The just suspended speed may be characterized by the Zwietering criterion (Zwietering, 1958), expressed below:

$$N_{js} = S\nu^{0.1}\left[\frac{g(\rho_s - \rho_l)}{\rho_l}\right]^{0.45} X^{0.13} d_p^{0.2} D^{-0.85} \tag{V.1}$$

where S is a dimensionless number, which incorporates the influence of the impeller and tank geometry and X is the mass ratio of suspended solids to liquid × 100, ρ_l and ν are the fluid density and kinematic viscosity respectively, and d_p the particle diameter. Note that the fluid and particle properties have a small influence on N_{js}, reflected by the small exponents on ν, d_p and X. More important are the impeller and vessel geometry, given by larger exponents on S and D.

The just suspended speed of particles in water agitated by a 45° PBT impeller with $D = T/3$, $C = T/4$ and $W = D/4$ were calculated. The S factor of 4.4 was obtained from the study of Mak (1992). The real blade width to impeller diameter ratio was $W = D/4.55$, but S for this particular case was not found in literature. Consequently, Mak's (1992) conditions provide an estimate. Note that the largest particle size from each class was used for the calculation (i.e. 300, 750 and 1000 μm), to ensure suspension of all particles. Results are given in Table V.1. The flow is fully turbulent under all conditions, indicated by the flow Reynolds number for experiments conducted in water (at the just suspended speeds), given in Table V.2.

Table V.1: Just suspended speed of the 45° PBT from the Zwietering correlation (1958), for various dispersed particle sizes and volume percentages, in water

Particle size (μm)	*Volume percentage dispersed phase (%)*						
	0.01	*0.02*	*0.1*	*0.2*	*0.3*	*0.4*	*0.5*
300	491	537	662	725	764	793	817
750	590	645	796	871	918	953	981
1000	625	684	843	922	972	1010	1039

Particle size (μm)	*Volume percentage dispersed phase (%)*						
	0.6	*0.7*	*0.8*	*0.9*	*1*	*2*	*3*
300	837	854	869	882	895	980	1035
750	1005	1025	1043	1060	1074	1177	1243
1000	1064	1086	1105	1122	1138	1247	1316

Table V.2: Flow Reynolds number with varying dispersed particle size and volume percentage, corresponding to N_{js} given in Table V.1

Particle size (μm)	*Volume percentage dispersed phase (%)*						
	0.01	*0.02*	*0.1*	*0.2*	*0.3*	*0.4*	*0.5*
300	9,239	10,111	12,465	13,642	14,383	14,933	15,374
750	11,098	9,048	12,219	13,389	17,275	17,936	18,466
1000	12,291	10,021	13,534	14,830	19,133	19,865	20,453

Particle size (μm)	*Volume percentage dispersed phase (%)*						
	0.6	*0.7*	*0.8*	*0.9*	*1*	*2*	*3*
300	15,745	16,066	16,349	16,604	16,835	18,447	19,471
750	18,912	19,297	19,637	19,943	20,221	22,157	23,387
1000	20,032	20,440	20,800	21,124	21,418	23,469	24,772

V.1.2 Particle Reynolds number

It was discussed in §2.4 that the particle Reynolds number may be used to characterise the particle's effect on the continuous phase turbulence, defined as follows:

$$\mathrm{Re}_p = \frac{\left|u - u_p\right| d_p \rho_l}{\mu} \tag{V.2}$$

where u_p and u are velocity vectors of the particle and surrounding fluid respectively. The particles' Reynolds number will be calculated in this section, to predict *a priori* the effect they may have on the fluid. The variables ρ_l, μ and d_p are known. However, the respective velocities are unknown before experiments. Micheletti and Yianneskis (2004) suggested that the slip velocity between the two phases can be regarded as the local value of the particle settling velocity (sometimes referred to as the terminal velocity). The particle *settling* or *terminal* velocity (V_{term}) is the steady-state velocity that a dense solid particle accelerates to in a quiescent fluid. It occurs when the drag force balances the buoyancy and gravitational force acting on the particle. Other studies (Nouri and Whitelaw, 1992) have also used the particle

terminal velocity as a substitute for the slip or relative velocity. Subsequently, the particle terminal velocity will be used to estimate Re_p, such that Equation (V.2) reduces to:

$$\mathrm{Re}_p = \frac{V_{term} d_p \rho_l}{\mu} \tag{V.3}$$

In Newtonian fluids, the settling velocity is calculated as follows (Tilton, 1997):

$$V_{term} = \left(\frac{4 g d_p (\rho_s - \rho_l)}{3 C_D \rho_l} \right)^{1/2} \tag{V.4}$$

where g is the gravitational acceleration (9.81 m s^{-2}) and C_D the drag coefficient which is dependent on Re_p. Correlations for the drag coefficient expand across many hydrodynamic regimes, the main ones being Stokes' law, Intermediate and Newton's law regime.

In Stoke's law regime, $\mathrm{Re}_p < 0.3$ and $C_D = 24 / \mathrm{Re}_p$. After substituting this definition combined with Equation (V.3) into Equation (V.4), the terminal velocity may be directly inferred as:

$$V_{term} = \frac{g d_p^2 (\rho_s - \rho_l)}{18 \mu} \tag{V.5}$$

In Newton's law or the turbulent regime, $1000 < \mathrm{Re}_p < 35 \times 10^4$ and $C_D = 0.445$. Once again, the terminal velocity may be directly obtained from Equation (V.4). Note that if the hydrodynamics of the solid suspension are assumed to be characterized by the Stoke's law or turbulent regimes as an initial approximation, it must later be checked whether Re_p obtained from the terminal velocity falls within the specified range.

Finally, in the Intermediate regime, $0.3 < \mathrm{Re}_p < 1000$ and $C_D = 18.5 / \mathrm{Re}_p^{3/5}$, an iterative procedure must be used to obtain the terminal velocity.

The largest particle diameter in each size class was used as the characteristic d_p for the terminal velocity calculation; i.e. 300, 750 and 1000 μm. In all three cases, Re_p did not satisfy limits of Stoke's law or turbulent regimes; the terminal velocity was obtained under the Intermediate regime. The particle terminal velocity and particle Reynolds numbers are given in Table V.3.

Note that the case discussed above considers the settling velocity of particles in a stagnant fluid. In an agitated solid suspension, it becomes more difficult to quantify the particle settling velocity due to the complex, turbulent hydrodynamic field and presence of particle-particle interactions, which modifies the flow field around the particles. It has been well accepted that the drag coefficient of particles in the Stokes's regime is unaffected by free stream turbulence. However, for particles in all other regimes, the drag coefficients in turbulent fluids are a function of both particle and flow field characteristics (Clift *et al.*, 1978). Many researchers have

attempted to characterise the settling velocity of particles in an agitated fluid (Nienow and Bartlett, 1974; Magelli *et al.,* 1990; Pinelli *et al.*, 1996). The general consensus amongst these studies is that the settling velocity in agitated suspensions is less than the equivalent velocity in a dormant fluid, indicating an increase in the drag coefficient.

Table V.3: Particle settling velocity, particle Reynolds number and drag coefficient for various particle sizes, obtained under the Intermediate regime

Particle size (μm)	V_{term} *(m s^{-1})*	Re_p	C_D
300	0.031	4.92	7.11
750	0.087	35.05	2.19
1000	0.140	104.74	1.14

Since the particle Reynolds numbers of all three sizes is almost the same as or less than O(100), it is anticipated that they will dampen the fluid turbulence, according to the theory of Hetsroni (1989). However the subsequent calculation of slip velocities in §6.7.3 showed that they were underestimated by a factor of five and nine for the 1000 and 750 μm particles respectively, in isolated regions within the discharge stream.

V.2 Continuous phase tracers

V.2.1 Stirred-cell technology for manufacturing particles

Tracer particles were made from the polymerization of styrene monomer, cross-linked with divinyl benzene (PS/DVB), incorporating fluorescent dye at a concentration of 1 mol m^{-3} polymer. All chemicals in the following description were used as received. Styrene +99% (Cat: S497-2), divinyl benzene (Cat: 1321-74-0) and polyvinyl alcohol (PVA) (Cat: 81386) were purchased from Sigma Aldrich. Dibenzoyl peroxide (BPO) 75% (Cat: 211781000) and sodium chloride (Cat: S/3160/53) were obtained from Fisher Scientific. The fluorescent dye (pyrromethene 597-8C9) was purchased from Exciton. Particle synthesis was carried out under the supervision of a postgraduate researcher working in the field of particle technology at Loughborough University, UK (Chris C. Webb).

The first stage involved the preparation of the styrene and toluene emulsion, containing the cross-linking agent DVB and initiator BPO. In the trial attempt, a 35 ml mixture of styrene and toluene (volumetric ratios 1:2), DVB (3 vol% of the styrene monomer) and a trace amount of BPO (0.11 g) was prepared. Fluorescent dye of the required concentration was added to the solution and mixed thoroughly. The purpose of the toluene was to swell the particles during droplet formation, and subsequently shrink them by evaporating the toluene at the end. This would enable control of the particle size. After the trial run failed to generate particles, it was decided not to use toluene (for reasons which will be explained later) and a mixture of only styrene (35 ml), DVB (3 vol% of the styrene monomer) and trace BPO (0.32 g) was used instead.

The polymerization was conducted in the presence of an aqueous solution comprising 2% PVA and 3.3% NaCl by mass in distilled water. PVA acted as a stabilising agent that helped to control the droplet size, and NaCl reduced the solubility of the monomer in the aqueous

solution. The following steps were implemented to prepare 500 ml of the solution. Approximately 17.34 g of NaCl was added to 600 ml of distilled water, which was heated and stirred simultaneously. When the solution temperature reached 70 °C, the heat was reduced and around 10.54 g of PVA was added to the solution incrementally. The solution was stirred at a temperature of 20 °C for approximately 2 hours, after which the heat was turned off. The mixture was left to stir for another 12 hours at room temperature, which yielded a clear PVA solution. Distilled water was added to the resulting solution to regain the required volume (500 ml).

The second stage was formation of emulsion droplets in a stirred cell. The cell was filled with 60 ml of the aqueous solution. Next, the styrene mixture was fed to the cell using a pumped glass syringe of maximum capacity 25 ml, at a rate of 0.4 ml min^{-1}. The cell had a height of $T = 165$ mm, and was equipped with a flat paddle impeller of diameter $D = 31$ mm that operated at a clearance of around 2 mm from the vessel base. The cell incorporated a 10 µm circular-pore membrane, from Micropore technologies Ltd. The mixture was stirred at a constant agitation rate under ambient conditions (with the impeller operating at 9 volts) until the entire feed was injected into the cell (which took approximately 1.5 hours). This generated an initial droplet diameter of ~50 µm.

The third part of the operation was polymerization of the styrene monomer within the emulsion droplets via suspension polymerization. After complete mixing, the emulsion was transferred to a stirred batch reactor where polymerization was initiated in the presence of BPO. The reactor had a height of $T = 170$ mm, filled with 400 ml of the 2% PVA and 3.3% NaCl solution. The impeller had a diameter of $D = 60$ mm, located at a clearance of $C = T/3$ from the vessel base. The reaction was carried out at 80 °C, with an impeller speed of 175 rpm for approximately 24 hours.

When the reaction stage was complete, the dyed polystyrene particles were crudely separated from the solvent by adding RO water to the solution, and left to standby for around 6 hours. The particles floated to the top (due to the toluene content) and retrieved from the surface. The wet particle slurry was cleaned by filtering through a Buchner funnel (lined with Whatman No. 5 filter paper) with an equivalent volume of RO water, thereby halving the concentration of PVA around the particles. This filtering process was repeated three times consecutively, reducing the end PVA concentration to approximately 0.25%. For normal (dye-free) polystyrene particles, the next logical step would be to wash the particles with acetone to remove the water, and further purify them in a Soxhlet extractor with toluene. However, when washing the particles with acetone, some dye was found to leak out of the polymer into the solvent. Consequently, cleaning in a Soxhlet extractor was not carried out, and the particles were filtered with water until the PVA concentration was assumed to be minimal.

The final stage involved drying the particles under ambient conditions for ~6 hours, and subsequently in a vacuum oven at 65 °C for ~24 hours, to remove the toluene content by evaporation. This process causes shrinking of the particles to obtain the desired size range. However, the final sample obtained after drying was found to be an agglomerated block; a failed attempt to create particles. This may have been because particles were not completely cleaned of the PVA solution from filtering alone, and the residual PVA caused agglomeration when dried.

As mentioned above, in the second attempt toluene was not used at all. The mixture was prepared from styrene, DVB, BPO, and fluorescent dye at a concentration of 1 mol m^{-3} polymer. In this case, the same stirred cell and membrane was employed to generate particles close to the required mean size (~30 μm) but with less control over the size distribution. The reaction and cleaning stages were carried out exactly as described above, apart from the final drying stage, which could be eliminated as there was no toluene in the particles. The particle sample was preserved in a wet form to prevent drying of the residual PVA and subsequent agglomeration. The final particle size was characterized using a Malvern Mastersizer, and the volume-average particle diameter was confirmed to be around 30 μm. The particles contained 1 mol m^{-3} polymer, and had a density of 1050 kg m^{-3}.

V.2.2 Selection of dye

The fluorescent dye was selected based on the following criteria:

- The dye must be able to absorb light at the laser wavelength (532 nm)
- The dye must emit fluorescence with an emission peak within the spectral sensitivity range of the camera. Common PIV cameras have spectral sensitivity between 400 and 700 nm
- The fluorescence spectrum must be distinct from the laser wavelength in order to facilitate optical filtering of its emission from Mie scattering
- The dye must be soluble in oil but insoluble in water

The last criterion arises from the preparation of the PS/DVB particles. As described in the previous section, an oil-based emulsion is passed through a membrane and stirred in an aqueous medium within the stirred cell. Thus, it is necessary for the dye to be soluble in oil for incorporation into the styrene monomer; at the same time it should be insoluble in water to minimise entrainment from the emulsion into the aqueous solution. This criterion posed the greatest limitation on the number of dyes which could be implemented. Rhodamine based dyes were found to be the most popular type for FPIV applications (Boedec and Simoens, 2001; Kosiwczuk *et al.*, 2005; Guido *et al.*, 2005), but they are highly soluble in water and subsequently rejected for the present case.

Generally, pyrromethene dyes are oil soluble and water insoluble (with the exception of pyrromethene 556). Specifically, pyrromethene 597-8C9 dye (Exciton) was found to satisfy all four criteria simultaneously as well as being the most oil soluble, hence selected for the current study. The dye has an absorption peak at $\lambda_{abs} = 527.8$ nm (close to the laser excitation wavelength of 532 nm), and fluorescence peak at $\lambda_{fl} = 590$ nm in diesel fuel. Pyrromethene dyes are not very solvo-chromatic, hence their wavelength changes would be small (5 to 10 nm at most) in the PS/DVB material. An example of the pyrromethene 597-8C9 dye used for LIF techniques may be found in the study of Wolff *et al.* (2007).

V.2.3 Particle size

Previous experience of researchers facilitating this operation has enabled particles to be produced within the size range of 30 to 300 μm with a reasonable size distribution (CV ~10%).

Smaller particles of the standard size range (~10 μm) could have also been produced by operating at a higher shear rate, although the size distribution of these particles would be significantly broader. Subsequently, the particle size was a deciding factor in the choice of operating parameters. A point to consider is that fluorescence emissions have a lower intensity in comparison to Mie scattering, and images of the smallest particles might not be recorded by the CCD camera. Higher sensitivity cameras would be required to capture the smallest particle sizes (Boedec and Simoens, 2001). In order to produce LIF images of comparable intensity to Mie scattering, a greater 'effective' thickness of the laser light sheet would be required (Kosiwczuk *et al.*, 2005). This is not desirable, as a thicker light sheet would cause objects to be out of focus in the image plane. Alternatively, since the fluorescence intensity is dependent on particle size, an option is to use bigger tracer particles. For this reason, 30 μm tracers were preferable, as well as the benefit of obtaining a narrower size distribution.

V.2.4 Stokes' number analysis

Standard PIV experiments employ 10 μm hollow glass spheres. Particles of this size are considered to be small enough to follow the flow field faithfully. In the same way, it is essential for the 30 μm fluorescent tracer particles (made in the laboratory) to follow the flow in order to estimate the fluid velocities reliably. This property could be verified by calculating the Stokes' number St, which provides an indication of the particle-fluid interactions. The Stokes' number is a dimensionless parameter; the ratio of the particle response time to the appropriate fluid time scale. It may be assumed that if $St \ll 1$, the particle response time is much smaller than the fluid time-scale, such that it has ample time to respond to changes in the fluid velocity. Accordingly, particles follow the fluid streamlines at approximately the same velocity. Conversely if $St \gg 1$, particles cannot respond to changes in the fluid velocity and are not affected appreciably by the flow field.

The particle response time is defined as the time required by a particle to reach 63% of its settling velocity. Under the Stokes' regime (where $\mathrm{Re}_p < 1$), the response time is given as:

$$\tau_p = \frac{d_t^2 \rho_t}{18\mu} \tag{V.6}$$

where d_t and ρ_t are the tracer particle diameter and density respectively (1050 kg m^{-3} and 30 μm), and μ the absolute fluid viscosity. The particle Reynolds number (satisfying operation in the Stokes' regime) and response time were found to be 2.5×10^{-4} and 5.2×10^{-5} s respectively.

A comparison of the response time could be made against the macro-scale (i.e. integral time scale) or micro-scale (i.e. Kolmogorov time scale). These parameters depend significantly on the flow under investigation. Subsequently this information was obtained from previous studies investigating the flow field generated by comparable PBTs. Pettersson and Rasmuson (1997) employed 3-D LDA to study six points in the flow field surrounding a PBT impeller. The authors obtained the macro time scales at the respective locations by integrating the autocorrelation coefficient of the fluctuating velocity component in three Cartesian directions, with respect to time. This yielded macro-time scales in the three directions at each point. The macro-time

scales at each point and corresponding Stokes' number are given in Table V.4. Refer to the paper for exact locations of the points.

In another study, Khan *et al.* (2004) calculated integral length scales for a field of view expanding across the whole vessel, by employing a multi-block approach. These length scales have been converted to integral time scales in the present case using information of the mean velocity in the corresponding regions as a proportionality factor as follows:

$$T_{E,i} = \frac{\Lambda_{u_i x_i}}{\overline{u_i}} \tag{V.7}$$

where $\Delta_{u_i x_i}$ is the 1-D longitudinal length scale obtained from integrating the autocorrelation coefficient of velocity component u_i with respect to direction x_i. $\overline{u_i}$ is the mean velocity component in the i^{th} direction. The integral time scales were obtained from the 1-D longitudinal length scale in the direction Δ_{vy} and mean axial velocity $\bar{v}$ near the impeller region and surface. Results of the Stokes' number are given in Table V.5.

The resulting Stokes' numbers listed in Table V.4 and Table V.5 indicate that $St << 1$ everywhere. The time scales obtained from both studies are of the same order of magnitude, providing confidence in the Stokes number estimates. Subsequently it may be assumed that the tracer particles are able to respond to the integral time scales sufficiently, and capture the mean fluid motions and turbulent kinetic energy.

Table V.4: Stokes' number of 30 µm tracer particles on comparison with integral time scales. Data obtained from Pettersson and Rasmuson (1997).

Point studied	***Flow direction***	$T_{E,i}$ ***(s)***	St ***(-)***
Point 1	Axial	0.029	0.0015
	Tangential	0.019	0.0023
	Radial	0.022	0.0020
Point 2	Axial	0.039	0.0011
	Tangential	0.012	0.0036
	Radial	0.016	0.0027
Point 3	Axial	0.048	0.0009
	Tangential	0.100	0.0004
	Radial	0.076	0.0006
Point 4	Axial	0.052	0.0008
	Tangential	0.050	0.0009
	Radial	0.039	0.0011
Point 5	Axial	0.090	0.0005
	Tangential	0.108	0.0004
	Radial	0.085	0.0005
Point 6	Axial	0.190	0.0002
	Tangential	0.120	0.0004
	Radial	0.150	0.0003

Table V.5: Stokes' number of 30 µm tracer particles on comparison with integral time scales. Data obtained from Khan *et al.* (2004).

Region	$\Delta_{v,y}$ *(m)*	$\bar{v}$ *(m s^{-1})*	T_E *(s)*	St *(-)*
Impeller	0.0114	1.13	0.010	0.0043
Surface	0.0247	0.10	0.247	0.0002

In order to obtain turbulence properties at the smallest scales (such as the dissipation rate), particles should be able to respond to changes in the flow field, which occur at the Kolmogorov time and length scale. Kolmogorov time scales (τ_η) are related to the dissipation rate via:

$$\tau_\eta \equiv \left(\nu/\varepsilon\right)^{1/2} \tag{V.8}$$

The smallest time scale can only be deduced from *a priori* knowledge of the maximum dissipation rate. Estimates reported in literature for PBT flow are given in Table V.6. The normalized values are also listed to portray the real difference between the estimates due to the difference in calculation method. Zhou and Kresta (1996) performed LDA experiments at different impeller speeds, and obtained the maximum dissipation rate via dimensional analysis. Sheng *et al.* (2000) and Khan (2005) employed the LES analogy, although the relatively low normalized estimate obtained by Sheng *et al.* (2005) may be due to the poor PIV resolution (with interrogation area of size 5×5 mm). All of these estimates were used to obtain the Kolmogorov time scale, and subsequently the Stokes' number.

Table V.6: Stokes' number of 30 µm tracer particles on comparison with Kolmogorov time-scales. Data obtained from various studies.

Author	*D/T*	*N (rps)*	$\varepsilon_{\max} / N^3D^2$	$\varepsilon_{\max}$ *(m^2 s^{-3})*	τ_η *(s)*	St *(-)*
Zhou and Kresta (1996)	0.333	5.95	2.47	3.34	5.E-04	0.08
		8.00	2.36	7.71	4.E-04	0.12
		9.83	2.62	15.1	3.E-04	0.17
		11.68	2.33	23.8	2.E-04	0.21
		13.33	2.44	37.1	2.E-04	0.26
Sheng et al. (2000)	0.349	1	0.58	0.01	0.013	0.00
Khan (2005)	0.333	5	9.20	10.75	3.E-04	0.14

Results of Table V.6 indicate that $St \ll 1$, hence there is confidence that the 30 µm tracer particles will follow the turbulent flow field under the listed experimental conditions. However the impeller speed required to suspend the largest dispersed particles in the fluid will be as high as approximately 1300 rpm (or ~21.67 rps), which will inevitably generate higher absolute dissipation rates, and smaller Kolmogorov time scales in accordance with Equation (V.8). By assuming that the dissipation rate scales with N^3D^2, the normalized estimates were used to predict the absolute maximum dissipation rates at the higher impeller speed, and subsequently the Kolmogorov time scales under these conditions were recalculated. Following, the Stokes' number was also estimated at this impeller speed. The results are shown in Table V.7.

Table V.7: Stokes' number of 30 µm tracer particles, on comparison with Kolmogorov time-scales, assuming operation at 21.67 rps

Author	N_{max} *(rps)*	ε_{max} *(m² s⁻³)*	τ_η *(s)*	St *(-)*
Zhou and Kresta (1996)	21.67	27.91	1.9E-04	0.229
	21.67	26.67	1.9E-04	0.224
	21.67	29.61	1.8E-04	0.236
	21.67	26.33	1.9E-04	0.222
	21.67	27.58	1.9E-04	0.228
Sheng et al. (2000)	21.67	6.52	3.9E-04	0.111
Khan (2005)	21.67	103.97	9.8E-05	0.442

As expected, the Stokes' numbers are higher than those obtained from estimates at lower impeller speeds, but are of the same order of magnitude and still smaller than unity. From this result it may be concluded that the 30 µm tracer particles are appropriate for tracking the continuous phase turbulence, and a suitable size for current FPIV experiments.

Nomenclature

Roman letters

a	Volume ratio of reagents in vessel to feed	[-]
a	x Cartesian coordinate of circle centre in Hough transforms	[m or pixels]
a_{ij}	Anisotropy tensor	[-]
$[a,b]_{\max}$	Coordinates of maximum peak on Hough transform planes	[m or pixels]
$[a,b]_{\text{peak}}$	Coordinates of high peak on Hough transform planes	[m or pixels]
A	Constant in dimensional analysis Equation (4.3)	[-]
A_a	Area of analyte in GCMS chromatogram	[-]
A_s	Area of internal standard in GCMS chromatogram	[-]
b	y Cartesian coordinate of circle centre in Hough transforms	[m or pixels]
b_{ij}	Normalized anisotropy tensor	[-]
b_t	Blade thickness	[mm]
B	Average intensity of an object in an image frame	[-]
c_i	Absolute concentration of substance i	[mol m^{-3}]
C	Impeller clearance from vessel base	[mm]
$\langle C_d \rangle$	Locally averaged volumetric concentration of particles from PIV images	[vol%]
C_D	Drag coefficient	[-]
C_i	Normalised concentration of substance i	[-]
C_s	Smagorinsky constant	[-]

d_p	Dispersed particle diameter	[mm]
d_t	Tracer particle diameter	[mm]
D	Impeller diameter	[mm]
D_q	Generalized dimension in multifractal model	[-]
D_{353}	Light absorption at 353 nm in the Beer-Lambert law	[-]
Da	Damköhler number	[-]
E	Engulfment rate coefficient	[s^{-1}]
E_{av}	Average engulfment rate coefficient	[s^{-1}]
E_r	Fraction of dissipation on secondary eddy of length $r(n)$	[$m^2 s^{-3}$]
E_t	Total dissipation in a primary eddy	[$m^2 s^{-3}$]
f_w	Median filter width in image processing	[mm]
f	Frequency	[s^{-1}]
f_D	Doppler shift between incident and scattered light in LDA	[s^{-1}]
f'	Normalized macro-instability frequency	[-]
$f^{\#}$	f-number of recording aperture	[-]
$F(f)$	Normalized PSD	[-]
g	Gravitational acceleration	[m s^{-2}]
G^o	Gibbs free energy under standard-state conditions	[kJ mol^{-1}]
$h(f)$	None-normalized PSD from a periodogram estimate	[-]
H	Water fill height	[mm]
H_f^o	Enthalpy of formation under standard-state conditions	[kJ mol^{-1}]
I	Pixel intensity in an image frame	[-]
I	Ionic strength	[mol l^{-1}]

I_t	Pixel intensity of tracer in an image frame	[-]
I_s	Pixel intensity of solid in an image frame	[-]
J	N^o of frames particle allowed to jump in particle tracking algorithm	[-]
k	Turbulent kinetic energy	[m^2 s^{-2}]
k_i	Rate constant of forward reaction i	[(m^3 mol^{-1})^n s^{-1}]
$k_i^{'}$	Rate constant of reverse reaction i	[(m^3 mol^{-1})^n s^{-1}]
K	Total kinetic energy	[m^2 s^{-3}]
K_i	Equilibrium constant of reaction i	[(m^3 mol^{-1})^n]
K_{ijhk}	Isotropic ratio	[-]
KE_r	Kinetic energy flow in radial direction	[W]
KE_z	Kinetic energy flow in axial direction	[W]
l	Characteristic eddy size	[m]
l	Optical path length across a quartz cell in the Beer-Lambert law	[m]
l_j	Length multiplier	[-]
L	Characteristic length scale	[m]
L_f	Resultant macro-scale	[m]
M_j	Measure multiplier	[-]
M_x	Number of intervals in the direction in Simpson's rule	[-]
n_{bl}	Number of impeller blades	[-]
n_B	Number of baffles	[-]
n_i	Moles of substance i	[mol]
N	Impeller speed	[s^{-1}]
N	Number of particles with a particular size and brightness in image	[-]

N_{js}	Just suspended impeller speed	[s^{-1}]
N_p	Number of particles in image for particle tracking	[-]
N_t	Total number of velocity fields in a data set	[-]
P	Power consumed by impeller	[W]
P_{CV}	Power consumed in control volume	[W]
P_o	Power number of impeller	[-]
$P(f)$	Spectral distribution function	[-]
pH*	Critical pH of iodine instability in Villermaux reaction scheme	[-]
Q_i	Coefficient vector for the one-dimensional Simpson's rule	[-]
Q_{ij}	Coefficient matrix for the two-dimensional Simpson's rule	[-]
q	Moments of generalized dimension D_q	[-]
r	Radius of circle in Hough transforms	[m or pixels]
r_i	Rate of reaction i	[mol m^{-3} s^{-1}]
r_s	Ratio of moles to GSMS chromatogram area of analyte	[mol]
$r_{\max}$	Most probable circle radius of highest peak in Hough transforms	[m or pixels]
r_{peak}	Highly probable circle radius in Hough transforms	[m or pixels]
r_s	Ratio of moles to GSMS chromatogram area of internal standard	[mol]
$r(n)$	Characteristic linear dimension of eddy from generation step n	[m]
R	Impeller radius	[m]
R	Ideal gas constant	[J K^{-1} mol^{-1}]
R_p	Search radius for particle in particle tracking algorithm	[m or pixels]
R_{u_i}	Autocorrelation function of velocity u'_i	[-]

Re	Reynolds number	[-]
Re_d	Droplet Reynolds number	[-]
Re_p	Particle Reynolds number	[-]
RF	GCMS calibration response factor	[-]
s_{err}	Combined axial and radial velocity error of solids in a phase-separated image	[m s^{-1}]
$\overline{s_{err}}$	Average of error s_{err} over all images in PIV data set	[m s^{-1}]
s_{ij}	Resolved scale strain rate tensor	[s^{-1}]
$\lvert s_{ij} \rvert$	Characteristic filtered strain rate	[s^{-1}]
S	Object area in an image frame	[pixels]
S	Dimensionless number in Zwietering correlation	[-]
Sc	Schmidt number	[-]
S_d	Shaft diameter	[mm]
St	Stokes' number	[-]
S^o	Entropy under standard-state conditions	[kJ mol^{-1} K^{-1}]
t	Time	[s]
t_b	Baffle thickness	[mm]
T	Vessel diameter	[mm]
T	Temperature	[K]
$T_{E,i}$	Macro-time scale	[s]
T_l	Trajectory length in particle tracking algorithm	[-]
T_1	Threshold to pick out Hough transform planes	[-]
T_2	Threshold to pick out Hough peaks	[-]

u	Radial velocity component	[m s^{-1}]
u_{err}	Radial velocity error of solids in a phase-separated image	[m s^{-1}]
u_i	Instantaneous fluid velocity in Cartesian direction i	[m s^{-1}]
$u_{i,p}$	Instantaneous particle velocity in Cartesian direction i	[m s^{-1}]
$\overline{u_i}$	Mean fluid velocity in Cartesian direction i	[m s^{-1}]
$u_{i,slip}$	Slip velocity in Cartesian direction i	[m s^{-1}]
u'	Characteristic turbulent fluid velocity	[m s^{-1}]
u'_i	Fluctuating fluid velocity in Cartesian direction i	[m s^{-1}]
$\tilde{u}_i$	rms fluid velocity in Cartesian direction i	[m s^{-1}]
u_s	Radial velocity of solids in solids-only image	[m s^{-1}]
$u_{s,sep}$	Radial velocity of solids in phase-separated solids image	[m s^{-1}]
u_t	Radial velocity of tracers in tracer-only image	[m s^{-1}]
$u_{t,sep}$	Radial velocity of tracers in phase-separated tracer image	[m s^{-1}]
u_η	Kolmogorov velocity scale	[m s^{-1}]
$u(l)$	Characteristic eddy velocity	[m s^{-1}]
v	Axial velocity component	[m s^{-1}]
v_{err}	Axial velocity error of solids in a phase-separated image	[m s^{-1}]
v_s	Axial velocity of solids in solids-only image	[m s^{-1}]
$v_{s,sep}$	Axial velocity of solids in phase-separated solids image	[m s^{-1}]
v_t	Axial velocity of tracers in tracer-only image	[m s^{-1}]
$v_{t,sep}$	Axial velocity of tracers in phase-separated tracer image	[m s^{-1}]
V	Vessel volume	[m^3]

V_{CV}	Volume occupied by control volume	[m^3]
V_{inj}	Injected feed volume in micromixing reactions	[m^3]
V_t	Total number of vectors in a given velocity field	[-]
V_{term}	Particle terminal velocity	[$m\ s^{-1}$]
V_{tip}	Blade tip speed	[$m\ s^{-1}$]
V_x	Number of vectors in x Cartesian direction	[-]
V_y	Number of vectors in y Cartesian direction	[-]
V_0	Initial tank volume in micromixing reactions	[m^3]
w	Tangential velocity component	[$m\ s^{-1}$]
w_b	Baffle width	[mm]
W	Blade width	[mm]
x	Axial Cartesian coordinate	[-]
x_i	Cartesian coordinate in direction i	[-]
x_{in}	Drop-in percentage of vectors after phase separation	[%]
x_{out}	Drop-out percentage of vectors after phase separation	[%]
X	Mass ratio of suspended solids ×100 in Zwietering correlation	[-]
X_i	Position in the image plane in direction i	[m]
X_S	Segregation index in Villermaux reaction scheme	[-]
$X_s\|_L$	Segregation index of pure liquid phase in Villermaux reaction scheme	[-]
$X_s\|_{LS}$	Segregation index of solid-liquid suspension in Villermaux reaction scheme	[-]
X_Q	Product distribution in Bourne reaction scheme	[-]
$X_Q\|_L$	Product distribution of pure liquid phase in Bourne reaction scheme	[-]

$X_Q\big\vert_{LS}$	Product distribution of solid-liquid suspension in Bourne reaction scheme	[-]
y	Radial Cartesian coordinate	[m]
Y	Yield of iodine under imperfect mixing conditions	[-]
Y_{TS}	Yield of iodine under totally segregated conditions	[-]
z	Tangential Cartesian coordinate	[m]

Greek symbols

α	Blade pitch angle	[°]
δ	Fringe spacing	[m]
δ_{ij}	Kronecker delta	[-]
Δ	Filter width in large eddy simulation analogy	[m]
Δr	Longitudinal separation between data pints	[m]
ΔT	Time between two PIV double-image frame exposures	[s]
Δ_{x_i}	Interval length between two points in x_i direction in Simpson's rule	[-]
ε	Turbulent kinetic energy dissipation rate	[$m^2 s^{-3}$]
$\overline{\varepsilon}$	Average turbulent kinetic energy dissipation rate	[$m^2 s^{-3}$]
$\overline{\varepsilon_{CV}}$	Average turbulent kinetic energy dissipation rate in control volume	[$m^2 s^{-3}$]
$\varepsilon_{\max}$	Maximum dissipation rate	[$m^2 s^{-3}$]
$\overline{\varepsilon_{SGS}}$	Reynolds averaged sub-grid scale dissipation rate	[$m^2 s^{-3}$]
ε_{353}	Molar extinction coefficient at 353 nm in the Beer-Lambert law	[$m^2 mol^{-1}$]
η	Kolmogorov length scale	[m]
θ	Angle or azimuthal direction in Polar coordinate system	[°]
κ	Wave number	[m^{-1}]
λ	Wavelength	[nm]

λ_{abs}	Fluorescent particle maximum absorption wavelength	[m]
λ_{fl}	Fluorescent particle maximum emission wavelength	[m]
Λ	Characteristic turbulent length scale	[m]
Λ_{u_i}	2-D integral length scale from autocorrelation of the velocity u_i	[m]
Λ_{u_i,x_j}	1-D integral length scale from autocorrelation of velocity u_i in direction x_j	[m]
μ	Absolute or dynamic viscosity	[Pa s]
ν	Kinematic viscosity	[$m^2 s^{-1}$]
ρ_l	Liquid density	[kg m^{-3}]
ρ_s	Solid particle density	[kg m^{-3}]
ρ_t	Tracer particle density	[kg m^{-3}]
σ	Number of discretized feed parts	[-]
τ_{ij}	Sub-grid scale stress tensor	[N m^{-2}]
$\tau(l)$	Characteristic eddy time scale	[s]
τ_p	Particle response time	[s]
τ_η	Kolmogorov time scale	[s]
ϕ	Ratio of local to average dissipation rate	[-]
ω_z	Vorticity z component	[s^{-1}]

Abbreviations

BPO	Dibenzoyl peroxide
CCD	Charge coupled device
CSD	Crystal size distribution
CFD	Computational fluid dynamics

DVB	Divinyl benzene	
ECA	Ethyl chloroacetate	
EtOH	Ethanol	
FEP	Fluorinated ethylene propylene	
FFT	Fast Fourier Transform	
FOV	Field of view	
FPIV	Fluorescent particle image velocimetry	
GCMS	Gas chromatography-mass spectrometry	
Hz	Hertz	$[s^{-1}]$
IA	Interrogation area	
kHz	kilohertz	$[s^{-1}]$
LDA/V	Laser Doppler anemometry/velocimetry	
LES	Large eddy simulation	
LIF	Laser induced fluorescence	
MI	Macro-instabilities	
Nd:YAG	Neodym-Yttrium-Aluminium Garnet	
NS	Navier-Stokes	
PBT	Pitched blade turbine	
PIV	Particle image velocimetry	
PS	Polystyrene	
PSD	Power spectral density	$[W\ Hz^{-1}]$
PTV	Particle tracking velocimetry	
PVA	Polyvinyl alcohol	
r.h.s	Right hand side	
rpm	Revolutions per minute	$[min^{-1}]$
RI	Refractive index	

RDT	Rushton disc turbine	
RO	Reverse osmosis	
SGS	Sub-grid scale	
SNR	Signal-to-noise	
TKE	Turbulent kinetic energy	$[m^2 s^{-2}]$
VTR	Video tape recording	
vol%	Volumetric concentration	[%]

References

Achenbach, E., **(1974)**, Vortex shedding from spheres, *J. Fluid Mech.,* **62**, 209-221.

Anselmet, F., Antonia, R. A. and Danaila, L., **(2001)**, Turbulent flows and intermittency in laboratory experiments, *Planetary and Space Science,* **49**, 1177-1191.

Atiemo-Obeng, V. A., Penney, W. R. and Armenante, P., **(2004)**, Solid-liquid mixing In: eds E. L. Paul, V. A. Atiemo-Obeng and S. M. Kresta, Handbook of industrial mixing: Science and practice*, John Wiley & Sons, Inc.,* New Jersey, 543-583.

Atsuhide, K., Yoshimichi, H. and Takuro, K., **(2007)**, PTV investigation of phase interaction in dispersed liquid-liquid two-phase turbulent swirling flow, *Exp. Fluids,* **42**(6), 871-880.

Awtrey, A. D. and Connick, R. E., **(1951)**, The absorption spectra of I_2, I_3^-, I^-, IO_3^-, S_4O_6 and $S_2O_3^-$. Heat of the reaction $I_3^-=I_2+I^-$, *J. Am. Chem. Soc.,* **73**(4), 1842-1843.

Bachalo, W. D., **(1994)**, Experimental methods in multiphase flows, *Int. J. Multiphase Flow,* **20**, 261-295.

Baldi, S., **(2004)**, Energy dissipation measurements in stirred vessels with Particle Image Velocimetry, *Ph.D Thesis,* King's College London, London, UK.

Baldi, S. and Yianneskis, M., **(2003)**, On the direct measurement of turbulence energy dissipation in stirred vessels with PIV, *Ind. Eng. Chem. Res.,* **42**, 7006-7016.

Baldi, S. and Yianneskis, M., **(2004)**, On the quantification of energy dissipation in the impeller stream of a stirred vessel from fluctuating velocity gradient measurements, *Chem. Eng. Sci.,* **49**, 2659-2671.

Baldyga, J. and Bourne, J. R., **(1989)**, Simplifications of micromixing calculations. I. Derivation and application of new model, *Chem. Eng. J.,* **42**, 83-92.

Baldyga, J. and Bourne, J. R., **(1990)**, The effect of micromixing on parallel reactions, *Chem. Eng. Sci.,* **45**(4), 907-916.

Baldyga, J. and Bourne, J. R., **(1999),** Turbulent mixing and chemical reactions*, John Wiley & Sons Ltd,* West Sussex, England.

Baldyga, J., Henczka, M. and Makowski, L., **(2001)**, Effects of mixing on parallel chemical reactions in a continuous-flow stirred tank reactor, *Chem. Eng. Res. Des.,* **79**(Part A), 895-900.

Barresi, A. A. **(1997)**, Experimental investigation of interaction between turbulent liquid flow and solid particles and its effects on fast reactions, *Chem. Eng. Sci.*, **52**(5), 807-814.

Barresi, A. A. **(2000)**, Selectivity of mixing-sensitive reactions in slurry systems, *Chem. Eng. Sci.*, **55**, 1929-1933.

Batchelor, G. K. and Green, J. T., **(1972)**, Determination of bulk stress in a suspension of spherical particles to order C-2, *J. Fluid Mech.,* **56**(DEC12), 401-427.

Batchelor, G. K. and Townsend, A. A., **(1949)**, The nature of turbulent motion at large wave-numbers, *Proc. R. Soc. London Ser. A-Mathematical and Physical Sciences,* **199**(1057), 238-255.

Bertrand, J. and Couderc, J. P., **(1985)**, Evaluation of the power consumption in agitation of viscous Newtonian or pseudoplastic liquids by two-bladed, anchor or gate agitators, *Chem. Eng. Res. Des.,* **63**(4), 259-263.

Bhattacharya, S. and Kresta, S. M., **(2004)**, Surface feed with minimum by-product formation for competitive reactions, *Chem. Eng. Res. Des.,* **82**(A9), 1153-1160.

Bittorf, K. J. and Kresta, S. M., **(2003)**, Prediction of cloud height for solid suspensions in stirred tanks, *Chem. Eng. Res. Des,* **81**(A5), 568-577.

Boedec, T. and Simoens, S., **(2001)**, Instantaneous and simultaneous planar velocity field measurements of two phases for turbulent mixing of high pressure sprays, *Exp. Fluids,* **31**(5), 506-518.

Bourne, J. R., **(2008)**, Comments on the iodide/iodate method for characterising micromixing, *Chem. Eng. J.,* **140**, 638-641.

Bourne, J. R. and Yu, S., **(1994)**, Investigation of micromixing in stirred tank reactors using parallel reactions, *Ind. Eng. Chem. Res.,* **33**, 41-55.

Bregains, J. C., Coleman, I. C., Ares, F. and Moreno, E., **(2004)**, Calculating directivities with the two-dimensional Simpson's rule, *IEEE Antennas and Propagation Magazine,* **46**(4), 106-112.

Brilman, D. W. F., Antink, R., van Swaaij, W. P. M. and Versteeg, G. F., **(1999)**, Experimental study of the effect of bubbles, drops and particles on the product distribution for a mixing sensitive, parallel-consecutive reaction system, *Chem. Eng. Sci*., **54**, 2325-2337.

Calabrese, R. V. and Stoots, C. M., **(1989)**, Flow in the impeller region of a stirred tank, *Chem. Eng. Prog.,* **85**(5), 43-50.

Chapple, D. and Kresta, S. M., **(1994)**, The effect of geometry on the stability of flow patterns in stirred tanks, *Chem. Eng. Sci.,* **49**(21), 3651-3660.

Chapple, D., Kresta, S. M., Wall, A. and Afacan, A., **(2002)**, The effect of impeller and tank geometry on power number for a pitched blade turbine, *Chem. Eng. Res. Des.,* **80**(A4), 364-372.

Chase, M. W., **(1998)**, *NIST-JANAF Themochemical Tables, Fourth Edition*, *J. Phys. Chem. Ref. Data, Monograph 9,* 1-1951.

Chen, R. C. and Fan, L. S., **(1992)**, Particle Image Velocimetry for characterizing the flow structure in three-dimensional gas-liquid-solid fluidized-beds, *Chem. Eng. Sci.,* **47**(13-14), 3615-3622.

Clark, R. A., Ferziger, J. H. and Reynolds, W. C., **(1979)**, Evaluation of subgrid-scale models using an accurately simulated turbulent flow, *J. Fluid Mech.,* **91**, 1-16.

Clements, P., Eagles, W. and Ozcan-Taskin, G., **(2006),** *Suspension of nanoparticle agglomerates in water-WP5,* Iterim technical note 5.3, BHR Group Ltd, Cranfield, Bedfordshire, UK.

Clift, R., Grace, J. R. and Weber, M. E., **(1978),** *Bubbles, Drops and Particles,* Academic Press, London.

Collicott, S. H., **(1992)**, Transition from particle image velocimetry to laser speckle velocimetry with increasing density, *Proceedings of the 6th International Symposium on Applied Laser techniques and fluid mechanics,* Instituto Superior Tecnico, Lisbon, Portugal.

Conway, B. E., **(1978)**, The Evaluation and Use of Properties of Individual Ions in Solution, *J. Solution Chem.,* **7**(10), 721-770.

Cooper, R. G. and Wolf, D., **(1968)**, Velocity profiles and pumping capacities for turbine type impellers, *Can. J. Chem. Eng.,* **46**, 94-100.

Crowe, C. T., Troutt, T. R. and Chung, J. N., **(1996)**, Numerical models for two-phase turbulent flows, *Ann. Rev. Fluid Mech.,* **28**, 11-43.

Cutter, L. A., **(1966)**, Flow and turbulence in a stirred tank, *AIChE J.,* **12**, 35-45.

Dantec Dynamics, **(2007)**, PIV principles, http://www.dantecdynamics.com/PIV/Princip/Index.html, Dantec Dynamics, 30-06-2007.

Delnoij, E., Westerweel, J., Deen, N. G., Kuipers, J. A. M. and Swaaij, W. P. M., **(1999)**, Ensemble correlation PIV applied to bubble plumes rising in a bubble column, *Chem. Eng. Sci.,* **54**(21), 5159-5171.

Derksen, J. J., **(2003)**, Numerical simulation of solids suspension in a stirred tank, *AIChE J.,* **49**(11), 2700-2714.

Derksen, J. J., Doelman, M. S. and Van den Akker, H. E. A., **(1999)**, Three-dimensional LDA measurements in the impeller region of a turbulently stirred tank, *Exp. Fluids,* **27**(6), 522-532.

Driscoll, K. D., Sick, V. and Gray, C., **(2003)**, Simultaneous air/fuel-phase PIV measurements in a dense fuel spray, *Exp. Fluids,* **35**(1), 112-115.

Ducci, A. and Yianneskis, M., **(2005)**, Direct determination of energy dissipation in stirred vessels with two-point LDA, *AIChE J.,* **51**(8), 2133-2148.

Eaton, J. K. and Fessler, J. R., **(1994)**, Preferential concentration of particles by turbulence, *Int. J. Multiphase Flow,* **20**, 169-209.

Eggels, J. G., Unger, F., Westerweel, J., Adrian, R. J., Friedrich, R. and Nieuwstadt, F. T. M., **(1994)**, Fully developed turbulent pipe flow: A comparison between direct numerical simulation and experiment, *J. Fluid Mech.,* **268**, 175.

Eigen, M. and DeMaeyer, L., **(1955)**, Untersuchungen uber die kinetic der neutralisation, *Z. Elektro Chem.,* **59**(10), 986-993.

Elghobashi, S. and Truesdell, G. C., **(1993)**, On the two-way intercation between homogeneous turbulence and dispersed solid particles. I: Turbulence modification, *Phys. Fluids A,* **5**(7), 1790-1801.

Eloranta, H., Honkanen, M. and Saarenrinne, P., **(2001)**, Measurements in two-phase flows with a combination of PIV and digital image processing techniques, *4th International symposium on particle image velocimetry,* Gottingen, Germany, 17-19 September.

Escudie, R., **(2001)**, Structure locale de l'Hydrodynamique generee par une Turbine Rushton, *Ph.D Thesis,* Institute National des Sciences Appliquees de Toulouse, Toulouse, France.

Escudie, R. and Line, A., **(2003)**, Experimental analysis of hydrodynamics in a radially agitated tank, *AIChE J.,* **49**(3), 585-603.

Fajardo, C. M., Smith, J. D. and Sick, V., **(2006)**, Sustained simultaneous high-speed imaging of scalar and velocity fields using a single laser, *Appl. Phys. B-Lasers and Optics,* **85**(1), 25-30.

Fan, J., Rao, Q., Wang, Y. and Fei, W., **(2004)**, Spatio-temporal analysis of macro-instability in a stirred vessel via digital particle image velocimetry (DPIV), *Chem. Eng. Sci.,* **59**, 1863-1873.

Ferrante, A. and Elghobashi, S., **(2003)**, On the physical mechanisms of two-way coupling in particle-laden isotropic turbulence, *Phys. Fluids,* **14**(2), 315-329.

Fournier, M. C., Falk, L. and Villermaux, J., **(1996)**, A new parallel competing reaction system for assessing micromixing efficiency - experimental approach, *Chem. Eng. Sci.,* **51**(22), 5053-5064.

Fukagata, A., Zahrai, S., Kondo, S. and Bark, F. H., **(2001)**, Anomolous velocity fluctuations in particulate turbulent channel flow, *Int. J. Multiphase Flow,* **27**, 701-719.

Gabriele, A., Nienow, A. W. and Simmons, M. J. H., **(2009)**, Use of angle-resolved PIV to estimate local specific energy dissipation rates for up- and down-pumping pitched blade agitators in a stirred tank, *Chem. Eng. Sci.,* **64**(1), 126-143.

Gimbun, J., **(2009)**, Scale-up of gas-liquid stirred tanks using coupled computational fluid dynamics and population balance modelling, *Ph.D Thesis,* Loughborough University, Loughborough, UK.

Gore, R. A. and Crowe, C. T., **(1989)**, Effect of particle size on modulating turbulent intensity, *Int. J. Multiphase Flow,* **15**(2), 279-285.

Gore, R. A. and Crowe, C. T., **(1991)**, Modulation of turbulence by a dispersed phase, *J. Fluids Eng. Trans. ASME,* **113**(2), 304-307.

Greensfelder, B. S. and Latimer, W. M., **(1931)**, The heat capacity and entropy of silver iodate from 16 to 300° absolute. The entropy of iodate ion. *J. Am. Chem. Soc.,* **53**(10), 3813-3817.

Grunefeld, G., Finke, H., Bartelheimer, J. and Kruger, S., **(2000)**, Probing the velocity fields of gas and liquid phase simultaneously in a two-phase flow, *Exp. Fluids,* **29**(4), 322-330.

Guichardon, P. and Falk, L., **(2000)**, Characterisation of micromixing efficiency by the iodide/iodate reaction system Part 1: experimental procedure, *Chem. Eng. Sci.,* **55**, 4233-4243.

Guichardon, P., Falk, L., Fournier, M. C. and Villermaux, J., **(1995)**, Study of micromixing in a liquid solid suspension in a stirred reactor, *A.I.Ch.E. Symp. Ser.* No. 305*,* **91**, 123-130.

Guichardon, P., Falk, L. and Villermaux, J., **(2000)**, Characterisation of micromixing efficiency by the iodide/iodate reaction system Part 2: Kinetic study, *Chem. Eng. Sci.,* **55**(19), 4245-4253.

Guido, P., Rojas, J. and Huelsz, G., **(2005)**, Simultaneous measurement of the solid and liquid phase velocities of flow in channels, *Ingenieria Hidraulica En Mexico,* **20**(3), 21-29.

Guillard, F., Tragardh, C. and Fuchs, L., **(2000)**, A study of turbulent mixing in a turbine-agitated tank using a fluorescence technique, *Exp. Fluids,* **28**, 225-235.

Guiraud, P., Costes, J. and Bertrand, J., **(1997)**, Local measurements of fluid and particle velocities in a stirred suspension, *Chem. Eng. J.,* **68**(2-3), 75-86.

Gunkel, A. A. and Weber, M. E., **(1975)**, Flow phenomena in stirred tanks. Part 1: The Impeller Stream, *AIChE J.,* **21**(5), 931-949.

Haam, S., Brodky, R. S. and Fasano, B., **(1992)**, Local heat transfer in a mixing reactor using the heat flux sensors, *Ind. Eng. Chem. Res.,* **31**, 1384-1391.

Hasal, P., Montes, J. L., Boisson, H. C. and Fort, I., **(2000)**, Macro-instabilities of velocity field in stirred vessel: detection and analysis, *Chem. Eng. Sci.,* **55**(2), 391-401.

Hasan, O. S., Alvarez, M. M., Muzzio, F. J. and Buettner, H. M., **(1999)**, Characterization of suspension flows using Particle Image Velocimetry (PIV), *AIChE Symposium series No 321,* **95**, 90-94.

Hassan, Y. A. and Canaan, R. E., **(1991)**, Full-field bubbly flow velocity measurements using a multiframe particle tracking technique, *Exp. Fluids,* **12**, 49-60.

Hassan, Y. A. and Philip, O. G., **(1997)**, A new artificial neural network tracking technique for Particle Image Velocimetry, *Exp. Fluids,* **23**(2), 145-154.

Hayward, A. T. J., **(1979)**, Flowmeters, *The Macmillan Press Ltd.*, London.

Hetsroni, G., **(1989)**, Particles-turbulence interaction, *Int. J. Multiphase Flow,* **15**(5), 735-746.

Hinze, J. O., **(1975),** Turbulence 2nd Edition, *McGraw-Hill,* New York.

Hishida, K., Sato, Y., Hanzawa, A. and Maeda, M., **(1995)**, Interactions between particle wake and turbulence in a water channel flow (PIV measurements and modelling for turbulence modification), *Proceedings of the 2nd International Conference on Multiphase Flow,* Kyoto, Japan, 4-7 April.

Hockey, R. M. and Nouri, J. M., **(1996)**, Turbulent flow in a baffled vessel stirred by a 60 degrees pitched blade impeller, *Chem. Eng. Sci.,* **51**(19), 4405-4421.

Huang, T. S., **(1981)**, Two-dimensional digital signal processing II*, Springer-Verlag,* Berlin.

Jarvis, S., **(2003)**, Premixed flame propagation and interaction with turbulent flow structures in a semic-confined combustion chamber, *Ph.D Thesis,* Loughborough University, Loughborough, UK.

Keane, R. D. and Adrian, R. J., **(1999a)**, Optimization of Particle Image Velocimeters with multiple pulsed systems, *Proceedings of the 5th International Symposium on Applications of Laser Techniques to Fluid Mechanics,* Lisbon, Portugal.

Keane, R. D. and Adrian, R. J., **(1990b)**, Optimization of Particle Image Velocimeters-1. Double Pulsed Systems, *Meas. Sci. Technol.,* **1**(11), 1202-1215.

Khalitov, D. A. and Longmire, E. K., **(2002)**, Simultaneous two-phase PIV by two-parameter phase discrimination, *Exp. Fluids,* **32**(2), 252-268.

Khan, F. R., **(2005)**, Investigation of turbulent flows and instabilities in a stirred vessel using Particle Image Velocimetry, *Ph.D Thesis,* Loughborough University, Loughborough, UK.

Khan, F. R., Rielly, C. D. and Brown, D. A. R., **(2006)**, Angle-resolved stereo-PIV measurements close to a down-pumping pitched blade turbine, *Chem. Eng. Sci.,* **61**(9), 2799-2806.

Khan, F. R., Rielly, C. D. and Hargrave, G. K., **(2004)**, A multi-block approach to obtain angle-resolved PIV measurements of the mean flow and turbulence fields in a stirred vessel, *Chem. Eng. Technol.*, **27**(3), 264-269.

Kiger, K. T. and Pan, C., **(2000)**, PIV technique for the simultaneous measurement of dilute two-phase flows, *J. Fluids Eng. Trans. ASME,* **122**(4), 811-818.

Kilander, J. and Rasmuson, A. C., **(2005)**, Energy dissipation and macro instabilities in a stirred square tank investigated using an LE PIV approach and LDA measurements, *Chem. Eng. Sci.,* **60**, 6844-6856.

Kosiwczuk, W., Cessou, A., Trinite, M. and Lecordier, B., **(2005)**, Simultaneous velocity field measurements in two-phase flows for turbulent mixing of sprays by means of two-phase PIV, *Exp. Fluids,* **39**(5), 895-908.

Kresta, S. M. and Wood, P. E., **(1991)**, Prediction of the three-dimensional turbulent flow in stirred tanks, *AIChE J.,* **37**(3), 448.

Kresta, S. M. and Wood, P. E., **(1993a)**, The mean flow field produced by a 45 degrees pitched blade turbine-Changes in the circulation pattern due to off bottom clearance, *Can. J. Chem. Eng.,* **71**(1), 42-53.

Kresta, S. M. and Wood, P. E., **(1993b)**, The flow field produced by a pitched blade turbine: characterization of the turbulence and estimation of the dissipation rate, *Chem. Eng. Sci.,* **48**, 1761-1774.

Laufhutte, H. D. and Mersmann, A. B., **(1985)**, Dissipation of power in stirred vessels, *Proceedings of the 5th European conference on mixing,* Wurzburg, West Germany, 10-12 June, 331-339.

Lee, K. C. and Yianneskis, M., **(1998)**, Turbulence properties of the impeller stream of a Rushton turbine, *AIChE J.,* **44**(1), 13-24.

Levy, Y. and Lockwood, F. C., **(1981)**, Velocity measurements in a particle laden turbulent free jet, *Combust. Flame,* **40**, 333-339.

Ljungqvist, M. And Rasmuson, A., **(2004)**, The two-phase flow in an axially stirred vessel investigated using phase-doppler anemometry, *Can. J. Chem. Eng.,* **82**, 275-288.

Lourenco, L. and Krothapalli, A., **(1986)**, The role of photographic parameters in laser speckle of particle image displacement velocimetry, *Exp. Fluids,* **5**(1), 29-32.

Lui, S., Meneveau, C. and Katz, J., **(1994)**, On the properties of similarity subgrid-scale models as deduced from measurements in a turbulence jet, *J. Fluid Mech.,* **275**, 83-119.

Lumley, J., **(1978)**, Computational modelling of turbulent flows, *Adv. Appl. Mech.,* **24**, 123-176.

Magelli, F., Fajner, D., Nocentini, M. and Pasquali, G., **(1990)**, Solid distribution in vessels stirred with multiple impellers, *Chem. Eng. Sci.,* **45**(3), 615-625.

Magelli, F., Fajner, D., Nocentini, M., Pasquali, G., Marisko, V. and Ditl, P., **(1991)**, Solids concentration distribution in slurry reactors stirred with multiple axial impellers, *Chem. Eng. Process.,* **29**(1), 27-33.

Mahouast, M., Cognet, G. and David, R., **(1989)**, Two-component LDV measurements in a stirred tank, *AIChE J.,* **35**(11), 1770-1778.

Mak, A. T. C., **(1992)**, Solid-liquid mixing in a mechanically agitated vessel, *Ph.D Thesis,* University College London.

Meneveau, C. and Sreenivasan, K. R., **(1991)**, The multifractal nature of turbulent energy dissipation, *J. Fluid Mech.,* **224**, 429-484.

Micheletti, M. and Yianneskis, M., **(2004)**, Study of fluid velocity characteristics in stirred solid-liquid suspensions with a refractive index matching technique, *P. I. Mech. Eng. E-J. Pro.,* **218**(4), 191-204.

Mittal, R., **(2000)**, Response of the sphere wake to freestream fluctuations, *Theor. Comp. Fluid Dyn.,* **13**, 397-419.

Montante, G. and Magelli, F., **(2007)**, Mixed solids distribution in stirred vessels: Experiments and computational fluid dynamics simulations, *Ind. Eng. Chem. Res.,* **46**, 2885-2891.

Montante, G., Micale, G., Magelli, F. and Brucato, A., **(2001)**, Experiments and CFD predictions of solid particle distribution in a vessel agitated with four pitched blade turbines, *Chem. Eng. Res. Des.,* **79**(A8), 1005-1010.

Montes, J. L., Boisson, H. C., Fort, I. and Jahoda, M., **(1997)**, Velocity field macro-instabilities in an axially agitated mixing reactor, *Chem. Eng. J.,* **67**, 139-145.

Myers, K. J., Ward, R. W. and Bakker, A., **(1997)**, A digital particle image velocimetry investigation of flow field instabilities of axial flow impeller, *J. Fluids Eng.,* **119**, 623-632.

Negi, A. S. and Anand, S. C., **(1985)**, A textbook of physical chemistry*, New Age International (P) Limited,* New Delhi, India, pp24.

Ng, K. and Yianneskis, M., **(2000)**, Observations on the distribution of energy dissipation in stirred vessels, *Chem. Eng. Res. Des.,* **78**(A3), 334-341.

Nienow, A. W. and Bartlett, R., **(1974)**, The measurement and prediction of particle-fluid slip velocities in agitated vessels, *Proceedings of the 1st European Conference on Mixing and Centrifugal Separation,* Cambridge, UK, 9-11 September, B1/1-15.

Nikiforaki, L., Montante, G., Lee, K. C. and Yianneskis, M., **(2003)**, On the origin, frequency and magnitude of macro-instabilities of the flows in stirred vessels, *Chem. Eng. Sci.,* **58**, 2937-2949.

Nocentini, M., Pinelli, D. and Magelli, F., **(2002)**, Dispersion coefficient and settling velocity of the solids in agitated slurry reactors stirred with multiple Rushton turbines, *Chem. Eng. Sci.,* **57**(11), 1877-1884.

Nolan, G. J. and Amis, E. S., **(1961)**, The rates of alkaline hydrolysis of ethyl aplha-haloacetates in pure and mixed solvents, *J. Phys. Chem.,* **65**(9), 1556.

Northrup, M. A., Kulp, T. J. and Angel, S. M., **(1991)**, Fluorescent Particle Image Velocimetry-Application to flow measurement in refractive index-matched porous-media, *Appl. Opt.,* **30**(21), 3034-3040.

Nouri, J. M. and Whitelaw, J. H., **(1992)**, Particle velocity characteristics of dilute to moderately dense suspension flows in stirred reactors, *Int. J. Multiphase Flow,* **18**(1), 21-33.

Owen, P. R., **(1969)**, Pneumatic transport, *J. Fluid Mech.,* **39**, 407-432.

Pahuja, S. and Longmire, E. K., **(1995)**, *Simultaneous two-phase PIV measurements in particle-laden jet flow,* Report 1995-3, Dept of Aerospace Engineering and Mechanics, University of Minnesota, Minneapolis, Minnesota.

Palmer, D. A. and Lietzke, M. H., **(1982)**, The equilibria and kinetics of iodine hydrolysis, *Radiochimica Acta,* **31**(1-2), 37-44.

Palmer, D. A., Ramette, R. W. and Mesmer, R. E., **(1984)**, Triiodide ion formation equilibrium and activity coefficients in aqueous solution, *J. Solution Chem.,* **13**(9), 673-683.

Papadopoulos, G. and Arik, E. B., **(2004)**, Scope of fundamental flow measurement techniques In: eds E. L. Paul, V. A. Atiemo-Obeng and S. M. Kresta, Handbook of industrial mixing: Science and practice*, John Wiley & Sons, Inc., New Jersey,* 202-206.

Papadopoulos, G. and Guillard, F., **(2003)**, Image-based diagnostics for flow field characterization, *11th International conference on computational methods & experimental measurements,* Halkidiki, Greece, 12-14 May.

Pastor, M., **(2007)**, Simple Particle Tracking, *Private Communication,* Laboratorio de Medios Granulares, Departamento de Fisica y Matematica Aplicada, Universidad de Navarra, Spain.

Pettersson, M. and Rasmuson, A. C., **(1997)**, Application of three-dimensional phase-Doppler anemometry to mechanically agitated crystallizers, *Chem. Eng. Res. Des.,* **75**(A2), 132-141.

Pinelli, D., Nocentini, M. and Magelli, F., **(1996)**, Modelling of the solid distribution in slurry reactors stirred with multiple impellers: influence of suspension characteristics, *Proceedings of CHISA'96, paper D1.2 [515],* Praha, 25-30 August.

Pope, S. B., **(2000)**, Turbulent flows*, Cambridge University Press,* Cambridge.

Press, W. H., Teukolsky, S. A., Vetterling, W. T. and Flannery, B. P., **(1992)**, Fortran numerical recipes 2nd Edition, *Cambridge University Press,* Cambridge.

Raffel, M., Willert, C. E., Wereley, S. T., Kompenhans, J., **(2007)**, Particle Image Velocimetry: A Practical Guide 2nd Edition, *Springer*, Berlin.

Ranade, V. V. and Joshi, J. B., **(1989)**, Flow generated by pitched blade turbines. 1. Measurements using laser Doppler anemometer, *Chem. Eng. Commun.,* **81**, 197-224.

Randall, R. B., **(1977)**, Application of B & K equipment to frequency analysis*, Bruel Kjaer,* Naerum, Denmark.

Rockwood, A. L., **(1987)**, Absolute half-cell entropy, Phys. Rev. A 36, 1525 - 1526 (1987), *Phys. Rev. A,* **36**, 1525-1526.

Rottenkolber, G., Gindele, J., Raposo, J., Dullenkopf, K., Hentschel, W., Wittig, S., Spicher, U. and Merzkirch, W., **(2002)**, Spray analysis of a gasoline direct injector by means of two-phase PIV, *Exp. Fluids,* **32**(6), 710-721.

Ruasse, M. F., Aubard, J., Galland, B. and Adenier, A., **(1986)**, Kinetic study of the fast halogen-trihalide ion equilibria in protic media by the Raman-laser temperature jump technique. A non diffusion-controlled ion-molecule reaction. *J. Phys. Chem.,* **90**(8), 4382-4388.

Saarenrinne, P., Piirto, M. and Eloranta, H., **(2001)**, Experiences of turbulence measurement with PIV, *Meas. Sci. Technol.,* **12**(11), 1904-1910.

Sakamoto, H. and Haniu, H., **(1990)**, A study on vortex shedding from spheres in a uniform flow, *ASME J. Fluids Eng.,* **112**, 386-392.

Scargiali, F., D'Orazio, A., Grisafi, F. and Brucato, A., **(2007)**, Modelling and simulation of gas–liquid hydrodynamics in mechanically stirred tanks, *Chem. Eng. Res. Des.*, **85**, 637–646.

Schafer, M., Yianneskis, M., Wachter, P. and Durst, F., **(1998)**, Trailing vortices around a 45 degrees pitched blade impeller, *AIChE J.,* **44**(6), 1233-1246.

Seol, D. G., Bhaumik, T., Bergmann, C. and Socolofsky, S. A., **(2007)**, Particle Image Velocimetry measurements of the mean flow characteristics in a bubble plume, *J. Eng. Mech-ASCE,* **33**(6), 665-676.

Sharp, K. V. and Adrian, R. J., **(2001)**, PIV study of small-scale flow structure around a Rushton turbine, *AIChE J.,* **47**(4), 766-778.

Sheng, J., Meng, H. and Fox, R. O., **(2000)**, A large eddy PIV method for turbulence dissipation rate estimation, *Chem. Eng. Sci.,* **55**(20), 4423-4434.

Smagorinsky, J., **(1963)**, General circulation experiments with the primitive equation I the basic experiment, *Monthly Weather Review,* **91**, 99-164.

Stanislas, M. and Monnier, J. C., **(1997)**, Practical aspects of image recording in Particle Image Velocimetry, *Meas. Sci. Technol.,* **8**(12), 1417-1426.

Stephenson, R. and Stuart, J., **(1986)**, Mutual binary solubilities: water-alcohol and water-esters, *J. Chem. Eng. Data,* **51**, 56-70.

Stern, J. H. and Passchier, A. A., **(1962)**, The heats of formation of triiodide and iodate ions, *J. Phys. Chem.,* **66**(4), 752-753.

Stoots, C. M. and Calabrese, R. V., **(1995)**, Mean velocity field relative to a Rushton turbine blade, *AIChE J.,* **41**(1), 1-11.

Sugioka, K. and Komori, S., **(2005)**, Drag and lift forces acting on a spherical droplet in homogeneous shear flow (in Japanese), *Trans JSME,* **71**(B), 7-14.

Tilton, J. N., **(1997)**, Fluid and Particle Dynamics In: eds R. H. Perry and D. W. Green, Perry's Chemical Engineer's Handbook 7th Edition, *McGraw-Hill,* New York, 50-51.

Togatorop, A., **(1995)**, Computational fluid mixing in stirred vessels, *Ph.D Thesis,* UMIST, UK.

Tsuji, Y. and Morikawa, Y., **(1982)**, LDV measurements of an air-solid two-phase flow in a horizontal pipe, *J. Fluid Mech.,* **120**, 385-409.

Tsuji, Y., Morikawa, Y. and Shiomi, H., **(1984)**, LDV measurements of an air-solid two-phase flow in a vertical pipe, *J. Fluid Mech.,* **139**(FEB), 417-434.

Tsuji, Y., Morikawa, Y., Tanaka, T. and Karimine, K., **(1988)**, Measurement of an axisymmetric jet laden with coarse particles, *Int. J. Multiphase Flow,* **14**(5), 565-574.

Van't Riet, K. and Smith, J. M., **(1975)**, Trailing vortex system produced by Rushton turbine agitators, *Chem. Eng. Sci*., **30**(9), 1093-1105.

Virdung, T. and Rasmuson, A. C., **(2003)**, PIV measurements of solid-liquid mixing at elevated concentrations, *11th European Conference on Mixing, 637th event of the European Federation of Chemical Engineering,* Bamberg, Germany, 14-17 October.

Virdung, T. and Rasmuson, A. C., **(2007a)**, Hydrodynamic properties of a turbulent confined solid-liquid jet evaluated using PIV and CFD, *Chem. Eng. Sci.,* **62**, 5963-5978.

Virdung, T. and Rasmuson, A. C., **(2007b)**, Measurements of continuous phase velocities in solid-liquid flow at elevated concentrations in a stirred vessel using LDV, *Chem. Eng. Res. Des.,* **85**(A2), 193-200.

Virdung, T. and Rasmuson, A. C., **(2008)**, Solid-liquid flow at dilute concentrations in an axially stirred vessel investigated using particle image velocimetry, *Chem. Eng. Commun.,* **195**(1), 18-34.

Westerweel, J., Dabiri, D. and Gharib, M., **(1997)**, The effect of a discrete window offset on the accuracy of cross-correlation analysis of digital PIV recordings, *Exp. Fluids,* **23**(1), 20-28.

Winardi, S. and Nagase, Y., **(1991)**, Unstable phenomenon of flow in a mixing reactor with a marine propeller, *J. Chem. Eng. Jpn.,* **24**, 243-249.

Wolf, D. and Manning, F. S., **(1966)**, Impact tube measurement of flow patterns, velocity profiles and pumping capacities in stirred vessels, *Can. J. Chem. Eng.*, **44**, 137-142.

Wolff, M., Delconte, A., Schmidt, F., Gucher, P. and Lemoine, F., **(2007)**, High-pressure Diesel spray temperature measurements using two-colour laser-induced fluorescence, *Meas. Sci. Technol.,* **18**, 697-706.

Wu, H. and Patterson, G. K., (1989), Laser-Doppler measurements of turbulent-flow parameters in a stirred mixer, Chem. Eng. Sci., 44(10), 2207-2221.

Wu, H., Patterson, G. K. and Vandoorn, M., **(1989)**, Distribution of turbulence energy dissipation rates in a Rushton turbine stirred mixer, Exp. Fluids, 8(3-4), 153-160.

Xie, L., Rielly, C. D., Eagles, W., Özcan-Taskin, G., **(2007)**, Dispersion of nano-particle clusters using mixed flow and high shear impellers in stirred tanks, *Chem. Eng. Res. Des.*, **85**(A5), 676-684.

Xie, L., Rielly, C. D., Özcan-Taskin, G., **(2008)**, Break-Up of Nanoparticle Agglomerates by Hydrodynamically Limited Processes, *J. Disper. Sci. Technol.*, **29**(4), 573-589.

Yeh, Y. and Cummins, H. Z., **(1964)**, Localized fluid flow measurements with an He-Ne laser spectrometer 1 (E), *Appl. Phys. Lett.,* **4**(10), 176-178.

Yianneskis, M., Popiolek, Z. and Whitelaw, J. H., **(1987)**, An experimental study of the steady and unsteady flow characteristics of stirred reactors, *J. Fluid Mech.,* **175**, 537-555.

Yianneskis, M. and Whitelaw, J. H., **(1993)**, On the structure of the trailing vortices around Rushton turbine blades, *Chem. Eng. Res. Des.,* **71**(A5), 534-550.

Yu, S., **(1993)**, Micromixing and parallel reactions, *Ph.D Thesis,* ETH Zurich.

Zachos, A., Kaiser, M. and Merzkirch, W., **(1996)**, PIV measurements in multiphase flow with nominally high concentration of the solid phase, *Exp. Fluids,* **20**(3), 229-231.

Zhou, G. and Kresta, S. M., **(1996)**, Impact of tank geometry on the maximum turbulence energy dissipation rate for impellers, *AIChE J.,* **42**(9), 2476-2490.

Zhou, G. and Kresta, S. M., **(1998)**, Correlation of mean drop size and minimum drop size with the turbulence energy dissipation and the flow in an agitated tank, *Chem. Eng. Sci.,* **53**(11), 2063-2079.

Zwietering, T. N., **(1958)**, Suspending of solid particles in liquid by agitators, *Chem. Eng. Sci.,* **8**(3-4), 244-253.